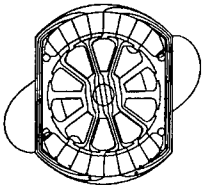
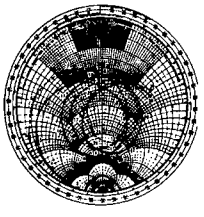
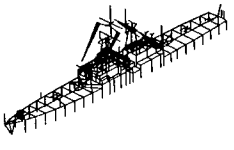
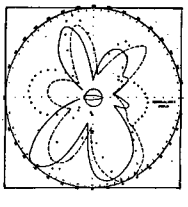
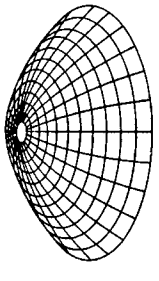
DISTRIBUTION STATEMENT A
Approved for Public Release
Distribution Unlimited











16th Annual Review of Progress in

APPLIED

COMPUTATIONAL

ELECTROMAGNETICS

at the

Naval Postgraduate School

Monterey, CA

March 20-24, 2000

CONFERENCE PROCEEDINGS

20000731 017

CONFERENCE PROCEEDINGS

VOLUME II

16th Annual Review of Progress in

APPLIED

COMPUTATIONAL

ELECTROMAGNETICS

at the

Naval Postgraduate School

Monterey, CA

March 20-24, 2000

TECHNICAL PROGRAM CHAIRMAN

Douglas Werner

Sponsored by

The Applied Computational Electromagnetics Society,

Naval Postgraduate School, Penn State University,
Utah State University, University of Wisconsin-Madison,
Michigan State University, Southwest Research Institute

DTIC QUALITY INSPECTED 3

Table of Contents i

2001 Call for Papers xii

2000 Symposium Program Committee xiv

Technical Program Chairman's Statement xv

ACES President's Statement xvi

ACES 2000 Short Courses xvii

Agenda xix

PLENARY SESSION I

"Efficient Extraction of S-parameters of Transmission Line Discontinuities for RF and Wireless Circuit Design", Raj Mittra 2

SESSION 1: FINITE ELEMENT METHODS Chairs: Jianming Jin and Peter Monk

"Transient Electromagnetic Scattering from Curved Dielectric/lossy 3D Bodies Using Covariant Projection Elements",
R. Ordovas, S.P. Walker and M.J. Bluck 4

"Towards an *hp*-adaptive Finite Element Method for Full-Wave Analysis of Waveguides"
L. Vardapetyan and L. Demkowicz 11

"An *hp*-Adaptive Finite Element Method for Maxwell's Equations"
L. Demkowicz 19

"Finite Element Method for Designing Plasma Reactors"
Leo Kempel, Paul Rummel, Tim Grotjohn and John Amrhein 28

"Finite-Element Domain Decomposition Through an Iterative Algorithm: Coupling Between Cavity-Backed Slots"
Anastasis C. Polycarpou and Constantine A. Balanis 35

"Investigation of the Bunting/Davis Functional When Used with Vector Finite Elements for Waveguide Analysis", Andrew F. Peterson and Sharib Wasi 43

"Numerical Methods for High Frequency Problems"
T. Huttunen and P. Monk 49

SESSION 2: OPTIMIZATION IN ELECTROMAGNETICS Chairs: Eric Michielssen and Dan Weile

"Design of Dual Band Frequency Selective Surfaces Using Genetic Algorithms"
A. Monorchio, R. Mittra, and G. Manara 56

"A Study of Cauchy and Gaussian Mutation Operators in the Evolutionary Programming Optimization of Antenna Structures"
Ahmad Hoorfar and Yuan Liu 63

"A Statistical Intercomparison of Binary and Decimal Genetic Algorithms""
Yee Hui Lee, Stuart J. Porter and Andrew C. Marvin 70

"The Compact Genetic Algorithm: A Litmus Test for Genetic Algorithm Applicability"
Daniel S. Weile, Eric Michielssen and David E. Goldberg 78

"Dipole Equivalent Circuit Optimization Using Genetic Algorithm"
Bruce Long, Ping Werner, and Doug Werner 86

"Computing the Electromagnetic Field in a Perturbed Configuration Using Modified" Reduced-Order Models"
R.F. Remis and P.M. van den Berg 93

"Some Further Results from FARS: Far-Field Analysis of Radiation Sources"
Edmund K. Miller 99

SESSION 3: NUMERICAL TECHNIQUES FOR PACKAGING AND INTERCONNECTS
Chairs: Omar Ramahi and Andreas C. Cangellaris

"A New Methodology for the Direct Generation of Closed-Form Electrostatic Green's Functions in Layered Dielectrics"
Andreas C. Cangellaris 108

"The Treatment of Narrow Microstrips and PCB Tracks in the FDTD Method Using Empirically Modified Coefficients", Chris J. Railton 115

"Time-Domain-Analysis of QTEM Wave Propagation and Crosstalk on Lossy Multiconductor Transmission Lines with Terminal Coupling"
Georg Mueller, Jan Wendel, and Karl Reiss 123

"An MPIE-Based Circuit Extraction Technique and its Applications on Power Bus Modeling in High-Speed Digital Designs"
Kim Fan, Hao Shi, James L. Knighten, and James L. Drewniak 130

"Non-Resonant Electromagnetic Simulation of Some Resonant Planar Circuits"
Yuriy O. Shlepnev 138

"FDTD Analysis of Conventional and Novel Delay Lines",
Omar M. Ramahi 146

"Complementary Operators for Frequency-Domain Methods: A Single Simulation Implementation", Omar M. Ramahi 152

SESSION 4: STUDENT PAPER COMPETITION Chair: Perry Wheless

"Systematic Studies in Annular Ring PBG Structures"
Todd M. Lammers, Shawn W. Staker, and Melinda Piket-May 160

"Fast Electromagnetic Analysis Using the Asymptotic Waveform Evaluation Method"
Dan Jiao and Jianming Jin 166

"A Domain-Decomposition/Reciprocity Technique for the Analysis of Arbitrarily-Shaped Microstrip Antennas with Dielectric Substrates and Superstrates Mounted on Circularly-Cylindrical Platforms"
R.J. Allard, D.H. Werner, and J.S. Zmyslo 173

"A New FDTD Scheme to Model Chiral Media"
A. Akyurtlu, D.H. Werner, and K. Aydin 181

"T-Matrix Computer Code Applied to Electromagnetic Field Penetration in Magnetic Resonance Imaging"
Rafael R. Canales, Luis F. Fonseca, Fredy R. Zypman 189

SESSION 5: INTERACTIVE POSTER SESSION

"Characteristics of Silicon Photoconductivity Under Near-Infrared Illumination"
Preston P. Young, Robert Magnusson, and Tim R. Holzheimer 198

"Characteristics of Fractal Antennas", Haruo Kawakami, Yasushi Ojiro, Yasushi Lizuka, Satoshi Kogiso and Gentei Sato 206

"Feigenbaum Encryption of Computer Codes"
R.M. Bevensee 214

"Extension of SuperNEC to Calculate Characteristic Modes", Thomas Abbott 221

"Review of Basic 3-D Geometry Considerations for Intelligent CEM Pre-Processor Applications", Kurt V. Sunderland 226

"Modelling of Loaded Wire Conductor Above Perfectly Conducting Ground by Using 3D TLM Method"
Nebojsa S. Doncov, Bratislav D. Milovanovic, and Vladica M. Trenkic 233

"Evanescent Tunneling and Quantile Motion of Electromagnetic Waves in Wave Guides of Varying Cross Section", E. Gjonaj 241

"A Modal Approach for the Calculation of Scattering Parameters in Lossfree and Lossy Structures Using the FI-Technique"
Rolf Schuhmann, Peter Hammes, Stefan Setzer, Bernd Trapp, Thomas Weiland 247

"A Modular Technique for the Calculation of Wave Guide Structures"
Johannes Borkes, Adalbert Beyer, and Oliver Pertz 255

SESSION 5: INTERACTIVE POSTER SESSION (cont)

"Wave Propagation Through 2D Clusters of Coupled Cylindrical Resonators"
Ross A. Speciale 263

"Design Software for Cylindrical Helix Antennas"
M. Slater and C.W. Trueman STUDENT PAPER COMPETITION 281

"The Analysis of a Center-Fed Helical Microstrip Antenna Mounted on a Dielectric-Coated Circular Cylinder Using the Reciprocity Theroem"
R.A. Martin and D.H. Werner 286

"Near to Far Field Transformation for a FDTD BOR with PML ABC and Sub-Grid Capability"
Vicente Rodriguez-Pereyra, Atef Z. Elsherbeni, and Charles E. Smith 294

"~~Computer Simulation of Radar Images of PEC Models of Complicated Objects~~"
~~Nickolai Zh. Kolev~~ PAPER WITHDRAWN - PAGES 302 THROUGH 307 ..... ~~302~~

PLENARY SPEAKER II

"Design on Computer - A Coming of Age Tom Cwik 308

SESSION 6: COMPUTATIONAL BIO-ELECTROMAGNETICS Chairs: Ray Luebbers and Susan Hagness

"Numerical Investigation of Two Confocal Microwave Imaging Systems for Breast Tumor Detection"
Susan C. Hagness, Xu Li, Elise C. Fear, and Maria A. Stuchly 310

"FDTD Studies on SAR in Biological Cells Exposed to 837 and 1900 MHz in a TEM Cell"
A.W. Guy 317

"Modelling of Personnel Electromagnetic Radiation Hazards", Alan Nott 325

"Modeling Interference Between Very Low Frequency Electromagnetic Fields and Implanted Cardiac Pacemakers"
Trevor W. Dawson and Maria A. Stuchly 333

"Using Computational Electromagnetics to Solve an Occupational Health and Safety Incident"
Timothy Priest, Kevin Goldsmith, and Dean DuRieu 341

"Analysis of Permanent Magnet Type of MRI Taking Account of Hysteresis and Eddy Current and Experimental Verification", Norio Takahashi, Siti Zubaidah, Takeshi Kayano, Koji Miyata and Ken Ohashi 349

SESSION 7: VIRTUAL REALITY IN REAL WORLD APPLICATIONS Chairs: Stan Kubina and Dennis DeCarlo

"A Virtual Radiation Pattern Range and Its Uses - C-130/Hercules HF Notch Antenna"
Stanley J. Kubina, Christopher W. Trueman, and David Gaudine 356

"HP Towel-Bar Antenna Location Study Aboard an H-3 Sikorsky Helicopter"
Saad N. Tabet, Carl D. Myers, and Dennis DeCarlo 365

"Improving Model Confidence through Metamorphosis"
Douglas R. Munn and C.W. Trueman 373

"Model Morphing for Insight into the HF Assessment Parameters"
Douglas R. Munn and C.W. Trueman 381

"3D Modeling of Complex Helicopter Structures: Predictions and Measurements"
Anastasis C. Polycarpou, Dong-Ho Han, Stavros V. Georgakopoulos,
Constantine Balanis 387

"Increasing the Productivity of NEC Analysis with Virtual Reality and 3D Laser Scanners"
Kevin J. Cybert and Daniel D. Reuster 395

"An Interactive HTML Based Multimedia Course on Antennas"
Ulrich Tuerk and Peter Russer 401

SESSION 8: EMC Chairs: Bruce Archambeault and Jim Drewniak

"Adding Imperfections to EMC FDTD Models as a Means of Increasing Accuracy"
Colin E. Brench 410

"Power Conversion Techniques for Portable EMI Sensitive Applications"
Reinaldo Perez 416

"Using the Partial Element Equivalent Circuit (PEEC) Simulation Technique to Properly
Analyze Power/Ground Plane EMI Decoupling Performance"
Bruce Archambeault 423

"EMI Model Validation and Standard Challenge Problems"
Bruce Archambeault and James L. Drewniak 431

"Modeling EMI Resulting from a Signal Via Transition Through Power/Ground Layers"
Wei Cui, Xiaoning Ye, Bruce Archambeault, Doug White, James Drewniak 436

"Techniques for Optimizing FEM/MoM Codes"
Y. Ji, T.H. Hubing, and H. Wang 444

"Numerical Modeling of Shielding by a Wire Mesh Box"
Gerald J. Burke and David J. Steich 452

SESSION 9: PROPAGATION Chairs: Steve Fast and Frank Ryan

"A Fast Quasi Three-Dimensional Propagation Model for Urban Microcells"
Joseph W. Schuster and Raymond J. Luebbers 462

"FDTD Techniques for Evaluating the Accuracy of Ray-Tracing Propagation Models for Microcells"
Joseph W. Schuster and Raymond J. Luebbers 470

"A Building Database Features Pre-Processor for 3D SBR/GTD Urban EM Propagation Models"
James Pickelsimer and Raymond Luebbers 477

"Toward a New Model for Indoor and Urban Propagation Using Percolation Theory"
G. Franceschetti, S. Marano, N. Pasquino, and I.M. Pinto 485

"Ray Tracing Algorithm for Indoor Propagation"
C.W. Trueman, R. Paknys, J. Zhao, D. Davis, and B. Segal 493

"Modeling Large and Small-Scale Fading on the DPSK Datalink Channel Using a GTD Ray-Tracing Model"
Kent Chamberlin, Mikhailo Seledtsov, and Petar Horvatic 501

"Rough Surface Forward Scatter in the Parabolic Wave Equation Model"
Frank Ryan 507

"A Comparison of Electromagnetic Parabolic Equation Propagation Models Used by the U.S. Navy to Predict Radar Performance"
Donald de Forest Boyer and Huong Pham 515

AUTHOR INDEX 523

SESSION 10: WAVELET AND TLM MODELING TECHNIQUES
Chairs: Wolfgang J.R. Hoefer and Peter Russer

"The Implementation of a High Level (1st-order) Haar Wavelet MRTD Scheme"
Enqiu Hu, Poman P.M. So, Masafumi Fujii, Wei Liu, and Wolfgang J.R. Hoefer 526

"Multi-Resolution Based TLM Technique Using Haar Wavelets"
Ismael Barba, Jose Represa, Masafumi Fujii, and Wolfgang J.R. Hoefer 534

"Formulation and Study of an Arbitrary Order Haar Wavelet Based Multi-resolution Time Domain Technique"
Costas D. Sarris and Linda P.B. Katehi 540

"Computational Optimization of MRTD Haar-Based Adaptive Schemes Used for the Design of RF Packaging Structures", Manos M. Tentzeris 548

"Time-Domain Simulation of Electromagnetic Wave Propagation in a Magnetized Plasma"
J. Paul, C. Christopoulos, and D.W.P. Thomas 556

SESSION 10: WAVELET AND TLM MODELING TECHNIQUES (cont)

"TLM Simulation of Patch Antenna on Magnetized Ferrite Substrate"
M.I. Sobhy, M.W.R. Ng, R.J. Langley, and J.C. Batchelor 562

"On the Practical Use of Layered Absorbers for the Simulation of Planar Microwave Circuits Using the SCN-TLM Method"
Juergen Rebel, Tobias Mangold and Peter Russer 570

"A Numerical Study of MEMS Capacitive Switches Using TLM"
Fabio Coccetti, Larissa Vietzorreck, Vitali Chtchekatourov, and Peter Russer 580

"Thin Wire Modeling with the TLMIE-Method"
S. Lindenmeier, C. Christopoulos, and P. Russer 587

"What Determines the Speed of Time-Discrete Algorithms?"
Tobias Mangold, Jurgen Rebel, Wolfgang J.R. Hoefer, Poman P.M. So, and Peter Russer 594

SESSION 11: TIME DOMAIN METHODS Chairs: Amelia Rubio Bretones and R. Gomez Martin

"Introducing a New Time-Domain Electromagnetic Field Solver LSFEM ™ TD-3D"
Craig C. Ouyang, B.N. Jiang, and Nina Liao 604

"Characteristic-Based Time-Domain Method for Antenna Analysis"
Dan Jiao, Jianming Jin and J.S. Shang 611

"Modeling of Thin-Wire Structures by Solving the EFIE in Time Domain"
Friedrich Schunn and Hermann Singer 619

"Time-Domain Analysis of Thin-Wire Loaded Antennas Using Integral Equations"
M. Fernandez Pantoja, A. Rubio Bretones, and R. Gomez Martin 627

"Haar MRTD Wave Propagation Through Isotropic Plasmas"
Ismael Barba, Jose Represa, Masafumi Fujii, and Wolfgang J.R. Hoefer 635

"Time-Domain Scattering from arbitrarily Shaped Metallic Shelters with Apertures: Numerical and Experimental Analysis"
Giuliano Manara and Agostino Monorchio 640

"Integral Equation Based Analysis of Transient Electromagnetic Scattering From Three Dimensional Inhomogeneous Dielectric Objects"
N.T. Gres, A.A. Ergin, B. Shanker, and E. Michielssen 647

"Computational Properties of Wavelet Based PEEC Analysis in Time Domain"
G. Antonini and A. Orlandi 654

"Time Domain Modeling of a Pulsed Horn-Dish Antenna"
M.J. Bluck, S.P. Walker and C. Thomas 662

PLENARY SPEAKER III

"Fast Solvers for Electromagnetic Simulations - A New Age Analysis Tool"
W.C. Chew 668

SESSION 12: MOMENT METHODS Chairs: Zachi Baharav and Ramakrishna Janaswamy

"Iterative Solvers for Dense Matrices - Application to Moment Method Matrices"
Juergen v. Hagen and Werner Wiesbeck 670

"Convergence Properties of the CFIE for Several Conducting Scatterers"
William Wood Jr., Kueichien Hill, William Kent, Robert Layden & Lisa Cravens 677

"Modeling of General Surface Junctions of Composite Objects in an SIE/MoM Formulation"
Joon Shin, Allen W. Glisson, and Ahmed A. Kishk 683

"A Novel Grid-Robust Higher-Order Vector Basis Function for the Method of Moments"
G. Kang, J.M. Song, W.C. Chew, K. Donepudi, and J.M. Jin 691

"Analytical Treatment of Green's Functions Singularities in Microstrip Structures"
E. Jimenez, F.J. Cabrera, J.G. Cuevas del Rio 699

~~"A Two-Stage Numerical Procedure for Extraction of Surface Wave Poles for Multilayered Media"~~
~~Ya-Xun Liu, Le-Wei Li, Tat-Soon Yeo, Pand-Shyan Kooi, and Mook-Seng Leong ..... 707~~
PAPER WITHDRAWN - PAGES 707 THROUGH 715

"Higher-Order Electromagnetic Modeling of Multilayer Microstrip Structures"
Feng Ling, Kalyan Donepudi, and Jianming Jin 716

SESSION 13: CONFORMAL ANTENNAS Chairs: Leo Kempel and Douglas Werner

"A Conformal, Flexible, Multifunction Communications Antenna"
T.R. Holzheimer 726

"Finite Printed Antenna Array Modeling Using an Adaptive Multi-Resolution Approach"
Lars S. Anderson, Yunus E. Erdemli, and John L. Volakis 734

"A Technique for Analyzing Radiation from Conformal Antennas Mounted on Arbitrarily-Shaped Conducting Bodies"
Dean Arakaki, Douglas H. Werner, and Raj Mittra 742

"Using Computational Electromagnetics and Monte-Carlo Methods to Locate Antennas on Aircraft"
Kevin Goldsmith, Paul Johnson, and Timothy Priest 750

"Coupling Phenomena in Horizontal and Vertical Polarized Aperture Coupled Patch Antennas on Cylindrical Surfaces"
D. Loffler, J. von Hagen, and W. Wiesbeck 758

SESSION 13: CONFORMAL ANTENNAS (cont)

"Modeling and Analysis of Wideband Conformal Antennas"
Keith D. Trott, Rene D. Guidry, and Leo C. Kempel 765

"Curvature Effects on a Conformal Log-Periodic Antenna"
Charles Macon, Leo Kempel, Keith Trott, and Stephen Schneider 772

SESSION 14: ANTENNA ARRAYS Chairs: Keith Lysiak and Nathan Cohen

"Problems of Characterising Array Manifolds for Naval Platform in HF Environments"
Linda Holtby 780

"Designing A VHF Wrap-Around DF Antenna Array Using NEC", Keith Lysiak 790

"Specifying A Direction Finding Antenna with Examples"
T.R. Holzheimer 798

"A High Efficiency Broad Band Wire Antenna System "
Kevin J. Cybert and Daniel D. Reuster 806

"Comparison of Calculations and Measurements of an Electronically Scanned Circular Array"
James M. Stamm, Michael W. Jacobs, and James K. Breakall 814

"Array Sidelobe Reduction by Small Position Offsets of Fractal Elements"
Nathan Cohen and Robert G. Hohlfeld 822

"The Radiation Characteristics of Recursively Generated Self-Scalable and Self-Similar Arrays"
D.H. Werner and P.L. Werner 829

SESSION 15: FAST AND EFFICIENCY METHODS Chairs: Weng C. Chew and Jiming Song

"Three Dimensional Scattering Analysis in Stratified Medium Using Fast Inhomogeneous Plane Wave Algorithm"
Bin Hu and Weng Cho Chew 838

"Multilevel Fast Multipole Algorithm for Analysis of Large-Scale Microstrip Structures"
Feng Ling, Jiming Song, and Jianming Jin 845

"A Novel Implementation of Multilevel Fast Multipole Algorithm for Higher-Order Galerkin's Method"
K.C. Donepudi, J.M. Song, Jianming Jin, G. Kang, and W.C. Chew 851

"Incomplete LU Preconditioner for FMM Implementation"
Kubilay Sertel and John L. Volakis 859

"A Fast, High-Order Scattering Code for Solving Practical RCS Problems"
J.J. Ottusch, J.L. Visher, and S.M. Wandzura 867

SESSION 15: FAST AND EFFICIENCY METHODS (cont)

"An Efficient Integral Equation Based Solution Method for Simulation of Electromagnetic Fields in Inhomogeneous Dielectric (Biological) Media"
E. Bleszynski, M. Bleszynski, and T. Jaroszewicz 874

"Efficient Solution of Large-Scale Electromagnetic Eigenvalue Problems Using the Implicity Restarted Arnoldi Method"
Daniel White and Joseph Koning 882

"Fast Fourier Transform of Functions with Jump Discontinuities"
Guo-Xin Fan and Qing Huo Liu 890

"Applications of Nonuniform Fast Transform Algorithms in Numerical Solutions of Integral Equations "
Q.H. Liu, X.M. Xu, and Z.Q. Zhang 897

SESSION 16: APPLICATIONS OF THE FIXED TECHNIQUE Chairs: Atef Elsherbeni and Wenhua Yu

"A Non-Dissipative Staggered Fourth-Order Accurate Explicit Finite Difference Scheme for the Time-Domain Maxwell's Equations"
A. Yefet and P.G. Petropoulos 906

"FDTD Method for Maxwell's Equations in Complex Geometries"
A. Ditkowski, K. Dridi, and J.S. Hesthaven 917

"FDTD Analysis of Tapered Meander Line Antennas for RF and Wireless Communications"
Chun-Wen Paul Huang, Atef Z. Elsherbeni, and Charles E. Smith 924

"FDTD Modeling of an Electron Cyclotron Resonance Reactor Driven by a Lisitano Coil"
Gaetano Marrocco, Fernando Bardati, and Francesco De Marco 930

"Modelling Microwave and Hybrid Heating Using FDTD"
J. Haala and W. Wiesbeck 936

"A Conformal Finite Difference Time Domain (CFDTD) Algorithm for Modeling Perfectly Conducting Objects"
Wenhua Yu, Raj Mittra, Dean Arakaki, and Douglas H. Werner 944

"A Finite-Difference Algorithm for Modeling of Conductive Wedges in 2D"
Piotr Przybyszewski 8 pages 951

"Advanced Techniques of Geometrical Modelling and CFDTD"
F. Rivas, J.P. Roa, and M.V. Catedra 7 pages 959

SESSION 17: HYBRID TECHNIQUES Chairs: Agostino Monorchio and P.H. Pathak

"A Three-Dimensional Hybrid Techniques for Combining the Finite Element and Finite Difference Methods in Time Domain"
Agostino Monorchio and Raj Mittra 968

"Vertical Antenna Near-Field Computation in Complex Environments by a Hybrid Method"
F. Bardati, E. Di Giampaolo, A. Durantini, and G. Marrocco 975

"3-D EM Problem Modelling by Geometry Decomposition and Combination of the FE, FDTD and BIE Techniques"
Hendrik Rogier, Daniel De Zutter, and Frank Olyslager 981

"Hybrid FDTD-Frequency Dependent Network Simulations Using Digital Filtering Techniques"
Ian Rumsey and Melinda Piket-May 988

"Study of Electrically-Short Thin-Wire Antennas Located in the Proximity of Inhomogeneous Scatterers Using a Hybrid NEC/FDTD Approach"
A. Rubio Bretones, R. Mittra, and R. Gomez Martin 995

"A Review of Some Hybrid High Frequency and Numerical Solutions for Radiation/Scattering Problems"
P.H. Pathak and R.J. Burkholder 1001

"An Hybrid Method Combining Integral Equations and Modal Expansion Applied to the RCS Modulation of Antennas and Rotating Fans"
Andre Barka and Paul Soudais 1006

"A 2D TLM and Haar MRTD Real-Time Hybrid Connection Technique"
Masafumi Fujii, Poman P.M. So, Enqiu Hu, Wei Liu, and Wolfgang J.R. Hoefer 1013

AUTHOR INDEX 1021

CALL FOR PAPERS



THE APPLIED COMPUTATIONAL ELECTROMAGNETICS SOCIETY

The 17th Annual Review of Progress in Applied Computational Electromagnetics
March 19 - 23, 2001
Naval Postgraduate School, Monterey, California
Share Your Knowledge and Expertise with Your Colleagues

The Annual ACES Symposium is an ideal opportunity to participate in a large gathering of EM analysis enthusiasts. The purpose of the Symposium is to bring analysts together to share information and experience about the practical application of EM analysis using computational methods. The symposium offerings include technical presentations, demonstrations, vendor booths, short courses, and hands-on workshops. All aspects of electromagnetic computational analysis are represented.

The ACES Symposium is a highly influential outlet for promoting awareness of recent technical contributions to the advancement of computational electromagnetics. Attendance and professional program paper participation from non-ACES members and from outside North America are encouraged and welcome.

Papers may address general issues in applied computational electromagnetics, or may focus on specific applications, techniques, codes, or computational issues of potential interest to the Applied Computational Electromagnetics Society membership.

Areas and topics

Computational studies of basic physics	Computer hardware issues
Examples of practical code application	Code validation
New codes, algorithms, code enhancements, and code fixes	Code performance analysis

Partial list of applications

Communications systems	Microwave components	Wireless	Radar Imaging
Remote sensing & geophysics	EMP EMI/EMC	Shielding Fiberoptics	Radar cross section
Dielectric & magnetic materials	MIMIC technology	Visualization	Fiberoptics
Non-destructive evaluation	Wave propagation	Eddy currents	Direction finding
Propagation through plasmas	Bioelectromagnetics	Inverse scattering	Antennas

Partial list of techniques

Diffraction theories	Moment methods	Physical optics
Frequency-domain & Time-domain techniques	Hybrid methods	Modal expansions
Finite difference & finite element analysis	Numerical optimization	
Integral equation & differential equation techniques	Perturbation methods	

INSTRUCTIONS FOR AUTHORS AND TIMETABLE

Submission Deadline - November 1, 2000: Electronic submission preferred (Microsoft Word). Otherwise submit three copies of a full-length, camera-ready paper to the Technical Program Chairman. Please supply the following data for the corresponding authors: name, address, email address, FAX, and phone numbers. **Authors notified of acceptance by December 1, 2000.**

PAPER FORMATTING REQUIREMENTS

The recommended paper length is 6 pages, with 8 pages as a maximum, including figures. The paper should be camera-ready (good resolution, clearly readable when reduced to the final print of 6x9 inch paper). The paper should be printed on 8-1/2x11 inch papers with 13/16 side margins, 1-1/16 inch top margin, and 1 inch on the bottom. On the first page, place title 1-1/2 inches from top with authors, affiliations, and e-mail addresses beneath the title. Single spaced type using 10 or 12 point font size, entire text should be justified (flush left and flush right). No typed page numbers, but number your pages lightly in pencil on the back of each page.

For all questions regarding the ACES Symposium please contact:
Leo C. Kempel, Technical Program Chair
Michigan State University, ECE Engr,
2120 Engineering Bldg, E. Lansing, MI 48824-1126
Tel: (517) 353-9944, Fax: (517) 353-1980,
E-mail: lkempel@ieee.org
or visit ACES on line at:http://aces.ee.olemiss.edu.

EARLY REGISTRATION FEES

ACES member	$300	Student/Retired/Unemployed	$130 (no proceedings)
Non-member	$350	Student/Retired/Unemployed	$165 (includes proceedings)

Each conference registration is entitled to publish two papers in the proceedings free of charge. Excess pages over a paper limit of 8 will be charged $15/page.

$500 BEST-PAPER PRIZE

A $500 prize will be awarded to the authors of the best non-student paper accepted for the 16th Annual Review. Papers will be judged by a special ACES prize-paper Committee according to the following criteria:

1. Based on established electromagnetic (EM) theory
2. Reliable data
3. Computational EM results
4. Practical applications
5. Estimates of computational errors
6. Significant new conclusions

$200 BEST STUDENT PAPER CONTEST

This will be for the best student paper accepted for the 17th Annual Review. (Student must be the presenter on the paper chosen). Submissions will be judged by three (3) members of the BoD. The prizes for the student presenter and his/her principal advisor will consist of: (1) free Annual Review registration for the following year; (2) one free short course taken during the 2001 or 2002 Annual Review; and (3) $200 cash for the paper.

2001 ACES Symposium Sponsored by: ACES, NPS, PSU, MSU, SWRI
In cooperation with: The IEEE Antennas and Propagation Society,
The IEEE Electromagnetic Compatibility Society and USNC/URSI

2000 Symposium Program Committee

for the

16th Annual Review of Progress

in

Applied Computational Electromagnetics

at the
Naval Postgraduate School
Monterey, CA

Technical Program Chairman
Douglas H. Werner
EE Department
Penn State University
211A Electrical Engineering East
University Park, PA 16802
Phone: (814) 863-2946
Fax: (814) 865-3359
Email: dhw@psu.edu

Technical Co-Chair
Pingjuan L. Werner
EE Department
Penn State University
211A Electrical Engineering East
University Park, PA 16802
Phone: (814) 865-2364
Fax: (814) 865-3359
Email: plw7@psu.edu

Technical Co-Chair
Randy L. Haupt
ECE Department
Utah State University
4120, Old Main Hill
Logan, UT 84322-4120
Phone: (435) 797-2840
Fax: (435) 797-3054
Email: haupt@ieee.org

Short Course Chairman
Susan C. Hagness
ECE Department
University of Wisconsin-Madison
1415 Engineering Drive
Madison, WI 53706-1691
Phone: (608) 265-5739
Fax: (608) 262-1267
Email: hagness@engr.wisc.edu

Vendor Chairman
Leo C. Kempel
ECE Department
Michigan State University
2120 Engineering Bldg.
E. Lansing, MI 48824-1126
Phone: (517) 353-9944
Fax: (517) 353-1980
Email: l.kempel@ieee.org

Publicity Chair:
Keith Lysiak
Southwest Research Institute
6220 Culebra Road
San Antonio, TX 78238-5166
Phone: (210) 522-5776
Fax: (210) 522-2709
Email: klysiak@swri.edu

Symposium Administrator
Richard W. Adler
ECE Dept/Code EC/AB
Naval Postgraduate School
Monterey, CA 93943-5121
Phone: (831) 646-1111
Fax: (831) 649-0300
Email: rwa@attglobal.net

Conference Secretary
Mrs. Pat Adler
822 Devisadero Street
Monterey, CA 93940-1913
Email: pba@attglobal.net

Advisory Committee:
Richard W. Adler, Naval Postgraduate School
Bruce Archambeault, IBM
Robert Bevensee, Boma Enterprises
Anthony Brown, Chilworth, UK
Andreas Cangellaris, University of Illinois
Allen W. Glisson, University of Mississippi
Eric Michielssen, University of Illinois
Guiseppe Pelosi, University of Florence
Ray Perez, Jet Propulsion Lab.
Andrew Peterson, Georgia Institute of Technology
Norio Takahashi, Okayama University
W. Perry Wheless, Jr., University of Alabama

PREFACE

On behalf of the Conference Technical Committee, I would like to personally welcome all of you, especially those from overseas, to the 16th Annual Review of Progress in Applied Computational Electromagnetics – the first ACES Conference of the new millennium, here at the Naval Postgraduate School in beautiful Monterey.

We are fortunate to have with us this year three highly-regarded plenary speakers, Raj Mittra, Tom Cwik and Weng Chew, who will be discussing the challenges in computational electromagnetics that await as we move into the new millennium. The technical sessions this year cover a wide variety of topics ranging from *Wavelet and TLM Modeling Techniques* to *Virtual Reality in Real-World Applications*. Of special significance this year are the good number of international participants, some of whom have organized sessions and will also be chairing and presenting papers in the conference. This will also be the first year that there will be a special session devoted to the Student Paper Competition. We hope that you will all take advantage of the interactive poster session, vendor exhibits and the excellent program of short courses that have been organized for this years' conference.

We would also like to take this opportunity to thank the Naval Postgraduate School for serving as the host for the ACES 2000 conference. Special thanks goes to Dick and Pat Adler for their unending dedication and tireless efforts on behalf of ACES. We want to specifically thank all those who have helped to make ACES 2000 possible by organizing and chairing sessions. Finally, I would like to extend my personal thanks to my technical program committee team members -- including co-chairs Randy Haupt and Ping Werner, vendor chair Leo Kempel, short course chair Susan Hagness, publicity chair Keith Lysiak, and ACES webmaster Etef Elsherbeni -- for all their hard work and dedication throughout the past year.

We hope that the conference will provide a unique opportunity for all of you to come together from around the world to share your knowledge in computational electromagnetics by renewing old acquaintances and forming new collaborations. We also hope that ACES 2000 will be a memorable and productive conference for each and every participant.

Best wishes in the new millennium!

Douglas H. Werner

Douglas H. Werner
Technical Program Chair
ACES 2000 Conference

ACES PRESIDENT'S STATEMENT

Welcome to the ACES 2000 conference! The ACES *Annual Review of Progress in Applied Computational Electromagnetics* now has a 16-year tradition of excellence that guarantees a pleasant and educational experience. CEM specialists worldwide, both members and non-members of ACES, know they can find our conference in Monterey during the third week of March. The Naval Postgraduate School has been a gracious host and afforded excellent accommodations to ACES over the years, but a school calendar change has brought into question the week or location for our future conferences. The ACES Board of Directors will study this issue carefully before recommending any change, as both our date and place have been so well known for so many years.

We again express our continuing gratitude and debt to Dick and Pat Adler for their (perennial) long hours devoted to ACES, including the conference local arrangements. Doug Werner and his capable conference team have put together an excellent technical program. I won't attempt to credit all his enthusiastic and capable assistants here, but please come hear Doug's opening remarks on Tuesday morning. Because the majority of our conference registrants continue to prefer a limited number of parallel sessions, ACES has restricted the number of accepted papers for the technical program this year. I hope you will appreciate and enjoy this distinctive feature of our conference. The ACES 2000 conference is more than just paper sessions, short courses, and award banquets, and ACES is actively striving to enhance your opportunities to have some quality time available for colleagues and friends, both old and new. If you see a way that we can further improve the structure and conduct of the conference, please do let us hear from you!

For all the news about ACES 2001 as it is becomes available, remember to visit our Web sit at aces.ee.olemiss.edu on a regular basis!

Perry Wheless
ACES President

ACES 2000 SHORT COURSES/WORKSHOPS

MONDAY 20 MARCH 2000

0830-1630	SHORT COURSE #1 (FULL-DAY) "Computational Electromagnetic Methods in Mobile Wireless Communication Design" Ray Perez, Jet Propulsion Laboratory
0830-1630	SHORT COURSE #2 (FULL-DAY) "XML and Modern Internet Technologies for Scientific Applications" Furrukh S. Kahn, Ohio State University.
0830-1630	SHORT COURSE #3 (FULL-DAY) "The Basics of The Finite Difference Time Domain Technique for Electromagnetic Application" Atef Z. Elsherbeni and Allen W. Glisson, University of Mississippi
0830-1630	SHORT COURSE #4 (FULL-DAY) "Techniques for Electromagnetic Visualization" Edmund K. Miller, Santa Fe, NM, and John Shaeffer, Marietta Scientific, Inc.
0830-1630	SHORT COURSE #5 (FULL-DAY) "EIGER - Electromagnetic Interactions Generalized: An Introduction to and Tutorial on the Software Suite" Robert M. Sharpe and Nathan J. Champagne, Lawrence Livermore National Laboratory William A. Johnson, Sandia National Laboratories, Donald R. Wilton, University of Houston, and J. Brian Grant, ANT-S.
0830-1130	HANDS-ON-WORKSHOP #6 (HALF-DAY, MORNING) "MATHCAD BASICS", Jovan Lebaric, Naval Postgraduate School.
1330-1630	HANDS-ON-WORKSHOP #7 (HALF-DAY, AFTERNOON) "MATLAB BASICS", Jovan Lebaric, Naval Postgraduate School.
0830-1630	SHORT COURSE #8 (FULL-DAY) "EMI/EMC Computational Modeling for Real-World Engineering Problems"" Omar Ramahi, Compaq Corporation, and Bruce Archambeault, IBM

PLEASE NOTE THAT A 10% DISCOUNT IS IN EFFECT FOR ALL WORKSHOPS TAKEN AFTER ATTENDING AN INITIAL WORKSHOP. THIS APPLIES TO THE GROUP OF WORKSHOPS FOR MATLAB AND MATHCAD.

FRIDAY 24 MARCH 2000

0830-1630	SHORT COURSE #9 (FULL-DAY) "Why is There Electromagnetic Radiation and Where Does It Come From?" John Shaeffer, Marietta Scientific Inc., and Edmund K. Miller, Santa Fe, NM
0830-1630	SHORT COURSE #10 (FULL-DAY) "Recent Advances in Fast Algorithms for Computational Electromagnetics" Weng Cho Chew, Jianming Jin, Eric Michielssen, and Jiming Song, University of Illinois at Urbana Champaign

ACES 2000 SHORT COURSES/WORKSHOPS (cont)

FRIDAY 24 MARCH 2000

0830-1630 HANDS-ON-WORKSHOP #11 (FULL-DAY)
"Method of Moments (MoM) Using MATHCAD"
Jovan Lebaric, Naval Postgraduate School

0830-1130 SHORT COURSE #12 (HALF-DAY, MORNING)
"Computational Electromagnetics Using Beowulf-Cluster Computers"
Tom Cwik and Daniel S. Katz, Jet Propulsion Laboratory

1330-1630 SHORT COURSE #13 (HALF-DAY AFTERNOON)
"Multiresolution FEM: Introduction and Antenna Applications"
John L. Volakis, University of Michigan and Lars Anderson, Agilent

SATURDAY 25 MARCH 2000

0830-1630 HANDS-ON-WORKSHOP #14 (FULL-DAY)
"FD/FDTD Using MATLAB"
Jovan Lebaric, Naval Postgraduate School, Monterey, CA

0830-1630 SHORT COURSE #15 (FULL-DAY)
"An Introduction to Radar Cross Section"
John Shaeffer, Marietta Scientific Inc.

AGENDA

The Sixteenth Annual Review of Progress in Applied Computational Electromagnetics

NAVAL POSTGRADUATE SCHOOL, MONTEREY, CALIFORNIA, U.S.A.
20-25 March 2000

Douglas Werner, Technical Program Chair

Randy Haupt, Symposium Co-Chair

Pingjuan Werner, Symposium Co-Chair

Susan Hagness, Short Course Chair

Leo Kempel, Vendor Chair

Keith Lysiak, Publicity Chair

Richard Adler, Symposium Administrator

Pat Adler, Conference Secretary

MONDAY MORNING 20 MARCH 2000

0700 – 0730	**CONTINENTAL BREAKFAST** (For short course and hands-on-workshop attendees only)	**Glasgow Courtyard**
0730 – 0820	**SHORT COURSE/HANDS-ON-WORKSHOP REGISTRATION**	**Glasgow 103**
0830-1630	**SHORT COURSE #1 (FULL-DAY)** "Computational Electromagnetic Methods in Mobile Wireless Communication Design" Ray Perez, Jet Propulsion Laboratory	**Ingersoll 280**
0830-1630	**SHORT COURSE #2 (FULL-DAY)** "XML and Modern Internet Technologies for Scientific Applications" Furrukh S. Khan, Ohio State University	**Glasgow 102**
0830-1630	**SHORT COURSE #3 (FULL-DAY)** "The Basics of The Finite Difference Time Domain Technique for Electromagnetic Application" Atef Z. Elsherbeni and Allen W. Glisson, University of Mississippi	**Ingersoll 122**
0830-1630	**SHORT COURSE #4 (FULL-DAY)** "Techniques for Electromagnetic Visualization" Edmund K. Miller, Santa Fe, NM, and John Shaeffer, Marietta Scientific, Inc	**Engr Auditorium**
0830-1630	**SHORT COURSE #5 (FULL-DAY)** "EIGER – Electromagnetic Interactions Generalized: An Introduction to and Tutorial on the Software Suite" Robert M. Sharpe and Nathan J. Champagne, Lawrence Livermore National Laboratory William A. Johnson, Sandia National Laboratories, Donald R. Wilton, University of Houston, And J. Brian Grant, ANT-S	**Ingersoll 265**
0830-1130	**HANDS-ON-WORKSHOP #6 (HALF-DAY, MORNING)** "MATHCAD Basics" Jovan Lebaric, Naval Postgraduate School	
0830-1630	**SHORT COURSE #8 (FULL-DAY)** "EMI/EMC Computational Modeling for Real-World Engineering Problems" Omar Ramahi, Compaq Corporation, and Bruce Archambeault, IBM	**Spanagel 101A**
0900-1200	**CONFERENCE REGISTRATION**	**Glasgow 103**

MONDAY AFTERNOON

1330-1630	**HANDS-ON-WORKSHOP #7 (HALF-DAY, AFTERNOON)** "MATLAB Basics" Jovan Lebaric, Naval Postgraduate School	
1400-1800	**CONFERENCE REGISTRATION**	**Glasgow 103**
1700	**BOD MEETING**	**SP 101A**
1900	**PUBLICATION DINNER**	

TUESDAY MORNING 21 MARCH 2000

0715 – 0745	**CONTINENTAL BREAKFAST**		**Glasgow Courtyard**
0740	**ACES BUSINESS MEETING**	**President Perry Wheless**	**Glasgow 102**
0745	**ACES Website Demo**	**Atef Elsherbeni**	**Glasgow 102**
0800	**WELCOME**	**Douglas Werner,** Penn State Univeristy	**Glasgow 102**
0815	**PLENARY SPEAKER:** "Efficient Extraction of S-parameters of Transmission Line Discontinuities for RF and Wireless Circuit Design"	**Raj Mittra,** Penn State University	**Glasgow 102**

SESSION 1: FINITE ELEMENT METHODS **Parallel with Sessions 2, 3 & 4)**
Chairs: Jianming Jin and Peter Monk

0920	"Transient Electromagnetic Scattering from Curved Dielectric/Lossy 3D Bodies Using Covariant Projection Elements"	R. Ordovas, S.P. Walker & M.J. Bluck
0940	"Towards an *hp*-Adaptive Finite Element Method for Full-Wave Analysis of Waveguides"	L. Vardapetyan & L. Demkowicz
1000	"An *hp*-Adaptive Finite Element Method for Maxwell's Equations: A Progress Report"	L. Demkowicz
1020	**BREAK**	
1040	"Finite Element Method for Designing Plasma Reactors"	Leo Kempel, Paul Rummel, Tim Grotjohn & John Amrhein
1100	"Finite-Element Domain Decomposition Through an Iterative Algorithm: Coupling Between Cavity-Backed Slots"	Anastasis C. Polycarpou & Constantine A. Balanis
1120	"Investigation of the Bunting/Davis Functional when used with Vector Finite Elements for Waveguide Analysis"	Andrew F. Peterson & Sharib Wasi
1140	"Numerical Methods for High Frequency Problems"	T. Huttunen & P. Monk
1200	**LUNCH**	

SESSION 2: OPTIMIZATION IN ELECTROMAGNETICS **(Parallel with Sessions 1, 3 & 4)**
Chairs: Eric Michielssen and Dan Weile

0920	"Design of Dual Band Frequency Selective Surfaces Using Genetic Algorithm"	A. Monorchio, R. Mittra & G. Manara
0940	"A Study of Cauchy and Gaussian Mutation Operators in the Evolutionary Programming Optimization of Antenna Structures"	Ahmad Hoorfar & Yuan Liu
1000	"A Statistical Intercomparison of Binary and Decimal Genetic Algorithms"	Yee Hui Lee, Stuart J.Porter & Andrew C. Marvin
1020	**BREAK**	
1040	"The Compact Genetic Algorithm: A Litmus test for Genetic Algorithm Applicability"	Daniel S. Weile, Eric Michielssen & David E. Goldberg
1100	"Dipole Equivalent Circuit Optimization Using Genetic Algorithm"	Bruce Long, Ping Werner & Doug Werner
1120	"Computing the Electromagnetic Field in a Perturbed Configuration Using Modified Reduced-Order Models"	R.F. Remis & P.M. van den Berg
1140	Some Further Results From FARS: Far-Field Analysis of Radiation Sources"	Edmund K. Miller
1200	**LUNCH**	

SESSION 3: NUMERICAL TECHNIQUES FOR PACKAGING AND INTERCONNECTS **(Parallel with Sessions 1,2, & 4)**
Chairs: Omar Ramahi and Andreas Cangellaris

0920	"A New Methodology for the Direct Generation of Closed-Form Electrostatic Green's Functions in Layered Dielectrics"	Andreas C. Cangellaris
0940	"The Treatment of Narrow Microstrips and PCB Tracks in the FDTD Method Using Empirically Modified Coefficients"	Chris J. Railton
1000	"Time-Domain-Analysis of QTEM Wave Propagation and Crosstalk on Lossy Multiconductor Transmission Lines with Terminal Coupling"	Georg Müller, Jan Wendel & Karl Reiß

TUESDAY MORNING 21 MARCH 2000

SESSION 3: NUMERICAL TECHNIQUES FOR PACKAGING AND INTERCONNECTS (cont)

1020	**BREAK**	
1040	"An MPIE-Based Circuit Extraction Technique and Its Applications on Power Bus Modeling in High-Speed Digital Designs"	Jun Fan, Hao Shi, James L. Knighten James L. Drewniak
1100	"Non-resonant Electromagnetic Simulation of Some Resonant Planar Circuits"	Yuriy O. Shlepnev
1120	"FDTD Analysis of Conventional and Novel Delay Lines"	Omar M. Ramahi
1140	"Complementary Operators for Frequency-Domain Method: A Single Simulation Implementation"	Omar M. Ramahi
1200	**LUNCH**	

SESSION 4: STUDENT PAPER COMPETITION **(Parallel with Sessions 1, 2 & 3)**
Chair: Perry Wheless

0920	"Systematic Studies in Annular Ring PBG Structures"	Todd Lammers, Shawn W. Staker, & Melinda Piket-May
0940	"Fast Electromagnetic Analysis Using the Asymptotic Waveform Evaluation Method"	Dan Jiao & Jianming Jin
1000	"A Domain-Decomposition/Reciprocity Technique for the Analysis Of Arbitrarily-Shaped Microstrip Antennas with Dielectric Substrates and Superstrates Mounted on Circularly-Cylindrical Platforms"	R.J. Allard, D.H. Werner, & J.S. Zmyslo
1020	**BREAK**	
1040	"A New FDTD Scheme to Model Chiral Media"	A. Akyurtlu, D.H. Werner, & K. Aydin
1100	"T-Matrix Computer Code Applied to Electromagnetic Field Penetration in Magnetic Resonance Imaging"	Rafael R. Canales, Luis F. Fonseca & Fredy R. Zypman
1200	**LUNCH**	

TUESDAY AFTERNOON

1300-1530	**INTERACTIVE POSTER SESSION**	**Ballroom, Herrmann Hall**
1300-1900	**VENDOR EXHIBITS**	**Ballroom, Herrmann Hall**
1500-1700	**WINE AND CHEESE TASTING**	**Ballroom, Herrmann Hall**

SESSION 5: INTERACTIVE POSTER SESSION **Ballroom, Herrmann Hall**

"Characteristics of Silicon Photoconductivity Under Near-Infrared illumination"	Preston P. Young, Robert Magnusson Tim R. Holzheimer
"Characteristics of Fractal Antennas"	Haruo Kawakami, Yasushi Ojiro, Yasushi Iizuka, Satoshi Kogiso & Gentei Sato
"Feigenbaum Encryption of Computer Codes"	R.M. Bevensee
"Extension of SuperNEC to Calculate Characteristic Modes"	Thomas Abbott

(THE PAPER "XPATCH 4..., BELOW IS BEING PRESENTED HERE ONLY; IT WAS NOT RELEASED IN TIME FOR INCLUSION IN THE PROCEEDINGS

"Xpatch 4: The Next Generation in High Frequency Electromagnetic Modeling and Simulation Software"	J. Hughes, J. Moore, S. Kosanovich, D. Kapp, R. Bhalla, R. Kipp, T. Courtney, A. Nolan, D. Andersh, F. German and J. Cook
"Review of Basic 3D Geometry Considerations for Intelligent CEM Pre-Processor Applications"	Kurt V. Sunderland
"Modelling of Loaded Wire Conductor Above Perfectly Conducting Ground by Using 3D TLM Method"	Nebojša S. Dončov, Bratislav D. Milovanović, Vladica M. Trenkić

TUESDAY AFTERNOON 21 MARCH 2000

1300-1530 **INTERACTIVE POSTER SESSION (cont)** **Ballroom, Herrmann Hall**

"Near to Far Field Transformation for a FDTD BOR with PML ABC and Sub-Grid Capability"	Vicente Rodriguez-Pereyra, Atef Z. Elsherbeni, Charles E. Smith
"Evanescent Tunneling and Quantile Motion of Electromagnetic Waves in Wave Guides of Varying Cross Section"	E. Gjonaj
"A Modal Approach for the Calculation of Scattering Parameters in Lossfree and Lossy Structures Using the FI-Technique"	Rolf Schuhmann, Peter Hammes, Stefan Setzer, Bernd Trapp, & Thomas Weiland
"A Modular Technique for the Calculation of Wave Guide Structures"	Johannes Borkes, Adalbert Beyer, & Oliver Pertz
"Wave Propagation Through 2D Clusters of Coupled Cylindrical Resonators"	Ross A. Speciale
"Design Software for Cylindrical Helix Antennas"	M. Slater, C.W. Trueman
"The Analysis of a Center-Fed Helical Microstrip Antenna Mounted on a Dielectric-Coated Circular Cylinder Using the Reciprocity Theorem"	R.A. Martin, & D.H. Werner
"Near to Far Field Transformation for a FDTD BOR with PML ABC and Sub-Grid Capability"	Vicente Rodriguez-Pereyra, Atef Elsherbeni & Charles Smith

WEDNESDAY MORNING

0715 – 0800 **CONTINENTAL BREAKFAST**

0815 **PLENARY SPEAKER** **Tom Cwik,** Jet Propulsion Laboratory **Glasgow 102**
"Design on Computer – A Coming of Age"

SESSION 6: COMPUTATIONAL BIO-ELECTROMAGNETICS **Parallel with Sessions 7 & 8)**
Chairs: Ray Luebbers and Susan Hagness

0920	"Numerical Investigation of Two Confocal Microwave Imaging Systems for Breast Tumor Detection"	Susan C. Hagness, Xu Li, Elise C. Fear & Maria A. Stuchly
0940	"FDTD Studies on SAR in Biological Cells Exposed to 837 and 1900 MHz in a TEM Cell"	A.W. Guy
1000	"Modelling of Personnel Electromagnetic Radiation Hazards Deliberation of a Novice"	Alan Nott
1020	**BREAK**	
1040	"Modeling Interference Between Very Low Frequency Electromagnetic Fields and Implanted Cardiac Pacemakers"	Trevor W. Dawson & Maria A. Stuchly
1100	"Using Computational Electromagnetics to Solve an Occupational Health and Safety Incident"	Timothy Priest, Kevin Goldsmith & Dean DuRieu
1120	"Analysis of Permanent Magnet Type of MRI Taking Account of Hysteresis and Eddy Current and Experimental Verification"	Norio Takahashi, Siti Zubaidah, Takeshi Kayano Koji Miyata & Ken Ohashi

SESSION 7: VIRTUAL REALITY IN REAL-WORLD APPLICATIONS **(Parallel with Sessions 6 & 8)**
Chairs: Stan Kubina and Dennis DeCarlo

0920	"A Virtual Radiation Pattern Range and Its Uses - C-130/Hercules HF Notch Antenna"	Stanley J. Kubina, Christopher W. Trueman David Gaudine
0940	"HF Towel-Bar Antenna Location Study Aboard an H3 Sikorsky Helicopter"	Saad N. Tabet, Carl D. Myers & Dennis DeCarlo
1000	"Improving Model Confidence through Metamorphosis"	Douglas R. Munn and Chris Trueman
1020	**BREAK**	
1040	"Model Morphing for Insight into the HF Assessment Parameters"	Douglas R. Munn and Chris Trueman
1100	"3D Modeling of Complex Helicopter Structures: Prediction and Measurements"	Anastasis C. Polycarpou, Dong-Ho Han Stavros V. Georgakopoulos & Constantine A. Balanis

WEDNESDAY MORNING 22 MARCH 2000

SESSION 7: VIRTUAL REALITY IN REAL-WORLD APPLICATIONS (cont)

1120	"Increasing the Productivity of NEC Analysis with Virtual Reality and 3D Laser Scanners"	Kevin J. Cybert & Daniel D. Reuster
1140	"An Interactive HTML Based Multimedia Course on Antennas"	Ulrich Türk & Peter Russer

SESSION 8: EMC **(Parallel with Sessions 6 & 7)**
Chairs: Bruce Archambeault and Jim Drewniak

0920	"Adding Imperfections to EMC FDTD Models as a Means of Increasing Accuracy"	Colin E. Brench
0940	"Power Conversion Techniques for Portable EMI Sensitive Applications"	Reinaldo Perez
1000	"Using the Partial Element Equivalent Circuit (PEEC) Simulation Technique to Properly Analyze Power/Ground Plane EMI Decoupling Performance"	Bruce Archambeault
1020	**BREAK**	
1040	"EMI Model Validation and Standard Challenge Problems"	Bruce Archambeault & James L. Drewniak
1100	"Modeling EMI Resulting from a Signal via Transition Through Power/Ground Layers"	Wei Cui, Xiaoning Ye, Bruce Archambeault Doug White, Min Li & James L. Drewniak
1120	"Techniques for Optimizing FEM/MoM Codes"	Y. Ji, T.H. Hubing, & H. Wang
1140	"Numerical Modeling of Shielding by a Wire Mesh Box"	Gerald J. Burke & David J. Steich

LUNCH

WEDNESDAY AFTERNOON

SESSION 9: PROPAGATION **(Parallel with Sessions 10 & 11)**
Chairs: Steve Fast and Frank Ryan

1320	"A Fast Quasi Three-Dimensional Propagation Model for Urban Microcells"	Joseph W. Schuster & Raymond J. Luebbers
1340	"FDTD Techniques for Evaluating the Accuracy of Ray-Tracing Propagation Models for Microcells"	Joseph W. Schuster & Raymond J. Luebbers
1400	"A Building Database Features Pre-Processor for 3-D SBR/GTD Urban EM Propagation Models"	James Pickelsimer & Raymond J. Luebbers
1420	"Toward a New Model for Indoor and Urban Propagation Using Percolation Theory"	G. Franceschetti, S. Marano, N. Pasquino, & I.M. Pinto
1440	"Ray Tracing Algorithm for Indoor Propagation"	C.W. Trueman, R. Paknys, J. Zhao, D. Davis, & B. Segal
1500	**BREAK**	
1520	"Modeling Large and Small-Scale Fading on the DPSK Datalink Channel Using a GTD Ray-Tracing Model"	Kent Chamberlin, Mikhailo Seledtsov & Petar Horvatic
1540	"Rough Surface Forward Scatter in the Parabolic Wave Equation Model"	Frank J. Ryan
1600	"A Comparison of Electromagnetic Parabolic Equation Propagation Models Used by the U.S. Navy to Predict Radar Performance"	Donald de Forest Boyer & Huong Pham

SESSION 10: WAVELET AND TLM MODELING TECHNIQUES **(Parallel with Sessions 9 & 11**
Chairs: Wolfgang J.R. Hoefer and Peter Russer

1320	"The Implementation of a High Level (1st-order) Haar Wavelet MRTD Scheme"	Enqiu Hu, Poman P.M. So, Masafumi Fujii, Wei Liu Wolfgang J. R. Hoefer
1340	"Multi-Resolution Based TLM Technique Using Haar Wavelets"	Ismael Barba, Jose Represa, Masafumi Fujii, Wolfgang J.R. Hoefer
1400	"Formulation and Study of an Arbitrary Order Haar Wavelet Based Multi-Resolution Time Domain Technique"	Costas D. Sarris & Linda P.B. Katehi

WEDNESDAY AFTERNOON 22 MARCH 2000

SESSION 10: WAVELET AND TLM MODELING TECHNIQUES (cont)

1420	"Computational Optimization of MRTD Haar-Based Adaptive Schemes Used for the Design of RF Packaging Structures"	Manos M. Tentzeris
1440	"Time-Domain Simulation of Electromagnetic Wave Propagation in a Magnetized Plasma"	J. Paul, C. Christopoulos & D.W.P. Thomas
1500	**BREAK**	
1520	"TLM Simulation of Patch Antenna on Magnetized Ferrite Substrate"	M.I. Sobhy, M.W. R. Ng, R.J. Langley & J.C. Batchelor
1540	"On the Practical Use of Layered Absorbers for the Simulation of Planar Microwave Circuits Using the SCN-TLM Method"	Jürgen Rebel, Tobias Mangold, & Peter Russer
1600	"A Numerical Study of MEMS Capacitive Switches Using TLM"	Fabio Coccetti, Larissa Vietzorreck, Vitali Chtchekatourov, Peter Russer
1620	"Thin Wire Modeling with the TLMIE-Method"	S. Lindenmeier, C. Christopoulos & P. Russer
1640	"What Determines The Speed of Time-Discrete Algorithms"	Tobias Mangold, Jürgen Rebel, Wolfgang J.R. Hoefer, Poman P.M. So, & Peter Russer

SESSION 11: TIME DOMAIN METHODS AND APPLICATIONS **(Parallel with Sessions 9 & 10)**
Chairs: Amelia Rubio Bretones and R. Gomez Martin

1320	"Introducing a New Time-Domain Electromagnetic Field Solver LSFEM™TD-3D"	Craig C. Ouyang, B.N. Jiang & Nina Liao
1340	"Characteristic-Based Time-Domain Method for Antenna Analysis"	Dan Jiao, Jianming Jin & J.S. Shang
1400	'Modeling of Thin-Wire Structures by Solving the EFIE in Time Domain"	Friedrich Schunn & Hermann Singer
1420	"Time-Domain Analysis of Thin-Wire Loaded Antenna Using Integral Equations"	M. Fernandez Pantoja, A. Rubio Bretones R. Gomez Martin
1440	"Haar MRTD Wave Propagation Through Isotropic Plasmas"	Ismael Barba, Jose Represa, Masafumi Fujii, Wolfgang J. R. Hoefer
1500	**BREAK**	
1520	"Time-Domain Scattering from Arbitrarily Shaped Metallic Shelters with Apertures: Numerical and Experimental Analysis"	Giuliano Manara & Agostino Monorchio
1540	"Integral Equation Based Analysis of Transient Electromagnetic Scattering from Three Dimensional Inhomogeneous Dielectric Objects"	N.T. Gres, A.A. Ergin, B. Shanker, & E. Michielessen
1600	"Computational Properties of Wavelet Based PEEC Analysis in Time Domain"	G. Antonini & A. Orlandi
1620	"Time Domain Modeling of a Pulsed Horn-Dish Antenna"	M.J. Bluck, S.P. Walker & C. Thomas

THURSDAY MORNING 23 MARCH 2000

0715 – 0800 **CONTINENTAL BREAKFAST**

0815 **PLENARY SPEAKER:** **W.C. Chew,** University of Illinois at Urbana-Champaign
"Fast Solvers for Electromagenetic Simulations – A New Age Analysis Tool"

SESSION 12: MOMENT METHODS **(Parallel with Sessions 13 & 14)**
Chairs: Zachi Baharav and Ramakrishna Janaswamy

0920	"Iterative Solvers for Dense Matrices –Applications to Moment Method Matrices"	Jürgen v. Hagen & Werner Wiesbeck
0940	"Convergence Properties of the CFIE for Several Conducting Scatterers"	William D. Wood, Jr., Kueichien C. Hill William J. Kent, Robert G. Layden & Lisa A. Cravens
1000	"Modeling of General Surface Junctions of Composite Objects in an SIE/MoM Formulation"	Joon Shin, Allen W. Glisson, & Ahmed A. Kishk
1020	**BREAK**	

THURSDAY MORNING 23 MARCH 2000

SESSION 12: MOMENT METHODS (cont

1040	"A Novel Grid-Robust Higher-Order Vector Basis Function for the Method of Moments"	G. Kang, J.M. Song, W.C. Chew, K. Donepudi, & J.M. Jin
1100	"Analytical Treatment of Green's Functions Singularities in Microstrip Structures"	E. Jiménez, F.J. Cabrera & J.G. Cuevas del Rio
1120	"Higher-Order Electromagnetic Modeling of Multilayer Microstrip Structures"	Feng Ling, Kalyan Donepudi & Jianming Jin

SESSION 13: CONFORMAL ANTENNAS **(Parallel with Sessions 12 & 14)**
Chairs: Leo Kempel and Douglas Werner

0920	"A Conformal, Flexible, Multifunction Communications Antenna"	T.R. Holzheimer
0940	"Finite Printed Antenna Array Modeling Using an Adaptive Multi-Resolution Approach"	Lars S. Andersen, Yunus E. Erdemli & John L. Volakis
1000	"A Technique for Analyzing Radiation from Conformal Antennas Mounted on Arbitrarily-Shaped Conducting Bodies"	Dean Arakaki, Douglas H. Werner & Raj Mittra
1020	**BREAK**	
1040	"Using Computational Electromagnetics and Monte-Carlo Methods to Locate Antennas on Aircraft"	Kevin Goldsmith, Paul Johnson & Timothy Priest
1100	"Coupling Phenomena in Horizontal and Vertical Polarized Aperture Coupled Patch Antennas on Cylindrical Surfaces"	D. Löffler, J. von Hagen & W. Wiesbeck
1120	"Modeling and Analysis of Wideband Conformal Antennas"	Keith D. Trott, Rene D. Guidry & Leo C. Kempel
1140	"Curvature Effects on a Conformal Log-Periodic Antenna"	Charles Macon, Leo Kempel, Keith Trott, Stephen Schneider

SESSION 14: ANTENNA ARRAYS **(Parallel with Sessions 12 & 13)**
Chairs: Keith Lysiak and Nathan Cohen

0920	"Problems of Characterising Array Manifolds for Naval Platforms in HF Environments"	Linda Holtby
0940	"Designing a VHF Wrap-Around DF Antenna Array Using NEC"	Keith Lysiak
1000	"Specifying a Direction Finding Antenna with Examples"	T. R. Holzheimer
1020	**BREAK**	
1040	"A High Efficiency Broad Band Wire Antenna System"	Kevin J. Cybert & Daniel D. Reuster
1100	"Comparison of Calculations and Measurements of an Electronically Scanned Circular Array"	James M. Stamm, Michael W. Jacobs & James K. Breakall
1120	"Array Sidelobe Reduction by Small Position Offsets of Fractal Elements"	Nathan Cohen & Robert G. Hohlfeld
1140	"The Radiation Characteristics of Recursively Generated Self-Scalable and Self-Similar Arrays"	D.H. Werner & P.L. Werner

THURSDAY AFTERNOON

SESSION 15: FAST AND EFFICIENT METHODS **(Parallel with Sessions 16 & 17)**
Chairs: Weng C. Chew and Jiming Song

1320	"Three Dimensional Scattering Analysis in Stratified Medium Using Fast Inhomogeneous Plane Wave Algorithm"	Bin Hu, & Weng Cho Chew
1340	"Multilevel Fast Multipole Algorithm for Analysis of Large-Scale Microstrip Structures"	Feng Ling, Jiming Song & Jianming Jin
1400	"A Novel Implementation of Multilevel Fast Multipole Algorithm for High-Order Galerkin's Method"	K.C. Konepudi, J.M. Song, J.M. Jin, G Kang & W.C. Chew
1420	"Incomplete LU Preconditioner for FMM Implementation"	Kubilay Sertel, & John L. Volakis

THURSDAY AFTERNOON 23 MARCH 2000

SESSION 15: FAST AND EFFICIENT METHODS (cont)

1440	"A Fast, High-Order Scattering Code for Solving Practical RCS Problems"	J.J. Ottusch, J.L. Visher & S.M. Wandzura
1500	**BREAK**	
1520	"An Efficient Integral Equation Based Solution Method for Simulation of Electromagnetic Fields in Inhomogeneous Dielectric (Biological) Media"	E. Bleszynski, M. Bleszynski & T. Jaroszewicz
1540	"Efficient Solution of Large-Scale Electromagnetic Eigenvalue Problems Using the Implicitly Restarted Arnoldi Method"	Daniel White & Joseph Koning
1600	"Fast Fourier Transform of Functions with Jump Discontinuities"	Guo-Xin Fan, & Qing Huo Liu
1620	"Applications of Non-Uniform Fast Transform Algorithms in Numerical Solutions of Integral Equations"	Q.H. Liu, X.M. Xu, & Z.Q. Zhang

SESSION 16: APPLICATIONS OF THE FDTD TECHNIQUE **(Parallel with Sessions 15 & 17)**
Chairs: Atef Elsherbeni and Wenhua Yu

1320	"A Non-Dissipative Staggered Fourth-Order Accurate Explicit Finite Difference Scheme for the Time-Domain Maxwell's Equations"	A. Yefet & P.G. Petropoulos
1340	"FDTD Method for Maxwell's Equation in Complex Geometries"	A. Ditkowski, K. Dridi & J.S. Hesthaven
1400	"FDTD Analysis of Tapered Meander Line Antennas for RF and Wireless Communications"	Chun-Wen Paul Huang, Atef Z. Elsherbeni Charles E. Smith
1420	"FDTD Modeling of an Electron Cyclotron Resonance Reactor Driven by an Lisitano Coil"	Gaetano Marrocco, Fernando Baardati Francesco De Marco
1440	"Modeling Microwave and Hybrid Heating Using FDTD"	J. Haala & W. Wiesbeck
1500	**BREAK**	
1520	"A Conformal Finite Difference Time Domain (CFDTD) Algorithm for Modeling Perfectly Conducting Objects"	Wenhua Yu, Raj Mittra, Dean Arakaki, & Doug Werner
1540	"A Finite-Difference Algorithm for Modeling of Conductive Wedges in 2D"	Piotr Przybyszewski
1600	"Advanced Techniques of Geometrical Modelling and CFDTD"	F. Rivas, J.P. Roa & M.F. Cátedra

SESSION 17: HYBRID TECHNIQUES **(Parallel with Sessions 15 & 16)**
Chairs: Agostino Monorchio and P. H. Pathak

1320	"A Three-Dimensional Hybrid Technique for Combining the Finite Element and Finite Difference Method in Time Domain'	Agostino Monorchio & Raj Mittra
1340	"Vertical Antenna Near-Field Computation in Complex Environments by a Hybrid Method"	F. Bardati, E. Di Giampaolo, A. Durantini, & G. Marrocco
1400	"3D EM Problem Modeling by Geometry Decomposition and Combination of the FE, FDTD and BIE Techniques"	Hendrik Rogier, Daniël De Zutter & Frank Olyslager
1420	'Hybrid FDTD-Frequency Dependent Network Simulations Using Digital Filtering Techniques"	Ian Rumsey & Melinda Piket-May
1440	"Study of Electrically-Short Thin-Wire Antennas Located in the Proximity of Inhomogeneous Scatterers Using a Hybrid NEC/FDTD Approach"	A. Rubio Bretones, R. Mittra & R. Gómez Martin
1500	**BREAK**	
1520	"A Review of Some Hybrid High Frequency and Numerical Solutions for Radiation/Scattering Problems"	P.H. Pathak & R.J. Burkholder
1540	"An Hybrid Method Combining Integral Equations and Modal Expansion Applied to the RCS Modulation of Antennas and Rotating Fans"	Andre Barka & Paul Soudais
1600	"A 2D TLM and Haar MRTD Real-Time Hybrid Connection Technique"	Masafumi Fujii, Poman P.M. So, Enqiu Hu, Wei Liu Wolfgang J. R. Hoefer

END OF TECHNICAL PAPERS

FRIDAY 24 MARCH 2000

0700 – 0730	**CONTINENTAL BREAKFAST** (For Short Course and hands-on-workshop attendees only)	**Glasgow Courtyard**
0730 – 0820	**SHORT COURSE/HANDS-ON-WORKSHOP REGISTRATION**	**Glasgow 103**
0830-1630	**SHORT COURSE #9 (Full Day)** Why is There Electromagnetic Radiation and Where Does It Come From?" John Shaeffer, Marietta Scientific Inc and Edmund K. Miller, Santa Fe, NM.	**Engr Auditorium**
0830-1630	**SHORT COURSE #10 (FULL-DAY)** "Recent Advances in Fast Algorithms for Computational Electromagnetics" Weng Cho Chew, Jianming Jin, Eric Michielssen and Jiming Song, University of Illinois at Urbana-Champaign	**Ingersoll 265**
0830-1630	**HANDS-ON-WORKSHOP #11 (FULL-DAY)** "Method of Moments (MoM) Using MATHCAD" Jovan Lebaric, Naval Postgraduate School	
0830-1630	**SHORT COURSE #12 (HALF-DAY, MORNING)** "Computational Electromagnetics using Beowulf-Cluster Computers" Tom Cwik and Daniel S. Katz, Jet Propulsion Laboratory	**Ingersoll 122**
1330-1630	**SHORT COURSE #13 (HALF-DAY, AFTERNOON)** "Multiresolution FEM: Introduction and Antenna Applications" John L. Volakis, University of Michigan, and Lars Andersen, Agilent	**Ingersoll 122**

PLEASE NOTE THAT A 10% DISCOUNT IS IN EFFECT FOR ALL WORKSHOPS TAKEN AFTER ATTENDING AN INITIAL WORKSHOP. THIS APPLIES TO THE GROUP OF WORKSHOPS FOR MATLAB AND MATHCAD.

SATURDAY 25 MARCH 2000

0700 – 0730	**CONTINENTAL BREAKFAST** (For Short Course and hands-on-workshop attendees only)	**Glasgow Courtyard**
0730 – 0820	**SHORT COURSE/HANDS-ON-WORKSHOP REGISTRATION**	**Glasgow 103**
0830-1630	**HANDS-ON-WORKSHOP #14 (FULL-DAY)** "FD/FDTD Using MATLAB" Jovan Lebaric, Naval Postgraduate School	
0830-1630	**SHORT COURSE #15 (FULL-DAY)** "An Introduction to Radar Cross Section" John Shaeffer, Marietta Scientific, Inc.	**Engr Auditorium**

SESSION 10

WAVELET AND TLM MODELING TECHNIQUES

Chairs: Wolfgang J.R. Hoefer and Peter Russer

The Implementation of A High Level (1st-order) Haar Wavelet MRTD Scheme

Enqiu Hu, Poman P.M. So, Masafumi Fujii, Wei Liu and Wolfgang J.R. Hoefer
Computational Electromagnetics Research Laboratory
Department of Electric and Computer Engineering
University of Victoria
PO BOX 3055, Victoria, British Columbia, Canada V8W 3P6
E-Mail: ehu@ece.uvic.ca

Abstract

In this paper, a 2D multiresolution time-domain (MRTD) scheme based on high level (1st-order) Haar wavelets is presented. The use of a 1st-order wavelet scheme in MRTD leads to coupled time step updating equations. The boundary conditions can be very easily and directly implemented, and the reconstructed total field distribution is smoother than the field distribution obtained with a 0-order uncoupled Haar MRTD scheme. The most important advantage of this new scheme is its potential for considerable savings in memory and computational time.

I. INTRODUCTION

Recently, the multiresolution time-domain (MRTD) approach based on wavelets has attracted the attention of many researchers in electromagnetic wave modeling. Battle-Lemarie[1], Haar[2], biorthogonal B-spline[3] and Daubechies[4,5] wavelets all have been tested as basic functions of MRTD.

The most important advantage of this new technique is its capability to provide an effective way for time and space adaptive gridding through thresholding of the field wavelet expansion coefficients. If the value of a wavelet coefficient falls below a certain threshold, it will simply be discarded. This reduces the information stored in memory, yet the accuracy of the computational results is hardly affected. As a result, the mesh appears effectively coarser at these wavelet locations. Furthermore, the position and the number of wavelet expansion coefficients with significant value change in each time step, creating a space and time adaptive dense mesh in regions of strong field variations, while maintaining a much coarser mesh elsewhere. Thus the MRTD method based on wavelets in combination with a thresholding technique leads to an enhanced spatial resolution while reducing computational expenditure.

In the case of Battle-Lemarie MRTD, when the field is sampled or injected, many terms of the field expansion coefficients must be considered by virtue of the nonlocal characteristics of the Battle-Lemarie wavelet functions. As compactly supported wavelets, Daubechies' wavelets and biorthogonal B-spline wavelets require less terms, but they still lead to greater computational effort. Moreover, the implementation of boundary conditions is very complicated for Battle-Lemarie wavelets, Daubechies' wavelets and biorthogonal B-spline wavelets MRTD schemes. In the case of 0-order Haar wavelet MRTD, it has been shown [2] that the scaling and wavelet updating equations are independent of each other. Coupling occurs only at source locations and at the boundaries. Hence, excitation and boundary conditions are usually implemented by interpolation. The resulting computational field distribution is not always smooth when the topology of the boundaries is complex.

In this paper, a 2D Multiresolution Time-Domain (MRTD) scheme based on high level (1st-order) Haar wavelets will be derived. By including 1st-order wavelets we obtain coupled MRTD updating equations everywhere, and the reconstructed total field distribution is smoother than that obtained by a 0-order uncoupled Haar MRTD scheme. The principal advantage of this new scheme is its potential to realize considerable savings in memory and computational time.

II. THEORTICAL FORMULATION

A. The Definition of the Basic Functions

We employ a definition of Haar scaling and mother wavelet functions that differs slightly from the original definition.

$$\phi(s)=\begin{cases}1 & |s|<0.5\\ 0.5 & |s|=0.5\\ 0 & elsewhere\end{cases} \tag{1a}$$

$$\psi(s)=\begin{cases}0.5 & s=-0.5\\ 1 & -0.5<s<0\\ 0 & s=0\\ -1 & 0<s<0.5\\ -0.5 & s=-0.5\\ 0 & elsewhere\end{cases} \tag{1b}$$

Each electric and magnetic field component is expanded using pulse functions $h_n(t)$ in time domain and Haar scaling functions $\phi_m(s)$ and r-order wavelet functions $\psi_m^{r,p}(s)$ in space domain, where

$$h_n(t)=\begin{cases}1 & for\ (n-0.5)\Delta t\le t<(n-0.5)\Delta t\\ 0 & elsewhere\end{cases} \tag{2a}$$

$$\phi_m(s)=\phi(\frac{s}{\Delta s}-m),\qquad s=x,y,z \tag{2b}$$

$$\psi_m^{r,p}(s)=2^{r/2}\psi(2^r(\frac{s}{\Delta s}-m)-p)\qquad r=0,p=0;r>0,p=\pm1,\pm2\quad \pm2^{r-1},s=x,y,z \tag{2c}$$

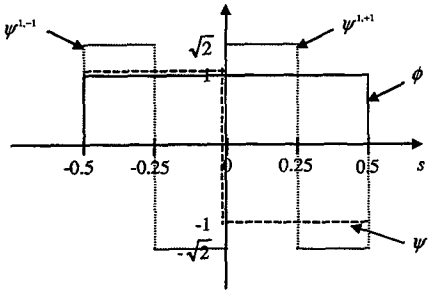


Fig. 1. 1D Haar scaling and wavelet basic functions in a field node

For 1st-order Haar wavelet MRTD the spatial basic functions in one coordinate direction for a field node are shown in Fig.1. The scaling and wavelet functions have the following important properties:

$$\left\langle \frac{\partial \phi_m(s)}{\partial s} \middle| \phi_{k+1/2}(s) \right\rangle = -\delta_{m,k} + \delta_{m,k+1} \quad (3a)$$

$$\left\langle \frac{\partial \phi_m(s)}{\partial s} \middle| \psi_{k+1/2}(s) \right\rangle = 0 \quad (4a)$$

$$\left\langle \frac{\partial \psi_m(s)}{\partial s} \middle| \phi_{k+1/2}(s) \right\rangle = 0 \quad (3b)$$

$$\left\langle \frac{\partial \psi_m(s)}{\partial s} \middle| \psi_{k+1/2}(s) \right\rangle = -\delta_{m,k} + \delta_{m,k+1} \quad (4b)$$

$$\left\langle \frac{\partial \psi_m^{1,-1}(s)}{\partial s} \middle| \phi_{k+1/2}(s) \right\rangle = \frac{\sqrt{2}}{2}\delta_{m,k} - \frac{\sqrt{2}}{2}\delta_{m,k+1} \quad (3c)$$

$$\left\langle \frac{\partial \psi_m^{1,-1}(s)}{\partial s} \middle| \psi_{k+1/2}(s) \right\rangle = \frac{\sqrt{2}}{2}\delta_{m,k} + \frac{3\sqrt{2}}{2}\delta_{m,k+1} \quad (4c)$$

$$\left\langle \frac{\partial \psi_m^{1,+1}(s)}{\partial s} \middle| \phi_{k+1/2}(s) \right\rangle = -\frac{\sqrt{2}}{2}\delta_{m,k} + \frac{\sqrt{2}}{2}\delta_{m,k+1} \quad (3d)$$

$$\left\langle \frac{\partial \psi_m^{1,+1}(s)}{\partial s} \middle| \psi_{k+1/2}(s) \right\rangle = -\frac{3\sqrt{2}}{2}\delta_{m,k} - \frac{\sqrt{2}}{2}\delta_{m,k+1} \quad (4d)$$

$$\left\langle \frac{\partial \phi_m(s)}{\partial s} \middle| \psi_{k+1/2}^{1,-1}(s) \right\rangle = \frac{\sqrt{2}}{2}\delta_{m,k} - \frac{\sqrt{2}}{2}\delta_{m,k+1} \quad (5a)$$

$$\left\langle \frac{\partial \phi_m(s)}{\partial s} \middle| \psi_{k+1/2}^{1,+1}(s) \right\rangle = -\frac{\sqrt{2}}{2}\delta_{m,k} + \frac{\sqrt{2}}{2}\delta_{m,k+1} \quad (6a)$$

$$\left\langle \frac{\partial \psi_m(s)}{\partial s} \middle| \psi_{k+1/2}^{1,-1}(s) \right\rangle = -\frac{3\sqrt{2}}{2}\delta_{m,k} - \frac{\sqrt{2}}{2}\delta_{m,k+1} \quad (5b)$$

$$\left\langle \frac{\partial \psi_m(s)}{\partial s} \middle| \psi_{k+1/2}^{1,+1}(s) \right\rangle = \frac{\sqrt{2}}{2}\delta_{m,k} + \frac{3\sqrt{2}}{2}\delta_{m,k+1} \quad (6b)$$

$$\left\langle \frac{\partial \psi_m^{1,-1}(s)}{\partial s} \middle| \psi_{k+1/2}^{1,-1}(s) \right\rangle = \delta_{m,k} - \delta_{m,k+1} \quad (5c)$$

$$\left\langle \frac{\partial \psi_m^{1,-1}(s)}{\partial s} \middle| \psi_{k+1/2}^{1,+1}(s) \right\rangle = 0 \quad (6c)$$

$$\left\langle \frac{\partial \psi_m^{1,+1}(s)}{\partial s} \middle| \psi_{k+1/2}^{1,-1}(s) \right\rangle = 0 \quad (5d)$$

$$\left\langle \frac{\partial \psi_m^{1,+1}(s)}{\partial s} \middle| \psi_{k+1/2}^{1,+1}(s) \right\rangle = \delta_{m,k} - \delta_{m,k+1} \quad (6d)$$

where $\langle f(s)|g(s)\rangle = \int_{-\infty}^{+\infty} f(s)g(s)ds$ denotes the inner product of the functions $f(s)$ and $g(s)$. δ is Dirac's delta function.

B. 1st-Order 2D MRTD Scheme

Consider Maxwell's curl equations for the TE polarization case with the propagation vector in the x-z plane and the electric field pointing in y-direction.

$$\frac{\partial E_y(x,z,t)}{\partial x} = -\mu \frac{\partial H_z(x,z,t)}{\partial t} \quad (7a)$$

$$\frac{\partial E_y(x,z,t)}{\partial z} = \mu \frac{\partial H_x(x,z,t)}{\partial t} \quad (7b)$$

$$\frac{\partial H_x(x,z,t)}{\partial z} - \frac{\partial H_z(x,z,t)}{\partial x} = \varepsilon \frac{\partial E_y(x,z,t)}{\partial t} + \sigma E_y(x,z,t) + J_y(x,z,t) \quad (7c)$$

The basic functions in each 2D field node on the x-z plane are tensor products of the sum of scaling and wavelet functions multiplied by the time pulse function as follows:

$$\phi_i(x)\phi_k(z)h_n(t), \quad (8a) \qquad \phi_i(x)\psi_k(z)h_n(t) \quad (8b)$$

$$\phi_i(x)\psi_k^{1,-1}(z)h_n(t) \quad (8c) \qquad \phi_i(x)\psi_k^{1,+1}(z)h_n(t) \quad (8d)$$

$$\psi_i(x)\phi_k(z)h_n(t) \quad (8e) \qquad \psi_i(x)\psi_k(z)h_n(t) \quad (8f)$$

$$\psi_i(x)\psi_k^{1,-1}(z)h_n(t) \quad (8g) \qquad \psi_i(x)\psi_k^{1,+1}(z)h_n(t) \quad (8h)$$

$$\psi_i^{1,-1}(x)\phi_k(z)h_n(t) \quad (8i) \qquad \psi_i^{1,-1}(x)\psi_k(z)h_n(t) \quad (8j)$$

$$\psi_i^{1,-1}(x)\psi_k^{1,-1}(z)h_n(t) \quad (8k) \qquad \psi_i^{1,-1}(x)\psi_k^{1,+1}(z)h_n(t) \quad (8l)$$

$$\psi_i^{1,+1}(x)\phi_k(z)h_n(t) \quad (8m) \qquad \psi_i^{1,+1}(x)\psi_k(z)h_n(t) \quad (8n)$$

$$\psi_i^{1,+1}(x)\psi_k^{1,-1}(z)h_n(t) \quad (8o) \qquad \psi_i^{1,+1}(x)\psi_k^{1,+1}(z)h_n(t) \quad (8p)$$

The field components are expanded in terms of the above basic functions

$$F_s(x,z,t)=\sum_{n=-\infty}^{\infty}h_{n+n_0}(t)\times\left\{\sum_{i=-\infty}^{\infty}\left[{}_{n+n_0}^{s}F_{i+i_0}^{\phi}\phi_{i+i_0}(x)+\sum_{r=0}^{\infty}\sum_{p}{}_{n+n_0}^{s}F_{i+i_0}^{\psi^{r,p}}\psi_{i+i_0}^{r,p}(x)\right]\right\}$$
$$\times\left\{\sum_{k=-\infty}^{\infty}\left[{}_{n+n_0}^{s}F_{k+k_0}^{\phi}\phi_{k+k_0}(z)+\sum_{r=0}^{\infty}\sum_{p}{}_{n+n_0}^{s}F_{k+k_0}^{\psi^{r,p}}\psi_{k+k_0}^{r,p}(z)\right]\right\} \quad (9a)$$

$$r=0,p=0;r>0,p=\pm1,\pm2\cdots\pm2^{r-1} \quad (9b)$$

$${}_{n+n_0}^{s}F_{i+i_0,k+k_0}^{\xi\varsigma}={}_{n+n_0}^{s}F_{i+i_0}^{\xi}\times{}_{n+n_0}^{s}F_{k+k_0}^{\varsigma} \quad F=E,H,J;\ s=x,y,z;\ \xi=\phi,\psi;\ \varsigma=\phi,\psi \quad (9c)$$

$$for\ E_y(x,z,t),\ F=E,\ s=y,\ n_0=0,\ i_0=0,\ k_0=0 \quad (9d)$$

$$for\ J_y(x,z,t),\ F=J,\ s=y,\ n_0=0,\ i_0=0,\ k_0=0 \quad (9e)$$

$$for\ H_x(x,z,t),\ F=H,\ s=x,\ n_0=1/2,\ i_0=0,\ k_0=1/2 \quad (9f)$$

$$for\ H_z(x,z,t),\ F=H,\ s=z,\ n_0=1/2,\ i_0=1/2,\ k_0=0 \quad (9g)$$

Subsequently, each field component is substituted in the Maxwell's component equations [7a-c], and following Galerkin's procedure and applying the Method of Moment, the resulting expressions are tested with the basic functions. By virtue of the inner product properties of the basic functions, we can obtain the time iterative difference equations for all expansion coefficients of all field components. The following are four examples of those equations.

$${}_{n+1}^{y}E_{i,k}^{\phi\phi}=\frac{2\varepsilon_{i,k}-\sigma_{i,k}\Delta t}{2\varepsilon_{i,k}+\sigma_{i,k}\Delta t}{}_{n}^{y}E_{i,k}^{\phi\phi}\frac{2\Delta t}{2\varepsilon_{i,k}+\sigma_{i,k}\Delta t}{}_{n+1/2}^{y}J_{i,k}^{\phi\phi}+\frac{2\Delta t}{(2\varepsilon_{i,k}+\sigma_{i,k}\Delta t)\Delta x\Delta z}$$
$$\times\left\{\begin{array}{l}-\Delta z\left[({}_{n+1/2}^{z}H_{i+1/2,k}^{\phi\phi}-{}_{n+1/2}^{z}H_{i-1/2,k}^{\phi\phi})+\frac{\sqrt{2}}{2}(-{}_{n+1/2}^{z}H_{i+1/2,k}^{\psi^{1,-1}\phi}+{}_{n+1/2}^{z}H_{i-1/2,k}^{\psi^{1,-1}\phi}+{}_{n+1/2}^{z}H_{i+1/2,k}^{\psi^{1,+1}\phi}-{}_{n+1/2}^{z}H_{i-1/2,k}^{\psi^{1,+1}\phi})\right]\\+\Delta x\left[({}_{n+1/2}^{x}H_{i,k+1/2}^{\phi\phi}-{}_{n+1/2}^{x}H_{i,k-1/2}^{\phi\phi})+\frac{\sqrt{2}}{2}(-{}_{n+1/2}^{x}H_{i,k+1/2}^{\phi\psi^{1,-1}}+{}_{n+1/2}^{x}H_{i,k-1/2}^{\phi\psi^{1,-1}}+{}_{n+1/2}^{x}H_{i,k+1/2}^{\phi\psi^{1,+1}}-{}_{n+1/2}^{x}H_{i,k-1/2}^{\phi\psi^{1,+1}})\right]\end{array}\right\} \quad (10a)$$

$${}_{n+1}^{y}E_{i,k}^{\phi\psi}=\frac{2\varepsilon_{i,k}-\sigma_{i,k}\Delta t}{2\varepsilon_{i,k}+\sigma_{i,k}\Delta t}{}_{n}^{y}E_{i,k}^{\phi\psi}\frac{2\Delta t}{2\varepsilon_{i,k}+\sigma_{i,k}\Delta t}{}_{n+1/2}^{y}J_{i,k}^{\phi\psi}+\frac{2\Delta t}{(2\varepsilon_{i,k}+\sigma_{i,k}\Delta t)\Delta x\Delta z}$$
$$\times\left\{\begin{array}{l}-\Delta z\left[({}_{n+1/2}^{z}H_{i+1/2,k}^{\phi\psi}-{}_{n+1/2}^{z}H_{i-1/2,k}^{\phi\psi})+\frac{\sqrt{2}}{2}(-{}_{n+1/2}^{z}H_{i+1/2,k}^{\psi^{1,-1}\psi}+{}_{n+1/2}^{z}H_{i-1/2,k}^{\psi^{1,-1}\psi}+{}_{n+1/2}^{z}H_{i+1/2,k}^{\psi^{1,+1}\psi}-{}_{n+1/2}^{z}H_{i-1/2,k}^{\psi^{1,+1}\psi})\right]\\+\Delta x\left[({}_{n+1/2}^{x}H_{i,k+1/2}^{\phi\psi}-{}_{n+1/2}^{x}H_{i,k-1/2}^{\phi\psi})+\frac{\sqrt{2}}{2}(3{}_{n+1/2}^{x}H_{i,k+1/2}^{\phi\psi^{1,-1}}+{}_{n+1/2}^{x}H_{i,k-1/2}^{\phi\psi^{1,-1}}-{}_{n+1/2}^{x}H_{i,k+1/2}^{\phi\psi^{1,+1}}-3{}_{n+1/2}^{z}H_{i,k-1/2}^{\phi\psi^{1,+1}})\right]\end{array}\right\} \quad (10b)$$

$$
{}_{n+1}{}^{y}E_{i,k}^{\phi\psi^{1,-1}} = \frac{2\varepsilon_{i,k}-\sigma_{i,k}\Delta t}{2\varepsilon_{i,k}+\sigma_{i,k}\Delta t}\,{}_{n}{}^{y}E_{i,k}^{\phi\psi^{1,-1}} - \frac{2\Delta t}{2\varepsilon_{i,k}+\sigma_{i,k}\Delta t}\,{}_{n+1/2}{}^{y}J_{i,k}^{\phi\psi^{1,-1}} + \frac{2\Delta t}{(2\varepsilon_{i,k}+\sigma_{i,k}\Delta t)\Delta x\Delta z}
$$

$$
\times\left\{\begin{array}{l}
-\Delta z\left[\left({}_{n+1/2}{}^{z}H_{i+1/2,k}^{\phi\psi^{1,-1}} - {}_{n+1/2}{}^{z}H_{i-1/2,k}^{\phi\psi^{1,-1}}\right) + \dfrac{\sqrt{2}}{2}\left(-{}_{n+1/2}{}^{z}H_{i+1/2,k}^{\psi^{1,-1}\psi^{1,-1}} + {}_{n+1/2}{}^{z}H_{i-1/2,k}^{\psi^{1,-1}\psi^{1,-1}} + {}_{n+1/2}{}^{z}H_{i+1/2,k}^{\psi^{1,+1}\psi^{1,-1}} - {}_{n+1/2}{}^{z}H_{i-1/2,k}^{\psi^{1,+1}\psi^{1,-1}}\right)\right] \\
+\Delta x\left[\left(-{}_{n+1/2}{}^{x}H_{i,k+1/2}^{\phi\psi^{1,-1}} + {}_{n+1/2}{}^{x}H_{i,k-1/2}^{\phi\psi^{1,-1}}\right) + \dfrac{\sqrt{2}}{2}\left(-{}_{n+1/2}{}^{x}H_{i,k+1/2}^{\phi\phi} + {}_{n+1/2}{}^{x}H_{i,k-1/2}^{\phi\phi} - {}_{n+1/2}{}^{x}H_{i,k+1/2}^{\phi\psi} - 3\,{}_{n+1/2}{}^{z}H_{i,k-1/2}^{\phi\psi}\right)\right]
\end{array}\right\} \tag{10c}
$$

$$
{}_{n+1}{}^{y}E_{i,k}^{\phi\psi^{1,+1}} = \frac{2\varepsilon_{i,k}-\sigma_{i,k}\Delta t}{2\varepsilon_{i,k}+\sigma_{i,k}\Delta t}\,{}_{n}{}^{y}E_{i,k}^{\phi\psi^{1,+1}} - \frac{2\Delta t}{2\varepsilon_{i,k}+\sigma_{i,k}\Delta t}\,{}_{n+1/2}{}^{y}J_{i,k}^{\phi\psi^{1,+1}} + \frac{2\Delta t}{(2\varepsilon_{i,k}+\sigma_{i,k}\Delta t)\Delta x\Delta z}
$$

$$
\times\left\{\begin{array}{l}
-\Delta z\left[\left({}_{n+1/2}{}^{z}H_{i+1/2,k}^{\phi\psi^{1,+1}} - {}_{n+1/2}{}^{z}H_{i-1/2,k}^{\phi\psi^{1,+1}}\right) + \dfrac{\sqrt{2}}{2}\left(-{}_{n+1/2}{}^{z}H_{i+1/2,k}^{\psi^{1,-1}\psi^{1,+1}} + {}_{n+1/2}{}^{z}H_{i-1/2,k}^{\psi^{1,-1}\psi^{1,+1}} + {}_{n+1/2}{}^{z}H_{i+1/2,k}^{\psi^{1,+1}\psi^{1,+1}} - {}_{n+1/2}{}^{z}H_{i-1/2,k}^{\psi^{1,+1}\psi^{1,+1}}\right)\right] \\
+\Delta x\left[\left(-{}_{n+1/2}{}^{x}H_{i,k+1/2}^{\phi\psi^{1,+1}} + {}_{n+1/2}{}^{x}H_{i,k-1/2}^{\phi\psi^{1,+1}}\right) + \dfrac{\sqrt{2}}{2}\left({}_{n+1/2}{}^{x}H_{i,k+1/2}^{\phi\phi} - {}_{n+1/2}{}^{x}H_{i,k-1/2}^{\phi\phi} + 3\,{}_{n+1/2}{}^{x}H_{i,k+1/2}^{\phi\psi} + {}_{n+1/2}{}^{x}H_{i,k-1/2}^{\phi\psi}\right)\right]
\end{array}\right\} \tag{10d}
$$

C. Boundary Conditions

Firstly consider perfect electric conductor (PEC) boundary conditions. According to the image principle, PEC walls can be modeled by imposing odd symmetry conditions for the tangential electric field. For the 0-order Haar wavelet MRTD scheme, the scaling and wavelet expansion coefficients are not coupled at the inner computational nodes, but only at the boundaries and at source nodes. Therefore, the PEC boundary conditions are usually implemented by combining scaling and wavelet expansion coefficients at the boundary nodes such that the total tangential electric field at those nodes is zero. In program implementation, the expansion coefficients are obtained by using the image principle and interpolation from the inner nodes so that the tangential electric field varies smoothly in front of boundary.

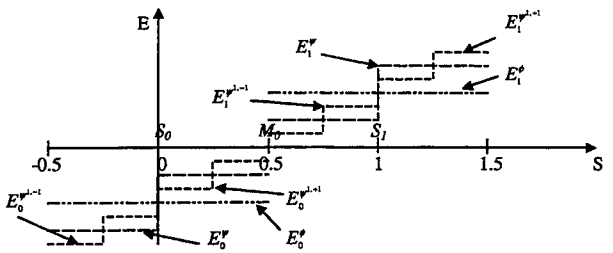


Fig.2. The left-hand side PEC boundary in one-dimensional case

For 1st-order Haar wavelet MRTD schemes, as can be seen from the above time iterative difference equations of the expansion coefficients, the scaling and wavelet expansion coefficients are coupled. All expansion coefficients at the PEC boundary nodes can simply be set. For simplicity, the

implementation of PEC boundary conditions is described in the one-dimensional case, the results can be extended directly to the two-dimensional case. The actual position of the boundary is one half of the mesh size away from the center of the boundary cell. Fig. 2 shows the left-hand side boundary of the computational domain. S_0 is the PEC boundary node. S_1 is the first electric field node from S_0 in the inner computational region. The precise boundary location is at M_0. The expansion coefficients of the node S_0 can be enforced by using those of the node S_1: $E_0^{\phi} = -E_1^{\phi}$, $E_0^{\psi} = E_1^{\psi}$, $E_0^{\psi^{i,-1}} = E_1^{\psi^{i,+1}}$, $E_0^{\psi^{i,+1}} = E_1^{\psi^{i,-1}}$. Hence, it is straightforward to implement PEC boundary conditions in this scheme.

Perfect magnetic conductor (PMC) boundary conditions can be imposed with equal ease. Perfectly Matched Layer (PML) absorbing boundary conditions can be implemented in a manner similar to the traditional FDTD method. The only difference is that each expansion coefficient must be handled independently in the PML.

D. Stability Condition

The stability condition for the high level wavelet 2D-MRTD scheme is

$$\Delta t \le \frac{1}{c\sqrt{(\frac{2^{r_x}}{\Delta x})^2 + (\frac{2^{r_z}}{\Delta z})^2}} \tag{11}$$

where c is the wave propagation velocity. r_x and r_z are the maximum order of wavelets in x and z direction respectively. Due to the use of 1st-order wavelets, the spatial discretization intervals Δx and Δz are four times greater than those of an equivalent FDTD grid. The 1st-order Haar wavelet MRTD thus yields the same space resolution as FDTD with a time step that is two times greater than that of FDTD. Therefore, when modeling a process for a given time duration, this new scheme needs only about 50% of the number of time steps required by the conventional FDTD.

E. Thresholding Technique

Thresholding is the most promising technique for reducing memory requirements. It reduces the amount of stored information by omitting expansion coefficients that are smaller than a threshold value. When implementing the thresholding technique, the field coefficients must be evaluated and checked against the threshold value at every time step. This will increase computational overhead and may lead to a larger cumulative error. Therefore, the tradeoff between computational efficiency and accuracy should be taken into consideration. An optimum procedure must be found that reduces memory requirements and maintains computational efficiency at the same time.

In our 1st-order Haar wavelet MRTD scheme, thresholding technique is implemented by combining a relative and an absolute thresholding procedure. The relative thresholding compares the wavelet expansion coefficients to a given fraction of the scaling expansion coefficient at the same cell and at each time step. All wavelet expansion coefficients that fall below this threshold value are eliminated from the subsequent calculations. When the scaling expansion coefficient itself is very small, the absolute threshold procedure is employed; the absolute threshold value is usually set to a fraction of the maximum field value at the source. Both thresholding procedures do not add any significant overhead in execution time. In our program implementation, a dynamic allocating array is used to save all scaling and wavelet expansion coefficients for each field node. At the same time, a flag variable must be added to record what wavelet expansion coefficients are saved in the above array. The array and the flag variable must be modified at each time step.

III. NUMERICAL VALIDATION

To validate this approach, we have performed two numerical examples.

Firstly, four simple air-filled square resonator cavities for which analytical solutions are available, are solved and compared with the FDTD and the 0-order Haar wavelet MRTD methods. The dimensions of these cavities are shown in Table I. To achieve the same order of computational accuracy, the same background mesh is used for all methods in each cavity. But the cell size of the 0-order Haar wavelet MRTD is twice that of FDTD while the cell size of the 1st-order Haar wavelet MRTD is four times that of FDTD. The computational results are shown in Table I. The errors of the 0-order Haar wavelet MRTD is a little larger than those of FDTD, but the results of the 1st-order Haar wavelet MRTD is almost the same as those of FDTD. At the same time, we have found that the waveform of the reconstructed field with 1-order Haar wavelet MRTD is much smoother. Thus the results indicate that 1-order Haar wavelet MRTD is much accurate than 0-order Haar wavelet MRTD even using the same accuracy meshes.

Table I. Comparison of the lowest resonant frequencies computed with different methods

Cavities sizes (mm×mm)	Analytical value (GHz)	FDTD			0-order Haar wavelet MRTD			1st-order Haar wavelet MRTD		
		Mesh size	Value (GHz)	Relative error	Mesh size	Value (GHz)	Relative error	Mesh size	Value (GHz)	Relative error
16×24	11.2598	16×24	11.2585	0.0115%	8×12	11.2570	0.0273%	4× 6	11.2581	0.0151%
16×32	10.4746	16×32	10.4711	0.0334%	8×16	10.4575	0.1632%	4× 8	10.4702	0.0420%
16×48	9.8755	16×48	9.8701	0.0547%	8×24	9.8515	0.2430%	4×12	9.8685	0.0709%
16×64	9.6571	16×64	9.6510	0.0631%	8×32	9.6298	0.2827%	4×16	9.6487	0.0988%

As the second example, a WR28 waveguide bandpass filter is analyzed to investigate the effect of thresholding on the accuracy and the memory saving. The waveguide is terminated at both ends by PML boundary conditions. The model is excited with a modulated Gaussian waveform source. Fig. 3 shows the total field distribution obtained with 1st-order Haar wavelet MRTD without thresholding at time $4000\Delta t$. Fig. 4 shows the computed S_{11} and S_{21} parameters with 1st-order Haar wavelet MRTD.

The memory saving is quantified by the wavelet expansion coefficient compression rate defined as

$$\alpha = \frac{\textit{Number of wavelet expansion coefficients omitted by thresholding}}{\textit{Total Number of scaling and wavelet expansion coefficients}} \times 100\%$$

Table II gives the computed resonant frequencies and memory saving obtained by using 1st order Haar wavelet MRTD (at time step 8000) and 0-order Haar wavelet MRTD (at time step 8000) with different threshold values. For comparison, the results obtained with TLM are also listed. The same background mesh is used for all three methods. As can seen from table II, 1st-order Haar wavelet MRTD can save much more memory, it is about 1.5 times that of 0-order Haar wavelet MRTD. The optimal relative threshold fraction is about 0.01%, and large memory savings (about 74%) are attainable by conserving a reasonable accuracy.

Table II. Comparison of frequencies and memory savings obtained with different methods

Relative Threshold fractions	TLM		0-order Haar wavelet MRTD			1st-order Haar wavelet MRTD		
	f_1 (GHz)	f_2 (GHz)	f_1 (GHz)	f_2 (GHz)	α (%)	f_1 (GHz)	f_2 (GHz)	α (%)
0.001%	31.2625	31.9449	31.5456	32.2330	41.35	31.3412	32.0236	65.45
0.005%			31.5572	32.2457	45.61	31.3471	32.0291	69.73
0.010%			31.5897	32.2789	49.58	31.3587	32.0413	73.95
0.050%			31.9175	32.6451	53.85	31.5379	32.2552	77.87

IV. CONCLUSIONS

A 2D 1st-order Haar wavelet multiresolution time-domain (MRTD) has been implemented. There are 4 basic functions for representing EM fields on each node in each coordinate direction by including 1st-order wavelets in MRTD. The new MRTD time step updating equations are coupled everywhere in the computational domain. PEC and PMC boundary conditions can be very easily and directly implemented without reducing computational accuracy. The reconstructed total field distribution is smoother than fields computed with a 0-order uncoupled Haar MRTD scheme. The most important advantage of this new scheme is its potential for considerable savings in memory and computational time. The presented scheme can be directly extended to three space dimensions.

REFERENCES

[1] M. Krumpholz, L. P. B. Katehi, "MRTD: New Time Domain Scheme Based on Multiresolution Analysis", *IEEE Trans. Microwave Theory and Tech.*, vol. 44, no. 4, pp. 555-571, April 1996.

[2] Masafumi Fujii and W. J.R. Hoefer, "A Three-Dimensional Haar-Wavelet-Based Multiresolution Analysis Similar to the FDTD Method-Derivation and Application", *IEEE Trans. Microwave Theory and Tech.*, vol. 46, no. 12, pp. 2463-2475, Dec. 1998.

[3] M. Aidam and P. Russer, "New High Order Time-Stepping Schemes for Finite Differences", *15th Annual Review of Progress in Applied Computational Electromagnetics*, Naval postgraduate School, Monterey, CA, pp. 578-585, Mar. 1998.

[4] M. Werthen and I. Wolff, "A Novel Wavelet Based Time Domain Simulation Approach", *IEEE Microwave and Guided Wave Letters*, vol. 6, no. 12, pp. 438-440, Dec. 1996.

[5] Y.W. Cheong, Y. M. Lee, K. H. Ra, J. G. Kang and C. C. Shin, "Wavelet-Galerkin Scheme of Time-Dependent Inhomogeneous Electromagnetic Problems", *IEEE Microwave and Guided Wave Letters*, vol. 9, no. 8, pp. 297-299, Aug. 1999.

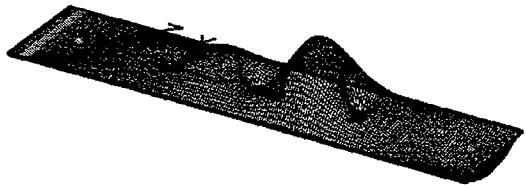


Fig. 3. The total field distribution obtained with 1st-order MRTD without thresholding at time 8000Δt.

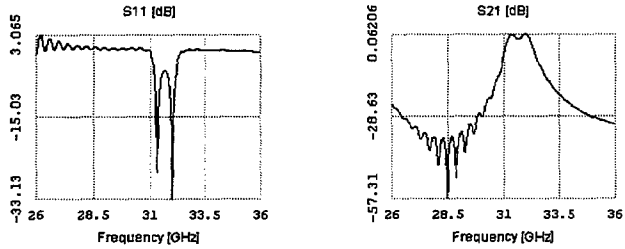


Fig. 4. S_{11} and S_{21} parameters obtained with 1st-order MRTD without threshold at time 8000Δt.

Multi-Resolution Based TLM Technique Using Haar Wavelets

Ismael Barba*, Jose Represa*, Masafumi Fujii, Wolfgang J.R. Hoefer****

*Dpto. Electricidad y Electrónica.
Univ. Valladolid
47011 Valladolid – SPAIN
Tel: +34 983 423224
Fax: +34 983 423217
E-Mail: ibarba@ee.uva.es, jrepresa@ee.uva.es

**Department of Electrical and Computer Engineering
Univ. of Victoria. P.O. Box 3055
Victoria B.C.
CANADA – V8W 3P6
Tel: +1 250 721 6025
Fax: +1 250 721 6230
E-Mail: fujii@ece.uvic.ca, whoefer@ece.uvic.ca

Abstract. **–A first Haar-wavelet based multi-resolution formulation of the TLM method is proposed. The technique is derived for the simplest 1-D case. To validate it, we have computed the resonant frequencies of a 1-D resonator bounded by two electric walls. Results have been compared with resonant frequencies obtained by the traditional TLM method, and with the analytical values.**

I INTRODUCTION

Multi-resolution time-domain (MRTD) techniques have recently been used to solve electromagnetic problems, using both Battle-Lemarie [1] and Haar [2] wavelets. They have usually been developed following the traditional FDTD update formalism.

In this paper, we have formulated a Haar-based multi-resolution technique in terms of the TLM method. In this derivation we have taken advantage of the equivalence between TLM and FDTD and thus capitalized on previous work performed with FDTD.

II FORMULATION

II.a. 1-D MRTD Basic Functions and Algorithm.

The Haar wavelet formulation has the advantage over other wavelet formulations that the resulting algorithm is similar to the traditional FDTD equations. However, in the multi-resolution method the equations are computed independently for each basis function. We can expand each field component in a combination of the Haar scaling (ϕ) and wavelet (ψ) functions [3]:

$$E_y(\bar{r},t)=\sum_{i=1}^{I}\sum_{n=1}^{N} h_n(t)\cdot\left\{{}^{y}_{n}E_i^{\phi}\cdot\phi_i(x)+{}^{y}_{n}E_i^{\psi}\cdot\psi_i(x)\right\} \qquad (1)$$

The notation is that used in [2], but reduced to one space dimension. We can expand the magnetic field (H_z) in orthonormal basis functions as well. If we substitute each component in Maxwell's equations, expressions identical to the traditional FDTD update equations are obtained, and they are formulated independently for each basis function coefficient.

II.b. 1-D FDTD-TLM Equivalence.

It is well known that the TLM method [4] is based on the isomorphism between Maxwell's equations and transmission line equations: the propagation of voltage and current impulses through a mesh of transmission lines is computed, yielding the equivalent electric and magnetic field components. The usual identities between TLM and field quantities are:

$$E \equiv V,\ I \equiv H \tag{2}$$

For example, the discrete voltage pulses at the nodes of a TLM mesh are given by:

$$V(\bar{r},t) = \sum_{i=1}^{I}\sum_{n=1}^{N} {}_{n}V_i \delta_n(t)\delta_i(x) \tag{3}$$

where $\delta_n(t)$, $\delta_i(x)$ are Dirac pulses at $t=n\Delta t$, $x=i\Delta x$, respectively. Theses voltage samples are equivalent to the discrete electric field samples:

$$E(\bar{r},t) = \sum_{i=1}^{I}\sum_{n=1}^{N} {}_{n}E_i h_n(t)\phi_n(x) \tag{4}$$

that can be computed and updated with FDTD. However, since the FDTD scheme has an equivalent TLM formulation, both algorithms should give the same result. If we now apply a Haar wavelet decomposition to the field in Eq. (4), we obtain the usual MRTD model in terms of scaling and wavelet functions [3]. Every set of basis functions is calculated independently with the FDTD updating procedure. By virtue of the equivalence given in Eq. (2), two separate TLM processes can be employed, one for each term of the field in Eq. (1). For example, in figures 1 and 2 the decomposition of a sinusoidal electric field (the first resonant mode between two parallel electric walls) is shown:

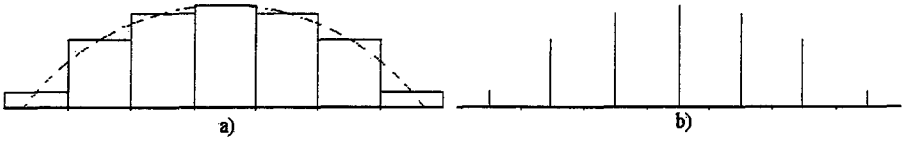


Figure 1. Scaling functions for a) Electrical Field b) Equivalent TLM mesh voltage.

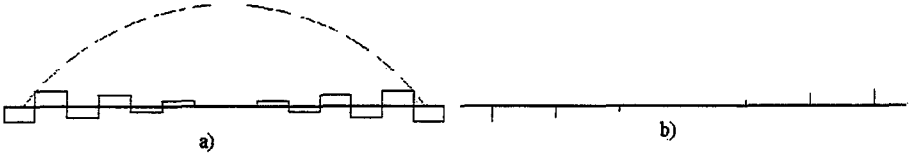


Figure 2. Wavelet functions: a) Electric Field wavelet functions. b) Equivalent pulses in the second TLM mesh.

II.b. Boundary Conditions.

As in FDTD-based MRTD, boundary conditions should be applied to the whole field/voltage, involving thus both TLM meshes. This can be handled in two ways:

a) An equivalent circuit, connecting both TLM meshes, can be calculated.
b) A condition for the total field can be applied at each boundary node to calculate the reflected pulses in the transmission lines.

To preserve the analogy with FDTD-based MRTD, we have employed the second option. For example, for a PEC wall placed in i=1, the voltage impulses incident on the node at i=1 in both TLM meshes are shown in figure 3.

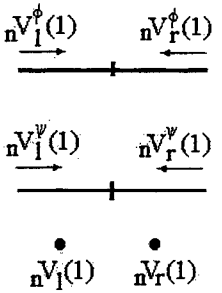


Figure 3. Incident pulses in both (scaling and wavelet equivalent) transmission lines, for i=1.

In this figure, $_nV_l^{\phi}(1)$ is the pulse incident from the left in the TLM mesh for the scaling function, for i=1, $_nV_r^{\phi}(1)$ is the pulse incident from the right in the same node. $_nV_l(1)$ is the total voltage in the left side of the cell ($_nV_l(1)=_nV^{\phi}(1)-_nV^{\psi}(1)$ equivalent to $^yE_l^{\phi}-^yE_l^{\psi}$), while $_nV_r(1)$ is the total field in the right side of the cell. Computing both fields, we obtain:

$$\begin{aligned} {}_nV_l(1) &= {}_nV^{\phi}(1)+{}_nV^{\psi}(1) = {}_nV_l^{\phi}(1)+{}_nV_r^{\phi}(1)+{}_nV_l^{\psi}(1)+{}_nV_r^{\psi}(1) \\ {}_nV_r(1) &= {}_nV^{\phi}(1)-{}_nV^{\psi}(1) = {}_nV_l^{\phi}(1)+{}_nV_r^{\phi}(1)-{}_nV_l^{\psi}(1)-{}_nV_r^{\psi}(1) \end{aligned} \tag{5}$$

Coefficients $_nV_r^{\phi}(1)$ and $_nV_r^{\psi}(1)$ can be calculated by means of the transmission coefficients between neighboring nodes. $_nV_l^{\phi}(1)$ and $_nV_l^{\psi}(1)$ can be calculated employing Eq. (5) and the fact that, if we place the PEC wall in $x=\Delta x/4$, $_nV_l(1)=0$. To obtain a second condition, we can require that there be no dispersion in the reflected signal. Finally, the equations for the PEC wall would be:

$$\begin{aligned} {}_nV_l^{\phi}(1) &= \frac{-{}_{n-1}V_r^{\phi}(1)+{}_{n-1}V_r^{\psi}(1)-{}_nV_r^{\phi}(1)-{}_nV_r^{\psi}(1)}{2} \\ {}_nV_l^{\psi}(1) &= \frac{{}_{n-1}V_r^{\phi}(1)-{}_{n-1}V_r^{\psi}(1)-{}_nV_r^{\phi}(1)-{}_nV_r^{\psi}(1)}{2} \end{aligned} \tag{6}$$

A similar reasoning would give us the boundary conditions for i=I.

III RESULTS

Resonant frequencies of a 1D resonator bounded by two electrical walls have been calculated. The separation between both walls is 0.3 m. That means the theoretical frequencies should be 0.5 - 1 - 1.5 - 2 ... GHz.

A first simulation has been performed by dividing the space between the walls into 30 cells, i.e., taking into account the different positions of the PEC walls in both schemes. The cell size of the TLM mesh is 0.01 m, and that of the MR-TLM is 0.0102m, so that the time steps are Δt=33.3 and 33.9 ps, respectively. We have performed 2000 time steps, employing both the traditional TLM method and our Multi-resolutive TLM formulation. Results are compared in table 1 and figure 4.

Table 1: Resonant frequencies in GHz of a 1D resonator bounded by two electric walls, discretized into 30 cells.

TLM	.50	1.00	1.50	2.00	2.50	3.00
MR-TLM	.50	1.00	1.50	2.00	2.50	3.00

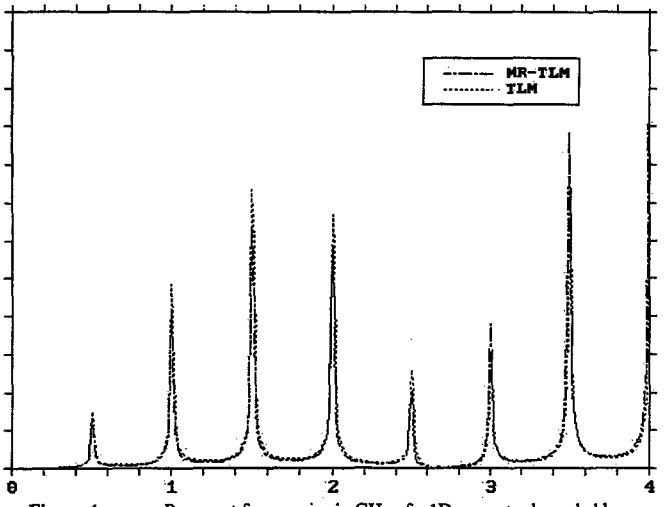


Figure 4. Resonant frequencies in GHz of a 1D resonator bounded by two electric walls, discretized into 30 cells.

If we reduce the number of cells between the two walls, a larger difference between both methods should be found in the subsequent figure. For example, if the number of nodes is 15 (i.e. Δx=0.02/0.0207m in every case, and Δt=66.7/69.0 ps). Results are shown in table 2, and figure 5.

Table 2: Resonant frequencies in GHz of a 1D resonator bounded by two electric walls, discretized into 15 cells.

TLM	.50	1.00	1.50	2.00	2.50	------	3.50
MR-TLM	.50	1.00	1.50	2.00	2.50	3.00	3.50

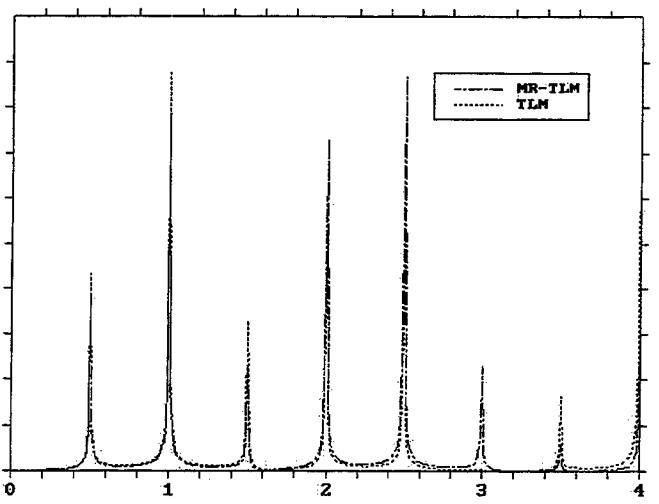


Figure 5: Resonant frequencies in GHz of a 1D resonator bounded by two electric walls, discretized into 15 cells.

A stronger reduction of the number of cells (10 nodes, i.e. Δx=0.03/0.0316m, Δt=100/105.3 ps), would lead to the results shown in table 3 and figure 6.

Table 3: Resonant frequencies in GHz of a 1D resonator bounded by two electric walls, discretized into 10 cells.

TLM	.50	1.00	1.50	-----	2.50	3.00
MR-TLM	.50	1.00	1.50	2.00	2.50	3.00

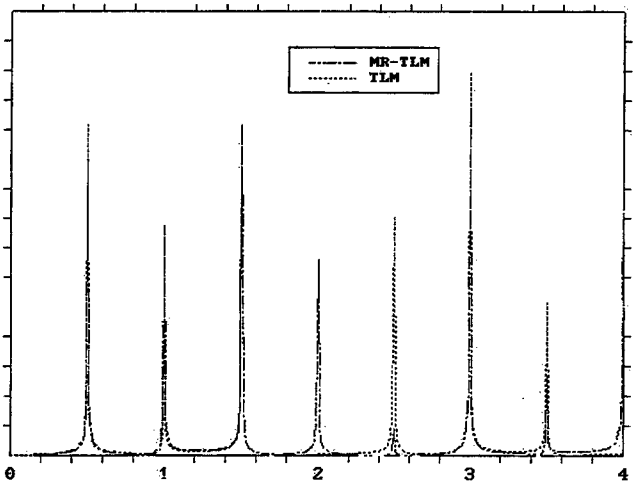


Figure 6: Resonant frequencies in GHz of a 1D resonator bounded by two electric walls, discretized into 10 cells.

IV CONCLUSION.

Haar wavelets have been applied to obtain a multi-resolution formulation of the TLM method. Resonant frequencies of a one-dimensional resonator formed by two electric walls have been computed to validate the 1D algorithm and boundary PEC boundary condition. Since a 1D TLM simulation is dispersion free, any error in the obtained frequencies could only be caused by errors in the sampling of the results and the DFT employed, provided that the boundary conditions and the algorithms themselves (TLM and MR-TLM) are properly formulated and implemented. Differences in the shape of spectral lobes are due to the different electrical position of the output probe (in the middle of a TLM cell, and at ¼ or ¾ of a MR-TLM cell, respectively).

V REFERENCES.

[1] M. Krumpholz and L.T.B. Katehi, "MRTD: New time-domain schemes based on multiresolution analysis", *IEEE Trans. Microwave Theory Tech.*, vol. 44, no. 4 pp. 555-571, Apr. 1996.

[2] M. Fujii and W. J.R. Hoefer, "A 3D Haar-Wavelet-Based Multiresolution Analysis Similar to the FDTD Method –Derivation and Application-", *IEEE Trans. Microwave Theory Tech.* Vol 46, No. 12, Dec. 1998.

[3] I. Daubechies, *Ten lectures on wavelets*, SIAM Rev, Philadelphia, PA, 1992.

[4] W. J.R. Hoefer, "The Transmission Line Matrix (TLM) Method". *Numerical Techniques for Microwave and Millimeter-Wave Passive Structures*". T. Itoh (Editor), pp. 496-591, John Wiley & Sons, New York 1989.

Formulation and Study of an Arbitrary Order Haar Wavelet Based Multiresolution Time Domain Technique

Costas D. Sarris and Linda P. B. Katehi
Radiation Laboratory
Department of Electrical Engineering and Computer Science
University of Michigan, Ann Arbor, 48109-2122 MI

Abstract

The use of wavelet bases for the discretization of Maxwell's equations via the Moment Method has led to the development of novel time domain schemes with inherently adaptive properties. Due to the latter, such schemes have attained significant economy in memory requirements when applied to electromagnetic and circuit problems. For robust, adaptive schemes, arbitrary order wavelet formulations have to be employed, in order to provide the capability of modeling arbitrarily fine geometric details of a given structure. In addition, one of the remaining challenges for multiresolution time domain techniques is to efficiently incorporate non-uniform time discretization in order to maximize their performance in terms of CPU time requirements. Both questions are addressed in this paper for the case of Haar wavelet basis.

1. INTRODUCTION

Time domain differential methods are becoming increasingly popular among the electromagnetic community as a consequence of their versatility and their ability to provide simulation results that are intuitively meaningful to circuit designers and microwave engineers. However, the poor scalability of the computational demands that methods such as the Finite Difference Time Domain (FDTD [1]) or the Transmission Line Matrix (TLM [2]) method present, has posed the significant question of deriving new techniques that can perform reasonably accurate computations, with computational requirements that can be met by nowadays computer performance.

In general, non-uniform meshing, based on adaptivity criteria can significantly improve the efficiency of a numerical scheme. Still, a remaining problem comes from the typically over-restrictive limitation that the minimum cell size of the grid imposes on the time step [3]. For this problem to be resolved, computationally burdensome techniques such as extrapolation or interpolation of field quantities at different mesh interfaces have been proposed in the past [4, 5]. Apart from the apparent complexity and the related computation time overhead that is related to the latter methods, the possibility of adaptive mesh refinements of various orders at several positions of the computational domain appears to be quite complicated within their context.

Wavelet based time domain techniques, such as the Multiresolution Time Domain Method (MRTD [6]), offer a promising alternative that overcomes the previously mentioned problems. Indeed, an adaptively non-uniform, moving mesh is effectively implemented by merely thresholding the time dependent wavelet coefficients of a field (or circuit) quantity series expansion at each time step. Such an approach leads to both memory and computation time economy for the reason that thresholded coefficients do not participate in operations that are carried out in subsequent time steps.

However, most research studies in this area have concentrated on either low order wavelet schemes (employing one or two [7, 8] wavelet levels), or on higher order wavelet schemes applied to structures

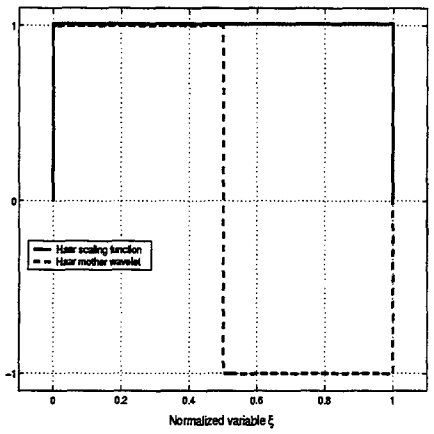


Figure 1: Haar scaling function and 0-wavelet.

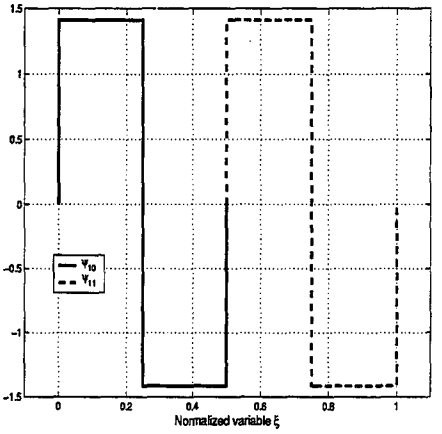


Figure 2: Haar wavelet functions of order 1.

that contain inhomogeneities of the order of the scaling function [9]. Hence, a remaining challenge for multiresolution techniques is to implement arbitrary order schemes that can model geometric details at the highest wavelet resolution, which may be much smaller than the scaling cell size. Applications of such schemes were recently presented [10] and a more detailed development for them is herein given. An operation count is approximated and inherent memory - computation time - accuracy trade-offs are discussed. Source and hard boundary modeling is also presented and validated. Finally, the problem of introducing time adaptive stepping is approached and some preliminary considerations are given.

Throughout this paper, the Haar basis is employed for all schemes that are derived. This is due to the relative simplicity of Haar Multiresolution Time Domain (MRTD) schemes, that constitute a generalization of Yee's FDTD. However, from a mathematical point of view, the same methodologies are to be followed for similar derivations in any wavelet basis.

2. FORMULATION OF ARBITRARY ORDER HAAR WAVELET MRTD

A. Definitions

For the extension of Haar MRTD to arbitrary orders, the following definitions are employed (the difference from similar definitions adopted in [8] and similar works should be noted).

The Haar scaling function is defined as a pulse (Figure 1) :

$$\phi(\xi) = \begin{cases} 1, & 0 \le \xi < 1 \\ 0, & otherwise \end{cases} \tag{1}$$

and the scaling function basis is produced by orthogonal translations of the latter:

$$\phi_k(\xi) = \phi(\xi - k) \tag{2}$$

The Haar mother wavelet function is defined as (Figure 1):

$$\psi(\xi) = \begin{cases} 1, & 0 \le \xi < 1/2 \\ -1, & 1/2 \le \xi < 1 \\ 0, & otherwise \end{cases} \tag{3}$$

and the basis is now produced by both translations and dilations, as shown in the definition:

$$\psi^r_{k,p}(\xi) = 2^{r/2}\psi(2^r(\xi - k) - p) \tag{4}$$

The parameter r denotes the wavelet resolution, while $p = 0, 1, \cdots, 2^r - 1$ denotes the position of the wavelet within a cell defined by a scaling function ϕ_k. First order Haar wavelet functions are depicted in Figure 2, for the role of p to become evident. In all previous definitions, the variable ξ is a normalized variable, representing for example in the case of a z-directed scaling/wavelet function, the ratio $z/\Delta z$, Δz being the cell size in z. direction.

B. Generalized Finite Difference Equations

An arbitrary order Haar MRTD scheme is now formulated for the transmission line equations (Telegrapher's equations) :

$$\frac{\partial v(z,t)}{\partial z} = -L\,\frac{\partial i(z,t)}{\partial t} \tag{5}$$

$$\frac{\partial i(z,t)}{\partial z} = -C\,\frac{\partial v(z,t)}{\partial t} \tag{6}$$

Voltage and current are expanded in a series of scaling and wavelet functions :

$$v(z,t) = \sum_{m,k} {}_kV^{\phi}_m\,\phi_m(z)\,h_k(t) + \sum_{m,k}\sum_{r,p} {}_kV^{\psi_{r,p}}_m\psi^r_{m,p}(z)\,h_k(t) \tag{7}$$

$$i(z,t) = \sum_{m,k} {}_{k+0.5}I^{\phi}_{m+0.5}\,\phi_{m+0.5}(z)\,h_{k+0.5}(t) + \sum_{m,k}\sum_{r,p} {}_{k+0.5}I^{\psi_{r,p}}_{m+0.5}\psi^r_{m+0.5,p}(z)\,h_{k+0.5}(t) \tag{8}$$

For the formulation of the scheme via the Method of Moments [6], integrals of the form :

$$\int_{-\infty}^{+\infty} f(\lambda)\,\frac{\partial}{\partial\lambda}g(\lambda)\,d\lambda \tag{9}$$

with :

$$\begin{aligned} f(\lambda) &= \phi_m(\lambda) \quad or \quad \psi^r_{m,p}(\lambda) \\ g(\lambda) &= \phi_{m'\pm 1/2}(\lambda) \quad or \quad \psi^{r'}_{m'\pm 1/2,p'}(\lambda) \end{aligned} \tag{10}$$

and $\lambda = x, y, z$ are evaluated in a closed form. Thus, finite difference equations for arbitrary orders of wavelet expansions can be derived, and write as follows :

$${}_{k+1}V^{\phi}_m = {}_kV^{\phi}_m - \frac{\Delta t}{C\Delta z}\left({}_{k+\frac12}I^{\phi}_{m+\frac12} - {}_{k+\frac12}I^{\phi}_{m-\frac12}\right) - \frac{\Delta t}{C\Delta z}\sum_{r,p} C(r,p)\left({}_{k+\frac12}I^{\psi_{r,p}}_{m+\frac12} - {}_{k+\frac12}I^{\psi_{r,p}}_{m-\frac12}\right) \tag{11}$$

$${}_{k+1}V^{\psi_{r,p}}_m = {}_kV^{\psi_{r,p}}_m - \frac{\Delta t}{C\Delta z}\,C(r,p)\left({}_{k+\frac12}I^{\phi}_{m+\frac12} - {}_{k+\frac12}I^{\phi}_{m-\frac12}\right)$$

$$-\frac{\Delta t}{C\Delta z}\sum_{r',p'}\left(\mathcal{D}_0(r,p,r',p')\,{}_{k+\frac12}I^{\psi_{r',p'}}_{m+\frac12} + \mathcal{D}_1(r,p,r',p')\,{}_{k+\frac12}I^{\psi_{r',p'}}_{m+\frac12}\right) \tag{12}$$

with :

$$\begin{aligned} &C(r,p) = 2^{\frac{r}{2}-1}\left(\delta_{p,2^{r-1}} - \delta_{p,2^{r-1}-1}\right) \\ &\mathcal{D}_i(r,p,r',p') = \\ &2^{\frac{r+r'}{2}}\{\psi(2^r(0.5 - i + \tfrac{p'}{2^{r'}}) - p) - 2\,\psi(2^r(0.5 - i + \tfrac{p'+0.5}{2^{r'}} - p) + \psi(2^r(0.5 - i + \tfrac{p'+1}{2^{r'}} - p)\} \\ &i = 0, 1. \end{aligned} \tag{13}$$

and $\delta_{k,\lambda}$ being Kronecker's delta function. Dual equations hold for current coefficients.

5. WAVELET EXCITATION AND HARD BOUNDARY MODELING

It has been already mentioned [8, 11] that Haar MRTD schemes with only zeroth order wavelets consist of uncoupled equations. In such schemes, wavelet coefficients become coupled to the scaling coefficients through the excitation and the boundary conditions [11]. A similar problem is encountered in the general case of an arbitrary order scheme, since by the multiresolution principle, a multiresolution decomposition of the approximation space V_k [12] as :

$$V_k = V_0 \oplus W_0 \oplus W_1 \oplus \cdots \oplus W_{k-1} \tag{14}$$

is equivalent to :

$$V_k = V_{k-1} \oplus W_{k-1} \tag{15}$$

The latter expression corresponds to a one wavelet level multiresolution analysis, in which scaling functions are combined with the (uncoupled) highest order wavelets of the former decomposition. Hence, in our experiments, a scaling excitation is sufficient to excite all wavelet terms except the highest order ones. For these terms , an explicit excitation scheme has been derived and validated, based on the application of continuity condition at planes within the excitation cell, generalizing the procedure described in [11]. These planes are defined by the scaling functions corresponding to the approximation space V_{k-1} (Figure 4).

For the modeling of hard boundaries, it is interesting to note that image theory can be applied in a straightforward way due to the form of Haar wavelets (Figure 3). Hence, perfect electric / magnetic conductors (PECs/PMCs) or short/open circuits in circuit geometries respectively, can be modeled by appropriate matching of wavelet functions. Such a modeling, applied to a TM^z incidence on a PEC is validated by the results shown in Figures 5-8 for a second order MRTD scheme. Total field pattern and second order wavelet coefficients for the tangential to the boundary magnetic field H_y are shown to assume the expected form in this case.

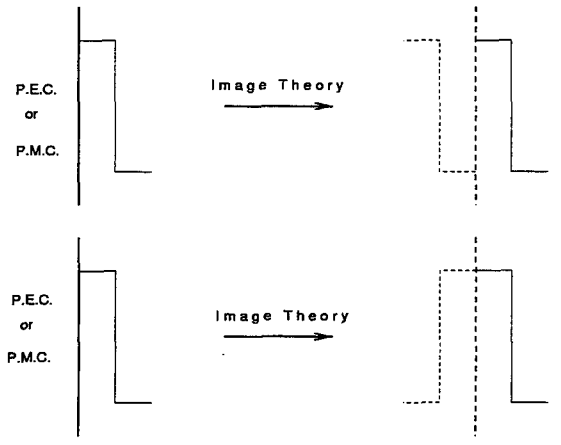


Figure 3: Image principle applied to hard boundaries : (-) image and (+) image, derived by multiplying the wavelet function by (+1), (-1) respectively.

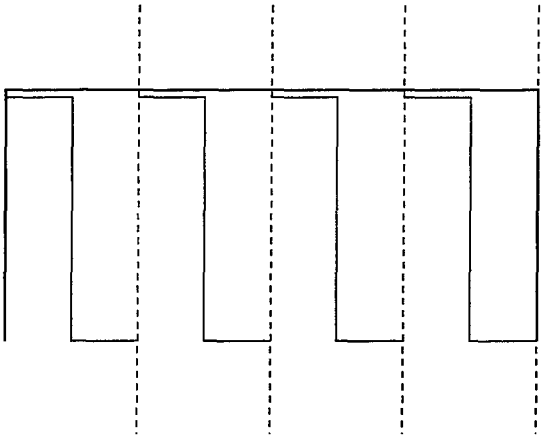


Figure 4: Excitation cell refined by four second order wavelets in a second order MRTD scheme. Dashed lines indicate the position of planes where the continuity condition is applied in the sense of [11].

4. EXECUTION TIME AND MEMORY ECONOMY IN NON - ADAPTIVE AND SPACE ADAPTIVE MRTD

A. Non – adaptive MRTD

The execution time budget of Haar MRTD is compared to the conventional FDTD without thresholding being taken into account. First, a stability analysis is performed, based on von Neumann's well known method [13] and verified by numerical experiments. It was found that the stability condition for a general three - dimensional scheme is :

$$\Delta t \leq \frac{1}{u_p} \frac{1}{\sqrt{\left(\frac{2^{R_x}}{\Delta x}\right)^2 + \left(\frac{2^{R_y}}{\Delta y}\right)^2 + \left(\frac{2^{R_z}}{\Delta z}\right)^2}} \tag{16}$$

(where u_p is the maximum phase velocity in the computational domain). In case $R_x = R_y = R_z = R$ and $\Delta x = \Delta y = \Delta z = \Delta$, a resolution of $\frac{\Delta}{2^{R+1}}$ is achieved by the MRTD technique, with a maximum time step :

$$\Delta t_{max}^{MRTD} = \frac{1}{\sqrt{3}u_p} \frac{\Delta}{2^R} \tag{17}$$

On the other hand, FDTD can achieve the same resolution with a time step [1]

$$\Delta t_{max}^{FDTD} = \frac{1}{\sqrt{3}u_p} \frac{\Delta}{2^{R+1}} = 0.5\Delta t_{max}^{MRTD} \tag{18}$$

The same relationship between Δt_{max}^{FDTD} and Δt_{max}^{MRTD} holds for the one dimensional scheme presented in 2.B . Then, taking into account all possible algebraic manipulations (*pairing of same order terms to avoid excessive multiplications*), the number of multiplications per scaling cell, per MRTD time step for MRTD schemes and FDTD is compared. The one dimensional scheme treated in section 2 is considered. Our measure of comparison takes into account both resolution refinement and the difference in time steps. Table 2 shows the results for MRTD orders of zero, one, two.

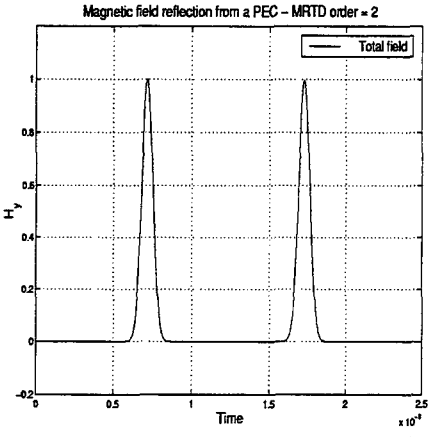


Figure 5: Total incident and reflected magnetic field from a PEC.

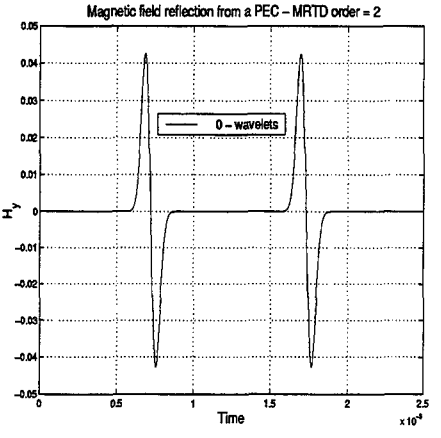


Figure 6: Zeroth order wavelet coefficients of incident and reflected magnetic field from a PEC.

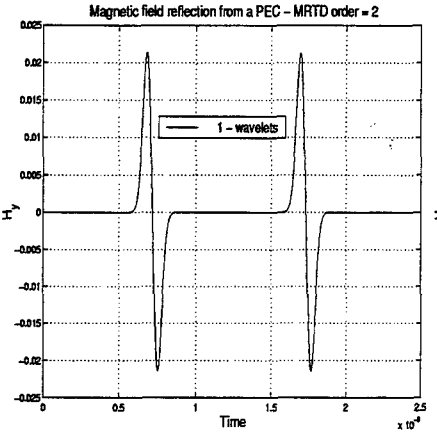


Figure 7: First order wavelet coefficients of incident and reflected magnetic field from a PEC.

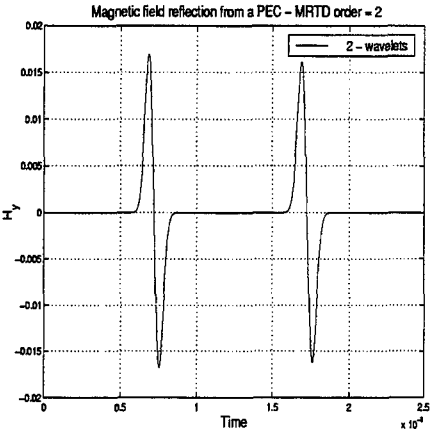


Figure 8: Second order wavelet coefficients of incident and reflected magnetic field from a PEC.

Table 1: Multiplications per scaling cell, per MRTD time step.

Order of MRTD resolution	MRTD	FDTD
0	2	4
1	13	8
2	38	16

It is evident, that with the exception of zero order Haar MRTD, higher order schemes involve *more* operations. Therefore, higher order schemes (at least for the Haar basis which is studied here) are meaningful and efficient only when they are combined with thresholding techniques.

B. Space Adaptive MRTD

Space adaptivity is introduced by means of coefficient thresholding as indicated in [14], at the expense of accuracy of the solution. Usually, wavelet based methods can tackle this trade - off relationship efficiently and, up to a point, the higher the order of the scheme that one uses, the more efficiently this is achieved [10]. For an advection equation, such as the system of transmission line equations, for R being the maximum wavelet resolution and N being the grid points that a conventional FDTD scheme uses, the operations per time step are for a space adaptive scheme [15] :

$$O\left(\sum_{r=0}^{R} n_r + \frac{N}{2^{R+1}}\right)$$

where n_r are the unthreshoded coefficients at resolution r. The latter expression shows the potential for attaining significant *time* savings with wavelet based solvers, when n_r is small as is the case in most applications [10, 14].

However, these time savings are attained at the expense of memory, since the use of data structures that "monitor" the sparsity of the vector of unknown coefficients step by step is necessary.

It should be also noted that grid coarsening is restricted by the Nyquist limit.

5. TIME ADAPTIVITY IN MRTD SCHEMES

A. Time Wavelets

Using wavelets in time, in a similar manner to which wavelet based spatial discretization is performed via Galerkin method, leads to a time adaptive gridding. Time adaptivity is again brought about by thresholding of time wavelet coefficients [16]. However, for the Haar basis, our numerical experiments have shown that the validity of this method is only limited to zero order wavelets [10]. Beyond that, it leads to unstable schemes. In general, the Wavelet - Galerkin technique does not yield stable time - stepping schemes, as can be seen from the roots of the finite difference equation for the scaling coefficients, when , for example, a Daubechies basis is used [17].

B. Adaptive Time Stepping

Time adaptive stepping is an important method to optimize the execution time requirements of a general wavelet based solver. The technique is presented in [15] and suggests that the update of terms which correspond to interactions between scaling - scaling, scaling - wavelet and wavelet - wavelet functions can be carried out at different time steps. These time steps are determined by the approximation space within each such interaction "lives". Terms that belong to successive approximation spaces (V_k and V_{k+1}) are updated at time steps that differ by a factor of two (higher resolution terms are updated twice as often as the next lower resolution terms). The advantage of this approach is that the highest wavelet resolution within the computational domain does not impose a restriction on the time step for the update of lower resolution terms.

Evidently, this algorithm cannot be implemented when E/H (or V/I) values are offset by half time step. If for example the magnetic field H is sampled at $(k+0.5)\Delta t$ then its value at $(k+0.5)\times 2\Delta t$, which is necessary for the update of terms that live in the second highest order approximation space, is not available and can only be interpolated. Therefore, all field values should be sampled at integer time steps.

Also, the implementation of the algorithm requires storage of unknown coefficients at "previous" time steps, the length of the storage window being related to the highest wavelet resolution (in particular, if R is the highest wavelet resolution introduced in the grid, 2^R previous time steps should be kept in memory).

6. CONCLUSION

The formulation and study of an arbitrary order Haar MRTD technique has been presented. It should be emphasized that the introduction of higher order wavelets only makes sense when it is combined with thresholding techniques that render the method space adaptive. It has also been mentioned that thresholding of wavelet coefficients is not only connected to memory but to time savings as well. Time adaptivity algorithms which, when introduced into spatially adaptive wavelet methods, have shown the promise of providing a highly efficient alternative to subgridding techniques, are currently under study.

7. ACKNOWLEDGEMENT

The authors wish to acknowledge the support of the U. S. Army Research Office to their research effort.

REFERENCES

[1] A. Taflove, "Computational Electrodynamics : The Finite Difference Time Domain Method", *Artech House, 1990.*

[2] W. J. R. Hoefer, "The transmission line matrix method - theory and applications", *IEEE Trans. Microwave Theory Tech., MTT-33, 882-893 (1985).*

[3] M. J. Berger, J. Oliger, "Adaptive Mesh Refinement for Hyperbolic Partial Differential Equations", *Journal of Computational Physics, 53, 484-512 (1984).*

[4] I. S. Kim, W. J. R. Hoefer, "A Local Mesh Refinement Algorithm for the Time Domain Finite Difference Method Using Maxwell's Curl Equations", *IEEE Trans. Microwave Theory Tech., MTT-38, no.6, June 1990, pp. 812-815.*

[5] M. Okoniewski, E. Okoniewska, M. A. Stuchly, "Three Dimensional Subgridding Algorithm for FDTD", *IEEE Trans. Antennas Propagat., AP-45, no.3, March 1997, pp. 422-429.*

[6] M.Krumpholz, L.P.B. Katehi, "MRTD: New Time Domain Schemes Based on Multiresolution Analysis", *IEEE Trans. Microwave Theory and Techniques, MTT-44, no.4, pp.555-561, April 1996.*

[7] K. Goverdhanam, L.P.B. Katehi, A. Cangellaris, "Applications of multiresolution based FDTD multigrid", *1997 MTT-S Digest, pp.333-336.*

[8] M. Fujii, W.J.R. Hoeffer, "Formulation of a Haar-wavelet based multiresolution analysis similar to the 3-D FDTD method", *1998 MTT-S Digest, pp.1393-1396.*

[9] M. Werthen, I. Wolff, "A novel wavelet based time domain simulation approach", *IEEE Microwave Guided Wave Lett., vol. 6, pp. 438-440,Dec. 1996.*

[10] C. D. Sarris and L. P. B. Katehi, "Multiresolution Time Domain Schemes with Space - Time Haar Wavelets" *1999 MTT-S Digest, pp. 1459-1462.*

[11] K. Goverdhanam, E. Tentzeris, L.P.B. Katehi, "Treatment of boundaries in Multiresolution based FDTD multigrid", *Presented at the 1998 ACES conference, Monterrey, CA.*

[12] I. Daubechies, "Ten Lectures on Wavelets", *Philadelphia, PA : SIAM, 1992.*

[13] J.C. Strikwerda, "Finite Difference Schemes and Partial Differential Equations ",*Wadsworth Inc., Belmont CA.*

[14] E.Tentzeris, R.Robertson, A.Cangellaris and L.P.B.Katehi, "Space- and Time- Adaptive Gridding Using MRTD", *1997 IEEE MTT-S Digest, pp.337-340.*

[15] E. Bacry, S. Mallat, G. Papanicolaou, "A wavelet based space - time numerical method for partial differential equations", *Technical Report 591, New York University, Courant Institute of Mathematical Sciences, November 1991.*

[16] E.Tentzeris, J.Harvey and L.P.B.Katehi, "Time Adaptive Time-Domain Techniques for the Design of Microwave Circuits", *IEEE Microwave and Guided Wave Letters, Vol.9, No.3, pp.96-98, March 1999.*

[17] K. Amaratunga, J. R. Williams, "Time Integration Using Wavelets", *SPIE, Vol. 2491, pp. 894-902.*

Invited to the Session: "Wavelet and TLM Modeling Techniques" organized by Dr. W. J. R. Hoefer in ACES 2000

COMPUTATIONAL OPTIMIZATION OF MRTD HAAR-BASED ADAPTIVE SCHEMES USED FOR THE DESIGN OF RF PACKAGING STRUCTURES

Manos M. Tentzeris
School of ECE, Georgia Institute of Technology, Atlanta, GA 30250-0250
(FAX : (404) 894-4641)
(e-mail:etentze@ece.gatech.edu)

Abstract

The MRTD adaptive gridding scheme that is based on the Haar expansion basis is discussed for arbitrary wavelet resolutions. Guidelines for the optimization of memory and execution time requirements are presented. A multi-time-stepping procedure enhances further the computational economies offered by a combination of absolute and relative thresholding of the wavelet values.
Keywords: Multiresolution, Time-Domain Techniques, Adaptive Gridding, Wavelets, Memory Compression, Thresholding, Haar

I Introduction - Discussion on the Haar expansion basis

Significant attention is being devoted now-a-days to the analysis and design of various types of RF Packaging structures (e.g. Flip-Chip, Multi-Layered Structures) used in Wireless and Computing applications. Though The finite-difference-time-domain (FDTD) scheme is one of the most powerful and versatile techniques used for numerical simulations, it suffers from serious limitations due to the substantial computer resources required to model such electromagnetic problems with medium or large computational volumes. Recently, MRTD (MultiResolution Time Domain Method) [1]-[9] has shown unparalled properties in comparison to Yee's FDTD. In a MRTD scheme the fields are represented by a two-fold expansion in scaling and wavelet functions with respect to time/space. Scaling functions guarantee a correct modelling of smoothly-varying fields. In regions characterized by strong field variations or field singularities, higher resolution is enhanced by incorporating multiple resolutions of wavelets in the field expansions. The major advantage of the use of Multiresolution analysis to time domain is the capability to develop time and space adaptive grids. This is due to the property of the wavelet expansion functions to interact weakly and allow for a spatial sparsity that may vary with time through a thresholding process. Haar expansion basis functions (Fig.(1)) provide a convenient tool for the transition from FDTD to MRTD due to their compact support, and to their similarity with the FDTD pulse basis [6]-[9]. Nevertheless, the enhancement of additional wavelet terms the number of which is different from cell to cell and for different time-steps requires a careful consideration of the memory and execution time overheads. In addition, the fact that the stability

limit of the time-step decreases as more resolutions are added requires the use of an effective multi-time-stepping algorithm, that will maintain the required accuracy without increasing significantly the execution time requirements.

II MRTD Scheme with Multiple Wavelet Resolutions

For simplicity, the 1D MRTD scheme for TEM propagation will be discussed. It can be extended to 2D and 3D in a straightforward way. The Electric (E_x) and the Magnetic (H_y) fields are displaced by half step in both time- and space-domains (Yee cell formulation) and are expanded in a summation of scaling (ϕ) and wavelet (ψ_r) functions in space and scaling components in time. For example, E_x is given by

$$E_x(z,t) = \sum_{m,i=-\infty}^{\infty} \left({}_mE^{\phi}_{x,i}\phi_i(z) + \sum_{r=0}^{r_{max}} \sum_{i_r=1}^{2^r} {}_mE^{\psi_{r,i_r}}_{x,i}\psi_i^{r,i_r}(z) \right) \phi_m(t) \quad , \tag{1}$$

where $\phi_i(z) = \phi(z/\Delta z - i)$ and $\psi_i^{r,i_r}(z) = 2^{r/2}\psi_0(2^r(z/\Delta z - i_r) - i)$ represent the Haar scaling and r-resolution wavelet functions located inside the $i-$cell. The conventional notation ${}_mE_{x,i}$ is used for the voltage component at time $t = m\Delta t$ and $z = i\Delta z$, where Δt and Δz are the time-step and the spatial cell size respectively. The notation for H_y is similar.

Substituting E_x,H_y in the TEM equations and applying Galerkin technique derives the following equations for H_y

$$\begin{aligned} {}_{m+0.5}H^{\phi}_{y,i-0.5} &= {}_{m-0.5}H^{\phi}_{y,i-0.5} - \frac{\Delta t}{\mu\Delta z}\left(E^{\phi}_{x,i} - E^{\phi}_{x,i-1} + \right. \\ &+ \left. \sum_{r=1}^{r_{max}} (c_{1,r,2^r,-1}\, E^{\psi_{r,2^r}}_{x,i-1} + c_{1,r,1,1}\, E^{\psi_{r,1}}_{x,i+1} + \sum_{i_{r1}=1}^{2^{r_{max}}} c_{1,r,i_{r1},0}\, E^{\psi_{r,i_r}}_{x,i}\right), \end{aligned} \tag{2}$$

$$\begin{aligned} {}_{m+0.5}H^{\psi_0}_{y,i-0.5} &= {}_{m-0.5}H^{\psi_0}_{y,i-0.5} - \frac{\Delta t}{\mu\Delta z}\left(E^{\psi_0}_{x,i} - E^{\psi_0}_{x,i-1} + \right. \\ &+ \left. \sum_{r=1}^{r_{max}} (c_{2,r,2^r,-1}\, E^{\psi_{r,2^r}}_{x,i-1} + c_{2,r,1,1}\, E^{\psi_{r,1}}_{x,i+1} + \sum_{i_{r1}=1}^{2^{r_{max}}} c_{2,r,i_{r1},0}\, E^{\psi_{r,i_r}}_{x,i}\right), \end{aligned} \tag{3}$$

$$\begin{aligned} {}_{m+0.5}H^{\psi_{r'>0,i_{r'}\in[1,2^{r'-1}]}}_{y,i-0.5} &= {}_{m-0.5}H^{\psi_{r',i_{r'}}}_{y,i-0.5} - \frac{\Delta t}{\mu\Delta z}\left(d_{r',i_{r'},1,-1}\, E^{\phi}_{x,i-1} + d_{r',i_{r'},2,-1}\, E^{\psi_0}_{x,i-1}\right. \\ &+ \sum_{r=1}^{r_{max}} (\delta_{i_{r'},1} e_{r',i_{r'},r,2^r,-1}\, E^{\psi_{r,2^r}}_{x,i-1} + \sum_{i_r=i_1}^{i_2} e_{r',i_{r'},r,i_r,0}\, E^{\psi_{r,i_r}}_{x,i}) \\ &+ \left. \delta_{i_{r'},2^{r'-1}}(d_{r',i_{r'},1,0}\, E^{\phi}_{x,i} + d_{r',i_{r'},2,0}\, E^{\psi_0}_{x,i})\right), \end{aligned} \tag{4}$$

$$\begin{aligned} {}_{m+0.5}H^{\psi_{r'>0,i_{r'}\in[2^{r'-1}+1,2^{r'}]}}_{y,i-0.5} &= {}_{m-0.5}H^{\psi_{r',i_{r'}}}_{y,i-0.5} - \frac{\Delta t}{\mu\Delta z}\left(d_{r',i_{r'},1,0}\, E^{\phi}_{x,i} + d_{r',i_{r'},2,0}\, E^{\psi_0}_{x,i}\right. \\ &+ \sum_{r=1}^{r_{max}} (\delta_{i_{r'},2^{i_{r'}}} e_{r',i_{r'},r,1,1}\, E^{\psi_{r,1}}_{x,i+1} + \sum_{i_r=i_1}^{i_2} e_{r',i_{r'},r,i_r,0}\, E^{\psi_{r,i_r}}_{x,i}) \\ &+ \left. \delta_{i_{r'},2^{r'-1}+1}(d_{r',i_{r'},1,-1}\, E^{\phi}_{x,i-1} + d_{r',i_{r'},2,-1}\, E^{\psi_0}_{x,i-1})\right) \end{aligned} \tag{5}$$

where: $i_1 = max[1, INT((i_r - 1)\,2^{-(r'-r)}) + 1]$ and $i_2 = min[2^r, INT(1 + i_r\,2^{-(r'-r)})]$. Also, the c,d and e coefficients can be calculated by the Galerkin technique correlating the respective wavelet and scaling functions and δ is the Kroenecker Delta. For example,

$$c_{1,r,i_r,p} = \int \phi_{i-0.5}(z)\frac{\partial \psi_{i+p}^{r,i_r}(z)}{\partial z}dz = 2^{r/2-1}(\delta_{i_r,2^r}(\delta_{p,-1} - \delta_{p,0}) + \delta_{i_r,1}(\delta_{p,1} - \delta_{p,0})) \qquad (6)$$

Through the split of the wavelet coefficients of resolution $r' > 0$ to two groups ($[1,..,2^{r'-1}]$ and $[2^{r'-1}+1,..,2^{r'}]$) the calculations are performed more efficiently in terms of the scaling and wavelet of 0-Resolution contributions. In addition, it is clear that the calculation of these wavelet coefficients require a significantly smaller number of terms than $2^{r_{max}+1}$, something that proves that the number of operations increase significantly slower than $O(2^{2(r_{max}+1)})$ as the maximum resolution r_{max} increases.

II.1 Hard Boundaries

Due to the finite-domain nature of the expansion basis, the Hard Boundary conditions (Perfect Electric/Magnetic Conductor) can be easily modeled. For example, if a P.E.C. exists at the $z = i\Delta z$, then the scaling E_x coefficient for the $i - cell$ has to be set to zero for each time-step m since the position of the conductor coincides with the midpoint of the domain of the scaling function. Nevertheless, the 0-resolution wavelet for the same cell has the value of zero at its midpoint; thus its amplitude does not have to be set to zero. To enforce the physical condition that the electric field values on either side of the conductor are indpendent from the files on the other side, TWO 0-resolution wavelet E_x coefficients have to be defined. The one (on the one side of P.E.C.) will depend on H_y values on this side only and the other (on the other side of P.E.C.) will depend on H_y values on that side only. Wavelet coefficients of higher-resolution with domains tangential to the position of P.E.C. have to be zeroed out as well. As far as it concerns the equations that update the coefficients of the magnetic field H_y, only E_x coefficients on the same side of the P.E.C. have to be used. The rest of the summation terms have to be replaced with coefficients derived applying the odd image theory for the electric field. A similar approach can be applied for the modeling of a Perfect Magnetic Conductor (P.M.C.).

It can be easily observed that for Wavelet Resolutions up to r_{max}, $2^{r_{max}+1}$ coefficients have to be calculated per cell per field component instead of one component in the conventional F.D.T.D. The derived gain is that the new algorithm has an improved resolution by a factor of $2^{r_{max}+1}$ that can vary from cell-to-cell depending on the field variations and discontinuities. In addition, MRTD can offer a significantly better E_x field resolution close to P.E.C.'s through the 0-Resolution Wavelet Double term with a negligible computational overhead per P.E.C. (the second 0-Resolution term). Conventional F.D.T.D. assumes a constant zero E_x distribution half-cell on either side of the P.E.C. by zeroing out its amplitude at the P.E.C. cell.

II.2 Field Reconstruction

The alternating nature of the wavelet functions guarantees the improved time-domain resolution of the MRTD scheme. Assuming that the H_y scaling and wavelet (0 to r_{max} resolutions) coefficients for a specific cell i have been calculated for $t = m\Delta t$, two values can be defined for the domain $[(i - 1. + (i_r - 1)2^{-r_{max}})\Delta z,\ (i + i_r 2^{-r_{max}})\Delta z]$ of each wavelet coefficient $\psi_i^{r_{max},i_r}$ of the maximum resolution r_{max}. As a result, a total number of $2^{r_{max}+1}$ subpoints/cell at the positions: $z = (i - 1. + (i_r - 0.5)\ 2^{-(r_{max}+1)})\Delta z$, for $i_r = 1, .., 2^{r_{max}+1}$ can be used for the total field value reconstruction:

$$ {}_{m-0.5}H_y^{total(i,r_{max},i_r)} = {}_{m-0.5}H_{y,i}^{\phi} + c_1\ {}_{m-0.5}H_{y,i}^{\psi_0} + \sum_{r=1}^{r_{max}} {}_{m-0.5}H_{y,i}^{\psi_{r,i'_r}} \psi_{r,i'_r}(z) \quad , \tag{7} $$

where: $i'_r = INT(2^r\ z) + 1$, and

$$ c_1 = \begin{cases} +1 & \text{if } i_r \leq 2^{r_{max}} \\ -1 & \text{if } i_r > 2^{r_{max}} \end{cases} $$

A similar expression can be derived for E_x component. It is obvious, that only $2 + r_{max}$ coefficients are required for the field reconstruction at each subpoint.

II.3 Dynamic Adaptivity - Thresholding

The fact that the wavelet coefficients take significant values only for a small number of cells that are close to abrupt discontinuities or contain fast field variations allows for the development of a dynamically adaptive gridding algorithm. One thresholding technique based on absolute and relative thresholds offers very significant economy in memory while maintaining the increased resolution in space where needed. For each time-step, the values of the scaling coefficients are first calculated for the whole grid. Then, wavelet coefficients with resolutions of increasing order are updated. As soon as all wavelet components of a specific resolution of a cell have values below the Absolute Threshold (that has to do with the numerical accuracy of the algorithm) or below a specific fraction (Relative Threshold) of the respective scaling coefficient, no higher wavelet resolutions are updated and the simulation moves to the update of the wavelet coefficients of the next cell. The same thresholding procedure is performed for both E_x and H_y components. of the respective medium(s). In this way, the execution time requirements are optimized, since for areas away from the excitation or discontinuities, only the scaling coefficients need to be updated. This is a fundamental difference with the conventional F.D.T.D. algorithms that cannot provide a dynamical time- and space- adaptivity even with grids of variable cell sizes (static adaptivity).

II.4 Multi-Time-Stepping Implementation

As it has been reported in [9], the maximum time step value that guarantees numerical stability for maximum wavelet resolution r_{max} is

$$ \Delta t^{(r_{max})} = \frac{\Delta z}{2^{r_{max}}\ c} \quad , \tag{8} $$

where c is the velocity of the light in the simulated medium and Δt, Δz are the time-step and the cell size respectively. The dynamically changing gridding that was described in the previous section allocates different values of maximum wavelet resolution throughout the grid for every time-step, thus deriving different values of stable time-steps from cell to cell. The easiest way to guarantee stability would be to identify the maximum used wavelet resolution and use the respective time-step. That would lead to a huge computational overhead of no practical gain especially for cells that a few or even no wavelet resolution is needed. On the other side, if different time-steps were to be used, the calculation of coefficients updated more often than the neighboring cells (high wavelet resolutions and smaller time-steps) would require the efficient interpolation of the values that are updated less often (larger time-steps). To simplify this procedure, the used time-steps in the grid are defined in powers of 2 starting from the smallest time-step (cells that use the highest wavelet resolution r_{max}), $\Delta t^{(r_{max})}$. For example, the used time-step for a cell that requires the wavelet calculation up to the $r_{use} < r_{max}$ resolution would get the value $\Delta t^{(r_{use})} = \Delta t^{(r_{max})} 2^{r_{max}-r_{use}}$.

After identifying the appropriate time-steps for each cell, a second-order backward interpolation is used to calculate field values for intermediate time instants. For example, if the calculation of E_x coefficients in one cell is performed with time-step $\delta t = \Delta t^{(r_1)}$ and the calculation of H_y in the neighboring cell is performed with a larger $\Delta t = \Delta t^{(r_2)} = \delta t\ 2^{r_1-r_2}$, there is the need for the calculation of H_y in $2^{r_1-r_2}$ subpoints between $m\Delta t$ and $(m+1)\Delta t$ for each time-step m. The interpolation process can be expressed as:

$$
\begin{aligned}
{}_{i_{int}}H_y &= [(0.5 + (i_{int} - 0.5)\frac{\delta t}{\Delta t})(1 + 0.5((i_{int} - 0.5)\frac{\delta t}{\Delta t} - 0.5))]\ {}_{m+0.5}H_y \\
&- [((i_{int} - 0.5)\frac{\delta t}{\Delta t} - 0.5)(1 + (i_{int} - 0.5)\frac{\delta t}{\Delta t} + 0.5)]\ {}_{m-0.5}H_y \\
&+ 0.5[(i_{int} - 0.5)\frac{\delta t}{\Delta t} - 0.5][(i_{int} - 0.5)\frac{\delta t}{\Delta t} + 0.5]\ {}_{m-1.5}H_y \quad , \qquad (9)
\end{aligned}
$$

for $i_{int} = 1, .., \frac{\Delta t}{\delta t} (= 2^{r_1-r_2})$ and can be applied to scaling and wavelet components. The use of the second-order scheme provides stability for thousands of time-steps. Using linear time interpolation was found to lead to instabilities and increased reflection error at the interface of the different time-steps. Though the interpolation process adds a computational overhead by requiring the storage of the coefficients for three time-steps, it improves significantly the requirements in execution time by performing the simulations at the maximum allowable time-step everywhere in the grid.

II.5 Validation Case

To validate the above approach, the MRTD algorithm was applied to the simulation of the TEM propagation of a Gaussian excitation at $z = 200\Delta z$ up to 3 GHz inside air dielectric ($\epsilon_r = \mu_r = 1$) for 1,000 time-steps with size $\Delta t = 0.95\Delta t^{r_{max}}$ for each cell's maximum used wavelet resolution r_{max} and 400 cells with $\Delta z = 2.5cm$. Wavelets up to 2-Resolution are enhanced wherever needed. A relative threshold of 10^{-4} and an absolute threshold of 10^{-6} offer an approximation error smaller than 0.4%. Fig.(2) which displays the reconstructed E_x field distribution at $t = 500\Delta z$ demonstrates

the fact that only 24 cells need to calculate the Wavelet Coefficients. Everywhere else E_x is close to zero and shows no variation; thus it requires the calculation of only scaling coefficients. (Memory Compression=94%). The fact that an interpolation scheme is used for the time-stepping allows for a time-step aspect ratio of $2^3 = 8:1$ in these two areas. In this way, the memory compression gain is transfered to the execution time as well without affecting the simulation accuracy. Fig.(3) which is a magnification of Fig.(2) for the area of increased resolution, proves the ability of Haar-based MRTD schemes with arbitrary wavelet resolutions to provide locally magnified accuracy through the accurate representation of field variations at multiple intracell subpoints. This optimized algorithm has been expanded in 2D and 3D and simulation results of practical RF Packaging structures (Flip-Chip, Emebedded Passives) will be presented at the conference. intracell subpoints.

III Conclusions

Various computational aspects concerning the Haar-based MRTD adaptive gridding scheme have been discussed and guidelines for the optimization of memory and execution time requirements have been presented. The use of absolute and relative thresholding of the wavelet coefficients has been combined with a multi-time-stepping procedure and has led to further economies. In addition, an optimized field reconstruction procedure allows for the quick and reliable demonstration of the increased resolution that is offered by the enhancement of multiple resolution of wavelets with minimum computational overhead. In this way, the Haar-based MRTD adaptive scheme has been proven to be a very efficient and reliable full-wave simulation tool for complex RF structures, such as RF Packaging geometries.

IV Acknowledgments

The author would like to thank the Packaging Research Center of Georgia Tech for their continuous support.

References

[1] E.Tentzeris, R.Robertson, A.Cangellaris and L.P.B. Katehi, "Space- and Time- Adaptive Gridding Using MRTD", Proc. MTT-S 1997, pp. 337-340.

[2] M.Krumpholz, L.P.B.Katehi, "MRTD: New Time Domain Schemes Based on Multiresolution Analysis", IEEE Trans. Microwave Theory and Techniques, vol. 44, no. 4, pp. 555-561, April 1996.

[3] E.Tentzeris, M.Krumpholz and L.P.B. Katehi, "Application of MRTD to Printed Transmission Lines", Proc. MTT-S 1996, pp. 573-576.

[4] R. Robertson, E. Tentzeris, M. Krumpholz, L.P.B. Katehi, "Application of MRTD Analysis to Dielectric Cavity Structures", Proc. MTT-S 1996, pp. 1861-1864.

[5] E.Tentzeris, R.Robertson, M.Krumpholz and L.P.B. Katehi, "Application of the PML Absorber to the MRTD Technique", Proc. AP-S 1996, pp. 634-637.

[6] E.Tentzeris, J.Harvey and L.P.B.Katehi, "Time Adaptive Time-Domain Techniques for the Design of Microwave Circuits", IEEE Microwave and Guided Wave Letters, Vol. 9, No. 3, pp. 96-98, 1999.

[7] K.Goverdhanam, E.Tentzeris, M.Krumpholz and L.P.B. Katehi, "An FDTD Multigrid based on Multiresolution Analysis", Proc. AP-S 1996, pp. 352-355.

[8] M.Fujii, W.J.R.Hoefer, "Formulation of a Haar-wavelet based Multiresolution Analysis similar to the 3-D FDTD Method", Proc. MTT-S 1998, pp. 1393-1396.

[9] C.Sarris and L.P.B.Katehi, "Multiresolution Time Domain (MRTD) Schemes with Space-Time Haar Wavelets", Proc. MTT-S 1999, pp. 1459-1462

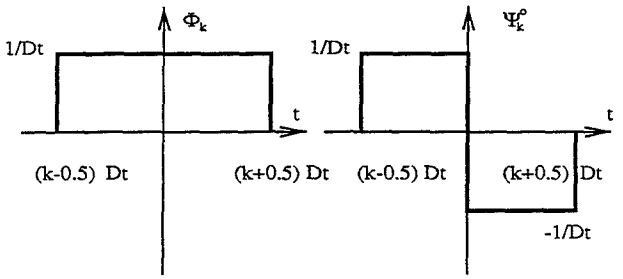


Figure 1: 0-Order Haar Function Basis.

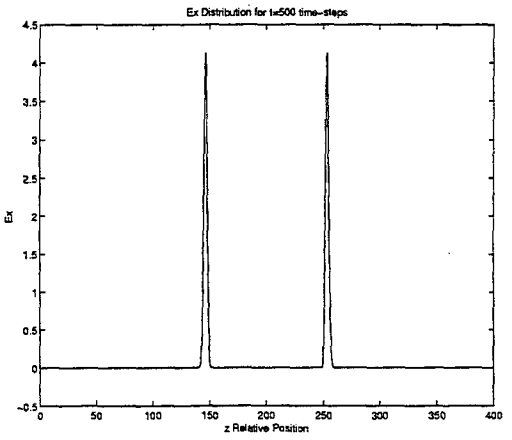


Figure 2: Demonstration of the Memory Compression of E_x Spatial Distribution at $t = 500\Delta t$.

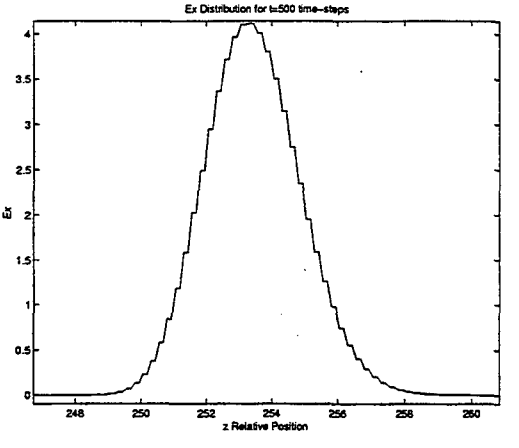


Figure 3: Demonstration of the Variable Resolution (Multipoint Intracell Representation) of E_x Spatial Distribution at $t = 500\Delta t$.

TIME-DOMAIN SIMULATION OF ELECTROMAGNETIC WAVE PROPAGATION IN A MAGNETIZED PLASMA

J.Paul, C.Christopoulos and D.W.P.Thomas

Electromagnetics Research Group, School of Electrical and Electronic Engineering
University of Nottingham, University Park, Nottingham, NG7 2RD, United Kingdom.
Fax: +44 (0)115 9515616, Email: jdp@eee.nott.ac.uk

Abstract: In this paper, a one-dimensional time-domain transmission-line model of electromagnetic wave propagation in a magnetized plasma is developed. The discretization procedure of the anisotropic Lorentzian conductivity function is based on bilinear $\mathcal{Z}$-transforms. The method is validated using a simple example with an analytic solution and applied to two examples of ionospheric propagation.

INTRODUCTION

The description of electromagnetic wave propagation in a magnetized plasma was first studied using the Finite-Difference Time-Domain (FDTD) method [1]. In a previous paper [2], Transmission-Line Modelling (TLM) was applied to the simulation of propagation in a magnetized plasma using the complex exponential discretization scheme [3]. Although this system is adequate for an initial model, it does not give an accurate amplitude and phase response at high frequencies. Thus in this paper, the conductivity tensor is discretized using the prewarped complex bilinear $\mathcal{Z}$-transform, which requires no more computational overhead and yields more accurate solutions.

As in the FDTD development [1], the approach is validated by comparing the plane wave reflection and transmission coefficients of a slab calculated using the time-domain method and analysis [4].

Finally, the method is applied to the simulation of propagation of low frequency waves in the ionosphere. The launch of a pulse from the ground and the high altitude dispersion of a pulse are studied. The results confirm that the dispersion of a pulse electromagnetic wave in a magnetized plasma leads to the formation of a whistler [5].

1. THEORY

In this section, the simulation of 1-D propagation in a magnetized plasma using TLM is developed. For further details of the approach and applications to other anisotropic materials, the reader is referred to [2].

If we consider one-dimensional propagation in x, with the static bias field also in x, in a non-dielectric, non-magnetic magnetized plasma, the conduction current is

$$\begin{bmatrix} J_{ey} \\ J_{ez} \end{bmatrix} = \begin{bmatrix} \sigma_e^{yy} & \sigma_e^{yz} \\ \sigma_e^{zy} & \sigma_e^{zz} \end{bmatrix} \cdot \begin{bmatrix} E_y \\ E_z \end{bmatrix} \qquad (1)$$

The conductivity tensor is

$$\begin{bmatrix} \sigma_e^{yy} & \sigma_e^{yz} \\ \sigma_e^{zy} & \sigma_e^{zz} \end{bmatrix} = \frac{\omega_p^2 \varepsilon_0}{(s+\nu_c)^2 + \omega_b^2} \begin{bmatrix} s+\nu_c & \omega_b \\ -\omega_b & s+\nu_c \end{bmatrix} \qquad (2)$$

In (2), the electron plasma frequency $\omega_p = \sqrt{N q^2/(\varepsilon_0 m)}$, where N is the number density of electrons, q is the electron charge and

m is the electron mass. Also in (2), the collision frequency is ν_c and the gyro-frequency $\omega_b = B_0\, q/m$ where B_0 is the static bias field.

The TLM representation of the electric conductivity tensor is [2]

$$\begin{bmatrix} g_e^{yy} & g_e^{yz} \\ g_e^{zy} & g_e^{zz} \end{bmatrix} = \frac{g_{e0}\,\nu_c}{(s+\nu_c)^2+\omega_b^2} \begin{bmatrix} s+\nu_c & \omega_b \\ -\omega_b & s+\nu_c \end{bmatrix} \quad (3)$$

In (3), $g_{e0} = \omega_p^2\,\varepsilon_0\,\eta_0\,\Delta\ell/\nu_c$ where η_0 is the impedance of free-space and $\Delta\ell$ is the space-step.

The elements of the conductivity tensor are second-order functions of frequency, and as described in [3], may be written as the real part of two complex first-order functions. Also because we are employing the bilinear $\mathcal{Z}$-transform for the discretization, to obtain an accurate mapping from the s to the $\mathcal{Z}$ plane, the functions in (3) are prewarped [6] using

$$\zeta = \nu_c/\omega_b \quad , \quad \omega_0 = \sqrt{\nu_c^2+\omega_b^2} \quad (4)$$

$$\nu_{cw} = \frac{2\zeta}{\Delta t}\tan\left(\frac{\omega_0\,\Delta t}{2}\right) \quad (5)$$

$$\omega_{bw} = \frac{2}{\Delta t}\sqrt{1-\zeta^2}\tan\left(\frac{\omega_0\,\Delta t}{2}\right) \quad (6)$$

where ζ is the damping ratio, ω_0 is the resonant frequency, Δt is the time-step, ν_{cw} is the warped collision frequency and ω_{bw} is the warped gyro-frequency. The prewarping operation conserves the d.c. gain and the damping ratio of the second-order function in the transformation to the $\mathcal{Z}$-domain. The prewarped complex form of (3) is

$$\begin{bmatrix} g_e^{yy} & g_e^{yz} \\ g_e^{zy} & g_e^{zz} \end{bmatrix} = g_{e0}\,\nu_c\,\Re\left\{ \frac{\frac{\nu_{cw}-j\omega_{bw}}{\nu_c-j\omega_b}}{s+(\nu_{cw}-j\omega_{bw})} \begin{bmatrix} 1 & -j \\ j & 1 \end{bmatrix} \right\} \quad (7)$$

where $\Re\{\cdot\}$ denotes the real part of a complex function. The discrete model of (7) follows from the bilinear transform $s \rightarrow (2/\Delta t)(1-z^{-1})/(1+z^{-1})$ and a partial fraction expansion to obtain

$$\begin{bmatrix} g_e^{yy} & g_e^{yz} \\ g_e^{zy} & g_e^{zz} \end{bmatrix} = \begin{bmatrix} g_{e0}^{yy} & g_{e0}^{yz} \\ g_{e0}^{zy} & g_{e0}^{zz} \end{bmatrix} + z^{-1} \begin{bmatrix} \bar{g}_e^{yy} & \bar{g}_e^{yz} \\ \bar{g}_e^{zy} & \bar{g}_e^{zz} \end{bmatrix} \quad (8)$$

In (8), the constant tensor is

$$\begin{bmatrix} g_{e0}^{yy} & g_{e0}^{yz} \\ g_{e0}^{zy} & g_{e0}^{zz} \end{bmatrix} = \Re\left\{ k_p \begin{bmatrix} 1 & -j \\ j & 1 \end{bmatrix} \right\} \quad (9)$$

where

$$k_p = \frac{g_{e0}\,\nu_c\,\Delta t(\nu_{cw}-j\omega_{bw})/(\nu_c-j\omega_b)}{2+\Delta t(\nu_{cw}-j\omega_{bw})} \quad (10)$$

Also in (8), the frequency-dependent tensor is

$$\begin{bmatrix} \bar{g}_e^{yy} & \bar{g}_e^{yz} \\ \bar{g}_e^{zy} & \bar{g}_e^{zz} \end{bmatrix} = \Re\left\{ \frac{\alpha_p}{1-z^{-1}\beta_p} \begin{bmatrix} 1 & -j \\ j & 1 \end{bmatrix} \right\} \quad (11)$$

where

$$\alpha_p = \frac{g_{e0}\,\nu_c\,\Delta t(\nu_{cw}-j\omega_{bw})4}{(\nu_c-j\omega_b)(2+\Delta t(\nu_{cw}-j\omega_{bw}))^2} \quad (12)$$

and

$$\beta_p = \frac{2-\Delta t(\nu_{cw}-j\omega_{bw})}{2+\Delta t(\nu_{cw}-j\omega_{bw})} \quad (13)$$

Incorporation of (8) into the TLM model is detailed in reference [2]. The time-domain algorithm requires the storage of 2 real numbers per electric field component.

2. VALIDATION

In this section, the approach is tested by comparing the plane wave transmission and reflection performance of a magnetized plasma slab calculated using the time-domain method and analysis [4]. Following the example studied in FDTD [1], the slab depth was 9mm, the space-step $\Delta\ell = 75\mu$m and the time-step was $\Delta t = \Delta\ell/c$. The plasma properties were $\omega_p = 2\pi \times 50 \times 10^9$, $\nu_c = 2 \times 10^{10}$ and $\omega_b = 3 \times 10^{11}$. The incident wave was a delta function, polarized in z. The transmission coefficients for circularly polarized waves were obtained from

$$T_{RCP}(\omega) = E_y^t(\omega) + jE_z^t(\omega)$$
$$T_{LCP}(\omega) = E_y^t(\omega) - jE_z^t(\omega)$$

The reflection coefficients were calculated using similar expressions involving the reflected fields.

Figs. 1 and 2 show close agreement between the reflection coefficient magnitudes and phases calculated using analysis and TLM. Similarly, Fig. 3 shows a similar correlation for the transmission coefficient magnitudes. Figs. 4 and 5 show the transmission coefficient phases. Although the transmission phases are not as accurate as the reflection phases, the results indicate that the prewarped model is yielding improved results c.f. [2].

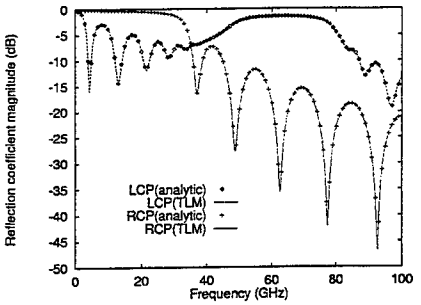


Figure 1: Reflection coefficient magnitudes

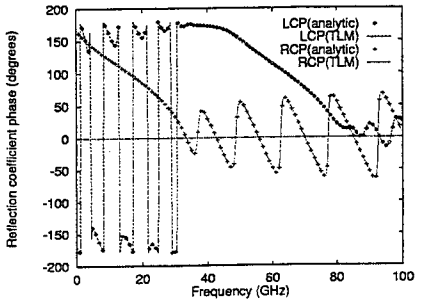


Figure 2: Reflection coefficient phases

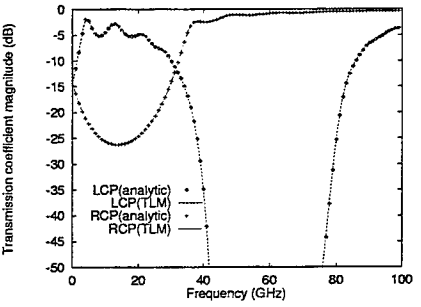


Figure 3: Transmission coefficient magnitudes

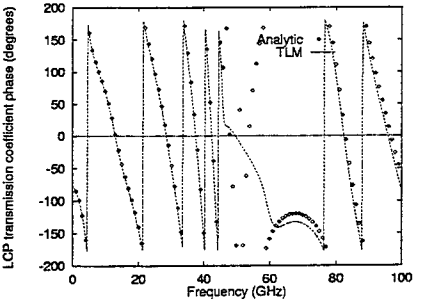


Figure 4: LCP transmission coefficient phase

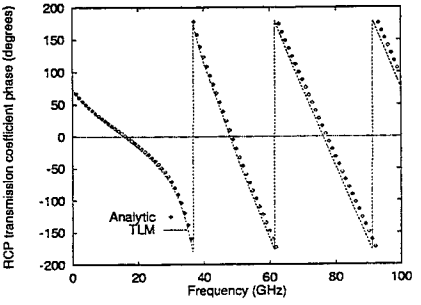


Figure 5: RCP transmission coefficient phase

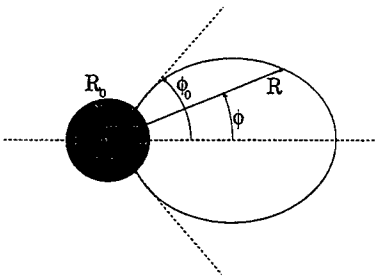


Figure 6: Geomagnetic field line

3. PROPAGATION IN THE IONOSPHERE

In the earth's ionosphere, the plasma frequency and the collision frequency are functions of the altitude above the ground. The gyro-frequency is a function of both altitude and geomagnetic latitude. In this section, the model is applied to the simulation of one-dimensional propagation along a geomagnetic field line as indicated in Fig. 6. This represents whistler mode propagation [5].

3.1. Geomagnetic field line

In Fig. 6, the mean earth radius $R_0 = 6371$km and the geomagnetic latitude of the field line at the earth's surface is ϕ_0. The geocentric radius at geomagnetic latitude ϕ is [5],

$$R = R_0 \cos^2\phi / \cos^2\phi_0 \qquad (14)$$

The gyro-frequency is given by

$$\omega_b = \omega_{b,eq} \left(\frac{R_0}{R}\right)^3 \sqrt{1 + 3\sin^2\phi} \qquad (15)$$

where the gyro-frequency at the equator $\omega_{b,eq} = 2\pi \times 880 \times 10^3$.

3.2. Electron density

To a first approximation, the electron density is assumed to be a simple Chapman layer [7],

$$N_c = N_0 \exp\left\{0.5\left(1 - z - \sec\chi\, e^{-z}\right)\right\} \qquad (16)$$

In (16), N_c is the electron density, N_0 is the maximum electron density and χ is the angle between the sun and the zenith. The reduced height is given by

$$z = \frac{A - A_0}{H(A)} \qquad (17)$$

where the altitude above the ground $A = R - R_0$ and the altitude of the maximum electron density with the sun overhead is $A_0 = 300$km. Also in (17), $H(A)$ is the local scale height [8], given by

$$H(A) = \frac{k\,T(A)}{\bar{m}(A)\,g(A)} \qquad (18)$$

where k is the Boltzmann constant, $T(A)$ is the temperature, $\bar{m}(A)$ is the mean molecular mass and $g(A)$ is the acceleration due to gravity. To a first approximation, the temperature as a function of altitude is,

$$\begin{aligned} T(A \le A_i) &= T_0 + k_l\, A \\ T(A > A_i) &= T_\infty - (T_\infty - T_i) e^{-k_h (A - A_i)} \end{aligned} \qquad (19)$$

In (19), the altitude of the temperature inversion is $A_i = 85$km, the ground temperature $T_0 = 282$K, the low altitude temperature gradient $k_l = -1.102$K/km, the electron temperature at high altitudes is $T_\infty = 3750$K, the inversion temperature $T_i = T_0 + k_l\, A_i$ and the high altitude temperature coefficient $k_h = 0.01105$/km.

The mean molecular mass in (18) is assumed constant at $\bar{m} = 3.97 \times 10^{-26}$kg and the acceleration due to gravity is

$$g(A) = g_0 \left(1 + \frac{A}{R_0}\right)^{-2} \qquad (20)$$

where $g_0 = 9.825$m/s.

For modelling the electron density at high altitudes, (16) must be modified to take into account the fall off in electron density due to the plasmapause [5]. This is approximated by multiplying (16) with an exponential function, i.e.,

$$N = N_c \exp\left\{-\frac{A - A_0}{A_p}\right\} \qquad (21)$$

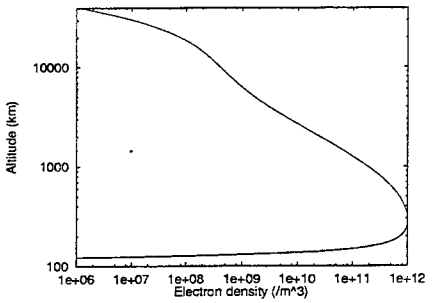


Figure 7: Electron density

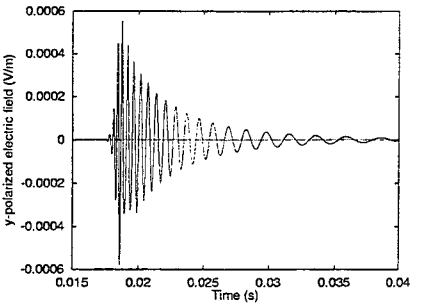


Figure 8: High altitude whistler, time-domain

where $A_p = 3500$km.

By combining (16) through (21), assuming the sun is overhead, i.e. $\chi = 0$, the maximum electron density $N_0 = 10^{12}\text{m}^{-3}$ and evaluating the electron density as a function of altitude, the profile of Fig. 7 is obtained. The approximation obtained is of the same order as the measured results for low and high altitudes shown in reference [7]. The plasma frequency follows from $\omega_p = \sqrt{N q^2/(\varepsilon_0 m)}$ and the collision frequency is approximately $\nu_c \sim N \times 7 \times 10^{-13}$ [5].

3.3. High altitude whistler

The high altitude dispersion of a derivative Gaussian pulse is shown in Fig. 8. The model consisted of 8000 cells of space-step $\Delta\ell \sim 0.278$km covering 5° of the geomagnetic field line indicated in Fig. 6 with $\phi_0 = 60°$. The pulse was launched at $\phi = 2.5°$ and the output was sampled for 60000 time-steps at $\phi = 1.25°$. The sample point was ~556km from the source point and the front of the pulse was observed after ~0.018s, indicating the speed of propagation of the pulse front of $\sim c/10$. This result agrees with the calculation in reference [8]: At the geomagnetic equator, for $\phi_0 = 60°$, $\omega_p \sim 85.7$kHz and $\omega_b \sim 13.75$kHz and the propagation speed of the whistler front

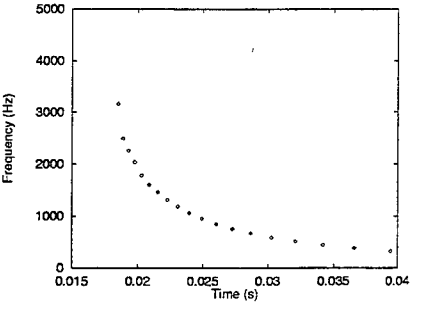


Figure 9: High altitude whistler, frequency-domain

is $c3\sqrt{3}\omega_b/(8\omega_p) \sim c/10$.

Fig. 9 shows the frequency content of the whistler as a function of time extracted by timing the zero-crossings. The figure indicates the expected frequency-dependent dispersion with the whistler nose frequency of $0.25\omega_b \sim 3.4$kHz [8].

3.4. Whistler launch

In Fig. 10, the launch of a z-polarized Gaussian derivative pulse from the ground into the lower ionosphere is shown. Also indicated in the figure is the shape of the electron density profile (c.f. Fig. 7). The model consisted of 8000 cells

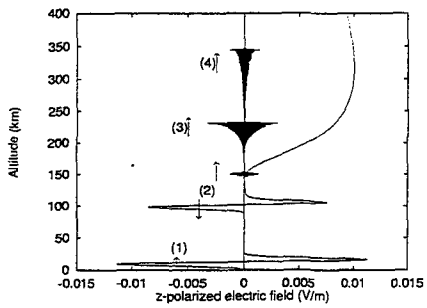


Figure 10: Whistler launch

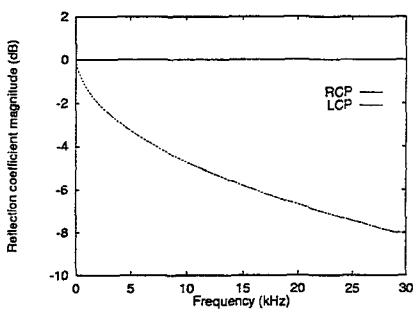


Figure 11: Reflection coefficient magnitude of the ionosphere

using a space-step of ~63.5m. The arrows on the curves indicate the direction of travel of the waves. Pulse (1) is the excitation observed after 400 time-steps. Pulse (2) shows the reflected and transmitted waves at the lower boundary of the ionosphere after 3000 time-steps. Pulses (3) and (4) show the transmitted wave scaled up by a factor of 10 after 30000 and 100000 time-steps. In Fig. 11 the reflection coefficient magnitudes for circularly polarized waves are shown. The figure indicates that only the LCP mode penetrates the ionosphere and the RCP mode is totally reflected.

CONCLUSIONS

This paper has dealt with the time-domain modelling of one-dimensional propagation in a magnetized plasma. The discretization scheme was based on a prewarped complex bilinear $\mathcal{Z}$-transform. Results obtained from the time-domain model for the reflection and transmission performance of a slab agreed closely with analysis. In the final part of the paper, the technique was applied to the simulation of propagation in the earth's ionosphere. The results obtained confirm that the frequency dispersion of a pulse travelling along a geomagnetic field line leads to the formation of a whistler.

REFERENCES

[1] F. Hunsberger, R. Luebbers, and K. Kunz. Finite-Difference Time-Domain Analysis of Gyrotropic Media—I: Magnetized Plasma. *IEEE Transactions on Antennas and Propagation*, 40(12):1489–1495, December 1992.

[2] J. Paul, C. Christopoulos and D. W. P. Thomas. Generalized Material Models in TLM—Part 2: Materials with Anisotropic Properties. *IEEE Transactions on Antennas and Propagation*, 47(10):1535–1542, October 1999.

[3] R. J. Luebbers and F. Hunsberger. FDTD for Nth-Order Dispersive Media. *IEEE Transactions on Antennas and Propagation*, 40(11):1297–1301, November 1992.

[4] V. L. Ginzburg. *The Propagation of Electromagnetic Waves in Plasmas.* Pergamon Press Ltd., Oxford, U.K., 1970.

[5] R. A. Helliwell. *Whistlers and Related Ionospheric Phenomena.* Stanford Univerity Press, Stanford, CA, 1965.

[6] J. Van de Vegte. *Feedback Control Systems.* Prentice-Hall Inc., Englewood Cliffs, NJ, 1994.

[7] J. K. Hargreaves. *The upper atmosphere and solar-terrestrial relations.* Van Nortrand Reinhold Co. Ltd., New York, 1979.

[8] J. A. Ratcliffe. *An introduction to the ionosphere and magnetosphere.* Cambridge University Press, London, 1972.

TLM SIMULATION OF PATCH ANTENNA ON MAGNETIZED FERRITE SUBSTRATE

M.I. Sobhy , M.W.R. Ng, R.J. Langley and J.C. Batchelor

The Electronic Engineering Laboratories,
The University of Kent at Canterbury
Canterbury, Kent, CT2 7NT, U.K.

email M.I.Sobhy@ukc.ac.uk
fax +44 1227 456084

Abstract

Patch antennas on magnetized ferrite substrate have useful properties like steerable beam direction, tunable resonance frequency and circular polarization. Conventional TLM (SCN) algorithm using open and short circuit stubs are not sufficient to model the magnetized ferrite substrate. A new TLM(SCN) algorithm has therefore been developed. General state equations are used to model the anisotropic and dispersive permeability of the magnetized ferrite substrate. Equivalent circuit for the magnetized ferrite substrate are first derived from the Polder permeability tensor and then transformed to state equations. The new TLM (SCN) algorithm is applied to compute the reflection coefficient S_{11} and the radiation pattern of a sample patch antenna on magnetized ferrite substrate. The algorithm is numerically stable and computed results agree with measurement.

I. INTRODUCTION

Microstrip patch antennas are widely used in communication system due to their conformal geometry and low production cost. Microstrip patch antennas on magnetized ferrite substrate have the further advantages not provided by conventional dielectric substrates. Beam direction and resonance frequency can be changed by varying the strength of the dc bias magnetic field [1]. Circular polarization occurs in the fundamental mode [2]. A planar antenna simulation tool based on the method of moment cannot deal with ferrite in magnetized state because of the anisotropic tensor permeability. In the original symmetrical condensed node (SCN) formulation of the TLM (Transmission Line Matrix) method, the dielectric properties of the media are simulated by three open circuited stubs, one for each direction of propagation and the magnetic properties by three short circuited stubs. Losses are simulated by three terminated stubs. However the dispersion in the media cannot be simulated. In this new TLM algorithm the non-linear, dispersive and anisotropic properties of the media are modelled by state equations [3]. In the new TLM(SCN) algorithm, the permittivity of the media is modelled by shunt transmission lines and an one-port equivalent circuit in the x,y and z directions respectively. The permeability is modelled by series transmission lines and an one-port equivalent circuit in the x,y and z direction respectively. The equivalent circuit of magnetized ferrite for the new TLM algorithm are first derived from the Polder tensor [4] as shown in equation (1).

$$\begin{bmatrix} B_x \\ B_y \\ B_z \end{bmatrix} = \begin{bmatrix} \mu_{xx} & \mu_{xy} & \mu_{xz} \\ \mu_{yx} & \mu_{yy} & \mu_{yz} \\ \mu_{zx} & \mu_{zy} & \mu_{zz} \end{bmatrix} \begin{bmatrix} H_x \\ H_y \\ H_z \end{bmatrix} = \begin{bmatrix} \mu & j\kappa & 0 \\ -j\kappa & \mu & 0 \\ 0 & 0 & \mu_0 \end{bmatrix} \begin{bmatrix} H_x \\ H_y \\ H_z \end{bmatrix}$$

where

$$\mu = \mu_0 + \chi$$

$$\chi = \frac{\gamma M_0 (\gamma H_0 + j\omega\alpha)}{(\gamma H_0 + j\omega\alpha)^2 - \omega^2} \qquad (1)$$

$$\kappa = \frac{-\omega\gamma M_0}{(\gamma H_0 + j\omega\alpha)^2 - \omega^2}$$

γ = Gyromagnetic ratio $\quad$ α = Damping factor

H_0 = D.C. Magnetic field $\quad$ M_0 = D.C. Magnetisation

The equivalent circuits of the Polder tensor for the new TLM algorithm are derived and shown in Fig.1.

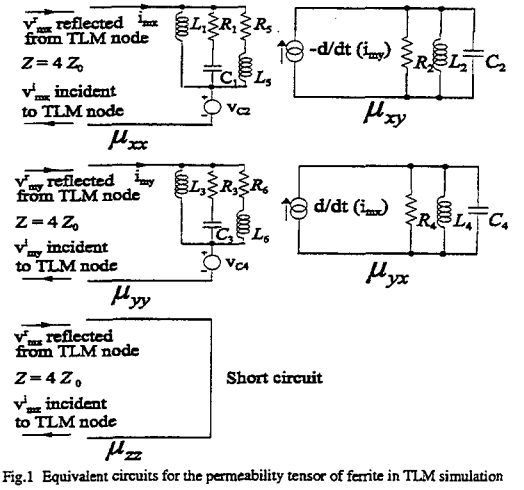


Fig.1 Equivalent circuits for the permeability tensor of ferrite in TLM simulation

The circuit elements in Figure 1 are given by

$$L_1 = L_3 = L_5 = L_6 = \frac{M_0 \Delta L}{H_0}\ ,\ L_2 = L_4 = \frac{M_0 \Delta L}{\gamma H_0^2}$$

$$C_1 = C_3 = \frac{\alpha^2 + 1}{\gamma^2 H_0 M_0 \Delta L}\ ,\ C_2 = C_4 = \frac{\alpha^2 + 1}{\gamma M_0 \Delta L}$$

$$R_1 = R_3 = \frac{\gamma M_0 \Delta L \alpha}{\alpha^2 + 1}\ ,\ R_2 = R_4 = \frac{M_0 \Delta L}{2 H_0 \alpha}\ ,\ R_5 = R_6 = \frac{\gamma M_0 \Delta L}{\alpha}$$

Gyromagnetic resonance effect is modelled by the parallel *LC* circuits and damping factor are modelled by resistors. Couplings between *x,y* and *z* directed magnetic fields are modelled by controlled voltage and current sources from the above equivalent circuits in Fig. 1. A set of state equations with 12 state variables can be derived to model the anisotropic permeability.

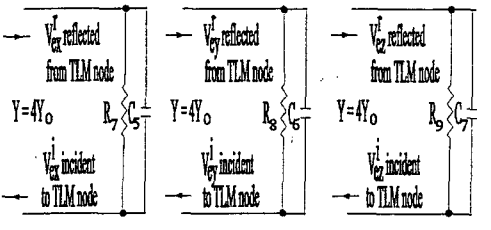


Fig. 2 Equivalent circuits for the permittivity of ferrite in TLM simulation

For the permittivity of ferrite the equivalent circuits used in the new TLM (SCN) algorithm are also derived and shown in Fig. 2. The elements in the equivalent circuits of Fig. 2 are given by

$$C_5 = C_6 = C_7 = (\varepsilon_r - 1)\varepsilon_0 \Delta L$$

$$R_7 = R_8 = R_9 = \frac{1}{\omega \delta (\varepsilon_r - 1)\varepsilon_0 \Delta L}$$

Where ε_r = Relative permittivity of the ferrite
ε_0 = Permittivity of air
δ = Loss tangent of ferrite
ΔL = TLM discretisation length

A set of state equations with 3 state variables are derived from the equivalent circuits in Fig. 2 . The overall state and output equations given in Equation (2).

$$\frac{dx}{dt} = Ax + Bv^r + B_n f(x, v^r) \qquad (2)$$
$$v^i = Cx + Dv^r$$

There are totally15 state variables required to model the permittivity and the tensor permeability of ferrite. In the overall state equations (2) the inputs are v^r the reflected voltages at the nodes. There are 6 output variables which are the six incident voltages v^i at the nodes. The functions $f(x, v^r)$ are used to represent the non-linearities in the ferrite. The inputs to the state equations are the reflected waves from the TLM (SCN) nodes to the equivalent circuits and are calculated using Equation (3). The TLM scattering equation which decouples the added effects of the media is given by equation (4). The LHS is the overall reflected voltages from the TLM(SCN) node and is the sum of two terms. The first term contains is the reflections if the media is free space and the second term is the added contribution from the media. The second term can be calculated if the permittivity and permeability are known and can be modelled by a set of state equations or equivalent circuits.

$$\begin{bmatrix} v^r_{ex} \\ v^r_{ey} \\ v^r_{ez} \\ \frac{1}{4}v^r_{mx} \\ \frac{1}{4}v^r_{my} \\ \frac{1}{4}v^r_{mz} \end{bmatrix} = \frac{1}{4} \begin{bmatrix} 1 & 1 & 0 & 0 & 0 & 0 & 0 & 0 & 1 & 0 & 0 & 1 \\ 0 & 0 & 1 & 1 & 0 & 0 & 0 & 1 & 0 & 0 & 1 & 0 \\ 0 & 0 & 0 & 0 & 1 & 1 & 1 & 0 & 0 & 1 & 0 & 0 \\ 0 & 0 & 0 & 1 & -1 & 0 & 1 & -1 & 0 & 0 & 0 & 0 \\ 0 & -1 & 0 & 0 & 0 & 0 & 0 & 0 & 1 & -1 & 0 & 0 \\ 1 & 0 & -1 & 0 & 0 & 0 & 0 & 0 & 0 & 0 & 1 & -1 \end{bmatrix} \begin{bmatrix} v^i_1 \\ v^i_2 \\ v^i_3 \\ v^i_4 \\ v^i_5 \\ v^i_6 \\ v^i_7 \\ v^i_8 \\ v^i_9 \\ v^i_{10} \\ v^i_{11} \\ v^i_{12} \end{bmatrix} \qquad (3)$$

The state equations are then solved numerically to obtain the outputs which are the incident waves from the equivalent circuits to the TLM(SCN) node. From these outputs of the state equations the total reflected voltage from the TLM(SCN) node can be calculated using Equation (4).

$$\begin{bmatrix} v_1^r \\ v_2^r \\ v_3^r \\ v_4^r \\ v_5^r \\ v_6^r \\ v_7^r \\ v_8^r \\ v_9^r \\ v_{10}^r \\ v_{11}^r \\ v_{12}^r \end{bmatrix} = \frac{1}{4} \begin{bmatrix} 0 & 1 & 1 & 0 & 0 & 0 & 0 & 0 & 1 & 0 & -1 & -2 \\ 1 & 0 & 0 & 0 & 0 & 1 & 0 & 0 & -2 & -1 & 0 & 1 \\ 1 & 0 & 0 & 1 & 0 & 0 & 0 & 1 & 0 & 0 & -2 & -1 \\ 0 & 0 & 1 & 0 & 1 & 0 & -1 & -2 & 0 & 0 & 1 & 0 \\ 0 & 0 & 0 & 1 & 0 & 1 & -2 & -1 & 0 & 1 & 0 & 0 \\ 0 & 1 & 0 & 0 & 1 & 0 & 1 & 0 & -1 & -2 & 0 & 0 \\ 0 & 0 & 0 & -1 & -2 & 1 & 0 & 1 & 0 & 1 & 0 & 0 \\ 0 & 0 & 1 & -2 & -1 & 0 & 1 & 0 & 0 & 0 & 1 & 0 \\ 1 & -2 & 0 & 0 & 0 & -1 & 0 & 0 & 0 & 1 & 0 & 1 \\ 0 & -1 & 0 & 0 & 1 & -2 & 1 & 0 & 1 & 0 & 0 & 0 \\ -1 & 0 & -2 & 1 & 0 & 0 & 0 & 1 & 0 & 0 & 0 & 1 \\ -2 & 1 & -1 & 0 & 0 & 0 & 0 & 0 & 1 & 0 & 1 & 0 \end{bmatrix} \begin{bmatrix} v_1^i \\ v_2^i \\ v_3^i \\ v_4^i \\ v_5^i \\ v_6^i \\ v_7^i \\ v_8^i \\ v_9^i \\ v_{10}^i \\ v_{11}^i \\ v_{12}^i \end{bmatrix} + \frac{1}{4} \begin{bmatrix} 4v_{ex}^i + v_{mz}^i \\ 4v_{ex}^i - v_{my}^i \\ 4v_{ey}^i - v_{mz}^i \\ 4v_{ey}^i + v_{mx}^i \\ 4v_{ez}^i - v_{mx}^i \\ 4v_{ez}^i + v_{my}^i \\ 4v_{ez}^i + v_{mx}^i \\ 4v_{ey}^i - v_{mx}^i \\ 4v_{ex}^i + v_{my}^i \\ 4v_{ez}^i - v_{my}^i \\ 4v_{ey}^i + v_{mz}^i \\ 4v_{ex}^i - v_{mz}^i \end{bmatrix} \quad (4)$$

II. TLM SIMULATION RESULTS

A 15mm long 0.7mm wide 50Ω microstrip line has been fabricated on a 1mm thick ferrite substrate . The ferrite medium is magnetized in the saturation region using a permanent magnet placed below and above the microstrip line sample. The simulation parameters are M_0=0.035 Tesla , γ=221000 rad m /sec A, H_0=234000 A/m, α=0.0056, ε_r=13.69, δ=0.0002, ΔL=0.1mm, Δt=0.1667ps and mesh size=47 x700x30. The S_{21} parameter has been measured using a vector network analyser. The TLM simulation results using a Gaussian excitation are shown in Fig. 3. The time domain results are transformed to the frequency domain using the FFT. The S_{21} parameter from the TLM simulation and measurement are compared and are shown in Fig.4. The simulated gyromagnetic resonance is in good agreement with the measurement.

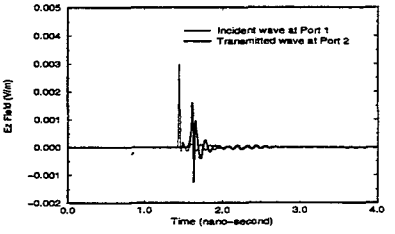


Fig. 3 TLM simulation of the microstrip line on magnetized ferrite substrate

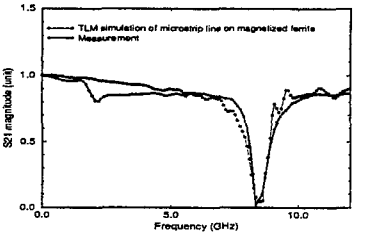


Fig. 4 The insertion loss S_{21} of the microstrip line on magnetized ferrite substrate

A microstrip patch antenna on ferrite substrate as shown in Fig. 5 has also been fabricated. The simulation parameters are M_0=0.035 Tesla , γ=221000 rad m /sec A, H_0=234000 A/m, α=0.0056, ε_r=13.69, δ=0.0002, ΔL=0.1mm, Δt=0.1667ps and mesh size=111x200x40. The simulated time domain results are shown in Fig. 6. The simulated and measured S_{11} are shown in Fig. 7. The patch antenna has a single resonance frequency at 8.2 GHz without magnetization. The new resonant frequencies at 6.4 , 7.0 ,and 8.75 GHz generated by the magnetized ferrite are simulated by the new TLM algorithm and are in close agreement with the measured results.

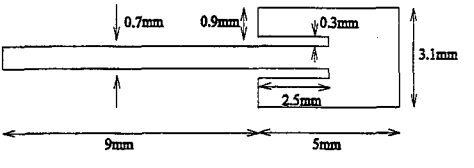


Fig. 5 Dimensions of the microstrip patch antenna

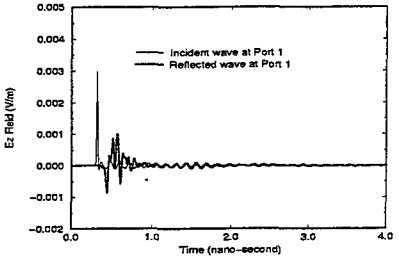


Fig. 6 TLM simulation of the microstrip patch antenna on magnetized ferrite substrate

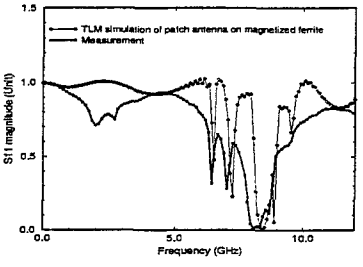


Fig. 7 The return loss S_{11} of the microstrip patch antenna on magnetized ferrite substrate

Far field radiation pattern of the antenna can be calculated by Fourier transform of the near field pattern[5]. Applying the equivalence principle the tangential electric fields on six rectangular surfaces enclosing the radiating patch antenna can be used as the near fields. The radiation efficiency of the patch antenna in Fig. 5 near the resonant frequency is so low that the measurement of the radiation pattern is buried in noise . Another patch antenna with resonant frequency at 4.66GHz was fabricated. Radiation pattern of this patch antenna on magnetized ferrite substrate has been computed using the new TLM algorithm and is shown in Fig 8. For the polarization in the angle psi direction in spherical coordinate a good agreement with the measured radiation pattern can be seen up to 60 degree azimuth. For the polarization in the angle theta direction, the measured power is low and noisy. The simulated and the measured power in the angle theta direction are of the same order of magnitude.

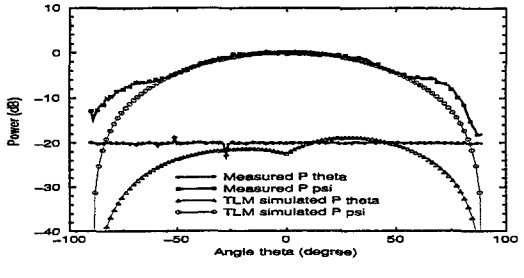


Fig. 8 Radiation pattern at 4.66 GHz of a patch antenna on magnetized ferrite substrate, angle psi = 0 degree

Simulation errors arise from the assumptions used in the formulation of the Polder tensor. The formulation assumes a completely saturated magnetization state, normal and uniform applied magnetic field and a constant damping factor at all frequencies. All the above assumptions are only approximations of the real magnetic properties of ferrite. Hysteresis loss is not included. The Polder tensor formulation of the ferrite permeability does not include the effect of the residue crystalline anisotropy field which cause gyromagnetic absorption at below 4GHz. Error in the measurement of the magnitude of the dc bias magnetic field causes differences in simulated and measured resonant frequencies. The space and time discretization used in the TLM method cause numerical dispersion and this also results in error in simulated resonant frequencies. Copper loss and the discontinuities at the coaxial to microstrip junction have not been included in the TLM simulation. Imperfect absorbing boundary condition used in TLM simulation can affect radiation pattern computed. All the above factors account for the differences in the simulated and measured results.

III. CONCLUSIONS

A new TLM (SCN) algorithm for ferrite media has been developed using state equations to model the media which is anisotropic, dispersive and non-linear. Time domain state equations models of the permeability of ferrite have been derived from the frequency domain Polder tensor. The new algorithm is numerically stable. The simulation results of a microstrip line and a patch antenna on magnetized ferrite medium in saturation region confirm the validity of the new algorithm.

IV. ACKNOWLEDGEMENT

The work of M.W.R. Ng is supported by research grant funded by the EPSRC U.K.

V. REFERENCES

[1] D.M. Pozar, and V. Sanchez, "Magnetic Tuning of a microstrip antenna on a ferrite substrate", Electronic Letter, 1998, V.24 , pp. 729-731.

[2] K.K. Tsang, and R.J. Langley, "Design of circular patch antennas on ferrite substrates" IEE Proc-Microw. Antenna Propag., Feb. 1998. V.145, pp.49-55

[3] L.R.A.X de Menezes and W.J.R. Hoefer, "Modelling of General Constitutive Relationships in SCN TLM", pp.854-860, IEEE Transaction on Microwave Theory and Techniques, Vol. MTT-44, No. 6, June 1996.

[4] A.J. Baden-Fuller, "Ferrite at Microwave Frequencies", pp.21-28, IEE1987.

[5] R.E. Collin, "Antenna and Microwave Propagation", pp164-182, McGraw Hill, 1985

On the Practical Use of Layered Absorbers for the Simulation of Planar Microwave Circuits using the SCN-TLM Method

Jürgen Rebel, Tobias Mangold and Peter Russer

Institut für Hochfrequenztechnik,Technische Universität MünchenArcisstr. 21, D-80333 Munich, Germany,
E-mail: rebel@hft.ei.tum.de, mangold@hft.ei.tum.de, russer@hft.ei.tum.de

Abstract

In this paper we report on the practical use of matched layer (ML) and perfectly matched layer (PML) absorbers for simulating planar microwave circuits using the SCN-TLM method. It emerges, that a recently proposed PML-SCN node suffers from serious stability problems when applied to layered three-dimensional problems and its practical use is hence very limited. However, revisiting the well-known matched layer technique, it emerges that a parabolic conductivity profile is not the best choice to achieve optimum absorption in contrast to common belief. Rather, the optimum conductivity profile depends on the number of matched layers. In the cases of 5 and 10 matched layer, a linear conductivity profile gave the best results in terms of minimum return loss, whereas for 15 matched layer, a steep profile witch $p = 2.4$ gave the best results. Furthermore, we show that the main source of reflection in the matched layer does not come from parasitic numerical reflections due to the abrupt change in conductivity, but from the differing dispersion in neighbouring media with different media parameters.

1 Introduction

When simulating planar microwave circuits it is necessary to truncate the computational domain by absorbing boundary conditions to eliminate unphysical reflections from truncating the mesh. For this, a number of absorbing boundary conditions have been proposed and intensively studied [1, 3, 10, 11]. Examples are boundary conditions obtained by discretizing one-way analytical conditions derived for the analytical wave equations [10] and Taylor's expansion of the plane wave solution [3]. Another approach is the use of discrete Green's functions [7].

Recently, Berenger suggested truncating the computational domain by an artificial medium known as *perfectly matched layer* (PML), which achieves a much better absorption than previously suggested absorbing boundary conditions [2]. For the use with the TLM method with symmetrical condensed node, there have been different approaches of implementing the PML. The first reported use of PML in TLM was given by Eswarappa and Hoefer where a FDTD implementation of PML was interfaced with the TLM computational domain [6].

A modified SCN simulating PML media was proposed by Dubard and Pompei [4]. Although the authors report various applications to three-dimensional antenna problems, in view of the results presented in this paper, it seems that this TLM PML node is numerically extremely critical which limits its practical use tremendously, especially when the PML layers are supposed to truncated layered inhomogeneous media.

Later, another unified PML-SCN algorithms were proposed by Ney et al. [11]. However, when using uniform PML-SCN algorithms, the authors also report stability problems of their implementation which also limit the practical use of their PML implementation.

For this, we revisited the well known matched layer technique as this Maxwellian absorber is absolutely stable as it consists of common symmetrical condensed nodes. Optimizing the conductivity profile of the matched layer yields sufficient absorption for calculating S-parameters in planar waveguide problems. It emerges, that in the studied examples, a linear conductivity profile yields the minimum return loss in contrast to common belief.

2 Implementation of Layered Absorbers

Planar microwave circuits commonly involve complicated layered substrates. Examples are multichip-module interconnects or planar inductors on Si substrates [9, 12]. Considering the cross-section of such realistic structures, one realizes that one has a very large number of regions with different media parameters such as permittivity, permeability and conductivity. This large number of regions is of course also present at the terminating walls of the computational domain. If one wants to use layered absorbers for such structures, each of these regions requires its own matched conditions in normal direction. Although it is not absolutely impossible to derive the necessary parameters for the ML or PML by hand, practically, it is necessary to automize the generation of the absorbing layers surrounding the computational domain.

We have implemented an automatic generator for generating these surrounding layers. The general algorithm of this generator shall be sketched briefly. Particularly for using PML, one can generally distinguish three different types of regions, i.e. plates for uniaxial PML, edges for biaxial PML and corners for triaxial PML. Our generator works list oriented, i.e. for each type of possible PML region a separate list is administrated. This allows the flexible declaration of layered absorbers in any combination. In waveguide structures, it may be sufficient to use PML at the ports of the structure. In radiation problems, such as characterization of microstrip antennas, PML may be desired at all sides of the computational domain. Of course, this generator can also be used for specifying a matched layer termination of the computational domain.

3 Stability Problems of the PML-Symmetrical Condensed Node

Although the use of the recently introduced PML symmetrical condensed node has been demonstrated by simulating planar antenna structures, we could not reproduce these results due to serious stability problems. The stability issue seems to be more profound, as others have made the same observations [8]. We could perfectly demonstrate the function of the PML in two dimensional parallel plate test structures. However, in three-dimensional problems, instabilities corrupted the solution after a few hundred time steps. To illustrate this, a coplanar waveguide with uniform mesh using cubic cells was terminated with five layers of PML, using the same parameters as Dubard et al. [5]. The geometry of the waveguide is depicted in Fig. 1 and the time-domain signals in Fig. 2. The other walls were terminated by simple matched load terminations as described in the next section. Although the PML seems to work at the beginning of the simulation, especially when compared to a reference solution using a very large domain and a waveguide truncated with matched load, after 1500 time steps the solution deteriorates.

To probe further into the nature of these instabilities, we studied a single PML-SCN cell in a simple TLM test code were we could easily switch between single and double precision arithmetic. For this one of the ports was excited by a Gaussian pulse which is formally equivalent to a PML cell interfacing a larger computational domain. Using single precision, strange round-off errors can be observed as shown

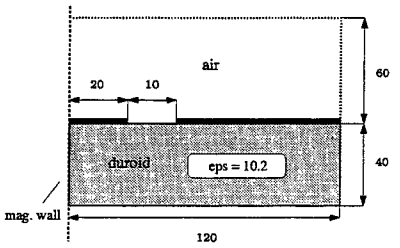


Figure 1: Dimensions of test coplanar waveguide with uniform cubic mesh in μm. Δl was chosen 2μm.

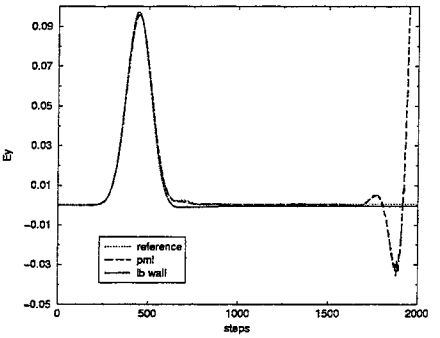


Figure 2: Coplanar waveguide terminated with PML.

in Fig. 3. However, using double precision, these round-off errors vanish, as indicated in Fig. 4. These results clearly indicate, that this implementation of the split field Berenger formulation of the PML is numerically rather problematic in case of the PML-SCN node.

Simulating real three-dimensional problems using double precision arithmetic, the stability problems still remained which indicates that not only round-off errors are responsible for the instabilities. Furthermore, we observed instability, when we excited four PML-SCN cells stacked as a square at the flat side. This indicates, that some unwanted modes in connection with round-off problems are responsible for the stability problems.

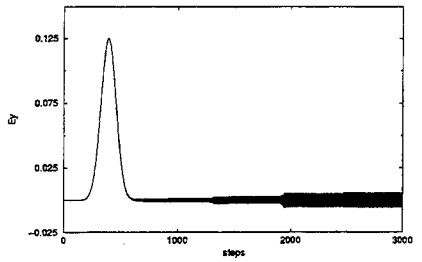


Figure 3: Single PML cell with Gaussian excitation using single precision arithmetic.

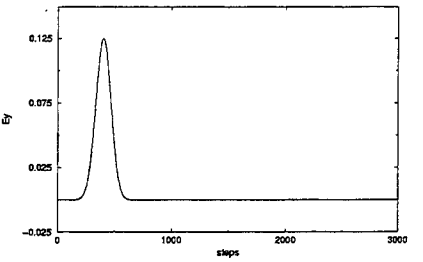


Figure 4: Single PML cell with Gaussian excitation using double precision arithmetic.

4 Matched Load Technique for Irregularly Graded Mesh

The least computational effort for modelling free space boundaries can be achieved by terminating transmission-lines of a TLM-SCN mesh touching the boundary plane with a reflection coefficient $r_{eff} = 0$. Within a stub-loaded TLM mesh a local reflection coefficient $r_{loc} \neq r_{eff}$ has to be used to achieve an effective reflection coefficient r_{eff}. For isotropic materials a local reflection coefficient r_{loc} is determined

by

$$r_{loc}\left(r_{eff}, \epsilon_r, \mu_r, (u,v,w)\right) = \frac{r_0 + r_{eff}}{1 + r_0 r_{eff}} \tag{1}$$

where

$$r_0 = \frac{\frac{g_{\|}}{g_{\perp}}\sqrt{\frac{\mu_r}{\epsilon_r}} - 1}{\frac{g_{\|}}{g_{\perp}}\sqrt{\frac{\mu_r}{\epsilon_r}} + 1} \qquad \text{with} \qquad \begin{array}{lll} g_{\|} & \in (u,v,w) & \| \quad V_i \\ g_{\perp} & \in (u,v,w) & \perp \quad V_i \end{array} \tag{2}$$

The variable terms $g_{\|}$ and $g_{\perp}$ represent the normalized geometric dimension of the adjacent TLM-cell in the directions parallel ($\|$) or perpendicular ($\perp$) to the polarization of the wave amplitude V_i on the transmission-line to be terminated. This termination of free space boundaries is comparable with absorbing boundary conditions of first order. Though their absorption is relatively low, they exhibit two main advantages over higher order models. There is no additional memory requirement or computational effort. Using matched load terminations, a return loss of around -30dB can be achieved in waveguide problems as indicated in Fig. 6. Similar loss figures were reported in [11].

5 Optimizing the Matched Layer Technique

In contrast to PML, a layered matched layer termination of the computational domain is unconditionally stable. For this, we studied the influence of various parameters, such as layer thickness, theoretical reflection coefficient, and conductivity profile more thoroughly in order to determine the optimum parameter combination. The theoretical reflection coefficient determines the maximum conductivity at the end of the ML. Following Ney et al. [11], we used the following conductivity profile

$$\sigma(L) = \sigma_{max}\left(\frac{L}{N}\right)^p, \tag{3}$$

where σ_{max} denotes the maximum matched layer electric conductivity at the outer layer N of the matched layer, $L \in 1, ..., N$ denotes the index of the matched layer. The maximum conductivity is calculated according to

$$\sigma_{max} = -\frac{a_{red}(p+1)\ln(R_0)}{2N\Delta l Z_0}, \tag{4}$$

with R_0 the theoretical reflection coefficient when the matched layer absorber is terminated by an electric wall and Z_0 the free space impedance. It emerged that using a constant $a_{red} = 1.0$ resulted in conductivity values, which changed the dispersion in neighbouring layers with different media parameters such that a worse absorption was achieved in contrast to using lower conductivity values. A value of $a_{red} = 0.1$ performed much better thus reducing the differences in dispersion between neighbouring layers.
In layered media, the matched condition is as follows

$$\frac{\sigma_e^i}{\epsilon^i} = \frac{\sigma_m^i}{\mu^i} = \frac{\sigma_e^{i+1}}{\epsilon^{i+1}} = \frac{\sigma_m^{i+1}}{\mu^{i+1}} = \cdots \tag{5}$$

To investigate the influence of the various parameters of the matched layer, a simple coplanar waveguide was studied using a uniform mesh with cubic cells. We studied the performance of the ML for two

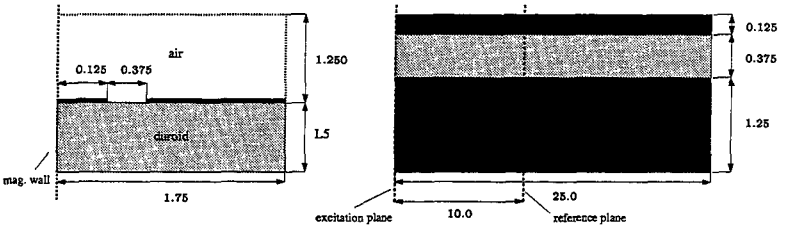


Figure 5: Details of the test coplanar waveguide used for optimizing the matched layer absorber. All dimensions in mm. Cubic cells with $\Delta l = 0.125$mm were used. The discretization is analogue to the cpw presented in [11].

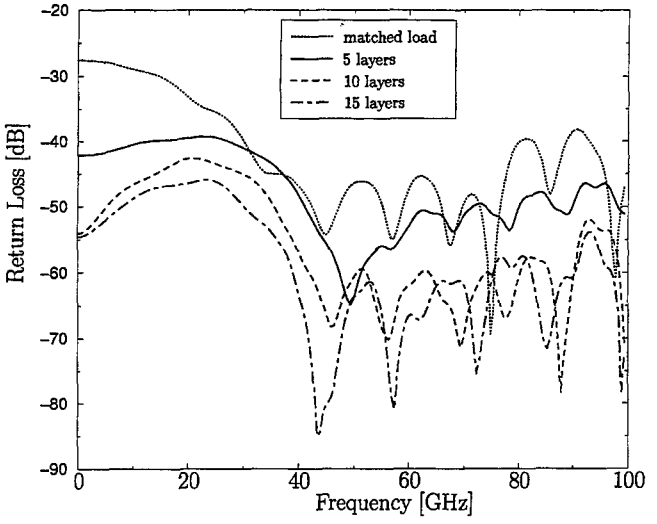


Figure 6: Minimum return loss curves for 5, 10 and 15 layers ML compared to matched load termination for CPW on substrate with $\varepsilon = 9.9$. For each ML thickness $R_0 = 1.0^{-4}$ yielded the best result. The profile coefficients are $p = 1.0$ for 5 and 10 ML and $p = 2.4$ for 15 ML.

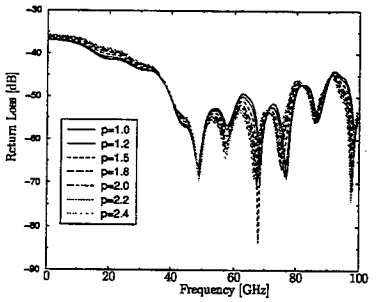


Figure 7: Return loss for 5 ML with $R_0 = 1.0^{-2}$ for CPW on substrate with $\varepsilon_r = 9.9$.

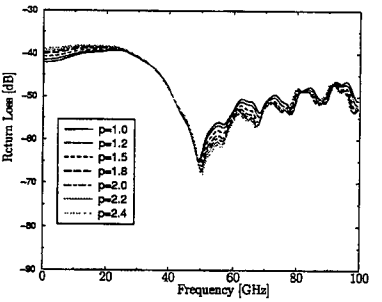


Figure 8: Return loss for 5 ML with $R_0 = 1.0^{-4}$ for CPW on substrate with $\varepsilon_r = 9.9$.

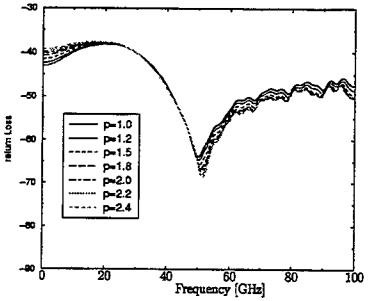


Figure 9: Return loss for 5 ML with $R_0 = 1.0^{-6}$ for CPW on substrate with $\varepsilon_r = 9.9$.

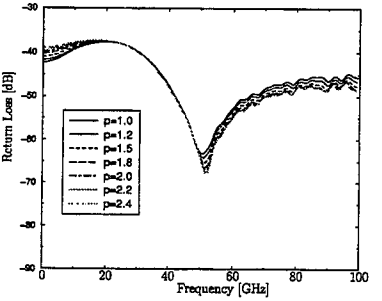


Figure 10: Return loss for 5 ML with $R_0 = 1.0^{-8}$ for CPW on substrate with $\varepsilon_r = 9.9$.

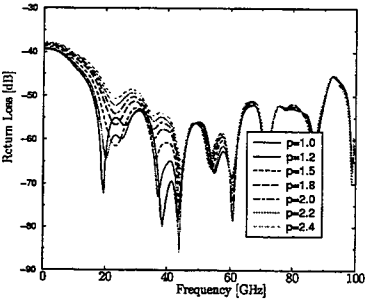


Figure 11: Return loss for 10 ML with $R_0 = 1.0^{-2}$ for CPW on substrate with $\varepsilon_r = 9.9$.

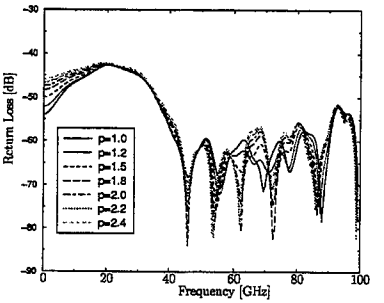


Figure 12: Return loss for 10 ML with $R_0 = 1.0^{-4}$ for CPW on substrate with $\varepsilon_r = 9.9$.

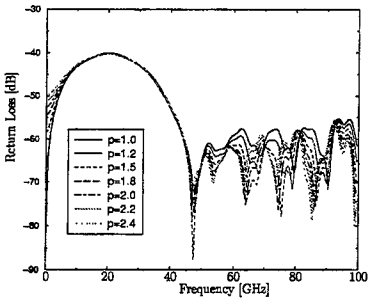


Figure 13: Return loss for 10 ML with $R_0 = 1.0^{-6}$ for CPW on substrate with $\varepsilon_r = 9.9$.

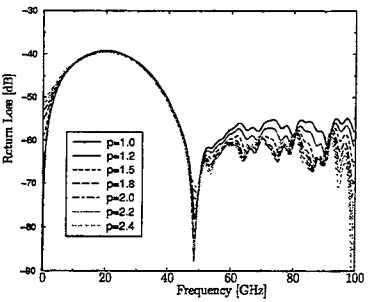


Figure 14: Return loss for 10 ML with $R_0 = 1.0^{-8}$ for CPW on substrate with $\varepsilon_r = 9.9$.

different substrates, one with $\varepsilon_r = 9.9$ and the other with $\varepsilon_r = 5.0$. The details are shown in Fig. 5. All other open sides were again terminated by matched load terminations.
We studied the influence of the conductivity profile, expressed by the exponential coefficient p in eqn. 3, on the absorption for three different layer thicknesses, i.e. five, ten, and 15 matched layers. In each case the profile coefficient is varied from $p = 1.0$ to $p = 1.2, 1.5, 1.8, 2.0, 2.2, 2.4$. The maximum conductivity is in each case varied by setting $R_0 = 1.0^{-2}, 1.0^{-4}, 1.0^{-6}, 1.0^{-8}$. The ML was always terminated with a matched load described in the previous section.

First, we want to compare the return loss curves for the CPW on a substrate with $\varepsilon = 9.9$ obtained using 5 matched layers, i.e. Fig. 7 to 10. Surprisingly, the difference between curves with different profile coefficient is less pronounced as previously expected. Below 20GHz, a difference of only $\pm$1dB can be recognized for different profiles. Interestingly, if R_0 is chosen too low, i.e. $\sim 1.0^{-2}$ the return loss is only 5dB less than the one obtained by using only a matched load termination is achieved in the lower frequency region (see Fig.7). By inspecting Fig. 7 to 10, one can find the optimum combination of parameters of the ML with 5 layers as $R_0 = 1.0^{-4}$ and $p = 1.0$ in Fig. 8. This parameter combination gives a uniform return loss of at least -40dB up to 20GHz.

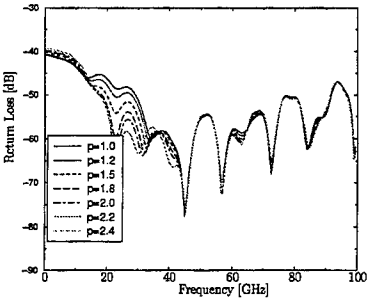


Figure 15: Return loss for 15 ML with $R_0 = 1.0^{-2}$ for CPW on substrate with $\varepsilon_r = 9.9$.

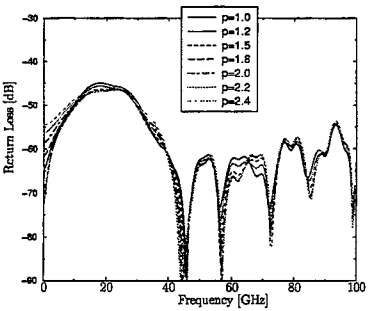


Figure 16: Return loss for 15 ML with $R_0 = 1.0^{-4}$ for CPW on substrate with $\varepsilon_r = 9.9$.

For comparison, the return loss for the 'best' combination of parameters chosen using the criteria mentioned above, for each ML thickness is shown in Fig.6. The curve, using simple matched load termination is also plotted.

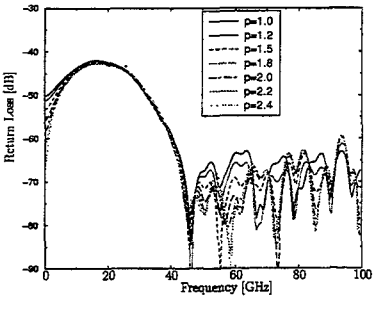


Figure 17: Return loss for 15 ML with $R_0 = 1.0^{-6}$ for CPW on substrate with $\varepsilon_r = 9.9$.

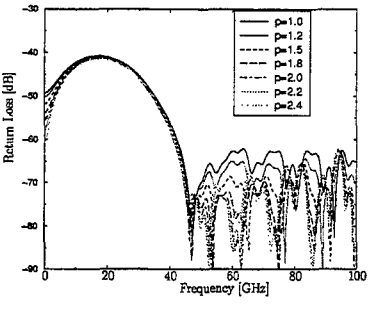


Figure 18: Return loss for 15 ML with $R_0 = 1.0^{-8}$ for CPW on substrate with $\varepsilon_r = 9.9$.

Increasing the number of ML to 10 results in a return loss of almost -50dB up to 10 GHz and -43dB up to 20 GHz for the optimum parameter combination $R_0 = 1.0^{-4}$ and $p = 1.0$, which can be found from Fig. 12. Again, if R_0 is chosen too low, as depicted in Fig. 11, the return loss is about 10dB better then when using a matched load termination. Compared to using 5 matched layers, the influence of the profile coefficient p is more pronounced when looking at Fig. 12 to 14, especially for $R_0 = 1.0^{-4}$ where varying p results in a $\pm$3dB change in return loss in the 0-10 GHz region.

A similar picture presents itself when 15 layers ML are used. Comparing Fig. 15 to 18 indicates that only for $R_0 = 1.0^{-4}$ the profile coefficient p has a pronounced influence on the return loss in the low frequency region. Again, the 'best' return loss up to 20 GHz is achieved for $R_0 = 1.0^{-4}$. However, using a steeper profile with $p = 2.4$ gives the lowest overall return loss up to 20 GHz, which is almost below -57dB everywhere in this region.

If we look at the return loss curves for the CPW on a substrate with approximately half the dielectric constant, i.e. $\varepsilon_r = 5.0$, Fig. 19 to 21, one immediately realizes that the more or less uniform low frequency absorption region extends up to approximately 40GHz. The absorption of the 5, 10, and 15 ML was investigated for $R_0 = 1.0^{-4}$ and the previously mentioned values of p. Interestingly, for 5 and 10 ML a linear profile, i.e. $p = 1.0$, yields the most uniform absorption, whereas in case of 15 ML a profile with $p = 2.4$ yields the most uniform absorption.

In Fig. 22 to 24, the return losses for the CPWs on the two substrates with identical ML parameters are compared. It is evident, that the media parameters of the substrate have a distinct influence on the performance of the ML absorber.

For the CPW with $\varepsilon_r = 5.0$ substrate, the absorption in the lower frequency region up to 40GHz is much better when compared to the return loss for the CPW on a substrate with $\varepsilon_r = 9.9$. In the latter case, the absorption in the upper frequency region is better. From this, it is clear that the differences in dispersion due to the different media parameters in neighbouring layered media have a stronger influence on the performance of the ML absorber as the parasitic reflections due to abrupt changes in conductivity.

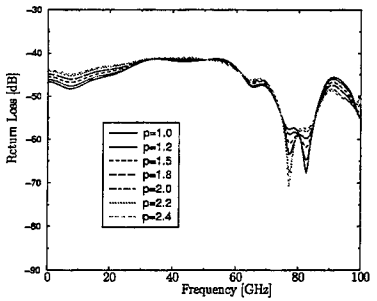


Figure 19: Return loss for 5 ML with $R_0 = 1.0^{-4}$ for CPW on substrate with $\varepsilon_r = 5.0$.

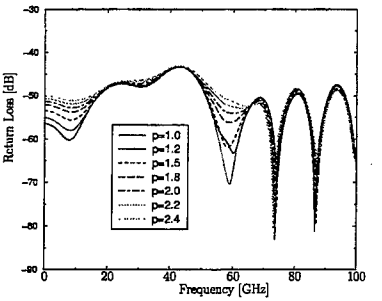


Figure 20: Return loss for 10 ML with $R_0 = 1.0^{-4}$ for CPW on substrate with $\varepsilon_r = 5.0$.

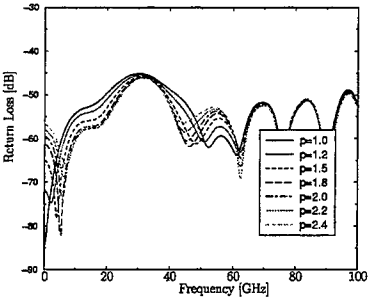


Figure 21: Return loss for 15 ML with $R_0 = 1.0^{-4}$ for CPW on substrate with $\varepsilon_r = 5.0$.

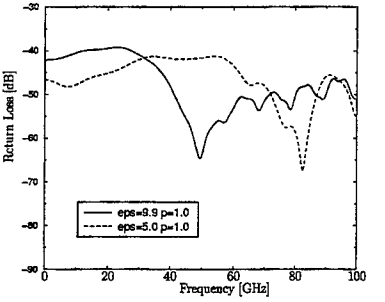


Figure 22: Comparison of return loss for 5 ML with $R_0 = 1.0^{-4}$ for CPW on substrates of $\varepsilon_r = 5.0$ and $\varepsilon_r = 9.9$.

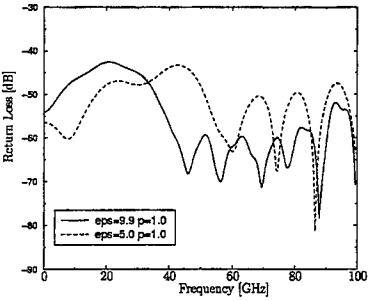


Figure 23: Comparison of return loss for 10 ML with $R_0 = 1.0^{-4}$ and $p = 1.0$ for CPW on substrates of $\varepsilon_r = 5.0$ and $\varepsilon_r = 9.9$.

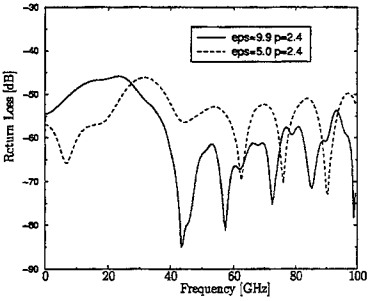


Figure 24: Comparison of return loss for 15 ML with $R_0 = 1.0^{-4}$ and $p = 2.4$ for CPW on substrates of $\varepsilon_r = 5.0$ and $\varepsilon_r = 9.9$.

6 Conclusion

In this paper we have investigated the performance of matched layer absorbers for truncating the computational domain in planar problems with layered substrates. The absorption of the ML was studied at the example of a coplanar waveguide on two different substrates with different permittivity. It was found that for 5 an 10 ML a linear conductivity profile yields the best absorption, whereas for 15 ML a profile coefficient of $p = 2.4$ yielded the most uniform absorption. Hence, one could say that the more ML are used the steeper the conductivity profile has to be. Moreover, we could show that in problems which involve layered media, the main source of reflection in the matched layer is due to different dispersion in neighbouring layers and not due to the abrupt change in conductivity, as previously thought.

Furthermore, we found that a recently proposed PML TLM node suffers from serious numerical problems which inhibits its practical use in problems with layered media.

7 Acknowledgment

One of the authors (J. Rebel) would like to thank Siemens AG for generously granting an Ernst-von-Siemens scholarship.

References

[1] A. Banai, F. Farzaneh, F. Ndagijimana, and P. Saguet, *An Interpretation of Instabilities in the Absorbing Boundary Conditions in TLM Method and an Improved Matched Termination Wall*, Int. J. Num. Modelling **11** (1998), 243–254.

[2] J.P. Berenger, *Three-dimensional perfectly matched layer for the absorption of electromagnatic waves*, Journal of Computational Physics **127** (1996), 363–379.

[3] Z. Chen, M. Ney, and W.J.R. Hoefer, *Absorbing and Connecting Boundary Conditions for the TLM Method*, IEEE Trans. Microwave Theory Tech. **41** (1993), no. 11, 2016–2024.

[4] J.L. Dubard and D. Pompei, *A Modified 3D-TLM Variable Node for the Berenger's Perfectly Matched Layer Implementation*, 13th Annual Review of Progress in Applied Computational Electromagnetics Digest (1997), 661–665.

[5] ———, *Optimization of the PML efficiency in 3D-TLM method*, private communication (1999).

[6] C. Eswarappa and W.J.R. Hoefer, *Implementation of berenger absorbing boundary conditions in tlm by interfacing fdtd perfectly matched layers*, Electron. Lett. **31** (1995), no. 15, 1264–1266.

[7] M. Krumpholz and P. Russer, *Discrete Time-Domain Greens Functions for Three-Dimensional TLM Modelling of the Radiating Boundary Conditions*, 9th Annual Review of Progress in Applied Computational Electromagnetics Digest **1** (1993), 458–466.

[8] S. LeMaguer, private communication at URSI conference 1999 (1999).

[9] T. Mangold and P. Russer, *Generation of Lumped Element Equivalent Circuits from Time-Domain Scattering Signals*, 14th Annual Review of Progress in Applied Computational Electromagnetics Digest (1998), 351–358.

[10] J. Morente, J. Porti, and M. Khalladi, *Absorbing Boundary Conditions for the TLM Method*, IEEE Trans. Microwave Theory Tech. **40** (1992), no. 11, 2095–2099.

[11] M. Ney, S. LeMaguer, and N. Pena, *Modeling of Absorbing Media for the Simulation of Open Boundaries in TLM*, Second Int. Workshop on TLM Modeling, Munich (1997), 91–102.

[12] H.D. Wohlmuth, W. Simbürger, H. Knapp, and A.L. Scholtz, *2GHz Meißner VCO in Si Bipolar Technology*, Proceddings of 29th European Microwave Conference (1999), 190–193.

A NUMERICAL STUDY OF MEMS CAPACITIVE SWITCHES USING TLM

FABIO COCCETTI, LARISSA VIETZORRECK, VITALI CHTCHEKATOUROV AND PETER RUSSER

INSTITUT FÜR HOCHFREQUENZTECHNIK, TECHNISCHE UNIVERSITÄT MÜNCHEN
ARCISSTR. 21, D-80333 MUNICH, GERMANY
EMAIL: {COCCETTI|VIETZORRECK|CHTCHEKA|RUSSER}@EI.TUM.DE

ABSTRACT. In this paper we investigate the RF behaviour of a microelectromechanical capacitive switch by the Transmission Line Matrix method (TLM). These microelectromechanical (MEMS) switches can be utilized for antenna and phased array applications for communication systems or automotive radar. The switch under study consists of a thin metallic membrane connected to the ground of a CPW line which - when actuated by a dc voltage - forms a virtual short with the center conductor of the CPW. It is demonstrated how the TLM algorithm can be applied for the calculation of the scattering parameters of both switching states.The crucial point for the analysis of those structures is the aspect ratio of the geometrical dimensions. Especially in the off-state, where the virtual short is realized by a 0.1 μm thin dielectric layer between the two electrodes, the discretization becomes problematical. Here the time domain analysis can solve this problem very elegantly by modeling the thin layer as a thick anisotropic medium with a very much higher dielectric constant in vertical direction. However, due to highly dispersive structure, a post-processing of time domain signal is necessary to avoid long calculation times and to suppress unwanted reflections at the not ideal absorbing boundary at the output planes. The signal is truncated suitably and then prolonged analytically by estimating the truncated part by a least square parameter estimation using AR models. The calculated results of a metal membrane switch show very good agreement to results obtained by other numerical methods.

1. INTRODUCTION

Since the first demonstration of a MEMS switch in 1971 [1] vivid research activities in this area have started due to the increasing demand on miniaturized elements and circuits. Rapid advances in bulk and surface micromachining techniques have enabled the fabrication of more and more complex three-dimensional components with great reliability. Different forms of MEMS switches in shunt and series configuration, developed mostly for phased array antenna applications, have been proposed recently [2, 3, 4, 5, 6].

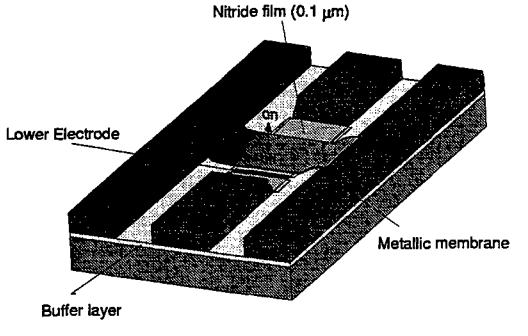


FIGURE 1. Geometry of a MEMS capacitive switch in on -and off position

In comparison with other switches, realized by PIN diodes, e.g., MEMS capacitive switches possess a better isolation and insertion loss, they exhibit a great linearity and the power consumption is zero in the activated position. Certainly there are some drawbacks like the the switching speed or the comparatively high switching voltage. Since the fabrication of those switches is a demanding technological process, there is a great need for suitable design tools for a numerical characterization with reasonable effort combined with a great accuracy.

In Fig. 1 the basic design of a single-pole single-through Ka-band shunt switch in coplanar technique is depicted. Unfortunately these metal membrane switches possess some features which make a numerical description of the purely high-frequency behavior quite difficult, especially the calculation of insertion/isolation and return loss in the different switching positions. They exhibit a layered structure on a bulk high-resistive silicon substrate with some extremely thin layers. For this switch the thickness of the nitride film, which prevents sticking of the two electrodes in the off-state, is in the range of 0.1 μm. Also the SiO_2 buffer layer, the lower electrode and the metallic membrane are very thin compared to the height of the substrate, the transverse dimensions and the length of the connecting transmission lines. This geometry considerably affects the discretization and hence the required memory and calculation times for all numerical methods.

In this contribution the TLM method is proposed for the numerical characterization of the RF behavior of this switch. The time domain method gives accurate results by using less memory than frequency domain methods. Employing an anisotropic model for the thin dielectric film avoids a too fine discretization as necessary in other methods. A suitable post-processing of the time domain signal applying a least square parameter estimation prevents long calculation times. Here we use it for the numerical improvement of the results, whereas in [7] it has been utilized for analytic calculations.

2. Analysis of different switching states

2.1. The on-state. In the on-state, when the membrane is not actuated, the thin nitride film upon the lower electrode can be neglected, as the influence on the capacity of the bridge is marginal due to its small thickness. The TLM analysis is carried out using $N_x = 268$, $N_y = 88$ and $N_z = 90$ nodes. The output ports are closed by matched impedance layers. 12000 time steps were chosen, since the Gaussian input pulse widens severely in the highly dispersive structure. Reflections occurring at the not ideal absorbing boundaries at the output ports can be suppressed in the time domain signal by filtering with simple window functions. The results are depicted in Fig. 3. and Fig. 4 and compared with numerical results obtained with the method of lines (MoL), working in frequency domain [8]. For the reflection coefficient a very good agreement can be observed. The slight difference in the transmission factor can be explained by taking into account substrate and conductor loss in the MoL, which is more significant for low frequencies, and the radiation loss considered by TLM. However, the agreement is also quite good bearing in mind the low value of the insertion loss.

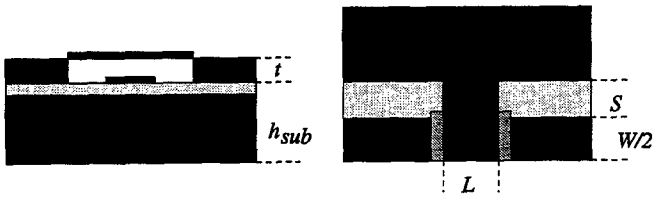


FIGURE 2. Layout and longitudinal section of the examined structure. The geometrical parameters of the CPW line are $W = 60$ μm, $S = 45$ μm, $t = 2.5$ μm, $L = 60\mu$m, $h_{sub} = 300$ μm, $\varepsilon_{Si} = 12.67$

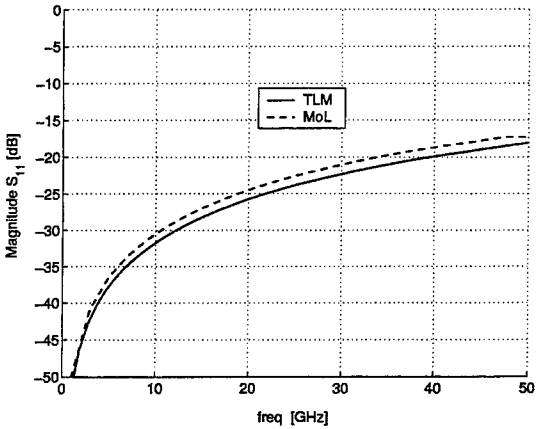


FIGURE 3. Return loss for the not actuated switch compared with numerical results obtained by the MoL

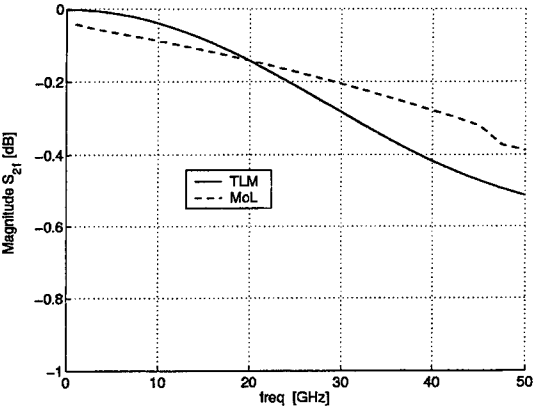


FIGURE 4. Insertion loss for the switch in on-position

2.2. **The off-state.** The analysis of the off-state is much more complicated for all numerical methods. The membrane is pulled down by applying an electrostatic force, forming a virtual short through the very thin nitride film. Here the thin film is considered by modeling the dielectric layer with the thickness t_d as anisotropic medium of thickness t_m with a dielctric constant

$$\overleftrightarrow{\varepsilon_r} = diag(\varepsilon_{r_x},\ \varepsilon_{r_y},\ \varepsilon_{r_z}) = diag\left(\varepsilon_r,\ \varepsilon_r,\ \frac{t_m}{t_d}\varepsilon_r\right) \tag{1}$$

Unfortunately the virtual short has a severe influence on the run of the time domain signal, which can be observed in Fig. 5.

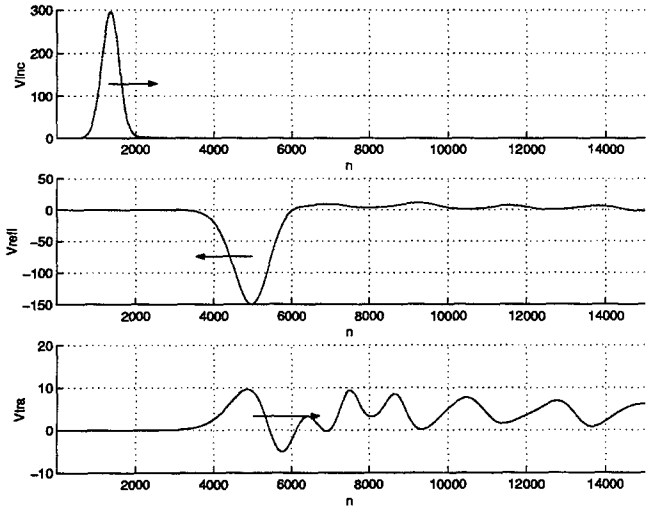


FIGURE 5. Incoming, reflected and transmitted time domain signals in the off-state

A truncation of the the signal after 15000 time steps leads to a considerable error after transformation in frequency domain. This can be seen in Fig. 6. and Fig. 7 (TLM without prolongation), where the artificial limited bandwidth of the time domain signal causes an unphysical behavior in the lower frequency band and a violation of the power conservation. A higher number of timesteps enforces not only a considerably higher calculation time, but also a larger amount of required memory, as the length of the transmission lines has to be increased in order to avoid a superposition with the reflected signal. To overcome this problem, the truncated time domain signal is completed by an predicted behavior, calculated by a least square parameter estimation using AR models.

2.3. **ARMA and AR models for the S-parameter estimations.** The using of the autoregressive-moving average (ARMA) and the autoregressive (AR) [9] models can be successfully applied for the linear prediction of a low-decayed impulse responses of HF devices. These models can be described for a m-channel process $s[n]$, $(n = 0 \dots N)$ by the system of the difference equations

$$\underbrace{\mathbf{s}[n] = -\sum_{k=1}^{d} \mathbf{A}[k] \cdot \mathbf{s}[n-k] + \sum_{k=0}^{r} \mathbf{B}[k] \cdot \mathbf{u}[n-k]}_{ARMA} = \underbrace{-\sum_{k=1}^{p} \mathbf{C}[k] \cdot \mathbf{s}[n-k] + \mathbf{u}[n]}_{AR} \qquad (2)$$

where $\mathbf{A}[k]$, $\mathbf{B}[k]$, $\mathbf{B}[k]$ - $m \times m$ complex matrices of the coefficients of the models; d, r, p - orders of the models, $\mathbf{u}[n]$ - a m-channel input process.

The matrix-shifting techniques as well as polynomial AR spectral estimation methods are usually used for the estimation of the complex coefficients of the models [10]. So the least squares estimation method,

which minimizes the error between samples of a process and samples of the model, can be used for the determination of the linear prediction $1 \times (p+1)$ block matrix forward $\mathbf{C}^f = (I, \mathbf{C}^f[1] \ldots \mathbf{C}^f[p])$ and backward $\mathbf{C}^b[k] = (\mathbf{C}^b[p] \ldots \mathbf{C}^b[1], \mathbf{I})$:

$$\mathbf{C}^f \cdot \mathbf{SS} = (\Re^f 0 \ldots 0), \qquad \mathbf{C}^b \cdot \mathbf{SS} = (0 \ldots 0\ \Re^b) \tag{3}$$

where $\Re^f$, $\Re^b$ are linear prediction error matrices and $\mathbf{SS}$ – for the case of the covariance approach – is the $(p+1) \times (p+1)$ block matrix with elements

$$\mathbf{SS}[i,j] = \sum_{k=p+1}^{N} \mathbf{s}[n-i] \cdot \overline{\mathbf{s}}^T[n-j] \tag{4}$$

For $m = 1$ the system of equations (3) can be significantly simplified

$$\overline{\mathbf{S}}^T\mathbf{S} \cdot \left\{ \begin{bmatrix} 1 \\ \mathbf{c}^f \\ \mathbf{c}^b \\ 1 \end{bmatrix} \right\} = \left\{ \begin{bmatrix} \rho^f \\ 0 \\ 0 \\ \rho^b \end{bmatrix} \right\} \tag{5}$$

where $\mathbf{S}$ - windowed, prewindowed or nonwindowed matrix of the process; $\mathbf{c}^f$, $\mathbf{c}^b$ - the vectors of linear prediction coefficients. The estimations of the forward and backward poles z_k, and the correspondent residues w_k can be also easy made by factorization of the polynomials, which can be created from the parameters $\mathbf{c}^f$ and $\mathbf{c}^b$, and by solving the linear equations

$$(\overline{\mathbf{Z}}^T\mathbf{Z})\mathbf{w} = \overline{\mathbf{Z}}^T \tag{6}$$

where Z - $p \times N$ Vandermonde matrix of the poles z_k. The accuracy of the models (2) depends on the values of d, r, p and should be optimized [9].

In contrast to [7] we use this method only to predict the future time response of the truncated signal. For this estimation only a part of the output signal is used, namely the oscillating part with decaying amlitude. The calculation of the prolongation is shown in Fig. 6 and Fig. 7.

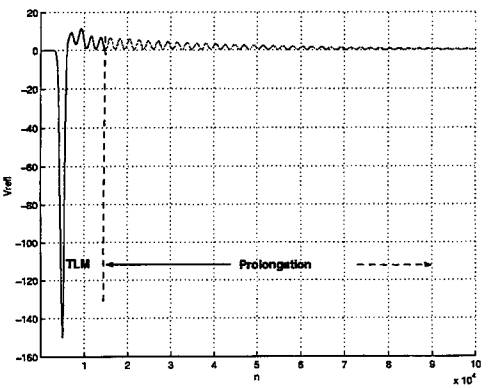


FIGURE 6. Prolongation of the reflected signal using a parameter estimation technique

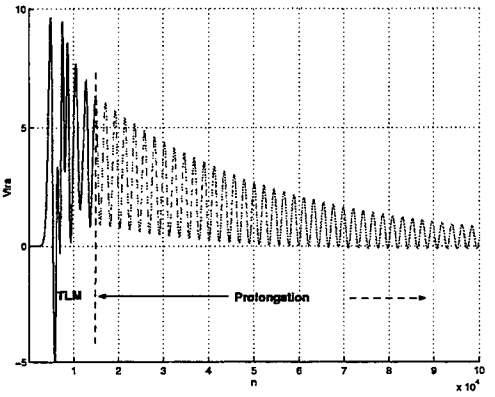


FIGURE 7. Prolongation of the transmitted signal using parameter estimation technique method

After a FFT of the signal into frequency domain, we observe a physically plausible run of the scattering parameters. In Fig. 8 it can be clearly seen, that the unphysical behavior for low frequencies has been corrected perfectly. Fig. 9 shows again a good correction of the behavior in the low frequency band. Here the comparison with the MoL can give here no final criterion for the judgement of the accuracy, as the MoL has to use approximate boundary conditions in the section of the membrane which can cause some deviations. A full discretization of the cross-section incorporating the thin layer would exceed the available computer memory.

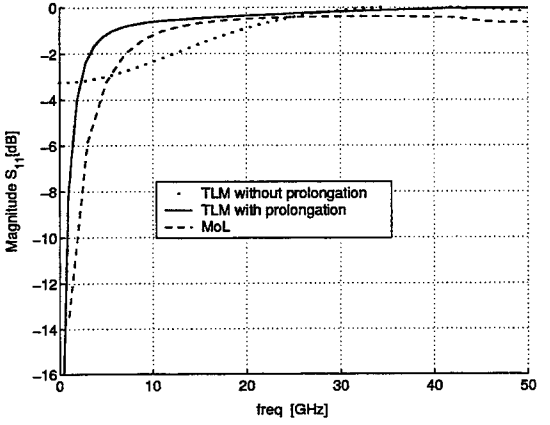


FIGURE 8. Return loss for the actuated switch compared with numerical results obtained by the MoL

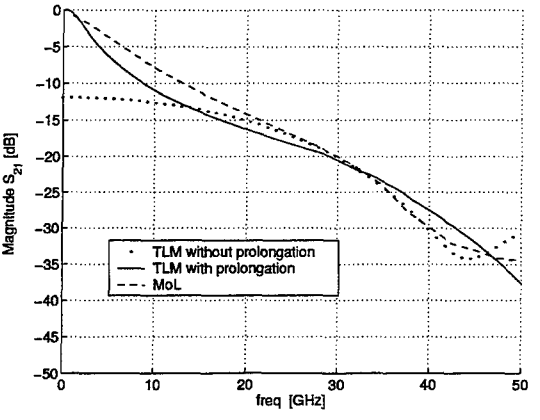


FIGURE 9. Isolation of the actuated switch

3. CONCLUSION

It was shown how a MEMS capacitive switch can be analyzed effectively by TLM. The analysis of the on-state of the switch requires no additional means for the calculation of the scattering parameters. A very good consistency with results obtained by the method of lines can be stated for both switching states. Less memory and computation time was spent by obtaining the same accuracy. For the off-state a post-processing of the time domain signal becomes necessary to avoid extreme calculation times. The reflection coefficient is corrected perfectly by predicting the truncated signal using a least square parameter estimation technique. The required amount of memory and computation time can be reduced drastically.

REFERENCES

[1] K.E. Petersen, "Micromechanical Membrane Switches on Silicon", *IBM J. Res. Develop.*, vol. 23, pp. 376–385, July 1971.

[2] C.L. Goldsmith, Z. Yao, S. Eshelman, and D. Denniston, "Performance of Low-Loss RF MEMS Capacitive Switches", *IEEE Microwave Guided Wave Lett.*, vol. 8, pp. 269–271, Aug. 1998.

[3] N.S. Barker and G.M. Rebeiz, "Distributed MEMS True-Time Delay Phase Shifters and Wide-Band Switches", *IEEE Trans. Microwave Theory Tech.*, vol. 46, pp. 1881–1890, Nov. 1998.

[4] S. Pacheco, C.T.C. Nguyen, and L.P.B. Katehi, "Microelectromechanical Electrostatic K-Band Switches", in *IEEE MTT-S Int. Symp. Dig.*, Baltimore, USA, June 1998, pp. 1569–1572.

[5] S. Chen, K. Suzuki, T. Marumoto, Y. Ara, and R. Iwata, "Design of Micromachined RF Switch", in *European Microwave Conference*, München, Germany, Oct. 1999, pp. 49–52.

[6] K.M. Strohm, C.N. Rheinfelder, A. Schurr, and J.-F. Luy, "SIMWIC Capacitive RF Switches", in *European Microwave Conference*, München, Germany, Oct. 1999, pp. 411–414.

[7] C. Eswarappa and W.J.R. Hoefer, "Fast S-Parameter Computation of a Microstrip Interdigital Filter Using TLM, Prony's and Digital Filtering Techniques", *Journal of Numerical Modelling*, vol. 9, pp. 237–248, 1996.

[8] L. Vietzorreck, "Modeling of the Millimeter-Wave Behavior of MEMS Capacitive Switches", in *IEEE MTT-S Int. Symp. Dig.*, Anaheim, USA, June 1999, pp. 1685–1688.

[9] S. Lawrence Marple Jr., *Digital Spectral Analysis*, Prentice Hall, Inc., New Jersey, USA, 1987.

[10] M. Haardt, *Efficient One-, Two- and Multidimensional High-resolution Array Signal Processsing*, Shaker Verlag, Aachen, 1997.

Thin Wire Modeling with the TLMIE-Method

S. Lindenmeier, C. Christopoulos*, P. Russer

Technische Universität München, Lehrstuhl für Hochfrequenztechnik
Arcisstrasse 21, D-80333, München, Germany; phone: +49 89 289 23378
fax: +49 89 289 23365, e-mail: lindenmr@hft.ei.tum.de
*School of Electrical and Electronic Engineering,
University of Nottingham, Nottingham, United Kingdom

Abstract

The hybrid Transmission Line Matrix-Integral Equation method (TLMIE) is extended in order to include the modeling of thin wire structures which are embedded into a TLM mesh. While the radiated field of the thin wire structures is modeled by the Integral Equation method, the incident field at the structures is modeled via the space discretizing TLM method. In this way it is possible to investigate the interaction of thin wire structures with an environment of non-uniform material using a relatively coarse TLM mesh compared to the size of the thin wire structure.

Introduction

Typical of many practical configurations in engineering is the presence of wire-like structures in the proximity of complex three-dimensional objects consisting of several materials. It is well known that integral equation (IE) methods [1,2] are well suited to the modeling of wire-like structures and that in contrast space discretizing methods like the FDTD method [3] and the TLM method [4,5] are well suited to modeling complex inhomogeneous objects. Methods have been developed for the implementation of thin wire modeling with the TLM algorithm but in these methods the wires are restricted in their geometrical structure [6,7]. It is therefore desirable that the modeler has the option of using each method, the TLM method and the IE method in its best domain of application and combining it in a hybrid to tackle complex practical configurations. This type of hybridization was demonstrated in a series of publications [8,9,10,11] for the case of two or more remote regions which are modeled in detail using a space discretizing method, the coupling between these regions through free space being done using IE type formulations.

In this paper the method is extended to include the modeling of arbitrary wire structures embedded in a region modeled by a space discretizing method. The benefits of this approach are that the wires can be modeled efficiently using an IE method without imposing the burden of modeling fine features on the space discretizing method which is modeling large volumetric features of the problem. In this way, several wires (eg. wire harnesses) may be modeled and embedded as pre-calculated elements in the global simulation. Also more intricate shapes such as spiral, helical antennas, twisted wires etc. can be pre-calculated and embedded in simulations without imposing significant computational burdens on the global simulation.

Theory

In many EMC problems we have to investigate the electromagnetic coupling between wire structures and objects placed in a non-uniform environment consisting of several materials like dielectrics, lossy material and conductors.

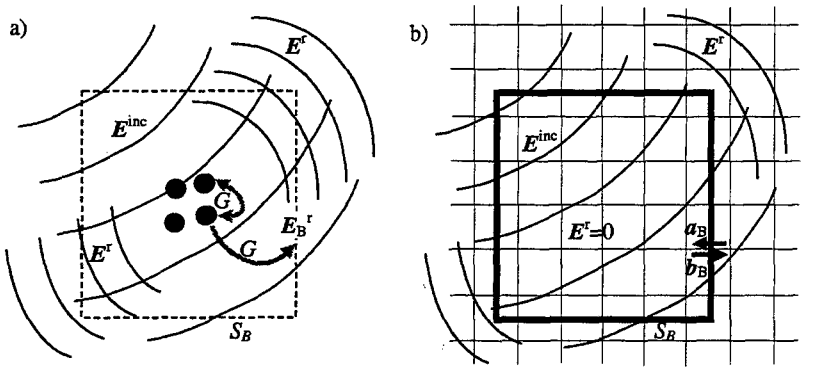


Fig.1 a): Derivation of the radiated field at the boundary surface S_B of the wire subregion;
b): Excitation of the radiated field by equivalent sources on the surface S_B

In order to obtain an accurate field modeling in the compound material we discretize the problem space including all the material into a discretized region where the field is modeled using the TLM method. Since the dimensions of the thin wire structures are far below the size of the TLM-elementary cells these structures can not be modeled accurately with the TLM method without employing special techniques. In order to achieve a highly accurate description of the wire structure in the TLM method we replace the wire structures by an equivalent source which is more extended in size than the thin wires and which is matched to the TLM mesh. This way we embed the wire in a wire subregion with the surface S_B. The surface S_B encloses the complete wire structure and is congruent with the boundaries of the TLM mesh cells. Applying the Schelkunoff Huygens surface equivalence theorem we derive the field at the surface S_B which yields an equivalent source to the wire radiation.

In the complete problem space inside and outside S_B we distinguish between the incident field E^{inc}, H^{inc} from all sources located outside S_B and the radiated field E^r, H^r from all sources located inside S_B. As a reaction to the incident field and due to other possible sources the field E^r, H^r is radiated from the wire (fig.1a). We consider the surface S_B which encloses the thin wire structures and where we define the field E_B, H_B, which is a superposition of the incident field $E_B{}^{inc}$, $H_B{}^{inc}$ and the radiated field $E_B{}^r$, $H_B{}^r$.

According to the Schelkunoff Huygens representation of the equivalence theorem, the tangential field components $E_B{}^r$, $H_B{}^r$ on the surface elements of the boundary surface S_B represent equivalent surface

currents which are sources of radiation. According to this theorem the equivalent surface currents generate the radiated field E^r, H^r outside the surface S_B which is equivalent to the radiated field of the thin wire structure. Inside the surface S_B the equivalent surface currents generate no radiated field (fig.1b). This means that in the TLM method a source of the field $E_B{}^r$, $H_B{}^r$ along the surface S_B leads to the excitation of the field E^r, H^r outside the surface S_B while inside the surface S_B no field E^r, H^r is excited.

The field distribution of the incident field is continuous and smooth and is not dependent to the wire structure. Hence the incident field in the time domain can be modeled by the TLM method in the whole problem region outside and inside the surface S_B.

The field $E_B{}^r$, $H_B{}^r$ at the boundary surface S_B we obtain from the current distribution on the wire structure via the dyadic Green's function in the time domain. The current distribution on the wire structure we obtain via the dyadic Green's function in the time domain, the boundary conditions at the wire surface and from the incident field E^{inc}, H^{inc} at the wire surfaces. This is shown in the following section.

Calculation of the current values on the wire structure

On the conductor surfaces we define the unity vector $\boldsymbol{u}$ which points in the direction of the conductor. We define the position of a point on the conductor by its distance s from the end of the conductor. All points on the conductor are defined by the three dimensional coordinates $\boldsymbol{r}(l)$.

Now we discretize the surfaces of the thin conductors along one dimension into wire segments with the index k. On each wire segment we define the current I_k and the tangential unity vector $\boldsymbol{u}_k$. The location of the wire segments is l_k. The index i is the time index of the current values. We expand the current vectors by the basis functions b_c:

$$I(\boldsymbol{r}(l),t)=\sum_k\sum_i I_{k,i}\,b_c(l-l_k,t-i\Delta t) \tag{1}$$

with

$$b_c(l-l_o,t-t_o)=\begin{cases}0 & \text{for}(l-l_o)\geq\frac{1}{2};(t-t_o)\geq\frac{1}{2}\\ 1 & \text{else}\end{cases} \tag{2}$$

In every time step the actual current values $I_{k,j}$ of the wire segments are derived via the Schelkunoff Huygens surface equivalence theorem [1,2], if we take into account the boundary conditions for the total field $\boldsymbol{E}_C$, $\boldsymbol{H}_C$ at the wire surface S_C. The following expression relates the current distribution along the conductor surfaces and the radiated field $\boldsymbol{E}_C{}^r$, $\boldsymbol{H}_C{}^r$ on the conductor surfaces S_C according to the surface equivalence theorem [2].

$$\boldsymbol{E}_C^r(\boldsymbol{r}(l),t)=\frac{1}{4\pi}\int_{S_c}\left[-\boldsymbol{u}'\frac{\mu}{R_c}\frac{\partial}{\partial t}I(l',t-\Delta t_c)+\boldsymbol{u}\frac{1}{\varepsilon}\frac{\partial}{\partial l}\left(\frac{1}{R_c}\int_0^t I(l',t-\Delta t_c)\;dt\right)\right]dl'\Bigg|_{R_c=r_c(l)-r_c(l');\Delta t_c=R_c/c_o} \tag{3}$$

where

$$R_c = |\boldsymbol{R}_c| = |\, \boldsymbol{r}_c(l) - \boldsymbol{r}_c(l')| \tag{4}$$

$$\Delta t_c = R_c / c_o \tag{5}$$

If we insert eqs. (1) and (2) into eq. (3) , we obtain the following approximation

$$\boldsymbol{E}^r_C(\boldsymbol{r}(l_k), j\Delta t) = \boldsymbol{E}^r_{Ck,j} = \sum_{l=1}^{n} \sum_{i=0}^{j} \boldsymbol{M}_{k,l,i}\, I_{l,i} \tag{6}$$

for the electric field values $\boldsymbol{E}^r_{Ck,j}$ which are defined in each time step $t=j\Delta t$ at the location $\boldsymbol{r}=\boldsymbol{r}(l_k)$ of the wire segments k. The vectors $\boldsymbol{M}_{k,l,i} = (M_x, M_y, M_z)^T_{k,l,i}$ contain the coupling coefficient vectors of the current values $I_{k,i}$ for the field components $(E^r_x, E^r_y, E^r_z)^T_{Ckl,j}$ of the radiated field.

At the surface S_C of the wire structure we obtain the total electric field $\boldsymbol{E}_C$, $\boldsymbol{H}_C$ by superposition of the incident field $\boldsymbol{E}_C^{inc}$, $\boldsymbol{H}_C^{inc}$ with the radiated field $\boldsymbol{E}_C^r$, $\boldsymbol{H}_C^r$. The incident field at all the segments k of the wire structure is derived from the wave amplitudes of the TLM simulation by the mapping introduced in [4].

$$\boldsymbol{E}^{inc}_{Ck,j} = \boldsymbol{E}^{inc}_C(\boldsymbol{r}(l_k), j\Delta t) = \boldsymbol{E}(\boldsymbol{a}_C, \boldsymbol{b}_C) \;\; ; \;\; \boldsymbol{H}^{inc}_{Ck,j} = \boldsymbol{H}^{inc}_C(\boldsymbol{r}(l_k), j\Delta t) = \boldsymbol{H}(\boldsymbol{a}_C, \boldsymbol{b}_C) \tag{7}$$

The position of the sampling points of the electromagnetic field in the TLM mesh is different from the position of the sampling points on the wire structure. We calculate the incident field values at the sampling points of the wire structure by interpolating the incident field values of the neighbored sampling points of the TLM mesh. The total field at the surface of the n wire segments k is

$$\boldsymbol{E}_{Ck,j} = \boldsymbol{E}^{inc}_{Ck,j} + \boldsymbol{E}^r_{Ckj} = \boldsymbol{E}^{inc}_{Ck,j} + \sum_{l=1}^{n} \sum_{i=0}^{j} \boldsymbol{M}_{k,l,i}\, I_{l,i} \tag{8}$$

We define the unity vectors $\boldsymbol{u}_k$, which are tangential to the wire segments k. From the boundary condition at the conducting surface we obtain

$$\boldsymbol{E}_{Ck,j} \cdot \boldsymbol{u}_k = 0 \tag{9}$$

and hence, with eq. (8)

$$\sum_{l=1}^{n} \left(\boldsymbol{M}_{k,l,j} \cdot \boldsymbol{u}_k \;\; I_{l,j}\right) = -\boldsymbol{E}^{inc}_{Ck,j} \cdot \boldsymbol{u}_k - \sum_{l=1}^{n} \sum_{i=0}^{j-1} \left(\boldsymbol{M}_{k,l,i} \cdot \boldsymbol{u}_k \;\; I_{k,i}\right) \tag{10}$$

Equation (10) can be solved for the actual current values $I_{k,j}$ of the wire segments in every time step. This can be done without a matrix inversion since there is a time retardation between the different current values on the conductor segments [12]. This means, that the current values $I_{l,j}$ of the actual

time step j are only coupled with the field values $E_{Ck,j}$ of the same segment $j=k$. Hence $M_{k,l,j}=0$, if $l\neq k$ and $M_{k,l,j}\neq 0$, if $j=k$. This yields for the actual current values

$$I_{k,j}=\frac{1}{M_{k,k,j}\cdot u_k}\left[-E^{inc}_{Ck,j}\cdot u_k-\sum_{l=1}^{n}\sum_{i=0}^{j-1}\left(M_{k,l,i}\cdot u_k\, I_{k,i}\right)\right] \tag{11}$$

Calculation of the field excitation at the boundary surface

Instead of modeling the thin wire structure with the TLM scheme we replace the thin wire structure by an equivalent source surface S_B (fig.1). On this surface we impress the field E_B, H_B during the whole TLM simulation. We derive the field E_B, H_B from the incident field E_B^{inc}, H_B^{inc} and from the field E^r_B, H^r_B which is radiated by the wire structure.

$$E_B=E_B^{inc}+E^r_B \quad ; \quad H_B=H_B^{inc}+H^r_B \tag{12}$$

The incident field is modeled by the TLM method. In every time step we superimpose the radiated field E^r_B, H^r_B on the boundary surfaces S_B to the incident field. E^r_B, H^r_B is derived from the current distribution along the conductor surfaces according to the surface equivalence theorem. We give numbers μ to all boundary surface elements. The field values $E_{B\mu}$, $H_{B\mu}$ of these surface elements are defined in the center of the surface elements. The indices j and i are the time indices at the destination points and at the source points respectively. At the boundary surface we obtain the radiated electromagnetic field by

$$E^r_{B\mu}(r_\mu,t)=\frac{1}{4\pi}\int_{L_c}\left\{-\frac{\mu}{R}\frac{\partial}{\partial t}I(l',t-\Delta t)u'+\frac{1}{\varepsilon}\frac{\partial}{\partial l}\left[I(l',t-\Delta t)\Delta t+\int_0^t I(l',t-\Delta t)dt\right]\frac{R}{R^3}\right\}dl'\Big|_{R=r_\mu-r_c'(l');\Delta t=R/c_o} \tag{13}$$

$$H^r_{B\mu}(r_\mu,t)=\frac{1}{4\pi}\int_{L_c}\left\{\frac{1}{R^3}\left[1+\Delta t\frac{\partial}{\partial t}\right]I(l',t-\Delta t)\; u'\times R\right\}dl'\Big|_{R=r_\mu-r_c'(l');\Delta t=R/c_o} \tag{14}$$

where

$$R=|R|=|r_\mu-r_c'(l')| \tag{15}$$

$$\Delta t=R/c_o \tag{16}$$

If we insert eqns. (1) and (2) into eqns. (13) and (14), we obtain the following approximation

$$E^r_{\mu,j}=\sum_{k=1}^{n}\sum_{l=0}^{j}P_{\mu,k,l}\,I_{k,l} \tag{17}$$

$$H^r_{\mu,j} = \sum_{k=1}^{n} \sum_{i=0}^{j} Q_{\mu,k,i}\, I_{k,i} \tag{18}$$

where the matrices $\boldsymbol{P}$ and $\boldsymbol{Q}$ contain the coupling coefficients of the current values.

The field values $\boldsymbol{E}_B$, $\boldsymbol{H}_B$ at the ports on the boundary surfaces of the TLM-regions are mapped on the TLM wave amplitudes $\boldsymbol{a}_B$ and $\boldsymbol{b}_B$, which are defined at the transmission lines which are cut by the surface S_B.

$$\begin{aligned} \boldsymbol{a}_B &= \boldsymbol{a}_B^{TLM} + \boldsymbol{a}_B^r \quad \text{with} \quad \boldsymbol{a}_B^r = \boldsymbol{a}\left(\boldsymbol{E}_B^r, \boldsymbol{H}_B^r\right); \quad \boldsymbol{a}_B^{TLM} = \boldsymbol{a}\left(\boldsymbol{E}_B^{inc}, \boldsymbol{H}_B^{inc}\right); \\ \boldsymbol{b}_B &= \boldsymbol{a}_B^{TLM} + \boldsymbol{a}_B^r \quad \text{with} \quad \boldsymbol{b}_B^r = \boldsymbol{b}\left(\boldsymbol{E}_B^r, \boldsymbol{H}_B^r\right); \quad \boldsymbol{b}_B^{TLM} = \boldsymbol{b}\left(\boldsymbol{E}_B^{inc}, \boldsymbol{H}_B^{inc}\right) \end{aligned} \tag{19}$$

The TLM wave pulses with the amplitudes $\boldsymbol{a}^r_B$ and $\boldsymbol{b}^r_B$ are representing the source of the electromagnetic field which is radiated from the wire structure. In every time step the excitation $\boldsymbol{a}_B$ and $\boldsymbol{b}_B$ excites the total field outside the boundary surface S_B while inside the surface only the incident field is excited.

Finally, in this method the following procedures are performed in every time step of the TLM simulation: In the whole problem space outside and inside the wire subregion the actual incident field is calculated by the TLM method. At the boundary surface the actual radiated field is calculated from the time history of the current distribution on the wire structure via the Schelkunoff Huygens theorem. After calculating the radiated field at the boundary surface in every time step, we can consider the radiated field values on the boundary surfaces as equivalent sources. Outside the wire subregion these equivalent sources excite the same electromagnetic field as the wire structure. The radiated field at the surface boundary is mapped onto the wave amplitudes of the TLM algorithm. These wave amplitudes are exciting the radiated field outside the wire subregion which is calculated by the TLM method, superposed to the incident field. Inside the wire subregion the equivalent sources are producing no electromagnetic field due to the surface equivalence theorem. Hence, inside the wire subregion only the incident field is modeled by the TLM method. Taking into account the actual incident field and the boundary conditions at the surface of the wire structure the actual current distribution on the wire structure is calculated via the Schelkunoff Huygens theorem from the former time history of the current distribution at the wire structure.

Conclusions

We have presented the theoretical basis which allows a hybrid model of wires to be constructed in an environment consisting of complex composite bodies. The wire model is based on the Integral Equation method while the rest of space is modeled by using time-domain space discretizing techniques. The two models are combined to form an integrated solution. The advantages of this approach are that the differential time-domain model is constructed without reference to the fine structure of the wires. An IE technique is used for the wires as it is better suited to this task. This development has the potential for describing efficiently complex wire structures which may be pre-calculated and inserted into large complex configurations.

References

[1] J.J.H. Wang " Generalized Moment Methods in Electromagnetics", John Wiley and sons, 1991

[2] K. Mei, "On the Integral Equations of Thin Wire Antennas", IEEE Trans. Antennas Propagation, AP-13(3), pp. 374-378, 1965

[3] S. Yee, "Numerical solution of initial boundary value problems involving Maxwell's equations in isotropic media," IEEE Trans. Antenna Propagat., Vol.14, pp. 302-307, May 1966.

[4] P.B. Johns, "A Symmetrical Condensed Node for the TLM-Method", IEEE Trans. Microwave Theory Tech., vol. MTT-35, no. 4, Apr. 1987, pp. 370-377

[5] W.J.R. Hoefer, "The Transmission Line Matrix (TLM) Method", Chapter 8 in "Numerical Techniques for Microwave and Millimeter Wave Passive Structures", edited by T. Itoh, J. Wiley, New York, 1989, pp. 496-591

[6] J.A. Porti, J.A. Morente, M. Khalladi, A. Gallego, "Comparison of Thin Wire Models for TLM Method", Electron. Lett., Vol. 28(8), pp. 728-729, 1992

[7] A. Wlodarczyk, V. Trenkic, R. Scaramuzza, C. Christopoulos, "Integrated Solution for Modelling of Multiconductors in TLM", IEEE Trans. Theory Tech., Vol. 46(12), pp. 2431-2437, 1998

[8] S. Lindenmeier, L. Pierantoni, P. Russer, „Hybrid Space Discretizing-Integral Equation Methods for Numerical Modelling of Transient Interferences", to be published in: IEEE Trans. EMC, Vol. 41, No. 4, 6 pages, Nov. 1999

[9] S. Lindenmeier, L. Pierantoni, P. Russer, "Numerical Modeling of Transient Radiated Interferences in Time Domain by the Hybrid ARB Method", International Journal of Numerical Modelling: Electronic Networks, Devices and Fields, Vol. 12, pp. 295-310, July 1999

[10] L. Pierantoni, S. Lindenmeier, P. Russer, "Efficient Analysis and Modeling of the Radiation of Microstrip Lines and Patch Antennas by the TLM-Integral Equation (TLM-IE) Method", International Journal of Numerical Modelling: Electronic Networks, Devices and Fields, pp. 329-340, July 1999

[11] L. Pierantoni, S. Lindenmeier, P. Russer, „A Hybrid Time Domain TLM-Integral Equation Method for Solution of Radiation Problems", *Progress in Applied Computational Electromagnetics 1998 ACES Symposium Digest*, pp.320-325 March 1998

[12] G. Cerri, S. Chiarandini, P. Russo, "Numerical Aspects in Time Domain Modelling of Arbitrarily Curved Thin Wire Antennas", International Journal of Numerical Modelling: Electronic Networks, Devices and Fields, Vol. 12, pp. 275-294, July 1999

WHAT DETERMINES THE SPEED OF TIME-DISCRETE ALGORITHMS ?

TOBIAS MANGOLD*, JÜRGEN REBEL*, WOLFGANG J.R. HOEFER**,
POMAN P.M. SO**, AND PETER RUSSER*

*INSTITUT FÜR HOCHFREQUENZTECHNIK,TECHNISCHE UNIVERSITÄT MÜNCHEN
, ARCISSTR. 21, D-80333 MUNICH, GERMANY
**COMPUTATIONAL ELECTROMAGNETICS RESEARCH LABORATORY, ECE-DEPARTMENT,
UNIVERSITY OF VICTORIA, VICTORIA, BC, CANADA V8W 3P6

ABSTRACT. In this paper we highlight a number of factors that determine the speed of iterative time-discrete algorithms, exemplified by various TLM codes. One of the main determining factors of computational code performance on state-of-the-art platforms is memory access and not the number of floating point operations per TLM node, as recently shown [3]. To show the influence of memory access, the performance of various TLM codes is compared on various platforms for the example of a microstrip via-hole connect and a simple cavity resonator. Conventionally optimized and memory-access optimized codes are compared. Further, strategies for optimizing memory access are discussed. In addition, the issue of software emulated floating point underflow handling in simulations is discussed. By exploiting memory acccess optimization strategies, one can achieve a speed-up of the code of up to 100%. However, the optimization strategies are somehow dependent upon the compiler. If memory access is suitably optimized, TLM codes show similar perfomance on Pentium based PCs and workstations independently of the employed operating system and compiler. The reason why the same code still runs faster on workstations than on PCs with similar clock speed is due to the higher memory bus clock frequency and more aggressive out-of-order execution and branch-line-prediction of the workstations.

1. INTRODUCTION

Conventional wisdom suggests that the performance of iterative field solving codes is mainly determined by the number of floating point operations per iteration. However, it was recently shown that on state-of-the-art platforms the limiting factor in TLM code performance is not the pure number of floating point operatons but memory access [3]. This is not only true for workstations but also for Pentium based PCs. In this paper, we present strategies to optimize code performance with respect to memory access. A platform independent measure for code performance is the number of processed TLM nodes per second. Using this measure, we compare the performance of various TLM codes on various platforms. Further, two canonical test problems are defined for evaluating the performance of TLM codes.

2. THE ROLE OF MEMORY ACCESS

2.1. **The Test Problems.** To verify the findings of [3], a more complex test problem than used in [3] was specified. A microstrip via-hole transition on a layered substrate was considered. The structure is shown in Fig. 1. The structure was discretized using cubic cells of 1mm size. The E^z-field below the microstrip was excited using a Gaussian transient. The voltage in the output microstrip line was monitored by computing the line integral over the E^z-field at one point (see Fig. 1). At the bottom of the substrate, a perfectly conducting ground metallization was assumed. To be independent of particular implementations, the simplest possible boundary conditions were imposed. Only electric, magnetic or simple impedance boundaries were considered. The absorbing boundary conditions of the microstrip via-hole transition were realized by medium dependent matched loads at the boundaries of the computational domain. The simulation was run for 1000 time steps to ensure that the complete mesh contained non-zero

TLM pulses. This avoids overestimating the code performance, as zero multiplications are handled faster in the CPU than non-zero multiplications.

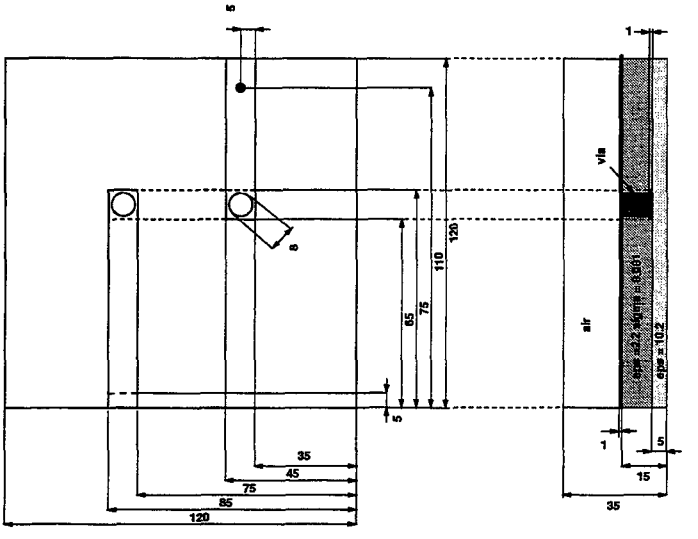


FIGURE 1. Layout of microstrip via-hole connect. All dimensions in mm.

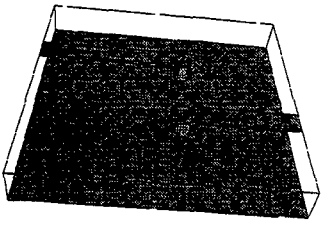


FIGURE 2. Three-dimensional view of TLM discretization obtained by tlm3dNG.

To highlight the role of memory access, a small problem that fitted into level I or level II cache of the CPU was also considered. It consisted of a simple air-filled cavity resonator of size 10mm×10mm×10mm. This cavity was discretized using 10×10×10, 20×20×20, and 40×40×40 cubic cells. Depending on the size of the CPU cache, only the 10×10×10 problem fitted into the cache, or on more advanced CPUs even the 20×20×20 problem fitted into the cache. For comparison, a finer

	platform	clock speed [MHz]	RAM [MB]	CPU	Cache	OS	Memory Bus Freq.
A	HP C-160	160	500	PA 8000	1MB extern	HP-UX 10.20	120MHz
B	HP C-360	360	500	PA 8500	1.5MB on chip	HP-UX 10.20	120MHz
C	PC	350	64	Pentium II	L1 32kB / L2 512kB	Linux	100MHz
D	PC	350	64	Pentium II	L1 32kB / L2 512kB	Windows 95	100MHz
E	Notebook	366	128	Pentium II	L1 32kB / L2 512kB	Windows 98	100MHz

TABLE 1. Data of the platforms employed for the performance study. OS stands for operating system.

discretization using 40×40×40 cells was also considered, to show the influence of the memory access on the performance, when the problem's process size no longer fitted into any cache memory.

2.2. **Details of Platforms and Codes.** The via-hole connect structure and the differently discretized cavities were run on various platforms involving various TLM codes and various operating systems. Table 1 gives an overview. We compared two TLM codes, one TLM code developed at the Technische Universität München, called tlm3dNG, and a commercially available code, namely MEFiSTo-3D^{TM} from Faustus Scientific Corporation, Victoria, BC, Canada. The codes differ in that the former is written in Fortran and the latter in C++. However, for the scattering routines themselves, which is always procedural code, C++ is eventually C and the optimization strategies suggested in section 3 equally apply. Both codes use for the SCN scattering the formulation of the scattering matrix following [2], which requires 54 additions/subtractions and 12 multiplications per scattering event. Only 12 quantities need to be stored. Moreover, the MEFiSTo-3D^{TM} program also allows using the general symmetrical condensed node (GSCN), which accounts for the constitutive parameters of the medium by using different impedances for the various arms of the symmetrical condensed node. A scattering with the GSCN requires 72 additions/subtractions and 42 multiplications if all stubs are considered. It follows the formulation of Trenkic [5]. The advantage of having three additional degrees of freedom is gained at the expense of a slight reduction of speed by typically 30 percent. In addition we have investigated various optimization strategies for improving the tlm3dNG code. Details can be found in section 3.

2.3. **Results.** To compare the performance of different TLM codes, we have defined a measure that is independent of the platform. We found that the number of scatter and connect events per second is particularly suitable and can be measured easily. To determine this number, we monitor the exact CPU time of the respective TLM process using system functions. This can easily be implemented in existing codes. As soon as the pure runtime of the TLM program is known, the performance in 1000 nodes per second (kilonodes/second) can be calculated. Simply multiply the number of nodes (TLM cells) used to discretize the structure by the number of time steps, then divide it by 1000 times the CPU runtime. The performance of the various codes when dealing with the microstrip via-hole transition on the various platforms is compiled in Table 2. The data for the cavity resonator, discretized using three different cell sizes, are shown in Tables 3 to 5. In all these tables, the first column indicates the platform, given in Table 1. The second column indicates the TLM code. The third column reports the performance values for the tlm3dNG and MEFiSTo-3D^{TM} codes using conventional compiler optimization. In the fourth column, the performance values for tlm3dNG using conventional compiler optimization in connection with data prefetching are given, and in the fifth column the data for the tlm3dNG code using compiler optimization, data prefetching and implicitly processing the connect operation are given. The optimization strategies are described in the following section.

Looking at the via-connect problem (Table 2) solved using the SCN, one realizes that before applying memory access optimization strategies, all codes show similar performance. The reason why the MEFiSTo-3D^{TM} code is slightly faster, may be due to some built-in optimization features of the commercial Windows C++ compiler, or it may be attributed to the different structure of the TLM

Performance of TLM codes in kilonodes/sec for microstrip via-hole transition				
mesh size	$120 \times 120 \times 35$			
iterations	1000			
platform	TLM-SCN code	conventionally optimized	conventionally optimized + data prefetching	conventionally optimized + data prefetching + implicit connect operation
A	tlm3dNG	668	943	1377
B	tlm3dNG	786	940	1425
C	tlm3dNG	675	-	1100
D	MEFiSTo-3D^{TM}	701	-	-
E	MEFiSTo-3D^{TM}	701	-	-

TABLE 2. Scattering performance of TLM codes for via-hole interconnect problem on various platforms and running under various operating systems, given in 1000 nodes per second [kilonodes/sec].

engines. However, when additional strategies for better memory access are used when writing the code, the impact is striking. Using data prefetching, the code can be made nearly 50% faster, and implicitly processing the connect operation produces a code nearly twice as fast! Implementing an implicit connect operation is thus an effective measure for accelerating the TLM algorithm. Comparing the speed of the tlm3dNG code achieved on workstations and PCs, one can recognize the influence of the system clock speed or memory bus frequency. The workstations are about 30% faster when simulating the via-connect problem.

The same picture is generated when comparing the performance values for the cavity resonator. The performance values for the workstations A and B in Tables 3 and 4, show the influence of the cache memory of the CPU. The 10×10×10 cells problem fits into the cache of each CPU. The 20×20×20 cells problem, fits only into the cache of platform B which has a bigger cache than the others (see Table 1).

Clearly, the process size of the 40×40×40 cells cavity problem does not fit into the cache of any machine which is obvious from the performance data in Table 5. Comparing the values for this problem with the data for the via-hole connect structure in Table 2, one sees the influence of the homogeneity of the data. Having a single computational domain, as in case of the air-filled cavity, the impact of optimization of memory access is clearly evident. The fact that the tlm3dNG code runs faster on workstations for uniform data is due to the more aggressive out-of-order execution and branch-line-prediction on these platforms.

3. Code Optimization Strategies

3.1. **Compile Time Optimization and Local Code Transformations.** Most of the optimization strategies commonly applied by modern compilers focus on the throughput of operations on the core CPU. Local code rearrangements performed by compiler optimization exploit processor features like pipelined processing or improve cache hit rates on a local scale. However, these compiler optimizations cannot deal with the problem of high memory bandwidth required by the TLM algorithm. Memory access time as a determining factor for TLM code performance becomes clearly evident when looking at the speedup of more then 400 % achieved for cache size problems (Table 4).

Therefore, code optimization needs to focus on memory access rather than the pure floating point performance. An optimization strategy addressing this issue is the so called 'data prefetching' offered by some state-of-the-art compilers. Instead of minimizing the number of operations, this optimization concept inserts dummy instructions that try to preload memory contents accessed in upcoming iterations

Performance of TLM codes in kilonodes/sec for cavity resonator				
mesh size		$10 \times 10 \times 10$		
iterations		10000		
platform	TLM-SCN code	conventionally optimized	conventionally optimized + data prefetching	conventionally optimized + data prefetching + implicit connect operation
A	tlm3dNG	1294	1280	1706
B	tlm3dNG	3086	2986	4016
C	tlm3dNG	1064	-	1852
D	MEFiSTo-3D™	1667	-	-
E	MEFiSTo-3D™	2000	-	-

TABLE 3. Scattering performance of TLM codes for cavity problem I on various platforms and running under various operating systems, given in 1000 nodes per second [kilonodes/sec].

Performance of TLM codes in kilonodes/sec for cavity resonator				
mesh size		$20 \times 20 \times 20$		
iterations		10000		
platform	TLM-SCN code	conventionally optimized	conventionally optimized + data prefetching	conventionally optimized + data prefetching + implicit connect operation
A	tlm3dNG	897	1180	1728
B	tlm3dNG	3474	3738	5138
C	tlm3dNG	821	-	1470
D	MEFiSTo-3D™	1212	-	-
E	MEFiSTo-3D™	808	-	-

TABLE 4. Scattering performance of TLM codes for cavity problem II on various platforms and running under various operating systems, given in 1000 nodes per second [kilonodes/sec].

into cache memory in parallel to the ongoing calculations. The results given in Table 2 point out the significant improvements obtained from such optimization strategies and demonstrate the importance of memory access for TLM code performance.

3.2. **Global Code Reorganization.** After applying all these well known optimization startegies, the resulting codes that follow the conventional TLM scheme with scatter (the notation according to [4] is used)

$$| b_{k+1} > = \mathbf{S} \, | a_k > \tag{1}$$

and connect operation

$$| a_{k+1} > = \mathbf{\Gamma} \, | b_{k+1} > \tag{2}$$

spend more time executing the connect operation Γ than the computationally expensive scattering operation **S** as listed in Table 6. This is again explained by memory access time. Scattering operates strictly

Performance of TLM codes in kilonodes/sec for cavity resonator				
mesh size		$40 \times 40 \times 40$		
iterations		1000		
platform	TLM-SCN code	conventionally optimized	conventionally optimized + data prefetching	conventionally optimized + data prefetching + implicit connect operation
A	tlm3dNG	721	1131	1653
B	tlm3dNG	847	1148	1830
C	tlm3dNG	761	-	1316
D	MEFiSTo-3D™	955	-	-
E	MEFiSTo-3D™	808	-	-

TABLE 5. Scattering performance of TLM codes for cavity problem III on various platforms and running under various operating systems, given in 1000 nodes per second [kilonodes/sec].

locally, resulting in a high cache hit rate, whereas the connect operation slows down the process due to accessing memory that is widespread over one-dimensional memory space.

Further performance improvements with striking code speed-ups are only possible by reorganizing the underlying algorithm and changing its memory access scheme on a global scale. One possible approach is the grouping of TLM operators of two subsequent time steps:

$$| a_{k+2} > = \underbrace{\mathbf{\Gamma} \cdot \mathbf{S} (\mathbf{\Gamma} \cdot \mathbf{S}}_{\mathbf{S}^*} | a_k >) \tag{3}$$

Defining distinct scattering operators $\mathbf{S}$ and $\mathbf{S}^*$ for even and odd time steps allows to implicitly process the connection operation. The same principle needs to be applied to field mapping and boundary conditions, respectively. From a programming point of view this formulation results in a dual implementation of every module with access to wave amplitudes a_k differing in memory access but not in functionality. The boost in code performance gained from this extra implementation work is most obvious for large problems as given in Table 2. Since memory access differs for the two scattering modules, we cannot expect an equal execution time for $\mathbf{S}$ and $\mathbf{S}^*$.

4. The Role of Software Emulated Floating Point Underflow Handling

On most platforms, the CPU monitors floating point underflow, and in case of detection it switches to a software emulation with higher precision [1]. Obviously, this will slow down the whole process. This feature is typically switched on by default on most platforms. Normally, if one has a single process, this effect is not noticed. However, in case of distributed computing, the performance of the slowest process determines the performance of the whole distributed process. To illustrate this, the mesh of a discretized coplanar waveguide was divided into 10 slices. Each slice constituted a single process, and the relative scattering times of each process were measured. All tlm3dNG processes were interconnected using the Parallel Virtual Machine (PVM). The waveguide is schematically depicted in Fig. 3. In Fig. 4, the relative scattering times versus time step are plotted for each process. In the fourth slice, we can recognize a sudden increase in relative scattering time after approximately 50 time steps. The increase lasts for about 25 time steps and dies out afterwards. This increase in scattering time propagates in the form of a 'shock wave' through all the slices along with the launched pulse. The explanation for this observation is as follows. The leading edge of the Gaussian field profile involves such low values of the TLM wave amplitudes that the CPU detects a floating point underflow. It switches to software emulation

microstrip via-hole connect			
mesh size iterations	120 × 120 × 120 1000		
optimization	conventional	conventional+ data prefetching	conventional+ data prefetching+ implicit connect operation
Start-Up [sec]	.36	.37	.37
Excitation [sec]	.11	.11	.16
Output [sec]	.06	.06	.04
Boundaries [sec]	42.13	41.91	41.59
Scat. I [sec]	256.34	200.04	99.11
Scat. II [sec]	-	-	212.22
Con. [sec]	342.12	293.53	-
Pure Scat.-Perf. [kilonodes/sec]	842	1021	1619
TLM-Perf. [kilonodes/sec]	786	940	1425

TABLE 6. CPU runtime in sec. of program modules when simulating the via-hole connect with tlm3dNG for various optimization strategies on a HP C-360 workstation. For comparison, the pure scattering performance, i.e. the number of processed nodes per cpu time taken for the scatter and connect operation alone, is also given in Table 6.

with enhanced accuracy and consequently, the scattering times strongly increase and the performance of the TLM code breaks down. As soon as the values of the pulses reach a certain level everywhere in the TLM mesh of each process, the numerical performance is as usual. This effect has a particularly strong impact on distributed processes, although it is common to all TLM computations. The software emulation of this floating point underflow has no influence on the accuracy of a TLM simulation and represents just an unwanted feature which slows down the field computation. Luckily, this feature can be easily switched off using compiler directives on most platforms. However, Intel Pentium processors seem to exhibit an inevitable preformance drop down to less than 50 % when operating at the edge of the defined floating point range, even if the floating point exception handling is switched off. This could not be observed on PCs running with AMD processors.

5. CONCLUSION

We have shown in this paper that the limiting factor in TLM code performance is indeed memory access. This was demonstrated by comparing the performance of various SCN-TLM codes on various commonly employed platforms when simulating two canonical problems. A realistic microstrip via-hole interconnect problem and a simple air-filled cavity resonator were considered. Various strategies for improving the data handling in procedural code have been proposed and verified. Applying data prefetching strategies and implicitly processing the connect operation wherever possible, speeds up the code by up to 100%. If suitable optimization strategies are used, TLM codes perform nearly equally well on workstations and Pentium based PCs. The reason why the same code runs faster on workstations than on PCs with similar clock speed is due to the higher memory bus clock frequency and more aggressive out-of-order execution and branch-line-prediction of the workstations. It was also found that the best optimization strategy for a particular platform is slightly compiler dependent. Moreover, it has been shown that the operating system (Linux or Windows) has no influence on the performance of a code, if the correct optimization strategy is pursued. The influence of the floating point underflow exception handling, which is common to all CPUs, on the performance of TLM codes has also been indicated.

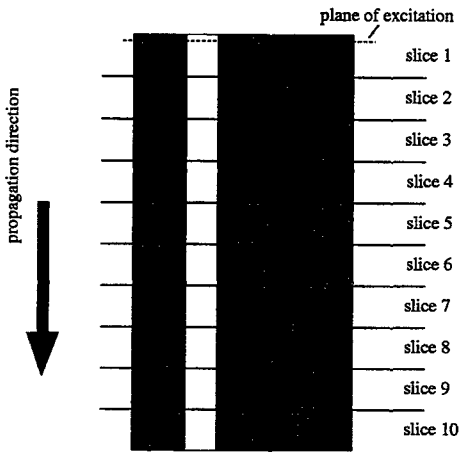


FIGURE 3. Schematic of coplanar waveguide computed by 10 interconnected distributed slices.

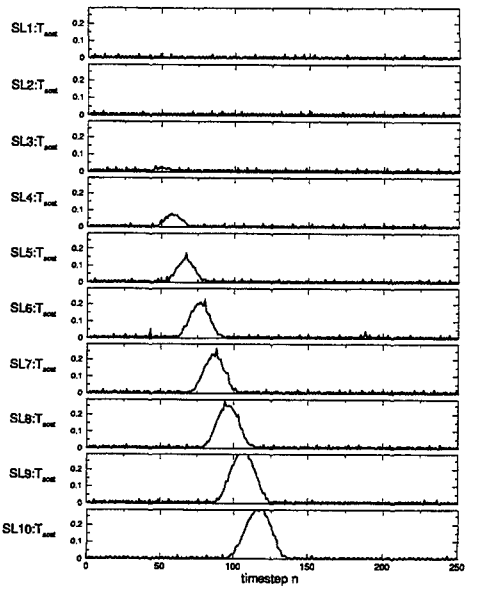


FIGURE 4. Relative scattering performance of each slice of the distributed TLM mesh.

REFERENCES

1. Hewlett-Packard Company, *HP-UX Floating-Point Guide*, Hewlett-Packard Company, 1996.
2. J.L. Herring, *Developments in the Transmission-Line Modelling Method for Electromagnetic Compatibility Studies*, PhD Thesis, University of Nottingham, 1993.
3. J. Rebel, T. Mangold, and P. Russer, *On the Performance of TLM-SCN Codes*, Proceedings of Third International Workshop on Transmission Line Matrix (TLM) Modelling (1999), 43–50.
4. P. Russer and M. Krumpholz, *The Hilbert space formulation of the TLM method*, Int. J. Num. Modelling **6** (1993), no. 1, 29–45.
5. V.Trenkic, C. Christopoulos, and T.M. Benson, *Development of a General Symmetrical Condensed Node for the TLM Method*, ieetm **46** (1996), no. 12, 2129–2135.

SESSION 11

TIME DOMAIN METHODS AND APPLICATIONS

Chairs: Amelia Rubio Bretones and R. Gomez Martin

INTRODUCING A NEW TIME-DOMAIN ELECTROMAGNETIC FIELD SOLVER LSFEM ™ TD-3D*

Craig C Ouyang (coyang@aaresearch.com)
B N Jiang (bnjiang@aaresearch.com)
Nina Liao (nina@aaresearch.com)
American Applied Research Inc.(AAR)
4441 N 103rd Street, Suite #5, Milwaukee, WI 53225, USA
Phone: 414 462 8632 Fax: 414 462 8633
Web site: www.aaresearch.com

Introduction

Although many electronic design automation tools are available, these tools generally suffer from problems of electromagnetic field solvers related to accuracy, efficiency and speed. Many available solvers, for example, provide an EMI analysis that solves for electric and magnetic fields in time and space domain using only the coupled Maxwell curl equations rather than complete Maxwell formulation. These algorithms based on incomplete Maxwell equations have been shown to give acceptable field and extraction results for low to medium frequencies. However, remarkable numerical errors appear at higher, e.g., Giga plus frequencies, and these errors increase with frequency. Numerical solutions at high frequencies, particularly at Giga Hertz level, diverge substantially from analytical solutions even fine meshes are used. This error is known as the "Gaussian Bug". For examples, in the paper "Numerical Errors in the Computation of Impedances by FDTD Method and Ways to Eliminate Them", IEEE Trans. Microwave & Guided Wave Letters, Vol. 5, No. 1, 1995, it showed examples of impedance extraction, e.g. for a coaxial line using the FD-TD method. The exact solution for the line impedance is known to be 50 Ohms. As the frequency climbs, however, the computed impedance values deviate. At frequencies of substantially 40 Giga Hertz, the computed impedance deviates from the exact solution by about 20%, and at higher frequencies, the discrepancy becomes even larger. These EMI analysis tools, therefore, are not sufficiently accurate for use with deep sub-micron circuits (semiconductor or electronic design packages in which the conductors are .25 microns in width and smaller) and high-speed digital design.

To eliminate these spurious solutions, prior art systems such as the FD-TD, FV-TD, and HPSS algorithms use special kinds of meshes in modeling. These methods require that the modeled circuit or electronics design package be divided into a very fine special mesh. For example, special "edge element" is used in conventional electromagnetic finite element methods. In calculations, only the tangential field components are included on the edge and the normal field components are ignored. Calculations performed using fine meshes require a significant amount of memory and also require significant computation time. Therefore, beside inaccuracy these prior art solutions are highly inefficient too. Furthermore, often the resultant coefficient matrix produced by these simulation engines may be non-symmetrical and non-positive-definite. Therefore, computing stability is problematic. Additionally, because the electromagnetic characteristics and performance of circuits and electronic design packages cannot be adequately simulated at high speeds, a lot of trial and error design cycles are required to produce each integrated circuit. Much as 60% of the silicon material is wasted in these trial-error processes.

As semiconductor technology advances, the need to provide accurate EMI field solver becomes increasingly important. Since today high-speed integrated circuits comprising increasingly large numbers of transistors are being constructed with increasingly smaller width conductors. The Gaussian bugs

* LSFEM ™: AAR patented technology

problem described above becomes increasingly important. Eliminating Gaussian bugs in the formulation level using appropriate methods will result significant computational profit in the EMI analysis.

For many years, American Applied Research group has developed systematic R&D to identify and solve the Gaussian bug problem [1-2]. Now it is able to provide the new time domain and frequency domain EMI field solver prototype, LSFEM TD-3D in the design tool arena. In this paper, we report the main results obtained in forming this new EMI solver to date to show its power in electromagnetic compatibility computation at up to high frequencies.

Basic Formulation for LSFEM TD-3D

The new EMI field solver LSFEM TD-3D is based on the full first-order Maxwell's differential Equations (Faradays' law, Ampere's law, Gauss' law (electric) and Gauss' law (magnetic)) to simulate the electromagnetic field and performances of electronic design packages. The simulation engine works on a plurality of linear algebraic equations, which are derived from Maxwell's Equations. To derive the equations, Maxwell's Equations are discretized in the time domain using appropriate numerical scheme, which provides an optimal approximation in time. A least square finite element method (LSFEM) is used to minimize the integral of the squares of the residuals over a meshed space domain, resulting in a set of linear algebraic equations. An iteration method is used to solve the set of algebraic equations determined above. Preferably, a parallel computing scheme is employed in the simulation to increase the speed of the overall system. Introducing parallel computing into the solution processes greatly increases the speed and efficiency of the overall system.

Checking the Source Code System

To check the correctness of the computing code, EMI examples are computed. They are firstly modeled to provide structural files or computer aided design (CAD) files. Then structural file representing the modeled example is "meshed" in the space domain by any preprocessor, using a node-based finite element discretization method. Preferably, the modeled circuit is "meshed" into a number of finite elements of varying shapes and sizes, wherein finer mesh is only employed in areas of greater interest.

Input data files to the solver include problem controlling file, node file, element file, and boundary condition and electromagnetic load file, which could be time-dependent. In the element file, information regarding the shape of the element, the material of each element in the design, and the nodes defining each element is associated with each element. Materials used in this solver include anisotropic cases

A user preferably selects the simulation module and design-test related initial and boundary conditions (excitations) for the simulation, time frames for the simulation, and other user-selectable information. The control module is provided for selecting among time domain, frequency domain and other simulation modules, and also to provide means for selecting time parameters. Then the EMI solution related to the defined boundary and initial value problems is established by using an iteration scheme. The output of the system preferably comprises data associating the magnetic and electric fields at each node in the modeled design for each time step over selected time period. Using this electromagnetic data base, various performances of the tested packages can be evaluated.

To accelerate the computing processes and enhance the efficiency, an adaptive mesh refinement procedure can be incorporated. To calculate a response using the iteration method, an initial guess is made as to the answer at former time step for each node. The difference between the results is retained as an error index, which can be used to change the size of the mesh locally.

The field solver part of the code therefore provides a time domain analysis of the modeled circuit or electronic design package. The time domain analysis by LSFEM-TD 3D code can be performed in two dimensions 2D, and three dimensions 3D. Output from the simulation solver can be used to compute time-dependent electromagnetic interference (EMI) fields between electronic components; time-dependent or frequency dependent parasitic extraction for critical nets, VLSI circuits, and system-on-a-chip; time delays and waveform evolutions; crosstalk & crosscoupling between conductors or electronic elements in the modeled design; power loss evaluations; electromigration, etc. Based on the LSFEM computing method, the resulted coefficient matrix is shown to be always a symmetrical and positive-definite. Therefore, computing stability using this LSFEM TD-3D code is guaranteed as we can see in the tests. Furthermore, super computing efficiency in terms of speed and memory used in problem modeling is clearly achieved.

Features of the results for various tests with the code including computing stability, convergence, correctness, accuracy, speed and efficiency will be briefly described in the following section of this paper.

Brief Description of the Tests

Test #1: Characteristic impedance extraction of a 50 Ω coaxial line. Fig. 1 shows the results. Here the results are under use of a 10 x 10 sparse mesh. Fourier transforms are used to convert from time domain to frequency domain. In this case, the LSFEM code gives accuracy within 1% for frequencies up to 40 Giga Hertz. While in the paper mentioned above in this paper, the author's estimation for the mesh required to obtain accuracy within 1% is finer than 100 x 100. Therefore, we can obtain much better modeling power from LSFEM code to give EMI analysis.

Test #2: Scattering by a circular cylinder. FE mesh is shown in Fig. 2(a). Comparison for the results regarding RCS is typically shown in Fig. 2(b). Here you can see the correctness of the LSFEM method and the code of LSFEM field solver. Fig. 3 shows the spurious solution given by two curl equations. In the near field, you can clearly see the area of spurious solution through comparison of both solutions by LSFEM and two curl equations.

Test #3: Scattering by a 3D sphere. Fig. 4 shows part of the meshed area. Here we use 5400 3D 8- node cubic elements and 6020 nodes to form the mesh. The code shows good computing stability, good convergence and good accuracy for thousands of time steps. Total scattering time for the signal analyzed reaches over 4166 pico-seconds.

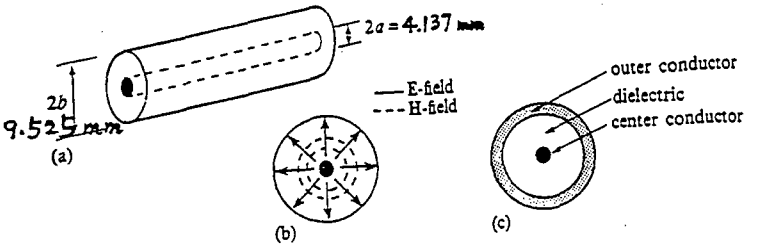
References

1). Bo-nan Jiang, The Least-Square Finite Element Method, Springer, 1998

2). C. Ouyang, Spurious Solutions in Computational Electromagnetics and the Least Square Finite Element Method - A Technical Review, AAR Report, No. 98-011, 1998

Figures

Coaxial Line



Coaxial Transmission Line: (a) Geometry (b) Field Profile (c) Construction

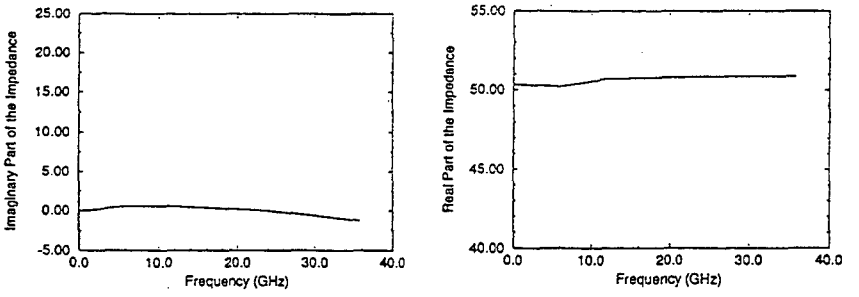
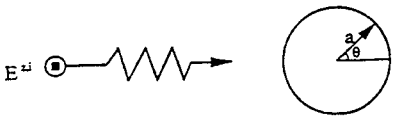
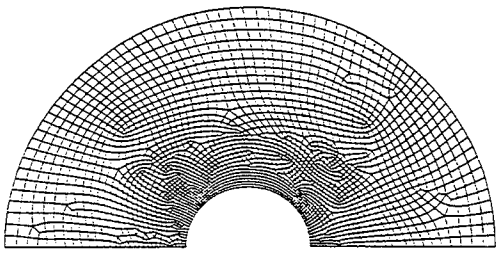


Fig. 1 Characteristic impedance of 50 Ω coaxial line by LSFEM TD-3D

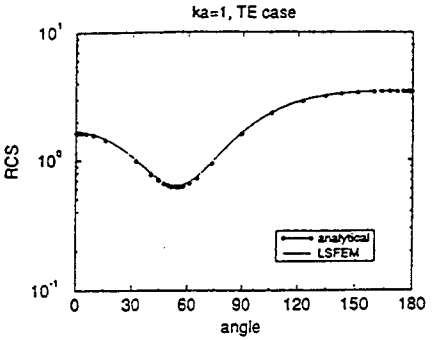


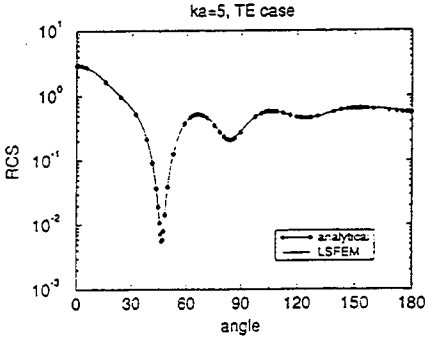
Scattering by a circular cylinder

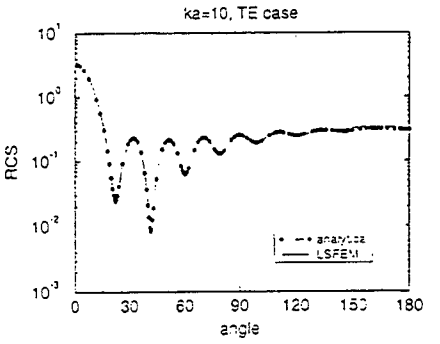


Finite element mesh

(a)

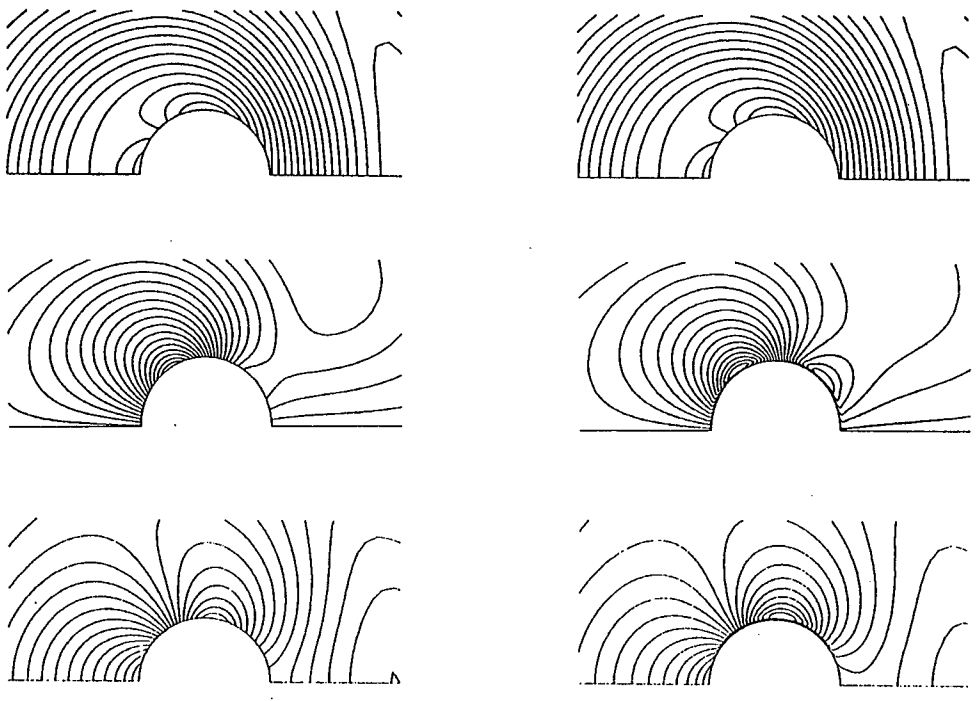






(b)

Fig. 2 Scattering by a circular cylinder under incident wave:
$E^{z,i} = Eo \sin(x\cos\alpha + y\sin\alpha - ct)$



Comparison of the solution of the full Maxwell's equations (left) and the two curl equations(right), TM case, $ka = 1$, E_z, H_x, H_y respectively (top to bottom).

Fig. 3 Spurious solutions given by incomplete Maxwell formulation and the correct solution by LSFEM TD-3D code

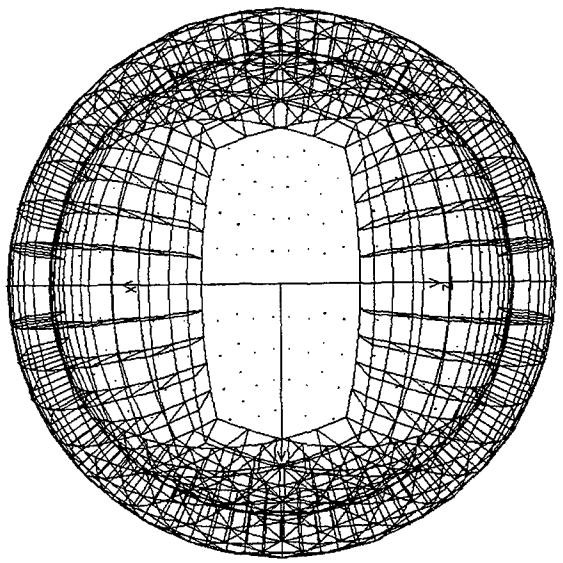


Fig. 4. FE mesh in computation for scattering by a sphere using LSFEM TD-3D

Characteristic-Based Time-Domain Method for Antenna Analysis

Dan Jiao[1], Jian-Ming Jin[1], and J. S. Shang[2]

[1]Center for Computational Electromagnetics
Department of Electrical and Computer Engineering
University of Illinois at Urbana-Champaign
Urbana, Illinois 61801-2991

[2]Air Vehicles Directorate
Air Force Research Laboratory
Wright-Patterson AFB, Ohio 45433-7913

Abstract

The characteristic-based time-domain method, developed in the computational fluid dynamics community for solving the Euler equations, is applied to the antenna radiation problem. Based on the principle of the characteristic-based algorithm, a governing equation in the cylindrical coordinate system is formulated directly to facilitate the analysis of body-of-revolution antennas, and also to achieve the exact Riemann problem. A finite difference scheme with the second-order accuracy in both time and space is constructed from the eigenvalue and eigenvector analysis of the derived governing equation. Rigorous boundary conditions for all the field components are formulated to improve the accuracy of the characteristic-based finite difference scheme. Numerical results demonstrate the validity and accuracy of the proposed technique.

1 Introduction

A variety of numerical methods have been extensively investigated to model antenna radiation problems. Basically, they can be divided into two classes: time-domain and frequency-domain methods. Between them, the time-domain method has received more attention recently over the frequency-domain counterpart. There are several reasons for its popularity. First, the parameters of interest to characterize an antenna generally change drastically with frequency. When the traditional frequency-domain methods are used for analysis, a set of algebraic equations must be solved repeatedly at many frequencies. This can be computationally expensive, and even become prohibitive, when an object of large electric size is considered. However, if the time-domain method is employed, one simulation will be sufficient to generate all the information in the frequency domain. As a result, the time-domain method greatly facilitates the modeling of antennas, especially the wideband antennas. Another attractive feature of the time-domain method is that it solves the time-dependent Maxwell's equations directly, and hence provides good physical insight into the radiation process. Furthermore, it removes the difficulty of handling material properties, which cannot be avoided easily by the frequency-domain methods. Although the time-domain method has to repeat the calculation for different incident angles when it deals with scattering problems,

this is not the case in antenna radiation problems because here the excitation is often fixed and the analysis usually requires one calculation.

In computational electromagnetics, a popular time-domain method is the finite-difference time-domain (FDTD) method, which was developed by Yee in 1966 [1]. This method is a mid-point, leap-frog algorithm with second-order accuracy in both time and space domains. Since it is a central difference scheme, it is naturally stable. The inaccuracy induced by improper boundary conditions, the discretization error, and the round-off error will continuously propagate through the entire computational domain. Since an absorbing boundary must be introduced to truncate the computation domain so that the infinite space can be simulated, the accuracy and stability of the FDTD scheme are restricted.

Maxwell's equations in time domain constitute a hyperbolic partial differential system, which is a pure initial-value problem [2-3]. Therefore, the characteristic-based algorithm [4-9], which was developed in the computational fluid dynamics community for solving the Euler equations, is found to be equally effective for solving Maxwell's equations in time domain. The basic approach of the characteristic-based method is to reduce the three-dimensional system of equations to an approximate Riemann problem in each spatial direction. The sequence of one-dimensional problem is then solved to obtain the solution to the original problem [4]. The characteristic-based algorithm has several advantages over other time-domain methods. First, it utilizes the unique feature of the hyperbolic differential system, which is that the given initial values, together with any possible discontinuities, are continued along the characteristics [2-3]. Consequently, if one of the coordinates of the system equation is aligned with the direction of the wave propagation, $\mathbf{E} \times \mathbf{H}$, the wave will continue to propagate along this direction, and hence no wave is reflected back. Therefore, it naturally eliminates the reflected wave from the truncated outer boundary. Second, it enforces the directional propagation of information for wave motion, because it conducts a detailed eigenvalue analysis. Forward differencing is adopted for the negative eigenvalues, and the backward one is used for the positive eigenvalues. This windward discretization provides a more robust stability than a central differencing scheme. Third, the governing equation can be easily cast into a generalized curvilinear coordinate system. It greatly accommodates the computation of electromagnetic fields around a complex scatterer. Another important feature of the characteristic-based method is that it can achieve a higher-order accuracy easily by using a higher-order interpolation or extrapolation scheme to construct the flux vector at the cell vertexes or interfaces.

Due to the above advantages of the characteristic-based algorithm, it has been applied to solving electromagnetic problems in recent years [4-9]. From a survey of the literature, it is found that the major concern at present is the scattering problem, and there has been little application of the method to antenna problems. However, it should be more advantageous to use this time-domain method to deal with the radiation problem, because the position of the source is fixed and therefore it is not necessary to repeat the calculation for different incident angles. However, the application of the characteristic-based method to the antenna radiation problem is not straightforward if the high accuracy is required. In this paper, a dipole antenna and a cylindrical monopole antenna are analyzed using the characteristic-based algorithm. In order to model these two kinds of antenna, we first formulate a governing equation, which is feasible for the body-of-revolution (BOR) problem. With this governing equation, the exact Riemann problem is then achieved, which enhances the accuracy of the numerical scheme. Next, a detailed eigenvalue and eigenvector analysis is conducted on the governing equation. A finite difference scheme with second-order accuracy in both time and space is constructed. Rigorous boundary conditions for all the field components on the surface of the perfect electric conductor (PEC) boundary are derived to improve the accuracy. Numerical examples are given to validate the proposed technique.

2 Formulation

If the characteristic-based algorithm is used directly for the analysis of a BOR antenna, the governing equation with six unknowns in Cartesian coordinate needs to be cast into the cylindrical coordinate system. This coordinate transformation induces errors in the characteristic-based scheme, because it transforms the original problem to an approximate Riemann problem. It also introduces the artificial difficulty in the enforcement of the boundary condition on the surface of the antenna and on the outer boundary of the computational domain. In this paper, we start from Maxwell's equations in the cylindrical coordinate system directly. By choosing unknowns wisely, the exact Riemann problem can be achieved. At the same time, the difficulty in implementing the boundary conditions can be removed.

2.1 Governing equations

For an antenna that is rotationally symmetric and excited by a rotationally symmetric source, the electromagnetic field is independent of the cylindrical coordinate ϕ. Therefore, Maxwell's equations can be expressed as two independent sets: one involves only the components D_z, D_ρ, B_ϕ (TM case), and the other involves only the components of B_z, B_ρ and D_ϕ (TE case). Taking the TM case as an example, the relevant Maxwell's equations become

$$\begin{aligned} \frac{\partial E_\rho}{\partial z} - \frac{\partial E_z}{\partial \rho} &= -\mu \frac{\partial H_\phi}{\partial t} \\ -\frac{\partial H_\phi}{\partial z} &= \epsilon \frac{\partial E_\rho}{\partial t} + J_\rho \\ \frac{1}{\rho}\frac{\partial (\rho H_\phi)}{\partial \rho} &= \epsilon \frac{\partial E_z}{\partial t} + J_z. \end{aligned} \tag{1}$$

Written in a flux vector form, the above equations become

$$\frac{\partial \mathbf{U}}{\partial t} + \frac{\partial \mathbf{F}_\rho}{\partial \rho} + \frac{\partial \mathbf{F}_z}{\partial z} = -\mathbf{J} \tag{2}$$

where

$$\mathbf{U} = \begin{Bmatrix} \rho D_z \\ \rho D_\rho \\ \rho B_\phi \end{Bmatrix} \tag{3}$$

and

$$\mathbf{F}_\rho = \begin{Bmatrix} -\rho B_\phi/\mu \\ 0 \\ -\rho D_z/\epsilon \end{Bmatrix}, \quad \mathbf{F}_z = \begin{Bmatrix} 0 \\ \rho B_\phi/\mu \\ \rho D_\rho/\epsilon \end{Bmatrix}, \quad \mathbf{J} = \begin{Bmatrix} \rho J_z \\ \rho J_\rho \\ \rho D_z/(\rho\epsilon) \end{Bmatrix}. \tag{4}$$

Since the flux vectors $\mathbf{F}_\rho$ and $\mathbf{F}_z$ are homogeneous functions of degree one with respect to the dependent variable $\mathbf{U}$, they can be expressed as the product of the dependent variables and the coefficient matrices,

$$\mathbf{F}_\rho = A\mathbf{U}, \quad \mathbf{F}_z = B\mathbf{U} \tag{5}$$

where the coefficient matrices A and B are

$$A = \begin{bmatrix} 0 & 0 & -\frac{1}{\mu} \\ 0 & 0 & 0 \\ -\frac{1}{\epsilon} & 0 & 0 \end{bmatrix}, \quad B = \begin{bmatrix} 0 & 0 & 0 \\ 0 & 0 & \frac{1}{\mu} \\ 0 & \frac{1}{\epsilon} & 0 \end{bmatrix}. \tag{6}$$

2.2 Eigenvalues and eigenvetors

The characteristic-based algorithm conducts a detailed eigenvalue and eigenvector analysis. The equations in the flux vector form are correspondingly split according to the sign of the eigenvalues. The forward difference is applied to compute the flux vectors associated with the negative eigenvalue, and the backward difference is adopted to evaluate the flux vectors identified with the positive eigenvalue. This process mimics the wave mechanism of information propagation, and hence provides a more robust stability than a central difference scheme.

The eigenvalues of the coefficient matrices A and B are the same, which are given by

$$\lambda = \left\{0, -\frac{1}{\sqrt{\mu\epsilon}}, \frac{1}{\sqrt{\mu\epsilon}}\right\}. \tag{7}$$

It is evident that the eigenvalues are nothing but the speed of the positively and negatively propagating waves.

The similarity matrices for diagonalization are constructed by using the eigenvectors as the column arrays as shown in the following equation

$$S_A = \begin{bmatrix} 0 & \sqrt{\frac{\epsilon}{\mu}} & -\sqrt{\frac{\epsilon}{\mu}} \\ 1 & 0 & 0 \\ 0 & 1 & 1 \end{bmatrix}, \quad S_B = \begin{bmatrix} 1 & 0 & 0 \\ 0 & -\sqrt{\frac{\epsilon}{\mu}} & \sqrt{\frac{\epsilon}{\mu}} \\ 0 & 1 & 1 \end{bmatrix} \tag{8}$$

which leads to

$$\mathbf{F}_\rho = S_A \lambda S_A^{-1}\mathbf{U}, \quad \mathbf{F}_z = S_B \lambda S_B^{-1}\mathbf{U}. \tag{9}$$

From equations (7) and (8), it is obvious that the derived eigenvalues and eigenvectors are invariant with respect to the dependent variables $\mathbf{U}$. As a result, the exact Riemann problem can be achieved with this formulation.

2.3 Flux vector splitting

The fundamental idea of the flux vector splitting is to process data according to the direction of wave propagation. The positively propagating wave is associated with the positive eigenvalue, and vice versa. As a consequence, the flux vectors $\mathbf{F}_\rho$ and $\mathbf{F}_z$ can be split as

$$\begin{aligned} \mathbf{F}_\rho &= A^+\mathbf{U} + A^-\mathbf{U} \\ \mathbf{F}_z &= B^+\mathbf{U} + B^-\mathbf{U} \end{aligned} \tag{10}$$

where

$$A^+ = \begin{bmatrix} \frac{1}{2\sqrt{\epsilon\mu}} & 0 & -\frac{1}{2\mu} \\ 0 & 0 & 0 \\ -\frac{1}{2\epsilon} & 0 & \frac{1}{2\sqrt{\mu\epsilon}} \end{bmatrix}, \quad A^- = \begin{bmatrix} -\frac{1}{2\sqrt{\epsilon\mu}} & 0 & -\frac{1}{2\mu} \\ 0 & 0 & 0 \\ -\frac{1}{2\epsilon} & 0 & -\frac{1}{2\sqrt{\mu\epsilon}} \end{bmatrix} \tag{11}$$

and

$$B^+ = \begin{bmatrix} 0 & 0 & 0 \\ 0 & \frac{1}{2\sqrt{\epsilon\mu}} & \frac{1}{2\mu} \\ 0 & \frac{1}{2\epsilon} & \frac{1}{2\sqrt{\mu\epsilon}} \end{bmatrix}, \quad B^- = \begin{bmatrix} 0 & 0 & 0 \\ 0 & -\frac{1}{2\sqrt{\epsilon\mu}} & \frac{1}{2\mu} \\ 0 & \frac{1}{2\epsilon} & -\frac{1}{2\sqrt{\mu\epsilon}} \end{bmatrix}. \tag{12}$$

A second-order accurate windward differencing can be constructed to form difference operators according to the sign of the eigenvalues,

$$\Delta\mathbf{U}_i = [-3\mathbf{U}_i + 4\mathbf{U}_{i+1} - \mathbf{U}_{i+2}]/2 \tag{13}$$

$$\nabla\mathbf{U}_i = [3\mathbf{U}_i - 4\mathbf{U}_{i-1} + \mathbf{U}_{i-2}]/2. \tag{14}$$

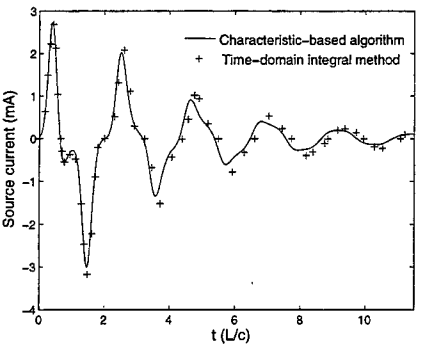


Figure 1: Electric current at the fed point of a center-fed dipole antenna with a Gaussian time-dependent voltage source.

The fractional-step method or the Runge-Kutta family of single-step multi-stage procedures can be employed to accomplish the time integration. In this paper, a single-step two-stage Runge-Kutta scheme is used to guarantee second-order accuracy in time.

3 Numerical examples

To demonstrate the validity of the proposed algorithm, a number of examples are considered here and the results are compared with other numerical or measured data.

The first example is a linear, center-fed dipole antenna [10]. The ratio of the radius to the length of the antenna, r/L, is equal to 0.00674. It is excited by a Gaussian time-dependent voltage source which takes the form of $V = \exp[-a^2(t - t_{max})^2]$, where $a = 1.5 \times 10^9$, $t_{max} = 1.43 \times 10^{-9}$ sec. The voltage source is fed to the antenna through a gap having a width of $L/20$ at the center of the antenna. Based on the equivalence principle, the gap is filled with PEC and a surface magnetic current M_ϕ is prescribed on the surface of the gap. This magnetic current is related to the voltage source by $M_\phi = V/d$, where d denotes the width of the gap, that is, $d = L/20$. The outer boundary of the computational domain is placed at a distance of L away from the antenna along both the ρ and z directions. The calculated current at the fed point is shown in Fig. 1. By performing the Fourier transform on the source current and the excitation voltage, the input admittance of the antenna can be obtained, which is shown in Fig. 2. Clearly, the calculated result agrees well with the result from the time-domain integral method [10].

The second example considered here is a monopole antenna fed through an image plane from a coaxial transmission line [11], the geometry of which is shown in Fig. 3. The parameters to characterize the monopole antenna are the height h and the radii of the inner and outer conductors of the coaxial line, a and b. In this example, the ratio of b to a is 2.3, and that of h to a is 32.8. The antenna is excited by the incident TEM wave within the coaxial line, which is given by

$$E_\rho(t) = V^i(t)/\rho \ln(b/a)$$
$$H_\phi(t) = V^i(t)/(2\pi\rho\eta) \qquad (15)$$

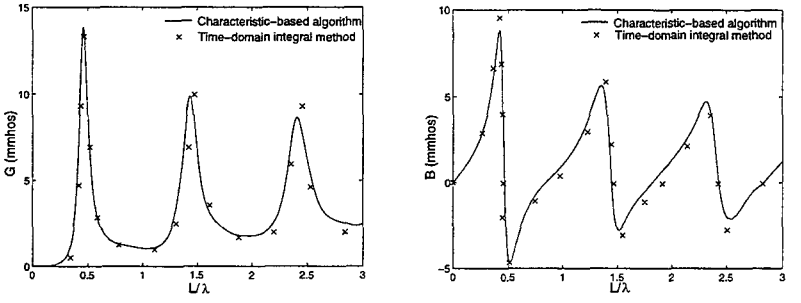


Figure 2: The input admittance of a center-fed dipole antenna. (a) Conductance. (b) Susceptance.

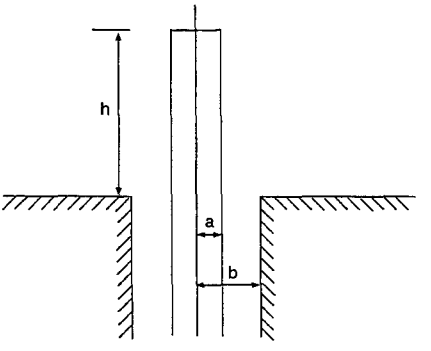


Figure 3: Geometry of a cylindrical monopole antenna fed through an image plane.

where $\eta = 60\ln(b/a)$, and

$$V^i(t) = \exp(-t^2/2\tau_p^2). \tag{16}$$

The internal reflection of the antenna is characterized by the time constant, τ_a, which is equal to h/c. In order to compare with the measured data in [11], the ratio of τ_p to τ_a is chosen to be 0.161. To apply the compatibility condition, the outer boundary is placed at a distance of h away from the tip of the monopole and the outer edge of the coaxial line. The calculated reflected voltage in the coaxial line is shown in Fig. 4. The reference plane to extract the reflected voltage can be chosen arbitrarily within the coaxial line, as long as only the TEM mode is present. The compatibility condition is also implemented here to suppress the incoming wave. From Fig. 4, it can be seen clearly that the numerical result agrees very well with the measured data.

Next, the input admittance of the monopole antenna is calculated. To compare with the result measured by Cooper [11], the ratio of b to a is chosen to be 3.0. The Gaussian pulse in the form of (19) is still employed to excite the antenna. After extracting the reflected voltage within the

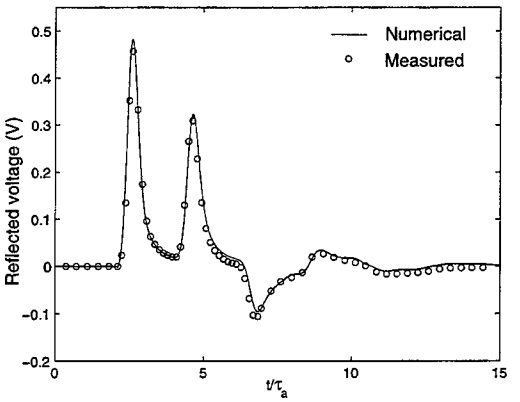


Figure 4: Reflected voltage in the coaxial line for a cylindrical monopole antenna excited by a 1-V Gaussian pulse: $b/a = 2.3$, $h/a = 32.8$, and τ_p/τ_a=0.161.

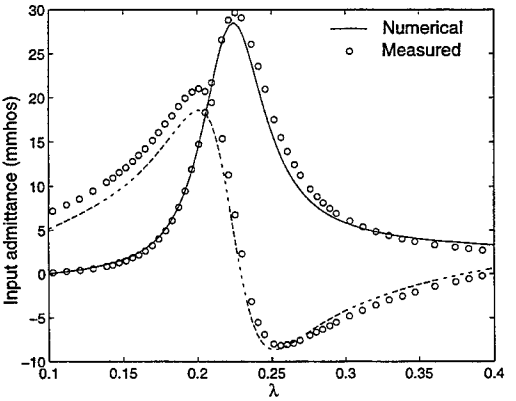


Figure 5: Input admittance of a cylindrical monopole antenna: $b/a = 3.0$.

coaxial line, a Fourier transform is performed on it as well as on the incident voltage to obtain the reflection coefficient at the reference plane. From the reflection coefficient, the input admittance at the aperture of the monopole antenna can be obtained. The result is shown in Fig. 5, which exhibits a good agreement with the measured value.

The method has also been applied to dielectric coated antennas successfully.

4 Conclusion

In this paper, a characteristic-based time-domain scheme is presented for antenna analysis. In combination with the unique feature of the BOR antenna, a governing equation is derived directly in the cylindrical coordinate system. It transforms the original initial and boundary value problem into an exact Riemann problem, and hence improves the accuracy of the characteristic-based scheme in a non-Cartesian coordinate system. It also facilities the enforcement of the PEC boundary conditions and compatibility condition. Numerical results are shown to demonstrate its effectiveness.

References

[1] K. S. Yee, "Numerical solution of initial boundary value problems involving Maxwell's equations in isotropic media," *IEEE Trans. Antennas Propagat.*, vol. 14, pp. 302–307, 1966.

[2] R. Courant and D. Hilbert, *Methods of Mathematical Physics, Volume II.* New York: Intersicence Publishers, 1965.

[3] A. Sommerfeld, *Partial Differential Equations in Physics.* New York: Academic Press, 1949.

[4] J. S. Shang, "Characteristic-based algorithms for solving the Maxwell equations in the time domain," *IEEE Antennas and Propagation Magazine*, vol. 37, pp. 15–25, June 1995.

[5] J. S. Shang and D. Gaitonde, "Characteristic-based, time-dependent Maxwell equations solvers on a general curvilinear frame," *AIAA Journal*, vol. 33, no. 3, pp. 491–498, March 1995.

[6] J. S. Shang and D. Gaitonde, "Scattered electromagnetic field of a reentry vehicle," *AIAA J. Spacecraft and Rockets*, vol. 32, no. 2, pp. 294–301, March-April 1995.

[7] J. S. Shang and M. F. Robert, "A comparative study of characteristic-based algorithms for the Maxwell equations," *Journal of Computational Physics*, vol. 125, pp. 378–394, 1996.

[8] J. S. Shang, "A fractional-step method for solving 3D, time-domain Maxwell equations," *Journal of Computational Physics*, vol. 118, pp. 109–119, 1995.

[9] J. L. Steger and R. F. Warming, "Flux vector splitting of the invisid gasdynamic equations with application to finite-difference methods," *Journal of Computational Physics*, vol. 40, pp. 263–293, 1981.

[10] A. J. Poggio and E. K. Miller, "Integral equation solutions of three dimensional scattering problems," in *Computer Techniques for Electromagnetics.* Chap. 4, Elmsford, NY: Permagon Press, 1973.

[11] J. G. Maloney, G. S. Smith and W. R. Scott, "Accurate computation of the radiation from simple antennas using the finite-difference time-domain method," *IEEE Trans. Antennas Propagat.*, vol. 38, no. 7, pp. 1059–1068, July 1990.

Modeling of Thin–Wire Structures by Solving the EFIE in Time Domain

Friedrich Schunn and Hermann Singer
Department of Theoretical Electrical Engineering
Technical University Hamburg–Harburg, Hamburg, Germany
email: schunn@tu-harburg.de

Abstract

Solving of the electric field integral equation (EFIE) using the method of moments (MoM) is a powerful tool in determining the time dependent current distribution on thin–wire structures. Modeling real life problems however requires consideration of the finite conductivity of the wires, consideration of lumped and distributed loads and the computation of the electromagnetic field in the vicinity of the structures. In this paper we present an extension of a time domain formulation for solving the EFIE for thin wires with regard to linear and non linear loads and scattered field computation.

1 Introduction

In [1] we presented a new numerical formulation to determine the time dependent current distribution on thin–wire structures excited by an arbitrary time varying field. The numerical formulation is based on the solution of an equation system formed by the mixed potential EFIE and continuity equation for thin wires. To solve this equation system we use the method of moments. The related current and linear charge density distributions are approximated by means of sets of basis functions. For the currents we use linear basis functions of triangular shape, and for the linear charge densities we use pulse basis functions. At wire junctions the current basis functions are slightly modified. They have to enable modeling of multiple connected wires without affecting the late–time stability of the formulation. The chosen current and charge approximations are similar to those in [2], which led to very good results in frequency domain. We also perform linear time discretization by using finite difference formulae.

For computation of scattered and radiated fields we make use of the electric scalar potential and magnetic vector potential. We compute both at suitable locations and differentiate them numerically with regard to space and time.

Considering loads, the EFIE used has to be modified. As long as the loads are passive elements the resulting matrix has to be modified only at elements of its principal diagonal. With linear loads the modified matrix is furthermore invariant with respect to time and has to be built up only once. It can then be used at every time step. With nonlinear loads matrix elements may change at each time step and special techniques or properties of the equation system have to be used in order to reduce computation time.

2 Numerical formulation

Assuming a perfectly conducting thin wire in a homogeneous and lossless medium with constant permittivity and permeability, the EFIE and continuity equation can be written as

$$\left[\frac{\partial \mathbf{A}}{\partial t} + \nabla\Phi\right]_{tan} = \mathbf{E}^{\mathrm{i}}_{tan}\,, \qquad \frac{\partial I}{\partial s} + \frac{\partial \lambda}{\partial t} = 0\,, \tag{1}$$

where $\mathbf{A}$ and Φ are the retarded magnetic vector and electric scalar potentials. I and λ are the induced electric current and linear charge density on the wire. s denotes the length variable along the wire. As excitation we use the electric field $\mathbf{E}^{\mathrm{i}}$ of an incident electromagnetic wave.

As reported in [1] we use the method of moments to solve (1). We approximate the current distribution with a set of triangular basis functions f_n and the linear charge density distribution with a set of pulse basis functions g_m:

$$I(s,t) = \sum_{n=1}^{N} I_n(t) f_n(s), \qquad \lambda(s,t) = \sum_{m=1}^{N+1} \lambda_m(t) g_m(s)\,. \tag{2}$$

As testing functions we use delta functions for the continuity equation and pulse basis functions in case of the EFIE. Applying the method of moments and replacing time and space derivatives with finite difference formulae yield

$$\frac{\Psi_n^{k+1} - \Psi_n^k}{\Delta t} = \frac{1}{2}\left(G_n^k + G_n^{k+1}\right)\,, \qquad \frac{\lambda_m^{k+1} - \lambda_m^k}{\Delta t} = -F_m^k\,, \tag{3}$$

where F_m^k is an expression for the current divergence at time step k and G_n is a function of the electric scalar potential and the incident electric field. $\Psi_n^{k+1} = A_n^{k+1} \cdot \Delta s$ contains the magnetic vector potential which is dependent on the electric current. The indices m, n correspond with the testing points (MoM) for the two equations.

To explain the Marching-On-in-Time (M–O–T) algorithm we assume that all quantities are known for time steps $0 \le k' \le k$ and we now want to know the values I_n^{k+1}, λ_m^{k+1}. With the continuity equation part of (3) new charge density values λ_m^{k+1} are computed. They lead to the new values G_n^{k+1} whereas the G_n^k are known from the time step before. We decompose the terms Ψ_n^{k+1} in a "self" contribution $\Psi_n^{\mathrm{s},k+1}$ that depends linearly on I^{k+1} values, and a "non–self" contribution $\Psi_n^{\mathrm{ns},k+1}$ which can be computed from known values $I^{k'}$. Thus we obtain the equation system

$$\mathbf{M}\, I^{k+1} = \Psi^{\mathrm{s},k+1} = \Psi^{k+1} - \Psi^{\mathrm{ns},k+1} \tag{4}$$

with the currents I^{k+1} as unknowns. Matrix $\mathbf{M}$ is sparse, diagonally dominant and contains mainly geometry information. Furthermore it is time invariant and needs to be set up only once at the beginning of the simulation. It can then be used again at every time step and leads to a considerable saving of computation time.

To ensure late–time stability we introduced a corrector step [1], in which the linear charge density λ^{k+1} and current I^{k+1} values are re–computed.

3 Field computation

The electromagnetic field in the vicinity of conducting structures is given by the superposition of the incident field and the scattered field. While we regard the incident field as excitation, and thus as known, we have to compute the scattered field. We do this by using the retarded electromagnetic potentials:

$$\mathbf{E}^s = -\nabla\Phi - \frac{\partial \mathbf{A}}{\partial t}, \qquad \mathbf{B}^s = \nabla \times \mathbf{A}. \tag{5}$$

Now consider a wire located on the z axis. At four points, which we obtain through small translations of the observation point in radial and axial direction, and at the observation point itself we compute the values for Φ and $\mathbf{A}$ at every time step. The scattered field contributions of the two potentials can be specified as

$$\nabla\Phi \approx \frac{\Phi_2 - \Phi_1}{\Delta r} \cdot \mathbf{e}_r + \frac{\Phi_4 - \Phi_3}{\Delta z} \cdot \mathbf{e}_z, \quad \nabla \times \mathbf{A} \approx -\frac{A_{z2} - A_{z1}}{\Delta r} \cdot \mathbf{e}_\phi, \quad \frac{\partial \mathbf{A}}{\partial t} \approx \frac{\mathbf{A}^{k+1} - \mathbf{A}^k}{\Delta t} \tag{6}$$

where the derivatives with respect to space and time have been replaced by finite difference formulae.

Using the retarded potentials directly we omit any far field approximations and are able to compute the electromagnetic field even at observation points very close to the conducting structure.

4 Wire junctions

In [1] we used current basis functions of type (I) from Fig. 1 for wire junctions. For each wire end at the junction point such a basis function has to be used. Δs_i denote the segment lengths on the connected wires and $\Delta l_i = \Delta s_i/2$.

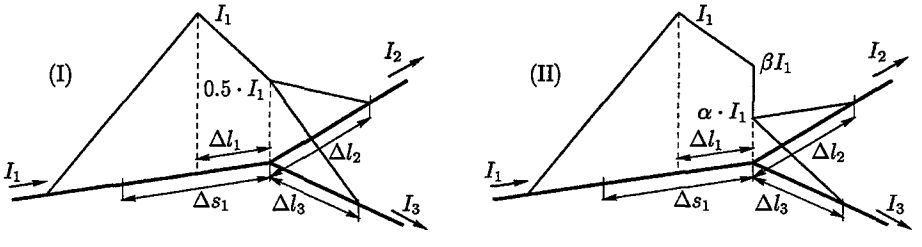


Figure 1: Basis functions for wire junctions

The basis functions of type (I) give good results as long as the number of connected wires is not to high (more than five). At higher numbers stability problems occur. With the modified basis functions of type (II) from Fig. 1 we have eliminated these stability problems. The difference

between the two types of basis functions are the heights of the current parts at the junction point. They are given by

$$\alpha = \frac{1}{n_j}, \qquad \beta = 1 - \frac{1}{n_j}, \tag{7}$$

where n_j is the number of connected wires at this wire junction. The basis functions of type (II) were first introduced in [3] for frequency–domain simulations. They ensure that Kirchhoff's law, one of the conditions for wire junctions, is also satisfied for the single basis function, whereas the basis functions of type (I) fulfill Kirchhoff's law only when we sum up the contributions of all basis functions adjoining this junction point.

5 Modeling linear loads

Modeling loads requires a modification of the EFIE. The additional voltage along the load has to be considered in the numerical model. The continuity equation is not affected by the load. The new EFIE can be written as

$$\frac{\partial \mathbf{A}_{tan}}{\partial t} + \frac{\partial \Phi}{\partial s} + \frac{\partial}{\partial s}\left[R\,I(t) + L\frac{\partial I}{\partial t} + \frac{1}{C}\int_{-\infty}^{t} I(\tau)d\tau \right] = \mathbf{E}^{\mathrm{i}}_{tan}. \tag{8}$$

In eq. (8) we regard the load as a lumped element that can be represented as a series connection of resistance, inductance and capacitance. To treat (8) numerically we have to perform similar transformations of the EFIE as those, which led from eq. (1) to eq. (3). In particular we have to discretize (8) with respect to time. We use a simple forward differentiation formula instead of the time derivative, that comes with the inductance

$$L\left.\frac{\partial I}{\partial t}\right|^{k} \approx L\frac{I^{k+1} - I^{k}}{\Delta t}, \tag{9}$$

and take advantage of the piecewise linear time history of the current:

$$\frac{1}{C}\int_{k\Delta t}^{(k+1)\Delta t} I(t)dt \approx \frac{1}{C}\left[I^{k}\cdot\Delta t + \frac{\Delta t}{2}\cdot\left(I^{k+1} - I^{k}\right)\right]. \tag{10}$$

In eq. (9) and (10) we also separate terms that depend on not retarded (not known) currents I^{k+1} from those that depend on retarded (already known) currents $I^{k'}$, $0 \le k' \le k$. Hence we obtain a new equation system

$$\left[\mathbf{M} + \Delta t\,\mathbf{R} + \mathbf{L} + \frac{\Delta t^2}{2}\mathbf{C}\right] I^{k+1} = \tilde{\Psi}^{k+1} - \Psi^{\mathrm{ns},k+1} \tag{11}$$

with the currents I^{k+1} as unknowns. $\mathbf{R}$, $\mathbf{L}$, and $\mathbf{C}$ represent matrices, that contain non–zero elements R_{ii}, L_{ii}, $1/C_{ii}$ only at positions of their principal diagonal that correspond to places

where load elements were located. In the geometry model the loads are positioned at the testing points for the EFIE. As long as the R, L, C values are linear, i.e. time invariant and as long as we keep $\Delta t = \text{const}_t$ the new system matrix is also time invariant. It needs to be built up only once and can be used at every following time step. The right hand side of the equation system has also changed. Besides the contributions due to the retarded potentials it contains also contributions related to the load elements.

We can imagine distributed loads or wires with finite conductivity as series connections of several lumped loads and model them in the same way as described above.

6 Modeling nonlinear loads

Modeling nonlinear loads is similar to modeling linear loads. The same formalism as described in section 5 is applied for modifying the EFIE. Differences occur when solving the equation system for the currents (4) and (11) respectively. The formalism leads to matrix elements, that may change at each time step. The most straight forward method would be to adjust the system matrix at each time step and use the usual solution scheme for the equation system. But this would require to find the inverse of the system matrix (or perform a LU decomposition of the matrix) at each time step. Also the amount of storage required for the matrix is twice (original matrix and inverse or LU decomposition). To overcome this increased requirements regarding computation time and storage special schemes for nonlinear loads have been developed. A good overview is given in [4] and [5].

At this stage we will consider only a single wire antenna loaded with a nonlinear load having an idealized diode–like characteristic. Let V_{NL} be the voltage along the nonlinear load. Its value is then given by

$$R_{NL} = \begin{cases} R_f\,, & \text{if} \quad V_{NL} > 0\,, \\ R_r\,, & \text{if} \quad V_{NL} \leq 0\,. \end{cases} \tag{12}$$

Since we consider only a single wire, our formulation yields for eq. (4) a matrix $\mathbf{M}$ that consists only of its principal diagonal. This is not the case with the procedure described in [4] and [5]. Thus we do not need a real matrix inversion or LU decomposition. We can therefore afford the "straight forward" method described above. Off–diagonal elements occur when wire junctions are involved or when the distance between two wires is smaller than $c \cdot \Delta t$, where Δt is the time step used and c the velocity of light. Since even in these cases matrix $\mathbf{M}$ is usually sparce, a resorting of the matrix can yield a block structure

$$\mathbf{M} = \begin{pmatrix} M_{11} & & & \\ & M_{22} & & \\ & & \ddots & \\ & & & M_{NN} \end{pmatrix} \tag{13}$$

where only the M_{ii}–Blocks have non–zero elements. Adjusting the matrix like in the "straightforward" method would be reduced to adjusting those blocks that contain nonlinear loads. In most of the cases this will result in a noticeable saving of computation time.

7 Numerical results

(1) With a first example (Fig. 2) we want to demonstrate the efficiency of the chosen basis functions for wire junctions. The structure consists of 26 wires of 0.5 m length and 1 mm radius each. For every wire 19 current basis functions were used. The structure is illuminated by an incident electromagnetic wave whose time history is given by a single puls of the form

$$E^{\mathrm{i}} = E_0 \sin^2(\pi t/T)\,, \quad E_0 = 1\ \mathrm{V/m}\,, \quad T = 2\ \mathrm{ns}\,. \tag{14}$$

The current in Fig. 2 shows that the results are stable for late times. It is the electric current in the middle of the wire marked with C. For validation, time domain (TD) results are compared with frequency domain (FD) results provided by CONCEPT (see [2]) by means of an inverse Fourier transform of the FD values.

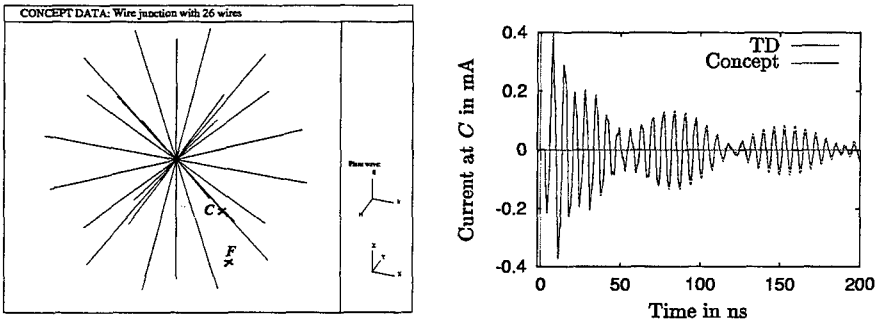


Figure 2: Wire junction with 26 wires; Current at point C.

Fig. 3 shows the E_x and H_y component of the resulting electromagnetic field at point F in Fig. 2. While the displayed E_x component is a pure scattered field component the contribution of the incident wave can clearly be seen at the first negative peak of the H_y component. Here again TD results are validated by comparison with FD results.

(2) We now consider modeling of linear loads. In Fig. 4 a R–L–C circuit is fed by a voltage source with the temporal behavior of a step function. The rise time of the source is $t_r = 1.5{\cdot}10^{-10}\,\mathrm{s}$. For the resulting current a solution can be found analytically. It is given by

$$i(t) = \frac{U_0 e^{-\frac{R}{2L}t}}{\omega L} \sin(\omega t)\,, \qquad \omega = \sqrt{\frac{1}{LC} + \left(\frac{R}{2L}\right)^2}\,. \tag{15}$$

For the numerical model we use four wires of 2 cm length. Each wire has a radius of 0.2 mm and was discretized using 9 segments. The voltage source is placed in the middle of wire 1 and the three load elements R, L, and C as a single lumped load in the middle of wire 3.

Modeling the load we have to consider that the loop has a self inductance $L_s = 64.87$ nH and therefore the load inductance used must be $L_l = 1\ \mu\mathrm{H} - L_s = 0.935\,\mu\mathrm{H}$. The value for L_s results from an approximation formula for the self inductance of rectangular loops [6].

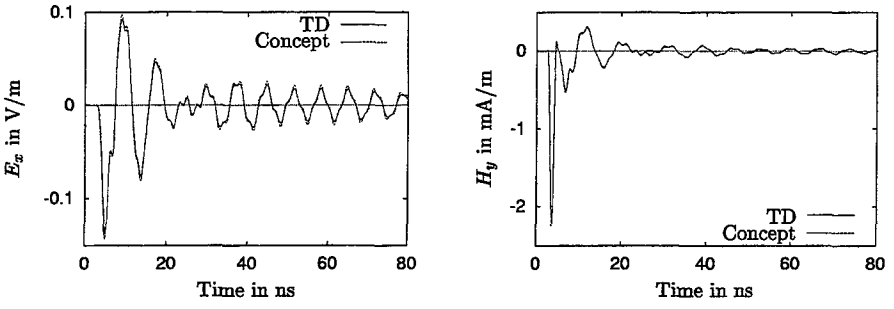


Figure 3: Electric and magnetic field at point F in Fig. 2.

Fig. 4 shows the current through the lumped load. As can be seen, numerical results (TD) match analytical results very well. The slight oscillations in the vicinity of the first positive peak are due to a traveling wave between the source voltage and the lumped load.

(3) As an example for nonlinear loads we reproduced results presented in [4]. A dipole is loaded at its center with a nonlinear resistor. The resistance is represented by $R_f = 50\ \Omega$ in the "forward" direction and $R_r = 5000\ \Omega$ in the "reverse" direction.

A voltage source is applied in series with the nonlinear element. The form of the voltage is $V(t) = 1\,\mathrm{V} \cdot e^{-[g(t-t_0)]^2}$, where $g = 1.73 \cdot 10^9\,\mathrm{s}^{-1}$ and $t_0 = 1.76 \cdot 10^{-9}\,\mathrm{s}$. To match the results given in [4] a dipole length of $L = 1$ m and a radius of $a = 6.739 \cdot 10^{-3}$ m were chosen. With this data the the dipole fatness parameter is found to be $\Omega = 2\ln(L/a) = 10$. 29 segments were used to model the antenna. Fig. 5 shows the current at the center of the dipole and the broadside radiated field according to that current. Similar to [4] the field has been "normalized" by the radial distance from the dipole to the observation point, i.e. the values for E_z have been multiplied with the radial distance. The results of Fig. 5 are essentially the same as presented in [4].

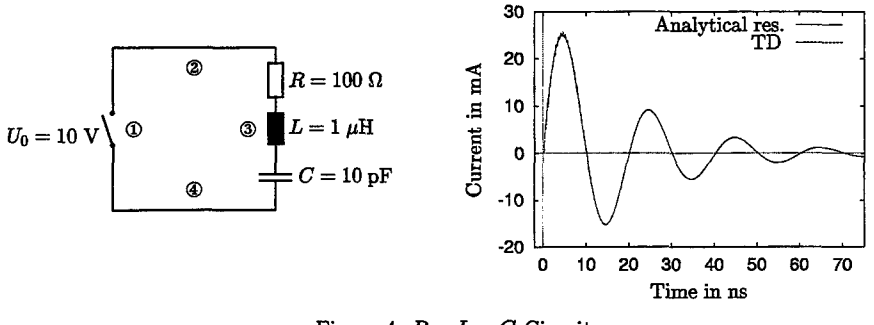


Figure 4: $R - L - C$ Circuit

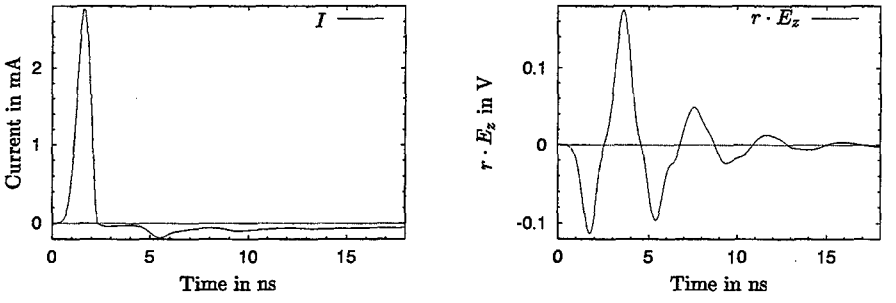


Figure 5: Current and radiated field of an antenna with a nonlinear load

8 Conclusions

The numerical technique developed in [1] has been improved with regard to modeling of wire junctions. Extensions for scattered-field computation and modeling of loads have been added. For the latter a modification of the used EFIE was necessary but did not affect late-time stability. The results presented have shown that our formulation is suitable for modeling general thin-wire structures. In case of nonlinear loads some extensions have yet to be made. Several other types of nonlinearities have to be added and computation time saving techniques for solving the current equation system have to be implemented.

References

[1] F. Schunn and H. Singer, "A New Numerical Formulation in Time-Domain Analysis of Thin-Wire Structures", Atlanta: IEEE APS Int. Symposium 1998, pp. 960–963.

[2] H.D. Brüns, "Pulserregte elektromagnetische Vorgänge in dreidimensionalen Stabstrukturen", Ph.D. Thesis, Universität der Bundeswehr, Hamburg, 1985.

[3] Th. Mader, "Berechnung elektromagnetischer Felderscheinungen in abschnittsweise homogenen Medien mit Oberflächenstromsimulation", Ph.D. Thesis, Techn. Univ. Hamburg-Harburg, Hamburg, 1992.

[4] J.A. Landt, "The Transient Response of Thin-Wire Antennas and Scatterers Loaded with Circuits and Nonlinear Elements", Los Alamos Nat. Lab., Los Alamos, Rep. LA-8242-MS, Feb. 1980.

[5] J.A. Landt, "Network loading of thin-wire antennas and scatterers in the time domain", Radio Science, Vol. 16, pp. 1241–1247, Nov.–Dec. 1981.

[6] H. Meinke and F.W. Gundlach, "Taschenbuch der Hochfrequenztechnik" 5. ed., Springer-Verlag, Berlin, Heidelberg, New-York, 1992.

Time-domain analysis of thin-wire loaded antennas using integral equations

M. Fernández Pantoja, (*) A. Rubio Bretones and R. Gómez Martín (**)
(*) Dpto. Electrónica. Universidad de Jaén, 23700 Linares (Jaén), Spain. (mariof@ujaen.es)
(**) Departamento de Física Aplicada, Facultad de Ciencias, Universidad de Granada, 18071, Granada, Spain. E-mail: arubio@goliat.ugr.es .

Abstract

A simple and efficient way to analyze the transient response of thin-wire antennas with arbitrarily connected passive linear elements is described. The method can be easily implemented in any existing code based on the solution, using a marching-on-in-time procedure, of the time-domain electric field integral equation for thin wires. Two examples of antennas designed using reactive loads are analyzed and the results compared with those obtained using the NEC code.

1. Introduction

It is well known that the broadband characteristics of thin-wire antennas can be governed by using continuous or discrete passive linear loadings, i.e. capacitors, inductances and/or resistances [1] -[3] . The transient analysis of the behavior of these loaded antennas might involve either frequency-domain analysis coupled with Fourier inversion or the application of direct time-domain techniques. The latter offers computational advantages when the antennas are used for short pulse radiation, and moreover, usually facilitates the understanding of the electromagnetic phenomena involved [4] ,[5] .

Among time-domain techniques, the Finite Difference Time Domain Method (FDTD), which is based on the direct solution of the time domain Maxwell's curl equations, is widely used due to its capability of dealing with complex geometries with arbitrary electrical properties [6] . However, the application of the FDTD to curved or arbitrarily oriented straight thin wires, even when they are not loaded, presents certain difficulties [7] ,[8] . On the other hand the time-domain electric field integral equation (TD-EFIE) solution using the method of moments in the time domain (MoM-TD) is well-suited for the study of thin wires embedded in a homogeneous environment [9] ,[10] and can also be used, via a hybrid technique [11] that combines the FDTD and MoM-TD methods, for analyzing complex geometries comprising thin wires in front of arbitrary inhomogeneous dielectric structures.

In the following we describe a simple method that allows us, with a straightforward and computationally efficient modification, to extend any code based on the solution of the TD-EFIE for perfect electric conducting thin wires, to analyze the transient response of wires with capacitive,

inductive and resistive loading, connected either in series or in parallel.

2. Time domain analysis of loaded antennas

The TD-EFIE for the case of a perfect electric conducting thin wire, derived by enforcing the boundary condition on the tangential electric field over the surface of the wire, is given by [4]

$$\hat{\mathbf{s}} \cdot \boldsymbol{E}^i(s,t) = \frac{1}{4\pi\varepsilon_0} \int_{\Gamma(s')} \left[\frac{\hat{\mathbf{s}} \cdot \hat{\mathbf{s}}'}{c^2 R} \frac{\partial}{\partial t'} I(s',t') + \frac{\hat{\mathbf{s}} \cdot \boldsymbol{R}}{cR^2} \frac{\partial}{\partial s'} I(s',t') - \frac{\hat{\mathbf{s}} \cdot \boldsymbol{R}}{R^3} q(s',t') \right] ds' \tag{1}$$

where: $\hat{\mathbf{s}}$ and $\hat{\mathbf{s}}'$ are tangent vectors to the wire axis of contour $\Gamma(s')$ at positions $s(\mathbf{r}) = s$ and $s(\mathbf{r}') = s'$; $I(s',t')$ and $q(s',t')$ are the unknown current and linear charge distribution at source point s' at retarded time $t' = t - R/c$ with $R = |\mathbf{r} - \mathbf{r}'|$; $\boldsymbol{E}^i(s,t)$ is the field applied to the observation point. The charge $q(s',t')$ can be expressed in terms of $I(s',t)$ by means of the equation of continuity.

The basis for solving (1) using the matching-point form of the MoM-TD, is the following: first, the wire length is approximated by N_S straight segments of length Δs and time is divided into N_T temporal intervals of duration Δt. Then, the current $I(s',t')$ is expanded into an appropriate set of spatial and temporal basis functions. The resulting equation is enforced at the space-time intervals by taking its inner product with a set of spatial and temporal weighting functions [4] , [9] . In general, this transforms (1) into a matrix equation, for each time step, of the form

$$\tilde{\boldsymbol{E}}_j^s + \tilde{\boldsymbol{E}}_j^i = \tilde{\boldsymbol{Z}}\, \tilde{\boldsymbol{I}}_j; \qquad j = 1, ..., N_T \tag{2}$$

where $\tilde{\boldsymbol{I}}_j$ is a vector whose N_S elements are the unknown coefficients of the expansion of $I(s',t')$ in terms of the chosen spatial basis functions at time t_j. The N_S elements of the column vector $\tilde{\boldsymbol{E}}_j^i$ are the tangential electric fields applied to the observation points on the wire, and $\tilde{\boldsymbol{E}}_j^s$ are the tangential electric fields scattered at the observation points and time t_j, by currents at previous times. Matrix $\tilde{\boldsymbol{Z}}$ is a matrix of interaction whose elements are time independent depending only on the geometry of the structure. From (2), $\tilde{\boldsymbol{I}}_j$ can be calculated, at each time step t_j, in terms of previously computed currents, by marching on in time.

As has been pointed out in [4] , the effect of passive loads connected in series along the wire can be easily included in (2) by just adding to its left hand side the unit length voltage drop, E_{load}, caused by the passive loads in opposition to the applied field.

$$E_{load}(s,t) = I(s,t)R_l(s) + L_l(s)\frac{\partial}{\partial t} I(s,t) + \frac{1}{C_l(s)} \int_{-\infty}^{t} I(s,\tau) d\tau \tag{3}$$

where $R_l(s)$, $L_l(s)$ and $C_l(s)$ are the values of the resistance, inductance and capacitance per unit length respectively, located at the observation point s. Expanding $I(s',t')$ in (3) as described above allows the evaluation of the derivative of the current and its integral in terms of the coefficients of the current expansion. A subsequent application of the point matching form of

the MoM leads to a matrix equation of the form (2) where the effect of the resistive loading is included in matrix $\tilde{\boldsymbol{Z}}$ [12] and the reactive loading in $\tilde{\boldsymbol{Z}}$ and in $\tilde{\boldsymbol{E}}^s_j$. Nevertheless, the extension of (3) to the case where the passive loads are connected in parallel is much more complicated because additional unknowns, corresponding to the current through each branch, are necessary.

To overcome this, we describe a simple technique that allows us, without introducing further unknowns, to analyze passive loads connected either in series or in parallel. The technique consists of replacing, at each time step, the connection of loads in a specific segment of length Δs, by an equivalent configuration formed by a resistor in series with a source voltage. To this aim, we start with the expressions of the voltage drop V^C_{j+1} across a segment of length Δs loaded with a capacitor, C, and the current I^L_{j+1} through a segment of the same length loaded with an inductance, L. At the time step $j+1$ they are expressed by:

$$\begin{aligned} V^C_{j+1} &= V^C_j + \frac{1}{C}\int_{t_j}^{t_{j+1}} I_C(\tau)d\tau \\ I^L_{j+1} &= I^L_j + \frac{1}{L}\int_{t_j}^{t_{j+1}} V_L(\tau)d\tau \end{aligned} \tag{4}$$

With the use of a trapezoidal rule to evaluate the integrals, the voltage through the capacitor is approximated by

$$V^C_{j+1} = \frac{\Delta t}{2C} I^C_{j+1} + (V^C_j + \frac{\Delta t}{2C} I^C_j) \tag{5}$$

and through the inductance by

$$V^L_{j+1} = \frac{2L}{\Delta t} I^L_{j+1} - (V^L_j + \frac{2L}{\Delta t} I^L_j) \tag{6}$$

where $\Delta t = t_{j+1} - t_j$ is the time step that is assumed to be constant.

Expression (5) illustrates that, at time step $j+1$, a capacitor can be treated as a resistance, $(\Delta t/2C)$, in series with a voltage source, $V^C_j + (\Delta t/2C) I^C_j$. Analogously, expression (6) shows that an inductor can be treated as a resistance, $(2L/\Delta t)$, in series with a voltage source, $-(V^L_j + (2L/\Delta t) I^L_j)$. This equivalence reduces any connection between passive elements, either in series or in parallel, to an equivalent resistance in series with an equivalent voltage source. In consequence the EFIE can be rewritten as

$$\begin{aligned} \hat{\mathbf{s}} \cdot \boldsymbol{E}^i(s,t) &= \frac{1}{4\pi\varepsilon_0}\int_{\Gamma(s')} \left[\frac{\hat{\mathbf{s}}\cdot\hat{\mathbf{s}}'}{c^2 R}\frac{\partial}{\partial t'} I(s',t') + \frac{\hat{\mathbf{s}}\cdot\boldsymbol{R}}{cR^2}\frac{\partial}{\partial s'} I(s',t') - \frac{\hat{\mathbf{s}}\cdot\boldsymbol{R}}{R^3} q(s',t') \right] ds' \\ &+ \sum_{n=1}^{loads} \frac{1}{\Delta s_n} \left(I(s,t) R^e_n + V^{e,n}(t) \right) \end{aligned} \tag{7}$$

where the sum on the left hand side runs on loaded segments and where R^e_n and $V^{e,n}$ are, respectively, the equivalent resistance and source voltage at the loaded segment s_n. By using the MoM-TD technique, equation (7) is transformed into the matrix equation

$$\tilde{\boldsymbol{E}}^s_j + \tilde{\boldsymbol{E}}^i_j = (\tilde{\boldsymbol{Z}} + \tilde{\boldsymbol{Z}}^L)\tilde{\boldsymbol{I}}_j; \qquad j = 1, ..., N_T \tag{8}$$

where $\tilde{\boldsymbol{Z}}^L$ is a diagonal matrix that includes the effect of the equivalent loads R^e along the antenna and does not depend on time. The contribution of the equivalent sources $V^e(t)$ along the antenna is included in $\tilde{\boldsymbol{E}}^s_j$. To calculate the equivalent sources at any segment and time step, it is only necessary to store the value of the current and voltage at that segment at the previous time step. Therefore, the method neither increases computational time nor requires the allocation of significant extra memory.

As an example, in the case where the passive RLC loads are connected in series, R^e and V^e_{j+1} become

$$\begin{aligned} R^e &= R + \frac{\Delta t}{2C} + \frac{2L}{\Delta t} \\ V^e_{j+1} &= V^C_j - V^L_j + (\frac{\Delta t}{2C} - \frac{2L}{\Delta t}) I_j \end{aligned} \tag{9}$$

and for a parallel connection of the same elements

$$\begin{aligned} R^e &= \frac{2\Delta t}{4C + \frac{(\Delta t)^2}{L} + \frac{2\Delta t}{R}} \\ V^e_{j+1} &= \left[I^C_j - I^L_j + (\frac{2C}{\Delta t} - \frac{\Delta t}{2L}) V^e_j \right] \frac{2\Delta t}{4C + \frac{(\Delta t)^2}{L} + \frac{2\Delta t}{R}} \end{aligned} \tag{10}$$

Any other combination of loads on a segment can be studied as the series combination of the two latter examples.

3. Numerical results

This section presents two examples of thin-wire loaded monopole antennas perpendicularly attached to a perfectly conducting ground plane with the feed point located at the junction with the ground plane. In both examples the antenna is excited by the gaussian pulse

$$V^i(t) = e^{-g^2(t-t_m)^2} \tag{11}$$

where $g = 5{\cdot}10^9\ s^{-1}$ and $t_m = 2.146/g\ s$ and the transient response is calculated including the described technique in the computer program DOTIG1 [9] -[10] . This program solves the TD-EFIE using the point-matching form of the moment method with the match points situated at the centres of the space-time intervals. The spatial and temporal variation of the current is represented by a two-dimensional Lagrangian interpolation of order two in each dimension (space and time) as the basis function.

The first example is a monopole antenna of length 16.3 cm and radius 1.5 mm. The monopole is loaded with five reactive elements as shown in the inset of Figure 1. The loads are one inductance $L = 1.257\ 10^{-8} H$, located at the feed point, and four capacitances $C_1 = 2.122\ 10^{-12} F$, $C_2 = 1.273\ 10^{-12} F$, and $C_3 = C_4 = 6.366\ 10^{-12} F$, which are located at 32.1 mm, 62.3 mm, 90.5 mm and 140.9 mm respectively from the feed point. Figure 1 shows the time evolution of the current at the

feed point. The real and imaginary parts of the input impedance of the antenna versus frequency calculated via Fourier transform using the method described and the Numerical Electromagnetic Code (NEC) [13] are shown in Figure 2. It can be seen that the two results are practically identical.

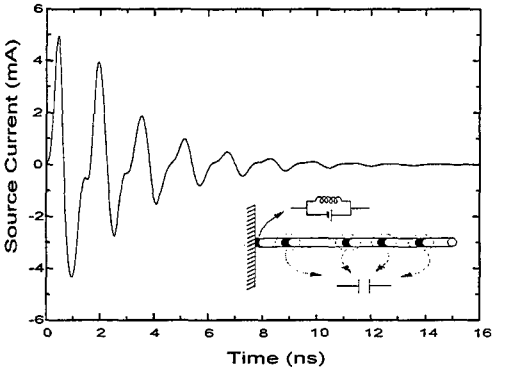


Figure 1. Time evolution of the current at the feed point. Inset, geometry of the series loaded monopole antenna. (Example 1)

As a second example a dual-band monopole antenna for cellular phones has been designed with operating frequency bands 824-894 MHz and 1.85-1.99 GHz. The length of the monopole is 10 cm and its radius 1.5 mm. The antenna is loaded with a resonant LC circuit located 4 cm from the feed point as shown in the inset of Figure 3. The values of the inductance and capacitance are L=1.365 $10^{-7}H$ and C=5.14 $10^{-14}F$ respectively. Figure 3 shows the evolution of the current at the feed point versus time, and Figures 4a and 4b the conductance and susceptance versus frequency, calculated using NEC and the proposed method. Again, there is an excellent agreement between the two sets of results.

4. Conclusions

This paper presents a simple and efficient method to extend any code based on the solution of the time domain electric field integral equation for perfectly conducting thin wires to include arbitrarily connected passive linear elements. The method does not require a significant increase

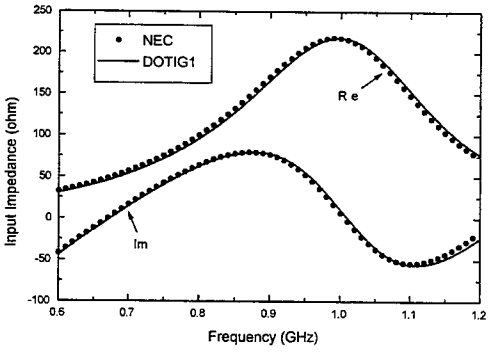


Figure 2. Real and imaginary parts of the input impedance of the antenna versus frequency. (Example 1)

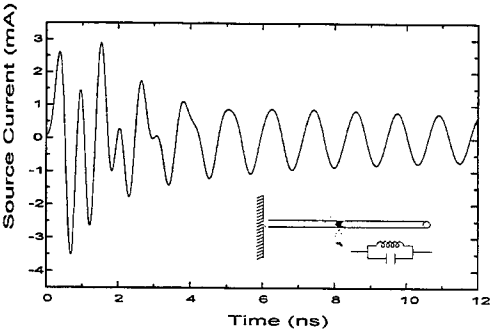


Figure 3. Time evolution of the current at the feed point. Inset, geometry of the dual-band monopole antenna. (Example 2)

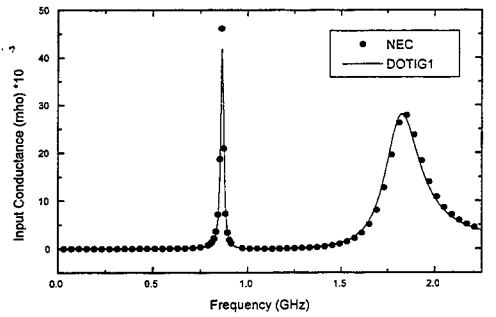


Figure 4a. Conductance versus frequency. (Example 2)

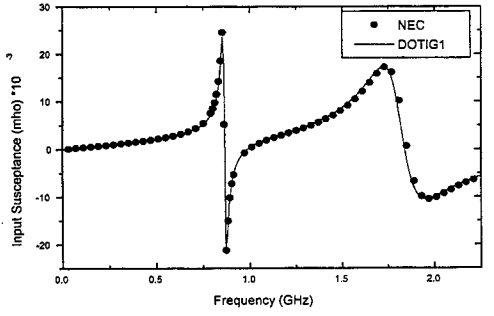


Figure 4b. Susceptance versus frequency. (Example 2)

in computational resources. For the sake of example two monopole antennas loaded in series and in parallel are analyzed. The results are found to coincide very well with those obtained using the NEC code.

Acknowledgments

Financial support was obtained from "Comisión Interministerial de Ciencia y Tecnología (CICYT)" through project TIC98-1037-C03-01 which is gratefully acknowledged.

References

[1] POPOVIC, B.D., DRAGOVIC, M.B. and DJORDJEVIC, A.R.: 'Analysis and synthesis of wire antennas' (Research Studies Press, Chichester, 1982)

[2] KANDA, M.: 'Time-domain sensors and radiators' in 'Time-domain measurements in electromagnetics' (Edited by E. Miller) (Van Nostrand Reinhold, New York, 1986)

[3] MONTOYA, T.P. and SMITH, G.S.: 'A study of pulse radiation from several broad-band loaded monopoles', *IEEE Trans. Antennas Propagat.*, 1996, **44** (8) pp. 1172-1182

[4] MILLER, E.K. and LANDT, J.A.: 'Direct time-domain techniques for transient radiation and scattering from wires', *Proc. IEEE,* 1980, **68** pp. 1396-1423

[5] MILLER, E.K.: 'Time-domain modeling in electromagnetics', *Journal of Electromagnetics Waves and Applications,* 1994, **8** (9/10) pp. 1125-1172

[6] TAFLOVE, A.: 'Computational electrodynamics' (Artech House, Boston, 1995)

[7] CANGELLARIS, C. and WRIGHT, D.B.: 'Analysis of the numerical error caused by the stair-stepped approximation in FDTD simulations', *IEEE Trans. Antennas Propagat.*, 1991, **39** (10) pp. 1518-1525

[8] MONTOYA, T.P. and SMITH, G.S.: 'Modeling staircase wires using FDTD method'. IEEE Antennas and Propagation International Symposium, July 1999, Orlando, USA, pp. 180-183

[9] RUBIO BRETONES, A., GÓMEZ MARTÍN, R. and SALINAS, A.: 'DOTIG1, a time domain numerical code for the study of the interaction of electromagnetic pulses with thin wire structures', *The International Journal for Computation and Mathematics in Electrical and in Electrical and Electronic Engineering (COMPEL)*, 1989, **8**, pp 39-61.

[10] GÓMEZ MARTÍN, R., SALINAS, A. and RUBIO BRETONES, A.: 'Time-domain integral equations methods for transient analysis', 1992, *IEEE Antennas and Propagation Magazine*, **34**, pp 15-23.

[11] RUBIO BRETONES, A., MITTRA, R. and GÓMEZ MARTÍN, R.: 'A hybrid technique combining the method of moments in the time domain and FDTD', *IEEE Microwave and Guided Wave Letters*, 1998, **8** (8) pp. 281-283

[12] SÁNCHEZ GARCÍA, I., RUBIO BRETONES, A. and GÓMEZ MARTÍN, R.: 'Pulse receiving characteristics of resistively loaded V antennas', *IEEE Electromagnetic Compatibility*, 1998, **40** (2) pp. 174-175

[13] BURKE, G.J. and POGGIO, A.J.: 'Numerical electromagnetic code (NEC)- method of moments'. Technical Documents 11, Naval Ocean Systems Center, San Diego, January 1981

Haar MRTD Wave Propagation Through Isotropic Plasmas

Ismael Barba*, Jose Represa*, Masafumi Fujii, Wolfgang J.R. Hoefer****

*Dpto. Electricidad y Electrónica.
Univ. Valladolid
47011 Valladolid – SPAIN
Tel: +34 983 423224
Fax: +34 983 423217
E-Mail: ibarba@ee.uva.es, jrepresa@ee.uva.es

**Department of Electrical and Computer Engineering
Univ. of Victoria. P.O. Box 3055
Victoria B.C.
CANADA – V8W 3P6
Tel: +1 250 721 6025
Fax: +1 250 721 6230
E-Mail: fujii@ece.uvic.ca, whoefer@ece.uvic.ca

Abstract. **– A Multi-Resolution Time-Domain (MRTD) technique based on Haar-wavelets has been applied to model the propagation of waves in an absorbing isotropic plasma. To validate this technique, we have computed the transmission coefficient of a plane wave through the plasma.**

I INTRODUCTION

Multi-resolution time-domain (MRTD) techniques have recently been used to solve electromagnetic problems, using both Battle-Lemarie [1] and Haar [2] wavelets.

In this paper, we have applied a multi-resolution technique based on Haar wavelets to model the propagation of waves in an absorbing isotropic plasma. To this end, we have discretized the convolution equation governing its behavior and solved it with a recursive technique [3]. We have compared the results with those obtained using a similar TLM formulation [4], and with theoretical results.

II FORMULATION

II.a. 2-D Basis Functions and Algorithm.

The Haar wavelet formulation has the advantage over other wavelet formulations that the resulting equations of the algorithm are similar to the traditional FDTD equations, with the difference that in the multi-resolution method the equations are computed independently for each basis function. We can expand each field component in a two-dimensional combination of the Haar scaling (ϕ) and wavelet (ψ) functions [5]:

$$E_y(\bar{r},t)=\sum_{i=0}^{I}\sum_{j=0}^{J}\sum_{n=0}^{N}h_n(t)\cdot\begin{Bmatrix} {}^{y}_{n}E^{\phi\phi}_{i,k}\cdot\phi_i(x)\phi_k(z) \\ +{}^{y}_{n}E^{\phi\psi}_{i,k}\cdot\phi_i(x)\psi_k(z) \\ +{}^{y}_{n}E^{\psi\phi}_{i,k}\cdot\psi_i(x)\phi_k(z) \\ +{}^{y}_{n}E^{\psi\psi}_{i,k}\cdot\psi_i(x)\psi_k(z)\end{Bmatrix} \quad (1)$$

The notation is that given in [6] for two dimensions of space. We can expand the remaining field components (H_x and H_z, in a TE mode) in orthonormal basis functions. We can substitute each component in Maxwell's equations, obtaining, as mentioned above, the same equations as the traditional FDTD (Yee's scheme), formulated independently for each basis function.

II.b. Discretization of the Causality Relationship in Linear Dispersive Media

In time domain and for a linear dispersive medium, the relationship between the displacement (**D**) and the electrical field (**E**) vectors can be expressed as follows [7]:

$$\mathbf{D}(t)=\varepsilon_\infty\varepsilon_0\mathbf{E}(t)+\varepsilon_0\chi(t)*\mathbf{E}(t) \quad (2)$$

where ε_0 is the permittivity of the vacuum, ε_∞ is the permittivity of the medium at very high frequencies, $\chi(t)$ is the time-domain electric susceptibility of the same medium [8], and * represents a convolution product. We can discretize this equation in our FDTD/MRTD mesh to obtain [3]:

$${}_{k}D=\varepsilon_0\left\{\varepsilon_{\infty}\cdot{}_{k}E+\sum_{m=0}^{k-1}\chi_m\frac{{}_{k-m}E+{}_{k-m-1}E}{2}\right\} \quad (3)$$

for each value of the spatial indices. k is the temporal index, and χ_m
Electric Susceptibility (GES)" and is defined, according to Luebbers *et al.* [9], as:

$$\chi_n=\int_{n\Delta t}^{(n+1)\Delta t}\chi(t')dt' \quad (4)$$

Thus, if we discretize Maxwell's curl equation:

$$\frac{\partial D_y}{\partial t}=\frac{\partial H_z}{\partial z}-\frac{\partial H_z}{\partial x}-\sigma E_y \quad (5)$$

for a medium with a conductivity σ, and we substitute Eq. (3) in the result, we get the equation describing the FDTD algorithm:

$$
{}_{n+1}E^{y}_{i,k} = \left\{ \begin{array}{l} \dfrac{2\varepsilon_\infty - \chi_1 - \dfrac{\sigma\Delta t}{\varepsilon_0}}{2\varepsilon_\infty + \chi_0 + \dfrac{\sigma\Delta t}{\varepsilon_0}}\,{}_{n}E^{y}_{i,k} \\ -\dfrac{1}{2\varepsilon_\infty + \chi_0 + \dfrac{\sigma\Delta t}{\varepsilon_0}} \sum_{m=1}^{n-1} {}_{n-m}E^{y}_{i,k}\left(\chi_{m+1} - \chi_{m-1}\right) \\ +\dfrac{2\Delta t}{\Delta z\varepsilon_0\left(2\varepsilon_\infty + \chi_0 + \dfrac{\sigma\Delta t}{\varepsilon_0}\right)}\left[\begin{array}{l} {}_{n+1/2}H^{x}_{i,k+1/2} \\ -{}_{n+1/2}H^{x}_{i,k-1/2} \end{array} \right] \\ -\dfrac{2\Delta t}{\Delta x\varepsilon_0\left(2\varepsilon_\infty + \chi_0 + \dfrac{\sigma\Delta t}{\varepsilon_0}\right)}\left[\begin{array}{l} {}_{n+1/2}H^{z}_{i+1/2,k} \\ -{}_{n+1/2}H^{z}_{i-1/2,k} \end{array} \right] \end{array} \right\} \qquad (6)
$$

We must perform this algorithm for each combination of scale and wavelet functions as shown in Eq. (1).

II.c. Plasma Modeling.

Under certain conditions [8], the frequency domain susceptibility of an isotropic plasma is given by:

$$
\chi(\omega) = \frac{\omega_p^2}{\omega(j\omega_c - \omega)} \qquad (7)
$$

where ω_c is known as "collision frequency", and ω_p as "plasma frequency". As it is explained in [9], an expression for the time-domain susceptibility can be found that is valid for every frequency, with the exception of ω=0, where the relationship is not causal:

$$
\chi(t) = \left(\frac{\omega_p}{\omega_c}\right)^2 \left(1 - e^{-\omega_c t}\right) \qquad t > 0 \qquad (8)
$$

if we apply Eq. 4 to this expression, we obtain a GES:

$$
\chi_m = \frac{\omega_p^2}{\omega_c}\Delta t - \left(\frac{\omega_p}{\omega_c}\right)^2 \left(1 - e^{-\omega_c \Delta t}\right) e^{-m\omega_c \Delta t} \qquad (9)
$$

We observe a constant term in the equation, but, as the GES is included in the MRTD algorithm by means of a substraction (χ_{m+1}-χ_{m-1}), this term vanishes, and the summation can be computed in a recursive way:

$$(\chi_{m+1} - \chi_{m-1}) = e^{-\omega_c \Delta t}(\chi_m - \chi_{m-2}) \tag{10}$$

III RESULTS

We have simulated the propagation of a plane wave through a plasma whose characteristic frequencies are ω_c=ω_p=1000 GHz. The computational domain is 10 x 5000 square cells, with Δx=0.42 μm. The sidewalls are magnetic (in order to support the propagation of a plane wave), and the end walls are placed far enough to avoid the reflection appearing in our simulation. The excitation is distributed between space steps 2080Δx and 2090Δx of the computational domain. The transmission coefficient between space positions (2110Δx -2120Δx) and (2210Δx -2220Δx) has been calculated, and the results are shown in Figure 1.

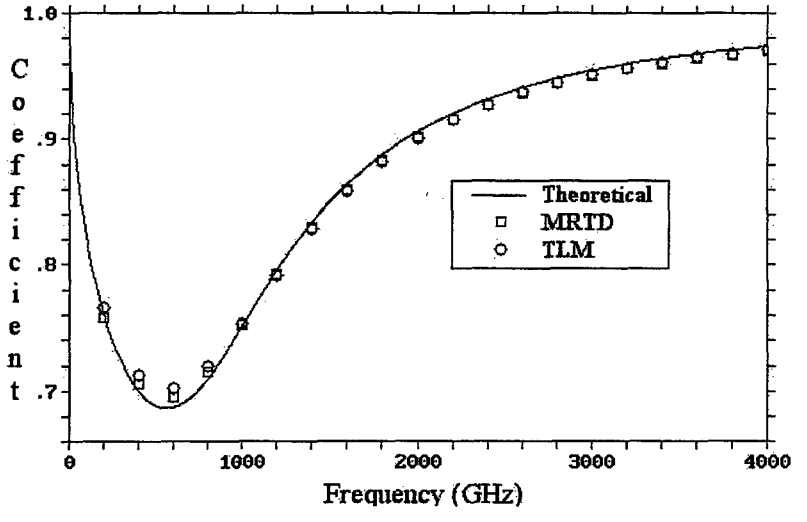


Figure 1. Transmission coefficient through 0.42 mm of plasma: comparison between data obtained with MRTD and TLM.

IV CONCLUSION.

A MRTD technique for the simulation of the propagation of waves in absorbing isotropic plasmas has been developed. Haar wavelets have been employed.

Results have been compared with those obtained with our own TLM modified algorithm [4] and with exact theoretical treatment. We observe a good agreement among them (the maximum error being around 1%), a better precision of the MRTD data being obtained, especially at low frequencies. The MRTD technique is particularly advantageous if wavelets are adaptively employed in situations where the nonuniformity of the fields varies dynamically, such as in the propagation of narrow pulses through a plasma.

V REFERENCES.

[1] M. Krumpholz and L.T.B. Katehi, "MRTD: New time-domain schemes based on multiresolution analysis", *IEEE Trans. Microwave Theory Tech.*, vol. 44, no. 4 pp. 555-571, Apr. 1996.

[2] M. Fujii and W. J.R. Hoefer, "A 3D Haar-Wavelet-Based Multiresolution Analysis Similar to the FDTD Method –Derivation and Application-", *IEEE Trans. Microwave Theory Tech.* Vol 46, No. 12, Dec. 1998.

[3] R. Siushansian and J. LoVetri, "A Comparison of Numerical techniques for Modeling Electromagnetic Dispersive Media", *IEEE Microwave and Guided Wave Letters*, vol. 5, no. 12, Dec. 1995.

[4] J. Represa, A.C.L. Cabeceira and I. Barba, "The Use of Sources for TLM Modeling of Complex Materials", *13th Annual review of progress in Applied Computational Electromagnetics. ACES 97*, pp 638-648. Monterey (CA), 1997.

[5] I. Daubechies, *Ten lectures on wavelets*, SIAM Rev, Philadelphia, PA, 1992.

[6] I. Barba, J. Represa, M. Fujii, W. J.R. Hoefer, "Multiresolution Model of Electromagnetic Wave Propagation in Dispersive Materials", *IEEE MTT Symposium.* Anaheim, CA, 1999.

[7] J.D. Jackson, *Classical Electrodynamics*, Wiley, New York 1962.

[8] L.D. Landau et al., Electrodynamics of Continuous Media. Elmsford NY: Pergamon, 1984.

[9] R. J. Luebbers, F. Hunsberger, K. S. Kunz, "A Frequency-Dependent Finite Difference Time-Domain Formulation for Transient Propagation in Plasma", *IEEE Trans. APP.*, Vol. 39, No. 1, Jan. 1991.

Time-Domain Scattering from Arbitrarily Shaped Metallic Shelters with Apertures: Numerical and Experimental Analysis

Giuliano Manara and Agostino Monorchio

Department of Information Engineering, University of Pisa, Pisa, Italy
via Diotisalvi 2, I-56126 Pisa, Italy. Tel. +39-050-568511, Fax. +39-050-568522
E-mail: manara@iet.unipi.it, mono@iet.unipi.it

Abstract. Numerical results obtained by the application of a stable marching-on-in-time solution scheme of the Electric Field Integral Equation (EFIE) are compared with experimental data relevant to the case of scattering from continuous metallic shelters with apertures. The experiments have been conducted in an Electromagnetic Pulse (EMP) hardware simulator, reproducing the plane wave illumination condition. The limits of applicability of the EFIE to the case of the transmission through apertures in perfectly electric conducting (PEC) bodies are discussed.

1. INTRODUCTION

Numerical techniques directly operating in time domain (TD), have recently received considerable attention in computational electromagnetics. Indeed, the availability of time-domain computer codes is of remarkable importance in a variety of applications in the field of electromagnetic compatibility, where the interest is often extended to wide frequency bands.

Among the algorithms proposed in the literature for electromagnetic scattering analyses in TD, we mention the marching-on-in-time formulation of the Method of Moments (MoM). A shortcoming of this algorithm is its intrinsic numerical instability: the calculated induced current and field distributions typically exhibit spurious fluctuations of growing amplitude and eventually diverge. These instabilities are introduced at the system discretization stage, *i.e.*, in the conversion of the Electric Field Integral Equation (EFIE) to a discrete space-time model. Similar problems arise in the application of the magnetic and combined field integral equations. In particular, the achievement of a stable numerical procedure strongly depends on how the original problem is discretized, both in space (size and shape of the spatial basis functions) and time (time step and shape of basis functions with respect to time) [1].

The limits of applicability of a numerically stable MoM solution of the Electric Field Integral Equation in Time Domain (EFIE-TD) are investigated in this paper with reference to the case of continuous structures realized by joining perfectly electric conducting (PEC) plates, in the presence of apertures in their walls. The case of PEC closed bodies has been already discussed in [2]. Here, simulation data are compared with results obtained from experiments performed on a set of canonical closed bodies with apertures. The experiments have been carried out in an open-site Electromagnetic Pulse (EMP) hardware simulator, reproducing plane wave illumination conditions. The induced current densities on the exterior surface of the metallic bodies have been measured by broad-band sensors, which are coupled to the magnetic fields tangential to the above surfaces.

Moreover, the electric field penetrating the interior region of a metallic shelter through an aperture has been measured by employing suitable field sensors. The measured current densities and field amplitudes have been therefore processed in order to eliminate the effects introduced by the measuring instruments chain and those of air humidity that strongly affects the results. It is worth pointing out that, due to the large time constants characterizing the measurement setup, comparisons between experimental and numerical data can be performed only if the employed method is stable also at late times; in our case this long term stability has been obtained by the analysis developed in [3].

2. A STABLE MOM-TD FORMULATION

A TD version of the EFIE suitable for solving the scattering problem of interest is described in this section and solved through a MoM approach. Let S be the exterior surface of a perfectly conducting body, which can be either closed or open, illuminated by an arbitrarily polarized plane wave; $\bar{E}^i$ denotes the incident electric field and $\bar{J}$ the surface current density induced on S.

Since the body is a perfect electric conductor, the tangential component of the total electric field on S must vanish. This leads to an integro-differential vector equation in the unknown induced current density $\bar{J}$. The forcing term of this equation is given by the tangential component of the incident electric field $\bar{E}^i_{\text{tang}}$:

$$\frac{\partial}{\partial t}\left[\frac{\mu}{4\pi}\int_S \frac{\bar{J}(\bar{r}',t-R/c)}{R}\,dS\right]-\nabla\left[\frac{1}{4\pi\varepsilon}\int_S \frac{1}{R}\int_{-\infty}^{t-R/c}\nabla\cdot\bar{J}(\bar{r}',\tau)\,d\tau\,dS\right]=\bar{E}^i_{\text{tang}}. \qquad (1)$$

In (1), $R=|\bar{r}-\bar{r}'|$ represents the distance between an arbitrarily located observation point $\bar{r}$ and a source point $\bar{r}'$ on S; $t-R/c$ is the retarded time and μ, ε are the permeability and permittivity of the medium surrounding the scatterer, respectively. In order to obtain a numerical solution of equation (1), a suitable expansion of the unknown current $\bar{J}(\bar{r},t)$ is employed. In particular, the spatial variation of surface currents induced on the body can be accurately approximated by discretizing its surface into N_T triangular patches over which a set of basis functions can be defined. As far as the temporal variation is concerned, a time discretization scheme can be assumed, provided that the time step ΔT is properly chosen. Hence, the surface current distribution can be numerically approximated as

$$\bar{J}(\bar{r},t)=\sum_{j=-\infty}^{+\infty}\sum_{n=0}^{N_e} I_{n,j}\,T_j(t)\,\bar{f}_n(\bar{r}), \qquad (2)$$

where N_e is the number of edges of the triangles which model the scatterer, excluding the boundary edges if S is open. Each unknown coefficient $I_{n,j}$ represents the value of the component of the surface current normal to the n-th edge at the instant $j\Delta T$.

The basis functions $\bar{f}_n(\bar{r})$ that have been utilized are known as "roof-top" functions [4]; they are defined over each triangle pair that discretizes the body surface (triangular patch modeling). Basis functions $T_j(t)$ with a triangular shape have been commonly used to discretize the temporal

evolution [1]. However, in order to guarantee the algorithm stability according to the criteria defined in the next section, different interpolating functions have been employed here. Specifically, pulses ensuring quadratic approximation over temporal sub-domains have been used. In particular, the second order polynomial used to describe time evolution over each sub-domain is an arc of the parabola passing through the samples at: $t=(j-1)\Delta T$, $t=j\Delta T$, and $t=(j+1)\Delta T$. The result is a continuous piece-wise quadratic function, with a piece-wise linear derivative, which is discontinuous at the integer multiples of ΔT, except when the function to be interpolated is exactly linear or quadratic.

From (1) and (2), adopting a testing procedure as that used in the frequency domain approach [4], the following set of equations is obtained at the instant $t_j = j\Delta T$:

$$\frac{l_n}{2}(\bar{\rho}_n^{c+}+\bar{\rho}_n^{c-})\cdot\frac{\partial\,\bar{A}(\bar{r}_n^*,t_j)}{\partial\,t}+l_n\left[\phi(\bar{r}_n^{c+},t_j)-\phi(\bar{r}_n^{c-},t_j)\right]= \\ =\frac{l_n}{2}(\bar{\rho}_n^{c+}+\bar{\rho}_n^{c-})\cdot\bar{E}^i_{tang}(\bar{r}_n^*,t_j)\ ,\ n=1,2,...,N_e. \tag{3}$$

In the derivation of (3), testing functions coincide with basis functions (Galerkin's method). Moreover, the vector potential $\bar{A}$ is evaluated at the center $\bar{r}_n^*$ of each edge, while the scalar potential ϕ is calculated at the centroid $\bar{r}_n^{c\pm}$ of each triangle $\Gamma_n^{\pm}$. Finally, $\bar{\rho}_n^{c\pm}$ denotes the same centroid with respect to the free vertices of the pertinent triangles, while l_n is the length of the edge.

For obtaining a numerical implementation of (3), we substitute explicit free-space expressions in TD for the vector and the scalar potential and approximate the surface current distribution as in (2). In particular, the use of the quadratic interpolating functions enables us to evaluate in a closed form the derivatives with respect to time in (3). Finally, a linear system of equations is obtained which relates the unknown coefficients $I_{n,j}$ to the incident electric field. It can be expressed in matrix form as follows:

$$\underline{I}(j+1)=\sum_{k=0}^{j}\underline{\underline{M}}^{-1}\cdot\underline{\underline{F}}_{j-k}\cdot\underline{I}(k)+\underline{\underline{M}}^{-1}\cdot\underline{\underline{B}}\cdot\underline{E}^i_{\text{tang}}(j), \tag{4}$$

where $\underline{I}(j)$ is a column vector with N_e elements representing the unknown coefficients at the instant t_j, $\underline{E}^i_{\text{tang}}(j)$ is the vector containing the values of the incident electric field at each edge at the same instant. The matrices $\underline{\underline{M}}$, $\underline{\underline{F}}_{j-k}$ and $\underline{\underline{B}}$ assume values depending upon both geometrical and temporal parameters; however, they do not explicitly depend on time. The first term at the right-hand side of (4) reveals the recursive nature of the system, since the coefficients at a fixed instant of time depend on the values assumed by the same coefficients at previous instants.

A previous analysis presented in [3] revealed the existence of a lower and an upper limit, $\Delta T_{\min}$ and $\Delta T_{\max}$, of the time step ΔT for which system stability is ensured. In particular, the above limits were found to depend on both size and shape of the triangular elements used for space discretization. Both $\Delta T_{\min}$ and $\Delta T_{\max}$ vary with the size of the patches as well with their quality factor [5] according to a simple proportionality law. Furthermore, $\Delta T_{\max}$ was also seen to be affected by the relative positions of the patches. In conclusion, the stability interval strongly

depends on the geometrical discretization of the body. In particular, the more uniform and regular is the patch modeling of the scatterer, the wider is likely to be the set of values of ΔT leading to a stable behavior of the algorithm. Depending on the scatterer and on the particular mesh employed, this interval may sometimes be void so that stability cannot be ensured. This frequently occurs when the body has wedges or tips. However, even if a stability interval does not exist, it is convenient to choose ΔT close to the values $\Delta T_{\min}$ and $\Delta T_{\max}$, in order to delay instability phenomena as much as possible. Further details can be found in [3].

3. Numerical and Experimental Results

The limits of applicability of the EFIE simulation scheme illustrated above in the case of shelters with apertures in their metallic walls are discussed in this section by referring to a set of comparisons between numerical and experimental data. In this case, among the various parameters that might be of interest, we quote the field penetrating the inside the shelters. However, it is well known that accurate results for this class of problems can be accomplished only when defining equivalent magnetic currents at the aperture [6]. This has been confirmed in our experiments performed on a cube with an aperture in one of its walls. In particular, we observed that quite a good agreement exists between simulations and measurements for what concerns the external induced currents as well as the near field external to the body. Nevertheless, the transmitted field inside the objects is not properly evaluated by the EFIE in time domain when the aperture is small.

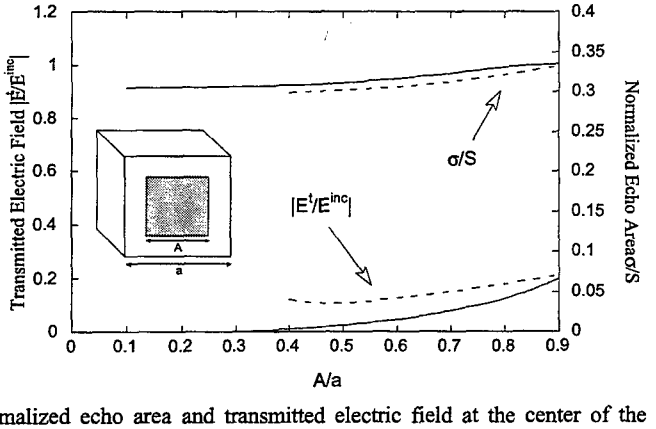


Figure 1. Normalized echo area and transmitted electric field at the center of the box as a function of the aperture dimensions. Continuous line: after [6]; dashed line: MoM-TD simulation.

This aspect has been summarized in Fig. 1, where the normalized echo area σ/S of a metallic cube with an aperture in one of its faces has been calculated and compared with results obtained by a MoM formulation in frequency domain which accounts for the equivalent magnetic currents on the aperture [6]. The operating frequency is chosen so that $a/\lambda=0.16$. As can be seen from the same figure, an overall agreement is present for all the values of the ratio a/A for what concerns the

normalized echo area. Conversely, the EFIE formulation gives very similar results to the MoM formulation with magnetic currents for the transmitted electric field only when the ratio A/a tends to one.

Measurements

The theoretical behavior described above has been confirmed by some experiments conducted in an Electromagnetic Pulse (EMP) hardware simulator, 95 m long, 28 m wide, and with a height of 19 m (Fig. 2).

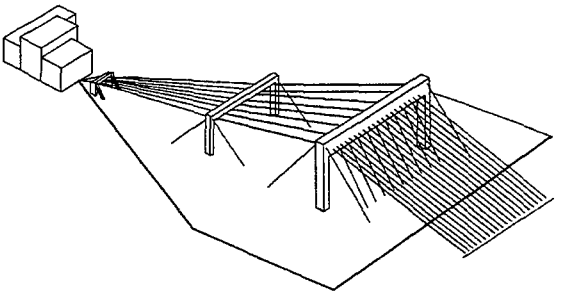


Figure 2. Configuration of the EMP hardware simulator where the experiments have been conducted.

The basis of the simulator is a metallic plane realized by a buried metallic grid while all the structures supporting the aerial lines are made of wood and kevlar to perturb the electromagnetic field distribution as less as possible. The effective test volume is a box with a basis of 10m×10m and a height of 6 m. A specific acquisition technique has been employed in the measurement procedure, which allows us to reconstruct the actual amplitude of the electric field impinging on the scattering object. This procedure relies on the definition and the evaluation of the system transfer function. In this way, the statistical approach is avoided and no averaging of the measurements is needed to compare the predicted and measured results. A detailed description of the instrument chain as well as of the acquisition procedure can be found in [2] and will not be reported here for the sake of brevity. Some apertures of different dimensions have been opened in a conducting cube 1 *m* on a side. In the following, we show two significant cases. In the first case, the top face of the conducting cube has been removed. In the other case, an aperture of dimensions 32 cm × 50 cm has been opened in one of the faces of the cube. In Fig. 2, we show the computed and measured electric field transmitted into the inside of an open cube whose upper face has been removed. The probe was located at a height of 40 cm from the ground and at the same distance from the remaining four walls. As can be seen from the same figure, the agreement between measured and computed results is very good for this case. Similar agreement has been obtained for the induced current densities and the near fields (field probe located close to the body but external to it). The presence of the ground plane in the EMP simulator has been accounted for in the simulations by doubling the dimensions of

the objects with respect to the ground plane, according to the image theorem, since they are actually in electric connection with the ground plane. The open cube has been meshed with 168 elements and the time step was set to $1.53 \cdot 10^{-9}$ sec.

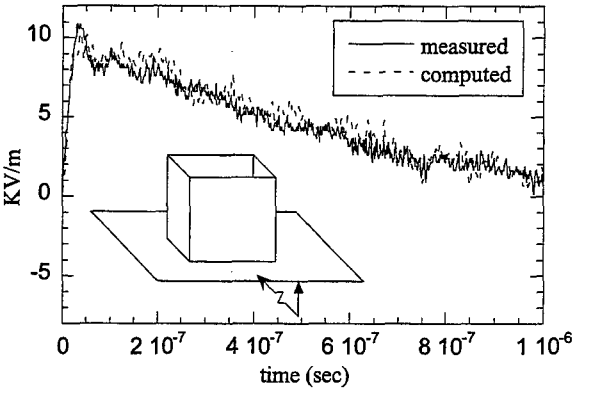


Figure 3. Electric field transmitted into the interior region of an open metallic box. Continuous line: measurements; dashed line: MoM-TD simulation.

In Fig. 3 we show a comparison between theory and experiment for the case of an aperture with smaller dimensions, *i.e.*, 32 cm × 50 cm with the smaller side lying on the edge of the cube. In particular, the induced current density at point A, located at the top face (open face) at a distance of about 20 cm from the left corner of the aperture, is plotted vs. time in the figure. The body has been discretized with 199 elements and the time step was set to $1.4984 \cdot 10^{-9}$ sec. Similar accordance between simulated and measured data has been obtained for the near field in the exterior region of the scattering body. Conversely, the EFIE in TD failed to adequately evaluate the transmitted field inside the body, confirming that a more general formulation involving the magnetic currents has to be used if one is interested in this parameter.

4. CONCLUSIONS

In this paper we addressed the problem of describing the transient scattering from metallic objects. Measurements have been conducted in an EMP hardware simulator and compared with the results obtained by applying a stable formulation of the MoM in time domain, in order to validate the latter numerical technique. A measurement procedure has been determined which allows us to reconstruct the actual amplitude of the electric field impinging on the scattering object avoiding a statistical approach. The agreement between simulated and measured data confirms the accuracy of both the simulation scheme and the measuring procedure. The limits of applicability of the proposed EFIE formulation have been discussed for the case of conducting bodies with apertures. We underline that a crucial point that allowed us to perform this comparative analysis was to obtain late time stability of the numerical procedure. Indeed, this is fundamental for simulating real experiments.

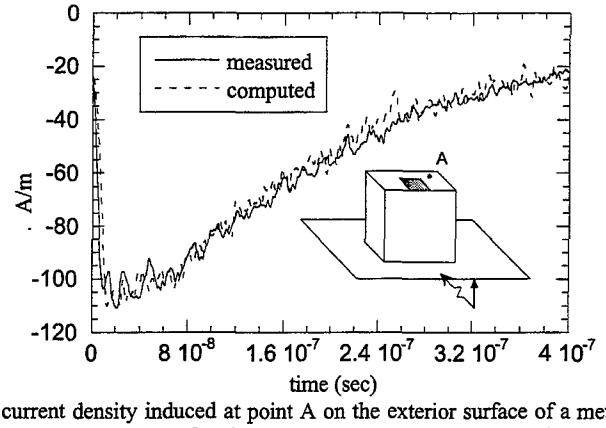


Figure 4. Surface current density induced at point A on the exterior surface of a metallic cube with an aperture on one of its upper. Continuous line: measurements; dashed line: MoM-TD simulation.

ACKNOWLEDGMENTS

The EMP simulator is a facility of C.I.S.A.M (Centro Interforze di Studi ed Applicazioni Militari) of the Italian Ministry of Defense, San Piero a Grado, Pisa. The authors wish to express their gratefulness to the personnel of C.I.S.A.M. for providing the measurements.

REFERENCES

[1] S. M. Rao and D. R. Wilton, "Transient scattering by conducting surfaces of arbitrary shape," *IEEE Trans. Antennas and Propagation*, Vol. 39, No. 1, pp. 56-61, Jan. 1991.

[2] G. Manara and A. Monorchio, "Experimental validation of a stable MoM procedure in time domain," *Proc. of the International Conference on Electromagnetics in Advanced Applications –ICEAA 99*, Torino, Italy, Sept. 13-21 1999, pp. 687-690.

[3] G. Manara, A. Monorchio and R. Reggiannini, "A space-time discretization criterion for a stable time-marching solution of the Electric Field Integral Equation," *IEEE Trans. Antennas and Propagation*, Special Issue on Advanced Numerical Techniques in Electromagnetics, Vol. 45, No. 3, pp. 527-532, March 1997.

[4] S. M. Rao, D. R. Wilton, and A. W. Glisson, "Electromagnetic scattering by surfaces of arbitrary shape," *IEEE Trans. Antennas and Propagation*, Vol. 30, No. 5, pp. 409-419, May 1982.

[5] D. A. Lindholm, "Automatic triangular mesh generation on surfaces of polyedra," *IEEE Trans. Magnetics*, Vol. 19, No. 6, pp. 2539-2542, Nov. 1983.

[6] T. Wang, R. F. Harrington, and J. R. Mautz, "Electromagnetic scattering from and transmission through arbitrary apertures in conducting bodies," *IEEE Trans. on Antennas and Propagation*, Vol. 38, No. 11, pp. 1805-1814, Nov.1990.

Integral Equation Based Analysis of Transient Electromagnetic Scattering from Three-Dimensional Inhomogeneous Dielectric Objects

N. T. Gres, A. A. Ergin, B. Shanker*, and E. Michielssen
Center for Computational Electromagnetics
Department of Electrical and Computer Engineering
University of Illinois at Urbana-Champaign
1406 W. Green St., Urbana, IL 61801
Phone: 217 244 2636 E-mail: gres@uiuc.edu

*currently affiliated with Iowa State University

Abstract

A novel technique for analyzing transient electromagnetic scattering from three-dimensional inhomogeneous dielectric targets is proposed. The electromagnetic volume equivalence principle is invoked to construct an integral equation for the electric flux density throughout the scatterer. This equation is solved using a marching-on-in-time scheme in which the electric flux density is expanded in space by volumetric rooftop basis functions defined on a tetrahedral mesh and in time by piecewise polynomial basis functions. The proposed method is validated for a representative dielectric structure by comparison of scattering data obtained with this method and various frequency domain techniques.

1. Introduction

This paper presents a volume time domain integral equation technique (VTDIE) for studying transient scattering from three-dimensional inhomogeneous dielectric objects. The analysis of electromagnetic phenomena in the presence of inhomogeneities is important for many applications. For instance, scattering by and detection of airborne particulates, medical diagnostics, interactions between antennas and biological bodies are all applications involving inhomogeneities. Furthermore, transient analysis capabilities are invaluable for studying wide-band or nonlinear systems.

If the scatterer is piecewise inhomogeneous, a surface integral equation method can be used [1] for analysis. For highly inhomogeneous bodies, a volume integral equation method as presented by Schaubert *et al.* [2],[3] for the analysis of frequency domain phenomena is more suitable. Here, Schaubert's work is extended to the time domain by constructing a VTDIE and solving it using a marching-on-in-time (MOT) scheme.

The paper is organized as follows: the construction of the VTDIE and formulation of the MOT method are presented in Section 2, results that validate the method are shown in Section 3, and conclusions to this study are presented in Section 4.

2. Formulation

Consider an inhomogeneous scatterer, occupying a volume V that resides in free space, defined as an unbounded medium with permittivity ε_0 and permeability μ_0. It is assumed that the scatterer is isotropic, lossless, and nonmagnetic with frequency independent permittivity $\varepsilon(\mathbf{r})$. The scatterer is illuminated by an incident electric field $\mathbf{E}^i(\mathbf{r},t)$ (Figure 1(a)), which is zero on V for time $t<0$. Our task is to determine the total electric field $\mathbf{E}(\mathbf{r},t)$ for all space and $t\geq 0$.

An integral equation for the electric flux density in V is derived to solve this problem. To facilitate this derivation, the total electric field is decomposed into incident and scattered components as

$$\mathbf{E}(\mathbf{r},t)=\mathbf{E}^i(\mathbf{r},t)+\mathbf{E}^s(\mathbf{r},t) \tag{1}$$

By invoking the volume equivalence principle, the scattered field is characterized by an equivalent volume current density $\mathbf{J}(\mathbf{r},t)$ that radiates in free space and is given by

$$\mathbf{J}(\mathbf{r},t)=\kappa(\mathbf{r})\partial_t\mathbf{D}(\mathbf{r},t) \tag{2}$$

where $\kappa(\mathbf{r})=\big(\varepsilon(\mathbf{r})-\varepsilon_0\big)/\varepsilon(\mathbf{r})$ is the contrast ratio and $\mathbf{D}(\mathbf{r},t)=\varepsilon(\mathbf{r})\mathbf{E}(\mathbf{r},t)$ is the electric flux density. The scattered electric field $\mathbf{E}^s(\mathbf{r},t)$ is expressed in terms of $\mathbf{J}(\mathbf{r},t)$ as

$$\mathbf{E}^s(\mathbf{r},t)=-\partial_t\mathbf{A}(\mathbf{r},t)-\nabla\phi(\mathbf{r},t) \tag{3}$$

where the magnetic vector potential $\mathbf{A}(\mathbf{r},t)$ and the electric scalar potential $\phi(\mathbf{r},t)$ are given by

$$\mathbf{A}(\mathbf{r},t)=\frac{\mu_0}{4\pi}\partial_t\int_V dv'\frac{\mathbf{J}(\mathbf{r}',\tau)}{R} \text{ and} \tag{4}$$

$$\phi(\mathbf{r},t)=-\frac{1}{4\pi\varepsilon_0}\int_V dv'\frac{1}{R}\int_{-\infty}^{\tau}d\xi\nabla'\cdot\mathbf{J}(\mathbf{r}',\xi) \tag{5}$$

In Equations (4) and (5) $R=|\mathbf{r}-\mathbf{r}'|$ denotes distance from the source to the field point and $\tau=t-R/c$ denotes retarded time where c is the free-space speed of light. Combining Equations (1)-(5) results in

$$\frac{\mathbf{D}(\mathbf{r},t)}{\varepsilon(\mathbf{r})}+\frac{\mu_0}{4\pi}\partial_t^2\int_V dv'\kappa(\mathbf{r}')\frac{\mathbf{D}(\mathbf{r}',\tau)}{R}-\frac{1}{4\pi\varepsilon_0}\nabla\int_V dv'\frac{\nabla'\cdot\kappa(\mathbf{r}')\mathbf{D}(\mathbf{r}',\tau)}{R}=\mathbf{E}^i(\mathbf{r},t),\ \forall\mathbf{r}\in V, \tag{6}$$

which is the desired integro-differential equation for $\mathbf{D}(\mathbf{r},t)$. Upon solving this equation for $\mathbf{D}(\mathbf{r},t)$, $\mathbf{E}^s(\mathbf{r},t)$ everywhere can be computed using Equations (2)-(5).

Equation (6) is solved using an MOT scheme. To this end, the electric flux density $\mathbf{D}(\mathbf{r},t)$ is discretized using a set of N_s spatial basis functions $\{\mathbf{f}_n(\mathbf{r})\}$ and N_t temporal basis functions $\{T_j(t)\}$ as

$$\mathbf{D}(\mathbf{r},t)=\sum_{n=1}^{N_s}\sum_{j=0}^{N_t-1}D_{n,j}\mathbf{f}_n(\mathbf{r})T_j(t), \tag{7}$$

where $\{D_{n,j}\}$ is the set of unknown expansion coefficients. The spatial basis functions used are the volumetric rooftop basis functions proposed by Schaubert *et al.* [2]. In order to define these functions, the scatterer V is approximated by a set of N_e tetrahedral elements $\{V_k\}$; the contrast ratio over element k is assumed constant and denoted κ_k. A spatial basis is associated with each triangular face S_n of the tetrahedral mesh. With reference to Figure 1(b), the spatial basis functions are defined as $\mathbf{f}_n(\mathbf{r})=a_n\boldsymbol{\rho}_n^{\pm}/(3v_n^{\pm})$ for $\mathbf{r}\in V_n^{\pm}$ and zero elsewhere; $V_n^{\pm}$ are the pair of tetrahedrons that share face n, a_n is the area of face n, and $v_n^{\pm}$ is the volume of $V_n^{\pm}$. The vector $\boldsymbol{\rho}_n^{+}$ is defined from the free vertex of V_n^{+} to the position vector $\mathbf{r}$; $\boldsymbol{\rho}_n^{-}$ is defined similarly except it is directed towards the free vertex of V_n^{-}. The convention used is superscripts refer to tetrahedrons and subscripts refer to triangles. An important property of these basis functions is that their normal components are continuous across each interior face. Therefore the boundary condition requiring continuity of the normal components of $\mathbf{D}(\mathbf{r},t)$ across material interfaces is satisfied within V. Only one tetrahedron is associated with those faces residing on the boundary of V; hence the corresponding spatial basis function is nonzero only over a single tetrahedron. Therefore, the number of spatial unknowns N_s equals the number of triangles in the tetrahedral mesh.

The temporal basis functions are chosen to be of the form $T_j(t)=T(t-j\Delta t)$, where Δt is the time step size. In this study, cubic polynomial interpolation bases [4] are used. The order of interpolation is chosen high enough to accommodate the derivatives that need to be evaluated in the vector potential contribution of the integral equation. The time step is chosen as $\Delta t=\pi/(5\omega_{\max})$ where $\omega_{\max}$ is the maximum frequency of the incident field.

The integral equation is now discretized using a Galerkin testing procedure. Upon substitution of the electric flux density given by Equation (7) into Equation (6), the resulting equation is tested at $t=t_j=j\Delta t$ with the spatial basis functions $\mathbf{f}_m(\mathbf{r})$, $m=1,...,N_s$, using the inner product $\langle\mathbf{f}(\mathbf{r}),\mathbf{g}(\mathbf{r})\rangle=\int_V dv\mathbf{f}(\mathbf{r})\cdot\mathbf{g}(\mathbf{r})$. To solve this system by MOT, all terms involving electric flux density values at time steps prior to t_j are moved to the right-hand side of the equation. In matrix form this yields

$$\overline{\mathbf{Z}}_0\mathbf{D}_j=\mathbf{V}_j-\sum_{k=1}^{j-1}\overline{\mathbf{Z}}_k\mathbf{D}_{j-k}, \tag{8}$$

where the m^{th} components of the vectors $\mathbf{D}_i$ and $\mathbf{V}_i$ are given by $D_{m,i}$ and $\left\langle\mathbf{f}_m(\mathbf{r}),\mathbf{E}^i(\mathbf{r},t_i)\right\rangle$, respectively, and the elements of the sparse interaction matrix $\overline{\mathbf{Z}}_i$ are given by

$$Z_{i,mn}=Z_{i,mn}^{self}+Z_{i,mn}^{\mathbf{A}}+Z_{i,mn}^{\phi}, \tag{9}$$

where the self $Z_{i,mn}^{self}$, vector potential $Z_{i,mn}^{\mathbf{A}}$, and scalar potential $Z_{i,mn}^{\phi}$ contributions to $Z_{i,mn}$ are given by

$$Z_{i,mn}^{self} = \left\langle \mathbf{f}_m(\mathbf{r}), T_{-i}(t)\mathbf{f}_n(\mathbf{r})/\varepsilon(\mathbf{r}) \right\rangle\Big|_{t=0} \tag{10}$$

$$Z_{i,mn}^{\mathbf{A}} = \frac{\mu_0}{4\pi}\left\langle \mathbf{f}_m(\mathbf{r}), \int_V dv' \partial_t^2 T_{-i}(\tau)\kappa(\mathbf{r}')\frac{\mathbf{f}_n(\mathbf{r}')}{R} \right\rangle\Big|_{t=0} \tag{11}$$

$$Z_{i,mn}^{\phi} = -\frac{1}{4\pi\varepsilon_0}\left\langle \mathbf{f}_m(\mathbf{r}), \nabla\int_V dv' T_{-i}(\tau)\nabla'\cdot\kappa(\mathbf{r}')\frac{\mathbf{f}_n(\mathbf{r}')}{R} \right\rangle\Big|_{t=0} \tag{12}$$

Equation (8) relates the expansion coefficients at the j^{th} time step to the incident field and the coefficients at prior time steps. Hence, all the expansion coefficients $D_{n,j}$ can be evaluated by starting at the first time step, forming the right-hand side, and solving Equation (8) at each time step. Equation (8) is solved iteratively using the transpose free quasi-minimal residual algorithm with initial guess equal to the solution of the previous time step. Stability of the MOT scheme is achieved without any special averaging methods and can be attributed to the implicit nature of the method, the presence of the strong self-term $\langle \mathbf{f}_m, \mathbf{D}/\varepsilon \rangle$ in the integral equation, and careful evaluation of the integrals.

Detailed formulas for the computation of $\overline{\mathbf{Z}}_i$ can be found in [2]. The volume and surface integrals that arise are computed using quadrature rules for tetrahedra and triangles [5],[6]. In this study, five point quadrature rules for tetrahedra and seven point quadrature rules for triangles are used for both evaluating the fields and testing purposes. When the source and field points are nearby in terms of the shortest excitation wavelength, the singularities are extracted by expanding integrals as:

$$\int du' T_{-i}(\tau)\frac{\mathbf{g}(\mathbf{r}')}{R} = \int du' \left(T_{-i}(\tau) - T_{-i}(t-t_c)\right)\frac{\mathbf{g}(\mathbf{r}')}{R} + \int du' T_{-i}(t-t_c)\frac{\mathbf{g}(\mathbf{r}')}{R} \tag{13}$$

where $\mathbf{g}(\mathbf{r})$ is either 1 or $\boldsymbol{\rho}_n^{\pm}$ and the integral is over either a tetrahedron or triangle. The expansion is offset by $t_c > R/c$ to ensure causality in the numerical implementation. The first term on the right-hand side is well-behaved and is computed numerically, while the second term is evaluated analytically using results from [7].

3. Results

This section presents results generated by the MOT scheme outlined in Section 2. The incident field is chosen to be an $\hat{\mathbf{x}}$ polarized modulated Gaussian plane wave propagating in the $\hat{\mathbf{z}}$ direction

$$\mathbf{E}^i(\mathbf{r},t) = \hat{\mathbf{x}}\cos\left[(ct - \mathbf{r}\cdot\hat{\mathbf{z}})\omega_0/c\right]e^{-(ct-\mathbf{r}\cdot\hat{\mathbf{z}}-6\sigma)^2/2\sigma^2} \tag{14}$$

where ω_0 is the center frequency and σ is the standard deviation. The effective maximum frequency of the signal is defined as $\omega_{max} = \omega_0 + 6c/\sigma$. At this frequency the signal power is down by over 150 dB from its peak value.

Results are given in terms of the frequency domain radar cross section $RCS(\hat{\mathbf{r}},\omega)$. The $RCS(\hat{\mathbf{r}},\omega)$ is obtained from the electric flux density generated with the MOT scheme by first computing the far-field signature:

$$\mathbf{E}^{far}(\hat{\mathbf{r}},t) = -\frac{\mu_0}{12\pi}(\bar{\mathbf{I}} - \hat{\mathbf{r}}\hat{\mathbf{r}})\partial_t^2 \sum_{n=1}^{N_s} a_n \left[\frac{\kappa_n^+}{v_n^+} \int_{V_n^+} \rho_n^+ D_n\left(t + \frac{\hat{\mathbf{r}}\cdot\mathbf{r}'}{c}\right) dv' + \frac{\kappa_n^-}{v_n^-} \int_{V_n^-} \rho_n^- D_n\left(t + \frac{\hat{\mathbf{r}}\cdot\mathbf{r}'}{c}\right) dv' \right] \tag{15}$$

This temporal signature is then transformed to the frequency domain yielding $\mathbf{E}^{far}(\hat{\mathbf{r}},\omega)$ from which the $RCS(\hat{\mathbf{r}},\omega)$ is obtained by

$$RCS(\hat{\mathbf{r}},\omega) = 10\log_{10}\left[4\pi \left|\mathbf{E}^{far}(\hat{\mathbf{r}},\omega)\right|^2 \Big/ \left|\mathbf{E}^{i}(\omega)\right|^2 \right] \tag{16}$$

where $|\mathbf{E}^i(\omega)|$ is the magnitude of the Fourier transform of the incident field given by Equation (14).

To validate this method, scattering from a dieletric spherical shell is studied. The inner shell radius is 0.75 m and the outer is 1 m; the permittivity is $2\varepsilon_0$. The parameters chosen for the incident pulse are $\sigma = 2\pi c/\omega_0 = 2.89$ m. The shell is discretized into 927 tetrahedrons yielding 2120 unknowns. At the effective maximum frequency there are approximately 10 spatial unknowns per wavelength in the dielectric. The method, referred to as the volume marching-on-in time method (VMOT) in the figures, is run for 400 time steps where the time step size is 0.493 ns.

The VMOT results are compared with those computed by a Mie series solution and a frequency domain volume methods of moments code (VMOM) [2]. First, the backscattered *RCS* is compared over the entire band of the incident pulse (Figure 2(a)). Next, the *RCS* is examined at a single frequency (Figure 2(b)). Good agreement is achieved.

4. Conclusions

An MOT scheme based on a volume integral equation has been described for transient scattering from inhomogeneous dielectric objects. It is based on rooftop basis functions defined over tetrahedral volume elements, which ensure field continuity. This technique has been validated through numerical examples. While the formulation presented here applies to dieletric bodies, this method can be easily extended to encompass scatterers with non-trivial permeabilities by including an equivalent magnetic current density and then solving a pair of equations for the electric and magnetic flux densities. The MOT scheme presented here is prohibitively expensive (it scales as $O(N_t N_s^2)$); work is

being done to accelerate it using the plane-wave time-domain algorithm [8], which would reduce the complexity to $O(N_t N_s)$.

Acknowledgements

This research was supported by the Air Force Office for Scientific Research via the MURI program under contract no. F49620–96–1–0025, the NSF under the grant ECS 95–02138, and by a Department of Energy Computational Science Graduate Fellowship.

References

[1] M. D. Pocock, M. J. Bluck, and S. P. Walker, "Electromagnetic scattering from 3-d curved dielectric bodies using time-domain integral equations," *IEEE Trans. Antennas Propagat.*, vol. 46, no. 8, pp. 1212-1219, Aug. 1998.

[2] D. H. Schaubert, D. R. Wilton, and A. W. Glisson, "A tetrahedral modeling method for electromagnetic scattering by arbitrarily shaped inhomogeneous dielectric bodies," *IEEE Trans. Antennas Propagat.*, vol. 32, no. 1, pp. 77-85, Jan. 1984.

[3] D. H. Schaubert and P. M. Meaney, "Efficient computation of scattering by inhomogeneous dielectric bodies," *IEEE Trans. Antennas Propagat.*, vol. 34, no. 4, pp. 587-592, Apr. 1986.

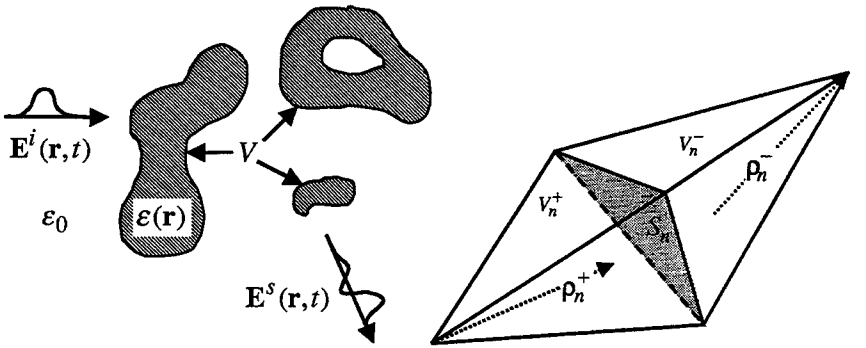
[4] G. Manara, A. Monorchio, and R. Reggiannini, "A space-time discretization criterion for a stable time-marching solution of the electric field integral equation," *IEEE Trans. Antennas Propagat.*, vol. 45, no. 3, pp. 527-532, Mar. 1997.

[5] K. S. Sunder and R. A. Cookson, "Integration points for triangles and tetrahedrons obtained from the gaussian quadrature points for a line," *Computers and Structures*, vol. 21, no. 5, pp. 881-885, 1985.

[6] P. Keast, "Moderate-degree tetrahedral quadrature formulas," *Computer Meth. Appl. Mechanics Eng.*, vol. 55, pp. 339-348, 1986.

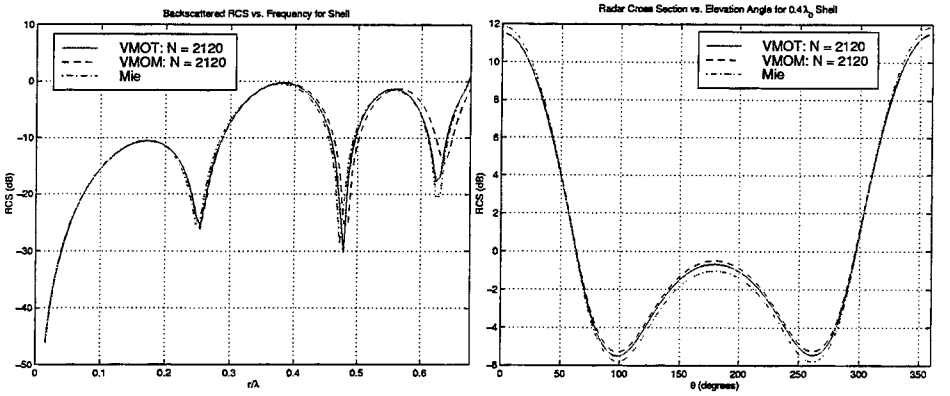
[7] D. R. Wilton, S. M. Rao, A. W. Glisson, D. H. Schaubert, O. M. Al-Bundak, and C. M. Butler, "Potential integrals for uniform and linear source distributions on polygonal and polyhedral domains," *IEEE Trans. Antennas Propagat.*, vol. 32, no. 3, pp. 276-281, Mar. 1984.

[8] A. A. Ergin, B. Shanker, and E. Michielssen, "The Plane-Wave Time-Domain Algorithm for the Fast Analysis of Transient Wave Phenomena," *IEEE Antennas and Propag. Mag.*, vol. 41, no. 4, pp. 39-52, Aug. 1999.



(a) (b)

Figure 1. (a) Scattering geometry. (b) Geometrical parameters associated with the n^{th} face.



(a) (b)

Figure 2. Scattering from a spherical shell. (a) Backscattered *RCS* vs. r/λ, where r/λ is the outer radius of the shell in wavelengths. (b) *RCS* vs. elevation angle for $r/\lambda = 0.4$.

COMPUTATIONAL PROPERTIES OF WAVELET BASED PEEC ANALYSIS IN TIME DOMAIN

G.Antonini, *IEEE Member*, A.Orlandi, *IEEE Senior Member*
antonini@ing.univaq.it , orlandi@ing.univaq.it

Department of Electrical Engineering, University of L'Aquila, I-67040 Poggio di Roio, L'Aquila, ITALY

***Abstract* – The use of wavelet basis functions for the efficient solution of Partial Element Equivalent Circuit (PEEC) models is studied. It is demonstrated that the use of wavelets for expansion and testing functions produces a sparse system matrix. Here, this effect are examined by varying the wavelets order, the thresholding level and decomposition levels.**

I. INTRODUCTION

The capability of the Partial Element Equivalent Circuit (PEEC) method [1,2] to model any electromagnetic problem – formulated in an integral equation form- by means of an equivalent circuit renders this technique very appealing. In the recent past, several advancements of this numerical technique has been developed: from the introduction of incident field and time delays [3] to hybrid models taking into account conductive surfaces and complex cables [4,5], up to the introduction of non-orthogonal elementary PEEC cells to improve the accuracy for complex geometries and to decrease the computational efforts [6]. Because the issue of stability for this algorithm in a marching-on-in-time solution has been already analyzed and stable implementations suggested [7] the only block preventing its widespread use appears to be its computational complexity. In order to facilitate the fast evaluation of transient electromagnetic fields by means of PEEC a wavelet approach has been developed [8]. This work continues that study and performs a parametric analysis of the sparsity and threshold properties of the resulting matrices due to the application of the wavelet transform [9] to a PEEC time domain solution. The paper is organized as follows: in Section II a brief derivation of the PEEC technique is given together with the application of the wavelet transform in order to decrease the number of non-zero entries in the global system matrix and hence speed-up the system solution. Section III is devoted to discuss the properties of the wavelet-transformed matrix for various types of wavelets and threshold's levels. In the same section the procedure is applied to the time-domain analysis of a multiconductor transmission line (MTL) and the results compared with those obtained by different approaches. At the end, Section IV draws some conclusions pointing out the main advantages of the proposed technique and some critical point that deserve more investigation.

II. PEEC BASIS AND WAVELET PEEC (W-PEEC) FORMULATION

The PEEC method is a numerical technique for the solution of integral equations in form of an equivalent circuit [1,2]. The electric field in the free space at a conductor can be written for the homogenous case as

$$\vec{E}^i(\vec{r},t)=\frac{\vec{J}(\vec{r},t)}{\sigma}+\mu\int_{v'}\frac{\partial\vec{J}(\vec{r}',t')}{\partial t}G(\vec{r}\,|\,\vec{r}')dv'+\nabla\frac{1}{\varepsilon}\int_{v'}G(\vec{r}\,|\,\vec{r}')\rho(\vec{r}',t')dv' \qquad (1)$$

where $t'=t-\frac{|\vec{r}-\vec{r}'|}{c}$ denotes the retardation time and c is the phase velocity of the medium. $\vec{J}$ is the current density flowing in the conductor, q is the charge density and $G(\vec{r}|\vec{r}')$ is the Green's function. In order to solve (1) for the unknowns $\vec{J}$ and ρ, the current and charge densities are spatially expanded in pulse basis functions. This results in a spatial discretization of the conductive regions into volume and surface cells. The circuit interpretation of the electromagnetic problem is obtained by weighting the resulting equation in the Galerkin approximation sense.
The development of the overall PEEC circuit is obtained by combining the resulting equation for the voltage drop along each appropriate direction in a conductor cell with the discrete version of the conservation of charge equation in form of KCL at each node in the equivalent circuit.

The elementary PEEC model is constituted by an inductive cell and two capacitive half cells as shown in Fig. 1. Having in mind this model three sets of equations can be written enforcing the Kirchoff voltage law (KVL) to both the longitudinal and vertical branches and the KCL to each capacitive node. Let the entire equivalent circuit contain N capacitive nodes and M inductor cells. A first set of equations is given by using KVL which takes the matrix form (capital bold letters refer to matrices):

$$-\mathbf{AV}-\mathbf{L}_P\frac{d\mathbf{I}_L}{dt}=\mathbf{V}_S \tag{2}$$

where $\mathbf{A}$ is the node-branch matrix, $\mathbf{V}$ are the capacitive nodes' potentials, in which $\mathbf{R}$ and $\mathbf{L}_P$ are the matrix of the conductors resistances (it is diagonal) and partial inductances respectively, $\mathbf{I}_L$ holds the inductor currents and $\mathbf{V}_S$ are the longitudinal voltage sources.

By applying the KCL at the node k (see Fig. 1b) there are four contributions: the currents on the branches n and n+1, the current on the capacitive branch towards infinity and the current I_{lumped} on the generic lumped element between nodes j and k. The KCL becomes

$$-\mathbf{I}_{lumped}+\mathbf{G}_{lumped}\mathbf{V}+\mathbf{C}_{lumped}\frac{d\mathbf{V}}{dt}+\mathbf{F}\frac{d\mathbf{V}_C}{dt}-\mathbf{A}^T\mathbf{I}_L=\mathbf{I}_S \tag{3a}$$

$$-\mathbf{AV}-\mathbf{L}_{lumped}\frac{d\mathbf{I}_{lumped}}{dt}=0 \tag{3b}$$

In (3a) and (3b) matrix operators $\mathbf{G}_{lumped}, \mathbf{C}_{lumped}\left(\frac{d}{dt}\right), \mathbf{L}_{lumped}\left(\frac{d}{dt}\right)$ are NxN matrices assembled according to the node-voltage analysis of a lumped-element circuit [15]. $\mathbf{I}_S$ is the excitation vector that describes the amount of current injected into the nodes by independent current sources, $\mathbf{F}$ is a NxN diagonal matrix operator in which $f_{kk}=\frac{1}{p_{kk}}$ and p_{kk} is the self potential coefficient of node k, $\mathbf{V}_C$ contains the voltage drops on the capacitances C_j. A third set of equations is given by the KVL applied to the vertical branches of the circuit in Fig. 1:

$$-\mathbf{V}+\mathbf{H}\mathbf{V}_C=0 \tag{4b}$$

where $\mathbf{H}$ is suitable NxN matrix whose entries are $h_{ki}=\frac{p_{ki}}{p_{kk}}$. The diagonal elements of this matrix are set to unity. These relations can be cast in the following set of differential equations

$$\begin{bmatrix} -\mathbf{1}_N & \left(\mathbf{G}_{lumped}+\mathbf{C}_{lumped}\frac{d}{dt}\right) & \mathbf{F}\left(\frac{d}{dt}\right) & -\mathbf{A}^T \\ 0 & -\mathbf{1}_N & \mathbf{H} & 0 \\ 0 & -\mathbf{A} & -\mathbf{R} & -\mathbf{L}_P\frac{d}{dt} \\ \mathbf{L}_{lumped}\frac{d}{dt} & -\mathbf{A} & 0 & 0 \end{bmatrix}\begin{bmatrix} \mathbf{I}_{L\,lumped} \\ \mathbf{V} \\ \mathbf{V}_C \\ \mathbf{I}_L \end{bmatrix}=\begin{bmatrix} \mathbf{I}_S \\ 0 \\ \mathbf{V}_S \\ 0 \end{bmatrix} \tag{5}$$

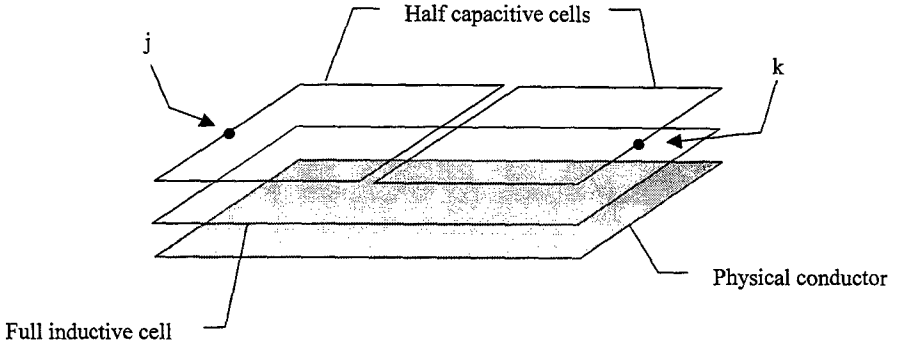
It can be easily shown that the product of matrices $\mathbf{F}$ and $\mathbf{H}^{-1}$ gives $\mathbf{F}\mathbf{H}^{-1}=\mathbf{P}^{-1}$. Wavelets are a class of recursively defined orthonormal basis functions. The complete orthonormal set is formed by taking dilations and translations of a single function $\psi(t)$

$$\psi_{j,k}(t)=2^{j/2}\psi(2^j t-k) \tag{6}$$

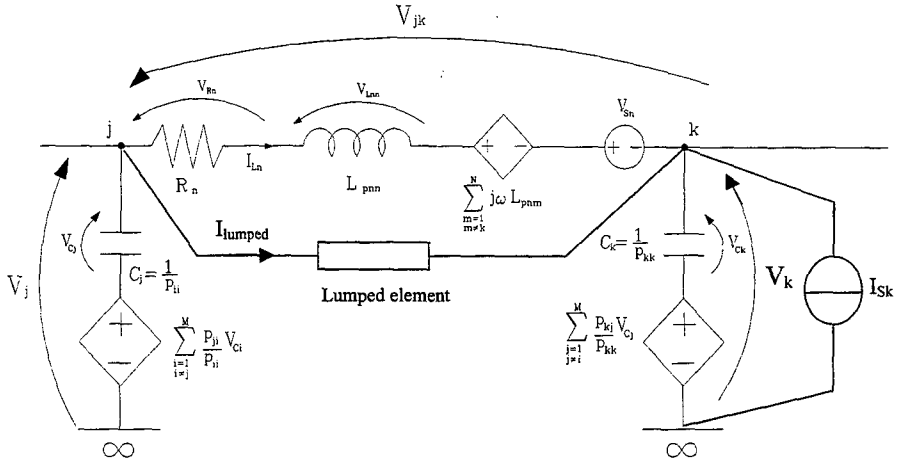
The function $\psi(t)$ has a companion, the scaling function $\varphi(t)$. Each of them are completely determined by a set of quadrature mirror filter coefficients, $h(n)$ and $g(n)$ as in [10]

$$\varphi(t)=\sqrt{2}\sum_{n=1}^{N_c}h(n)\varphi(2t-n) \tag{7}$$

$$\psi(t)=\sqrt{2}\sum_{n=1}^{N_c}g(n)\varphi(2t-n) \tag{8}$$



(a)



(b)

Fig. 1 – Elementary PEEC cell: a) discretization of the physical conductor, b) equivalent PEEC circuit.

In order to obtain the wavelet formulation of the PEEC method from equation (5) the wavelet representation of the time-derivative operator $\frac{d}{dt}$ is needed. In representing such operator in a wavelet basis, the so-called non-standard form [11] (NS-form) is chosen. The NS-form algorithm leads to a process of complexity $O(N)$ while its standard form counterpart requires N^2 operations. Generally a truncated matrix representing the derivative operator in the NS-form has more zero entries than its standard form and, since the number of operations is proportional to the number of non zero entries, it is desirable to perform computation directly using a matrix represented in the NS-form. The property of vanishing moments, typical of orthonormal basis functions, causes the wavelet coefficients corresponding to entries far from the diagonal to be smaller than the diagonal ones allowing the thresholding process. The NS-form of the wavelet matrix operator $\mathbf{T}$ (representation of $\frac{d}{dt}$) is given by a chain of triplets

$$T = \left\{ A_j \quad B_j \quad \Gamma_j \right\}_{j \in Z} \tag{9}$$

and admits a recursive definition

$$T_j = \begin{bmatrix} A_{j+1} & B_{j+1} \\ \Gamma_{j+1} & T_{j+1} \end{bmatrix} \tag{10}$$

The matrix elements α_{ml}^{j} , β_{ml}^{j} , γ_{ml}^{j} of $\mathbf{A}_j$, $\mathbf{B}_j$, Γ_j and r_{ml}^{j} of $\mathbf{T}_j$ are computed as in [8] and, therefore, the representation of $\frac{d}{dt}$ is completely determined. The application of the Wavelet Transform to the system of equations (5) gives

$$\begin{bmatrix} -\mathbf{1}_{N,w} & \left(\mathbf{G}_{lumped,w} + \mathbf{C}_{lumped,w}\mathbf{T}\right) & \mathbf{F}_w\mathbf{T} & -\mathbf{A}_w{}^T \\ 0 & -\mathbf{1}_{N,w} & \mathbf{H}_w & 0 \\ 0 & -\mathbf{A}_w & -\mathbf{R}_w & -\mathbf{L}_{P,w}\mathbf{T} \\ \mathbf{L}_{lumped,w}\mathbf{T} & -\mathbf{A}_w & 0 & 0 \end{bmatrix} \begin{bmatrix} \mathbf{I}_{L\,lumped,w} \\ \mathbf{V}_w \\ \mathbf{V}_{C,w} \\ \mathbf{I}_{L,w} \end{bmatrix} = \begin{bmatrix} \mathbf{I}_{S,w} \\ 0 \\ \mathbf{V}_{S,w} \\ 0 \end{bmatrix} \tag{11}$$

where $\mathbf{T}$ is the sparse representation of the differential operator and $\mathbf{I}_{s,w}$ and $\mathbf{V}_{s,w}$ are the wavelet transforms of the exciting sources. Combining the previous equations the final system in the unknown nodal potential is obtained

$$\left[\mathbf{A}_w{}^T\left(\mathbf{L}_{lupmed,w}\mathbf{T}\right)^{-1}\mathbf{A}_w + \mathbf{G}_{lupmed,w} + \mathbf{C}_{lumped,w}\mathbf{T} + \mathbf{A}_w{}^T\left(\mathbf{R}_w + \mathbf{L}_{P,w}\mathbf{T}\right)^{-1}\mathbf{A}_w + \mathbf{P}_w{}^{-1}\mathbf{T}\right]\mathbf{V}_w = \mathbf{I}_{S,w} - \mathbf{A}^T\left(\mathbf{R}_w + \mathbf{L}_{P,w}\mathbf{T}\right)\mathbf{V}_{S,w} \tag{12}$$

which can be rewritten as

$$\mathbf{Y}_w\mathbf{V}_w = \tilde{\mathbf{I}}_S \tag{13}$$

where $\tilde{\mathbf{I}}_{S,w}$ takes into account the lumped and the distributed sources expanded in the chosen wavelet basis. Having the wavelet basis a local support the matrix $\mathbf{T}$ has a banded structure with few nonvanishing codiagonals. Due to the high sparsity of the $\mathbf{T}$ matrix, the matrices $\mathbf{L}_{lumped,w}$, $\mathbf{A}_w$, $\mathbf{C}_{lumped,w}$ and $\mathbf{R}_w$ have the same sparse structure. Great advantages in computing time can be achieved by using a sparse treatment of equation (13). When the wavelet coefficients of the nodal potential have been evaluated, all the other expansion coefficients can be obtained from the Kirchhoff equations in the transformed domain. Finally the physical time domain solutions are derived by means of the reconstruction algorithm

$$V_i(t) = \sum_{k=-\infty}^{+\infty} V_{a,i}^{j_0}(k)\varphi_{j_0,k}(t) + \sum_{k=-\infty}^{+\infty}\sum_{j=j_0}^{N_d} V_{d,i}^{j}(k)\psi_{j,k}(t) \tag{14a}$$

$$I_m(t) = \sum_{k=-\infty}^{+\infty} I_{a,m}^{j_0}(k)\varphi_{j_0,k}(t) + \sum_{k=-\infty}^{+\infty}\sum_{j=j_0}^{N_d} I_{d,m}(j,k)\psi_{j,k}(t) \tag{14b}$$

in which $V_{a,i}^{j_0}(k)$, $I_{a,m}^{j_0}(k)$ and $V_{d,i}^{j_0}(k)$, $I_{d,m}^{j_0}(k)$ are the approximation and detail coefficients of the nodal potential $V_i(t)$ of the cell i and current $I_m(t)$ of the cell m respectively and N_d is the finer decomposition level.

III. RESULTS AND DISCUSSION

The parametric analysis is carried on a structure that consists in a 10 cm long two conductors transmission line with frequency independent parameters (see Fig. 2). The conductors width and thickness are w = 360 μm and t = 36 μm respectively. The line is excited by a voltage source V_S set to a gaussian pulse:

$$V_S = V_0 \exp((t - t_d)^2/(2\Delta^2)) \quad (15)$$

where V_0 = 1 V, center t_d = 10 ns, and semi-width Δ = 2.12 ns and the source internal resistance is R_S = 50 Ω. The loads are resistive terminations indicated as R_{FE1} = 10 Ω, R_{NE2} = 75 Ω and R_{FE2} = 10 Ω. The short-circuit condition on R_{FE1} is also considered.

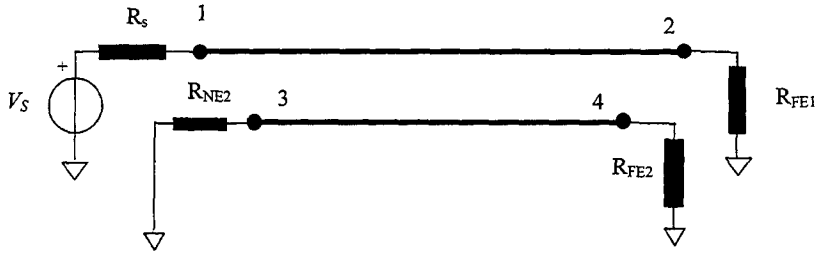


Fig. 2 - MTL and load terminations:
R_S = 50 Ω, R_{NE2} = 75 Ω, R_{FE1} = 10 Ω and R_{FE2} = 10 Ω.

As orthonormal basis are used the Daubechies wavelets (db) of seven different orders, from 3 to 9. The decomposition level chosen to obtain the transformed system (13) is N_d = 2. The property of vanishing moments, typical for these basis functions, causes the wavelet coefficients corresponding to entries far from the main diagonal of $\mathbf{Y}_w$ to be smaller than those close to the diagonal. To take advantage of this, elements of $\mathbf{Y}_w$ that are smaller than an element threshold τ are discarded and the remaining elements of $\mathbf{Y}_w$ are stored in a sparse matrix form. This allows matrix-vector multiplications to be carried out in a time proportional to the number of non zero elements in the sparse matrix, speeding the solution of (13). As in [12] the chosen threshold is

$$\tau = \frac{\delta}{M} \left\| \mathbf{Y}_w \right\|_\infty \quad (16)$$

where δ is a constant, M is the dimension of $\mathbf{Y}_w$ and $\left\| \mathbf{Y}_w \right\|_\infty = \max_i \sum_{j=1}^{M} |Y_w(i,j)|$. The values of τ changes as the decomposition level and wavelet order change. For the application in Fig. 2 Table I reports the threshold values.

TABLE I – THRESHOLD VALUES AS FUNCTION OF WAVELET ORDER AND DECOMPOSITION LEVEL.

Wavelet Order	N_d = 2	N_d = 3
3	51.287	24.544
4	34.567	19.567
5	28.963	13.619
6	24.038	11.306
7	20.181	9.504
8	17.659	8.256
9	15.483	7.345

Defining the *sparsity* of a matrix as the percentage of non-zero entries in the matrix, it is significant to show how the wavelet order affects the sparsity of $\mathbf{Y}_w$. This results in Fig. 3 where as the wavelet order increases the sparsity decrease up to the 42.78 %.

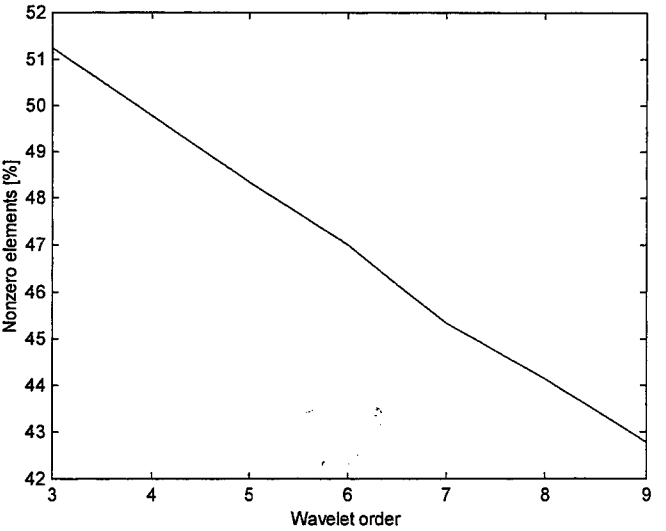


Fig. 3 – Percent sparsity of matrix $\mathbf{Y}_w$ for increasing wavelet order.

The sparsity is also dependent on the decomposition level. Table II gives, for different wavelet order and decomposition levels, the percentage of non-zero entries in $\mathbf{Y}_w$.

TABLE II – PERCENT MATRIX SPARSITY AS FUNCTION OF WAVELET ORDER AND DECOMPOSITION LEVEL.

Wavelet Order	$N_d = 2$	$N_d = 3$
3	51.2429	36.9130
4	50.1022	35.7640
5	48.3381	34.4762
6	47.0017	33.6725
7	45.3298	32.4155
8	44.1456	31.4535
9	42.7800	30.3467

It is interesting to note how with the increasing of the decomposition level the threshold decreases. One would expect that the sparsity of the matrix would have an opposite trend. In the case of wavelet decomposition this is not true (as shown by the two last columns of Table II) because the entries of matrix $\mathbf{Y}_w$ are strongly dependent on the decomposition level. Although the thresholded matrix retains only the 30% of the elements of $\mathbf{Y}_w$ the information contents it is not lost and good solution accuracy can be obtained. As measure of this accuracy we use the relative error between the solution computed using the full matrix $\mathbf{Y}_w$ in (13) and the solution using the thresholded sparse matrix. Fig. 4 shows the transient behavior of

such an error evaluated for the terminal voltage V_{FE2} when the line is matched; Fig. 5 gives the error of the same voltage when the termination resistance $R_{FE1} = 0$.

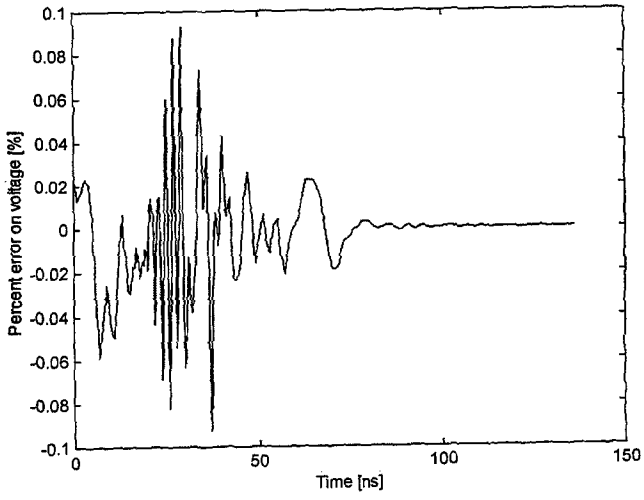


Fig. 4 - Percent error on voltage V_{FE2} for matched load and wavelet order equal to 9.

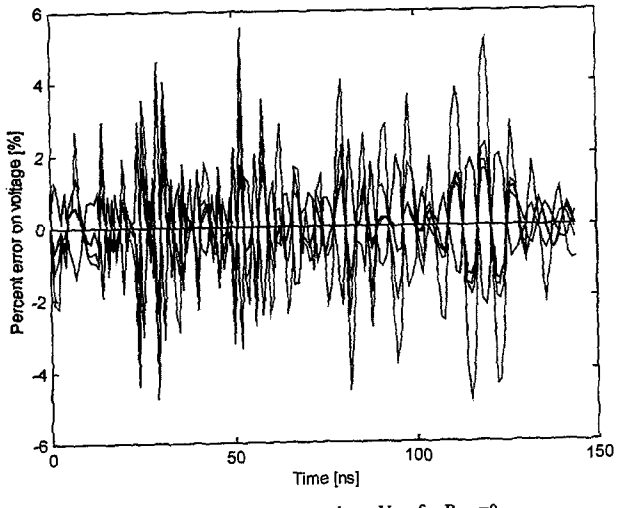


Fig. 5 – Percent error on voltage V_{FE2} for R_{FE1}=0 and different wavelet order.

Figures 4 and 5 reveal the capability of the wavelet basis to accurately represent very fast transients. Although the percent errors are very small, it should be noted that in the case of short circuit (R_{FE1}=0) – when the reflections along the transmission line are more preponderant than in the matched case – the percent error increases.

IV. CONCLUSIONS

A wavelet formulation for the PEEC method in time domain has been presented pointing out some numerical features of the wavelet decomposition; the described use of classical wavelet basis reduces the global solution time of a constant factor. The thresholding of the wavelet-transformed matrix has shown the capabilities of these basis functions in retaining the essential content of information also with an high degree of sparsity.

REFERENCES

[1] A.E. Ruehli, "Equivalent circuit models for three-dimensional multiconductor systems" *IEEE Trans. Microwave Theory Tech.*, vol. 22, n. 3, March 1974, pp. 216-221.

[2] A.E. Ruehli, "Circuit oriented EM modeling techniques for EMC", in *Proc. of 12th Int. Zurich Symposium and Technical Exhibition on EMC*, Zurich, CH, February 18-20, 1997.

[3] A.E.Ruehli, J.Garret, C.R.Paul, "Circuit models for 3D structures with incident field", in *Proc. of IEEE 1993 Int. Symp. on Electromagnetic Compatibility*, Dallas, TX, August 9-13, 1993.

[4] G.Antonini, S. Cristina, A. Orlandi, "PEEC modeling of lightning protection systems: full-wave formulation and circuit solution", *IEEE Trans.on Electromag. Compatibility*, vol. 40 , n. 4, November 1998, pp. 481-491.

[5] G.Antonini, S.Cristina, A.Orlandi, "Three dimensional model for conductive enclosures with apertures and attached cables", *Proc. of 13th Int. Zurich Symp. & Tech. Exhibition on EMC*, Zurich, Switzerland, February 16-18, 1999, pp. 245-250.

[6] A. E. Ruehli, G. Antonini, A. Orlandi, "Extension of the Partial Element Equivalent Circuit Method to Non-Rectangular Geometries", in *Proc. of 1999 IEEE International Symposium on EMC*, 2-6 August, 1999, Seattle, WA, USA.

[7] J.E. Garrett, A.E. Ruehli, C.R. Paul, "Accuracy and Stability Improvements of Integral Equation Models Using the Partial Element Equivalent Circuit (PEEC) Approach", *IEEE Transactions on Antennas and Propagation,* vol. 46, n. 12, December 1998.

[8] G.Antonini, A.Orlandi, A.Ruehli, "Speed-up of PEEC method by using a wavelet transform", submitted to 2000 IEEE International Symposium on EMC, 21-25 August, 2000, Washington DC, USA.

[9] G.Beylkin, "Wavelets, Multiresolution Analysis and Fast Numerical Algorithms", *INRIA Lectures*, May 1991, pp. 1-36.

[10] C.S.Burrus, R. Gopinath, H. Guo, *Wavelets and Wavelet Transforms. A primer*, Prentice Hall, New York, USA, 1998.

[11] G.Beylkin, J.M. Keiser, "On the adaptative numerical solution of non linear partial differential equations in wavelet basis", *Journal of Computational Physics*, vol. 132, 1997, pp. 233-259.

[12] R.L.Wagner, W.C.Chew, "A study of wavelets for the solution of electromagnetic integral equations", *IEEE Trans. Antennas and Propagat.*, vol. 43, n.8. August 1995, pp.802-810.

Time domain modelling of a pulsed horn - dish antenna

M J Bluck[1], S P Walker[1], C Thomas[2]

[1]Imperial College [2]Defence Evaluation and Research Agency

m.bluck@ic.ac.uk, s.p.walker@ic.ac.uk

Abstract: We describe the development of a hybrid integral equation time domain / physical optics time domain approach to the analysis of a horn - dish pulsed antenna, intended to transmit very short duration, well-focused pulses. The hybridisation developed is shown to be effective, with good internal consistency achieved, and to provide the ability to perform design studies and optimisations.

1. INTRODUCTION

In this paper we will outline the modelling of a horn - dish antenna system intended to transmit short pulses of EM energy.

The requirement is to produce a short high energy pulse in the far field, which is spatially as narrow as possible, and which temporally has suffered as little smearing as possible in its focussing and transmission. In particular, the initial rise time of the exciting signal should be preserved.

The feed to the transmitter is a short (~100ps) signal from a high voltage (~10kV) pulse generator, which is directed along a stripline, through a horn, and onto a dish. From here it is reflected away to produce the required far field.

Our intention was to develop methods to model this system, to provide a tool for analysis and design optimisation, and to demonstrate the methods to at least proof of principle stage.

2. SYSTEM SPECIFICATION

The working configuration adopted for model development purposes was as shown in Figure 1. It comprised a pair of parallel plates forming a simple transmission line, diverging and widening to form a horn, facing towards a large dish. The transmission line region was filled with dielectric of relative permittivity 2, with the high voltage pulsed signal introduced via a co-axial feed at its upstream end.

Some dimensions and other data are given in Table 1.

Pulse: Gaussian, fwhm (ps)	140
Dish diameter (m)	2.0
Dish focal length (m)	0.866
Horn mouth to the plane of the rim of the dish (m)	0.58

Table 1: Dimensions and other data.

3. MODELLING

Issues

The overall size of the device is of order 3m, and the pulse width of interest is ~40mm, making the problem electrically large. The problem is also a truly time domain one.

There are of course many powerful tools for antenna analysis in the frequency domain. These are mostly based on the method of moments[1-3], with an increasing number of frequency domain finite element treatments appearing[4], typically with domain closure achieved by hybridisation with an integral equation treatment[5]. These are restricted to structures of relatively modest electrical size. Larger components would generally be treated by an optical technique, hybridised to the method of moment treatment as appropriate[6]. Given the truly time dependent nature of the problem, they are not an attractive option here.

An FDTD approach[7] would have involved a rather large analysis, and with the dish being curved, and the horn plates not lying in co-ordinate planes, would have been vulnerable to staircasing effects, requiring fine discretisation.

The approach we adopted was a combination of integral equation time domain (IETD) analysis[8-10] for the horn, hybridised to a physical optics time domain (POTD)[11] treatment of the dish.

Formulation

The hybrid treatment adopted may be summarised:

(i) Compute the surface field history on the horn in isolation using the usual integral equation (here, the MFIE) in the time domain.

(ii) Compute the fields induced on the dish by the surface horn fields, using a time domain physical optics approximation on the dish, and using as the excitation for this an integral over the (retarded) surface fields on the horn.

(iii) Compute the time dependent near and far fields around the structure by integration of the retarded surface fields on the dish and horn, from whatever point it is desired to evaluate the field.

Feed region and horn

We begin the integral equation analysis at the end of the transmission line, where the plates begin to diverge and widen. (Modelling of the details of the feed and line would be better done by FDTD, and this was the intent of another part of this work, involving others, which did not proceed.) We must then represent adequately the entry of the wave from the transmission line into this diverging region of the horn. We model the field propagating down the line into the throat as a plane wave localised in the throat area. We make the approximation that the field being emitted from the transmission line is determined only by events and geometry upstream; the field entering the integral equation region is a 'given'. Integrations over this 'source plane' in the throat region serve as the excitation to the integral equation model, taking on the role of the incident wave term. It is to be expected that the far field eventually produced is independent of the details of the modelling of this source plane, and indeed computations in which source plane areas differing by a factor of 16 were used will be seen shortly to yield essentially identical results.

The MFIE is then evaluated for the horn in isolation; effects of the dish are neglected. The justification is two-fold. (i) The fields scattered back to the horn from the dish should be an order smaller than those directly induced on the horn by the source. (ii) Causality means that any influence on the fields on the dish which this does have will be some two horn-dish transit times after the main peak arrives at the dish. The early fields, which are of prime interest, are thus wholly unaffected by the approximation.

The dish

The dish is large, and the local radius of curvature of its pec surface is much greater than the wavelengths of interest, allowing fields induced on it to be estimated using the physical optics approximation. The excitation for this, the 'incident wave', is obtained by integration over the surface of the horn, with of course the horn surface fields being evaluated at the appropriate retarded times.

The far field

Far (and near) fields are found from integration over both the dish and horn. Note that for the far field the '$1/R$' term dominates over the $1/R^2$, leaving a far-field temporal dependence (mostly) determined by the time derivative of the pulse fed to the system.

4. RESULTS

Dish location and sizing

The dish diameter, focal length and horn - dish separation are the main degrees of freedom available in ensuring that as much as possible of the energy leaving the horn impinges on the dish (subject to the observation that decreasing the separation too much makes the horn ever less of a 'point source', and harms focussing). We used an assessment of the spatial distribution of transmitted energy to guide the dish design. The time integral of the square of the modulus of the **H** field provides an indication of the energy passing a point. Values were computed on 2m radius circles in the **E** and **H** planes centred on the mouth of the horn. This is shown in Figure 2.

From this a dish diameter of 2.0 m was tentatively adopted, arranged to subtend a full angle of 120 degrees, with a view to capturing as much energy as practical within this constraint. The mouth of the horn was located 0.58m from the

plane of the rim of the dish. For the mouth of the horn then to be at the focus required that the directrix of the parabola be located 1.16m from the origin of co-ordinates.

Far field produced

The time dependent far (E) field, on boresight, is shown in Figure 3.

The relative angular distribution of the energy transmitted from the dish, evaluated at a distance of 100m from the dish in each of the E and H planes, is shown in Figure 4. The actual quantity plotted is the time integral of $|\mathbf{H}|^2$.

Validation and verification

Comparison with empirical formula

There is an empirical formula for evaluation of far-field intensities from a horn:

$$|\mathbf{E}| \approx \frac{L}{4\pi dc}\left(\frac{dV}{dt}\right)$$

where L is characteristic of the horn mouth size, d the distance away, c the speed of light, and $\frac{dV}{dt}$ some average value during the pulse rise.

Taking d= 100m, L = 0.25m, and the derivative as $(10^4)/(140\text{x}10^{-12})$ gives an E of

460 Vm^{-1} at 10m

or ~50 Vm^{-1} at 100 m.

or ~5 Vm^{-1} at 1000 m.

Our computation gave a peak field, after focusing by the dish, of 210 Vm^{-1} at 100 m. Being a modest multiple of the approximate empirically predicted field due to the horn alone, this is certainly plausible. Actual results will be discussed further below.

Source plane modelling

In Figure 5 and Figure 6 are shown the radiation patterns of the horn alone with a series of source planes differing by a factor of 16 in area. As is seen, essentially identical results are obtained in all cases.

Time integral of the far field

The far scattered field is dominated by quantities proportional to the time derivative of the field; terms proportional to the field itself decline with one higher power of the distance away ($1/R^2$, rather than $1/R$). Since the excitation is Gaussian, whilst the far field will not be a pure differentiated Gaussian, we expect the field there to be both positive and negative, and would hope that the time integral of the far field was small. (An alternative interpretation of this statement is that 'DC' components will not propagate to the far field.)

The time integral of the boresight far field was computed. To provide a measure against which to assess 'small', the time integral of the modulus was also evaluated. The ratio of these integrals was 100:1, providing a very satisfying assurance of the internal consistency of all the various calculation stages.

Frequency spectrum of the far field

The frequency spectrum of the input pulse, a Gaussian, is itself a half-Gaussian, with a significant DC / low frequency component. For the reasons discussed above, we would expect this zero frequency part not to be present in the far field. Figure 7 shows a frequency spectrum of the pulse eventually reaching the far field. The zero frequency component has been eliminated, providing further evidence of the internal consistency of the calculations.

5. DISCUSSION AND CONCLUSIONS

The combination of integral equation time domain and physical optics time domain methods assembled seem well able to model the pulsed antenna. Internal quantitative consistency is good, and behaviour predicted is qualitatively as would be expected.

REFERENCES

1. P. Kirby, J. G. Lizius, J. G. Morgan, and J. C. Wood, CLASP - a new, general-purpose Method of Moments Scattering Code, *IEE Proc. Int.Conf.Comput.Electrom.*, 1, pp. 137-140, 1991.

2. J. L. Volakis, Carlos-3D; A general purpose three dimensional method of moments scattering code, *IEEE A-P Magazine*, 35, 1993.

3. R. F. Harrington, *Field Computation by Moment Methods*. New York: MacMillan, 1968.

4. P. P. Silvester and R. L. Ferrari, *Finite Elements for Electrical Engineers*, 2 ed. Cambridge: Cambridge University Press, 1990.

5. J. M. Jin and J. L. Volakis, A finite element-boundary integral method for scattering and radiation by two- and three-dimensional structures, *IEEE A-P Magazine*, 33, pp. 22-32, 1991.

6. U. Jakobus and F. M. Landstorfer, Current-Based Hybrid Moment Method Analysis of Electromagnetic Radiation and Scattering Problems, *ACES Journal*, 10, pp. 38-39, 1995.

7. A. Taflove, *Computational Electromagnetics; The Finite Difference Time Domain Method*. Boston: Artech House, 1995.

8. E. K. Miller, Time-domain modelling in electromagnetics, *Journal of Electromagnetic Waves and Applications*, 8, pp. 1125-1172, 1978.

9. R. Gomez Martin, A. Salinas, and A. Rubio Bretones, Time-Domain Integral Equation Methods For Transient Analysis, *IEEE Antennas and Propagation Magazine*, 34(3), pp. 15-22, 1992.

10. S. P. Walker, Developments in time domain integral equation modelling at Imperial College, *IEEE A-P Magazine*, 39, pp. 7-19, 1997.

11. S. P. Walker, M. J. Bluck, and M. J. Vartiainen, Hybridisation of curvilinear time domain integral equation and time domain optical methods for electromagnetic scattering analysis, *IEEE Tr. Ant and Prop*, 46, pp. 318-324, 1998.

FIGURES

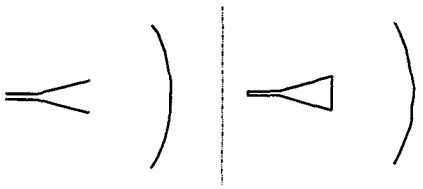


Figure 1: Schematic of the feed - horn - dish combination: elevation and plan views.

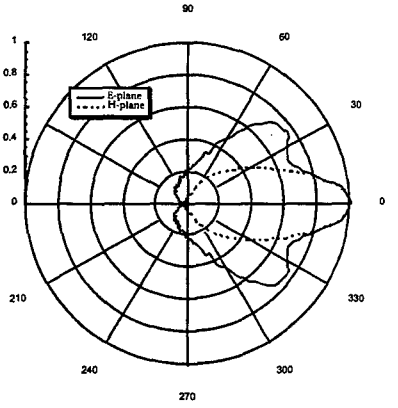


Figure 2 Time integrals of $|H|^2$ on circles of 2m radius centred on the mouth of the horn in the E and H planes

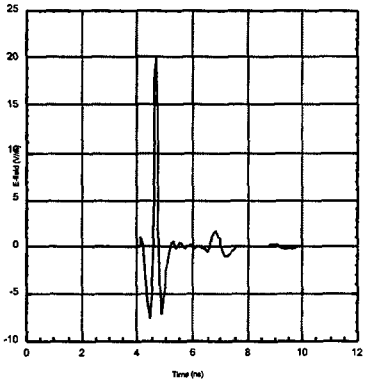


Figure 3 The E field on boresight versus time evaluated at distances of 1000m from the dish. .

(Arbitrary time datum.)

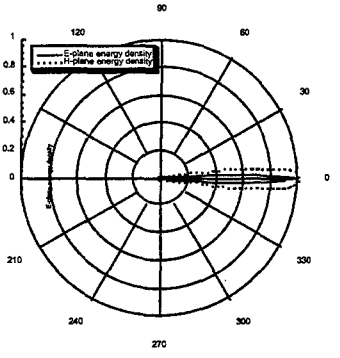


Figure 4 Angular distribution of the energy transmitted from the dish, evaluated at a distance 1000m from the dish

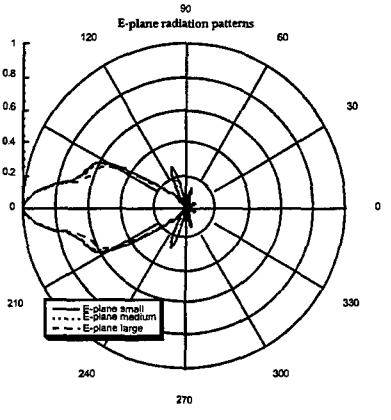


Figure 5 Radiation pattern of the horn alone (at a frequency of 3 GHz, extracted from the pulsed result by Fourier transformation): E plane, with the three different source regions. Note that the scale on these graphs is linear, not logarithmic

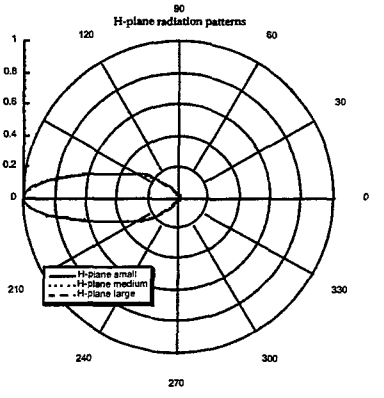


Figure 6 Radiation pattern of the horn alone (at a frequency of 3 GHz, extracted from the pulsed result by Fourier transformation): H plane, with the three different source regions. Note that the scale on these graphs is linear, not logarithmic

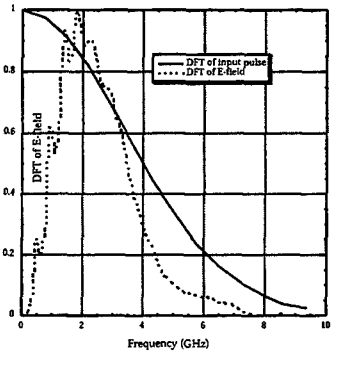


Figure 7 Fourier transforms of E-field on boresight @1000m and input pulse versus frequency

PLENARY SESSION III

W.C. Chew

Fast Solvers for Electromagnetic Simulations-A New Age Analysis Tool

W.C. Chew

Center for Computational Electromagnetics
Department of Electrical and Computer Engineering
University of Illinois at Urbana-Champaign
Urbana, IL 61801-2991

Abstract

This talk will overview the development of solution techniques for Maxwell's equations as an analysis tool. It reviews the solution techniques that were prevalent around the beginning of the 20th century. During that period, closed form solutions were sought for simple shape objects such as spheres, cylinders, half-planes, half-spaces, etc. That was the age of simple shapes. As the demand of science and engineering called for solutions to more complex problems, scientists and engineers developed approximate methods to solve Maxwell's equations approximately. This was often the combined use of asymptotic and perturbation methods. Examples of such are the asymptotic high-frequency methods in scattering, the small perturbation method in rough surface scattering, and the match asymptotic methods in boundary value problems, multiscale analysis in random media, and optics. Consequently, a larger class of solutions can be sought by such techniques, empowering the solutions available to Maxwell's equations. This was the age of approximations.

The advent of computer technology spurred interests in solving Maxwell's equations numerically. Much of these works were to find the corresponding matrix equations, which were sufficiently well posed and represented a high fidelity representation of the original Maxwell's equations. This lifted the restriction on solution types solvable for Maxwell's equations, and greatly expanded the scope and versatility of Maxwell's solvers. That was the age of numerical solvers. However, due to the inefficiency in the solution techniques, only small problems can be solved.

The most recent developments of analysis methods for Maxwell's equations are the fast solvers. These fast solvers have been developed for electrostatics, electrodynamics, as well as fast solvers that are continuously valid from static to electrodynamics; for the frequency and time domains, as well as for layered media. These fast solvers use resources that are orders of magnitude smaller than traditional numerical solvers. Their importance in electromagnetic simulations is as important as fast Fourier transforms in signal and image processing. It is quite certain that these solvers will precipitate a revolution in analysis methods in electromagnetics. Problems that required 10 years of computer time to solve in the past can now be solved within a day.

SESSION 12

MOMENT METHODS

Chairs: Zachi Baharav and Ramakrishna Janaswamy

Iterative Solvers for Dense Matrices — Applications to Moment Method Matrices

Jürgen v. Hagen Werner Wiesbeck

Institut für Höchstfrequenztechnik und Elektronik, Universität Karlsruhe
Kaiserstr. 12, 76199 Karlsruhe, Federal Republic of Germany
email: Juergen.vonHagen@etec.uni-karlsruhe.de

Abstract

The efficient solution of linear systems of equations is of considerable interest in computational electromagnetics. Dense system as they arise in Moment Method solutions are usually solved by a general *LU* factorisation (Gauss algorithm). Iterative algorithms are widely used when systems with sparse matrices must be solved. This paper analyses how iterative algorithms can be applied to the dense matrices of Moment Method solutions. Two test cases are studied closer.

1 Introduction

Many numerical methods for electromagnetic problems necessitate the solution of large linear systems of equations like the following

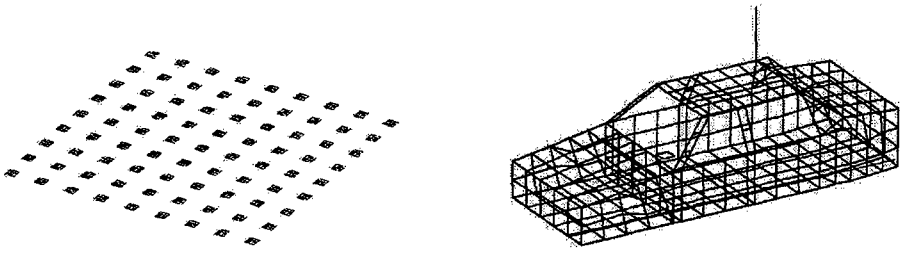
$$AX = B \tag{1}$$

with matrix A, excitation vector B and solution vector X. The vectors have n elements for the n unknowns, the matrix is then square with size $n \times n$.

The efficient solution of such linear systems of equations is of considerable interest. A decrease of computation time for one frequency step can decrease significantly decrease the overall computation time for a broad band computation. Presented here is the potential use of iterative algorithms for the solution of systems with dense matrices. One major issue is hereby the actual computer hardware the code is supposed to run on. Today, the use of hardware dependent libraries allows to achieve almost the theoretical maximum performance on a given processor. After presenting some characteristics of modern CPUs, we investigate the possible use of iterative algorithms by looking at two test cases.

Mathematically the eigenvalues and the singular values of the coefficient matrix have a significant influence on the convergence of iterative solvers, we therefore investigate the position of eigenvalues of two Moment Method matrices, and how a preconditioning can influence the position of the eigenvalues.

In this paper we use two moderately large matrices. One is taken from a recent paper [1] and produced by a 9 by 9 array of wiregrids. The second one is taken from the example files coming with Wiregrid (see html://www.emss.co.za/) and models a car. Pictures of the two models are shown in Fig. 1. The number of unknowns is 1944 for the array and 694 for the car.



(a) 9 by 9 array of wiregrids.

(b) Car model.

Figure 1: Wiregrid models used for NEC to produce Moment Method matrices.

2 Solving Linear Systems of Equations

2.1 Iterative algorithms for sparse matrices

Local methods like the finite difference or the finite element method involve the solution of systems with sparse matrices (i.e. most of the matrix elements are zero). The solution of these matrices is made by using iterative methods which produce a converging series X_i for the solution vector X by multiplications with the matrix A and possibly its transpose A^T. The computational cost is therefore proportional to the square of the number of non-zero elements for sparse matrices. This is then multiplied with the number of iterations.

Various iterative methods are known [2]. Usually a method is not used directly on the linear system itself, but on a modified system by applying a preconditioner

$$S_1 A S_2 X = S_1 B \tag{2}$$

with the preconditioner matrices S_1 and S_2. The intelligent use of preconditioning matrices S can significantly increase the convergence rate to solve (1).

2.2 Direct and iterative algorithms for dense matrices

In contrast to the local methods global methods as the Moment Method produce a system where the coefficient matrix A is dense, that is that all elements of A are non-zero and not neglect-able. The method of choice for solving systems with general matrices is the Gauss elimination. It comes with a computational cost of $\mathcal{O}\left(\frac{2}{3}n^3\right)$, hence increases with the third power of the number of unknowns.

Iterative algorithms compute again the solution vector by subsequent multiplying an iterate by the system matrix. Therefore the computation cost is the number of iterations times the square of the number of unknowns N. If the number of iterations is much less than the number of unknowns, the iterative algorithm will produce a result in a shorter time than the direct method.

Table 1: Run times for a 9 by 9 array of wiregrid patches

algorithm	$f = 299.8$ MHz factor in s	solution in s	total in s	$f = 500.0$ MHz factor in s	solution in s	total in s
original *LU*	378.19	1.10	379.29	376.79	1.13	377.92
LAPACK *LU*	72.76	0.44	73.20	75.47	0.45	75.92

A big influence on the computation time has the actual hardware the code is running on. Beside the ability of the compiler to produce highly optimised code, the programming of the code for a particular hardware is one major parameter for high performance code.

3 Computer Hardware Considerations

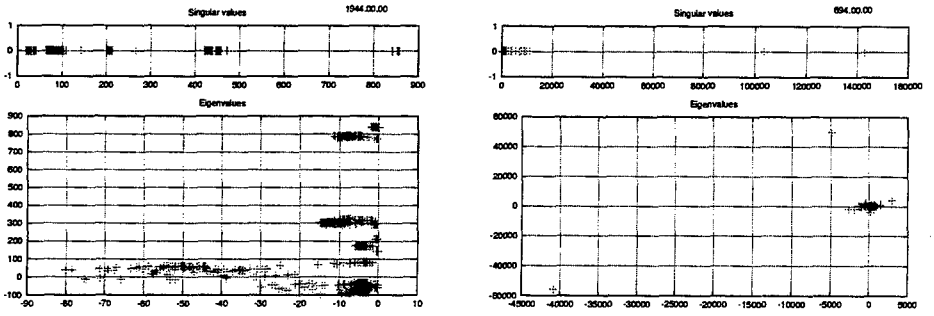
Modern computers are fitted with CPUs which implement many features known from high-end computers 10 years ago. Parallel computing, pipelining and integrated multiply-adds are included along with multiple stage cache memories in most modern RISC processors known in workstations and also in CISC processors as in PC computers. High programming skills are needed to use these high performance possibilities. As each processor has its own characteristics, these skills are also highly architecture dependent. Therefore the use of machine dependent libraries (BLAS, LAPACK, QMRPACK and the like) is mandatory to achieve the best performance.

The use of blocked algorithms [3, 4] for the well-known Gauss *LU* factorisation uses the memory system in an optimised way and allows to achieve almost the theoretical maximum performance on a given hardware. Table 1 shows a comparison of computation times for a text-book implementation of a Gauss *LU* factorisation in NEC 4, and the corresponding high performance implementation making use of the processors abilities (run times on IBM SP nodes, see [1]. Other run times in this paper are on HP C160 workstations).

4 Eigenvalues and Iterative Solvers

The distribution and position in the complex plane of the eigenvalues and the singular values of a coefficient matrix have a decisive influence on the convergence of iterative solvers. Different algorithms depend on either the eigenvalues or the singular values: The Conjugate Gradient Methods for the normal equations (CGN) is solely dependent on the singular values, whereas the Conjugate Gradient Squared (CGS) and the Biconjugate Gradient (BCG) are also influenced on the position of the eigenvalues in the complex plane [5]. We therefore determine the eigenvalues and the singular values for the above matrices.

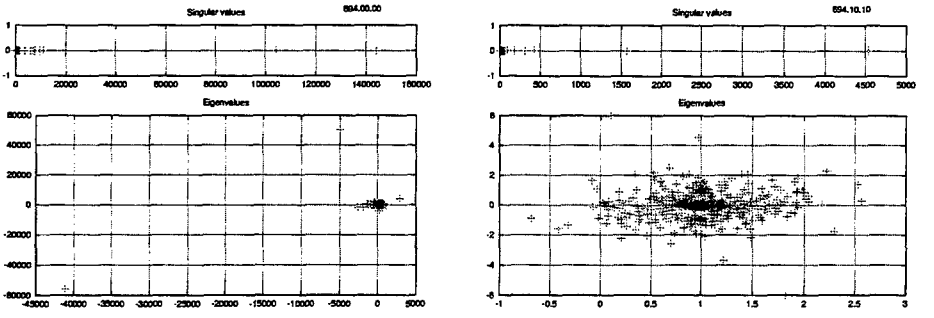
In Fig. 2 the eigenvalues and the singular values are shown for an unsorted matrix (basically the segments are numbered in an arbitrary way). The eigenvalues are all scattered around in the



(a) 9 by 9 array

(b) Car

Figure 2: Singular Values and Eigenvalues of the Two Test Cases - Unsorted.



(a) Sorted

(b) Sorted + Block Preconditioner

Figure 3: Singular Values and Eigenvalues of the Car Matrix. Elements are Sorted by Geometrical Proximity.

complex plane, there are two very large singular values and two widely eigenvalues scattered in the complex plane, rendering convergence very slow.

Now the segments are numbered so that two geometrically close segments are also close in the matrix. The eigenvalues and the singular values are shown in Fig. 3. The sorting of the elements can be considered as a preconditioning with the permutation matrices. The run-times obtained for the two cases is reported along with the results for the unsorted matrix in Tab. 2 and Tab. 3. As the matrix for the array case is already well sorted, no sorting was necessary in this case. It can be seen that no convergence was achieved for the car, the linear system is not solvable with a brute force application of an iterative algorithm.

Whereas the array of wiregrids is building a strongly diagonally dominant matrix, the unsorted

Table 2: Run-times for Test Case Array. - NC = No Convergence.

Algorithm	Preconditioner	Addtl. Storage	Iterations	Runtime / s
Blocked LU	-	-	-	162.62
TFQMR	-	0	127	62.12
TFQMR	scaling	0	74	36.56
TFQMR	band	37.4 MB	10	14.94
TFQMR	block (3 blocks)	19.22 MB	6	97.12

matrix for the car case is not exhibiting this dominance. The intensity plots in Fig. 4 shows clearly a strong main diagonal for the array case, but a very uniform matrix for the car case. The array has a very strong dominant main diagonal, hence the use of iterative solvers is possible. Iterative algorithms are less advised for the car due to the unfavourable structure of the matrix.

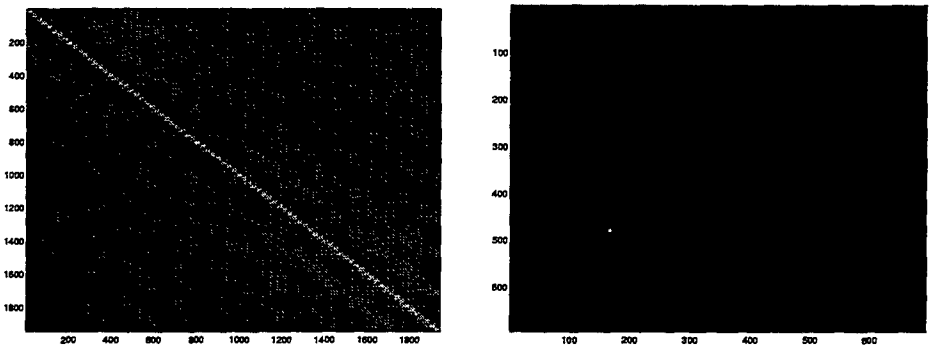
4.1 Preconditioned iterative algorithms

In Tab. 2 and Tab. 3 we report the run times for different preconditioners. The iterative algorithm used for all computations is the Transpose free quasi minimum residual iterative algorithm [6]. During our computations this algorithm converged the fastest.

The first preconditioner is the so-called Jacobi scaling preconditioner. The main diagonal elements are normalized by two diagonal matrices S_1 and S_2. The additional memory usage is just one vector of size n, as only the nonzero elements of S_1 and S_2 have to be held. Additionally the two vectors have the same elements so that one vector is sufficient.

The second preconditioner is the block preconditioner. The left precondition matrix S_1 is formed by a block diagonal matrix. The blocks on the main diagonal are the inverse of the same blocks in the system matrix A. The matrix $S_1 A$ has identity blocks on the main diagonal and dense subdiagonal blocks. It is closer to the identity which can be very well seen in the eigenvalue plot in Fig. 3. The eigenvalues are much closer to unity, the singular values are much lower. An iterative solver will converge in fewer steps.

The third preconditioner is a band matrix of the inverse of the main diagonal plus several sub-diagonals. The result of the preconditioner matrix and the system matrix $S_1 A$ will again be closer to the identity. In the tables can be seen that convergence can be achieved even for the car case, however with more memory requirements. For the small matrix size of 694 elements, the run times for the preconditioned iterative algorithms are higher than the corresponding Gauss factorisation. For bigger matrices this can revert, so that iterative solvers with an intelligent preconditioner may solve big systems faster than a direct algorithm.



(a) 9 by 9 array

(b) Car

Figure 4: Intensity Plots of the Two Test Matrices.

Table 3: Run-times for Test Case Car. - NC = No Convergence.

Algorithm	Preconditioner	Addtl. Storage	Iterations	Runtime / s
Blocked LU	-	-	-	2.5
TFQMR	-	0	NC	
TFQMR	sorting	-	NC	
TFQMR	scaling	-	NC	
TFQMR	band	2.2 MB	NC	
TFQMR	block (3 blocks)	2.4 MB	NC	
TFQMR	sorted + band	2.2 MB	269	24.25
TFQMR	sorted + block (3 blocks)	2.2 MB	248	18.0

5 Conclusions

The position of the eigenvalues and the singular values of two test Moment Method matrices were investigated. Iterative solvers seem to work well for Moment Method matrices if these are diagonally dominant. This can sometimes be forced by properly ordering the elements related to their geometrical position. Furthermore the use of sophisticated preconditioner is advisable for the application of iterative algorithms to dense matrices.

One of the best ways to improve the overall performance of linear algebra codes is to use the architecture specific libraries to obtain nearly the theoretical maximum performance.

Acknowledgements

The iterative solvers used are included in the QMRPACK package available at Netlib. Their use is acknowledged.

References

[1] J. v. Hagen, R. Mittra, and D. H. Werner, "MMSNEC – multiple matrix solver NEC," *15th Annual Review of Progress in Appl. Comp. Electromagnetics,* Monterey, CA, USA, Mar. 1999.

[2] R. W. Freund, G. H. Golub, and N. Nachtigal, "Iterative solution of linear systems," *Acta Numerica,* vol. 1, pp. 57–100, 1991.

[3] E. Anderson, Z. Bai, C. Bischof, J. Demmel, J. Dongarra, J. D. Corz, A. Greenbaum, S. Hammarling, A. McKenney, S. Ostrouchov, and D. Sorensen, *LAPACK Users' Guide.* Philadelphia, PA, USA: SIAM, 1992.

[4] G. H. Golub and C. F. van Loan, *Matrix Computations.* Baltimore and London: The Johns Hopkins University Press, 1996.

[5] N. M. Nachtigal, S. C. Reddy, and L. N. Trefethen, "How fast are nonsymmetric matrix iterations?," *SIAM Journal on Matrix Analysis and Applications,* vol. 13, pp. 778–795, July 1992.

[6] R. W. Freund and N. M. Nachtigal, "A transpose-free quasi-minimal residual algorithm for non-Hermitian linear systems," *SIAM Journal on Scientific Statistical Computing,* vol. 14, pp. 470–482, Mar. 1993.

Convergence Properties of the CFIE for Several Conducting Scatterers

William D. Wood, Jr. and Kueichien C. Hill
Air Force Research Laboratory
2591 K Street, Building 254
Wright-Patterson AFB OH 45433-7602

William J. Kent, Robert G. Layden, and Lisa A. Cravens
Mission Research Corporation
3975 Research Blvd.
Dayton OH 45430

Abstract

We investigate the numerical convergence properties of the combined field integral equation (CFIE). The result of the moment method based on the CFIE is known to approach the correct solution as the grid density increases, but we show that the rate of convergence can strongly depend on the choice of the CFIE parameter α. The dependence is shown to be greatest when the scattering is dominated by non-specular mechanisms. We present numerical results for a conducting sphere, trihedral corner reflector, ogive, and thin rod.

1 Introduction

Surface integral equations (SIEs) form the basis of most so-called "numerically exact" computational electromagnetics scattering computer software (codes). They possess the desirable properties of surface (rather than volume) discretization and exact coupling between physically separated components of the scatterer. As computer capabilities increase, codes based on SIEs may be applied to larger and larger problems, and the results are often not evaluated against rigorous convergence analyses [1]. In many cases, "rules of thumb" are used blindly. Such "rules of thumb" are derived based on experience gained by researchers and practitioners over (hopefully) years of use. However, they are prone to be relied upon in situations far different than those in which they were derived. Often, "rules of thumb" are accepted unquestioningly as gospel, and can, in some instances, lead to grave difficulties. The Air Force is actively pursuing highly accurate computational results for various canonical target shapes for use as radar cross section (RCS) measurement calibration standards, which drives the requirement for accurate SIE-based codes.

2 CFIE Formulation

The combined field integral equation (CFIE) is very popular in the analysis of closed conducting scatterers. It is based on the electric and magnetic field integral equations (EFIE and MFIE, respectively) and was first developed to solve the problem of real-valued eigenvalues of the EFIE and MFIE. The EFIE can be written

$$\hat{n} \times \vec{E}^{\text{inc}} = \frac{1}{jkY} \hat{n} \times \text{P.V.} \int_S \left\{ -k^2 \vec{J}\, \varphi + \nabla'_s \cdot \vec{J}\, \nabla' \varphi \right\} ds' \quad (1)$$

while the MFIE is written

$$\hat{n} \times \vec{H}^{\text{inc}} = \frac{1}{2} \vec{J} - \hat{n} \times \text{P.V.} \int_S \vec{J} \times \nabla' \varphi \, ds' \quad (2)$$

where $\vec{E}^{\text{inc}}$ and $\vec{H}^{\text{inc}}$ are the incident fields, S is the surface of the conducting scatterer, $\hat{n}$ is the outward unit normal, P.V. $\int$ is a principal value integral, $k = 2\pi/\lambda$ is the wavenumber of the surrounding medium, Y is the intrinsic admittance of the surrounding medium, $\vec{J} = \hat{n} \times \vec{H}$ on S, and $\varphi = \exp(-jk|\vec{r} - \vec{r}'|)/(4\pi|\vec{r} - \vec{r}'|)$ is the Green function for the (suppressed) $\exp(j\omega t)$ time convention.

Mitzner is often credited as originating the CFIE [2]; Poggio and Miller [3] present it as

$$\{(1-\alpha)(1/2 - \mathcal{L}) + \alpha \hat{n} \times \mathcal{M}\} \vec{J} = (1-\alpha) \hat{n} \times \vec{H}^{\text{inc}} + \alpha Y \hat{n} \times \left(\vec{E}^{\text{inc}} \times \hat{n} \right) \quad (3)$$

where $\mathcal{L}$ is the integral operator in (1), $\mathcal{M}$ is the integral operator in (2), and α is an arbitrary real constant between 0 and 1. α effectively weights the contribution of the EFIE and MFIE: $\alpha = 0$ degenerates to the MFIE, $\alpha = 1$ degenerates to the EFIE, and $\alpha = 0.5$ weights the EFIE and MFIE equally.

Along with possessing no real-valued eigenvalues, the CFIE is also generally better conditioned than either the EFIE or MFIE. It is this latter property that is most attractive to computer software writers, as it tends to reduce sensitivity to numerical errors in computing the impedance matrix terms, or, in the case of iterative solution, reduces the number of iterations necessary to reach a given residual threshold. In the spirit that the EFIE and MFIE should be weighted equally, many practitioners have adopted a "rule of thumb" that a value of $\alpha = 0.5$ is appropriate to use in nearly all cases. However, as we shall show in the following sections, the accuracy of the results can vary alarmingly with α, especially when non-specular scattering mechanisms dominate the far-field scattering.

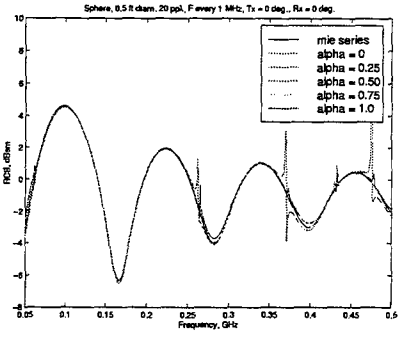


Figure 1: Monostatic RCS of a 6-inch diameter conducting sphere, comparison of CFIE to Mie series. The spikes are seen in the pure MFIE and EFIE results only. Curves are well-converged at a discretization density of 20 points/λ.

3 Numerical Results

Here we present numerical result for four conducting geometries, analyzed using mature, well-known moment method codes. The first target is the sphere, useful because it has an exact series analytical reference solution. The second target is a corner reflector whose RCS is dominated by specular scattering mechanisms. The third target is an ogive, with scattering properties exhibiting a large dynamic range as a function of angle and the presence of dominant non-specular scattering mechanisms. The fourth target is a thin rod, which also has strong "second order" physics dominating its RCS.

3.1 Sphere

The sphere is the one target for which results can be obtained to very high accuracy without using a method of moments computational approach, since the Mie series solution is available [4]. Comparison of a portion of the scat-

tering spectrum using MFIE, EFIE, and CFIE (for various values of α) as well as a Mie series solution is shown in Figure 1. This illustrates the need for the CFIE: values of $\alpha = 0$ (MFIE) and $\alpha = 1$ (EFIE) result in spurious resonance-type phenomena which are clearly anomalies. The CFIE was originally introduced to control these problems [2]. The figure shows that the anomalies occur for both EFIE and MFIE, but do not exist in the CFIE results for $0.25 < \alpha < 0.75$. As can be seen from the curves, the choice of the numerical value of α for this case is fairly irrelevant: the agreement with the Mie series is reasonably close. Often for problems in general, a value of $\alpha = 0.5$ is chosen somewhat arbitrarily, and the discretization is set at computationally affordable value, usually at about 20 points per wavelength for the highest frequency needed. As will be seen in the following paragraphs, this may not be an appropriate strategy in general.

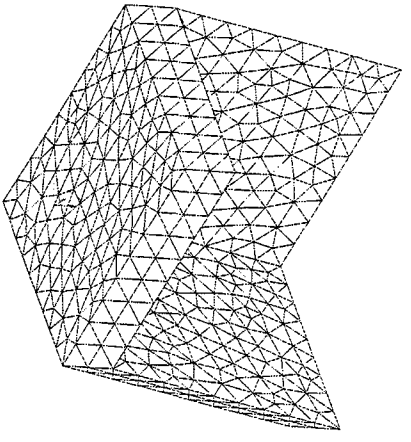


Figure 2: Trihedral Geometry. The trihedral is built out of 0.375-inch thick plates, exterior edges beveled at 45°. The three interior (reflecting) surfaces are square, 3 inches by 3 inches each.

3.2 Trihedral Corner Reflector

The trihedral corner reflector is a target that has recently come under scrutiny for use as a high-RCS calibration standard for scattering measurements. Each of the three reflecting surfaces is a 3-inch by 3-inch square, the thickness of each plate is 0.375 inches, and the exterior edges are beveled at 45°. The trihedral geometry is shown in Figure 2. The maximal monostatic RCS is presented when the projection onto the incident field plane is largest.

Like the sphere, the scattering from the trihedral is dominated by a specular mechanism. However, the CFIE calculations show a significant variation as a function of grid density and α, as shown in Figure 3. For some applications, the variation in RCS is within tolerance, but for calibration purposes the variation translates directly into overall RCS measurement uncertainty. Indeed, measurement uncertainty is bounded below by uncertainty in the reference RCS of the calibration standard.

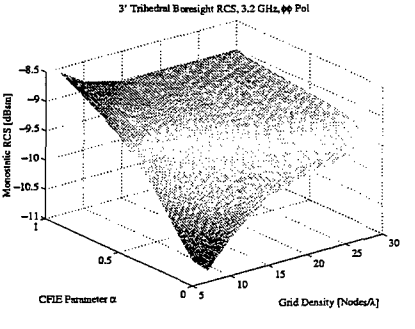


Figure 3: Monostatic RCS of trihedral. Computations were made with a general-purpose MoM code using an iterative matrix solver employing the fast multipole method.

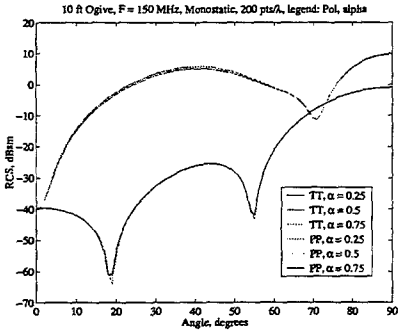


Figure 4: Monostatic RCS of the 10-foot ogive at 150 MHz. Results are plotted for both polarizations and α equal to 0.25, 0.50, and 0.75. Discretization density is 200 points/λ! Note that the lower curves ($\phi\phi$ pol) are well converged, but there is still some separation in the $\theta\theta$ pol as a function of α.

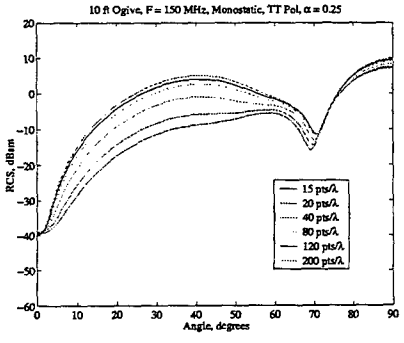


Figure 5: Monostatic RCS of the 10-foot ogive at 150 MHz, $\theta\theta$ polarization. Results are plotted for various discretization densities. Note that at 40 points/λ the results are far from converged, even though such a fine discretization is normally considered more than sufficient.

3.3 Conducting Ogive

The conducting ogive is an object which is very useful for RCS measurement range diagnostics. At nose-on incidence, it has low backscattering levels in both principal polarizations, and its wideband signature has trends opposite to that of a sphere: it starts high at low frequencies, and slowly falls as frequency increases. In the "downrange" domain, its signature is seen as principally dominated by tip responses, so that target mounting levels can be easily diagnosed and controlled, especially for large geometries. The ogive can exhibit high dynamic range (50-70 dB from nose to side at high frequencies) and, being a body of revolution (BOR), is in principle calculable using a "numerically exact" BOR formulation of a CFIE code [5]. The results given here are for a large conducting ogive target, 10 feet in length and one foot in diameter at the center (recall that an ogive is formed by rotating a circular arc about its chord). At one polarization (E-field in the scan plane, *i.e.*, $\theta\theta$ polarization), a traveling wave dominates the near nose-on scattering for a significant angular extent near 30° off the ogive axis. Although this is very clear at frequencies where the object is electrically large, we show lower frequency results only, due to computer run-time considerations. Figure 4 depicts the results for both principal polarizations for the 10-foot ogive at 150 MHz. Results for a range of α values are shown. For the non-traveling wave polarization ($\phi\phi$, or "PP" on the plots), all three curves are identical on this scale. Note that this was obtained using 200 points per wavelength. Figure 5 gives the results for α set at 0.25, for various values of points per wavelength. The inaccuracies seen in the traveling wave lobes is very high indeed, and is still almost 10 dB from the final converged answer at discretization of 40 points per wavelength. Note that many engineering computations are performed at a maximum of 20 points per wavelength due to problem size and computer time constraints. Similar results have been obtained for various values of α; the convergence for some α values is faster than others. All eventually converge to the same curve

sets as in Figure 4, but at discretization values far higher than is practical for many computational problems.

3.4 The Long Thin Rod

Another calibration target of interest to the RCS measurement range is the long thin rod. At 0° elevation (rod axis horizontal to the ground), there is a co-polarization signature ($\theta\theta$ and $\phi\phi$) from the rod, but no cross-polarization signatures ($\theta\phi$ and $\phi\theta$). However, at 45° elevation (rod axis forms a 45° angle with respect to the ground), both co-polarization and cross-polarization signatures exist. The $\theta\phi$ and $\phi\theta$ signature should be the same when the 45° elevated rod is broadside to the radar. This configuration provides a check for the cross-polarization quality of the measurement. Even though for this case the pattern cut is not on one of the principal planes of a BOR target, BOR codes can still be used to generate the theoretical results. This is done by calculating the $\theta\theta$ and $\phi\phi$ signatures at 0° elevation then performing a coordinate transformation to correctly predict the signature for the desired pattern cut. The cross-polarization arises due to the coordinate transformation. The results shown in Figures 6 and 7 are for 0° elevation at 140 MHz. The rod is 12 feet long with a 1.66 inch diameter. For $\theta\theta$ polarization the EFIE results converge at a grid density of 50 points per wavelength while the CFIE (with $\alpha = 0.5$) fails to converge even at 120 points per wavelength. For $\phi\phi$ polarization the CFIE results converge at 90 points per wavelength while the EFIE still has not converged at 120 points per wavelength. This case demonstrates that the choice of α and grid density is highly sensitive to polarization, even for the same target!

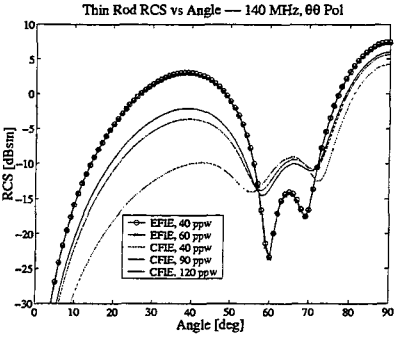


Figure 6: Monostatic RCS of long thin rod at 140 MHz, $\theta\theta$ polarization. The rod is 12 feet long and 1.66 inches in diameter. EFIE means $\alpha = 1$ and CFIE means $\alpha = 0.5$; 'ppw' means points/λ. Note the very poor convergence of the CFIE results.

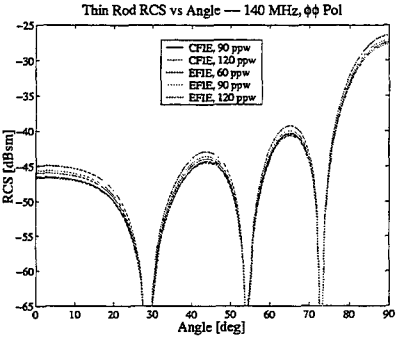


Figure 7: Monostatic RCS of long thin rod at 140 MHz, $\phi\phi$ polarization. Note the poor convergence of the EFIE for $\phi\phi$ polarization.

4 Conclusions

In this paper, we have discussed the role of the combined field integral equation in computational electromagnetics, concentrating on its convergence properties. We have presented results showing that we must use CFIE because it

controls the "resonance anomalies" that plague pure EFIE and MFIE results. These anomalies are unpredictable and will be found in wideband results that are needed in modern scattering analyses. We have demonstrated that the accuracy of the CFIE results depend very strongly on both the value of α weighting the EFIE and MFIE contribution, and the fineness of discretization (points per wavelength). The most distressing aspect we discovered is that the value of α that produces the fastest convergence is problem-dependent and may or may not be consistent with matrix condition number. The quickest convergence is usually found for targets that are dominated by specular-type scattering mechanisms (*e.g.*, sphere, cylinder, corner reflector), and is not overly sensitive to choice of α for most (but not all) applications. The slowest convergence is exhibited for long thin scatterers which support traveling waves, such as the ogive and the rod. In particular, convergence of the traveling wave lobe is exquisitely sensitive to the choice of α. Convergence properties at lower frequencies may or may not show the same trends at higher frequencies. In other words, if $\alpha = 0.75$ gives the fastest convergence at 150 MHz (where it is easy to run a thorough and wide-ranging convergence test), it may or may not be the fastest-converging α for 10 GHz (where such a test would be impractical in terms of computational resources). It is this lack of a generalizable rule that causes the most concern among the authors. We hope that further research can quantify the reasons for this in the near future.

References

[1] Pflug, D.R., "Some present and future aspects of the quality of solution in computational electromagnetics," in *14th Annual Review of Progress in Applied Computational Electromagnetics*, 1998, vol. 1, pp. 42–49.

[2] Mitzner, K.M., "Numerical solution of the exterior scattering problem at eigenfrequencies of the interior problem," in *1968 Fall URSI Meeting Proceedings*, 1968.

[3] Poggio, A.J. and Miller, E.K., "Integral equation solutions of three-dimensional scattering problems," in *Computer Techniques for Electromagnetics*, Mittra, R., Ed., pp. 159–265. Hemisphere, Washington, D.C., 1987.

[4] Van De Hulst, H.C., *Light Scattering by Small Particles*, John Wiley & Sons, New York, 1957.

[5] Medgyesi-Mitschang, L.N. and Putnam, J.M., "Electromagnetic scattering from axially inhomogeneous bodies of revolution," *ieee-tap*, vol. AP–32, no. 8, pp. 797–806, Aug. 1984.

Modeling of General Surface Junctions of Composite Objects in an SIE/MoM Formulation

Joon Shin, Allen W. Glisson, and Ahmed A. Kishk
Department of Electrical Engineering
University of Mississippi, University, MS 38677

Abstract This paper discusses the modeling of various kinds of surface junctions in an SIE/MoM (Surface Integral Equation / Method of Moments) formulation applied to complex objects consisting of arbitrarily shaped conducting and dielectric bodies. Methods of describing various types of junctions and systematically incorporating them in numerical solutions are presented. The procedures are of interest for the specific application of arbitrarily shaped dielectric resonator antennas and their associated feed structures and packaging. An E-PMCHW formulation in conjunction with a moment method procedure using generalized triangular basis functions is presented to deal with such general junctions.

I. Introduction

The modeling of general surface junctions in an SIE/MoM formulation is considered in this work. The specific application leading to this study is that of a dielectric resonator (DR) antenna. Since an experimental study of a cylindrical dielectric resonator (DR) antenna was reported in 1983 [1], this antenna has drawn continued interest because of its small size, efficiency, and potential ability to perform multiple antenna tasks via simple mode coupling mechanisms. The configuration of a DR antenna may range from a very simple one which allows analytic solutions to a very complex one. A typical structure for a DR antenna is a DR element of high dielectric constant excited by a single feed such as a microstripline or coaxial cable. Various shapes and combinations of DR elements as well as various feed structures have been suggested, however, which may improve the antenna performance in the areas of bandwidth, power handling, and antenna efficiency.

Rigorous SIE analysis methods for non-trivial DR antenna configurations have been available mainly for body of revolution (BOR) objects [2,3]. This work results from an interest in the analysis of DR antennas of more arbitrary configurations, which may include general 3D objects comprising an arbitrary combination of conducting and/or dielectric bodies of arbitrary shapes, using an SIE/MoM method with triangular patch basis functions. The junction modeling problem has been considered in previous works for conducting surfaces [4], for dielectric surfaces [5], simple combinations of both for BOR objects [2,3,6,7], and for a general case of conducting, dielectric, resistive, and impedance boundary condition surfaces [8]. This work attempts to provide a formalism for systematically describing junction models for a wide variety of junction types.

II. Formulation

A. Problem Description

The geometry under consideration is a general inhomogeneous body with N_R dielectric regions, each of which may contain conducting bodies as well as impressed sources as shown in Fig. 1.

The regions have permittivities ϵ_i and permeabilities μ_i, where $i = 1, \ldots, N_R$. Both ϵ_i and μ_i may be complex to represent lossy materials. Non-zero thickness conducting bodies denoted by R_0 may occupy any parts of the space. Infinitely thin conducting bodies can reside in any region, at interfaces between regions, or they may penetrate from one region to another. All conductors are considered to be PEC (Perfect Electric Conductor) material. One of the regions, region R_1 in Fig. 1, may be of infinite extent. The total fields in each region are denoted by $\mathbf{E}_i$ and $\mathbf{H}_i$, where $i = 0, 1, 2, \ldots, N_R$, for electric and magnetic fields, respectively, and $i = 0$ denotes PEC regions with $\mathbf{E}_0 = \mathbf{H}_0 = \mathbf{0}$. The time variation, $e^{j\omega t}$, is assumed and suppressed throughout.

Any two adjacent regions, R_i and R_j, are separated by a surface denoted by $S_{ij}(t_s, t, f)$, where t_s is the type of the surface, and t and f are the 'to-region' and the 'from-region' of the surface, respectively, which define the region connectivity and the surface orientation. The interface between a non-zero thickness conducting body and a dielectric region also forms a surface denoted in the same way with the 'from-region' being region zero. An infinitely thin conducting body in a dielectric region forms yet another type of surface with the 'from-region' being the same as the 'to-region. Thus, as shown in Fig. 1, there are four types of surfaces specified by t_s —

- Type-0 ($t_s = 0$, pf0) ; interface between a conducting body and a dielectric region,
- Type-1 ($t_s = 1$, pf1) ; infinitely thin conducting body within a dielectric region,
- Type-2 ($t_s = 2$, pf2) ; infinitely thin conducting body between two dielectric regions, and
- Type-3 ($t_s = 3$, df) ; dielectric interface between two dielectric regions.

When more than two surfaces meet at a curved line segment, they form a junction. Depending on the numbers and types of the surfaces at a junction, there are a variety of possible junction types, all of which are considered in this study.

Each region R_i is surrounded by a closed surface S_i^C and is associated with an inward normal unit vector $\hat{\mathbf{n}}_i$. The surface interface between regions R_i and R_j, if one exists, is denoted as S_{ij}, for any i and j, $i = 1, \ldots, N_R$, $j = 0, 1, \ldots, N_R$. Thus, S_i^C is the set of all interface surfaces S_{ij}, where j represents all region numbers that interface with region R_i. Note that $S_{ij} = S_{ji}$ for $j \neq 0$; however, the normal unit vectors $\hat{\mathbf{n}}_i$ and $\hat{\mathbf{n}}_j$ are in opposite directions to each other on S_{ij}.

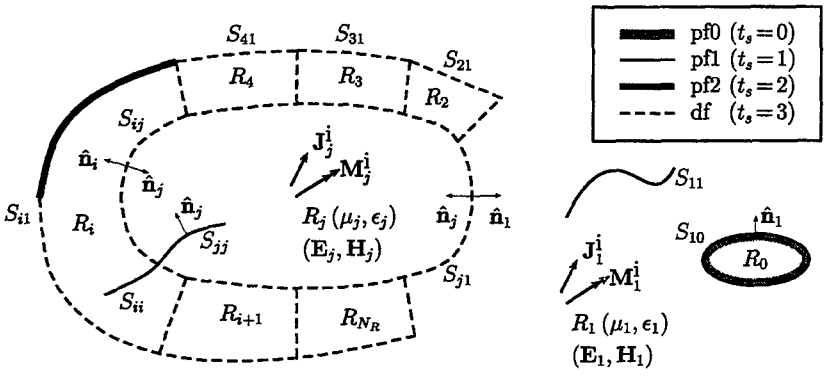


Fig. 1. General geometry under consideration.

B. The Field Equivalences

According to the equivalence principle [9], the original problem can be decomposed into N_R auxiliary problems, one for each dielectric region. To obtain the auxiliary problem for region R_i, the impressed sources of the original problem are retained only in region R_i and the boundaries of the region are replaced by equivalent surface currents radiating in a homogeneous medium with the constitutive parameters of region R_i. Electric currents are used for the conducting surfaces, while electric and magnetic currents are used for the dielectric boundaries. The electric and magnetic currents appearing on opposite sides of a dielectric interface in different auxiliary problems are taken equal in magnitude and opposite in direction to assure the continuity of the tangential components on these boundaries as they are continuous in the original problem. In this procedure, the fields produced within the region boundaries by the equivalent currents and the impressed sources in region R_i must be the same as those in the original problem, while the zero field is produced outside these boundaries. The electric and magnetic currents along S_i^C are $\mathbf{J}_i = \hat{\mathbf{n}}_i \times \mathbf{H}_i$ and $\mathbf{M}_i = \mathbf{E}_i \times \hat{\mathbf{n}}_i$, respectively.

A system of surface integro-differential equations can be obtained by enforcing the boundary conditions of continuity of the tangential components of electric field on the conducting surfaces and both electric and magnetic fields on the dielectric surfaces. This results in the E-PMCHW formulation [6] when there is no junction in the problem. For problems having general junctions, however, it is not easy to express the integral equation system explicitly apart from the testing procedure. Thus the system of integral equations is presented in the next section after describing the junction modeling and the basis functions.

C. Modeling of Junctions in the Moment Method Solution

Arbitrarily shaped surfaces are discretized in triangular patches and the equivalent surface currents are approximated by expansions in the RWG basis functions on the patches, which are expressed as [10]

$$\mathbf{J}(\mathbf{r}) \cong \sum_{n=1}^{N_{T_j}} I_n \mathbf{B}_n^{T_j}(\mathbf{r}; S_{T_n}^+, S_{T_n}^-) \tag{1}$$

where,

$$\mathbf{B}_n^{T_j}(\mathbf{r}) = \begin{cases} \pm \boldsymbol{\rho}_n^{\pm}/h_n^{\pm}, & \mathbf{r} \in S_{T_n}^{\pm} \\ \mathbf{0}, & \text{otherwise,} \end{cases} \tag{2}$$

N_{T_j} is the number of electric basis functions, and $S_{T_n}^{\pm}$ are the positive/negative domains or the from-/to- faces of the basis function, respectively. For magnetic currents, $\{\mathbf{B}_n^{T_m}\}_{n=1}^{N_{T_m}}$ can be defined similarly. The testing functions $\mathbf{T}_n^{T_j}$ and $\mathbf{T}_n^{T_m}$ are also taken to be the same as (2). With the basis and testing functions defined we have a matrix equation

$$\begin{bmatrix} \mathbf{Z}^{T_j T_j} & \mathbf{T}^{T_j T_m} \\ \mathbf{T}^{T_m T_j} & \mathbf{Y}^{T_m T_m} \end{bmatrix} \begin{bmatrix} |I^{T_j}\rangle \\ |I^{T_m}\rangle \end{bmatrix} = \begin{bmatrix} |V^{T_j}\rangle \\ |V^{T_m}\rangle \end{bmatrix} \tag{3}$$

When there are general surface junctions, the current related to an unknown coefficient may exist on many different surfaces. In such cases, the expression (1) is not rigorous enough. For example, there is an electric current on a dielectric surface in the region R_i equivalent problem and another one flowing in the opposite direction in the region R_j problem, represented by '$-I_n$'

as shown in Fig. 2(a). The expression in (1) for the electric currents has this sort of implication for the basis functions $\mathbf{B}_n^{T_j}$ when the domain of the unknown involves a dielectric interface. When more than two dielectric surfaces meet at a junction, this scheme does not work. Thus for general junctions, we seek another way of expressing the generalized current more rigorously. We will use two different basis functions for the same unknown coefficient related to a dielectric surface as shown in Fig. 2(b). In other words, the unknown coefficient has a multiplicity of two when it represents the electric or magnetic current on the dielectric face. Extending this to the general case, the generalized current is defined in terms of the generalized basis functions as

$$\mathbf{C}(\mathbf{r}) = \{\mathbf{J}(\mathbf{r}), \mathbf{M}(\mathbf{r})\} = \{\sum_{n=1}^{N_{T_j}} I_n \mathbf{B}_n(\mathbf{r}), \sum_{n=1+N_{T_j}}^{N} I_n \mathbf{B}_n(\mathbf{r})\} \tag{4}$$

where,

$$\mathbf{B}_n(\mathbf{r}) = \mathbf{B}_k^{T_j}(\mathbf{r}), \;\; \mathbf{B}_{n_v}(\mathbf{r}) = \mathbf{B}_{k_v}^{T_j}(\mathbf{r}), \;\; \tau_n = \tau_k, \qquad \text{with } k = n, \qquad \text{if } \; n \le N_{T_j} \tag{5}$$

$$\mathbf{B}_n(\mathbf{r}) = \mathbf{B}_k^{T_m}(\mathbf{r}), \;\; \mathbf{B}_{n_v}(\mathbf{r}) = \mathbf{B}_{k_v}^{T_m}(\mathbf{r}), \;\; \tau_n = \tau_k, \qquad \text{with } k = n - N_{T_j}, \qquad \text{if } \; n > N_{T_j} \tag{6}$$

$$N = N_{T_j} + N_{T_m}$$

$$\mathbf{B}_k^{T_j}(\mathbf{r}) = \sum_{v=1}^{\tau_k} \mathbf{B}_{k_v}^{T_j}(\mathbf{r}; ff_{k_v}, tf_{k_v}, R_{k_v}) \tag{7}$$

$$\mathbf{B}_k^{T_m}(\mathbf{r}) = \sum_{v=1}^{\tau_k} \mathbf{B}_{k_v}^{T_m}(\mathbf{r}; ff_{k_v}, tf_{k_v}, R_{k_v}) \tag{8}$$

$\mathbf{B}_{n_v}$ = the v^{th} basis function of I_n, $v = 1, ..., \tau_n$

$\mathbf{B}_{k_v}^{T_j}, \mathbf{B}_{k_v}^{T_m}$ = RWG basis function defined over the corresponding patches as in (2)

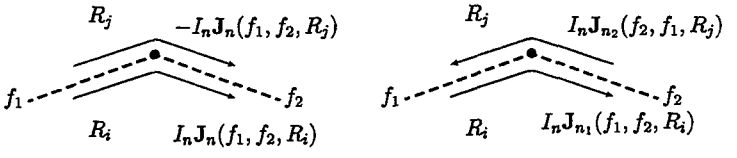
τ_n = multiplicity of the unknown coefficient, $I_n = \begin{cases} n_{dfn}, & n_{dfn} = n_{tf} \\ n_{dfn} + 1, & \text{otherwise} \end{cases}$

n_{tf} = total number of faces (surfaces) connected to the junction for I_n

n_{dfn} = number of dielectric faces (surfaces) related to I_n

ff_{n_v}, tf_{n_v} = from-face and to-face of $\mathbf{B}_{n_v}$.

R_{n_v} = region of $\mathbf{B}_{n_v}$.



(a) Conventional representation (b) New representation

Fig. 2. Two methods of representing basis functions.

Notice that there is one-to-one correspondence between $\mathbf{B}_{n_v}^{T_j}$ or $\mathbf{B}_{n_v}^{T_m}$ and the parameter set $\{ff_{n_v}, tf_{n_v}, R_{n_v}\}$. The numbers of unknowns and basis functions for a given junction or edge are determined from the types and numbers of the faces connected to the junction by considering proper boundary conditions at the junction. The methods of determining them and systematically incorporating them in the MoM solutions have been developed. Examples of modeling general junctions are shown in Fig. 3, where J_n and M_n are used instead of $\mathbf{B}_n^{T_j}$ and $\mathbf{B}_n^{T_m}$, respectively. The generalized testing functions $\{\mathbf{T}_m^{T_j}\}_{m=1}^{N_{T_j}}$, $\{\mathbf{T}_m^{T_m}\}_{m=1}^{N_{T_m}}$, and $\{\mathbf{T}_m\}_{m=1}^{N}$ are also defined in a similar manner. We also define $\mathbf{C}_i$, the generalized current for the region R_i equivalent problem, as

$$\mathbf{C}_i(\mathbf{r}) = \{\mathbf{J}_i(\mathbf{r}), \mathbf{M}_i(\mathbf{r})\} \tag{9}$$

where

$$\mathbf{J}_i(\mathbf{r}) = \sum_{n=1}^{N_{T_j}} I_n \sum_{v=1}^{\tau_n} \delta_{n_v i}^S \mathbf{B}_{n_v}(\mathbf{r}; ff_{n_v}, tf_{n_v}, R_{n_v}) \tag{10}$$

$$\mathbf{M}_i(\mathbf{r}) = \sum_{n=N_{T_j}+1}^{N} I_n \sum_{v=1}^{\tau_n} \delta_{n_v i}^S \mathbf{B}_{n_v}(\mathbf{r}; ff_{n_v}, tf_{n_v}, R_{n_v}) \tag{11}$$

$$\delta_{n_v i}^S = \text{source contribution coefficient} = \begin{cases} 1, & R_{n_v} = R_i \\ 0, & \text{otherwise} \end{cases}$$

With the set of basis functions in (4–8), one may apply the boundary conditions of tangential field continuity at each sub-domain of the basis functions. By merely applying the boundary conditions, however, the total number of equations may be greater than the number of the unknowns because of the multiplicity of some unknowns related to junctions. The usual methods of solving equations apply only when the number of equations equals to the number of unknowns, N. Such a set of N equations can be obtained by taking the n^{th} integral equation as the set of simultaneous integral equations (or summation of them) which satisfy the proper boundary conditions on the subdomains of the basis functions ($\mathbf{B}_{n_v}, v = 1, ..., \tau_n$) related to the unknown coefficient, I_n. It is possible to get such a surface integral equation system by testing with the generalized testing functions as follows

$$\sum_{i=1}^{N_R} \langle\, \mathbf{E}_i^S(\mathbf{C}_i)|_{\tan}, \sum_{u=1}^{\tau_m} \delta_{m_u i}^F \mathbf{T}_{m_u} \,\rangle = -\sum_{i=1}^{N_R} \langle\, \mathbf{E}_i^i|_{\tan}, \sum_{u=1}^{\tau_m} \delta_{m_u i}^F \mathbf{T}_{m_u} \,\rangle, \quad m = 1, 2, ..., N_{T_j} \tag{12}$$

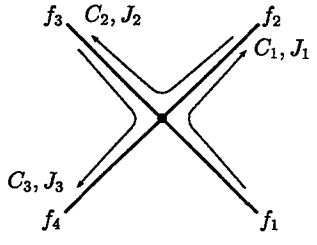
$$\sum_{i=1}^{N_R} \langle\, \hat{\mathbf{n}}_i \times \mathbf{H}_i^S(\mathbf{C}_i), \sum_{u=1}^{\tau_m} \delta_{m_u i}^F \mathbf{T}_{m_u} \,\rangle = -\sum_{i=1}^{N_R} \langle\, \hat{\mathbf{n}}_i \times \mathbf{H}_i^i, \sum_{u=1}^{\tau_m} \delta_{m_u i}^F \mathbf{T}_{m_u} \,\rangle,$$
$$m = N_{T_j} + 1, ..., N_{T_j} + N_{T_m}, \tag{13}$$

where,

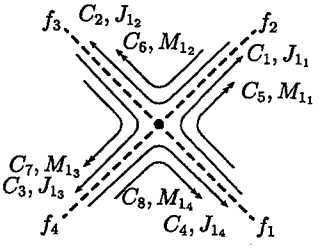
$$\langle\, \mathbf{f}, \mathbf{g} \,\rangle = \int_S \mathbf{f} \cdot \mathbf{g}\, ds$$

$$\delta_{m_u i}^F = \text{field contribution coefficient} = \begin{cases} 1, & R_i = R_{m_u} \\ 0, & \text{otherwise} \end{cases}$$

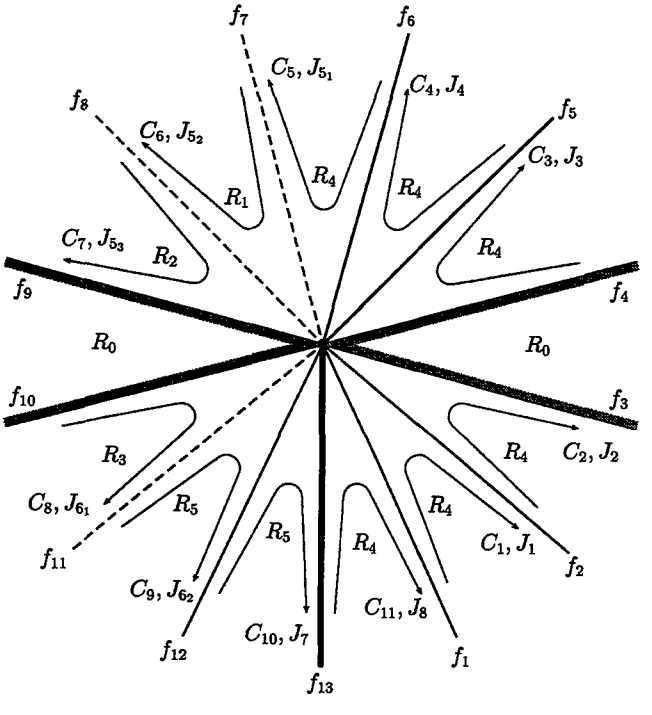
$$R_{m_u} = \text{region of the testing function, } \mathbf{T}_{m_u},$$



(a) All faces are pfl ($n_{tf} = n_{pf1} = 4$).



(b) All faces are df ($n_{tf} = n_{df} = 4$).



(c) A general case ($n_{tf} = 13, n_{pf0} = 4, n_{pf1} = 5, n_{pf2} = 1, n_{df} = 3$).

Fig. 3. Modeling of general surface junctions. ($C_i, i = 1, 2, 3, ...$, is an entry-counting index.)

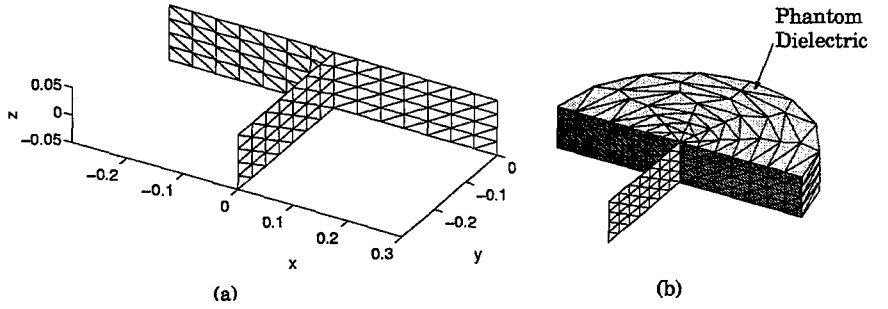


Fig. 4. A test case. (a) PEC alone (b) with phantom dielectric.

and $(\mathbf{E}_i^S,\ \mathbf{H}_i^S)$ and $(\mathbf{E}_i^i,\ \mathbf{H}_i^i)$ are the scattered fields due to $\mathbf{C}_i$ and incident fields, respectively. Equations (12) and (13) are the E-PMCHW formulation [6] extended to general junctions. Substituting $\mathbf{C}_i$ into (12) and (13), the impedance matrix and excitation vector elements in (3), $Z_{mn}^{T_jT_j}$ and $V_m^{T_j}$, for example, are expressed as

$$Z_{mn}^{T_jT_j} = \sum_{i=1}^{N_R} \langle\, [\mathbf{E}_i^S(\sum_{v=1}^{\tau_n} \delta_{n_v i}^S \mathbf{B}_{n_v}(\mathbf{r}'; ff_{n_v}, tf_{n_v}, R_{n_v}))]|_{\tan}, \sum_{u=1}^{\tau_m} \delta_{m_u i}^F \mathbf{B}_{m_u}(\mathbf{r}; ff_{m_u}, tf_{m_u}, R_{m_u}) \,\rangle,$$
$$n = 1, ..., N_{T_j} \text{ and } m = 1, ..., N_{T_j} \quad (14)$$

$$V_m^{T_j} = -\sum_{i=1}^{N_R} \langle\, \mathbf{E}_i^i|_{\tan}, \sum_{u=1}^{\tau_m} \delta_{m_u i}^F \mathbf{B}_{m_u}(\mathbf{r}; ff_{m_u}, tf_{m_u}, R_{m_u}) \,\rangle, \quad m = 1, ..., N_{T_j} \quad (15)$$

Some subroutines of EMPACK [11] have been used for the integrations over the triangular domains which appear in (14) implicitly.

III. Numerical Results

A T-shape junction of three 0.1-m wide and 0.3-m long PEC strips is taken as an example. For comparison a semi-circular cylinder of phantom dielectric having 0.1-m height and 0.3-m radius is attached to the T-shape junction as shown in Fig. 4. The z-directed surface currents along the contour lines, $(-0.3, 0, 0) \rightarrow (0.3, 0, 0)$ and $(0, 0, 0) \rightarrow (0, -0.3, 0)$, located at the center of each strip are computed for a plane wave excitation. The plane wave is expressed as $\mathbf{E}^{inc} = E_o\, e^{k_o \hat{k}^i \cdot \mathbf{r}}$, where, $\hat{k}^i = -\hat{x}\cos\phi^i \sin\theta^i - \hat{y}\sin\phi^i \sin\theta^i - \hat{z}\cos\theta^i$, $E_o = E_\theta^i(\hat{x}\cos\theta^i\cos\phi^i + \hat{y}\cos\theta^i\sin\phi^i - \hat{z}\sin\theta^i)$, $\theta^i = \phi^i = 45°$, $E_\theta^i = 1$, $k_o = 2\pi f\sqrt{\mu_o \epsilon_o}$, and $f = 300$ MHz. The results in Fig. 5 show very good agreement as well as the expected singularities at the end of the strips.

IV. Conclusion

A systematic procedure for modeling of the general junctions of any combination of conducting and/or dielectric bodies in an SIE/MoM formulation has been presented. With the successful modeling of general junctions, it is possible to apply the E-PMCHW formulation to a large class of problems including dielectric resonator antennas of complex configuration.

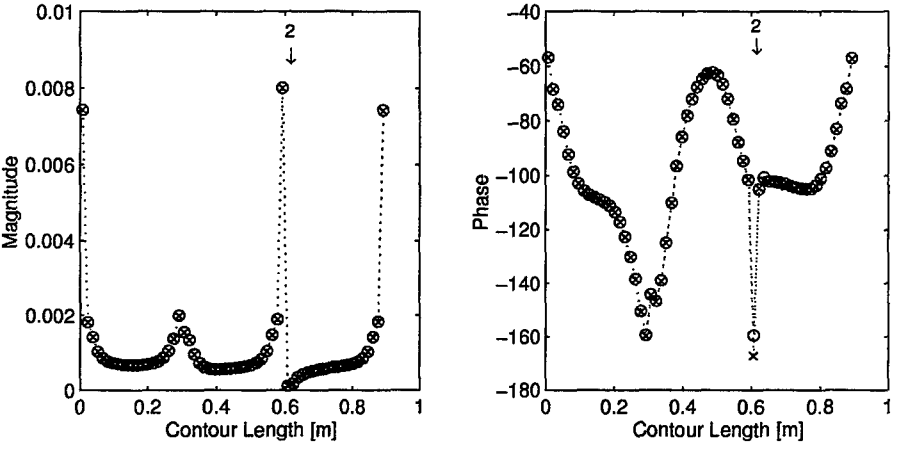


Fig. 5. z-directed current densities along the contours ($\circ$; PEC alone, $\times$; with phantom dielectric). The arrows denote the start of the second contour.

V. Acknowledgment

This work was supported by The Army Research Office under grant No. DAAG55-98-0308.

References

[1] S. A. Long, M. W. McAllister, and L. C. Shen, "The resonant cylindrical dielectric cavity antenna," *IEEE Trans. Antennas Propagat.*, vol. AP-31, pp. 406-412, Mar. 1983.

[2] T. E. Durham and C. G. Christodoulou, "Integral equation analysis of dielectric and conducting bodies of revolution in the presence of arbitrary surfaces," *IEEE Trans. Antennas Propagat.*, vol. AP-43, No. 7, pp. 674-680, July 1995.

[3] G. P. Junker, A. A. Kishk, A. W. Glisson, "Multiport network description and radiation characteristics of coupled dielectric resonator antennas," *IEEE Trans. Antennas Propagat.*, vol. AP-46, pp. 425-433, Mar. 1998.

[4] S. U. Hwu and D. R. Wilton, "Electromagnetic scattering and radiation by arbitrary configurations of conducting bodies and wires," Technical Report TR 87-17, Applied Electromagnetics Laboratory, University of Houston, May 1989.

[5] L. N. Medgyesi-Mitschang and J. M. Putnam, "Electromagnetic scattering from axially inhomogeneous bodies of revolution," *IEEE Trans. Antennas Propagat.*, vol. AP-32, pp. 797-806, Aug., 1984.

[6] A. A. Kishk and L. Shafai, "Different formulations for numerical solution of single or multibodies of revolution with mixed boundary conditions, *IEEE Trans. Antennas Propagat.*, vol. AP-34, pp.666-673, May 1986.

[7] J. M. Putnam and L. N. Medgyesi-Mitschang, "Combined field integral equation formulation for inhomogeneous two- and three-dimensional bodies: The junction problem," *IEEE Trans. Antennas Propagat.*, vol. AP-39, pp. 667-672, May, 1991.

[8] J. M. Putnam and L. N. Medgyesi-Mitschang, "Generalized method of moments for three-dimensional penetrable scatterers," *J. Opt. Soc. Am. A.* vol.11, No.4, pp.1384-1398, Apr. 1994.

[9] R. F. Harrington, *Time harmonic electromagnetic fields.* New York: McGraw-Hill, 1961.

[10] S. M. Rao, D. R. Wilton, and A. W. Glisson, "Electromagnetic scattering by surfaces of arbitrary shape," *IEEE Trans. Antennas Propagat.*, vol. AP-30, pp.409-418, May 1982.

[11] S. V. Yesantharao, "EMPACK — A software toolbox of potential integrals for computational electromagnetics," M.S. Thesis, University of Houston, 1989.

A Novel Grid-Robust Higher-Order Vector Basis Function for the Method of Moments

G. Kang, J. M. Song, W. C. Chew, K. Donepudi, and J. M. Jin

Center for Computational Electromagnetics
Department of Electrical and Computer Engineering
University of Illinois at Urbana–Champaign
Urbana, IL 61801-2991, USA

1 Introduction

Recently, higher-order numerical methods have received intense attention in computational electromagnetics [1]–[4] because of their ability to represent fields/currents and model geometries more accurately than conventional low-order methods. Among the present higher-order methods, one class uses higher-order basis functions in projection methods such as the finite element method (FEM) and Galerkin-based method of moments (MoM) [1]–[3]. The other class uses the Nystrom approach with high-order discretization [4].

In the first class of higher-order methods, the basis functions used to expand the unknown surface current have an important property in that their normal components are always continuous across the sides of triangular patches representing the surface of the object to be analyzed. This property precludes the infinite accumulation of electric charges along the patch sides and thus permits the use of Galerkin's method in the solution of the integral equation for the surface current. Among the various efforts on the development of higher-order basis functions, Wandzura [1] constructed a hierarchy of higher-order functions, in which the well-known Rao-Wilton-Glisson (RWG) function [5] is the natural first member. Graglia *et al.* [2] developed a set of fully interpolatory higher-order vector basis functions of the Nedelec type [6] in a unified manner, also based on the RWG function.

In the second class of higher-order methods, the unknown surface currents are represented by their samples at a set of discrete points on the surface of the object [4]. The Nystrom approach is then employed to discretize the integral equation to be solved. Additional efforts are often required to deal with the singular integrals by using local correction techniques, which use either the LU decomposition or the singular value decomposition (SVD) to solve certain matrix equations.

Comparing the two classes of higher-order methods discussed above, the first class produces more accurate solutions for the same number of unknowns. However, the evaluation of the integrals in the first class of methods is more time consuming because there are two fold integrations to be evaluated numerically. Additionally, the basis functions used in the first class require the mesh of triangular patches to be well connected: a side of a triangular patch has to be entirely shared by another patch and no vertices of a triangular patch can reside in the middle of its neighboring patch's sides. This requirement is also found in the FEM. However, for many practical applications, this requirement is too stringent and it precludes the use of defective meshes.

This paper proposes a set of novel, grid-robust, higher-order vector basis functions for the MoM solution of integral equations for three-dimensional (3D) electromagnetic problems. These

basis functions are defined over curvilinear triangular patches and represent the unknown electric current density within each patch using the Lagrange interpolation polynomials. The highlight of these basis functions is that the Lagrange interpolation points are chosen to be the same as the nodes of the well-developed Gaussian quadratures. As a result, the evaluation of the integrals in the MoM is greatly simplified. Additionally, the surface of an object to be analyzed can be easily meshed because the new basis functions do not require the side of a triangular patch to be entirely shared by another triangular patch. The proposed basis functions are implemented with point-matching for the MoM solution of the electric-field integral equation (EFIE), the magnetic-field integral equation (MFIE), and the combined-field integral equation (CFIE). Numerical examples are presented to demonstrate the higher-order convergence and the grid robustness for defective meshes using the new basis functions.

2 Vector Basis Functions

Given an object, its surface can be meshed into curvilinear trianglular patches. The current on the surface can then be represented as a summation of the currents on each of the patches:

$$\mathbf{J}(\mathbf{r}) = \sum_{p=1}^{P} \mathbf{J}_p(\mathbf{r}) \tag{1}$$

where $\mathbf{J}_p(\mathbf{r})$ denotes the current on the pth patch. The $\mathbf{J}_p(\mathbf{r})$ can be interpolated by the Lagrange interpolator:

$$\mathbf{J}_p(\mathbf{r}) = \sum_{i=1}^{I_p} \bar{\mathbf{L}}_{(i,p)}(\mathbf{r}) \cdot \mathbf{J}_p(\mathbf{r}_i) \tag{2}$$

where $\mathbf{r}_i$ $(i = 1, 2, \ldots, I_p)$ are the interpolation points and $\bar{\mathbf{L}}_{(i,p)}(\mathbf{r})$ is called the interpolator with the property that

$$\bar{\mathbf{L}}_{(i,p)}(\mathbf{r}_j) = \bar{\mathbf{I}}\delta_{ij} \tag{3}$$

where δ_{ij} is the Kronecker delta function and $\bar{\mathbf{I}}$ is the unit dyadic. Equation (2) can also be interpreted as the expansion of the current using $\bar{\mathbf{L}}_{(i,p)}(\mathbf{r})$ as the basis functions and $\mathbf{J}_p(\mathbf{r}_i)$ as the unknown expansion coefficients, which are to be determined.

With the property in Equation (3), the evaluation of the surface integrals in the MoM can be greatly simplified. For example, consider a surface integral over a triangular patch

$$\int_{\triangle_p} f(\mathbf{r}, \mathbf{r}') \bar{\mathbf{L}}_{(i,p)}(\mathbf{r}') \cdot \mathbf{J}_p(\mathbf{r}_i) dS' \tag{4}$$

where $f(\mathbf{r}, \mathbf{r}')$ is the kernel, which may be singular at $\mathbf{r} = \mathbf{r}'$. When the point $\mathbf{r}$ is not close to the point $\mathbf{r}'$ in triangular patch p, the Gaussian quadrature yields

$$\sum_{s=1}^{I} w_s(\mathbf{r}_s) f(\mathbf{r}, \mathbf{r}_s) \bar{\mathbf{L}}_{(i,p)}(\mathbf{r}_s) \cdot \mathbf{J}_p(\mathbf{r}_i) \tag{5}$$

where I is the number of points in the quadrature rule and w_s denote the weighting coefficients. If the quadrature points are the same as the interpolation points in the Lagrange polynomial, Equation (3) can be used to give

$$w_i(\mathbf{r}_i) f(\mathbf{r}, \mathbf{r}_i) \bar{\mathbf{I}} \cdot \mathbf{J}_p(\mathbf{r}_i) \tag{6}$$

which greatly simplifies the result of integration.

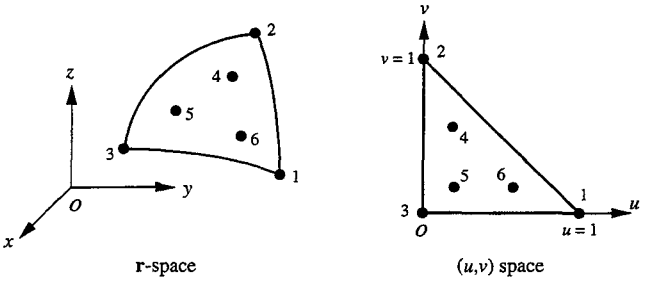


Figure 1: A curvilinear triangular patch in the $\mathbf{r}$ space mapped to a planar right-angle triangle in the (u, v) space.

To design the basis functions $\bar{\mathbf{L}}_{(i,p)}(\mathbf{r})$, we first map a curvilinear triangular patch in the $\mathbf{r}$ space into the (u, v) space, as shown in Figure 1. Since the surface current has two degrees of freedom, we can write any surface current in the (u, v) space as

$$\mathbf{J} = \frac{1}{J_{ac}}[J_u \mathbf{u} + J_v \mathbf{v}] \tag{7}$$

where

$$\mathbf{u} = \frac{\partial \mathbf{r}}{\partial u}, \qquad \mathbf{v} = \frac{\partial \mathbf{r}}{\partial v} \tag{8}$$

$$J_{ac} = \sqrt{g_{11} g_{22} - g_{12} g_{21}} \tag{9}$$

in which

$$g_{11} = \mathbf{u} \cdot \mathbf{u}, \quad g_{12} = g_{21} = \mathbf{v} \cdot \mathbf{u}, \quad g_{22} = \mathbf{v} \cdot \mathbf{v}. \tag{10}$$

From Equation (7), the current at any point $\mathbf{r}_i$ on the patch can be written as

$$\mathbf{J}_i = \frac{1}{J_{aci}}[J_{iu} \mathbf{u}_i + J_{iv} \mathbf{v}_i]. \tag{11}$$

The current $\mathbf{J}$ can then be interpolated by the Lagrange interpolator as

$$\mathbf{J} = \sum_{i=1}^{I_p} \frac{1}{J_{aci}} L_i(u, v)[J_{iu} \mathbf{u}_i + J_{iv} \mathbf{v}_i] \tag{12}$$

where $L_i(u, v)$ is a two-dimensional Lagrange interpolator with the property that

$$L_i(u_j, v_j) = \delta_{ij}. \tag{13}$$

Equation (12) can also be written as

$$\begin{aligned} \mathbf{J} &= \sum_{i=1}^{I_p} \frac{1}{J_{aci}} L_i(u, v)[\mathbf{u}(g_{i22} \mathbf{u}_i - g_{i12} \mathbf{v}_i) + \mathbf{v}(g_{i11} \mathbf{v}_i - g_{i21} \mathbf{u}_i)] \cdot \mathbf{J}_i \\ &= \sum_{i=1}^{I_p} \bar{\mathbf{L}}_i(u, v) \cdot \mathbf{J}_i. \end{aligned} \tag{14}$$

Table 1: Information about the vector basis functions and the chosen quadrature rules.

Order of basis functions	Number of interpolation points	Accuracy of quadrature rule	Unknowns in each patch
0	1	1	2
1	3	2	6
2	6	4	12
3	12	7	24

It then remains to design $\tilde{\mathbf{L}}_i(u,v)$ in the $\mathbf{r}$ space to satisfy Equation (3) or $L_i(u,v)$ in the (u,v) space to satisfy Equation (13). In addition, we also hope the Lagrange interpolation polynomials $L_i(u,v)$ to have the following properties. First, the interpolation points are distributed inside a triangular patch. Second, the interpolation points are the same as the nodes of a Gaussian quadrature rule. Third, the chosen interpolation points should give the highest degree of accuracy among the quadrature rules that have the same number of interpolation points.

The three properties above provide a guideline to choose the Gaussian quadratures. Once the quadrature points are chosen, one can proceed to find the explicit expression of $L_i(u,v)$. In the (u,v) space, we can define the space of n-degree polynomials [7] as

$$P_n^2 = \text{span}\{u^i v^j; i,j \geq 0; i+j \leq n\} \tag{15}$$

such that the dimension of the space is

$$\dim P_n^2 = C_{n+2}^2 = \frac{(n+2)(n+1)}{2}. \tag{16}$$

For $n=1$, $\dim P_n^2 = 3$, and $P_n^2 = \text{span}\{1,u,v\}$, and in this case, we choose the interpolation points from the three-point quadrature rules. For $n=2$, $\dim P_n^2 = 6$, and $P_n^2 = \text{span}\{1,u,v,u^2,uv,v^2\}$, and consequently, we choose the interpolation points from the six-point quadrature rules. This can be extended to the higher-order ones in a straightforward manner.

Once the polynomials P_n^2 are chosen, $L_i(u,v)$ can be determined by solving the matrix equation

$$\begin{bmatrix} P_1(u_1,v_1) & P_1(u_2,v_2) & \cdots & P_1(u_n,v_n) \\ P_2(u_1,v_1) & P_2(u_2,v_2) & \cdots & P_2(u_n,v_n) \\ \vdots & \vdots & \ddots & \vdots \\ P_n(u_1,v_1) & P_n(u_2,v_2) & \cdots & P_n(u_n,v_n) \end{bmatrix} \begin{bmatrix} L_1(u,v) \\ L_2(u,v) \\ \vdots \\ L_n(u,v) \end{bmatrix} = \begin{bmatrix} P_1(u,v) \\ P_2(u,v) \\ \vdots \\ P_n(u,v) \end{bmatrix} \tag{17}$$

where (u_i,v_i) denote the interpolation points. If the Vandermonde determinant of the above equation is nontrivial, $L_i(u,v)$ can be obtained uniquely. Therefore, an additional requirement for the interpolation points is that they should guarantee $|VDM| \neq 0$.

Table 1 lists the information about the zeroth-, first-, second-, and third-order vector basis functions that are designed based on the procedure described above. The zeroth-order basis function is the same as the well-known pulse function. For the zeroth-, first-, and second-order basis functions, we choose the quadrature rules [8] whose number of points matches the degrees of polynomials, $\dim P_n^2$. For the third-order basis functions, we find that the available 10-point Gaussian quadratures [9], [10] yield an ill-conditioned matrix in Equation (17). Hence, we choose to use the Gaussian quadrature with 12 points [11], which yields a well-conditioned matrix. In addition, the 12-point Gaussian quadrature rule has the 7th degree of accuracy while the aforementioned 10-point

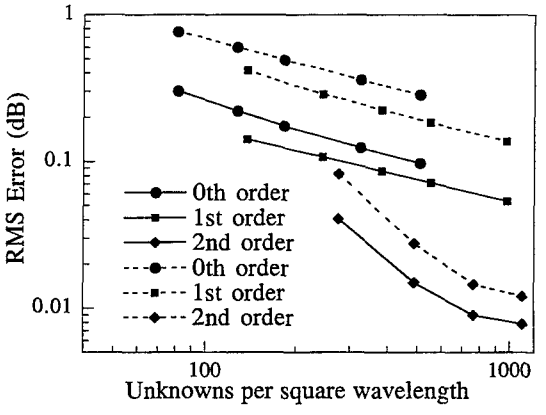


Figure 2: RMS error in the bistatic RCS versus the number of unknowns per square wavelength obtained using the CFIE. The solid lines correspond to $\alpha = 0.2$ and the dash lines correspond to $\alpha = 0.5$.

rules have only the 4th or 5th degree of accuracy. This choice yields a little more unknowns, but it also gives a higher integration accuracy. For the third order, the polynomial space is spanned by

$$\{1, u, v, u^2, uv, v^2, u^3, u^2v, uv^2, v^3, u^3v, uv^3\}. \tag{18}$$

3 Numerical Results

We have successfully implemented the new basis functions in the MoM solution of the EFIE, MFIE, and CFIE using the point-matching approach. The EFIE and MFIE are given by

$$\hat{\mathbf{t}} \cdot \frac{i\omega\mu}{4\pi} \int_s \bar{\mathbf{G}}(\mathbf{r}, \mathbf{r}') \cdot \mathbf{J}(\mathbf{r}') dS' = -\hat{\mathbf{t}} \cdot \mathbf{E}_{inc} \tag{19}$$

and

$$\frac{\mathbf{J}(\mathbf{r})}{2} - \frac{1}{4\pi} \hat{\mathbf{n}} \times \nabla \times \int_s g(\mathbf{r}, \mathbf{r}') \mathbf{J}(\mathbf{r}') dS' = \hat{\mathbf{n}} \times \mathbf{H}_{inc}(\mathbf{r}) \tag{20}$$

respectively, where $\bar{\mathbf{G}}(\mathbf{r}, \mathbf{r}')$ is the dyadic Green function, $g(\mathbf{r}, \mathbf{r}')$ is the scalar Green function, $\hat{\mathbf{t}}$ and $\hat{\mathbf{n}}$ denote the tangential and normal unit vectors on the surface s, respectively, and finally $(\mathbf{E}_{inc}, \mathbf{H}_{inc})$ denote the incident fields. The CFIE is simply a linear combination of EFIE and MFIE:

$$\alpha \text{EFIE} + (1 - \alpha)\eta \text{MFIE} \tag{21}$$

where α denotes the combination constant, usually chosen from 0.2 to 0.8, and η is the free-space wave impedance. For the singular integrals in the EFIE and MFIE, Duffy's transformation [12] is used for their evaluation.

A conducting sphere having a diameter of 1 m is used to test the MoM solution using the new higher-order vector basis functions. The parameter used in the study is the root-mean-square

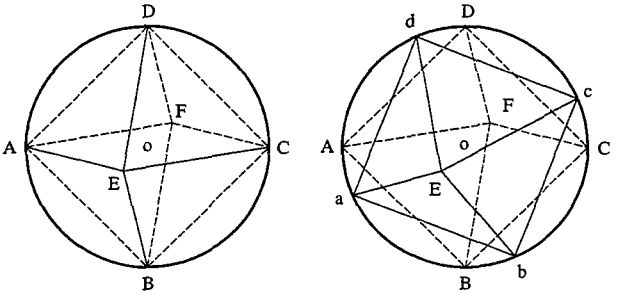


Figure 3: (a) An inscribed regular octahedron. (b) The front half of the octahedron is rotated by an angle of $\Delta\phi$.

(RMS) error defined as

$$\text{RMS} = \sqrt{\frac{1}{N_s}\sum_{i=1}^{N_s}|\sigma_{\text{ref}} - \sigma_{\text{cal}}|^2} \tag{22}$$

where σ_{cal} denotes the calculated radar cross section (RCS) and σ_{ref} denotes the reference Mie solution, both measured in dB, and N_s is the number of sampling points, which are the angles of observation here.

Figure 2 shows the convergence behavior of the higher-order basis functions obtained at 0.3 GHz. It is clear that when the number of unknowns increases, the results obtained using higher-order basis functions converge more quickly than those of lower-order ones. This is particularly true when a high solution accuracy is desired.

Next, the proposed basis functions are validated on defective meshes. Here, a defective mesh refers to one in which an edge of a triangular patch is partially, instead of totally, shared by another triangular patch, or in other words, two neighboring triangular patches partially share one edge. The validation is carried out on a 1-λ diameter sphere using the MFIE with the third-order basis functions. By mapping the triangles of an inscribed regular octahedron onto the surface of the sphere, we obtain an exact description of the sphere with well-connected curvilinear triangular patches, as illustrated in Figure 3(a). If we rotate the front half of the octahedron by an angle of $\Delta\phi$ and then map the eight triangles onto the surface of the sphere, we obtain a defective mesh, which also describes the sphere exactly, as shown in Figure 3(b). By subdividing each of the eight triangles into four subtriangles, we generate a mesh with 32 triangular patches, which is used for the study here. Figure 4 shows the RMS error as a function of the rotating angle $\Delta\phi$. It is seen that the RMS errors from a series of defective meshes are within ± 0.004 dB of the RMS error of the well-connected mesh, which is 0.013 dB. This demonstrates clearly the grid-robustness of the proposed new higher-order basis functions.

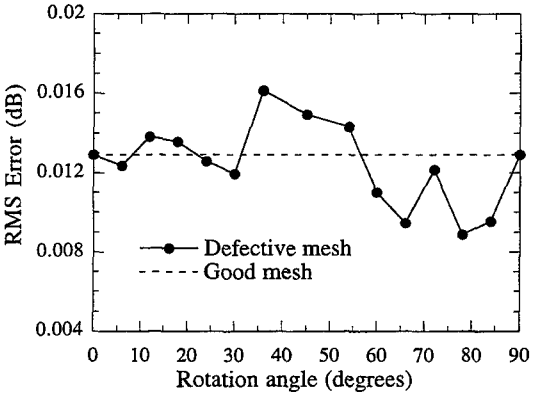


Figure 4: RMS error in the bistatic RCS versus the angle of rotation.

4 Conclusion

A set of novel, grid-robust, higher-order vector basis functions was proposed for the MoM solution of integral equations for 3D electromagnetic problems. These basis functions were defined over curvilinear triangular patches and based the Lagrange interpolation polynomials. The Lagrange interpolation points were chosen to be the same as the nodes of the Gaussian quadratures, which greatly simplified the evaluation of the integrals in the MoM. The new basis functions were also applicable to defective meshes where the side of a triangular patch is only partially shared by another triangular patch. The proposed basis functions were implemented with point-matching for the MoM solution of the EFIE, the MFIE, and the CFIE. Numerical examples were presented to demonstrate the higher-order convergence and the grid robustness for defective meshes.

References

[1] S. Wandzura, "Electric current basis functions for curved surfaces," *Electromagnetics* , vol. 12, pp. 77–91, 1992.

[2] R. D. Graglia, D. R. Wilton, and A. F. Peterson, "Higher order interpolatory vector bases for computational electromagnetics," *IEEE Trans. Antennas Propagat.*, vol. 45, pp. 329–342, March 1997.

[3] K. Donepudi, G. Kang, J. M. Song, J. M. Jin, and W. C. Chew, "Higher-order MoM implementation to solve integral equations," *IEEE AP-S international Symposium*, July 11–16, Florida, USA, vol. 3, pp. 1716–1719, 1999.

[4] L. S. Canino, J. J. Ottusch, M. A. Stalzer, J. L. Visher, and S. Wandzura, "Numerical solution of the Helmholtz equation in 2D and 3D using a high-order Nystrom discretization," *J. Comput. Phys.*, vol. 146, pp. 627–663, 1998.

[5] S. M. Rao, D. R. Wilton, and A. W. Glisson, "Electromagnetic scattering by surfaces of arbitrary shape," *IEEE Trans. Antennas Propagat.*, vol. 30, pp. 409–418, May 1982.

[6] J. C. Nedelec, "Mixed finite elements in R^3," *Numerische Mathematik*, vol. 35, pp. 315–341, 1980.

[7] J. S. Hesthaven, "From electrostatics to almost optimal nodal sets for polynomial interpolation in a simplex," *SIAM J. Numer. Anal.*, vol. 35, no. 2, pp. 655–676, April 1998.

[8] D. A. Dunavant, "High degree efficient symmetrical Gaussian quadrature rules for the triangle," *Int. J. Numer. Meth. Eng.*, vol. 21, pp. 1129–1148, 1985.

[9] E. De Doncker, "New Euler-Maclaurin expansions and their application to quadrature over the s-dimentional simplex, " *Math. Comput.*, vol. 33, no. 147, pp. 1003–1018, July 1979.

[10] J. N. Lyness and D. Jespersen, "Moderate degree symmetric quadrature rules for the trinagle," *J. Inst. Maths Applics*, vol. 15, pp. 19–32, 1975.

[11] K. G. Hamburg, "The construction of symmetric cubature formulas for the square and the triangle, " *Computing*, vol. 40, pp. 229–240, 1988.

[12] M. G. Duffy, "Quadrature over a pyramid or cube of integrands with a singularity at a vertex," *J. Numer. Anal.*, vol. 19, no. 6, pp. 1260–1262, Dec. 1982.

Analytical treatment of Green's functions singularities in microstrip structures

E. Jiménez, F.J. Cabrera, E.T.S.I. Telecomunicación, U.L.P.G.C., Spain
Campus de Tafira S/N, Las Palmas 35017
eugenio@cibeles.teleco.ulpgc.es, francis@cibeles.teleco.ulpgc.es

J.G. Cuevas del Río, E.T.S.I. Telecomunicación, U.P.M., Spain
Ciudad Universitaria S/N, Madrid 28040. gustavo@xyz.ssr.upm.es

1 The microstrip problem.

The current distribution on a microstrip structure radiates an electric field given by Pocklington's integral equation

$$\overline{E}(\bar{r}) = j\omega\mu_0 \iint_S \overline{\overline{G}}(\bar{r};\bar{r}')\overline{J_s}(\bar{r}')\, ds'$$

In order to solve Pocklington's equation for the current density $\overline{J_s}$, the method of moments (MoM for short) is employed. MoM solves this equation dividing the structure into M different segments called *patchs*. The unknown current distribution, $\overline{J_s}$, is written as a linear combination of two-dimensional *basis* functions which are defined over rectangular segments.

$$\overline{J_s} = \sum_{i=1}^{M} I_{x_i} J_{x_i}(x',y')\hat{x} + \sum_{i=1}^{M} I_{y_i} J_{y_i}(x',y')\hat{y} \tag{1}$$

Basis functions can be written as the product of two independent variable functions; $J_x(x,y) = T(x)Q(y)$ and $J_y(x,y) = Q(x)T(y)$. Usually, the longitudinal component has a piecewise sinusoidal or triangular variation and the tranversal component has a constant distribution. So, the shape of one of these *basis* functions can be something like figure 1. The components of the diadic Green's function can be written using G_x and G_v Sommerfeld integrals.

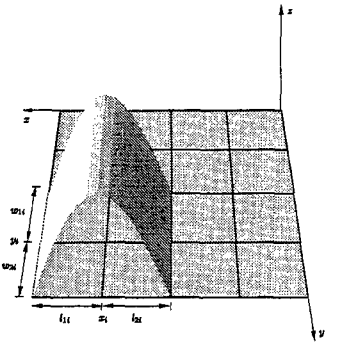


Figure 1: Basis function.

$$G_{E_{xx}} = \frac{j}{2\pi k_0^2}\left[k_0^2 G_x + \frac{\partial^2}{\partial x^2} G_v\right] \quad (2)$$

$$G_{E_{xy}} = \frac{j}{2\pi k_0^2}\left[\frac{\partial^2}{\partial x \partial y} G_v\right] = G_{E_{yx}} \quad (3)$$

$$G_{E_{yy}} = \frac{j}{2\pi k_0^2}\left[k_0^2 G_x + \frac{\partial^2}{\partial y^2} G_v\right] \quad (4)$$

Projecting the electric field along the x and y axis and using Galerkin's method, Pocklington's equation will reduce to a matrix equation:

$$\begin{pmatrix} Z_{xx}^{ij} & Z_{xy}^{ij} \\ Z_{yx}^{ij} & Z_{yy}^{ij} \end{pmatrix}_{2M\times 2M} \begin{pmatrix} I_x^i \\ I_y^i \end{pmatrix}_{2M\times 1} = \begin{pmatrix} V_x^j \\ V_y^j \end{pmatrix}_{2M\times 1} \quad \begin{matrix} i = 1..M \\ j = 1..M \end{matrix} \quad (5)$$

The elements of the matrix $[Z]$ are integrals of the following type.

$$\int_{x_i-l_{1j}}^{x_j+l_{2j}} dx' \int_{x_i-l_{1i}}^{x_i+l_{2i}} dx' \int_{y_i-w_{1i}}^{y_i+w_{2i}} dy' \int_{y_j-w_{1i}}^{y_j+w_{2j}} F_i(x';y')\ F_j(x;y)\ G(x-x',y-y')dy \quad (6)$$

where G is the Green's function of in a grounded dielectric slab and $F_i(x',y')$ and $F_j(x,y)$ are *basis* or *weight* functions.

Table 1 shows the value of these functions for each integral. This kind of integrals are defined over rectangular shapes. Since the functions F_i and F_j are defined within *patches*, the couple between *patches* i and j has to be

	Integral 1			Integral 2		
	$F_i(x';y')$	$F_j(x;y)$	$G(x,y;x',y')$	$F_i(x',y')$	$F_j(x,y)$	$G(x,y;x',y')$
Z_{xx}	$T_i(x')$	$T_j(x)$	$G_x(x,y;x',y')$	$\frac{\partial T_i(x')}{\partial x'}$	$\frac{\partial T_j(x)}{\partial x}$	$G_v(x,y;x',y')$
Z_{xy}	$\frac{\partial T_i(y')}{\partial y'}$	$\frac{\partial T_j(x)}{\partial x}$	$G_v(x,y;x',y')$	–	–	–
Z_{yx}	$\frac{\partial T_i(x')}{\partial x'}$	$\frac{\partial T_j(y)}{\partial y}$	$G_v(x,y;x',y')$	–	–	–
Z_{yy}	$T_i(y')$	$T_j(y)$	$G_x(x,y;x',y')$	$\frac{\partial T_i(y')}{\partial y'}$	$\frac{\partial T_j(y)}{\partial y}$	$G_v(x,y;x',y')$

Table 1: $[Z]$ functions.

computed by parts. This calculation will be accomplished through the sum of the couplings of each one of the subdomains in which is divided *patch* i with each one of the subdomains of *patch* j.

Terms V_x and V_j are obtained using a the delta-gap voltage excitation model. This model assumes the excitation is accomplished through a voltage source applied within a infinitesimally small gap. Terms $[Z]$ are quadruple integrals that can be directly calculated using a Gauss-Laguerre quadrature but their cost would be too large. To minimize this cost, a domain change transforming (6) to a double sum of double integrals is accomplished. Using this transformation, the calculation time reduces considerably.

$$\begin{aligned} &\int_{x_i-l_{1j}}^{x_j+l_{2j}} dx' \int_{x_i-l_{1i}}^{x_i+l_{2i}} dx' \int_{y_i-w_{1i}}^{y_i+w_{2i}} dy' \int_{y_j-w_{1i}}^{y_j+w_{2j}} F_i(x';y')\ F_j(x;y)\ G(x-x',y-y')dy \\ &= \sum_{L=1}^{12}\sum_{K=1}^{12} \int_{ULI_L}^{ULS_L} du \int_{VLI_K}^{VLS_K} f_{TT_L}(u)\cdot f_{TT_K}(v)\cdot G(\sqrt{2}u + x_j - x_i, \sqrt{2}v + y_j - y_i)dv \end{aligned} \quad (7)$$

The integration limits in (7) are different for each integral and once (7) has been obtained, the elements of the matrix $[Z]$ are numerically calculated.

2 Behaviour of Green's functions.

As shown in 2, 3 and 4, the components of the diadic Green's function can be written using two auxiliar functions; G_x and G_v. These two functions are also known as Sommerfeld integrals or Hankel transforms and their analytical

expressions are:

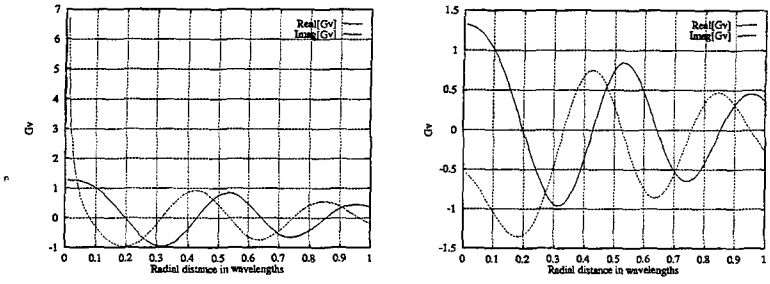
$$G_x = \int_0^\infty \frac{\xi}{D_{te}} J_0(\rho\xi) d\xi \tag{8}$$

$$G_v = \int_0^\infty \frac{N}{D_{te} D_{tm}} \xi J_0(\rho\xi) d\xi \tag{9}$$

for a substrate of height d, dielectric constant ϵ_r and losses factor $\tan\delta$.

$$D_{te} = k_2 - jk_1 \cot(k_1 d) \quad D_{tm} = \epsilon_t k_2 + jk_1 \tan(k_1 d) \quad N = k_2 + jk_1 \tan(k_1 d)$$
$$k_2 = \sqrt{k_0^2 - \xi^2} \quad k_1 = \sqrt{\epsilon_t k_0^2 - \xi^2} \quad \epsilon_t = \epsilon_r(1 - j\tan\delta)$$

The behaviour of the integrands in G_X and G_v when $\xi \to \infty$ is something like $F_\infty(\xi) = \sum_{n=0}^{N} \xi^n c_n$ which corresponds to a Laurent series expansion of the integrand at $\xi \to \infty$ taken along the real axis (there is an essential singularity at ∞). These terms can be integrated analytically and the asymptotic terms are in the form $S^\infty(\rho) = \sum_{n=0}^{N} \frac{c_n}{\rho^n}$. By extracting the asymptotic value of the integral, the singularity due to zero radial distance has been removed and can be analytically treated. For instance, let's go and see Sommerfeld integrals with and without the zero radial distance singularity (figures 2 and 3). Substrate parameters are $\epsilon_r = 12.8$, $h = 0.12\lambda_0$ and $\tan\delta = 0.01$



(a) With singularity

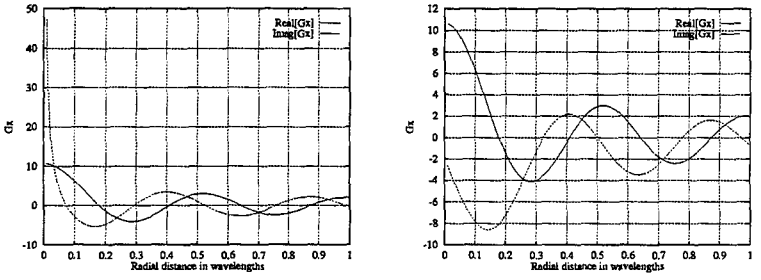
(b) Without singularity

Figure 2: G_v with and without singularity.

3 Computing [Z] terms.

Acording to the latter section, G_x and G_v can be written as $G_\alpha = \frac{c_0}{\rho} + G_{smooth}$ so Z terms in (7) can be divided into two terms. Depending on the kind of *basis* and *testing* functions, the contribution of the singularity to the integral can be analytically computed. The other term can be calculated using a gaussian like cuadrature.

In general, one chooses as basis functions the set of functions that have the ability to accurately represent the unknown function while minimizing the computational effort requiered to employ it.



(a) With singularity

(b) Without singularity

Figure 3: G_x with and without singularity.

The unknown current distribution can be represented using piecewise sinusoids as:

$$T_i(x') = \begin{cases} \frac{\sin[k_e(l_{1i} + x' - x_i)]}{\sin(k_e l_{1i})} & \text{if } x_i - l_{1i} \leq x' \leq x_i \\ \frac{\sin[k_e(l_{2i} - x' + x_i)]}{\sin(k_e l_{2i})} & \text{if } x_i \leq x' \leq x_i + l_{2i} \\ 0 & \text{elsewhere.} \end{cases} \tag{10}$$

$$Q_i(y') = \begin{cases} \frac{1}{w_{1i} + w_{2i}} & \text{si } y_i - w_{1i} \leq y' \leq y_i + w_{2i} \\ 0 & \text{elsewhere.} \end{cases} \tag{11}$$

where k_e is the propagation effective constant; usually $k_e = \frac{2\pi}{\lambda_0 \sqrt{\frac{\varepsilon_r + 1}{2}}}$. This kind of model is very good but it makes expressions like (7) very expensive to compute and the singular term cannot be analytically calculated.

On the other hand, one can use picewise linear functions to represent the current.

$$T_i(x') = \begin{cases} \frac{l_{1i} + x' - x_i}{l_{1i}} & \text{if } x_i - l_{1i} \leq x' \leq x_i \\ \frac{l_{2i} - x' + x_i}{l_{2i}} & \text{if } x_i \leq x' \leq x_i + l_{2i} \\ 0 & \text{elsewhere.} \end{cases} \tag{12}$$

$$Q_i(y') = \begin{cases} \frac{1}{w_{1i} + w_{2i}} & \text{si } y_i - w_{1i} \leq y' \leq y_i + w_{2i} \\ 0 & \text{elsewhere.} \end{cases} \tag{13}$$

This model isn't as good as the piecewise sinusoid but it has two advantages over it. First it's faster and simpler. Second the contribution of the singular term can be analytically computed. Using this model, one can use a simpler numerical cuadrature (vg. four points instead of eight) when computing terms with singularities (overlaped *patchs*) because the main contribution to (7) comes from an analytical formula. No numerical integration is needed to include the singular term.

4 Results.

In this section, we are going to show some results obtained analysing two microstrip structures using four different schemes.

- Piecewise sinusoids for *basis* and *testing* functions and an eight point gaussian quadrature to compute the numerical terms of (7).
- Piecewise lineal for *basis* and *testing* functions and an eight point gaussian quadrature to compute the numerical terms of (7). No analytical integral computed for the singular term.
- Piecewise lineal for *basis* and *testing* functions and a four point gaussian quadrature to compute the numerical terms of (7). No analytical integral computed for the singular term.
- Piecewise lineal for *basis* and *testing* functions and a four point gaussian quadrature to compute the numerical terms of (7). Singular term is analytically computed.

4.1 Microstrip hybrid.

The geometry of this structure is shown in figure (4) and it was meshed using 56 overlapped rectangular patches.

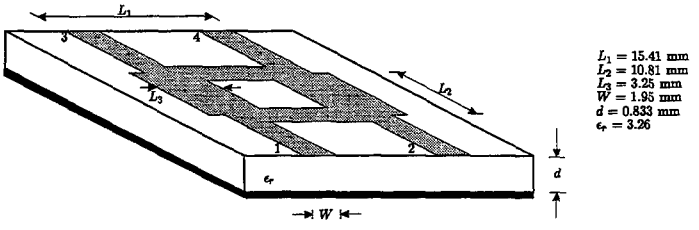
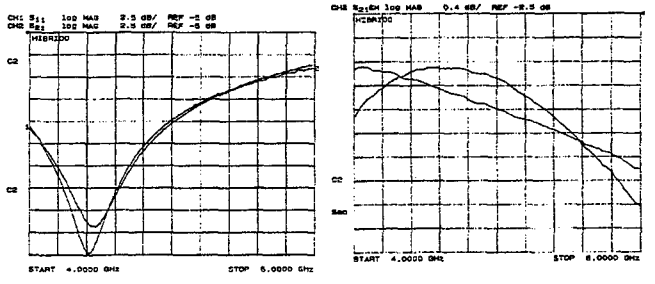


Figure 4: Hybrid geometry.

One prototype was built and measured and the results are shown in figure (5).



(a) S11 and S21 (b) S31 and S41

Figure 5: Hybrid measurements.

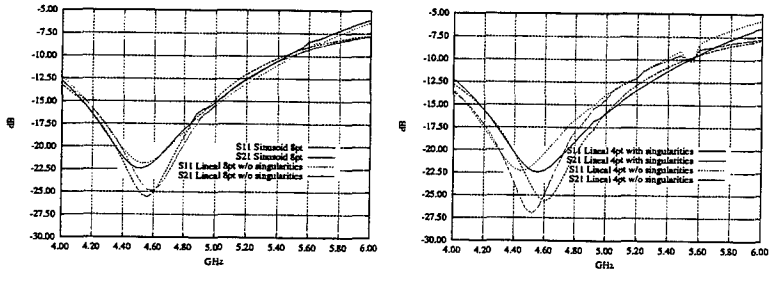


Figure 6: Calculated parameters.

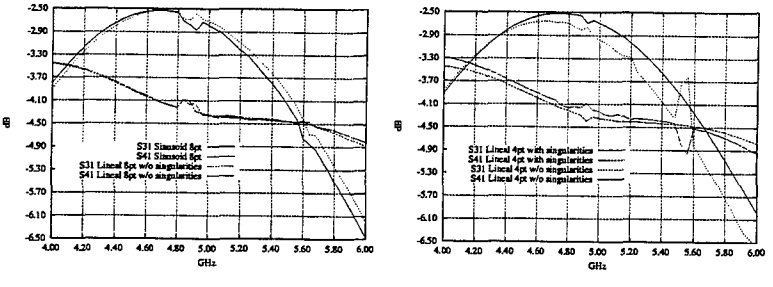
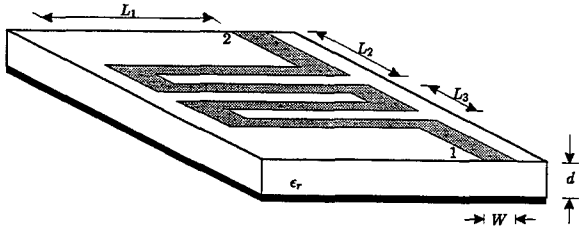


Figure 7: Calculated parameters.

4.2 Microstrip meander.

The geometry of this structure is shown in figure (8) and it was meshed using 42 overlapped rectangular patches.



$L_1 = 18.58$ mm
$L_2 = 20.44$ mm
$L_3 = 5.08$ mm
$W = 1.86$ mm
$d = 0.833$ mm
$\epsilon_r = 3.26$

Figure 8: Meander geometry.

One prototype was built and measured and the results are shown in figure (9).

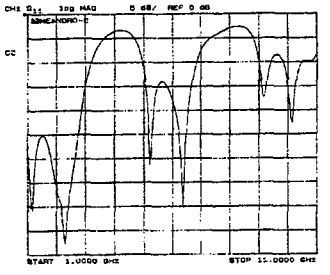


Figure 9: Meander measurements.

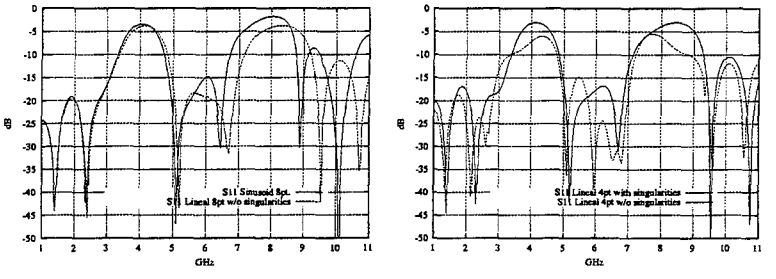


Figure 10: Calculated parameters.

5 Conclusions.

Table (2) shows timing for the computed simulations measured in seconds per frecuency. Simulations were made in a Pentium III 450 MHz machine. As one can see, piecewise lineal model with four points including analytical singular terms is, as least, as good as piecewise linear with eight points and 3.7 times faster. Piecewise lineal with four points without singularities is clearly bad and very inestable. Piecewise sinusoid is better than the other models simulating the meander because it's well suited for modeling current distributions along narrow strips. On the other hand it's eight times slower.

Structure	Sinusoid	Lin 8pt	Lin 4pt w/o	Lin 4pt with
Meander	128	56	15	15
Hybrid	256	118	31	31

Table 2: Simulation timing.

References

[1] J.R. Mosig and F.E. Gardiol, *"Analytical and numerical techniques in the Green's function treatment of microstrip antennas and scatterers."*, IEE Proc., Vol 130, Pt. H, No 2, March 1983.

[2] J.R. Mosig and T.K. Sarkar, *"Comparison of quasi-static and exact electromagnetic fields from a horizontal electric dipole above a lossy dielectric backed by an imperfect ground plane."*, IEEE Trans. MTT, vol MTT-34, No 4, April 1986.

[3] M. Marin, S. Barkeshli and P.H. Pathak, *"Efficient analysis of planar microstrip geometries using a closed-form asymptotic representation of the grounded dielectric slab Green's function."*, IEEE Trans. MTT, vol MTT-37, No 4, April 1989.

[4] E. Jiménez, F. Cabrera, J. G. Cuevas, "Sommerfeld: A Fortran Library for Computing Sommerfeld Integrals", *IEEE Antennas and Propagat. Society International Symposium*, Baltimore, p 966-969,Jul. 1996.

SORRY! PAPER WAS PULLED

SORRY! PAPER WAS PULLED

SORRY! PAPER WAS PULLED

SORRY! PAPER WAS PULLED

SORRY! PAPER WAS PULLED

SORRY! PAPER WAS PULLED

SORRY! PAPER WAS PULLED

SORRY! PAPER WAS PULLED

SORRY! PAPER WAS PULLED

Higher-Order Electromagnetic Modeling of Multilayer Microstrip Structures

Feng Ling, Kalyan Donepudi, and Jian-Ming Jin

Center for Computational Electromagnetics
Department of Electrical and Computer Engineering
University of Illinois at Urbana-Champaign
Urbana, Illinois 61801-2991

Abstract

A higher-order method of moments is presented for the analysis of microstrip structures in a multilayer medium. It is shown that this higher-order method has a better convergence rate than the conventional lower-order methods. Several examples are given to demonstrate the accuracy and efficiency of this method.

1 Introduction

Full-wave electromagnetic modeling of microstrip structures has become essential in the analysis and design of microstrip antennas and circuits. A variety of methods having been developed for this purpose, which can be divided into two broad classes: the differential-equation based approach and the integral-equation based approach. For microstrip structures in a multilayer medium, the integral-equation based method of moments (MoM) is more attractive since the method allows us to formulate the problem in terms of surface integrals instead of volume integrals.

A critical factor for an efficient and accurate MoM analysis is the choice of basis functions. Traditional numerical modeling employs roof-top functions for rectangular discretization or Rao-Wilton-Glisson (RWG) functions [1] for triangular discretization. These functions are complete to the zeroth order. As a result, a very fine discretization is often required to yield an accurate solution. This leads to a large matrix equation, which is expensive to solve. In addition, the numerical solution converges slowly to the exact one when the discretization is made finer. A solution to this problem is to employ higher-order basis functions, which have a better convergence rate and can yield an accurate solution with a rather coarse discretization. The better convergence of higher-order basis functions has been demonstrated previously in the spectral method [2] and the p-version finite element method [3]. In this paper, we present an MoM using higher-order interpolatory basis functions for electromagnetic modeling of microstrip structures in a multilayer medium.

2 Formulation

Consider a microstrip structure in a multilayer medium. A well-known integral equation for this problem [4] is given by

$$\hat{n} \times \left[-j\omega\mu_0 \langle \tilde{\mathbf{G}}^A(\mathbf{r}, \mathbf{r}'), \mathbf{J}(\mathbf{r}) \rangle + \frac{1}{j\omega\epsilon_0} \nabla \langle G^\Phi(\mathbf{r}, \mathbf{r}'), \nabla' \cdot \mathbf{J}(\mathbf{r}') \rangle \right] = -\hat{n} \times \mathbf{E}^a(\mathbf{r}) \tag{1}$$

where $\mathbf{J}$ denotes the electric current density on the microstrip and $\mathbf{E}^a$ is the applied field, which is the incident field in the absence of the microstrip for scattering problems or a delta gap source for circuit problems. The $\bar{\mathbf{G}}^A$ and G^Φ are the Green's functions for the vector and scalar potentials, respectively. In general, the Green's function for a multilayer medium can be written as

$$G(\rho, z|z') = \frac{1}{2\pi}\int_0^\infty \tilde{G}(k_\rho, z|z')J_0(k_\rho\rho)k_\rho dk_\rho \tag{2}$$

where $\tilde{G}$ is the spectral domain counterpart of G, which can be derived analytically [5]. To circumvent the time-consuming numerical integration, we employ the complex image method [6]-[10], which yields a closed-form expression.

To apply the MoM, the microstrip is discretized into triangular elements and the unknown current is expanded by a set of vector basis functions on triangular elements

$$\mathbf{J}(\mathbf{r}) = \sum_{n=1}^{N} I_n \mathbf{\Lambda}_n(\mathbf{r}) \tag{3}$$

where $\mathbf{\Lambda}_n$ is the basis function and N is the number of unknowns.

For each triangular element (Fig. 1), we define a set of area coordinates (ξ_1, ξ_2, ξ_3), where ξ_i vaires linearly across the element, reaching one at the ith vertex and zero along the opposite edge, which is defined as the ith edge. The well-known zeroth-order basis functions are given by

$$\mathbf{\Lambda}_i(\mathbf{r}) = \frac{1}{2A}(\xi_{i+1}\boldsymbol{\ell}_{i-1} - \xi_{i-1}\boldsymbol{\ell}_{i+1}), \quad i = 1, 2, 3 \tag{4}$$

where A is the area of the element and $\boldsymbol{\ell}_{i\pm1}$ are constant vectors defined along the $(i \pm 1)$th edges. Note that $\hat{n}_i \cdot \mathbf{\Lambda}_i$ is constant on edge i and $\mathbf{\Lambda}$ is linearly varying along edge $i-1$ and $i+1$, as shown in Fig. 2. Also noting that

$$\nabla\xi_i = \hat{n}_i \frac{\ell_i}{2A}, \tag{5}$$

we find the divergence of $\mathbf{\Lambda}$ as

$$\nabla \cdot \mathbf{\Lambda} = \frac{1}{A}. \tag{6}$$

The zeroth-order basis function is also known as the RWG basis function [1].

The higher-order interpolatory vector basis functions on a given triangular element are constructed by multiplying the zeroth-order basis functions with a set of polynomial functions [11]

$$\mathbf{\Lambda}^\beta_{ijk}(\mathbf{r}) = N_\beta \frac{(p+2)\xi_\beta \hat{\alpha}_{ijk}(\boldsymbol{\xi})}{i_\beta}\mathbf{\Lambda}_\beta(\mathbf{r}) \tag{7}$$

where β denotes the edge number associated with the zeroth-order basis function, i, j, k are the indexes for labeling the interpolation points, which satisfy $i + j + k = p + 2$, and i_β takes $i, j,$ or k for $\beta = 1, 2,$ or 3, respectively. The normalization coefficients N^β_{ijk} are given by

$$N_\beta = \frac{p+2}{p+2-i_\beta}\ell_\beta. \tag{8}$$

The $\hat{\alpha}_{ijk}(\boldsymbol{\xi})$ is the polynomial function defined in terms of shifted Silvester-Lagrange polynomials $\hat{R}$ as

$$\hat{\alpha}_{ijk}(\boldsymbol{\xi}) = \hat{R}_i(p+2, \xi_1)\hat{R}_j(p+2, \xi_2)\hat{R}_k(p+2, \xi_3) \tag{9}$$

where the shifted Silvester-Lagrange polynomial is given by

$$\hat{R}_i(p,\xi) = \begin{cases} \frac{1}{(i-1)!}\prod_{k=1}^{i-1}(p\xi - k), & 2 \le i \le p+1 \\ 1, & i = 1. \end{cases} \tag{10}$$

The number of degrees of freedom is $(p+1)(p+3)$ on a triangular element for the basis functions of order p. The first-order basis functions so obtained are shown in Fig. 3.

Substituting (3) into (1) and applying Galerkin's procedures, we obtain a matrix equation

$$\bar{\mathbf{Z}} \cdot \mathbf{I} = \mathbf{V}. \tag{11}$$

For calculating the matrix elements, the double surface integrals are evaluated using Gaussian quadrature when the two elements do not overlap. When they do, the method proposed by Duffy [12] is employed to evaluate the singular integral. The solution of this matrix equation gives the current distributions on the conductor surface, from which the radar cross section (RCS) or S-parameters can be extracted [13].

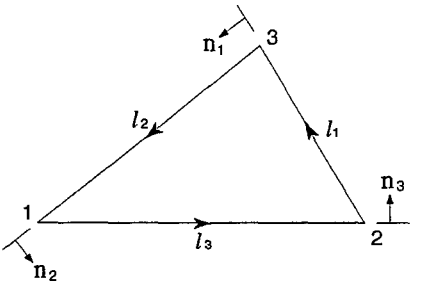


Figure 1: Notations of a triangle.

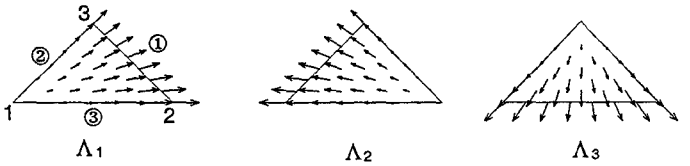


Figure 2: The zeroth-order basis function.

3 Numerical Results

The convergence behavior of the higher-order MoM is first analyzed using a microstrip patch antenna as an example. The patch is 40 mm by 40 mm, which resides on a substrate with relative

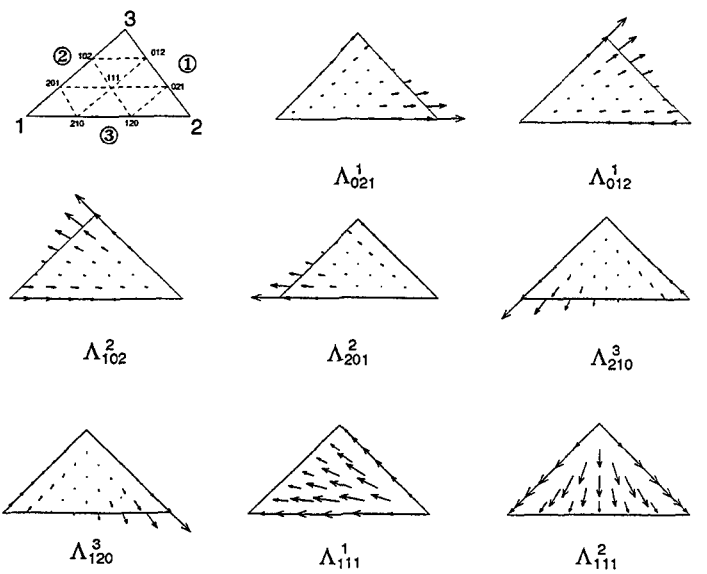


Figure 3: The first-order basis function.

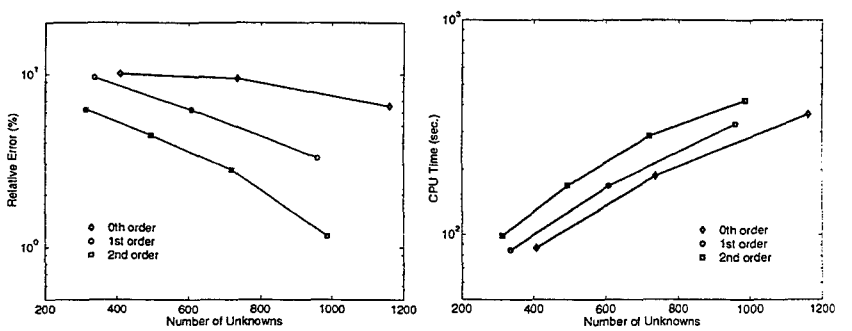


Figure 4: Convergence behavior of high-order basis function. (a) Relative error versus number of unknowns. (b) CPU time versus number of unknowns.

permittivity 2.17 and thickness 1.58 mm. The incident plane wave is assumed to be $\hat{\theta}$ polarized

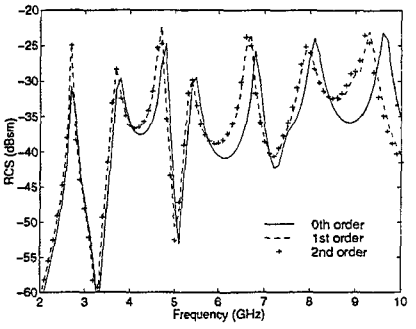


Figure 5: Backscattered RCS ($\sigma_{\theta\theta}$) versus frequency for a rectangular microstrip antenna [14].

with the incident angle $(\theta^i, \phi^i) = (60°, 45°)$. The frequency is 10 GHz. The $\hat{\theta}$ component of backscattered RCS is calculated. The simulation is carried out at various levels of discretization for basis functions with different orders. The error is plotted in Fig. 4(a) by computing $|\sigma - \sigma_{ref}|/|\sigma_{ref}|$ where σ_{ref} is the referenece RCS result by running the third-order scheme at a discretization of 400 triangles. The corresponding CPU time for matrix filling is given in Fig. 4(b). From the figures, we observe that for the same number of unknowns, the higher-order scheme gives more accurate results and the CPU time are comparable for different order schemes. For small problems, the higher-order schemes has more CPU time because the singular and near interaction terms are relatively dominant. When the problem size becomes large, the higher-order schemes become be more efficient than the lower-order ones.

As the first example, we calculate the backscattered RCS of a microstrip patch antenna [14]. All the parameters are the same as those in the previous convergence analysis except for the patch size. Here, the size is 36 mm by 26.6 mm. The zeroth-, first-, and second-order schemes are employed for a coarse discretization with 24 triangles. As can be seen from Fig. 5, the zeroth-order scheme does not give an accurate result, especially at high frequencies, whereas the first- and second-order schemes converge to the accurate result. The numbers of unknowns for the zeroth-, first-, and second-order approaches are 29, 106, and 231, respectively.

The next example is a crossed dipole antenna in a double-layer medium [10], [15]. The two crossed dipoles are on the top layer, which have different lengths so that the dual frequency operation is achieved. One is 11.9 mm long and the other is 10.2 mm long. Both of them are 1.7 mm wide. The feeding lines are on the bottom layer, which are 2.2 mm wide. The substrates have the same relative permittivity 2.17. The bottom layer is 0.8 mm thick and the top one is 1.6 mm thick. The coarse discretization is shown in Fig. 6(a). Different order basis functions are employed. The S-parameters are plotted in Fig. 6(b)-(d), which show that the higher-order basis functions give more accurate results. The numbers of unknowns for the zeroth-, first-, second-, and third-order approaches are 61, 246, 555, and 988, respectively.

The last example is a microstrip filter [16]. The photonic bandgap effect can be achieved from this structure. The coarse discretization is shown in Fig. 7(a). The zeroth- and first-order approaches are employed here, which have 347 and 1274 unknowns, respectively. The S-parameters are given by Fig. 7(b) and (c).

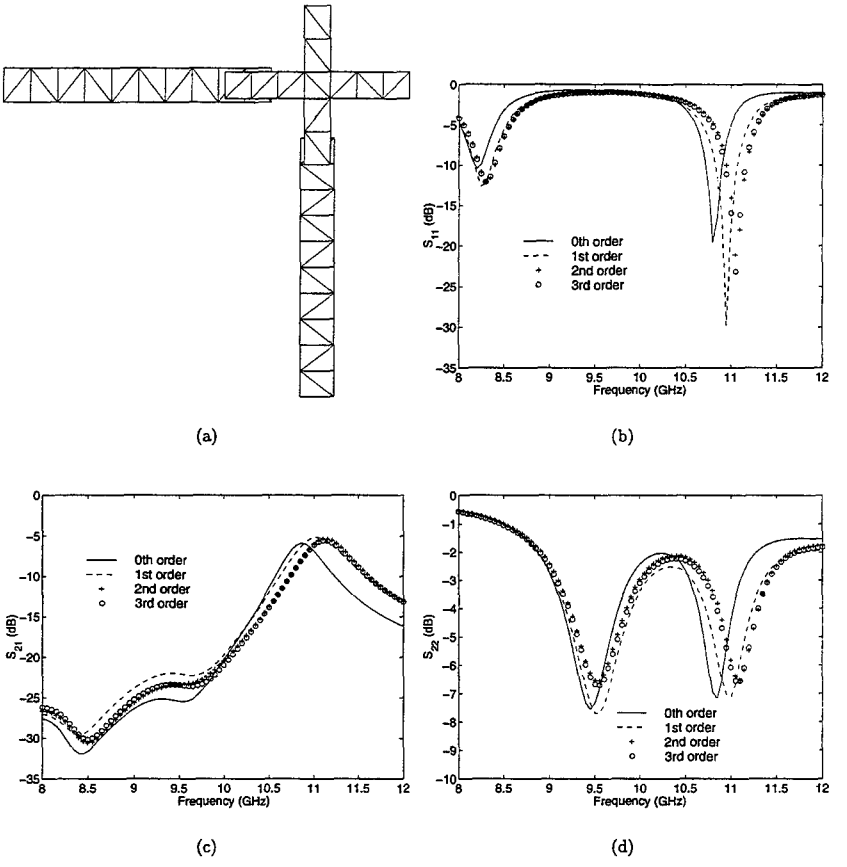


Figure 6: The S-parameters of a crossed dipole antenna [10], [15].

4 Conclusion

A higher-order method of moments is presented for the analysis of microstrip structures in a multilayer medium. It is shown that this higher-order method has a better convergence rate than the conventional lower-order methods. Several examples are given to demonstrate the accuracy and efficiency of this method.

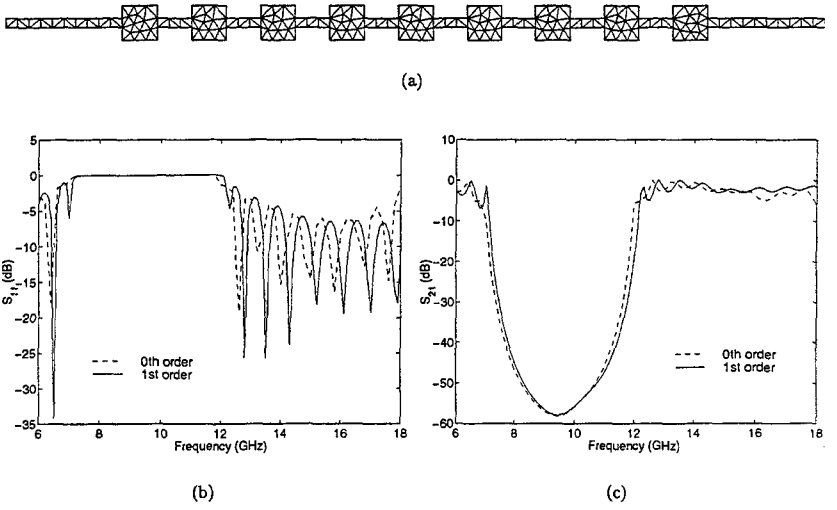


Figure 7: The photonic bandgap effect of a microstrip filter [16].

References

[1] S. M. Rao, D. R. Wilton, and A. W. Glisson, "Electromagnetic scattering by surface of arbitrary shape," *IEEE Trans. Antennas Propagat.*, vol. 30, pp. 409-418, May 1982.

[2] C. Canuto, M. Y. Hussaini, A. Quarteroni, and T. A. Zang, *Spectral Methods in Fluid Dynamics*, Berlin: Springer-Verlag, 1987.

[3] B. A. Szabó and I. Babuška, *Finite Element Analysis*, New York: Wiley, 1991.

[4] J. R. Mosig, "Arbitrarily shaped microstrip structures and their analysis with a mixed potential integral eqtation," *IEEE Trans. Microwave Theory Tech.*, vol. 36, pp. 314–323, Feb. 1988.

[5] W. C. Chew, *Waves and Fields in Inhomogeneous Media*, Piscataway: IEEE Press, 1995.

[6] D. G. Fang, J. J. Yang, and G. Y. Delisle, "Discrete image theory for horizontal electric dipole in a multilayer medium," *IEE Proc.-H*, vol. 135, pp. 297-303, Oct. 1988.

[7] Y. L. Chow, J. J. Yang, D. G. Fang, and G. E. Howard, "A closed-form spatial Green's function for the thick microstrip substrate," *IEEE Trans. Microwave Theory Tech.*, vol. 39, pp. 588-592, Mar. 1991.

[8] R. A. Kipp and C. H. Chan, "Complex image method for sources in bounded regions of multilayer structures," *IEEE Trans. Microwave Theory Tech.*, vol. 42, pp. 860-865, May 1994.

[9] M. I. Aksun, "A robust approach for the derivation of closed-form Green's functions," *IEEE Trans. Microwave Theory Tech.*, vol. 44, pp. 651-658, May 1996.

[10] F. Ling, D. Jiao, and J. M. Jin, "Efficient electromagnetic modeling of microstrip structures in multilayer media," *IEEE Trans. Microwave Theory Tech.*, vol. 47, pp. 1810-1818, Sept. 1999.

[11] R. D. Graglia, D. R. Wilton, and A. F. Peterson, "Higher order interpolatory vector bases for computational electromagnetics," *IEEE Trans. Antennas Propagat.*, vol. 45, pp. 329-342, March 1997.

[12] M. G. Duffy, "Quadrature over a pyramid or cube of integrands with a singularity at a vertex," *J. Numer. Anal.*, vol. 19, pp. 1260–1262, Dec. 1982.

[13] F. Ling and J. M. Jin, "Scattering and radiation analysis of microstrip antennas using discrete complex image method and reciprocity theorem," *Microwave Opt. Tech. Lett.*, vol. 16, no. 4, pp. 212-216, Nov. 1997.

[14] E. H. Newman and D. Forrai, "Scattering from a microstrip patch," *IEEE Trans. Antennas Propagat.*, vol. 35, pp. 245-251, Mar. 1987.

[15] R. Gillard, J. Corre, M. Drissi and J. Citerne, "A general treatment of matched terminations using integral equations— modeling and application," *IEEE Trans. Microwave Theory Tech.*, vol. 42, pp. 2545-2553, Dec. 1994.

[16] H. Contopanagos, L. Zhang, and N. G. Alexopoulos, "Thin frequency-selective lattices integrated in novel compact MIC, MMIC, and PCA architectures," *IEEE Trans. Microwave Theory Tech.*, vol. 46, pp. 1936-1948, Nov. 1998.

SESSION 13

CONFORMAL ANTENNAS

Chairs: Leo Kempel and Douglas Werner

A Conformal, Flexible, Multifunction Communications Antenna

T. R. Holzheimer
Raytheon Systems Company
Aircraft Integration Systems
Greenville, Texas 75403

Abstract:

Certain applications are constrained in available surface area for the location of multiple antennas. A solution to this was developed and tested that is both conformal and flexible with multifunction capability. The antenna has capabilities in the VHF, UHF and L-Band frequency bands. It has both transmit and receive capability in both VHF and UHF and receive only for L-Band. The VHF portion handles 50 Watts CW and the UHF capability is 200 Watts CW. The antenna described has 3.0 inches of flexure with a 19 inch square aperture in a 3.75 inch overall height. The UHF portion has both low and high angle modes. This antenna required a new method of installation and removal from arbitrary curved surfaces. Successful flight testing has occurred. Several modifications were made and limited data is presented illustrating its multifunction capability.

Introduction:

The typical antenna farm installation consists of a single antenna for every function and frequency band of interest. This can quickly result in a lack of available surface area for antenna installation. Typical solutions call for deletion of antennas or combinations of antennas.[1] .The problem is further aggravated by potential transmitter coupling, maintaining required field of view and meeting single antenna performance in a multifunction aperture. Mating conformal antenna(s) to an arbitrary surface is still a major problem. This solution requires a pliant or flexible antenna with multifunction capability. This has been investigated by several groups with solutions such as the flexible tape array that is minimally flat with a small amount of allowable bending.[2] A second antenna solution is the flexible cushion that is laid on any available surface.[3] These antennas are all limited to a single antenna function. The effort reported here resulted in a solution whereby antenna apertures are combined in a single aperture.

Antenna Requirements:

The antenna was designed for installation on a multitude of different shaped surfaces. Figure 1 defines the antenna and the localized directions for installation. The antenna has multiple communication capability in the VHF and UHF bands and receive only capability for GPS L1 and L2 frequencies. The requirements are summarized in Table I.

Table I. Conformal, Flexible Multifunction Antenna Requirements

Frequency Bands: VHF - 118 to 174 MHz
UHF - 240 to 320 MHZ
GPS - L1 and L2

Polarization: VHF - Vertical
UHF (Mode 0) - RHCP
UHF (mode 1) - Vertical
GPS - RHCP

Azimuthal Coverage: 360 degrees

Elevation Coverage: VHF - Standard Monopole
UHF (mode 0) - Upper Hemisphere
UHF (mode 1) - Standard Monopole
GPS - Upper Hemisphere

Gain: VHF - 0 dBli
UHF (mode 0) - +3.5 dBic
UHF (mode 1) - +3 dBli
GPS - +3 dBic

VSWR: VHF - 2.0:1 with 2.5:1 maximum
UHF - 2.0:1 with 2.5:1 maximum
GPS - 2.0:1 maximum

Power Handling: VHF - 50 Watts CW
UHF - 200 Watts CW
GPS - Receive Only

Pressure: 2.0 psi (4.0 psi ultimate) on Edges
10.0 psi (20.0 psi ultimate) on Top Surface

Weight: Less Than 25 Pounds

Size: 19 inches Square, 3.75 inches in Height

Solution:

The antenna solution is shown in figure 2. The antenna is extremely pliant with built-in flexure from fore to aft. The antenna weighed 20 pounds and met all power handling and required frequency band operation. Every requirement from Table I was met except for UHF mode 1 that requires a feed modification. However, it is noted that mode 1 performance is a goal.

The antenna solution uses four point feeding of an air loaded patch antenna for UHF.[4] VHF is handled with a broadband matched whip antenna inclined at 30 degrees aft. GPS is handled with a high 'K' stacked patch antenna located slightly off centerline in the fore area of the VHF antenna. The antennas were all positioned on the UHF antenna for minimized coupling. The UHF antenna center is a zero field point that allowed the installation of all decoupling and matching components in a centrally located cylinder.

Problems Discovered and Resolutions:

The GPS antenna function operated flawlessly with no interactions with VHF or UHF communications due to a built-in filter and two octave frequency separation. However, VHF energy did couple to UHF communications due to close proximity and the minimal 66 MHz frequency separation. This coupling was fixed with a small amount of inductance and attenuation using a coaxial line matching transformer inserted at the VHF feedpoint.

The UHF function also exhibited the problem of changing matching condition with flexure of the aperture and installation on the arbitrary curved surface. These problems were corrected with identical feed point match in four places that made flexure changes benign to antenna performance.

The antenna is installed via an insulating layer of proprietary adhesive, that can be removed, providing for a quick install and de-install of the antenna. The UHF antenna was tuned with the insulating layer on a simulated ground plane providing maximum gain over frequency. This accounted for dramatic variations in gain with installation. Figure 3 shows the gain at UHF when the antenna is incorrectly installed. Figure 4 shows the gain at UHF when the antenna is correctly installed.

Measurements:

Measurements were made on all functions. GPS was well within the required VSWR and gain. VHF exhibited a worst case 2.4:1 VSWR. UHF mode 0 is 1.5:1 VSWR maximum while mode 1 was 3.4:1 VSWR maximum. Radiation patterns were obtained and were as expected with no frequency dropouts or angular dropouts. Figure 5 shows a typical VHF radiation pattern. Figure 6 shows a typical set of un-normalized UHF mode 0 radiation patterns. A slight skewing was discovered in the UHF mode 0 function, but it changed slightly with installation and in all cases was acceptable. The UHF mode 1 function radiation patterns are close to theory, but the gain is lower than expected. Gain at VHF is + 5 dBli and + 3 dBic for GPS. UHF mode 0 has gain of + 3.5 dBic.

Summary:

A conformal, flexible multifunction communications antenna was developed, demonstrated and is still operating in the field. The antenna has been flown and can be installed and de-installed from a multitude of curved surfaces. All functions met the specifications in Table I except for UHF mode 1. A solution for this deficiency has been developed and is being presently pursued.

References:

[1] Lo, Y. T. and Lee, S. W., Antenna Handbook: Theory, Applications, and Design, Van Nostrand Reinhold Company, New York, 1988.

[2] Joy, Ed, "Doing Away With Satellite Dishes: Flat "Window Curtain" Antenna Offers Alternative For TV, Phone & Other Signals," Research News, Press Release, Georgia Institute of Technology, 4 March, 1994.

[3] Ball Aerospace and Communications Group, Telecommunication Products Division, UHF Satcom Antenna Data Sheet for AN0624A.

[4] D. H. Schaubert, F. G. Farrar, A. Sindoris and S. T. Hayes, "Microstrip Antennas with Frequency Agility and Polarization Diversity," IEEE Trans. AP, Vol. AP-29, No. 1, January, 1981, pp 118-123.

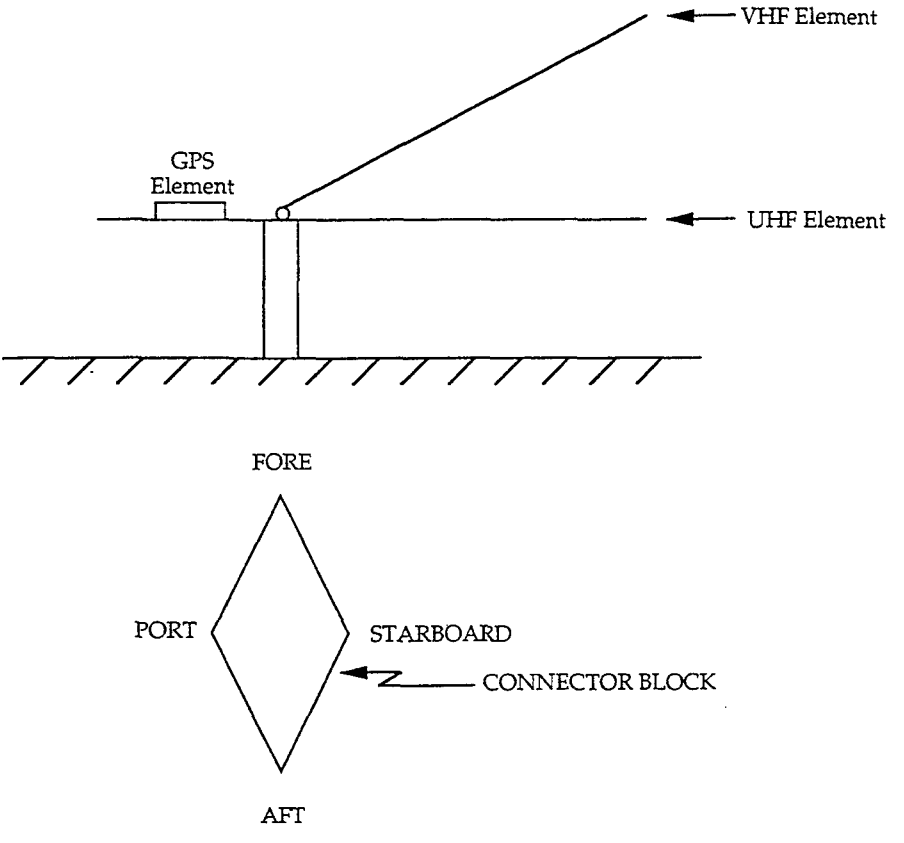


Figure 1. Conformal, Flexible, Multifunction Antenna Drawing With Directions.

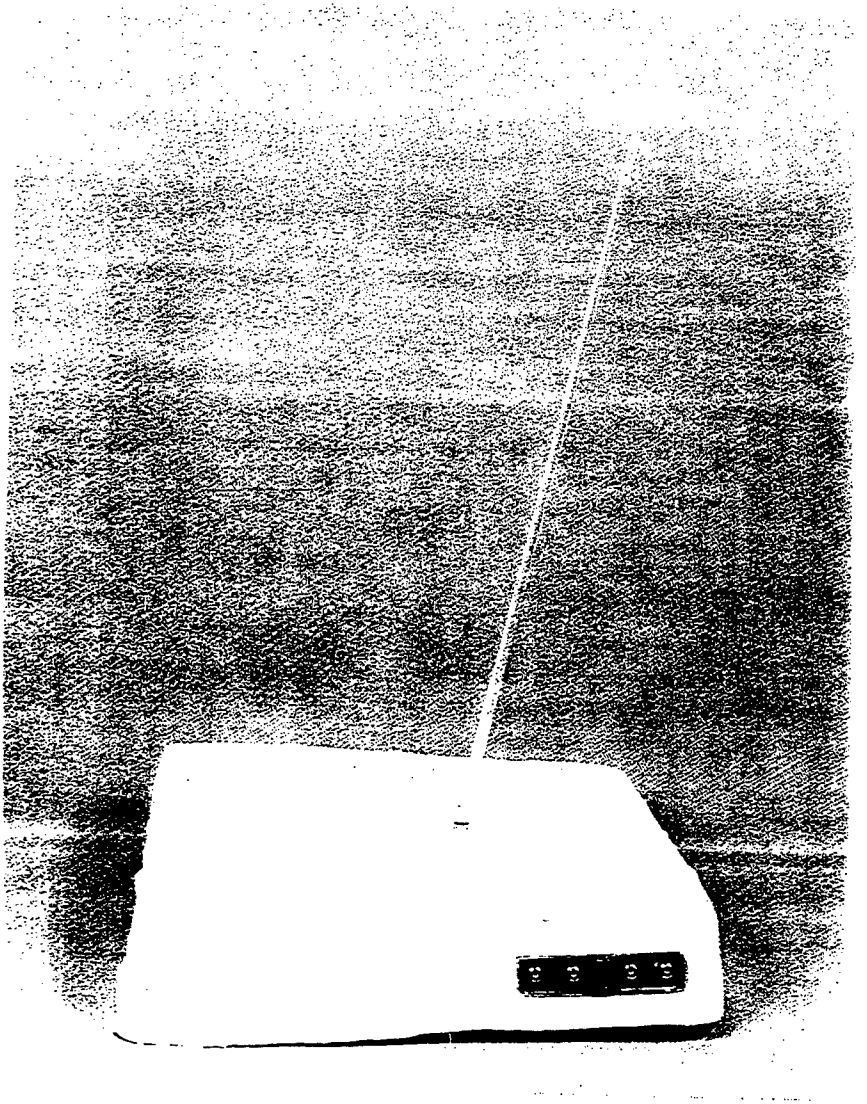


Figure 2. Conformal, Flexible, Multifunction Antenna Solution.

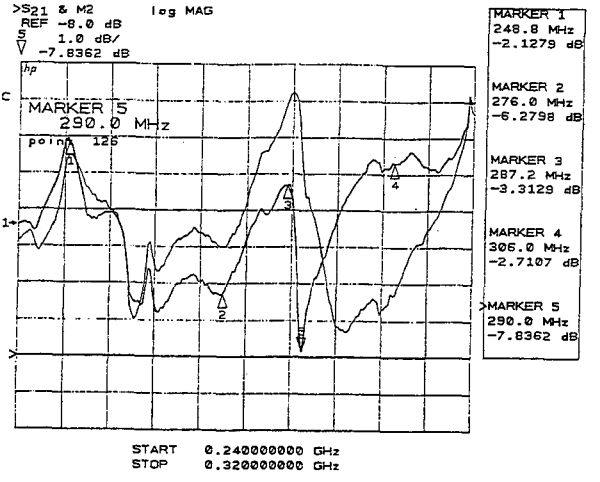


Figure 3. UHF Mode 0 Gain, Incorrectly Installed.

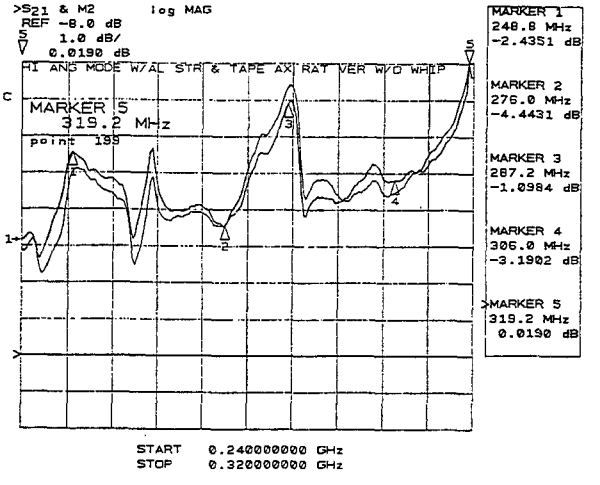


Figure 4. UHF Mode0 Gain, Correctly Installed.

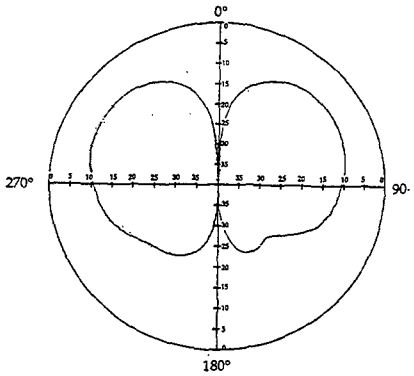


Figure 5. Typical VHF Radiation Pattern.

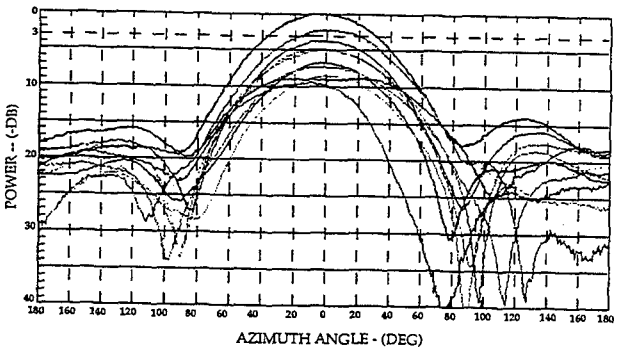


Figure 6. Typical UHF Radiation Patterns.

Finite printed antenna array modeling using an adaptive multi-resolution approach

Lars S. Andersen, Yunus E. Erdemli and John L. Volakis*
Radiation Laboratory, EECS Department, University of Michigan
Ann Arbor, MI 48109-2122, USA
E-mail : {andersen, yunusee, volakis}@umich.edu

Abstract

Accurate and efficient modeling of finite printed antenna arrays is of increasing practical importance. This paper presents an adaptive multi-resolution approach for performing such modeling. Its merits for single elements are demonstrated and the extension to finite arrays is discussed.

1 Introduction

Multi-functionality, broad bandwidth and size requirements are important issues in printed antenna design. Printed antennas meeting such demands often incorporate complex materials and fine features as part of their construction and hence part of these antennas often require a very high resolution for proper numerical modeling. High resolution is also needed for accurate feed modeling and input impedance computations. Accurate modeling of finite arrays of such multi-function or broadband elements presents additional challenges. The demands for high resolution result in an excessive number of unknowns which cannot easily be handled using traditional numerical methods, even when fast integral or hybrid techniques are employed.

In this paper, we discuss a new approach for accurate and efficient modeling of finite printed antenna arrays which may incorporate fine features. To overcome the difficulties in modeling the feed region, fine geometric details and complex or dense materials, the hybrid finite element / boundary integral (FE/BI) method [1] is employed in conjunction with hierarchical mixed-order tangential vector finite elements (TVFEs) for tetrahedra [2]. Such TVFEs avoid any need for re-meshing while allowing accurate modeling of rapid field variations provided the order of the approximation within each element is determined properly. This can be done adaptively which eliminates the need for human choices as part of the modeling process. To overcome the difficulties in modeling the finite nature of the array, we discuss an approach which is based on the fast spectral domain algorithm (FSDA) formulation for infinite periodic arrays [3] but employs a modified aperture Green's function which accounts for edge effects in an approximate manner. This modification influences the matrix-vector products within the iterative solver algorithm and has a minimal effect on the central processing unit (CPU) time requirements for the iterative solver. Hence, the CPU time requirements for the proposed approach are comparable to those for FSDA infinite array analysis. However, although the proposed approach is not exact, it is more accurate than simply utilizing a truncated infinite array solution as the latter approach does not incorporate edge effects at all.

This paper is organized as follows. Section 2 briefly outlines the adaptive refinement strategy adopted in the paper. Section 3 offers some numerical results demonstrating the merits of the proposed adaptive multi-resolution modeling approach for a single antenna element. Section 4 discusses the proposed approach for finite antenna arrays. Section 5 concludes the paper.

2 Adaptive refinement strategies

In this paper, a conceptually very simple adaptive refinement strategy is adopted. Following a FE/BI solution with mixed-order TVFEs of order 0.5, we determine the degree of error in each element via an error indicator. A refined solution is then computed where a certain pre-specified percentage of the elements having the highest degree of error are modeled with mixed-order TVFEs of order 1.5 and the remaining elements are again modeled with mixed-order TVFEs of order 0.5. Three different error indicators are presented below.

For a general three-dimensional electromagnetic problem, we discretize the computational domain into N^e tetrahedral elements denoted by T^e, $e = 1, \cdots, N^e$, each having 4 faces denoted by F_i^e, $i = 1, \cdots, 4$. The center of T^e and F_i^e is denoted by $C(T^e)$ and $C(F_i^e)$, respectively, and the unit normal vector to F_i^e directed out of the element T^e is denoted by $\hat{n}_i^e$. The lowest order FE/BI solution leads to an approximation of the electric flux density $\mathbf{D}$ within and on the boundary of each element T^e. On the face F_i^e, we let $\mathbf{D}_i^{e,\text{in}}$ denote the value of $\mathbf{D}$ evaluated in T^e and let $\mathbf{D}_i^{e,\text{out}}$ denote the value of $\mathbf{D}$ evaluated in the element bounding T^e. As discussed in [4], three suitable error indicators for an element e are

$$EI_1(e) = |\mathbf{D}(C(T^e))| \tag{1}$$

$$EI_2(e) = \max_i \left\{ |\hat{n}_i^e \cdot (\mathbf{D}_i^{e,\text{in}} - \mathbf{D}_i^{e,\text{out}})|_{C(F_i^e)} \right\} \tag{2}$$

$$EI_3(e) = \max_i \left\{ \int_{F_i^e} |\hat{n}_i^e \cdot (\mathbf{D}_i^{e,\text{in}} - \mathbf{D}_i^{e,\text{out}})|^2 dS \right\} \tag{3}$$

The corresponding error indicators for a sub-domain of elements are simply the maximum of the error indicators for the elements comprising the sub-domain.

3 Single antenna element analysis

We consider a metallic printed bowtie antenna backed by a rectangular cavity recessed in an infinite metallic ground plane, as illustrated in Fig. 1 (side view) and Fig. 2 (top view). The cavity-backed patch antenna is situated in free space characterized by the permittivity ε_0 and the permeability μ_0. The cavity dimensions are 48 cm $\times$ 64 cm $\times$ 12 cm. The interior metallic cavity walls are covered with an artificial absorber of permittivity $(1 - j2.7)\varepsilon_0$, permeability $(1 - j2.7)\mu_0$ and thickness 4 cm. This absorber layer would not be part of an actual antenna but is merely a well-established computational tool that serves to approximately simulate a metallic printed bowtie antenna situated in free space. The specific printed bowtie antenna consists of two isosceles triangular patches characterized by the opening angle 67.38° and the maximum width 24 cm. The bowtie patches are centered in the cavity aperture and fed by a probe of constant current connecting the two triangular patches.

An antenna very similar to the above was discussed by Collin [5] and is expected to cover the UHF channels 14 to 83 spanning the frequency range [450 MHz, 900 MHz] when used with a 300 Ω feed line. That is, the real and imaginary parts of the input impedance are expected to hover around 300 Ω and 0 Ω, respectively, in this frequency range.

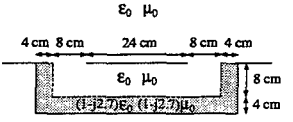


Figure 1: Side view of a metallic printed bowtie antenna backed by an air- and absorber-filled rectangular cavity recessed in an infinite metallic ground plane.

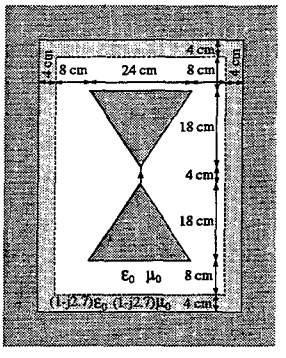


Figure 2: Top view of a metallic printed bowtie antenna backed by an air- and absorber-filled rectangular cavity recessed in an infinite metallic ground plane.

For analysis and evaluation of the proposed error indicators, we discretize the boundary integral (BI) surface and the patch into a coarse (56 antenna triangles and 330 BI triangles) and a fine (160 antenna triangles and 1030 BI triangles) mesh. These surface meshes are extruded into the cavity to form three prism layers. Each prism is broken into three tetrahedra and four different TVFE options are applied. First, the mixed-order TVFE of order 0.5 throughout the cavity for the coarse mesh. Second, the mixed-order TVFE of order 0.5 throughout the cavity for the fine mesh. Third, the mixed-order TVFE of order 1.5 throughout the cavity for the coarse mesh. Fourth, the mixed-order TVFE of order 0.5 in conjunction with the mixed-order TVFE of order 1.5 in regions found adaptively (20% of the TVFEs are of order 1.5) for the coarse mesh. The adaptive refinement is carried out for each of the error indicators EI_1, EI_2 and EI_3 given by (1)-(3) on a sub-domain by sub-domain basis only with a sub-domain being three adjacent prisms extruded from a surface triangle (386 sub-domains for the coarse mesh).

Real and imaginary parts of the input impedance as a function of frequency are given in Fig. 3 for the first three TVFE options (no adaptivity). Instead of the strongly resonant behavior characterizing cavity-backed patch antennas, we observe the expected slightly oscillatory behavior of the real and imaginary parts. Mixed-order TVFEs of order 0.5 for the fine mesh and mixed-order TVFEs of order 1.5 for the coarse mesh give similar results that are better (real parts closer to $300\,\Omega$ and imaginary parts closer to $0\,\Omega$) than those with mixed-order TVFEs of order 0.5 for the coarse mesh. Although mixed-order TVFEs of order 0.5 for the fine mesh and mixed-order TVFEs of order 1.5 for the coarse mesh give similar results, the latter approach is more attractive than the former in terms of memory and CPU time requirements.

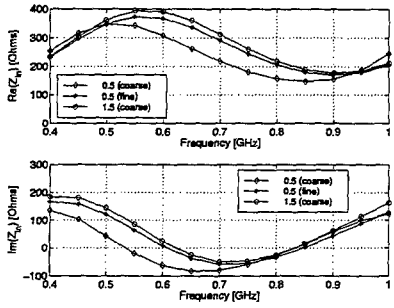


Figure 3: Real and imaginary part of the input impedance for the metallic bowtie patch antenna in Fig. 1-2.

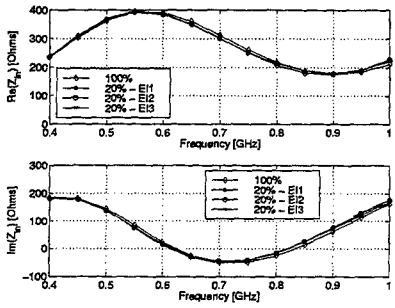


Figure 4: Real and imaginary part of the input impedance for the metallic bowtie patch antenna in Fig. 1-2.

To demonstrate the merits of adaptive refinement, Fig. 4 shows the real and imaginary parts of the input impedance as a function of frequency for the coarse mesh with mixed-order TVFEs of order 1.5 throughout the cavity and with 80% mixed-order TVFEs of order 0.5 and 20% mixed-order TVFEs of order 1.5 found via adaptive refinement using EI_1, EI_2 and EI_3 on a sub-domain by sub-domain basis. The results are almost indistinguishable expressing that we can accurately predict the behavior of the antenna using only 20% mixed-order TVFEs of order 1.5. This presents a significant memory and CPU time improvement at virtually no cost.

To illustrate the regions of refinement, we consider a cross-section of the mesh parallel to the antenna with the boundaries of the metallic cavity and antenna marked with thick black lines. As mentioned previously, the tetrahedral volume mesh is grown from a triangular surface mesh in a cut in the plane of the bowtie patches by extruding it into three prism layers and breaking each prism into three tetrahedra. Since we consider sub-domain by sub-domain refinement only, 0 or 9 tetrahedra can be refined corresponding to a given triangle in the cross-section. In the following, a white / dark gray triangle indicates that 0 / 9 tetrahedra are being refined. The regions of refinement at 0.7 GHz (close to the center of the frequency band of operation) are shown in Fig. 5. Although they are seen to differ slightly for the three different error indicators, they all show the general trend of predicting the feed area and, to a lesser extent, the corners of the triangular patches as the regions where mixed-order TVFEs of order 1.5 are applied.

4 Finite antenna array analysis

Accurate and efficient analysis of large finite arrays is of significant interest for practical phased-array applications. A fast but approximate approach is to consider the array as infinite in order to reduce the complexity of the problem by studying only a unit cell of the periodic structure. This approach has been shown to be accurate and efficient for radar cross section (RCS) computation of finite cavity arrays when utilizing the hybrid FE/BI technique [6]. In [6], the scattering pattern for a finite array was obtained by multiplying the pattern for a single unit cell of the corresponding infinite array with the proper array factor. Alternatively, one can simply truncate the infinite array solution in the finite array region. This truncation is carried out by generating the finite array near

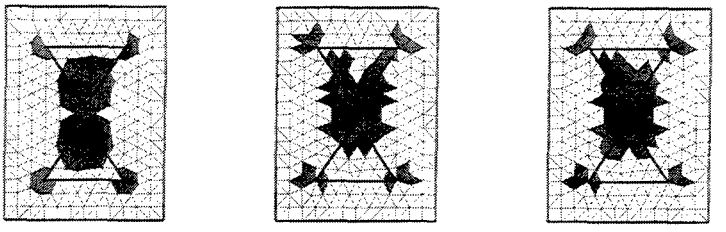


Figure 5: Regions of refinement for the metallic bowtie patch antenna in Fig. 1-2 with EI_1 (left), EI_2 (middle) and EI_3 (right).

fields using an infinite array unit cell solution along with the periodic phase shift imposed by the Floquet mode series. As an application of this approach, we consider the radiation from slot antenna arrays (Fig. 6). Radiation patterns of 3×3 and 5×5 slot antenna arrays are given in Fig. 7 for the truncated infinite array solutions along with corresponding finite array solutions obtained via rigorous but inefficient finite array analysis (brute force simulation of all array elements). As seen, the truncated infinite array patterns agree reasonably well with the exact finite array patterns in this case. However, for composite structures involving complex materials, we expect the agreement between the exact finite array solution and the approximate one based on the infinite array to be less acceptable. Furthermore, we emphasize that neither of the two approximate approaches incorporate the finiteness of the array into the analysis. That is, edge effects are not taken into account.

In the literature, there have been important attempts for accurate and efficient finite array analysis by taking advantage of the infinite array solution while including the edge effects. In [7], edge effects are taken into account through a convolution of the associated infinite array spectra with the finite array footprint. Poisson's sum formula (PSF) for finite sums is employed to obtain an infinite series representation from a finite series one. However, the incomplete form of the PSF which does not include explicit end point contributions is used, as recently pointed out in [8]. As discussed in [8], it is important to consider the complete PSF which contains explicit end-point contributions in order to evaluate array surface currents accurately. To emphasize the use of the complete PSF for a two-dimensional finite array, the array factor of a 41×41 uniform planar array is considered in Fig. 8 for a $0.5\lambda_0$ spacing and the scan direction $(\theta, \phi) = (30°, 45°)$. As seen in Fig. 8, the incomplete PSF results in error at angles far from the main beam and yields incorrect locations for pattern nulls and lobes. This is similar to the one-dimensional example given in [8]. Here, we employ the complete form of the PSF in our analysis which is presented in the following.

In dealing with the computational burdens of finite arrays, we introduce a new approach for pattern computation. The approach is based on the FSDA formulation for infinite periodic arrays [3]. However, we instead employ a modified aperture Green's function which is obtained by using the complete PSF to account for edge effects in an approximate manner. This modification influences the matrix-vector products within the iterative solver algorithm and has a minimal effect on the CPU time requirements for the iterative solver. As a result, the CPU time requirements for finite array analysis are comparable to those for infinite array analysis. Below, we briefly discuss the formulation of the proposed approach.

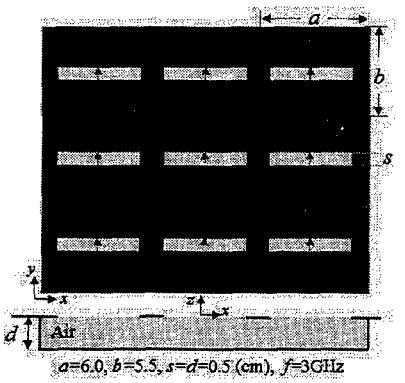


Figure 6: Slot antenna array geometry.

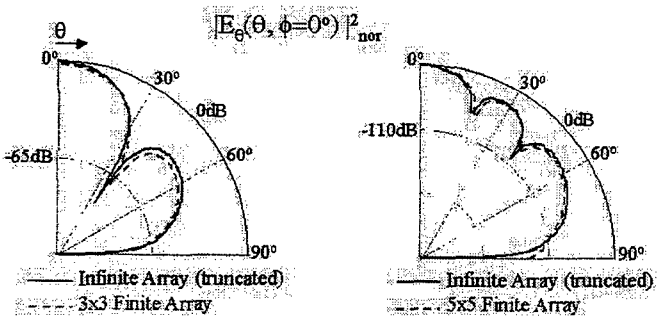


Figure 7: Slot antenna array radiation patterns.

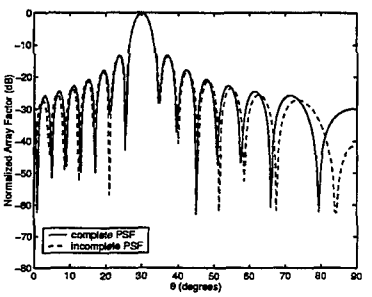


Figure 8: Array factor of a 41x41 uniform planar array with an element spacing of $0.5\lambda_0$ and the scan direction $(\theta, \phi) = (30°, 45°)$.

The FSDA [3] employs the spectral domain Green's function to efficiently evaluate the BI matrix-vector products carried out within an iterative solver. Instead of explicitly generating all BI matrix elements, the actual current distribution is summed up in the spectral domain in each iteration and the spectral Floquet mode series is computed only once per weighting function. Thus, the FSDA results in a CPU time complexity of $O(N)$ as well as a memory demand of $O(N)$ for a given fixed set of modes. Compared to the adaptive integral method (AIM) [9], the FSDA leads to enormous speed-ups of about two orders of magnitude for relatively small numbers of unknowns [3]. In the proposed approach, we take advantage of the speed and memory superiority of the FSDA.

We begin with a truncated infinite array Green's function representation. For a finite periodic array with $(2M_x+1)\times(2N_y+1)$ elements, the free space periodic Green's function can be written

$$G_p(\mathbf{r},\mathbf{r}') = \frac{1}{A}\sum_{m=-M_x}^{M_x}\sum_{n=-N_y}^{N_y}\frac{1}{2jk_{zmn}}e^{-jk_{zmn}|z-z'|}e^{-j\mathbf{k}_{tmn}\cdot(\rho-\rho')} \tag{4}$$

where the notation of [10] is used. Using a procedure similar to that in [7], we then employ the complete PSF on the doubly finite series in (4) to obtain an infinite series representation convolved with a pulse function representing the footprint of the finite array. This convolution operation is easily carried out since it involves an impulse function. Considering the discretized version of the BI by applying Galerkin's testing with the well-known Rao-Wilton-Glisson basis functions $\mathbf{b}_q(\mathbf{r})$ [11], we end up with the representation

$$\langle \mathbf{b}_q(\mathbf{r}), \mathbf{H}(\mathbf{r})\rangle = \frac{Y_0}{k_0 A}\sum_{p=1}^{N_{BI}} E_p[F_1^{qp}+F_2^{qp}+F_3^{qp}+F_4^{qp}] \ , \ q=1,...,N_{BI} \tag{5}$$

where E_p represent N_{BI} electric field expansion coefficients and $F_i^{qp}(i=1,2,3,4)$ are given by

$$F_1^{qp} = C_1\sum_{m=-M_x}^{M_x}\sum_{n=-N_y}^{N_y}\tilde{\mathbf{b}}_q(\mathbf{k}_{tmn})\cdot\tilde{\bar{\mathbf{G}}}(\mathbf{k}_{tmn})\cdot\tilde{\mathbf{b}}_p^*(\mathbf{k}_{tmn}) \tag{6}$$

$$F_2^{qp} = C_2\sum_{m=\pm M_x}\sum_{n=\pm N_y}\tilde{\mathbf{b}}_q(\mathbf{k}_{tmn})\cdot\tilde{\bar{\mathbf{G}}}(\mathbf{k}_{tmn})\cdot\tilde{\mathbf{b}}_p^*(\mathbf{k}_{tmn}) \tag{7}$$

$$F_3^{qp} = C_3\sum_{m=\pm M_x}\sum_{n=-N_y}^{N_y}\tilde{\mathbf{b}}_q(\mathbf{k}_{tmn})\cdot\tilde{\bar{\mathbf{G}}}(\mathbf{k}_{tmn})\cdot\tilde{\mathbf{b}}_p^*(\mathbf{k}_{tmn}) \tag{8}$$

$$F_4^{qp} = C_4\sum_{m=-M_x}^{M_x}\sum_{n=\pm N_y}\tilde{\mathbf{b}}_q(\mathbf{k}_{tmn})\cdot\tilde{\bar{\mathbf{G}}}(\mathbf{k}_{tmn})\cdot\tilde{\mathbf{b}}_p^*(\mathbf{k}_{tmn}) \tag{9}$$

where * and $\tilde{}$ denote complex conjugation and spectral domain representation, respectively, and C_i are constants determined by the geometry of the unit cell. Also, $\tilde{\bar{\mathbf{G}}}(\mathbf{k}_{tmn})$ is the discrete version of the spectral domain half space dyadic Green's function as given in [6]. The four terms F_i^{qp} in (5) are due to the complete PSF and represent the finiteness of the array. That is, they take into account edge effects. They are readily implemented in the context of the FSDA as outlined in [3].

We note that the computational domain for the finite array analysis is only a single unit cell (as in the case of an infinite array) and that we still consider the phase boundary conditions within the finite element volume [10]. However, as compared to the approach of simply truncating the infinite array solution, the proposed methodology provides superior accuracy since it includes edge contributions.

5 Conclusions

This paper presented an adaptive multi-resolution approach for accurate and efficient modeling of finite antenna arrays. Its merits for single elements were demonstrated and its extension to finite arrays was discussed.

References

[1] J.L. Volakis, A. Chatterjee, and L.C. Kempel. *Finite element method for electromagnetics.* IEEE Press, USA, 1998.

[2] L.S. Andersen and J.L. Volakis. 'Hierarchical tangential vector finite elements for tetrahedra'. *IEEE Microwave and Guided Wave Letters*, vol. 8, pp. 127-129, March 1998.

[3] T.F. Eibert and J.L. Volakis. 'Fast spectral domain algorithm for rapid solution of integral equations'. *Electronics Letters*, vol. 34, pp. 1297-1299, 25th June 1998.

[4] L.S. Andersen. *Multi-resolution methods for simulation and design of antennas.* PhD thesis, University of Michigan, 1999.

[5] R.E. Collin. *Antennas and radiowave propagation.* McGraw-Hill Book Company, USA, 1985.

[6] J.M. Jin and J.L. Volakis. 'Scattering and radiation analysis of three-dimensional cavity arrays via a hybrid finite-element method'. *IEEE Transactions on Antennas and Propagation*, vol. AP-41, pp. 1580-1586, November 1993.

[7] A.K. Skrivervik and J.R. Mosig. 'Analysis of finite phase arrays of microstrip patches'. *IEEE Transactions on Antennas and Propagation*, vol. AP-41, pp. 1105-1113, August 1993.

[8] O.A. Civi, P.H. Pathak, and H.-T. Chou. 'On the Poisson sum formula for the analysis of wave radiation and scattering from large finite arrays'. *IEEE Transactions on Antennas and Propagation*, vol. AP-47, pp. 958-959, May 1999.

[9] E. Bleszynski, M. Bleszynski, and T. Jaroszewicz. 'AIM : Adaptive integral method for solving large-scale electromagnetic scattering and radiation problems'. *Radio Science*, vol. 31, pp. 1225-1251, September-October 1996.

[10] T.F. Eibert, J.L. Volakis, D.R. Wilton, and D.R. Jackson. 'Hybrid FE/BI modeling of 3-D doubly periodic structures utilizing triangular prismatic elements and an MPIE formulation accelerated by the Ewald transformation'. *IEEE Transactions on Antennas and Propagation*, vol. AP-47, pp. 843-850, May 1999.

[11] S.M. Rao, D.R. Wilton, and A.W. Glisson. 'Electromagnetic scattering by surfaces of arbitrary shape'. *IEEE Transactions on Antennas and Propagation*, vol. AP-30, pp. 409-418, May 1982.

A Technique for Analyzing Radiation from Conformal Antennas Mounted on Arbitrarily-Shaped Conducting Bodies

Dean Arakaki, Douglas H. Werner, and Raj Mittra
Department of Electrical Engineering
The Pennsylvania State University
University Park, PA 16802

1. ABSTRACT

This paper presents an efficient method to solve the problem of radiation from conformal aperture and microstrip antennas mounted on arbitrarily-shaped conducting bodies. The method, based on the surface equivalence and reciprocity principles, uses a combination of the Finite Difference Time Domain (FDTD) and Method of Moments (MoM) techniques to substantially improve the computational efficiency of the radiation pattern calculation. When the geometry and location of the radiating element are modified, only a small portion of the overall analysis requires re-simulation. This leads to a significant improvement in computational efficiency over presently-used techniques, and can substantially improve design efficiency when included in an optimization loop. The technique is first validated by solving two canonical problems, namely a thin slot which is oriented either axially or azimuthally on an infinitely long, perfectly conducting cylinder. These patterns are then compared to those produced by the same slots mounted on finite-length cylinders. Finally, patterns are computed for a cavity-backed elliptical patch antenna mounted on an infinite-length PEC cylinder and compared to patterns computed by an alternate method.

2. INTRODUCTION

Low profile conformal antennas for use on mobile communications systems are receiving widespread attention due to the advantages of minimized aerodynamic friction and radar cross-sectional area, reduced risk of antenna structural damage, and simplified construction requirements over conventional types. Since this type of antenna has a complex configuration and is usually mounted on a large structure, the simulation of these antennas continues to be a challenge. Methods that will accommodate complex structures such as FDTD and the Finite Element Method (FEM) require an excessive number of volume elements for large bodies. Surface methods such as the Method of Moments (MoM) that can model large structures are limited to relatively simple material compositions such as homogeneous or layered material structures. Thus, any of these methods used alone cannot efficiently model a typical conformal antenna; hence, the need for a combination of techniques.

Several combinations of simulation techniques have been used; the hybrid method used in this paper includes the MoM and FDTD. These methods were selected for their strengths in modeling large arbitrarily-shaped homogeneous conducting bodies and relatively small regions with a complex material structure, respectively. The link between the two methods is the reciprocity theorem, which relates the currents and fields between two systems [1-3].

The hybrid method used in this paper reduces computational requirements for the calculation of radiation patterns, especially when the shape of the radiating element and location on the mounting structure are modified. For most configurations, the size and shape of the mounting structure is fixed: the proposed method exploits this constraint by requiring analysis on this part of the problem only once. Instead of re-simulating the entire structure to obtain the aperture field distribution for every element shape and location change, this approach requires a re-simulation in the vicinity of the element only if the element shape is changed. The proposed hybrid method eliminates the need to carry out multiple computationally-intensive matrix operations encountered in the use of other simulation methods.

Since the FDTD technique is well-suited to the analysis of complex inhomogeneous structures, it is used to model the region which includes the cavity-backed conformal antenna and a sufficient volume around it to account for the effects of the surrounding environment on the radiating aperture field distribution. Through the surface equivalence principle, equivalent currents are found and the cavity region is closed with a perfect electrical conductor (PEC). The resulting structure, which can be large relative to the radiating aperture and of arbitrary shape, is analyzed by the MoM technique, since this method approximates the surface with triangular element discretization. This enhances both computational accuracy and efficiency via the use of a closely-fitting surface mesh of the PEC object, as opposed to using a volume discretization, which would be required in the FDTD method.

3. APPROACH

This paper utilizes the reciprocity principle to divide the original problem into two parts [1-3]. A reciprocity approach is also applied in [4]; however, the Finite Element Method (FEM) is used to compute the equivalent magnetic currents on surface $\mathbf{S_1}$ instead of the Finite Difference Time Domain (FDTD) technique. First, we analyze the region containing the conformal antenna, which is typically inhomogeneous. The FDTD method is used for this analysis to derive equivalent electric and magnetic currents $\mathbf{J}$ and $\mathbf{M}$ on the surface $\mathbf{S_1}$ (see Fig. 1) of the radiating aperture of the antenna. Next, $\mathbf{S_1}$ is backed by a perfect electrical conductor (PEC) to short out the electric currents and the problem reduces to that of computing the radiation from these magnetic currents located on the *closed* PEC body. This calculation takes into account the shape of the PEC body in the vicinity of the antenna.

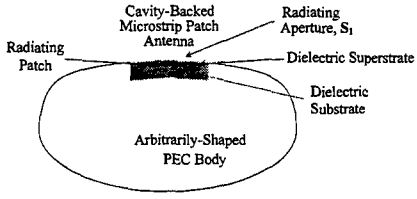


Fig. 1 Problem Geometry

The second step entails the application of the reciprocity principle to address the pattern computation problem. By invoking the reciprocity principle, we can write

$$\int_v \mathbf{E}_1 \cdot \mathbf{J}_2 \, dV = -\int_v \mathbf{H}_2 \cdot \mathbf{M}_1 \, dV \tag{1}$$

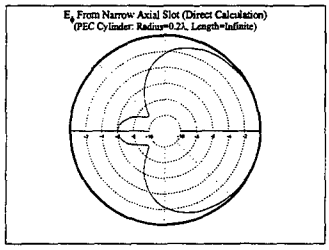
Our objective is to compute $\mathbf{E}_1$ radiated by $\mathbf{M}_1$ at a far-zone observation point **P**. We proceed by solving for the surface electric currents flowing on the closed PEC body by illuminating it with an infinitesimal dipole source $\mathbf{J}_2$ placed at location **P**. This problem is well-suited for handling by the Method of Moments (MoM). From the electric currents, the equivalent surface magnetic fields $\mathbf{H}_2$ are determined and by performing the integration on the right-hand side of (1), the desired field $\mathbf{E}_1$ is computed.

Note that once $\mathbf{H}_2$ is determined for the entire mounting structure, only $\mathbf{M}_1$ requires recalculation if the radiating element changes shape or location. The volume integral on the right-hand side of (1) reduces to the surface area of the superstrate (see Fig. 1). This re-simulation requires only a small percentage of the time required for a full-wave analysis of the entire mounting structure.

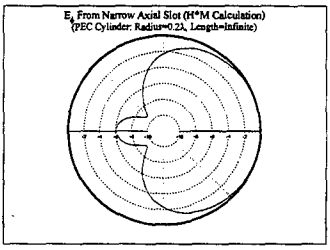
4. NUMERICAL RESULTS

To illustrate the procedure, we first compute the radiation pattern produced by a thin slot mounted on an infinite-length PEC cylinder. The slots are oriented in two directions: along the cylinder's axis (axial) and in the circumferential (azimuthal) direction. For the axial orientation, the aperture fields in the slot are ϕ-polarized (across the narrow width of the slot); thus, the $|E_\phi|$ pattern was computed. For the reciprocity calculation, the far-zone dipole source must be polarized in the same direction; therefore, analytical formulas taken from [5] to determine surface currents generated by a TE^z plane wave were used to obtain the necessary H fields (from the surface electric currents). For the azimuthal slot, the polarization of the aperture field is in the z-direction; thus, surface currents generated by a TM^z plane wave were used in the reciprocity pattern computation for $|E_\theta|$. The slot field variation was assumed to be cosinusoidal (dominant mode) and uniform along the length and width of the slot, respectively, for both orientations.

The reciprocity-approach patterns are compared to analytical formulations for these configurations [5] and are found to be in exact agreement (see Figs. 2 and 3 below).

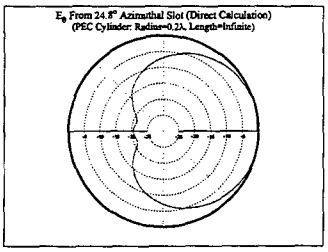


$|E_\phi|$ *vs.* ϕ Pattern (Direct) for Axial Slot in PEC Cylinder (Radius=0.2λ, Length=∞)

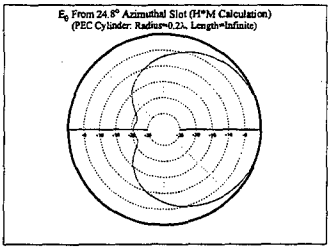


$|E_\phi|$ *vs.* ϕ Pattern (H*M) for Axial Slot in PEC Cylinder (Radius=0.2λ, Length=∞)

Fig. 2 Radiation Patterns: Axial Slot on Infinite-Length PEC Cylinder: Computation by Analytical (Direct) *vs.* Reciprocity (H*M) Methods



$|E_\theta|$ *vs.* ϕ Pattern (Direct) for Azimuthal Slot (24.8°) in PEC Cylinder (Radius=0.2λ, Length=∞)



$|E_\theta|$ *vs.* ϕ Pattern (H*M) for Azimuthal Slot (24.8°) in PEC Cylinder (Radius=0.2λ, Length=∞)

Fig. 3 Radiation Patterns: Azimuthal Slot on Infinite-Length PEC Cylinder: Computation by Analytical (Direct) *vs.* Reciprocity (H*M) Methods

The above patterns are computed for slots mounted on a 0.2λ radius PEC cylinder. The subtended angle for the azimuthal slot is 24.8°, which is identical to the one in the example considered in [5].

Simulations were then carried out on finite-length cylinders. Since analytical formulas do not exist for surface currents generated by plane waves incident on finite-length cylinders, a numerical code (MoM) was used to obtain these currents. For the axial slot, the polarization of the slot aperture and therefore the far-zone dipole source are ϕ-directed. Hence, the truncation in the z-direction has a minimal effect on the pattern. This can be seen in the figure below which plots the patterns produced by axial slots mounted on 1λ, 2λ, and, infinite length PEC cylinders.

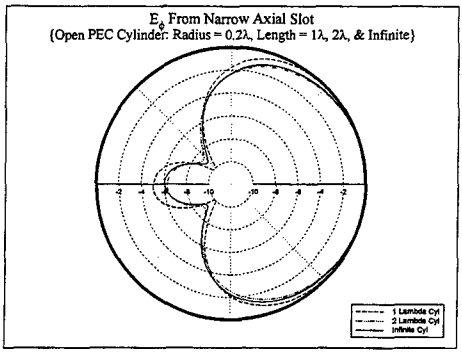
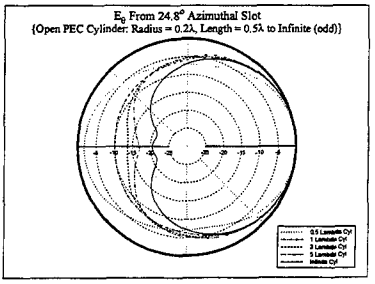
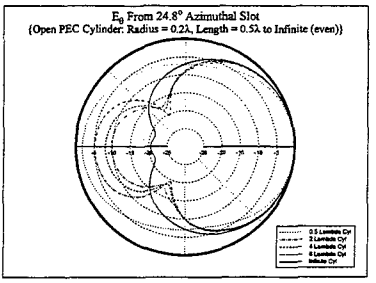


Fig. 4 $|E_\phi|$ vs. ϕ Radiation Patterns: Axial Slot on Finite-Length PEC Cylinders

The solid line represents the pattern for an axial slot mounted on an infinite cylinder. Thus, for a 2λ-length cylinder, the pattern has essentially converged to the infinite case. The pattern for the 1λ-length cylinder shows a higher back lobe level and deeper nulls caused by an enhanced standing wave presence created by the decreased distance to the truncated edge.

For the azimuthal slot, since the length of the cylinders had a significant impact on the shape of the patterns – an odd versus an even number of wavelengths – they are presented separately (see Fig. 5 below).





$|E_\theta|$ *vs.* ϕ: Odd λ-Length Cylinder

$|E_\theta|$ *vs.* ϕ: Even λ-Length Cylinder

Fig. 5 Radiation Patterns: Azimuthal Slot on Finite-Length PEC Cylinders

Again, the solid line shows the pattern produced by an azimuthal slot mounted on an infinite-length cylinder. The large back lobes for the even wavelength case are due to the current pattern formed on the finite cylinder when illuminated by a z-polarized plane wave. Since the truncation direction (z) is in the same direction as the

polarization of the plane wave, standing waves are formed with the number of peaks equaling the number of wavelengths. For the even wavelength case, the ϕ-cut at the z-midpoint passes through a local minimum in the current pattern on the lit (incident) side and a small local maximum on the shadow side of the cylinder. It is this shadow side peak that causes the large back lobe which appears in the patterns for the even case. For the odd case, the ϕ-cut at the z-midpoint passes through a local maximum on the lit side and a local minimum on the shadow side. This results in a smaller back lobe.

While the patterns appear to converge to the infinite case more closely for the odd wavelength case, both cases tend toward the infinite case as the length of the cylinder increases. The standing wave effects diminish only after the cylinder has reached a substantial length (beyond what could be simulated here), at which point both the odd and even wavelength cases begin converging to the infinite length case.

Finally, the radiation pattern produced by a cavity-backed elliptical patch antenna covered by a superstrate and mounted on an infinite-length PEC cylinder was computed. The radius of the cylinder is $0.631\lambda_o$ ($0.5\lambda_o + 0.2\lambda_d$). The patch considered for this analysis is elliptical with major and minor axes of $0.25\lambda_d$ and $0.2\lambda_d$, respectively, and was placed inside a rectangular block of dielectric ($\varepsilon_r = 2.33$) of length $1\lambda_d$ (x'-direction) and width $0.8\lambda_d$ (y'-direction) with a thickness of $0.2\lambda_d$. The major axis of the ellipse was aligned with the cylinder axis. A diagram of the conformal antenna is shown in Fig. 6 below.

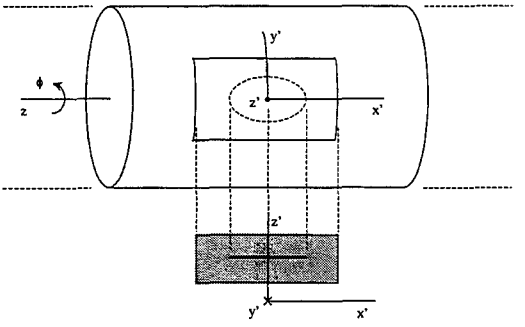
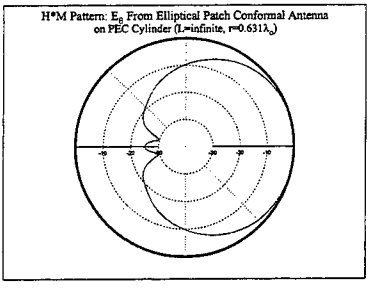
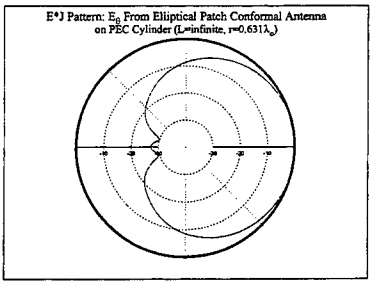


Fig. 6 Elliptical Patch Antenna Mounted on Infinite PEC Cylinder

The current distribution on the surface of the PEC cylinder is first calculated by analytical methods [5], followed by a computation of the electric fields (computed by a locally conformal FDTD code [6]) on the surface of the superstrate. The patch antenna is linearly polarized along the cylinder z-axis (patch x'-axis), hence the $|E_\theta|$ field ($\theta = 90°$) pattern is computed. This requires the computation of the surface electric currents produced on the cylinder by a z-polarized plane wave, which produces only z-directed currents. Therefore, only the x'-polarized aperture fields on the superstrate surface contribute to this pattern.

The resulting patterns were constructed by summing the complex dot-product of the electric current and electric field for each point on the surface of the superstrate and repeating this calculation while rotating the array of surface currents in the ϕ-direction. This dot-product is effectively the same as $\mathbf{H}_2 \bullet \mathbf{M}_1$ which appears on the right-hand side of (1), due to the normal vector being common to both vector quantities. The resulting pattern (H*M in Fig. 7 below) is compared to another obtained via the reciprocity theorem applied in a different manner. In this second approach, an infinite-length dielectric coated cylinder is considered, for which analytical formulas for the electric field inside the dielectric produced by an incident plane wave have been derived. The electric currents generated on the patch due to the feed (placed on the x'-axis halfway between the center and left edge) were computed using an MoM code. The MoM formulation assumes that the dielectric and backing ground plane are infinite in extent. These currents are then combined with the electric fields inside the dielectric at the location of the patch, and integrated over the surface of the patch to produce the radiation pattern. This plot is denoted E*J in the figure below.





$|E_\theta|$ *vs.* ϕ: H*M Approach $|E_\theta|$ *vs.* ϕ: E*J Approach

Fig. 7 $|E_z|$ Radiation Patterns: H*M *vs.* E*J Reciprocity Approach

The two patterns are seen to compare well. The H*M approach pattern has a slightly higher back lobe level, most likely due to the truncation of the radiating aperture area. If the aperture area is increased, the relative energy transmitted in the forward direction will increase resulting in a reduced back lobe. Since the patterns compare well, the selected aperture size is considered sufficient.

5. CONCLUSIONS

This paper has presented an efficient method for determining radiation patterns for arbitrarily-shaped conformal antennas. Several examples were presented illustrating the procedure for computing a pattern using the reciprocity approach. The technique was first verified against known radiation patterns, then extended to more complex structures. The pattern produced by a cavity-backed elliptical patch antenna was also computed

and compared to a pattern constructed using an alternate method. The patterns were shown to be in good agreement.

The paper shows how results obtained for the mounting structure can be used for any radiating element shape and location on the structure in the computation of the radiation pattern. This feature of the technique results in significant improvements in computational efficiency when the shape or location of the radiating element is varied. Further work is being pursued on curved radiating patches using an extension of the present locally-conformal FDTD algorithm for the magnetic current calculation. The effect of curvature on the flat patch approximation to pattern computation will be addressed and quantified in terms of finding the limit when the approximation is no longer accurate.

REFERENCES

[1] R. Mittra, S. Dey, S. Chakravarty, and N. V. Veremey, "Reciprocity Approach to Pattern Computation of a Microstrip Antenna Operating in a Complex Environment," *IEEE AP-S International Symposium*, Atlanta, GA., 1998, pp. 1138-1141.

[2] D. H. Werner, G. D. Mouyis, and R. Mittra, "A Reciprocity Approach for Determining Radiation Patterns of Patch Antennas on Circularly-Cylindrical Platforms," *IEEE AP-S International Symposium*, Atlanta, GA., 1998, pp. 1582-1585.

[3] D. H. Werner, G. D. Mouyis, R. Mittra, and J. S. Zmyslo, "A Reciprocity Approach for Calculating Radiation Patterns of Arbitrarily Shaped Patch Antennas Mounted on Circularly-Cylindrical Platforms," *Proceedings of the 15th Annual Review of Progress in Applied Computational Electromagnetics (ACES)*, Naval Postgraduate School, Monterey, CA., March 15-20, 1999, pp. 508-515.

[4] J. M. Jin, J. A. Berrie, R. Kipp, and S. W. Lee, "Calculation of Radiation Patterns of Microstrip Antennas on Cylindrical Bodies of Arbitrary Cross Section," *IEEE Trans. Antennas Propagat.*, vol. 45, no. 1, pp. 126-132, Jan. 1997.

[5] R. F. Harrington, *Time-Harmonic Electromagnetic Fields*, McGraw-Hill, New York: 1961.

[6] S. Dey, R. Mittra, and S. Chebolu, "A Technique for Implementing the FDTD Algorithm on a Nonorthogonal Grid," *Microwave and Optical Technology Letters*, vol. 14, no. 4, March 1997.

Using Computational Electromagnetics and Monte-Carlo Methods to Locate Antennas on Aircraft

Kevin Goldsmith, Paul Johnson and Timothy Priest
Defence Science and Technology Organisation
Department of Defence, Australia
kevin.goldsmith@dsto.defence.gov.au

1. ABSTRACT

A radio navigation system on a small aircraft was unlocking on approach to a number of Australian military bases. Flight trials to establish the cause of the problem proved inconclusive. Air Operations Division (AOD) of the Defence Science and Technology Organisation (DSTO) was asked to investigate the problem, to review the flight trials, and to resolve the issue.

An approach was developed to integrate Geometrical Theory of Diffraction (GTD) modelling of the electromagnetics problem, using a simplified flight model, and a Monte-Carlo simulation, to allow an informed decision to be made on the antenna location based on operational needs. The paper describes the process undertaken, the results of the modelling process, the Monte-Carlo simulation results and the measure of performance chosen for this particular problem. The paper also describes how this approach may be applied to other circumstances.

2. INTRODUCTION

Finding the optimum location of antennas on aircraft is notoriously difficult, especially so on military aircraft. Location decisions are often dominated by engineering or aerodynamic constraints, partly out of need, but also by default, because of difficulty in assessing the operational implications of a particular location. Excellence in radio navigation system performance, based on operational effectiveness, is all an aircraft operator really cares about. Optimum antenna location is a small but critical part of good system performance.

Computational methods for analysis of antenna/aircraft interaction are available but they are large consumers of processing time. However, recent improvements in the performance/cost ratio of computers have made feasible the proper analysis of the likely behaviour of an antenna on a given aircraft.

Aircraft/antenna interaction is commonly quite complex, mainly due to the size and shape of the aircraft compared with the wavelength of the transmission. Complex interaction produces complex radiation patterns, hence the conventional radiation plots are completely inadequate. The use of radiation patterns in two or three dimensions provides considerably more insight, however their interpretation is still difficult and the operational impact of the interaction is not revealed.

To investigate the performance of a radio-navigational (RN) system, two-dimensional radiation patterns were calculated for two possible antenna locations on a small single-engine aircraft, at a frequency of 1000 MHz. It was found that the patterns are of limited value in selecting the correct location, due to difficulties in interpretation and the unknown impact of the location on operational performance. This paper presents a solution to this problem by the integration of a computed antenna pattern with typical approach profiles in a Monte Carlo simulation. This technique gives a measure of performance of the system in flight to allow a choice based on operational effectiveness. Using this technique, the efficacy of various locations can be compared by analysing the antenna performance over thousands of simulated RN instrument approaches, providing more comprehensive information at considerably lower cost than actual flights.

In time, it is expected that this approach will aid in the locating of antennas during aircraft design, and also will provide an alternative method of presenting this complex information to aircraft operators, pilots and military mission planners. For the specialist in Computational Electromagnetics (CEM), this paper emphasizes the need to present the results of computation in understandable and computer effective forms.

3. MODELLING RADIATION PATTERNS OF ANTENNA

3.1. Computational Electromagnetics Codes

There are many computational techniques that can be employed in solving electromagnetic problems. (See [1] for a review). For antenna radiation pattern analysis, the most important techniques are the Method of Moments (MOM) and the Geometrical Theory of Diffraction (GTD). The MOM technique [2] involves the creation of a model of the structure under investigation with short wire segments. A matrix solution of the impedance equation allows the current in each segment, and hence by summation, the total electromagnetic (EM) field to be calculated. Unfortunately, this technique is not suitable for analysis of electrically large structures (i.e. large compared with wavelength), because the number of segments and hence computing time required for solution grows rapidly. For a moderately complicated structure of 1500 wire elements, the frequency limit is approximately 300 MHz. This limit is remarkably independent of computing power, since solution time varies as the fourth power of frequency when creating three-dimensional models.

The second technique, GTD, is a ray-tracing method with its roots in Physical Optics [3]. It is only suitable for electrically large structures, and is the technique used in this paper. The structure under investigation is represented by a series of basic geometrical shapes ie flat plates and cylinders. It is illuminated by EM waves and the reflected and diffracted radiation at any point can be found and summed to find the total field.

The software code GEMACS (Generalised Electromagnetic code for the Analysis of Complex Systems) implements both MOM and GTD, together with other techniques [4][5]. GEMACS has been used for the calculation of the antenna patterns in this paper.

3.2. GTD model of aircraft

A GTD model of the front underside of a typical single-engine propeller-driven aircraft was created using 40 flat plates, and 9 cylinders. The model is shown in Figure 1. The model has been reduced to the minimum number of plates and cylinders as this is the most effective method for controlling computational speed without sacrificing antenna pattern accuracy. We chose to model the type of aircraft which has a cavity and doors associated with the front nose wheel, but whose main undercarriage doors retract flush with the wing surface. This was to best represent a typical high speed single engine aircraft.

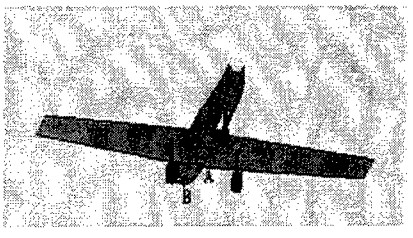


Figure 1: GTD model of a small single engine propeller aircraft, and the locations of the two antennas (A & B). The antenna location A is slightly off centre and behind the line connecting the main wheels. The antenna location B is further towards the rear of the model and along the centreline of the fuselage.

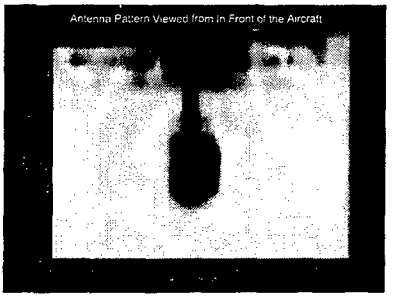


Figure 2: The original location 2D antenna pattern looking toward the aircraft with the undercarriage down. Dark areas are 60dB down on the light areas.

3.3. A quick look

The first attempt at looking at this problem was to use the model to evaluate the field that could be seen if you were to look directly at the front of the aircraft. While the RN system is primarily a receiver, the principle of reciprocity has been used to simplify the computational workload. The results of this first attempt are shown in figure 2. Confidence in these results was obtained by a process of modeling the aircraft without undercarriage, with nose-wheel but no bay doors and with bay doors open but no nose-wheel. The additional modeling was done to assess the sensitivity of the model and the modeling code to model features. The results of figure 2 clearly show that small changes in the aircraft attitude have the potential to produce large changes in the received signal strength. Attitude changes in the order of one degree can change the received signal by approximately 50 dB. This evidence was sufficient to indicate why the flight trials had been inconclusive and demonstrated the need for a more thorough investigation of the problem. These results also demonstrated the need to move the antenna to a better location.

3.4. Radiation patterns for two antenna locations

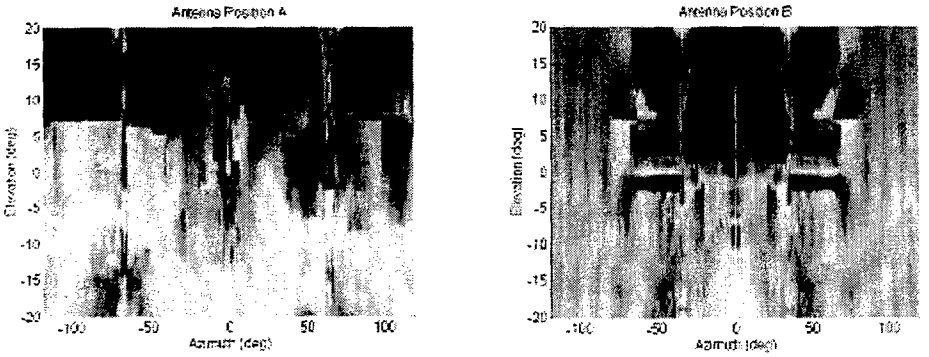
Spherical sources of radiation emitting at 1000 MHz (using a GEMACS command) were located at each of two possible antenna sites, and the far field radiation patterns were calculated every degree for a range of angles: -120 to 120 degrees in azimuth, and -20 to 20 degrees in elevation (relative to the

horizon). Each radiation pattern took approximately 100 hours of computing time on a fast workstation (SUN Ultra 2, rated at 505 SPECfp92).

The radiation patterns obtained are shown in figure 3 as greyscale plots. These patterns are complex, but provide abundant information more readily than a series of traditional polar diagram plots.

The two patterns are very different. Pattern B is symmetrical, as might be expected from the central location of the corresponding antenna. Likewise, pattern A is decidedly asymmetric. Pattern A shows more high elevation absorption than B, as might be expected from its location in line with wings, therefore performance in turns will be poorer. Pattern B only shows high elevation absorption in the forward direction, when the fuselage is in the line of sight of the transmitter. Performance in turns for location B should be better. In addition, both patterns show attenuation due to the main landing wheels [for A at (-70,-18) and (65,-18) and B at (±40,-18)] and the front nose wheel [for A at (0,-12) and B at (0,-9)].

Other than making gross observations like the above, it is difficult to see how antenna performance differences between the two locations will affect subsequent navigational system performance. To try and extract more useful information from antenna patterns, Monte Carlo simulations of typical instrument approaches were performed, and coupled with the radiation patterns to obtain predictions of operational, in-flight antenna performance.



(a) (b)

Figure 3: Greyscale antenna radiation plots, for the two antenna locations (a) A and (b) B, showing attenuation of the antenna signal over a wide area. (0,0) is straight ahead, positive elevations are above the nose, and positive azimuths are to starboard (right). The scale represents a range of -60 dB, from light 0dB to dark -60dB.

4. SIMULATION OF ANTENNA PERFORMANCE

4.1. An example instrumented approach

An approximate flight path, typical of RN instrument approach, with representative random perturbations superimposed was modelled. No attempt has been made to accurately simulate an

aircraft approach, nor have we utilised an accurate flight model or wind models to calculate the attitude of the aircraft with high-fidelity.

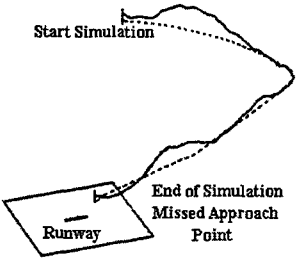


Figure 4: Schematic representation of an example instrument approach (full line) and nominal approach (dashed). The vertical scale is multiplied by a factor of 10.

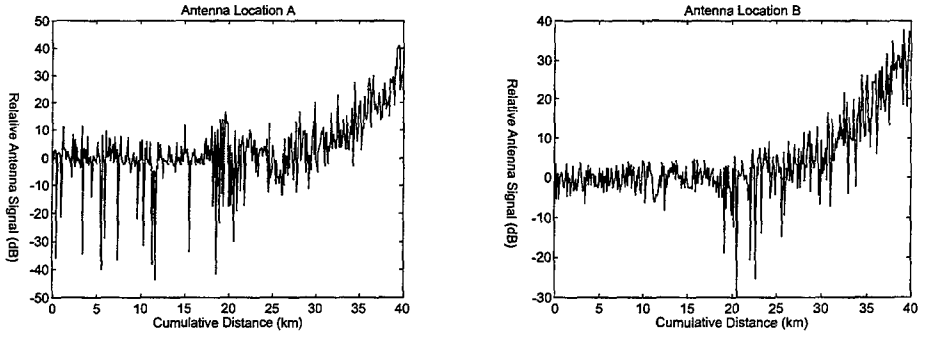
The nominal flight path (shown dashed in Fig 4), follows an arc of radius 20 km at not less than 3000 feet (900 metres) altitude. The aircraft then turns towards the beacon a few degrees in advance of the heading of the runway. A 3 degree glideslope is followed, so that by the Missed Approach Point (MAP), about 2 km out, the aircraft is above 500 feet (170 metres) altitude. At this point the pilot normally decides whether to proceed with the landing, in which case he aligns with the runway, otherwise the landing is aborted. The flight path beyond the MAP has not been considered, since after this point the RN system has lower operational importance until the next approach.

We have used an algorithm to make the aircraft follow the nominal flight path, allowing random deviations of the order of a hundred metres laterally and in height. Simple feedback rules provide an additional level of realism: the aircraft is encouraged to return to the flight path more strongly when below the nominal height than when above it; and stricter adherence to the nominal flight path is prescribed when the aircraft gets closer to the beacon. A simulated approach is given in Fig. 4.

The aircraft's position is sampled every 100m, which is appropriate given the resolution of the antenna radiation patterns. For each position, the aircraft's attitude is initially oriented as follows: the heading is made to coincide with the track the aircraft is following; the wings are made level; and the pitch is set to zero. On top of this are then superimposed fluctuations in roll, yaw and pitch, which are deviates chosen from normal (Gaussian) distributions of standard deviations of 2.5, 2.5 and 5 degrees respectively. These values represent realistic perturbations for a single engined aircraft in a realistic atmospheric environment. Once the attitude of the aircraft is fixed, the apparent location of the beacon is calculated in the coordinate frame of the aircraft, and finally the signal attenuation is calculated from databases representing the radiation patterns given earlier, together with an inverse-square correction.

These simplifying assumptions reduce the fidelity of the simulation of the flight but result in a computationally fast program with sufficient fidelity. In this way, demonstration of the technique and what it has to offer in terms of predicting antenna performance can be achieved.

For a given flight, the antenna signal strength as a function of time, or in this case total distance travelled can be computed. Two such plots are given in figure 5 for the two antennas.



(a) (b)

Figure 5: Plot of antenna signal strength as a function of distance flown by aircraft for antenna in location (a) A and (b) B.

The shape of the plots are similar: a level of 0dB is maintained for the first 20km, before steadily increasing towards +40dB for the next 20km. This corresponds to the arc phase and final glideslope respectively. The antenna in position A shows a higher number of large signal drops when following the arc. This is consistent with the expectations described above because in this position the aircraft has the beacon located at +90 degrees in relative azimuth, and the drops occur when the aircraft rolls more than a few degrees towards the beacon, shielding the antenna with the wing. The antenna in position B shows a higher number of moderate signal drops when following the glideslope. This is consistent with the dark areas of figure 2(b) for nose down pitch attitudes.

Plots such as those in figure 5 still give very little insight into the correct place to locate the antenna, because the operational aspects of the system were not included in the analysis. Both locations have a modest number of large signal drops but at different phases of the flight. Further processing of the Monte-Carlo results is necessary.

4.2. Measuring Performance

If the simulated approach is repeated many times, we are able to derive statistical information or average behaviour of the antennas and hopefully the attached RN systems. The statistical information will only have meaning if it describes some measure of the performance of the system. In this case we suspected that any automatic gain control in the RN systems would have considerable difficulty in coping with the large, rapid fluctuations in the received signal. The measure of performance was chosen to be the lowest probability of large fluctuations in the received signal during a flight.

We performed 1000 approaches, to obtain a series of data like the examples shown above. Signal fluctuation is defined as the magnitude of the difference in signal obtained between two consecutive

aircraft positions separated by the 100m sample distance, ie the rate of change of the signal with respect to distance (hence time). In figure 6, we plot the cumulative number of fluctuations as a function of the fluctuation size, expressed as a fraction of the total number of fluctuations (N).

If the RN system was able to cope with fluctuations up to 30 dB within the time taken to fly 100m, then an antenna location that produced the lowest probability of fluctuation at and above 30 dB would give the best system performance. For this case, fluctuations greater than 30 dB are seen 3% of the time for antenna location A, and only 0.3% for location B. Therefore if the RN system has performance problems with 30 dB signal variations in short distances (times), the best antenna location is B. In general, the antenna in location A shows more fluctuations of all sizes than location B, as curve A is always above curve B. From this analysis it is expected that B would be the preferred location for such an antenna.

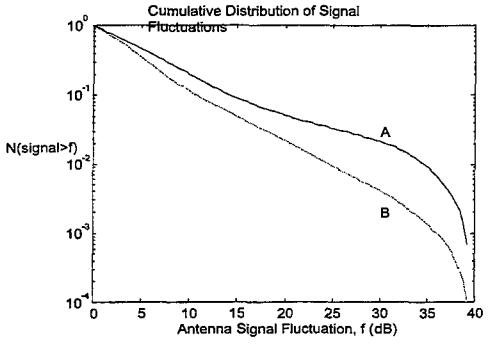


Figure 6: Cumulative distribution of signal fluctuations for antenna locations A & B. The fluctuation is the change in signal from sampled location of the aircraft to the next sample (100 metres apart).

Another example of the use for this method is to answer the question "How many times does the system drop out due to a loss of signal?" For this case the data used for plots of figure 5 are used directly and the cumulative number of signal drops below a receiver threshold are compared over a significant number of flights. This gives a different measure of the influence of antenna position on antenna performance and system performance, and may lead to a different location considered to be better.

4.3. Other Factors

Conventional computational approaches to examine the coupling between the chosen location and other antenna systems also needs to be completed. The optimum place for this in the smart antenna siting process is highly situation dependent. In this case, the aircraft did not have any other systems in the RN band so the choice of location was not complicated.

In all cases of this modeling approach it is necessary to examine the sensitivity of the modeling to model error and the plethora of simplifying assumptions. In most cases this can only be done by changing model parameters and repeating the process. The single factor most likely to produce a poor result for this method is the choice of performance measure.

4.4. Proof of the concept

This work was completed for a real aircraft problem. The modification suggested by this work was trialed in a series of flights, along with other possible solutions. The antenna location that performed the best was position B as expected. This modification has now been included in the entire fleet.

5. CONCLUSIONS

It is possible with modern CEM codes and reasonable computing power to obtain high frequency radiation patterns of antennas located on a relatively complex structure. Two-dimensional plots in themselves represent an advance in presenting such data over a series of traditional polar diagrams, but are not sufficient for system level decision making.

In addition, with a Monte Carlo simulation of a typical RN aircraft instrument approach, useful operational information about the performance of the antenna and its system can be obtained. This presents both a useful tool for choosing the initial location of the antenna, and an improved way of representing installed antenna performance data to the aircraft operators. The method presented here can also be used to predict installed antenna performance and justify changes to the position of antennas in poorly performing systems based on sound quantitative analysis. In general the method is not limited to aircraft navigation systems, it can be applied to a large variety of communication and surveillance problems.

6. REFERENCES

[1] Sadiku M. N. O., "Numerical Techniques in Electromagnetics", CRC Press (1992)
[2] Harrington R.F., "Matrix Methods for Fields Problems", Proc. IEEE, Vol 55, pp136-149 (1967).
[3] Kouyoumjian R.G., "The Geometrical Theory of Diffraction and its Applications" in Numerical and Asymptotic Techniques in Electromagnetics (ed. Mittra), Springer-Verlag, New York (1975)
[4] Coffey E.L., Coffey N.W., Kadlec D.L., "GEMACS Source Book", Rome Air Development Centre, Final Technical Report, RADC-TR-88-102 (1988)
[5] Coffey E.L., Coffey N.W., Kadlec D.L., "GEMACS Version 5 - Engineering Manual", Rome Air Development Centre, Final Technical Report, RADC-TR-90-360 Volume II (1990)

Coupling Phenomena in Horizontal and Vertical Polarized Aperture Coupled Patch Antennas on Cylindrical Surfaces

D. Löffler, J. von Hagen, W. Wiesbeck

Institut für Höchstfrequenztechnik und Elektronik, Universität Karlsruhe, Kaiserstraße 12, 76128 Karlsruhe, Germany, e-mail: Dietmar.Loeffler@etec.uni-karlsruhe.de

Abstract

Conformal antennas are an essential part in future communication and sensor systems as the integration of antennas in curved surfaces is requested more and more. Most of these conformal antennas have to work in a phased array manner using different excitation amplitudes and phases for each array element. The synthesis of this excitation coefficients requires exact knowledge about the coupling within the array, especially when small beamwidth or low side lobe levels are desired.
Aperture coupled feeding technique is an excellent choice if broadband patch antennas are needed. However, up to now, no data about the coupling behaviour of these aperture coupled antennas were published.
This paper presents measured scattering parameters for four combinations of polarization and position. The different coupling phenomena encountered during the measurements are identified and rated according to their influence on the excitation of the single elements. Finally some conclusions for the design of this type of antenna are drawn.

Introduction

Future broadband communication and sensor systems require efficient low profile antennas over a reasonable frequency bandwidth, which need to be integrated in existing curved surfaces either to hide the antenna due to aesthetically reasons or to minimize drag for aerodynamically reasons or both. Besides the conformal fit to the given surface the antenna should offer a variety of beamforming and beamsteering capabilities some of which are difficult to obtain with fixed planar antennas.
A good approach to this variety of requirements is a microstrip patch antenna with a aperture coupled feeding, as depicted in fig. 1, to achieve broadband behaviour. As most of the surfaces show primarily a curvature in one direction, e.g. a wing of a plane, naturally a cylindrical setup is the first one to be studied.
For a phased array operation of this conformal antenna the knowledge of the coupling in the array is mandatory if narrow beams or low side lobes are desired. In this contribution the coupling within an aperture coupled microstrip patch antenna on a cylindrical surface is studied

for horizontal (ϕ-directed) and vertical (z-directed) polarization with different element spacing in horizontal and vertical direction.

Four geometry types

In planar microstrip patch phased arrays the coupling is distinguished in E- and H-plane coupling, respectively. This is simply due to the fact that from the 2 parameters polarization and geometry, which determine the coupling, the geometry is invariant to rotations around a axis perpendicular to the array and therefore only the polarization is left as parameter.

However, in cylindrical arrays the geometry as well as the polarization have to be taken into account to determine the coupling. The 4 principal arrangements are depicted in fig. 2. Fig. 2a shows a E-plane coupling along the curvature, fig. 2d shows the E-plane coupling along the not curved direction. The H-plane coupling along the curvature is depicted in fig. 2c whereas the H-plane coupling along the non-curved surface is shown in fig. 2b.

These four different cases have to be treated separately. Additionally, the position of the slot relative to the cylinder's height is an important parameter, as the measurements show.

Measured coupling

To study the coupling effects for the different geometries according to fig. 2 under practical conditions, 4 different sets of 2 element arrays have been built and characterized. Fig. 3 shows the 5 measured setups for the

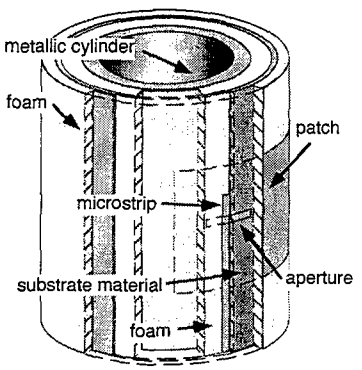


Fig. 1: 3D-view of an aperture coupled patch on a cylindrical surface

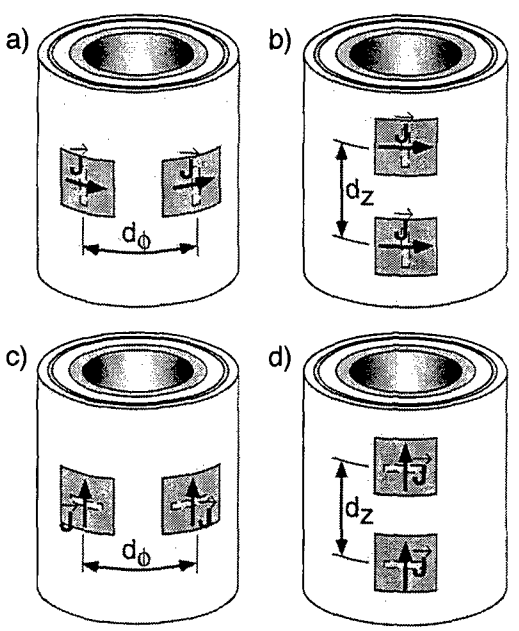


Fig. 2: The 4 different arrangements of geometry and polarization: a) ϕ-polarization with ϕ-directed element spacing, b) ϕ-polarization with z-directed element spacing, c) z-polarization with ϕ-directed element spacing, d) z-polarization with z-directed element spacing

ϕ-polarized 2x1 array with different element distances in ϕ-direction. The realized element distances in ϕ-direction are 0.4 λ_0 (69.2°), 0.5 λ_0 (86.5°), 0.7 λ_0 (121.2°), 0.9 λ_0 (155.8°) and 1.04 λ_0 (180°) where the distance is measured between the center of the elements along the circumference in the "patch plane".

The 6 measured setups for the z-polarized 1x2 array with different element distances in z-direction are depicted in fig. 4. The realized element distances in z-direction are 0.35 λ_0, 0.4 λ_0, 0.5 λ_0, 0.7 λ_0, 0.9 λ_0 and 1.04 λ_0 where the distance is measured along the z-direction between the center of the elements.

The geometry of the cylindrical structure was the same for all the setups and consists of a central metallic cylinder (r = 7.5 mm), a foam spacer of 22.5 mm, a RT/Duroid 5880 feeding substrate (0.508 mm) and a 10 mm foam layer as patch substrate. The patches themselves are etched on a 35 µm kapton-foil and glued to the foam material. The height of the cylinder was h = 180 mm. As the design frequency is 2.45 GHz all distances are normalized to that particular wavelength.

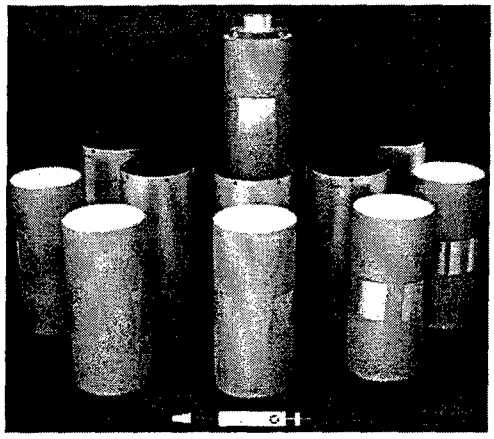


Fig. 3: Aperture coupled antenna structures for the measurement of the coupling in ϕ-direction in a ϕ-polarized array according to fig. 2a. The carrying structure in the middle shows a single element and is surrounded by the bent feed network substrate (the slots can be seen very clearly) and the patches on their foam substrate. The realized distances are (from the left to the right) 1.04 λ_0, 0.9 λ_0, 0.7 λ_0, 0.5 λ_0 and 0.4 λ_0.

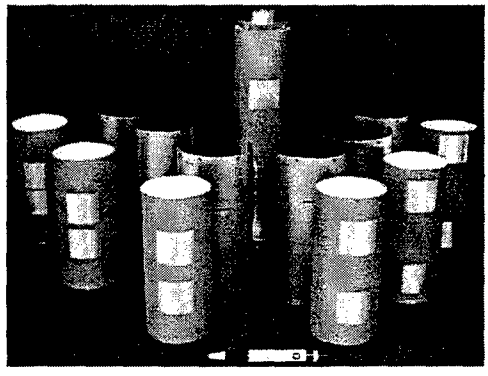


Fig. 4: Aperture coupled antenna structures for the measurement of the coupling in z-direction in a z-polarized array according to fig. 2d. The carrying structure in the middle shows a single element and is surrounded by the bent feed network substrate (the slots can be seen very clearly) and the patches on their foam substrate. The realized distances are (from the left to the right) 0.35 λ_0, 0.4 λ_0, 0.5 λ_0, 0.7 λ_0, 0.9 λ_0 and 1.04 λ_0.

Input reflection coefficient

As known from planar arrays coupling can have severe influence on the input reflection coefficient of the array elements [1]. That also happens to the cylindrical array. The measured input reflection coefficient for the ϕ-polarized elements as a function of the E-plane distance around the circumference is plotted in fig. 5. In the frequency range between 2 GHz and 2.5 GHz the same behaviour as in planar arrays occurs, coupling shifts the peak of the return loss towards higher frequencies. Between 2.5 GHz and 2.85 GHz, however, this phenomenon is dominated by the coupling of the slots to the TE_{111} resonance of the multilayer coaxial cavity inside the antenna. Furthermore the circumference at that frequency reaches a value of 2 wavelengths so an additional resonance in the patch substrate occurs. Above 2.85 GHz the input reflection coefficient again behaves like in a planar array with the exception of the resonance at 3.5 GHz, which is the TE_{114} resonance of the coaxial cavity coupled to primarily by the microstrip feed lines.

Fig. 6 shows the influence of H-plane coupling on the return loss along the planar surface of the cylinder. As in the planar case the input reflection coefficient is less affected by H-plane coupling what leads to nearly identical curves below 2.4 GHz. The coupling to the TE_{111} resonance at 2.6 GHz is weaker than in the case of fig. 5. This is due to the fact that the slots are moved symmetrically upwards and downwards (see fig. 4), what reduces the coupling of the slots to this mode. But the same movement increases the

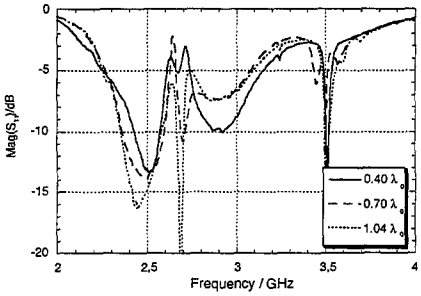


Fig. 5: Return loss of a ϕ-polarized element in a 2x1 element array for ϕ-directed element spacing of 0.4 λ_0, 0.7 λ_0 and 1.04 λ_0.

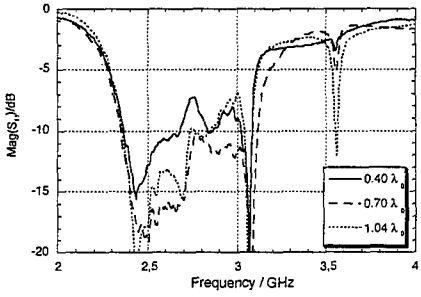


Fig. 6: Return loss of a ϕ-polarized element in a 1x2 element array for z-directed element spacing of 0.4 λ_0, 0.7 λ_0 and 1.04 λ_0.

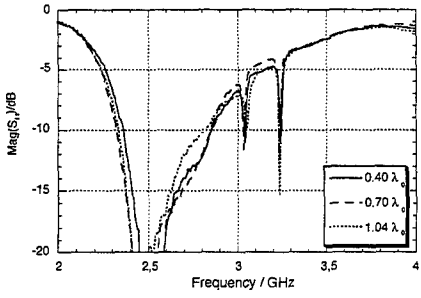


Fig. 7: Return loss of a z-polarized element in a 2x1 element array for ϕ-directed element spacing of 0.4 λ_0, 0.7 λ_0 and 1.04 λ_0.

coupling to the TEM_4 resonance at 3 GHz. Also here the TE_{114} resonance 3.5 GHz occurs, but this time the slots are more involved in the coupling to this mode what leads to a higher distance dependence in the form of the resonance peak.

The return loss of fig. 7 again is a function of H-plane coupling, which, like in the case of fig. 6, does not influence much the input reflection coefficient. For a distance of 0.4 λ_0 the peak of the return loss tends to shift towards higher frequencies. The peak at 3 GHz is caused again by weak coupling to the TEM_4 resonance by the feed lines. The feed lines also cause a coupling to the TE_{113} resonance at 3.25 GHz.

Fig. 8 shows an input reflection coefficient influenced by E-plane coupling along the planar z-direction. The frequency shift of the input reflection coefficient can be estimated by the form of the curves above 2.6 GHz. At the design frequency however, the coupling to the TEM_3 resonance, which strongly affects the 0.4 λ_0 distance, hides any other effects. The peaks around 3 GHz, 3.25 GHz and 3.5 GHz again mark the coupling to the TEM_4, TE_{113} and TE_{114} resonance.

Coupling between elements

The coupling in the E-plane around the circumference of the cylinder is plotted in fig. 9. Generally the coupling is quite high reaching values above -5 dB. The coupling generally drops with increasing distance slower than in the H-plane, what is well known from planar arrays. The sharp peak around 2.6 GHz is due to the TE_{111} resonance which influences the coupling according to the location of the feed lines and slots. This geometry

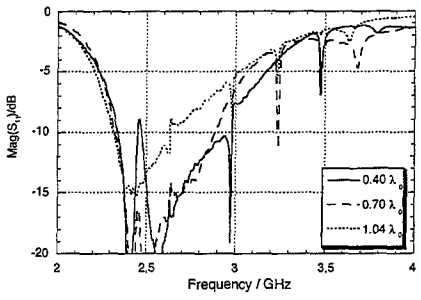


Fig. 8: Return loss of a z-polarized element in a 1x2 element array for z-directed element spacing of 0.4 λ_0, 0.7 λ_0 and 1.04 λ_0.

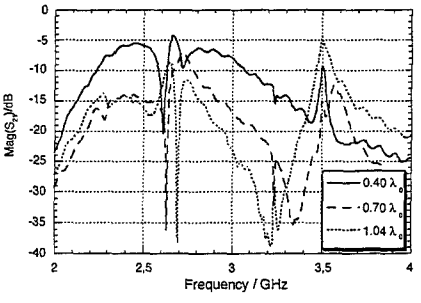


Fig. 9: Coupling between ϕ-polarized elements in a 2x1 element array for ϕ-directed element spacing of 0.4 λ_0, 0.7 λ_0 and 1.04 λ_0.

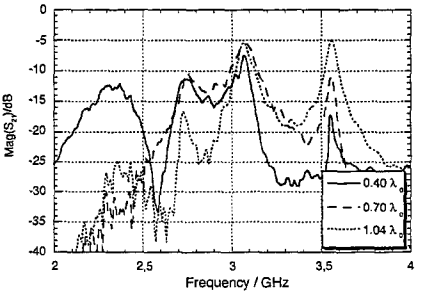


Fig. 10: Coupling between ϕ-polarized elements in a 1x2 element array for z-directed element spacing of 0.4 λ_0, 0.7 λ_0 and 1.04 λ_0.

dependence is even more visible around 3.5 GHz at the TE_{114} resonance. Due to the field configuration of the TE_{11} mode the coupling for the 180° (1.04 λ_0) separation (-4.3 dB) is higher than for the 0.7 λ_0 (121.2°) separation (-15 dB).

Fig. 10 shows H-plane coupling along the planar z-direction. The coupling is generally lower than in the case of fig. 9 but higher than in fig. 10. The resonances again disturb the global behaviour of the curves. This time the TE_{111} resonance decreases the coupling as the elements are moved symmetrically upwards and downwards to establish the desired separation (see fig. 4). The TE_{112} resonance around 2.75 GHz, the TEM_4 resonance around 3 GHz and the TE_{114} resonance at 3.5 GHz show very geometry-dependent behaviour of the coupling, sometimes inverting the "normal" behaviour of the curves (TE_{114} resonance: 1.04 λ_0 separation compared to 0.4 λ_0 separation).

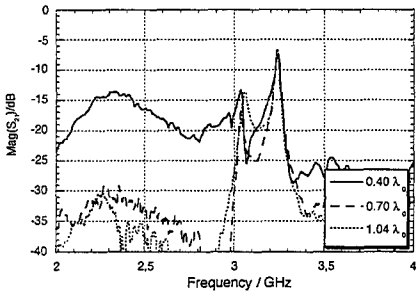


Fig. 11: Coupling between z-polarized elements in a 2x1 element array for ϕ-directed element spacing of 0.4 λ_0, 0.7 λ_0 and 1.04 λ_0.

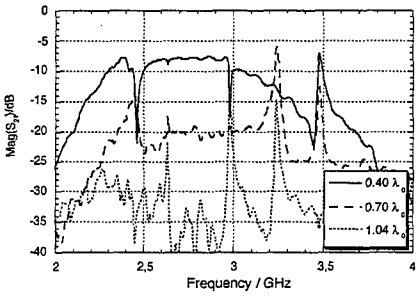


Fig. 12: Coupling between z-polarized elements in a 1x2 element array for z-directed element spacing of 0.4 λ_0, 0.7 λ_0 and 1.04 λ_0.

The H-plane coupling around the circumference of the cylinder depicted in fig. 11 shows the lowest coupling encountered during these measurements. The coupling drops very fast with increasing distance and is less affected by resonances. Only 2 resonances at 3 GHz (TEM_4 resonance) and 3.25 GHz (TE_{113} resonance) occur, because the polarization (orientation of the slots) and the location of the slots are bad for coupling to the resonances in the coaxial cavity.

The E-plane coupling along the planar z-direction is depicted in fig. 12. The coupling in this plane is stronger than in both H-planes but generally weaker than the E-plane coupling around the circumference depicted in fig. 9. Like in fig. 11 for the H-plane the z-polarization also shows in the E-plane less sensitivity for the resonances. Also here all the resonances (TEM_3 at 2.45 GHz, TEM_4 at 3 GHz, TE_{113} at 3.25 GHz and TE_{114} at 3.5 GHz) show a geometry-dependence of the coupling.

The different effects

The dominant coupling effect between these cylindrical aperture coupled patches is the resonance, either in the coaxial cavity or as a circumferencial resonance in the patch substrate coupled to by surface waves. This effect is narrowband and geometry-dependent [2].

The other more broadband effect is the propagation of surface waves, which causes the difference between E- and H-plane. Fig. 13 shows the nearfield of a ϕ-directed dirac current source (Green's Functions in space domain) to vizualize the propagation of a surface wave. The plot clearly shows a difference in magnitude of the nearfield between the direction parallel to the current and perpendicular to the current. The field and hence the coupling is much stronger parallel to the source, which of course is the E-plane.

In the cylindrical case this surface wave pattern in conjunction with the finite ϕ-direction causes high coupling because the surface wave energy "radiated" in the ϕ-direction can not be lost, so it stays within the system and causes coupling.

Other coupling effects (like radiation, etc.) are negligible.

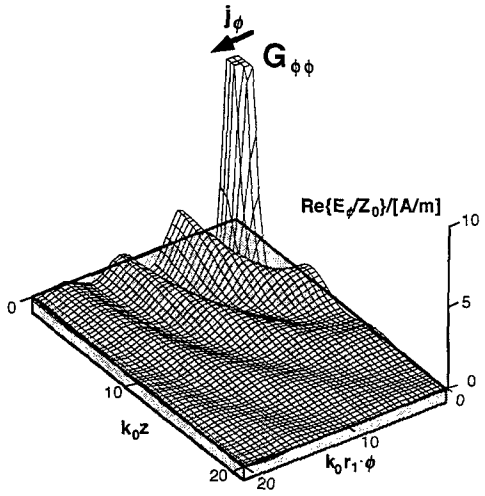


Fig. 13: Nearfields of a ϕ-directed dirac current sources (Green's Functions in space domain) to vizualize the propagation of a surface wave. The calculation parameters are chosen to show the surface wave effect, hence only a single layer substrate is used with a inner radius r: k_0r = 10, a substrate thickness d: k_0d = 0.2 and ε_r = 3.5.

Conclusions

The coupling phenomena within an cylindrical aperture coupled microstrip patch antenna are more complicated than in a planar microstrip patch antenna. As in the planar case the coupling in the E-plane is generally stronger than the coupling in the H-plane. Within both planes (E-plane and H-plane) the ϕ-polarization causes higher coupling than the z-polarization, because the energy is somehow trapped in the ϕ-direction. However, this effect is weaker than any coupling to a structural resonance, which dominates the coupling behaviour in the corresponding frequency range.

Comparing the input reflection coefficient and the coupling of both polarizations the ϕ-polarization is much more affected by the resonances than the z-polarization because the slot orientation of the ϕ-polarization is more "useful" for the coupling to the resonances.

References

[1] F. Rostan, W. Wiesbeck, "Design considerations for aperture coupled microstrip patch phased arrays taking into account mutual coupling effects," *Internat. Conference on Antennas and Propagation ICAP'97,* Edinburgh, UK, April 14-17, 1997, pp. 1.237-240

[2] N. Marcuvitz (ed.), *Waveguide Handbook,* McGraw-Hill, New-York, Toronto, 1951

Modeling and Analysis of Wideband Conformal Antennas

Keith D. Trott and Rene D. Guidry
Mission Research Corp
147 John Sims Parkway
Valparaiso, FL
(850)729-0855 (voice)
trott@mrcfl.com

Leo C. Kempel
Michigan State University
Radiation Lab
East Lansing, MI
(517)353-9944
kempel@egr.msu.edu

Abstract

Mission Research Corporation (MRC), in collaboration with Michigan State University (MSU) and Analytic Designs, Inc. (ADI) is applying unique, state-of-the-art computational electromagnetics (CEM) tools to investigate the performance parameters of wide bandwidth, multi-modal, conformal antennas. The antenna modeling is coupled with the CEM via a user-friendly graphical user interface (GUI). We will discuss our efforts to develop mesh generators for these types of antennas, the application of various finite element-boundary integral (FE-BI) engines for computation, and the interface through the GUI. We will also discuss the use of these special meshes with our FE-BI CEM tools to predict antenna performance parameters such as radiation pattern and impedance. This work was sponsored by AFRL/SNRP under contract # F33615-98-C-1223.

Introduction

The MRC Team's FE-BI CEM tools permit rapid analysis and design of conformal antennas, with particular emphasis on wide bandwidth, multi-modal antennas. These antennas are cavity-backed and flush-mounted on planar, cylindrical, and doubly-curved surfaces. Our CEM tools are based on the finite element-boundary integral (FE-BI) method. This CEM technology is uniquely capable of modeling complex geometrical and material properties. Below we present a brief summary of the FE-BI method.

Finite Element Boundary Integral (FE-BI) Method

Hybrid finite element methods (HFEM) have been explored for several years, most often being called either the finite element-boundary integral (FE-BI) or the finite element-integral equation (FE-IE) method. Both combine finite element and integral equation techniques. Unfortunately, a general FE-IE method is not currently feasible due to heavy computational resource demand. In such a case, electric and magnetic currents are needed on the mesh boundary as well as the three components of the interior field. All IE formulations result in full matrices due to global coupling; hence, the two currents on the mesh boundary impose an excessive computational burden in terms of memory and compute cycles. Therefore, FE-IE formulations typically are restricted to specialized situations such as cavity-backed patches or slots recessed in an infinite metallic surface. In this case, the FE-IE method can be formulated such that it requires only one current (magnetic) over the apertures located within the ground plane or circular cylinder [1]. Accordingly, the memory and computational requirements associated with the mesh boundary is minimized. In addition, very large apertures can be efficiently modeled by exploiting Toeplitz symmetry, present in the IE sub-matrix, provided these apertures lie in a metallic ground plane or circular cylinder and uniform

sampling is used on the mesh boundary. Figure 1 illustrates the application of the FE-IE (or FE-BI) method.

The MRC Team has been a leading innovator in custom FE-BI solutions for antenna analysis [2]. FE-BI is the only leading CEM technology capable of providing the geometric fidelity, efficiency, and accuracy required for demanding conformal antenna design and characterization.

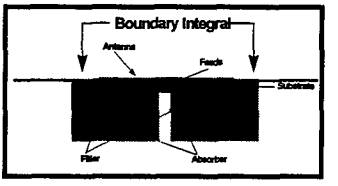


Figure 1: Application of FE-BI to a conformal antenna. *Note the reduced computational volume.*

Anisotropic Planar FE-BI Computer Codes

Our planar codes all use the half-space Green's function and have basically the same capabilities given by:

- Plane wave incidence
- Filamentary feed models
- Radar cross section calculation
- Power gain calculation for radiation analysis
- Voltage at feed pins due to plane wave reception
- Input impedance calculation
- Anisotropic materials
- Resistive (R-card) treatments

Anisotropic materials can be specified by fully populated symmetric or asymmetric permittivity or permeability tensors.

Brick Elements:

MRC developed and delivered a Fortran computer code called LM_BRICK. This FE code uses brick elements to discretize the volume as well as expand the unknown electric field. Validation has been performed by comparison with XBRICK results for a patch antenna for both scattering and radiation.

Prism Elements:

MRC developed and delivered a Fortran computer code called PRISM. This FE code uses right prism elements to discretize the volume as well as to expand the unknown electric field. PRISM also has the added capability to model superstrates and substrates. This code has been run on many of the antenna models and validated against existing data when available.

Tetrahedral Elements:
MRC developed and delivered a Fortran computer code called TET. This FE code uses tetrahedral elements to discretize the volume and expand the unknown electric field. TET also extends the capability of PRISM by including the capability to model non-planar cavity bottoms. This code has been run extensively on the LPA and validated against existing data.

Anisotropic FE-BI Cylindrical Computer Code:
To investigate the effects of curvature, MRC developed and delivered a tetrahedral element code for a cylindrical geometry. This code uses a special cylindrical tetrahedral element and the cylindrical Green's function for the boundary integral. This code is an improvement over the technique in [1].

Automatic Mesh Generators
We have developed a stand-alone C language code for each type of antenna we are modeling. These codes are integrated with a graphical user interface (GUI) currently under design by ADI. The basis of the mesh generators is Carnegie-Mellon's (CMU's) TRIANGLE Planar Surface Mesher. It is written in C (source code is freely available), uses X-Windows interface for mesh viewing, and we currently have it running on our SGI and other machines using Linux. We have developed mesh generators for the log-periodic, the equiangular spiral, the archimedean spiral, the sinuous spiral, and the Vivaldi notch. We also have generators for rectangular and circular patch antennas. The antenna codes are actually mesh generator interfaces used to create the input files used by TRIANGLE. TRIANGLE creates the triangular mesh, based on the input parameters specified by the user when a specific antenna code is run. SHOWME, also developed by CMU, is used to view the resulting mesh. Once the mesh files have been generated by TRIANGLE, an MRC developed code (INTERFACE) is used to create an input file for PRISM, TET, or CYL_TET (our FE-BI codes). The FE-BI code is then used to calculate various electromagnetic parameters such as input impedance, radiation patterns, and far-field patterns. A discussion of these meshers can be found in [3]

Our discussion will concentrate on the circular antennas. The associated polarization of the circular antennas is given below:

- Circular log-periodic (linear polarization)
- Spiral (circular polarization)
- Sinuous Spiral (dual circular or linear polarization)

Log-Periodic Geometry:
MRC developed a mesh generator for the Log Periodic Antennas (LPAs) with TRIANGLE. We can model a 4-arm LPA with any desired number of teeth. An example of a 4-arm LPA is shown in Figure 2.

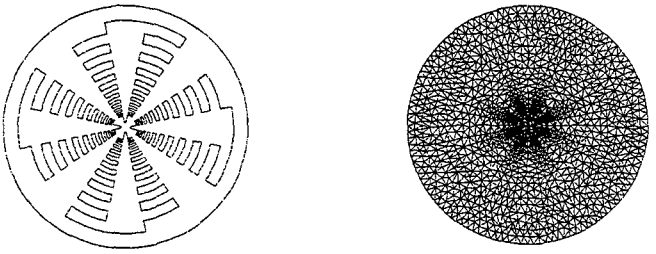


Figure 2: Log Periodic geometry and associated mesh

Spiral Mesh Generators

Mesh generators have been developed for 2-arm, 4-arm, and 8-arm equiangular and archimedean spiral antennas. We have also developed a mesh generator for a 4-arm sinuous spiral antenna. The user can specify typical spiral antenna attributes such as the antenna flare rate, maximum amount of rotation of the spiral arms, and initial distance between the antenna arms. Figure 3, Figure 4, and Figure 5 show examples of the various spiral antenna models and their associated meshes.

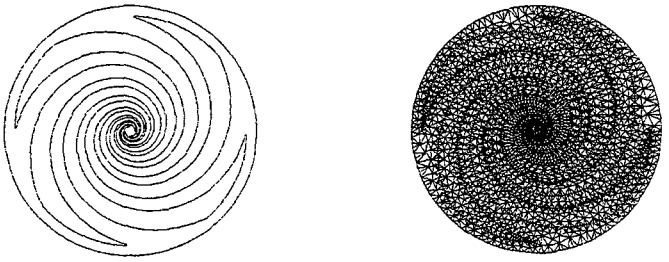


Figure 3: Equiangular spiral geometry and associated mesh

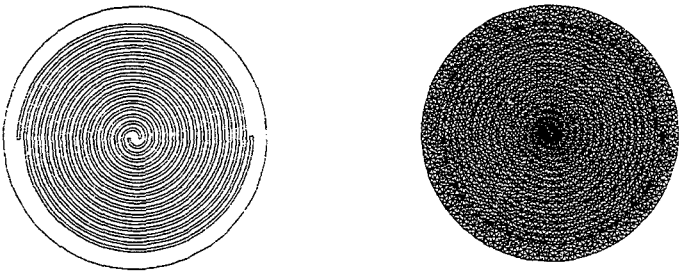


Figure 4: Archimedean spiral geometry and associated mesh

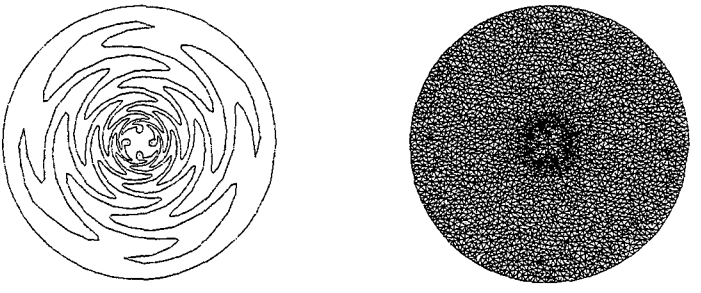


Figure 5: Sinuous spiral geometry and associated mesh

Graphical User Interface (GUI)

The GUI is being designed and implemented by ADI. It has been originally designed to run on SGI machines; however, we are also porting it to Linux machines. It consists of various pop-up screens that guide the user through setting up the geometry, generating the mesh, selecting the appropriate FE engine to solve the problem, provide input to the selected FE engine, and then provide post processing. Figure 6 shows the initial pop-up window. Selections are made from here.

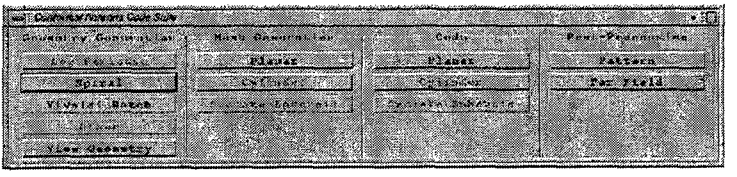


Figure 6: Initial Pop-up window. *Selects geometry, mesh generation, FE engine, and post processing*

Next, we pick "Spiral" to generate a spiral antenna geometry. From this window, another window is displayed that enables selection of the various antenna parameters. This is shown in Figure 7.

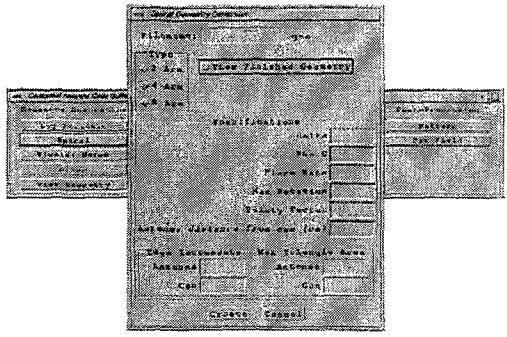


Figure 7: Pull down menu for constructing a spiral geometry. *Select spiral parameters.*

Next, the mesh needs to be generated. Figure 8 shows the inputs available through this window. The geometry can also be viewed. Figure 9 shows an example of a spiral antenna.

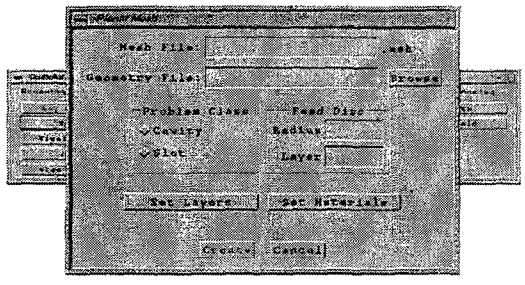


Figure 8 Mesh menu. *Mesh parameters are input here.*

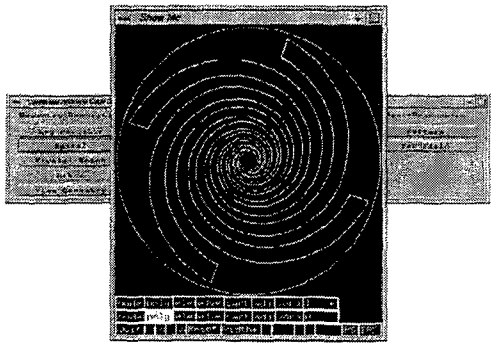


Figure 9: View Geometry button. *Displays geometry with "Show Me".*

Antenna Performance Prediction

We have discussed our efforts to develop an antenna design suite consisting of the antenna mesh generators for wideband, multi-modal antennas, choice of FE-BI techniques, and post processing options. The meshes enable accurate and efficient modeling of the performance for these antennas using the FE-BI method. These are all combined into a user-friendly GUI to make a useful tool engineers can easily use to determine design parameters that optimize performance of these antennas to solve real-world problems.

References

[1]. L.C. Kempel, J.L. Volakis, and R.J. Sliva, "Radiation by cavity-backed antennas on a circular cylinder," *IEE Proceedings, Pt. H*, 95.

[2]. L.C. Kempel & K.D. Trott, "Progress in modeling complex conformal antennas using the finite element-boundary integral method", URSI Radio Science Meeting, Atlanta, GA, June 98

[3]. K.D. Trott and R.D. Guidry, "Modeling Wideband Antennas using FE-BI Techniques", Proceedings of 1999 ACES Symposium, Mar 99

Curvature Effects on a Conformal Log-Periodic Antenna

Charles Macon, Leo Kempel, Michigan State University
Keith Trott, Mission Research Corporation
Stephen Schneider, Air Force Research Laboratory

Abstract

The impact of curvature on the resonant input resistance of a conformal, circular log-periodic antenna was investigated using the finite element-boundary integral method. The antenna was modeled as conformal to the surface of a perfectly conducting, infinite circular cylinder. The curvature of the cylinder was varied and the input resistance was calculated over a frequency range of 6-20 GHz using a finite element-boundary integral program. The behavior of the input resistance with respect to curvature was compared to that of a similarly mounted conformal square patch antenna. From this investigation, it is evident that the resonant input resistance of the log-periodic antenna is invariant with respect to changes in curvature.

I. Introduction

Log-periodic antennas belong to a class of broadband antennas for which the performance, as defined by the radiation pattern and impedance, is practically independent of frequency over a large bandwidth. This characteristic is achieved through the specification of an antenna geometry, such that the electrical characteristics of the antenna varies periodically as the logarithm of the frequency [1]. The motivation for this study lies in the fact that designers may sometimes find it necessary to place conformal antennas on the curved surfaces of aircraft, satellites or other types of vehicles. The effect of the supporting platform on the input impedance must be considered for matching purposes.

In this investigation, the finite element-boundary integral (FE-BI) method was utilized to calculate the input impedance of the antenna. The FE-BI method is versatile in that it permits the specification of anisotropic materials within the computational volume and is capable of modeling structures with both metallic and dielectric components as well as arbitrary shape. The FE-BI method utilizes a boundary integral to terminate the finite element mesh by relating the tangential electric and magnetic fields on the mesh surface. The FE-BI equations are derived from the weak form of the vector wave equation and are given as follows [2]:

$$\int_V \left[\nabla\times\mathbf{W}_i\cdot\bar{\bar{\mu}}_r^{-1}\cdot\nabla\times\mathbf{W}_j\right]dV - k_0^2\int_V\left[\mathbf{W}_i\cdot\bar{\bar{\varepsilon}}_r\cdot\mathbf{W}_j\right]dV + jk_0\int_{S_R}\left[\frac{\left(\hat{n}_R\times\mathbf{W}_i\right)\cdot\left(\hat{n}_R\times\mathbf{W}_j\right)}{R_e}\right]dS$$

$$-k_0^2\int_{S_a}\int_{S_a}\left[\mathbf{W}_i\cdot\hat{z}\times\bar{\bar{G}}_{e2}\times\hat{z}\cdot\mathbf{W}_j\right]dS'dS = f_i^{int} + f_i^{ext}$$

The first term is associated with the magnetic field, the second term is associated with the electric field, the third term accounts for resistive transition conditions, while the last term on the left-hand side is the boundary integral term. The two terms on the right-hand side are functions of the interior and exterior excitation, respectively [3]. Note that Galerkin's testing procedure is utilized, whereby the basis function $\mathbf{W}_j$ is functionally identical to the test function $\mathbf{W}_i$. Also note that the boundary condition on the metallic surface is implicit in the dyadic Green's function of the second kind used in the boundary

integral term. This formulation obviates the need for an equivalent electric current, thereby reducing the number of unknowns and associated computational cost.

II. Modeling and Simulation

A square patch antenna conformal to the surface of an infinite conducting cylinder was modeled using the FE-BI computer model described above. The dimensions of the square patch antenna are as follows: 2.5cm x 2.5cm metal patch with a 5cm x 5cm aperture and a .0762cm substrate thickness. This patch is illustrated in Figure 1. The patch antenna is fed

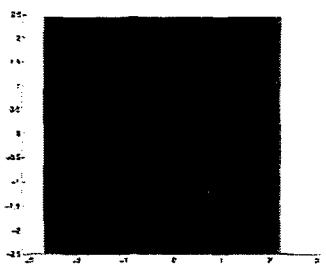


Figure 1. Patch antenna and the feed points for circumferential and axial polarizations.

along a centerline of the antenna and three rotational states are considered: 0°, 45°, and 90°.This corresponds to: axial, mixed, and circumferential polarizations. The input impedance about the resonance for this antenna is illustrated in Figure 2. As shown, the input resistance's dependence on the feed location is determined by the rotational state of the antenna. For axial and to a lesser extent mixed polarizations, the value of the input resistance at resonance depends on the cylinder curvature. On the other hand, for circumferential polarization, the input resistance is invariant with respect to cylinder curvature. Such a dependence is described elsewhere,

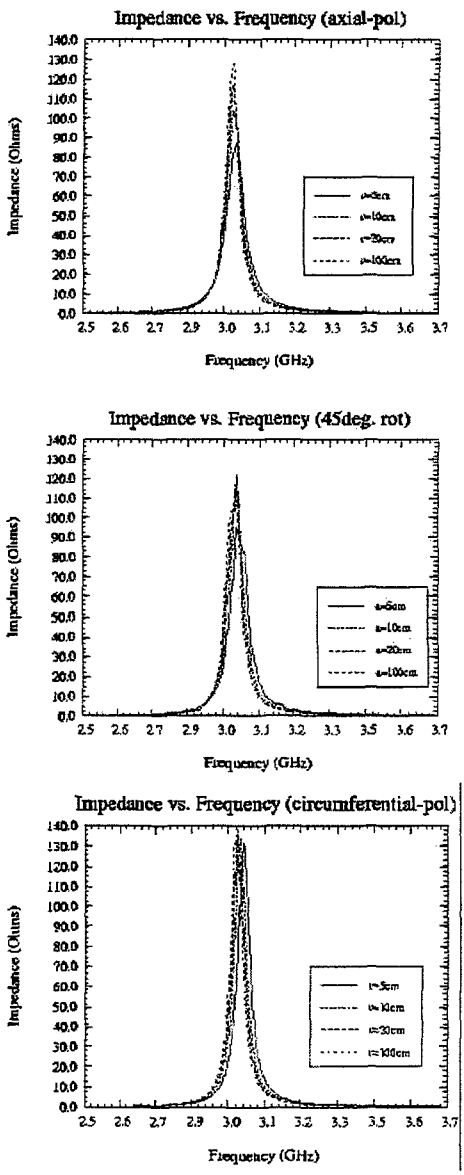
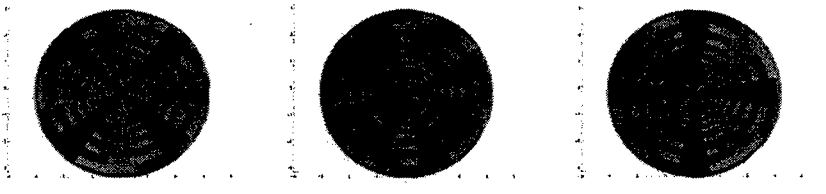


Figure 2. Resistance of a patch antenna for three different rotations on a cylinder: 0, 45, and 90 degrees.

though not for the mixed polarization case [4]-[5].

The consequence of the rectangular patch antenna's potential dependence on rotational state is a practical one. Care must be taken in the construction of arrays of such antennas and in the mounting of the array on a curved surface so that a good match to the feed network is obtained.

Such considerations motivated the subject of this study: the dependence of circular log-periodic (LPA) antennas on rotational state. The LPA was chosen since among all wide bandwidth, multi-modal antennas in practical use, it appears to be the most likely candidate for curvature dependence. This is due to its relative asymmetry with respect to rotation as compared to spiral, sinuous spiral, and other multi-mode antennas. A complementary four arm LPA has several distinct rotational state possibilities. Three of these are illustrated in Figure 3: 0, 22.5, and 45 degrees.



Case 1 Case 2 Case 3

Figure 3. Three orientations of the LPA on a cylinder: 0, 22.5, and 45 degrees.

For this study, the different rotational states can be considered as points on a compass. For the 0 degree case, the metallic arms of the LPA are aligned with the N-E-S-W points on a compass and the apertures align with NE-SE-SW-NW points on the compass. The 45 degree case is the complement (e.g. the metal arms align along NE-SE-SW-NW and the apertures align along N-E-S-W points). The 22.5 degree case is part way between the other two cases.

For this investigation, the resonance behavior of a four-arm, log-periodic antenna was analyzed as the curvature varied. The antenna was modeled as conformal to the surface of an infinite conducting cylinder. The following geometrical parameters describe the antenna: α=67.5°, β=22.5°, τ=0.80, R_0 = 0.129 and R_1 = 0.3 as described in [6]. A homogeneous cavity fill of permittivity $\varepsilon_r \approx 3.2$ was used through out this study. An infinite circular cylinder provides a computationally tractable representation of the types of curved structures on which the antenna could be mounted. A tetrahedral mesh was used to described the cavity volume. The impact of curvature on the input resistance for three distinct orientations was studied. As illustrated in Figure 3, each case represents a distinct rotation of the antenna with respect to the vertical cylinder axis. The excitation frequency range used in this study is 6-20 GHz. The antenna was excited at four feed points but, for the sake of brevity, only the results at two representative feed points (in case 1, the North and East arms) were presented in this paper. The curvature was altered by changing the cylinder radius (e.g. ρ=100cm, 20cm, 10cm and 5cm). The input resistance for mode 1 (progressive phase shift of 90°) versus the excitation frequency at each feed point was calculated using a FE-BI program and plotted, as shown in Figure 4.

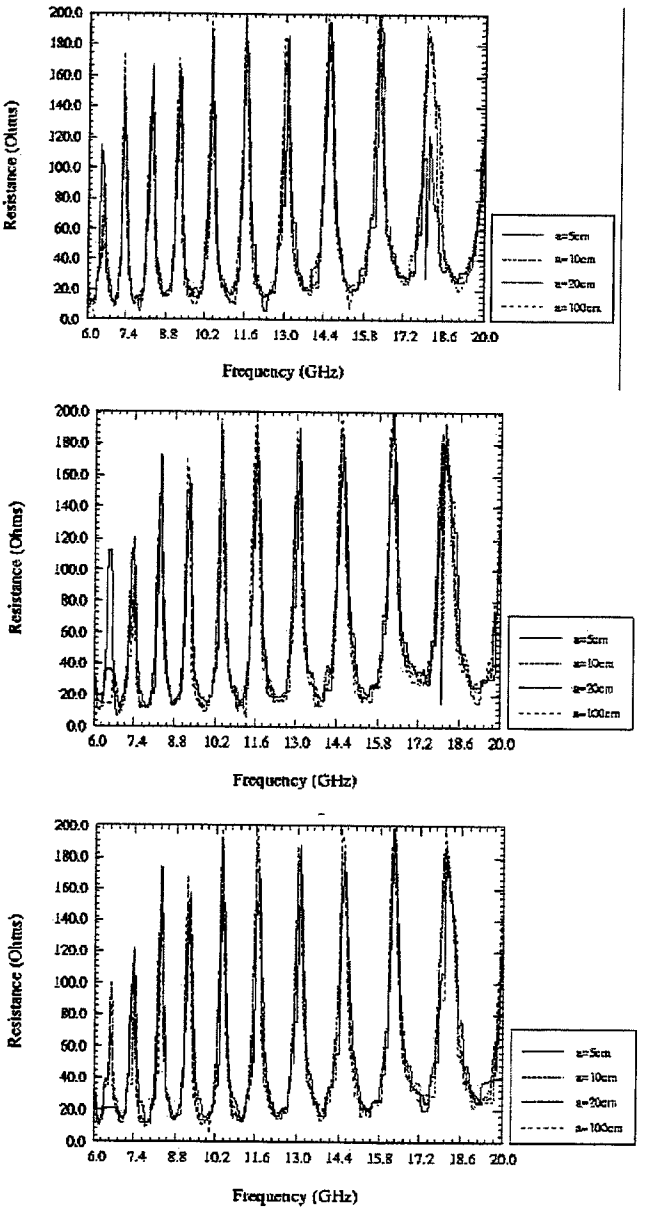


Figure 4. Input resistance for various curvatures measured at the North feed.

The input resistance at the East feed (as shown for case 1) is presented in Figure 5.

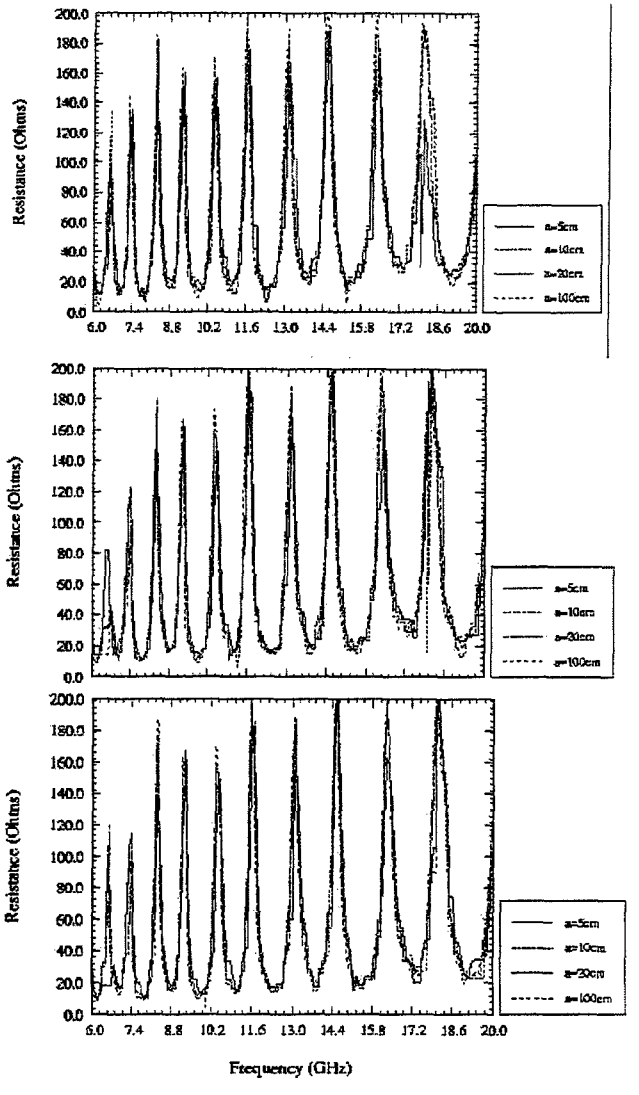


Figure 5. Input resistance for various curvatures measured at the East feed.

As seen in Figures 4 and 5, the input resistance for the antenna arms (for case 1) aligned along the North and East axes is invariant with respect to curvature. Due to the symmetry in this complementary LPA design, we may extend those conclusions to the South and West feeds as well.

III. Conclusions

We conclude that the reason for this invariance lies with the operational mode of a circular LPA. As a wide bandwidth antenna, radiation at different frequencies can be attributed to different portions of the antenna. The antenna is fed near the center of the antenna. Electromagnetic fields are guided by a tapered microstrip transmission line until a quarter-wave stub is encountered. At that point, radiation occurs. Accordingly, high frequency radiation emanates near the center of the LPA while low frequency radiation occurs at the extremity of the antenna. The curvature of the cylinder increases as the frequency increases (this is the fundamental reason the patch antenna can be sensitive to curvature); hence the high frequency fields "see" a ellectrically larger cylinder than do the lower frequency fields. For the patch antenna, the input resistance depends on the normal fields beneath the patch and these are different for axial and circumferential polarization. Indeed, it can be shown that the normal fields beneath a circumferentially polarized patch are invariant with respect to curvature [4]. However, unlike the patch antenna whose input resistance depends on the field underneath the resonant antenna, the LPA's resistance is invariant to curvature. The reason is likely due to the fact that the resonant structure (the quarter-wave stubs) are distant from the feed point. Note that the resonant stubs do appear as loads to the microstrip line and result in resonant lines in the spectral responses shown in Figures 4 and 5. Further investigation is warranted to tighten our understanding of this curvature invariant phenomena.

In this paper, we investigated the impact of curvature on a popular wide bandwidth multi-mode antenna: the circular log-periodic antenna. We found, unlike the case of a patch antenna, that the input resistance is not dependent on the curvature of the antenna itself. This has important practical implications since it permits the design of such antennas using efficient planar design methods. It also relives the antenna integration team of the responsibility to carefully align these antennas on the supporting structure (e.g. aircraft, automobile, etc.).

The conclusions reached in this study are for shallow cavity (substrate only) circular log-periodic antennas excited in mode 1 (total phase shift around the antenna of 360°) [7]. Further investigations will be undertaken to extend our conclusions to more general cases.

References

[1] R. H. DuHamel and F. R. Ore, "Logarithmically Periodic Antenna Designs," 1957 I.R.E. National Convention Record, Part I, pp. 139-151.

[2] L.C. Kempel, "Implementation of Various Hybrid Finite Element-Boundary Integral Methods: Bricks, Prisms, and Tets," Department of Electrical and Computer Engineering., Michigan State University.

[3] J. L. Volakis, A. Chatterjee, and L. C. Kempel, Finite Element Methods for Electromagnetics, New York: IEEE Press, 1998.

[4] K. M. Luk, K.F. Lee and J. S. Dahele, "Analysis of the Cylindrical-Rectangular Patch Antenna," IEEE Transactions on Antennas and Propagation, vol. 37, No. 2, Feb. 1989.

[5] L.C. Kempel, J.L. Volakis, and R.J. Sliva, "Radiation by cavity-backed antennas on a circular cylinder," *IEE Proc.-Microw. Antennas Propag.*, **142**(3), pp. 233-239, June 1995.

[6] W. L. Stutzman and G. A. Thiele, Antenna Theory And Design, 2nd ed., John Wiley & Sons, Inc.,1998
[7] R.G. Corzine and J.A. Mosko, "Four-arm spiral antennas," Artech House, 1990.

SESSION 14

ANTENNA ARRAYS

Chairs: Keith Lysiak and Nathan Cohen

©British Crown Copyright DERA/1999
Published with the permission of the Defence Evaluation and Research Agency on behalf of Controller HMSO.

Problems of characterising array manifolds for naval platforms in HF environments.

Linda Holtby
DERA Portsdown West
Hampshire, England.
October 1999

Acknowledgements:

The author would like to acknowledge the work by Roke Manor Research Limited in conjunction with this investigation, and in particular to thank Mr David Sadler for his support.

1.0 INTRODUCTION:

This paper explores some of the problems encountered when attempting to accurately calibrate ship DF arrays, particularly at HF, and for skywave signals.

Traditionally, a ship array response has been calculated using the geometry of the array, suitable positions on the superstructure have been allocated, then the whole arrangement is calibrated by sailing the ship in a circle and taking bearings on signals of known azimuth (elevation was not considered). For several years, copper scale models characterised on a model range have been seen as an appropriate substitute for the full-scale platform, and used as a 'first step' generating the calibration data. More recently, work has been done to evaluate the validity manifolds generated from CAD wireframe models.

The object of the research discussed in this paper is to evaluate the validity of copper and NEC (Numerical Electromagnetic Code) array manifolds. Ideally we would like to make wireframe models so accurate that the manifold for a ship DF array can be accurately predicted using software alone. This would enable quick re-calibration of an array where a modification has been made either to the array, or to the surrounding platform.

2.0 METHODS FOR GENERATING DF MANIFOLDS:

A manifold is a data set consisting of a collection of steering vectors that characterise the response of the DF array. Manifolds can be generated by geometric calculation, measurement (of the full-scale system or of a scale model) or by electromagnetic simulation.

The more data points that are collected (increments in azimuth, elevation and frequency, plus orthogonal polarisations) the more accurate the potential DF response of the array, however, the time required to characterise the array increases accordingly. To represent an array over the entire HF band, it is recommended that the frequency step size be around 5% of the centre frequency, with closer frequency spacing in the region of significant platform structural resonance. The required steps in azimuth and elevation can be assessed according to antenna beamwidths and the algorithms to be used, but are typically of the order of 2° and 3° respectively. The step size of all parameters is determined with reference to the required DF accuracy of the system, the algorithm to be used, and the environment stability.

2.1 Geometric Manifold:

This is simply a description (in phase) of where the elements of the array are physically with respect to one another. All elements are assumed to have identical radiation patterns being identically aligned.

2.2 Full-scale calibration:

In other words, sailing the ship in a circle within radio range of transmitters whose position is precisely known. Arguably, this is still the most accurate method of calibrating the array, although it is not practical to take data points above low elevations.

2.3 Scale models:

Scale models have an advantage in that the calibration signal can be accurately controlled in azimuth, elevation and polarisation. There are problems associated with obtaining high elevation test signals in the far field, and in the timescale required to collect sufficient measurements to characterise over a full half-hemisphere. There are also difficulties in assessing how accurately the model represents the full-sized array.

2.4 Computer models:

Computer simulated manifolds produced by analysis of wireframe CAD models are a recent method of generating array manifolds. At present, producing a complex wireframe model with sufficient detail to represent a cluttered platform is time intensive. Running the segmented model through a package such as NEC to produce a manifold at the appropriate frequency of interest is processor intensive. However, once a wireframe model for a particular platform has been produced, it can be modified and re-used with little extra effort. Similarly the run-time required to produce the manifold for the arrays should reduce rapidly as computer processing power and speeds increase. The main aim of the work described in this paper is to assess the validity of NEC manifolds in representing the full size array.

3.0 WORK DONE:

The procedure for collecting the data used to characterise the manifolds investigated is discussed in this section.

3.1 Full-scale array measurement:

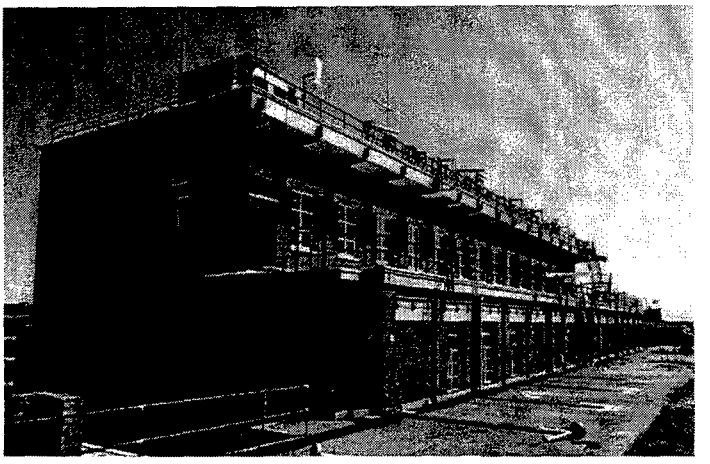


Figure 1 – The full-scale array - Photograph of the Fraser building with DF array mounted.

For the full-size platform, an array of 10 loops were mounted on a building at DERA Fraser (8 of which were used). The building was modified with steel strapping so that it better emulated the conductivity of a ship hull. The site was chosen because it faced directly onto a beach, and signals used in the trial propagated over seawater. Signals were transmitted from a boat and from transmitters suspended by balloons flown from the boat, at a range of 1500m (far field) from the array. The positions of the transmitters were checked with GPS and by optical means (theodolite). Measurements were taken for the responses of the array elements over 7 trials frequencies (between 2MHz and 26MHz). The manifold used for the full-sized structure was simply the geometry of the elements in the array, and was only defined in one polarisation. The signals measured were groundwave and expected to be vertically polarised.

3.2 Copper Model:

A 1:50 scale copper model of the Fraser site was constructed. This carried detail relevant to the highest frequency in use, and included site features likely to affect the responses of the elements in the array. The maximum (full-scale) distance between elements on the array was 35m, the overall site was some 150m in length. This allowed scope for investigation into how much the surrounding structures contributed to the aperture of the array. The copper model array manifold was populated for the 7 frequencies used in the Fraser boat trials, and in two orthogonal polarisations (H and V). The steps in azimuth and elevation were 2° and 3° respectively.

In addition to the boat trials data, signal data was also collected on an 8-channel DF rack (synchronous measurement) connected to the scale model. The signals were transmitted from the probe antenna on the model range boom. This ensured that the signals generated were of controlled DOA and polarisation, and had the same degree of curvature to the wavefront as the calibration measurements.

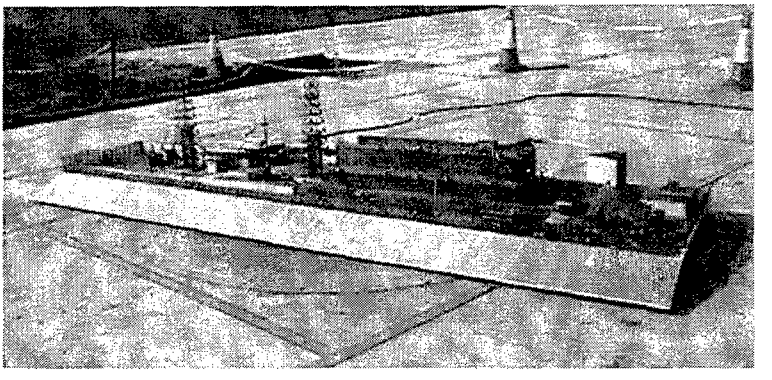


Figure 2: Photograph of the 1:50 scale model of Fraser on the model range turntable.

3.3 NEC models:

In the first instance, a very simple NEC model was generated for comparison purposes (using the 7 frequencies for the boat trial data). The model only represented the building carrying the array, with the loop positions defined as per the geometry. It was not anticipated that this would accurately emulate either the full-scale array or the copper model, since the major structures on the site (such as the radar towers) were omitted.

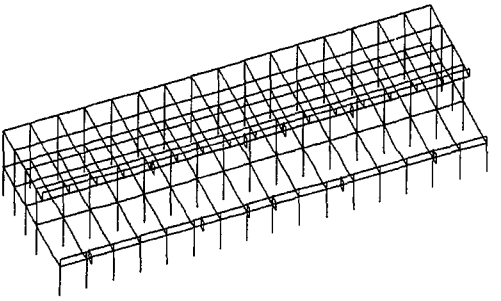


Figure 3: Simple wireframe model used for initial NEC manifold.

A complex wireframe model was then constructed which contained all the detailed structure of the full Fraser site. The model was segmented to produce an output file to allow NEC to generate a manifold at the chosen frequency. The higher the frequency the manifold is being calibrated for, the more segments that are required (smaller wavelengths). Extra detail (more segments) were incorporated around the antenna elements.

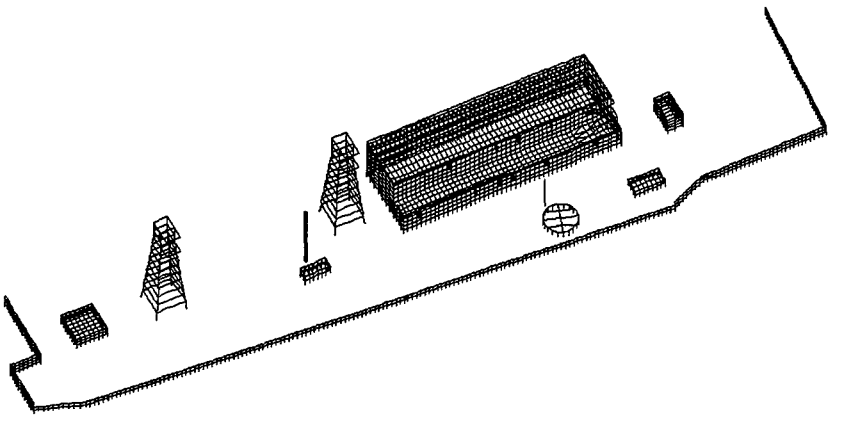


Figure 4: The 6500-element wireframe model used for detailed NEC simulation manifold.

The number of segments required for a detailed structure can be prohibitive. The full wireframe model segmented for 20.99MHz amounted to 6500 segments (using $\lambda/10$ segments). The wireframe model was initially reduced to around 5000 segments by stripping off the fence line, as it was felt that such a degree of fine grain structure (not significantly close to the array loops) was probably unnecessary for the manifold to be accurate. The 6500 segment version ran successfully, after 50 hours and with an upgrade to 1Gbit of RAM on the PC, (8 hours per frequency). Both manifolds were used to assess the impact of the fenceline on the modelled array response.

A manifold was produced in the far field at 20.99MHz, for use with the boat trials tracking data. A manifold was also produced at 16.019MHz, using a signal source specified at a distance equivalent to that of the probe from the copper model (around the near field boundary) for use with the data collected on the model range.

Normally a NEC generated manifold assumes 'true' far field, using a planar wavefront excitation. However a facility exists which allows for signal source range to be specified. Using the 'near field request' a curved wavefront can be simulated. In theory, the range of the original boat trial could be modelled as a 'near field' request, as the distance of the signal source is not infinite, although it is in the far field.

4.0 ISSUES TO CONSIDER:

4.1 Problems with manifold comparison:

Even if the copper model were to perfectly represent the full-scale site, the manifold would contain fine grain structure not present in the geometric manifold. This would give rise to differences in the DF results using the two manifolds, even without errors in the model calibration process.

The copper model manifold is defined in two orthogonal polarisations, whereas the Fraser (geometric) manifold was not. Therefore a direct comparison of DF accuracy between this and the scale model manifold is of reduced value. The trials data was anticipated to be vertically polarised (groundwave over 1.5km) so both manifolds were assessed using MUSIC, with vertical polarisation selected in the case of the 'copper' manifold.

Initial analysis of the tracking data collected at Fraser suggests mode conversion of the signals arriving at the loops. This cannot be accurately evaluated, as there may be phase errors in the definition of the 'copper' manifold masking or diluting the effect.

4.2 Problems with the full-scale platform:

The manifold for the array, being simple geometric calculation, assumes that the elements have identical radiation patterns, all aligned in the same direction. Analysis of the trials data demonstrates that the Fraser geometric manifold sufficiently described the array to give good results in azimuth, but gave less accurate results in elevation. Electromagnetic modelling of the array demonstrated that the loops mounted on the Fraser building had similar, but not identical radiation patterns. A geometric manifold would thus be inappropriate in the case of an array with elements having dissimilar radiation patterns.

4.3 Problems with the model range:

The calibration process used for the scale model manifold in our investigation was initially found to be inconsistent. Several factors contributed to this, the two main factors being environmental effects and inappropriate measurement procedure.

4.3.1 Errors due to environmental effects:

- Instability in the probe position (due to gusts of wind flexing the boom arm). A movement of 15cm at 1GHz is equivalent to $\lambda/2$, so introducing significant phase error into the measurements.
- Changes in temperature (particularly for long cable runs). For measurements taken over a protracted time period, some change in temperature is inevitable. It has been found that temperature variations can induce a corresponding phase variation in the measured signal.

- Rainfall/humidity inducing pronounced phase swings in the measured signal. Over a slightly longer time scale, a change in the water-content of the surrounding ground can also give rise to errors (where the conductivity of the ground-plane is significantly altered).

4.3.2 Inappropriate measurement procedure:

These give rise to the most avoidable errors; problems encountered include the following:

- Facilities that allow for only one channel to be measured at a time. This implies that any changes in the environment from one channel to the next (or frequency, or polarisation to the next) causes fluctuations specific to that one element response. If channels are calibrated separately, the elements are inherently being characterised with different calibration sources (with subtly different DOA, no matter how carefully the measurements are arranged).
- Any change to the position of the model. This is a practical limitation for any calibration incorporating curvature of the wavefront. Any change in the centre of rotation of a scale model during a calibration run (such as incorrect repositioning after vital maintenance) will cause errors in the manifold.
- Alignment of the 'origin' of the array to true north, or 0° in Azimuth. Errors in aligning the model in this plane will cause an error in DF azimuth (which should be fairly uniform throughout the manifold).
- Not including a reference probe on the model. The use of such a probe would eliminate fluctuations in the signal level in the calibration path, such as those due to environmental change or drift in equipment parameters.

4.3.3 Curvature of the wavefront:

There is a fundamental problem where calibration for skywave is concerned. For groundwave or low elevation signals, adequate far-field measurements can be taken at all frequencies (providing the site has a large enough groundplane and is uncluttered). However, for elevations above 10°, using a boom and turntable arrangement, it is not feasible to produce sufficiently far field signals for arrays of an appropriate aperture (except at the lowest frequencies of interest). A manifold calibrated this way is potentially less accurate with increasing elevation (depending on the height of the model). If a signal source is at true far field, the array is seen as a single point, and the centre of rotation is irrelevant. The greater the proximity of the probe to the model, the greater the phase errors across the aperture of the array.

Calibrating for skywave significantly increases the measurement time (by a factor of ×30 if increments of 3° in elevation are used).

Using a dedicated near field arrangement (using far field conversion techniques) was not an option for our study as there were no facilities available catering for the lower frequencies of interest at HF.

4.4 Problems with the NEC models:

NEC solves Maxwell's equations by a method of moments for a collection of wires or surface patches excited by voltage sources or an incident plane electromagnetic wave. In our analysis we used wire grids to model conducting surfaces.

The method is limited by the number of moments used and by the approximation on how currents flow. Wires are treated as one-dimensional structures, and NEC assumes that currents only flow axially. This does not take circumferential (or radial) currents into account, and must give rise to some modelling error.

The more detail that is used to describe an array (the array here being defined as the whole structure, with the elements being regarded as excitation points on the array), the more accurate the manifold. However, the more detail that is used, the more computationally intensive the process. The NEC manifold produced is equivalent to a matrix of all the element radiation patterns for the array (each taking the overall structure into account). Obtaining accuracy in the magnitude of the radiation response is relatively straightforward. The phase is less straightforward, and an accuracy of within 5° of the 'truth' is suggested as a desirable goal.

4.6 Problems with Skywave:

In addition to the 'near field' problem of the model range, there was another factor causing the response in elevation to be poor. The DF response (not the accuracy) for all of the manifolds under investigation was worse for elevation than for azimuth. This is a function of the shape of the array being used, having aperture much shorter in elevation than in azimuth. Therefore the array had 'deaf' response to skywave, having poor resolution in elevation. This problem will affect all arrays of similar profile.

5 EVALUATION OF THE MANIFOLDS OBTAINED:

The evaluation of the manifolds produced is not straightforward. Essentially this was a 3-way comparison, initially with no common reference. The methodology employed was as follows:

- Compare geometric results of the far field Fraser data with that of far field NEC models. This gives an indication of the difference between the simple wireframe model and the simple geometry, and then between the simple and the complex wireframe models (without introducing the factors encountered on the model range).
- Compare the manifold obtained from the copper model with the detailed NEC manifold stimulated with corresponding curved wavefront. This compares the NEC model to the copper model without introducing phase errors due to the proximity of the boom probe to the model. This is to gain an indication of how well the NEC model emulates the copper model, having a similar level of complexity and overall aperture.
- Compare the manifold from the same (detailed) NEC model excited with a planar wavefront and then with a signal defined at appropriate 'near' source. This is to gain an appreciation of the degree of DF error induced by the curved wavefront.
- The validity of the copper model in representing the full-scale Fraser site may then be inferred, on the basis of eliminating the factors that make direct comparison impractical.

A Matlab evaluation tool (written by Roke Manor Research Limited) was used for the manifold comparison. The software was modified to allow loading of externally generated manifolds. The manifolds were then tested using a DF algorithm and signal data obtained in the boat trial or on the model range. Manifold interpolation routines are required to permit DF processing of signals recorded at different frequencies to the manifold data.

6 FINDINGS:

6.1 The geometric manifold:

As the Fraser array had elements with fairly similar radiation patterns, the geometric array was expected to accurately predict the response of the array. This would be less true for any signal 'endfire' to the array or originating from behind the building. All of the trials data was generated within a 150° arc mainly broadside to the array.

6.2 The simple NEC manifold:

The very basic NEC model was derived from the geometry of the array this was also anticipated to give a reasonable DF response to the trials data. As the trials data was groundwave, and thus single (vertical) polarisation, this manifold gave good DF results using a single polarisation (MUSIC) algorithm.
The 'basic' NEC manifold performed less well with skywave signals generated on the model range (using both polarisation sensitive and insensitive algorithms). This is probably because the signals collected with the copper model would be affected by the local scattering from the detailed metal structures surrounding the array elements. The more complex NEC manifolds produced later took the surrounding structural detail into account, and performed better with the range data.

6.3 The copper model:

There are problems in assessing whether the copper model accurately emulated the conductivity and reflectivity of the Fraser site. The reflective surfaces around the elements produce local scattering (effectively multipath), which widen the beamwidth of the array. Although measures were taken to make the Fraser building emulate a conducting structure at the frequencies of interest, there was no way of quantifying the accuracy of the representation.

6.4 The copper model manifold:

Using the trials data, the geometric and the 'basic' NEC manifolds compared quite well, whereas the copper model manifold gave a very different response. This indicated that there were problems either with the copper model or with the way it was characterised. On the main Fraser site (and on the models), there was a large tower within a few meters of the end of the 'array'. At one of the trial frequencies the tower height represented a quarter wavelength, and this was expected to alter the phase centre of the array. Measurements were taken of the copper model with the tower present and with the tower down. While differences between the two manifolds produced were noted, the repeatability of the original manifold ('tower up') was found to be suspect. Thus reliable conclusions could not be drawn from the data.

6.5 Model range phase stability with temperature.

To investigate the apparent phase instability of the copper model measurements, an attempt was made to assess the impact of the environmental variations. A test was conducted whereby a 1/4 wave monopole was placed on the turntable, and a fixed 1GHz signal was monitored over a 24 hour measurement period.

During the experiment the phase of the measured signal was seen to suffer an apparent diurnal fluctuation of around 40°. The phase variation appeared to roughly track the measured ambient temperature. The exposure of sections of cable in the calibration path to the elements (sunlight etc.) was found to be a significant factor. In addition, it was found that rain induced a more dramatic phase swing (possibly due to a combination of greater cooling effects and humidity between the channel connections), a variation of 120° being recorded at one instance *(see figure 5)*. Note that the smaller fluctuations seen on the trace corresponded to clouds obscuring the sun. The substitution of a phase-stable coax on the boom significantly reduced this effect, as demonstrated in the second sweep plot *(see figure 6)*. Note that the second run was conducted on a windy day, with no direct sunlight (but with no rainfall), so sharp fluctuations shown on this trace give an indication as to the phase excursions induced by wind gusts (2° worst case, ±0.5° typical), with some underlying temperature effects still evident. Further experimentation revealed that errors due to boom movement in a gusting 15-knot wind over a short duration (i.e. no temperature variation) measured ±0.5° at 1.2GHz.

Until recently, the model range facility was used to characterise individual elements and their coupling to the surrounding platform. This involved measuring field strengths and producing amplitude patterns, thus a deficiency in the phase stability of the system would not be readily apparent.

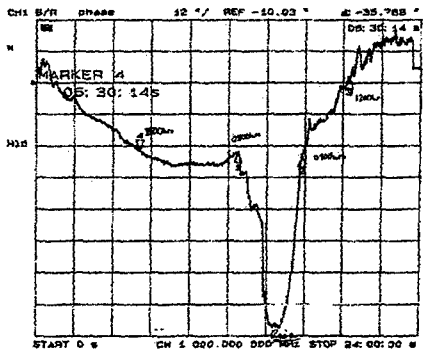


Figure 5: Phase drift of original calibration cable over a 24-hour sweep (with temperature).

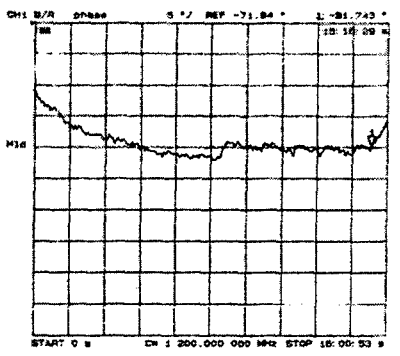


Figure 6: Phase response with phase-stable coax in calibration path[1]

6.6 Detailed NEC manifolds:

Using the signal data collected at Funtington range (controlled in polarisation and DOA), the analysis of the DF response of each of the 3 NEC models indicates that the more complex models give the greatest accuracy. This is expected since the 'basic' NEC model takes no account of the surrounding structures, and does not contain any fine grain structure (such as the metal staircase near element 5).

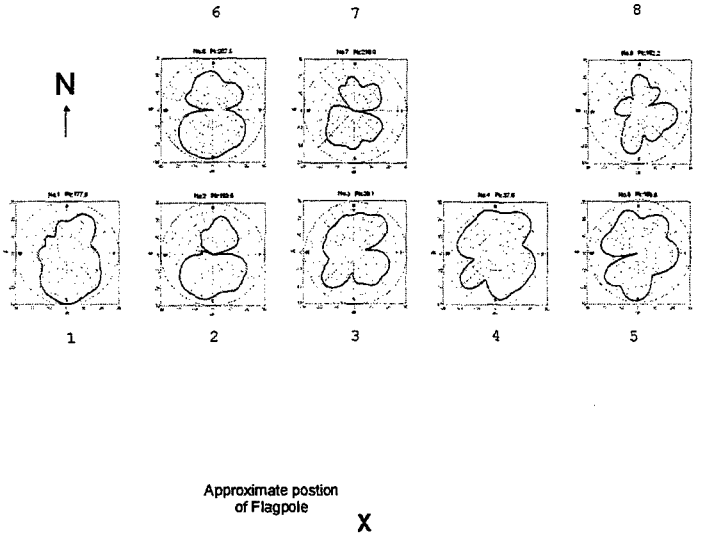


Figure 7: Polar element radiation patterns in 'NEC' array at 7.556MHz (flagpole resonant).

The inclusion of the fence line in the model gave better results than its omission, which implied that this structure had significant influence on the aperture of the array. It was also noted that at one of the test frequencies (7.566MHz), a fairly insignificant structure on the site had a pronounced influence on the response of the array. A small flagpole (9.5m in height) is visible to the south of the main array on the Fraser site, this appears as a slim vertical line on the wireframe model *(see figure 4)*. A structure of 9.93m in height represents $\lambda/4$ at 7.556MHz and would be resonant. Figure 7 shows a set of polar plots for the elements, as they appear on the array (viewed from above) and their response to a groundwave (vertically polarised) signal. The approximate position of the flagpole in relation to the array is marked 'X', and nulls are evident in the radiation patterns of the elements that appear to point towards the resonant structure.

7 CONCLUSIONS:

Measurement errors and process errors on the model range invalidated the copper model manifold in this instance. Most problems arose from the fact that the model range was principally designed to characterise single antennas and their coupling to the surrounding structure, or arrays of small physical dimensions. The phase-instability of the original cable to the boom probe was a major source of measurement errors. Synchronous measurement of all elements on an array is desirable at any one frequency, as it eliminates errors due to environmental changes, or fluctuations in the probe position. Where channels are characterised separately, they are not truly calibrated for the same incoming signal.

Where a large copper model is used on a range with a boom and turntable arrangement, the centre of rotation of the model becomes significant due to curvature of the wavefront. Although the phase taper across the array may not cause gross DF errors, moving the centre of rotation between measurements will cause serious errors in the manifold. Copper models (characterised with appropriately controlled facilities) are still useful from the point of view that test signals can be generated for any azimuth, elevation or polarisation.

At the wavelengths corresponding to the low end of the HF band (around 100m), a large aperture is required to achieve reasonable DF accuracy. In addition, larger arrays give greater resolution at a given frequency, allowing discrimination between close proximity signals. Where the aperture of an array becomes large enough to pose problems for scale modelling, computer-generated manifolds may prove the only practical solution.

During the course of this work, a polarisation sensitive algorithm was assessed in parallel with the manifolds under investigation. Where an array has elements with diverse radiation patterns the response of the array will span the polarisation space. Characterising an array in two orthogonal polarisations enables signals of any polarisation to be captured and thus be available for DF.

At present, the run-time for a highly detailed wireframe model at a single frequency is comparable with the measurement time required on a model range, however, this will reduce as computer processing speeds increase. Computer simulated arrays offer flexibility, and once mature, will provide a cost effective and fast calibration tool where modification of an array or platform has occurred. The natural progression to this is work is to use computer-generated manifolds to compare the performance of various DF algorithms under certain situations. For example, with correlated multipath (typical of HF), short duration signals (giving insufficient samples for HOS) or multiple target signals over a wide range of SNR.

The traditional view of the array as a set of elements with a geometric relationship is challenged where non-identical elements and reflective structures are involved. On a model range for example, it is not sufficient to measure the individual element responses and post-process for the phase relationships. The phase centre of the array is suspect where a resonant structure is close to the array, and the overall aperture of the array is altered. The array should be viewed as a single antenna with various 'excitation points'.

DESIGNING A VHF WRAP-AROUND DF ANTENNA ARRAY USING NEC

Keith Lysiak, klysiak@swri.edu
Southwest Research Institute, San Antonio, Texas

ABSTRACT

The Numerical Electromagnetic Code (NEC) was used to design a VHF wrap-around DF antenna array. A prototype array was constructed and extensive antenna response measurements were made at the SwRI antenna range. The measured responses matched the numerically modeled results very well with an overall mean correlation value of 0.986. NEC also produced beamformer characteristics very similar to the modeled characteristics. The numerically modeled results were used to produce array manifolds to estimate DF performance. An overall DF performance of less than 1 degree RMS error was obtainable using the NEC generated array manifold. This is a first order indication that the array design is very robust.

INTRODUCTION

The design of direction-finding (DF) antenna arrays is a complex task. Numerous factors can affect DF performance. In complex scattering environments, accurate information about the interaction of the antenna elements with the surrounding environment is crucial to determining DF performance. Most DF systems are required to operate over a broad frequency range which means that structural resonances within the band of operation are important. These resonances can significantly distort the antenna response patterns and decrease the array performance. Fortunately, a few key characteristics of the array beam response can be used to estimate the DF performance.

A DF antenna array design was required which could be mounted on a wide variety of tower or mast types ranging from telephone poles to water towers with minimal modifications. An adaptable fool-proof mounting design was desired that would simplify correct installation. Two performance characteristics of primary interest were the mainbeam width and maximum sidelobe level of the beamformed response. The array design was developed using the Numerical Electromagnetics Code Version 4 (NEC4) [1]. Numerical modeling can be a powerful tool to accurately calculate the individual antenna element responses and beamformer response characteristics. The array responses calculated by NEC were processed using a MATLAB DF algorithm to produce beamformer response patterns. Statistical analysis of these patterns provided the root-mean-squared beamwidth and maximum sidelobe level over all azimuths. By minimizing these two beamformer response characteristics, a optimal and robust array was designed.

The best numerical design was used to build an experimental array for testing. The mounting structure was adjustable so that data for a number of geometrical configurations could be acquired. This provided an increased confidence in the NEC modeling by having numerous array geometries for data comparison. It was hoped that in the future, NEC could be used to design and predict the performance of unique installations eliminating the need for individual site measurements.

The numerically modeled data for the DF arrays was compared to experimental data in several ways. Individual element patterns were compared as magnitude and phase or real and imaginary components. The element responses were processed using a beamforming DF algorithm to predict beam response characteristics. And finally, the experimental data was cross-correlated with the numerically modeled data to provide a complete comparison between the experimental and numerically modeled array responses.

ARRAY DESIGN

The objective of this project was to design a wrap-around VHF array with robust DF performance that would permit installation around a wide range of tower types. This development permits the installation of a DF array in an environment in which clear access to the top of the tower is not available. The primary focus was on triangular structures such as standard Rohn towers, but the analysis technique is also applicable to a variety of mountings including ship masts. After an initial survey (using numerical modeling) of different numbers of antenna elements in circular and triangular arrangements, a triangular arrangement of nine elements was chosen. Numerical modeling of this array placed on a Rohn G-45 tower section indicated very good DF performance. **Figure 1** shows the numerical model.

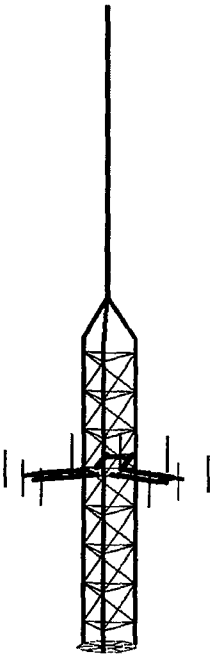


Figure 1 *Numerical Model of Wrap-Around Array*

EXPERIMENTAL ARRAY CONSTRUCTION

An adjustable nine-element array based on the numerical model was built for measurements at the SwRI range. The experimental array can be adjusted to match the nine configurations modeled with NEC. There were two primary objectives for the measurements. The first was to prove through experimental data that the array was capable of performing well over a range of radii and element separations. The second was to show a close correlation between the numerically modeled and the experimental data indicating that the numerical model could be used to predict the DF performance for other configurations. This will eliminate the need to perform measurements for each array installation. The antenna consisted of nine matched dipole elements arranged on three sides of a triangular array. Each side contained three elements placed in a straight line. The array was mounted to a Rohn G-45 tower section. The entire assembly was then mounted on the antenna rotator as shown in **Figure 2.**

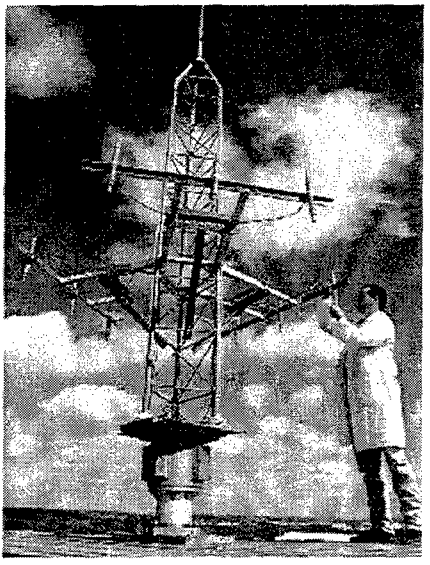


Figure 2 *Experimental DF Antenna Array Mounted on Rotating Tower Structure*

TOWER TEST FACILITY

Measurements were conducted at the outdoor antenna test range located at SwRI. This antenna range consists of an all-wood multi-tiered tower approximately 70 feet tall with a transmitter located on the ground approximately 1100 feet form the test antenna. The antenna arrays being tested can be rotated through 360 degrees of azimuth under remote control to measure antenna patterns (magnitude and phase). The measurement system has the capability of simultaneously measuring 12 RF channels relative to a reference channel. Relative amplitude and phase data are typically recorded at one-degree azimuth increments. The phase and amplitude reference is an auxiliary dipole antenna placed

approximately 20 feet below the test array. The RF channels are routed through a sequencer, which selects one channel for output into a dual-channel receiver. The other input comes from the reference antenna.

ARRAY MEASUREMENTS

The antenna array was tested in nine different configurations over a range of frequencies. The configurations consist of three radii and three element spacings. Each of the nine configurations were tested at 121.5, 157, and 243 MHz. Additionally, three configurations were tested over the range of 120 to 240 MHz at 10MHz intervals. The measurements were taken by transmitting at the desired frequency and rotating the antenna array through 360 degrees in azimuth.

NUMERICAL MODELED AND EXPERIMENTAL DATA

An initial comparison of the numerical and experimental data was done graphically. **Figure 3** shows a typical magnitude response of a single element. The elements used for this application are vertical monopoles with nearly omni-directional patterns. In the magnitude response we see the effects of mutual coupling between elements and the structure. Magnitude responses generally agree well within 1 dB.

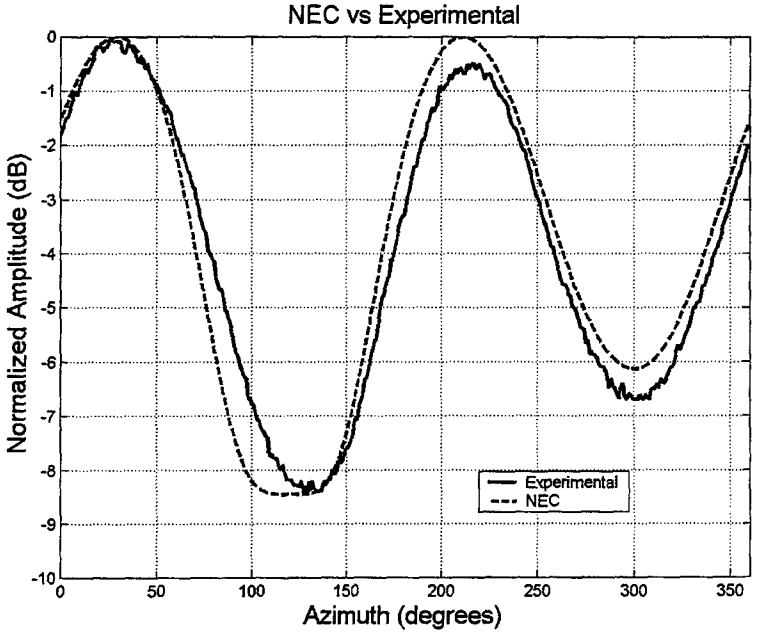


Figure 3 *Typical Magnitude Comparison of Numerical Modeled versus Experimental Antenna Response*

Figure 4 shows a typical phase response of a single element. In the phase response we see primarily the rotation of the element about the center point of the array and distortion effects only on as a second order effect. The phase responses generally matched well within 10 degrees. NEC provided a very good estimation of the experimental antenna response patterns.

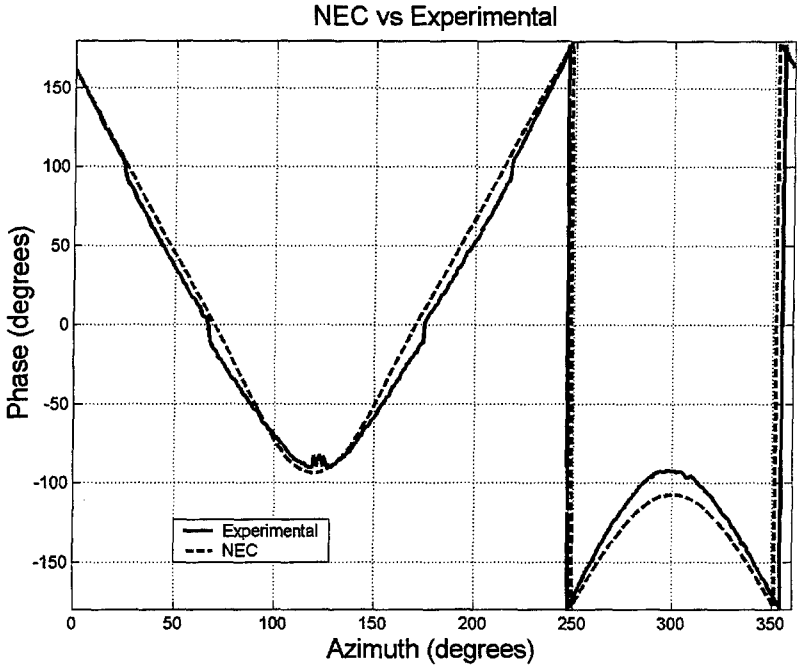


Figure 4 *Typical Phase Comparison of Numerical Modeled versus Experimental Antenna Response*

The experimental array performed very well as a DF array as predicted by the initial numerical model. For the nine configurations tested, the beamwidth was generally below 20 degrees and the maximum sidelobe level never exceeded -2.0 dB with respect to the main beam maximum response. For the DF systems used at SwRI, sidelobes within 0.5 dB of the mainlobe are generally acceptable. Not only did the experimental version of this array perform very well, it performed almost exactly as predicted by the numerical model. **Figure 5** shows a comparison for two beamform response characteristics as functions of frequency. The top plot shows RMS beamwidth, the lower plot shows the maximum sidelobe level relative to the mainbeam.

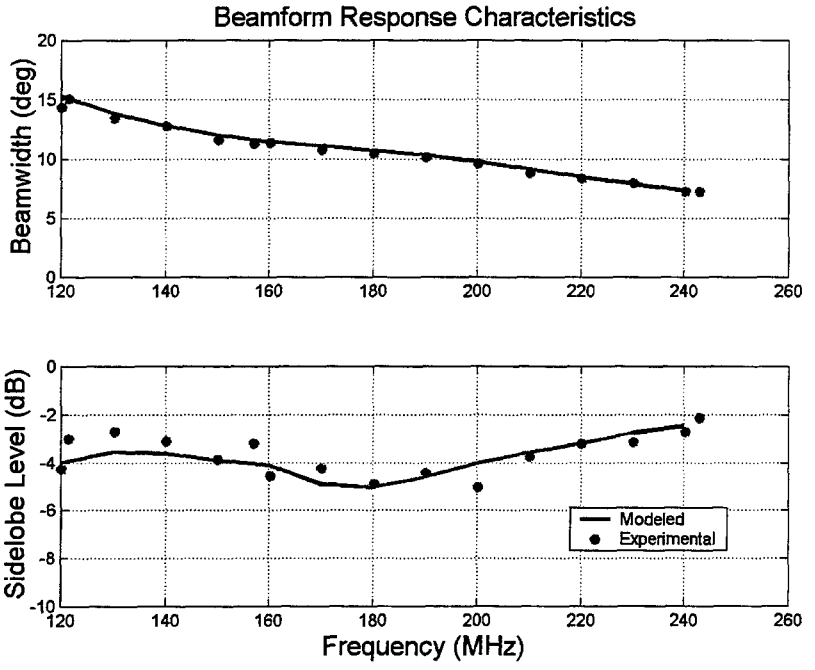


Figure 5 *Comparison of Numerical Modeled and Experimental Beamform Characteristics*

The degree of match of the individual antenna patterns and the beamformer characteristics led to the question of how well the predicted array manifold matched the details of the experimental array manifold. To determine the match, the numerically modeled array manifold was use a the calibration manifold and compared to the experimental array manifold. A standard deviation of DF bearing error was calculated as a function of frequency. A mean correlation value between the modeled and experimental data sets was also calculated at matched azimuths as a function of frequency. **Figure 6** shows a sample for one array configuration. The bearing error using the NEC calibration remains below 1 degree. This indicates the feasibility of using NEC to generate calibration array manifolds. The mean correlation is greater than 0.98 for all configurations and frequencies and the overall mean correlation between NEC and the experimental data was 0.986. As a reference point the mean correlation of the repeat data sets was 0.994. The numerical model can not be expected to do better than the measured repeatibility.

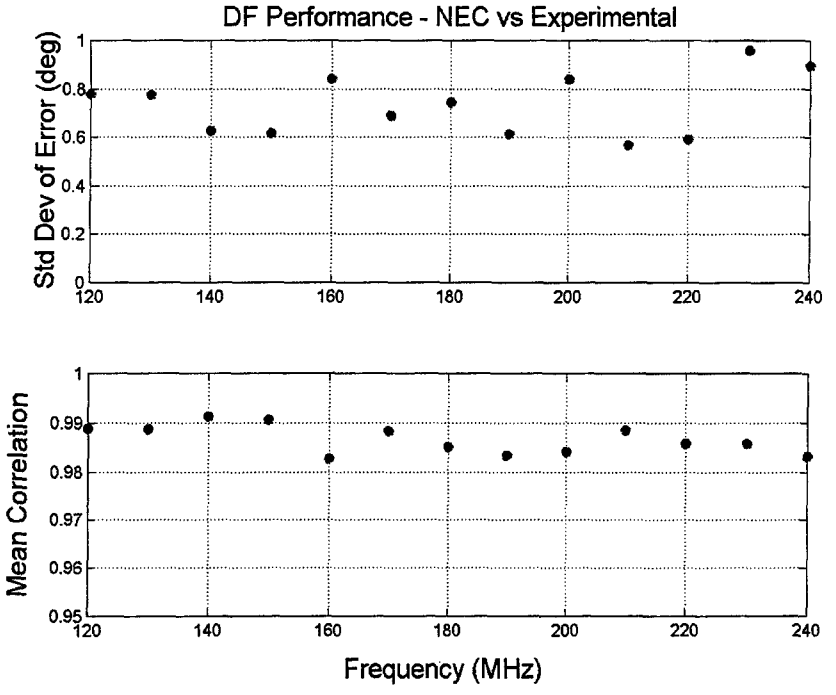


Figure 6 *Standard Deviation of Error and Figure-of-Fit between Numerical Modeled and Experimental Array Manifolds*

The exceptional comparison of the NEC data to the experimental is extremely encouraging. This agreement means that numerous investigations can be conducted using only the NEC model without the need for additional measurements. Based on the initial success of this project, several other related areas of interest will be examined. Among them are investigations of effects caused by very large towers, guy wires, and the existence of nearby scatters such as other antennas. Additional information about these effects and a full summary of the overall numerical model performance will be presented in the conference.

CONCLUSIONS

NEC worked exceptionally well for designing a VHF wrap-around DF antenna array. A general array configuration was designed for optimal DF performance and constructed for experimental measurements. A comparison of individual response patterns, beamformer response pattern characteristics, and array manifold correlations indicated that the numerically modeled data matched the experimentally measured data very well.

All project objectives were met or exceeded. The wrap-around array design met all design criteria. The numerically modeled results were not only accurate enough to design the array but also accurate enough to predict DF performance and be used as a calibration array manifold. SwRI now has the tools to predict the performance and create array manifolds for the wrap-around array when mounted on a large variety of towers and masts.

REFERENCES

1. Burke, Gerald J., "Numerical Electromagnetics Code - NEC-4, Method of Moments, Part I: User's Manual" UCRL-MA-109338, Lawrence Livermore National Laboratory, Livermore, CA January 1992,

2. Lysiak, Keith A., "NEC Model Results for Shipboard Shielded Crossed Loop Antennas with Scale-Model Range Data", Applied Computational Electromagnetics Conference Proceedings, pg.1012, March 1998

3. Knorr, Jeffery B., "Application of Computational Electromagnetics to Shipboard HFDF System Simulation", Applied Computational Electromagnetics Conference Proceedings, pg.182, March 1997

4. Skinner, William E., "Computer Simulation of AN/SRD-19 Mast Mounted DF Antenna by Numerical Electromagnetic Code (NEC)", Thesis, Naval Postgraduate School, NPS-62-80-024TR, December 1980

Specifying A Direction Finding Antenna With Examples

T. R. Holzheimer
Raytheon Systems Company
Aircraft Integration Systems
Greenville, Texas 75403

Abstract:

Direction Finding (DF) antennas are typically implemented in linear interferometers, resulting in very high angle of arrival (AOA) accuracy. Several DF antennas have been built of the 360 degree, circular variety. Three antennas are discussed that cover the frequency range from 0.5 to 18 GHz and exhibiting AOA accuracies of 0.5 to 1.0 degrees RMS. In optimizing these antennas, a set of DF system specifications have been determined that apply to all types of DF antenna systems. Specifications addressing these generic DF antenna system requirements can be defined to provide desired performance.

Introduction:

Numerous high accuracy DF antennas have been described in numerous papers and textbooks over the years.[1] A 0.5 degrees RMS, high accuracy, 2 to 18 GHz 360 degree azimuthal DF antenna has been described and presented at Antenna Applications Symposiums in 1995 and a similar version covering 0.5 to 2 GHz and 1 to 18 GHz has been reported at the 1999 Symposium.[2] Most DF antenna arrays use low gain elements such as spirals and dipoles. Some interferometers use medium gain horns if the depth is available. They are typically implemented in linear interferometer format and suffer field of view limitations on the order of +/- 60 degrees in Azimuth.

A full 360 degree field of view is typically provided with circular arrays. The earliest types used low gain omni-directional elements. Subsequent investigators looked at using directional antennas such as flared notches. A multitude of different beamformers have been investigated as well as antenna elments with varying types of polarization capabilities. Derivations and explanations of the synthesis used to produce AOA from a circular array have been previously reported and will not be repeated here.

The circular DF antennas evaluated are of the simultaneous modal phase type. Figure 1 illustrates the different phase modes that follow periodic functions of 360 degrees, i.e., N X 360 degrees, where N is the modal phase order. These phase modes are typically setup with beamformers such as, Butler matrix or Rotman Lens. Figure 2 shows the basic four element block diagram for the phase and amplitude only type of beamformer. Amplitude information can be obtained with the addition of an additional network or beamformer.

Specifying DF Antenna Requirements:

The DF antenna is difficult to separate from the DF antenna processor that applies the AOA algorithm. The DF antenna and processor are tightly coupled and are best specified together. The perfect array, with no coupling, can provide a full unambiguous field of view. Realistic situations and installations yield ambiguity rates and RMS AOA accuracies that are driven by element spacing and signal to noise ratio (SNR) as in linear interferometers. The required specifications are summarized in Table I.

Table I. Required DF System Specifications.

1. RMS AOA versus Frequency.

2. Unambiguous Data Rate versus Frequency.

3. Untagged Ambiguity Rate versus Frequency.

4. RMS AOA Accuracy versus Signal to Noise Ratio.

5. Unambiguous Data Rate versus Signal to Noise Ratio.

6. Untagged Ambiguous Data Rate versus Signal to Noise Ratio.

Table I provides terms that can be evaluated and used in determining AOA accuracy for a complete DF system. Good data is labeled as unambiguous data rate, while bad data is defined as untagged ambiguity rate. This says that based on the use of, typically, proprietary algorithms and calibration, data can be made more accurate and false AOA's can be minimized and identified. Data will illustrate this later. The addition of SNR provides the difficulty in separating the DF antenna from the DF processor which can include active amplifiers and receivers.

A generic, 2 to 18 GHz, linear interferometer will yield 1 degree RMS AOA accuracy with less than 4% ambiguity rate and a greater than 90% unambiguous data rate all down to a SNR of 8 dB. A generic, 0.5 to 2 GHz, linear interferometer will yield 1 degree RMS AOA accuracy with less than 5% ambiguity rate and a greater than 90% unambiguous data rate all down to a SNR of 8 dB. In both cases the linear interferometer will have a field of view of +/- 60 degrees in azimuth and +/- 30 degrees in elevation.

360 Degree DF antenna Examples:

Two 360 degree DF antennas are pictured in figures 3 and 4.[3] Figure 3 shows the 2 (1) to 18 GHz version while figure 4 shows the 0.5 to 2(18) GHz version. The numbers in parentheses show the full frequency range that the DF antenna is capable of operating over. In all cases a residual 6.1 degree (one sigma) phase pair tracking error was used as a typical post calibrated, wide-bandwidth, phase discriminating receiver. The first two references also compare to a 11.1 degree residual phase pair tracking error. A Raytheon Systems Company proprietary algorithm was invoked using a metric to determine the AOA accuracy.

The 2 to 18 GHz version circular DF antenna exhibits RMS AOA accuracy of 0.6 degrees, a 95% average unambiguous data rate and a 3% untagged ambiguity rate. The roll-offs with drop in SNR to 8 dB are as expected. This DF antenna is also useable down to 1 GHz. Figure 5 shows the RMS AOA accuracy versus Frequency.

The 0.5 to 2 GHz version exhibits RMS AOA accuracy averaging 0.71 degrees and maximum of 1 degree. Amplitude information is included in the ambiguity rate determination in order to meet the 5% desired. Figure 6 shows the RMS AOA accuracy versus frequency over the 1 to 2 GHz portion of its operational band.

Implementation Issues:

In all the configuration examples for the circular DF antenna, the beamformer used was a Butler matrix, but it could have also been a Rotman Lens. Low noise amplifiers, filters and switch's may be required in order to provide the DF antenna and processor intermodulation product immunity. Depending on the individual antenna elements

used, the DF antenna aperture can be relatively light weight, but the processor can be substantial when including the receivers. The desired diameter of the circular antenna is the smallest possible which is also true for the desired length of the linear interferometer. However, there is a tradeoff between size, AOA accuracy, un-blocked field of view and DF antenna placement.

Summary:

It is extremely difficult to separate the DF antenna from the DF processor. Developing overall DF antenna system requirements is the best way to pursue the DF antenna, keeping in mind the desired DF system specifications listed in table I. Aperture size must be carefully investigated in order to keep installation limitations minimized. The installation itself must be carefully evaluated as this can determine to what extent and how much calibration must be implemented in the DF system. As shown, the DF system specifications can apply to any DF antenna such as the linear interferometer or circular DF antenna.

References:

[1] T. R. Holzheimer, "High Accuracy DF Antenna Using COTS Hardware,' Antenna Applications Symposium, Monticello, Illinois, 20-22 September, 1995, pp 11-1 to 11-30.

[2] T. R. Holzheimer, "An Implementation of a 0.5 to 2.0 GHz Circular 360 Degree Direction Finding Antenna,' Antenna Applications Symposium, Monticello, Illinois, 15-17 September, 1999, pp 374-404.

[3] T. R. Holzheimer, "360 Degree DF Antenna," Patent Pending, 20 November, 1998.

[4] R. H. Jaeger, T. R. Holzheimer, et. Al., "Coaxial Cavity Antenna," Patent Pending, 20 October, 1998

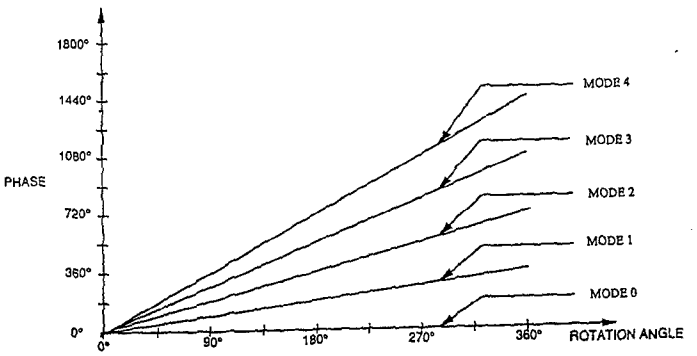


Figure 1. Modal Phase Versus Rotation Angle.

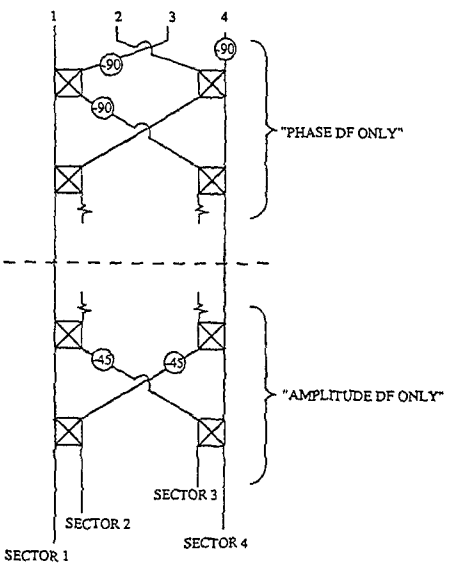


Figure 2. Phase Only verus Amplitude Only DF.

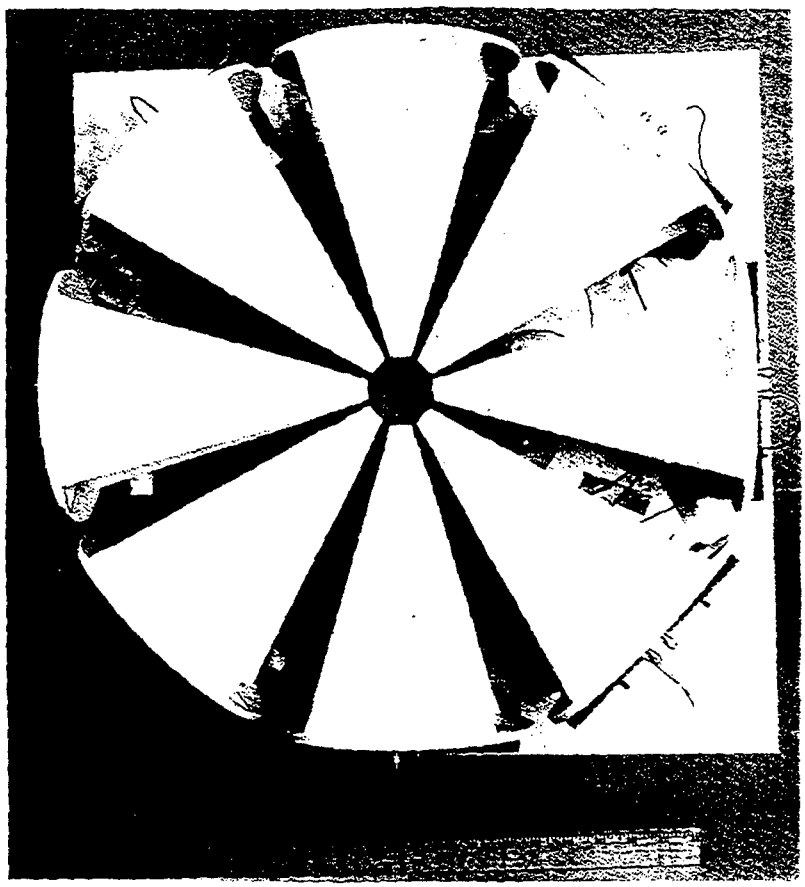


Figure 3. 2 to 18 GHz, Patent Pending, 360 Degree Circular DF antenna.

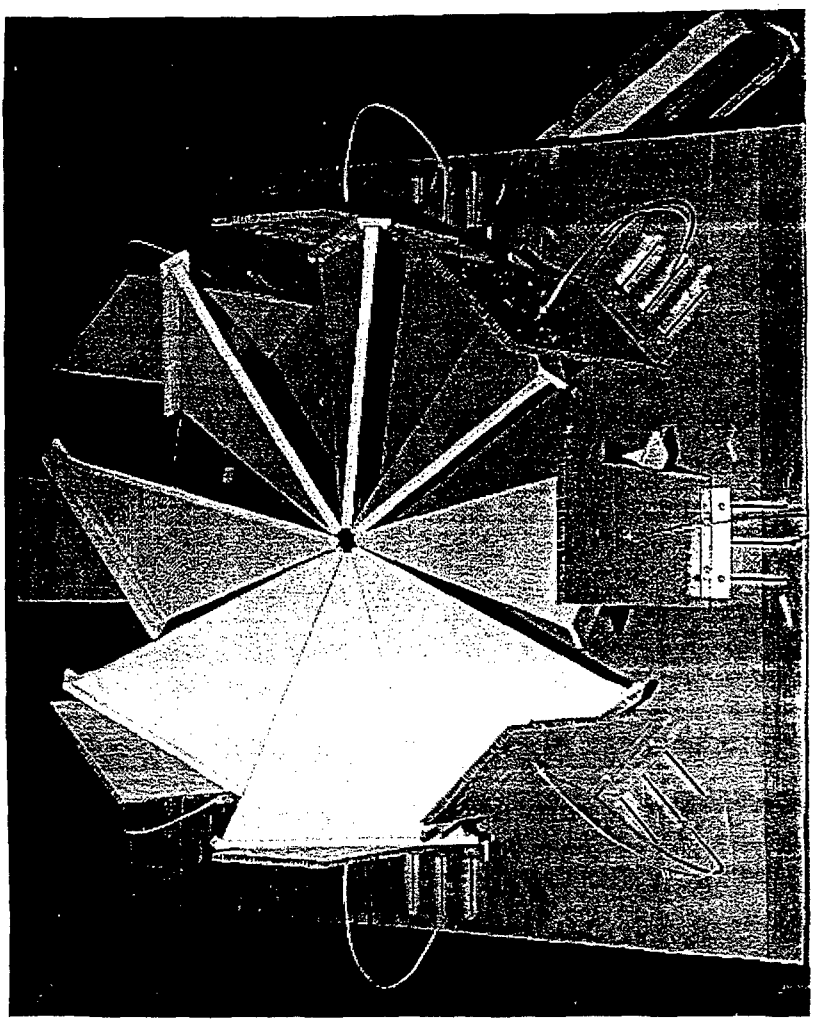


Figure 4. 0.5 to 2 GHz, Patent Pending, 360 Degree DF Antenna

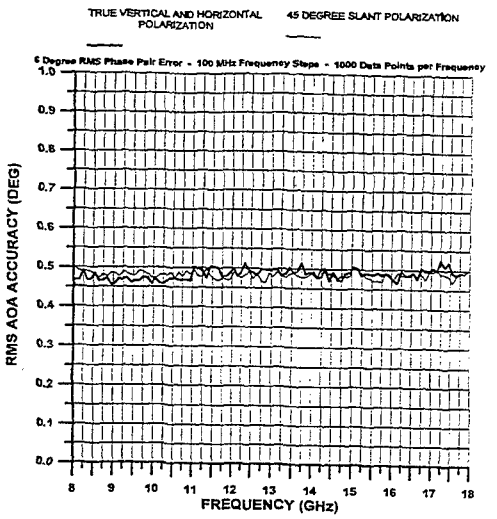


Figure 5. RMS AOA Accuracy versus Frequency, Typical for 2 to 18 GHz Circular DF Antenna.

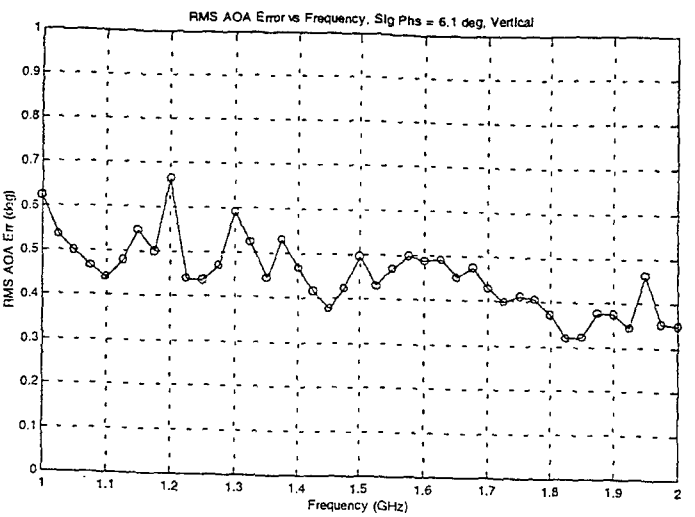


Figure 6. RMS AOA Accuracy versus Frequency, Typical for 1.0 to 2 GHz Circular DF Antenna.

A High Efficiency Broad Band Wire Antenna System

Kevin J. Cybert and Daniel D. Reuster
ARINC
Annapolis, MD 21401
Kcybert@arinc.com and Dreuster@arinc.com

1. Introduction

The performance of any antenna system is defined as the product of the antenna's efficiency and the antenna's directivity. For wire antennas, the directivity of the antenna is strictly a function of the antenna's electrical length and the efficiency of the antenna is strictly a function of how well the input impedance of the antenna is matched to the characteristic impedance of the transceiver (usually 50 ohms). The input impedance of a wire antenna is also a function of the electrical length of the antenna. While a vertical monopole antenna over a ground plane exhibits optimal gain for the frequency at which the antenna is approximately a quarter wavelength, maximizing the efficiency of a wire antenna system over a broad frequency band requires more advanced methods.

For traditional broadband wire antennas, inductor-capacitor circuit traps (referred to simply as "traps") have been inserted into the wire antennas in an effort to utilize a single wire antenna element for non-contiguous multiple frequency transmission and reception. This approach usually entails that the existing wire antenna be designed for the lowest frequency (longest wavelength) of interest, and that the other frequencies of interest are sufficiently different such that the resonant bandwidths of the inserted traps do not interfere with one another. Over the years, many design variations have been implemented since the concept was first patented in 1941 [1-3]. While many claims have been made regarding the number of resonant frequencies and the bandwidths associated with each of the resonant frequencies, all of the previous designs share one common characteristic limitation: no previous trapped wire antenna design provides continuous coverage across the complete frequency band of interest. In order for the traditional trapped wire antenna design to function properly, there must exist gaps in the frequency band, which are at least as large as the resonant bandwidths of the inductor-capacitor circuit traps.

While these prior assemblies are adequate for some applications, they cannot meet the broadband efficiency, directivity, and tuning response time needs of newer system requirements, such as with frequency agile radios.

2. Theory of Operation

The general purpose of the new antenna design is to provide a high efficiency, broadband, wire antenna system. The system is intended to provide continuous RF coverage while maintaining maximum antenna gain and stable input impedance. A significant aspect and feature of the new antenna design is the use of a plurality of wire antenna elements of different characteristics such that regions of stable and acceptable impedance characteristics can be utilized on each antenna element for part of the total frequency band of operation. Total band coverage is achieved by combining the stable and acceptable impedance characteristics of each segment such that these segments overlap in frequency coverage enough to provide the desired frequency response across the entire band of operation.

Another significant aspect and feature of the new antenna design is the placement of RF traps on the antenna elements such that the antenna pattern is controlled for that segment of the antenna element's frequency region of operation. Significant lobing of the pattern is prevented by the RF traps acting as band-stop filters limiting the current distributions to their fundamental operating regions. Total band coverage is achieved with a plurality of antenna elements and a corresponding plurality of RF traps that control the operation of different segments to provide total frequency coverage across the band of operation.

An example of one such a high efficiency, broadband, trapped wire antenna system, consisting of two wire antennas and four inductive-capacitive traps, is shown in Figure 1. The inductive-capacitive traps serve to limit the RF current flowing along the wires at various frequencies allowing the antenna system to appear to have physical lengths that correspond directly to the wavelength of interest. The bold arrows in Figure 1 represent these currents. In essence, the two-wire antenna system is broken up into six sub-antenna systems, each of which is capable of simultaneous transmission or reception. The two-wire trapped antenna network is then connected to the transmitter(s) via a series of RF filters and matching networks.

The connection network is used both to direct the radiated signal to the correct sub-band antenna and to impedance match, if required, the resultant sub-band antennas to the transceiver. Hence, each resulting antenna sub-band has a RF filter and impedance matching network associated with it to passively select the proper antenna and ensure maximum efficiency. Maximum antenna efficiency, at any given frequency, is obtained by matching the input impedance of the antenna to the characteristic impedance of the transmitter. The technique of adjusting the electrical length of the wire antennas with the inductive-capacitive traps also serves as a passive first order method of stabilizing the antenna's input impedance.

The trapped antenna network is designed such that the longest wire element corresponds to the first resonant length of the lowest design frequency (largest wavelength). For the monopole case, this length is approximately a quarter wavelength and for the dipole class, this length approximately a half wavelength. At this frequency (the lowest design frequency), none of the inductive-capacitive traps are active and the set of band-pass filters directs the signal to the proper antenna. Because the antenna is resonant at this particular frequency, the matching network does little to no work in ensuring that the antenna is properly impedance matched to the transceiver.

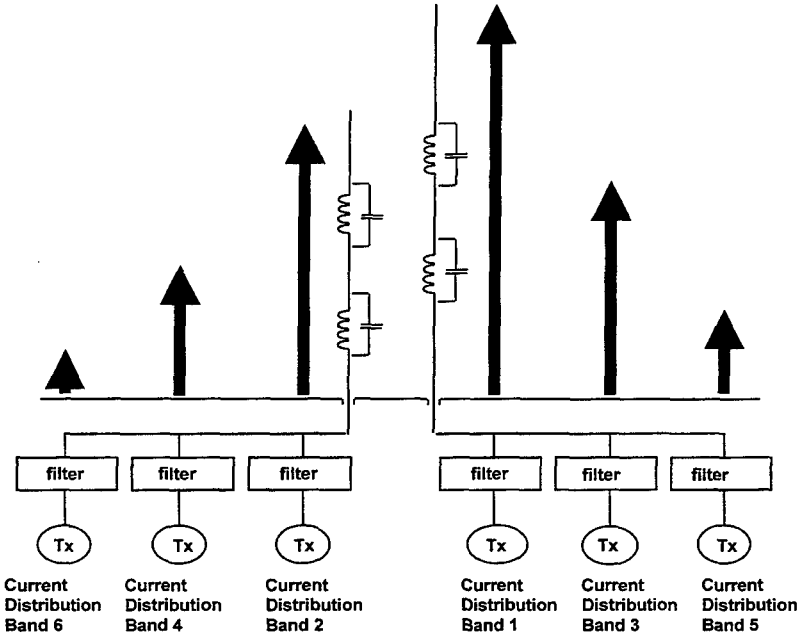


Figure 1. Banded Current Distributions

As the frequency is increased, the longest wire element is no longer resonant and the matching network begins to play a more active role in ensuring that the input impedance of the antenna is properly matched to the transceiver. This process continues until the longest wire element is too far from resonance to function at the pre-set efficiency level. In this region, the filter set transitions the signal from the existing wire element to the adjacent (second longest) wire element whose length has been designed to the resonant length of the switch over frequency. All of the inductive-capacitive traps are still not active and all that has occurred is that the signal is transitioned to a different radiating structure that is more efficient.

As the frequency is increased further, the matching network associated with the second longest antenna sub-element begins to match the impedance of the element to that of the transceiver. Again, this process continues until the radiation efficiency of the second antenna element transitions below the efficiency level of the next element. At this point, the band-pass filter transitions the signal back over to the first antenna wire.

This time, the upper most inductive-capacitive trap is active, stopping any RF current flow to the upper portion of the wire. The location of the upper most inductive-capacitive trap is set such that the clipped wire element is now once again resonant at the new higher frequency.

As the frequency is increased further, the matching network associated with the third sub-element adjusts to ensure that the impedances of the antenna and transceiver are properly matched. Once again, this process continues until the third longest wire element is too far from resonance to efficiently function. The signal is then once again transitioned over by the band-pass filter and antenna element impedance to the other antenna wire.

At this new higher frequency, the upper most inductive-capacitive trap on the shorter antenna wire is now active, stopping any RF current flow to the upper portion of the shorter antenna wire. Once again, the clipped wire element is resonant at this higher frequency. This entire process is continued until all of the inductive-capacitive traps existing on both wire elements have been utilized.

When the frequency is raised to a point that the shortest antenna element no longer radiates above the pre-set efficiency level, the antenna system has reached its upper frequency limit. While this process has been described for a two-wire antenna network, the design may be extended to include any number of wire elements containing any number of inductive-capacitive traps.

3. Prototype HF Antenna System

A prototype antenna was design and built which utilized two long wire antennas and four traps to achieve coverage over the entire HF band (2 to 30 MHz). The new dual-wire trapped-antenna is designed to replace an existing antenna system consisting of two equal length wires. The dual-wire trapped-antenna consists of two wire antennas of different lengths. The first wire had the same length as the existing antenna and the other wire length was approximately half the length of the existing antenna. Each wire antenna had two traps installed along it. A 11.5 MHz trap and a 20 MHz trap were installed on the longer wire with the 20 MHz located nearer to the antenna feed. A 14.7 MHz trap and a 28.7 MHz trap were installed on the shorter wire with the 28.7 MHz trap nearer to the antenna feed.

The dual wire trapped antenna system was designed and analyzed using computer simulation techniques. The trapped wire antennas were modeled using NEC-4 [4] running on Silicon Graphics and Sun Workstations. The analysis was performed on both the long and short wire antennas for frequencies from 2 to 30 MHz in 1 MHz increments. The computed real input impedance for both the trapped wires is shown in Figure 2.

Prototype antennas where then constructed to demonstrate the modeled antenna results. The antenna test platform utilized was of the same size and shape as that of the upper half of the aircraft that the existing antenna system was originally designed to operate with. The aircraft test platform was chosen in order to demonstrate the performance improvement of the dual-wire

trapped-antenna over the existing antenna configuration. The test platform was built out of wood and covered with screen. The actual feeds that are used on the aircraft were incorporated into the test platform. The antenna impedance was measured for each test using an HP Vector Impedance Meter from 2 to 30 MHz in 0.1 MHz steps.

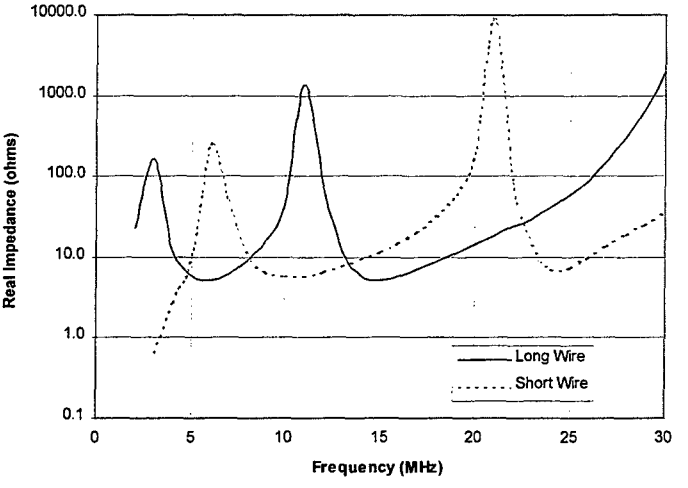


Figure 2. Modeled Dual Wire Trapped Antenna – Real Impedance

The measured data shows that the prototype dual wire trapped antenna performed as predicted. The measured results correlate fairly closely with the modeled results. The comparisons between the measured and modeled results are shown in Figure 3 for the trapped long wire antenna and Figure 4 for the trapped short wire antenna. The minor differences between the modeled and measured results are mainly due to the fact the traps were not resonant at their actual design frequency. This was primarily due to the capacitors that were used in the traps. The capacitors were commercial capacitors that were accurate to within ±20%. In addition, the tuning of the inductive coils was performed by manually shorting out the turns of the coil. This is a coarse method of tuning and can lead to small variations in the inductor values. These differences can be eliminated in the future by the use of variable capacitors in the traps.

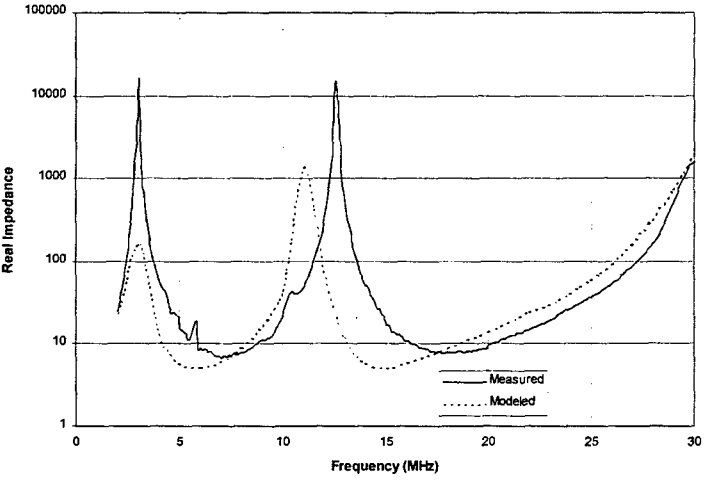


Figure 3
Measured vs. Modeled Real Impedance Data for the Trapped Long Wire Antenna

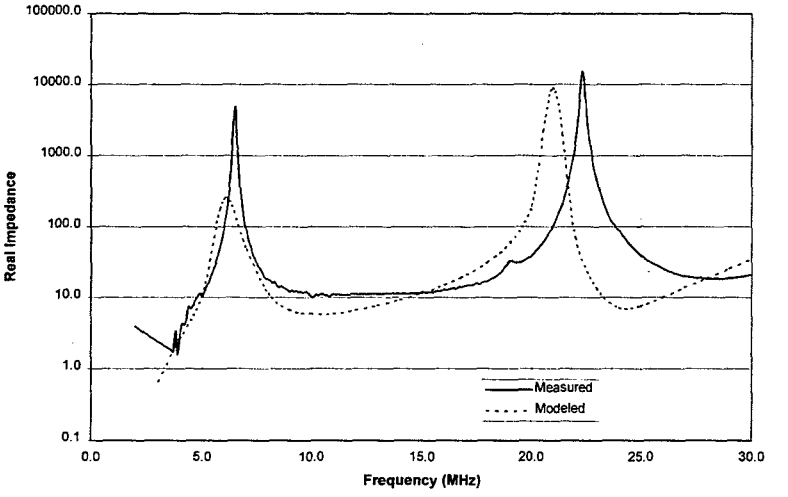


Figure 4
Measured vs. Modeled Real Impedance Data for the Trapped Short Wire Antenna

4. Impedance Matching Advantages

As can be seen from Figure 2, the real input impedance variations of the long and short wires are completely out of phase with one another; hence, when one is unstable, the other is stable. This offset in impedance is a direct result of the four traps (two on each wire) which were installed into the system. Each wire has two resonance points. These resonance points are offset so that when one of the wires has a high resonance point, the other antenna wire has an acceptable impedance value. Therefore, the system can switch back and forth between the two wires and maintain reasonable input impedance across the entire band of operation. The frequency bands can be divided as follows:

Frequency (MHz)	Antenna Wire
2 to 3.5	Long
3.5 to 6.5	Short
6.5 to 10.5	Long
10.5 to 19.5	Short
19.5 to 26.5	Long
26.5 to 30	Short

By utilizing these frequency bands, the new trapped long wire antenna will be significantly easier and quicker to impedance match. Also, the imaginary impedance is monotonic across each of the frequency bands. This will allow the matching circuit to be very simple, requiring only one variable reactive component. Figure 5 shows the real input impedance of the dual wire trapped antenna as each antenna wire is used according to the table above.

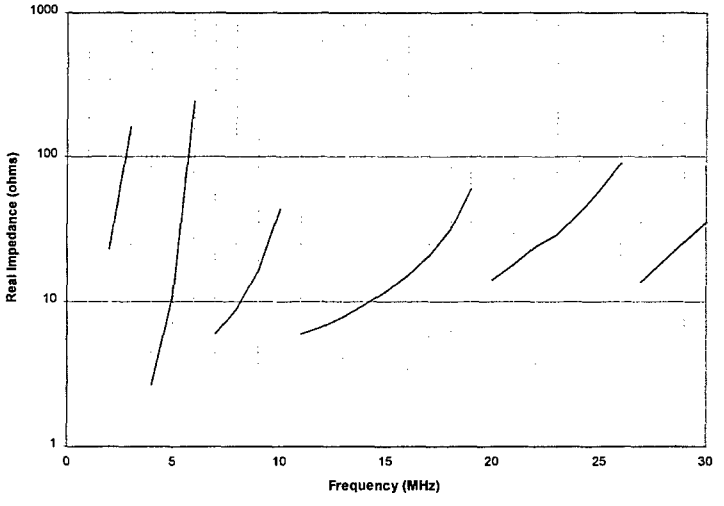


Figure 5. Dual Wire Trapped Antenna Real Input Impedance

5. Conclusion

Although many trapped antenna designs exist in both the amateur radio and military communication realms [1-3], all of these antenna designs are multi-band systems, which are designed to work at a finite set of predetermined frequencies. By utilizing multiple wire elements and controlling their current distributions utilizing RF traps, a truly broadband antenna has been developed rather than a multi-band antenna which is commonly associated with RF trap technology.

The dual-wire trapped-antenna design offsets the resonance points of the two wires so that they do not coincident in frequency. By shifting the resonances, the antennas can now be broken into frequency bands that have stable real impedance values and have monotonic imaginary impedance values. This improved input impedance performance allows for much easier impedance matching. The required matching network will be much simpler than the existing networks needed and will be able match any frequency very quickly.

Finally, the dual-wire trapped-antenna system concept was proven by the use of computer modeling. The prototype antenna design was based upon numerical optimization of the computer models. The measured results of the prototype antenna closely matched the predicted results obtained from the computer modeling. The dual wire trapped antenna system is applicable to any wire type antenna system having elements configured as monopoles, dipoles, or slots. ARINC currently holds the patent for the new high efficiency broad band wire antenna system (Patent Number: 5767812).

References

[1] H. K. Morgan, Patent #2,229,865 "RF Traps"

[2] D. R. Newcomb, Patent #4,222,053 "Multi-Band Vertical Antenna"

[3] R. S. Abramo, Patent #5,600,335 "High-Power Broadband Antenna"

[4] G. J. Burke, Numerical Electromagnetic Code – NEC4, Lawrence Livermore National Laboratory, January 1992.

COMPARISON OF CALCULATIONS AND MEASUREMENTS OF AN ELECTRONICALLY SCANNED CIRCULAR ARRAY

James M. Stamm
Naval Air Warfare Center–Aircraft Division
stammjm@navair.navy.mil

Michael W. Jacobs and James K. Breakall
The Pennsylvania State University
mwj116@psu.edu
jimb@psu.edu

ABSTRACT

A circular array is modeled using two independent moment method codes. The array utilizes closely spaced high-gain end-fire elements to maximize the volumetric efficiency of an ellipsoidal enclosure, while minimizing the number of elements requiring control. An initial element was designed with an optimizer based upon the NEC4 engine; however, the use of moderately thick wires, wire-wire spacings of approximately one diameter, and non-trivial feeds required a wire/plate code for accurate element performance prediction. At the same time, efficient modeling of the entire array required a second code with a discrete body-of-revolution (DBOR) capability. Both electromagnetic codes were used in conjunction to arrive at a complete array design. With the exception of the highest frequency, where balun difficulties were plainly evident, correlation between predicted and measured results are very good.

1. INTRODUCTION

Utilization of multiple electromagnetic codes is sometimes necessary for modeling antennas. Frequently, the capabilities and strengths of a particular code are well suited to the geometry of a given antenna, whereas another code is appropriate for modeling other additional features. At times, one must incorporate certain geometrical features into the antenna design to meet desired performance criteria, criteria that may not be well represented by any one piece of modeling software. This paper describes such an array, where the element design was completed with a wire/plate code called WIPL-D [1], and the array modeling was performed with NEC4. The array we are referring to is an experimental prototype for a UHF Electronically Scanned Array (UESA), which is proposed as a replacement for the current mechanically rotated radar array which is mounted atop the Navy's E-2C. A surveillance radar realizes numerous benefits when instantaneous 360° beam agility is available; however, support for such a retrofit is difficult to come by unless the replacement antenna provides equal or superior performance. This is a difficult task not because of the inherent geometry of circular arrays, but rather because the end-fire architecture results in considerable unused space in the center of the ellipsoidal radome. The radome center is also where the greatest vertical separation exists. Monopole arrays provide a simple way of utilizing the space in the center of the radome, but result in vertical polarization, which is undesirable for low frequency over sea radars. The array described herein is the

result of an aggressive effort try to obtain the maximum gain possible, while providing sidelobes in the 30-40 dB range.

2. ANTENNA ELEMENT DESIGN & MODELING RESULTS

The Yagi-Uda was selected as the array element because of its high gain, simple feed arrangement, and transparency to orthogonally polarized antennas that may be located behind it. In order to handle very high power and prevent corona discharge from wire ends, ¾ inch diameter tubing was selected. From previous circular array studies [2], it was determined that 50-60 elements were required to obtain the desired sidelobes while maintaining the desired azimuth plane beamwidth.

A challenge is imposed by the need for this many elements. Assuming a Yagi reflector length of approximately $\lambda/2$, elements operating at the UHF radar band are limited to about two feet in length (measured along the boom) for a 24-foot radome. Such an arrangement would lead to poor volumetric utilization. The Yagis can be lengthened by applying some type of shortening scheme to the rearmost elements, such as the disk on a tophat monopole. We elected to bend the wires on the reflector, driven wire (we avoid the term driven element to avoid confusing this with an *array element*), and the first two directors. This method enabled the Yagi to be lengthened by a factor of nearly two. Various other types of elements, such as the cubical quad, were tried with little success. The quad appears to be an attractive choice for the circular array configuration because the reflector (from a top-down perspective) is only about $\lambda/4$ in length, allowing a much longer element. One finds quickly, though, that the strong mutual coupling between the vertical wires of adjacent elements causes the active element VSWR to deteriorate rapidly as the quad is lengthened.

The first element was optimized with the NECOPT optimizer [3]. Initially, the shortening stubs were arranged in a symmetric manner, as shown in Fig. 1(a). It was then discovered that with 60 elements, coupling of the adjacent elements was severe enough to result in array (reflection) efficiencies of around 60%. Considerable experimentation resulted in the element shown in Fig. 1(b). In this configuration, coupling between adjacent pairs of shortening stubs is considerably reduced. By introducing the odd-angled shortening stubs and reducing the number of elements to 54, array reflection efficiencies of approximately 90-95% were observed in the NEC4 model. The array can be modeled efficiently with NEC using the GR card (circular symmetry)—a 54 element array with 13,000 segments can be run in about 9 minutes on a 300 MHz PC.

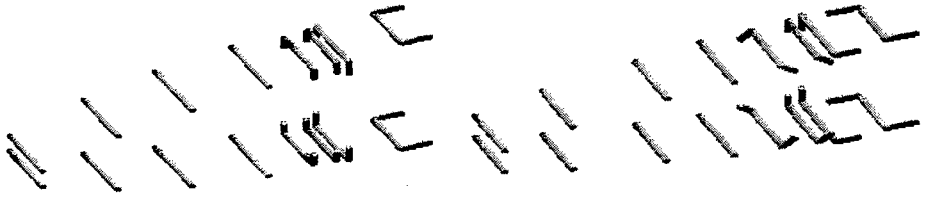


Figure 1—Elements with (a) symmetric and (b) odd shortening stubs. These elements were both designed to a 37 Ω characteristic impedance.

A single full-size element was built and VSWR tested on an HP 8510C network analyzer. Results were disappointing, as the VSWR at the upper portion of the band was poor. Several characteristics of the geometry lead to non-uniform currents (circumferentially) on the surface of the wires, a violation of the fundamental assumption used in the NEC formulation. The use of thick wires in conjunction with closely spaced wires (in particular, the spacing between the driven wire and first director is only about one wire diameter) leads to non-uniform currents. The close spacing is required to obtain the desired bandwidth. The corners also induce non-uniform currents, but we showed in a previous paper [4] that NEC appears to handle thick wires with 90° corners nearly perfectly. The last characteristic responsible for non-uniform currents is the feed. The final arrangement included a parallel plate feed that attaches to one side of the driven wire. The NEC E-field voltage source model assumes that the electrical field is completely uniform in the gap region. The parallel plate feed results in a decreased resonant frequency. Simply shortening the driven wire is not an effective means of compensation, since the shortening scheme removes the actual alignment of the stubs at the end and their associated mutual coupling.

In order to accurately predict the element performance, a new model was created using the WIPL-D package. WIPL-D uses a combination of plates and wires in an EFIE approach. Instead of using wires like NEC, the rearmost wires were "built" from plates as eight-sided hollow tubes. To reduce the total number of unknowns, the five wires in the front (directors 3-7) wires were modeled as uniform tubes of current as would be done in NEC. These wires, in addition to having no feedpoints, have no 90° bends and are displaced far enough from each other that the current can be assumed to be uniformly distributed along the wire circumference.

The WIPL-D model revealed instantly why the VSWR at the upper band edge was poor. From Fig. 2(a), we see that the radiation resistance drops rapidly above 440 MHz. The WIPL-D model was used to make adjustments such that the radiation resistance was flattened. In addition, it increased enough to work directly with a 50 Ω characteristic impedance. The resulting element is shown in Fig. 3.

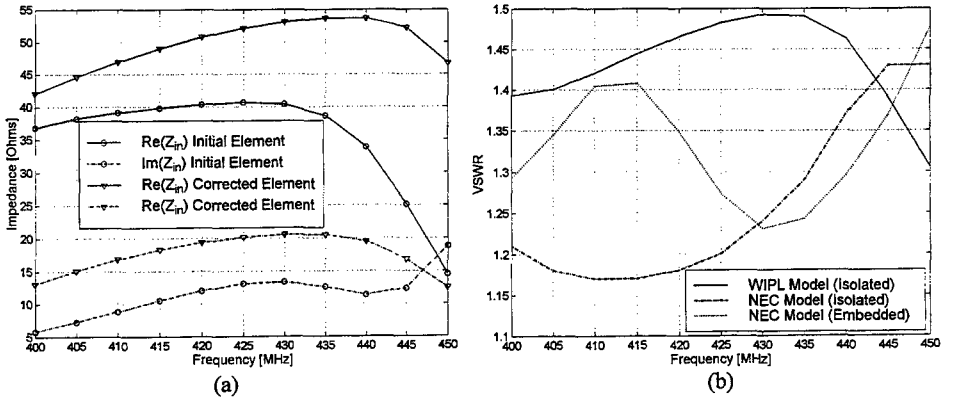


Figure 2—(a) Impedance of element of Figs. 1(b) and 3. (b) VSWR (50 Ω) of isolated and embedded element (of Fig. 3)



Figure 3—Top-down view of final wire/plate hybrid WIPL-D model.

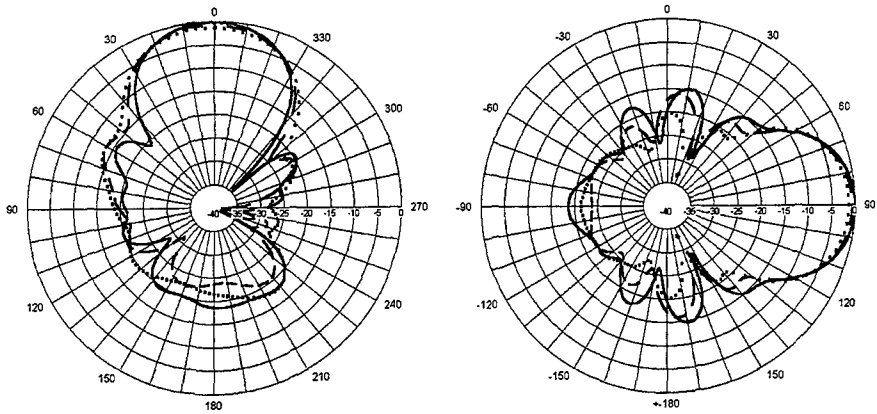
The gain of both element models was corrected by integrating the radiation pattern over all space. Interestingly, the NEC model required significant corrections at all frequencies. This is attributed at least in part to the optimization process. Since the optimizer seeks to minimize an error function that is based upon the code outputs, the optimizer will attempt to find the "Achilles heel" of the code. Optimistic results are expected from such an automated process, subject to the accuracy of the code and the particular model in question.

Table I shows the computed gain of the element on its boresight, correction factors, and corrected boresight gain for both the NEC and WIPL models. Once corrected, both models agree at all points within the band to an error of less than 0.1 dB.

TABLE I
UNCORRECTED AND CORRECTED BORESIGHT DIRECTIVITIES FOR NEC AND WIPL MODELS

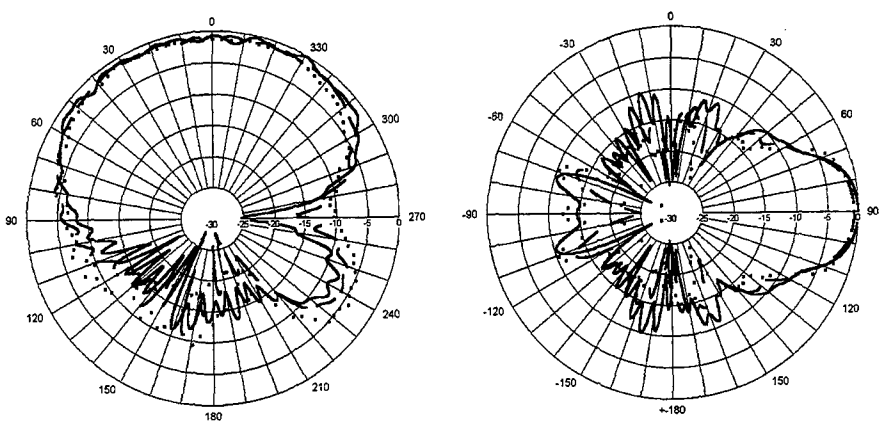
Freq (MHz)	Computed Dir. (dBi)		Correction (dB)		Corrected Dir. (dBi)	
	NEC	WIPL	NEC	WIPL	NEC	WIPL
400	13.06	12.49	-0.48	0.08	12.58	12.57
425	13.70	13.02	-0.53	0.08	13.17	13.10
450	14.30	13.48	-0.67	0.09	13.63	13.57

Since WIPL does not yet have the rotational symmetry capability, all array modeling was performed with NEC. While differences in the isolated element VSWR are observable in Fig. 2(b), the differences are not overwhelming. Radiation patterns from the two codes are in good agreement. In Figs. 4 and 5 are the isolated and embedded element patterns.



(a) (b)

Figure 4—Principal plane cuts of (a) azimuth, and (b) elevation patterns of isolated element at 400 (...), 425 (- -), and 450 (–) MHz. Peak value of the graph is 13.6 dBi.



(a) (b)

Figure 5—Principal plane cuts of (a) azimuth, and (b) elevation patterns of embedded element at 400 (...), 425 (- -), and 450 (–) MHz. Peak value of the graph is 9.7 dBi.

3. MEASUREMENT RESULTS

A complete ¼ scale model of the array was fabricated at Penn State University and shipped to NAWCAD Patuxent River for testing. Measurements included azimuth and elevation cuts for isolated elements, as well as azimuth cuts for embedded element patterns. Table II provides a comparison between the modeled and measured beamwidths and gains of the isolated element. Table III summarizes the available gains and beamwidths, synthesized from measured embedded element patterns. Results are include for a 27-element uniform excitation, and 27/54 element low sidelobe excitation resulting from an iteratively weighted least squares (LS) method, as defined in [5].

It should be noted that the balun was not included in the electromagnetic models. The best performance of a prototype element was observed with a split-wire balun, attached directly at the feedpoint. However, because of the difficulty in fabrication, its fragile nature (at the scale model size), and time constraints, the split-wire version was replaced with more easily fabricated remote bazooka balun.

TABLE II
COMPARISON OF NEC MODELED AND MEASURED RESULTS (ISOLATED ELEMENT)

	NEC			Measured		
Freq	Azimuth	Elevation	Gain	Azimuth	Elevation	Gain
(MHz)	BW (°)	BW (°)	(dBi)	BW (°)	BW (°)	(dBi)
400	48.9	41.0	12.6	48.0	41.3	12.5
425	45.6	38.6	13.1	44.2	39.4	13.1
450*	41.4	36.4	13.6	43.4	38.8	12.6

TABLE III
SUMMARY OF MEASURED (SYNTHESIZED) ARRAY PATTERNS

Freq (MHz)	Excitation	Gain (dBi)	Az BW (°)	Peak Sidelobe (dB rel Max)
400	Uniform	20.42	7.3	11
	27 LS	19.83	8.2	26
	54 LS	19.23	7.8	35
	54 LS	19.65	8.2	40
425	Uniform	21.04	6.7	10
	27 LS	20.22	8.1	30
	54 LS	19.50	7.7	35
	54 LS	20.15	8.2	40
450	Uniform	18.60	7.0	9
	27 LS	15.22	8.1	24
	54 LS	14.95	7.9	35
	54 LS	NA	NA	40



Figure 6—1/4 scale model array.

Azimuth cuts of the embedded elements are shown below in Fig. 7. Isolated element measurements are not shown, for lack of space.

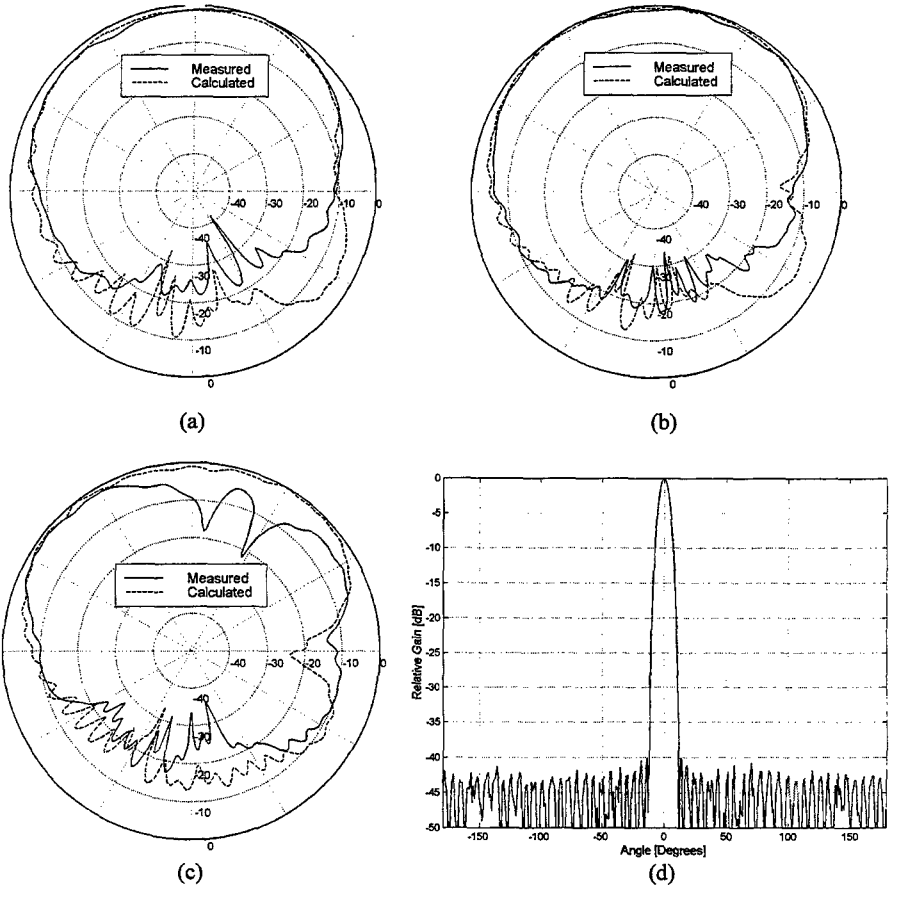


Figure 7—Computed vs. measured azimuth patterns of embedded element at (a) 400 MHz, (b) 425 MHz, (c) 450 MHz. (d) Low sidelobe pattern synthesized from 425 MHz (1.7 GHz) measured data with all elements active.

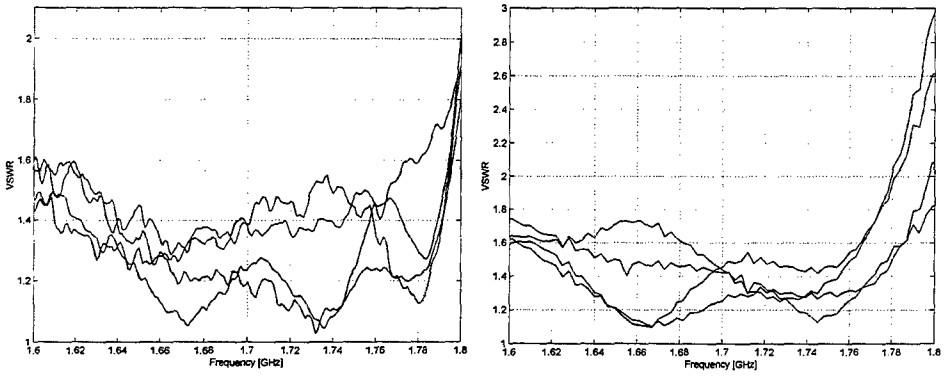


Figure 8—Samples of (a) isolated and (b) embedded element VSWR at the scale frequency.

4. CONCLUSIONS

A complete 54-element circular array was designed using both the WIPL-D and NEC4 codes. WIPL-D proved to be critical for obtaining an acceptable element design, while NEC's ability to exploit the inherent rotational symmetry of the problem was essential for modeling the entire array. Feedline radiation at 450 MHz, resulting from the partially ineffective bazooka balun, caused the single exception to a superbly correlated set of modeling and measurement results. Measured azimuth and elevation plane beamwidths of the isolated element were within about 1° of that modeled at 400/425 MHz. The measured boresight gains at these frequencies were within 0.1 dB of that observed from the models. Excellent correlation of measured and modeled embedded element patterns is also evident in Figs. 7(a) and 7(b).

REFERENCES

1. B. M. Kolundzija, J. S. Ognjanovic, T. K. Sarkar, R. F. Harrington, *WIPL: Electromagnetic Modeling of Composite Wire and Plate Structures.* Artech House, Inc. Dedham, Massachusetts: 1998

2. J. M. Stamm, and J. K. Breakall, "A Parameter Study of the Circular Array", submitted to *IEEE Trans. Antennas Propagat.*, February, 2000.

3. J. K. Breakall, J. S. Young, R. J. Bauerle, A. I. McDowell and T. A. Erdley, "Numerical Electromagnetics Code Optimization Design Software (NECOPT)," *10th Annual Review of Progress in Applied Computational Electromagnetics*, Naval Postgraduate School, Monterey, CA, 1994.

4. J. M. Stamm, M. Fenton, and J. K. Breakall, "Comparison and Results for Models of a Thick Bent-Wire Dipole using NEC4 and WIPL", *15th Annual Review of Progress in Applied Computational Electromagnetics*, Naval Postgraduate School, Monterey, CA, 1999.

5. C. A. Olen and R. T. Compton Jr., "A Numerical Pattern Synthesis Algorithm for Arrays", *IEEE Trans. Antennas Propagat.*, vol. 38, pp. 1666-1676, October 1990.

Array Sidelobe Reduction by Small Position Offsets of Fractal Elements

By Nathan Cohen[1,2] and Robert G. Hohlfeld[1,3]
fractenna@aol.com hohlfeld@buphy.bu.edu

[1]Fractal Antenna Systems, 2 Ledgewood Place, Belmont, MA 02478
[2]Science and Engineering Program, Metropolitan College, Boston University, Boston, MA 02215
[3]Center for Computational Science, Boston University, Boston, MA 02215

ABSTRACT

Small (sub-wavelength) position offsets of antenna array elements is a known technique for reducing array sidelobes, particularly when grating sidelobes are present in the array beam pattern. However this method is of limited benefit as the individual antenna elements are a significant fraction of a wavelength in size and so the available space to adjust their positions is too small to be effective. Mutual coupling also proves a constraint. Fractal antenna elements, which are resonant, low loss, of moderate bandwidth, and a smaller fraction of a wavelength in size can be used successfully to exploit this method of array sidelobe reduction. With fractal elements, more "real estate" of the phased array is available to accommodate position adjustments that reduce array sidelobes. We show an example of such a system as a 4×4 array of Minkowski-2 antenna elements, spaced at nominal separations of λ and have sizes of $\lambda/8$, with offsets of order $\lambda/8$ from a uniform distribution. Sidelobe reductions of 5-10 dB relative to an array of quarter-wavelength dipoles are shown in NEC4 simulations. The method proves amenable to use in conjunction with tapering.

1. Introduction

Sidelobe magnitude is an important design consideration for many phased array systems. Reducing the size of sidelobes reduces the power from interfering sources in phased arrays used for receivers with corresponding gains in system performance. Complementary advantages are obtained for phased arrays used for transmission. Development of a new or modified technique for sidelobe reduction in phased array design has implications for a wide range of practical problems.

A phased array (used as a receiver) may be viewed as measuring a sampling of the electromagnetic field impinging on it. In the Fourier domain, the phased array has response over spatial frequencies corresponding to the inverses of all the relative separations of the array elements. Since there are only a limited number of elements and a finite set of relative spacings, sampling in the Fourier domain is necessarily incomplete, which results in sidelobes in the array beam pattern. When the sampling in the Fourier domain is so incomplete as to violate Nyquist's theorem, *i.e.* with element spacings greater than $\lambda/2$, grating sidelobes appear which are the result of aliasing in the spatial Fourier domain. Additionally, the use of uniform arrays produces periodic sampling of selected spatial frequencies, enhancing periodic sidelobes.

These general theoretical considerations motivate strategies for improving phased array performance by arranging the antenna elements so as to sample more efficiently the spatial Fourier domain, while keeping the number of elements small. Some examples of such approaches include randomly distributed elements and/or fractally distributed elements in phased arrays (Kim and Jaggard, 1986). Generally, these methods seek to subtract elements from very large arrays to achieve reasonable performance.

In this paper we consider designs close to the canonical phased array designs, and then modify these designs by offsetting array elements so as to improve array performance by improving sampling in the spatial Fourier domain. Usually, this would not be considered as an attractive approach because the antenna elements in a typical phased array, *e.g.* a half-wavelength dipole, cannot be offset by any significant amount without running into other array elements, or yielding problems from mutual coupling. However, if we construct a phased array with fractal antenna elements, the antenna elements can be smaller by a factor of two or three, and we then have sufficient space to explore the effects of antenna offsets on the array beam pattern. We will consider examples in one and two dimensions with the array fractal elements. Simulation results from NEC4 will be presented that illustrate the performance of such an array.

2. Mathematical Discussion

We develop here the mathematical formalism describing sidelobe reduction by sub-wavelength offsets of the positions of antennas in the phased array. The formalism is based on the description of a uniformly spaced one-dimensional array as described in Balanis (1997) and in many other references. The array factor of an N element array of elements uniformly spaced with separation d is:

$$AF = \sum_{n=1}^{N} \exp\left[j(n-1)(kd\cos\theta + \beta)\right], \tag{1}$$

where $k = 2\pi/\lambda$ is the wavenumber of the electromagnetic wave, θ is the azimuth angle, and β is the beam steering angle. We want to extend this formalism by putting in d_n, the position of the nth antenna in explicitly. For the case of linear spacing, $d_n = d(n - 1)$, and if an offset or "dither" of δ_n in the position of the nth element is allowed,

$$d_n = d(n-1) + \delta_n \,. \tag{2}$$

and so if we incorporate the dithered positions in the expression for the array factor, we obtain

$$AF = \sum_{n=1}^{N} \exp\left[jk\left((n-1)d + \delta_n\right) + j(n-1)\beta\right]$$
$$= \sum_{n=1}^{N} \exp\left[j(n-1)(kd\cos\theta + \beta)\right]\exp\left[jk\delta_n \cos\theta\right]. \quad (3)$$

This expression allows us to understand the mechanism by which introducing spatial offsets in antenna position can lead to a reduction in the size of sidelobes. As can be seen in equation (1), the array factor is a sum of exponential factors, *i.e.* phasors, and so at any given angle and beam steer, the beam power depends on whether this phasor sum adds constructively or destructively. Introducing a spatial offset of the antenna element positions, multiplies these phasor terms by another complex exponential which changes their phase, and hence affects whether the phasor sum is adding constructively or destructively at any particular azimuth angle and beam steer angle. Different choices for the δ_ns will enhance or diminish different features in the beam pattern. Appropriate optimization schemes can be constructed for choosing the δ_ns in different phased array design problems, but development of that subject is beyond the scope of the present paper.

Equation (3) lets us illustrate this point with a simple 1-D example. Consider a baseline array with $N = 8$ and $d = \lambda/2$, with uniform excitation at each element. We calculate the beam pattern of that array at a zero beam steer angle and show the polar diagram of the beam pattern for reference in Figure 1A. To illustrate the effects of introducing the offsets in the element positions we arbitrarily chose, with no effort to select an optimal solution, a vector δ of offsets (in 1-D) for the element positions given by

$$k\delta = (0.0, 0.25, 0.5, 0.75, -0.25, -0.5, -0.75, 0.0). \quad (4)$$

The resulting beam pattern is given in Figure 1B. In both beam patterns, 40 dB of dynamic range of the beam is plotted, normalized relative to the amplitude of the main beam at $\theta = 90°$. The main beam in both cases has an amplitude of 18.03 dB absolute. In the baseline case the first sidelobe has an amplitude of

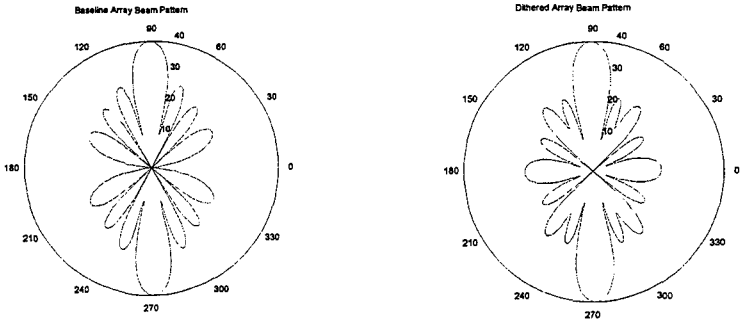


Figure 1: Beam pattern at left is for an 8 element linear array of uniformly excited elements spaced at intervals of $\lambda/2$. At right is the beam pattern resulting when the positions of this array are adjusted by the offset vector given in equation (4). The amplitude of the first sidelobe has been reduced by 3.6 dB. A substantial gain in performance has been obtained, although the choice of offsets has not been optimized.

5.26 dB, *i.e.* 12.76 dB down from the main beam, while in the case with the positions adjusted, the first sidelobe is at 1.67 dB, *i.e.* 16.36 dB down from the main beam. The offsets have improved the performance of the array in terms of the first sidelobe amplitude by 3.6 dB. In the case with offsets, the second sidelobe appears at a higher amplitude than the first sidelobe.

It is clear that adjusting the antenna positions has significantly changed the sidelobe structure in the array beam pattern, including the presence of a new sidelobe at end-fire. The offsets chosen here are merely illustrative, rather than intended to optimize array performance overall. Other choices of offsets can be made to optimize particular properties of the array beam pattern as desired.

3. Description of the Fractal Antenna Element and Array Motivation

Fractal elements incorporate self-similarity in order to change the operational characteristics of the antenna (Cohen, 1995). The elements under consideration here consist of fractal loops with a rectangular motif, dubbed Minkowski (Koch) fractal island loops (Cohen, 1995). These, among others, have been identified to have shrunken sizes (about $\lambda/8$ wave on a side) while maintaining very high efficiency. These loops, in iteration 2, have impedances of order 30 ohms real, and two parallel current maxima. This effectively gives this loop higher field strength than expected from the radiation resistance given by the small loop approximation (Cohen and Hohlfeld, 1996)

These 'MI2' loops were chosen because their small size when resonant allows greater versatility in the spatial offsets to be used. Furthermore, unlike other small elements, such as $\lambda/8$ dipoles, MI2 is self-resonant and requires no additional loading components, which produce higher losses. Finally, the useable bandwidth of the MI2 far exceeds that of other small loaded antennas of the same size, due to the higher radiation resistance caused by the two current maxima.

It has been known for some time (Kim and Jaggard, 1986) that random, fractal distributions of elements on an array lead to sidelobe reduction. However, such reduction requires rather large offsets from a uniform distribution. Thus we were motivated here to show that fractal *elements*, through their smaller size, self resonance, and greater bandwidth, offer a practical realization of sidelobe reduction in arrays of small form factor, and/or arrays which have limited 'real estate' for small offsets.

4. Phased Array Simulation

Aided by the one-dimensional analytical simulations, we chose to simulate the two dimensional array of fractal elements using the method of moments engine NEC4. Accuracy of mutual coupling and ohmic losses further guided us to choose this route.

Each MI2 element consisted of 100 wires sampled by 2 to 3 segments per wire. We chose an array of 4×4 elements separated, without offsets, by λ at 450 MHz in vertical and horizontal dimensions. We had the option, and used, voltage weighting of each element in the array to produce tapering with 0.5-1-1-0.5 tapering per column. Furthermore, we employed constant phase offsets on elements 2 and 3 of each array column, to produce consistent sidelobe reduction across a variety of steering angles.

We offset or 'dithered' the spatial position of the elements to produce the sidelobe reduction suggested by the one-dimensional case. These ditherings were not designed for optimization but for illustrating the effect. We considered a maximum horizontal dither of about $\lambda/8$ and tried several cases to determine typical sidelobe reductions.

As a comparison, as above, we used uniformly spaced, loaded $\lambda/4$ dipole elements to simulate a typical array of patch-sized elements. This array was tapered as above for each column and was phase steered uniformly per column.

To save computational time, neither array was backed by a reflector, and thus the results yielded bi-directional beam patterns in both cases.

5. Results and Discussion

Figure 2 shows the uniform dipole array, with accompanying azimuthal power patterns in Figures 3 and 4 for zero and 30 degrees steer, respectively. Similarly, the fractal element array and its concurrent results are found in Figures 5 through 7.

The results indicate dramatic sidelobe reductions for the fractal element array. In particular, at 30 degrees off boresite, the dipole array suffers from a grating sidelobe, which is reduced by 9.4 dB in the fractal element array. Other sidelobes experience reductions of 3-5 dB.

We note that the improvements for the MI2 panel array simulations are even larger than we obtained for the 1-D case considered in section 2. In the 1-D case we are modifying the structure of ordinary sidelobes in an array with $\lambda/2$ spacing, while in the MI2 panel simulations the original spacings were by λ. and the amplitudes of the grating sidelobes was reduced.

6. Conclusions

Using fractal elements offers an opportunity to reduce sidelobes through a dithered offset, of order $\lambda/8$. Here we have demonstrated that this proves a practical means of achieving such reductions, without large offsets in the array. The method further benefits from more conventional methods of sidelobe reductions, such as tapering, and can be used in conjunction with it.

Acknowledgements

We thank Misha Filippov for technical discussions. Patents pending.

7. References

Balanis, Constantine A. (1997): **Antenna Theory: Analysis and Design, 2nd Edition**, (John Wiley & Sons, Inc.: New York).

Cohen, N. (1995): " Fractal Antennas Part 1", *Communications Quarterly*, Summer, 7.

Cohen, N., and Hohlfeld, R. G. (1996): "Fractal Loops and the Small Loop Approximation", *Communications Quarterly*, Winter, 77.

Kim, Y., and Jaggard., D. (1986), "The Fractal Random Array", *Proc. IEEE*, **74**, 1278.

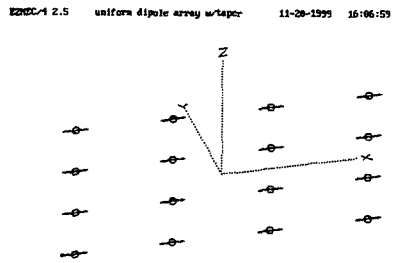


Figure 2: Baseline dipole array for NEC4 simulations. A 4 × 4 array of uniformly spaced loaded dipoles with taper as indicated in the text.

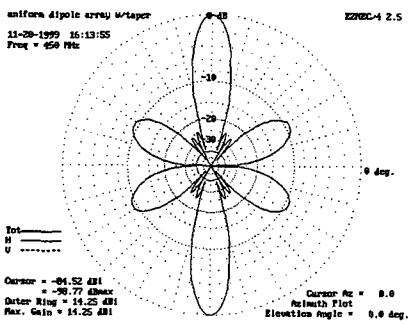


Figure 3: Zero beam steer beam pattern for the baseline dipole array shown in Figure 2.

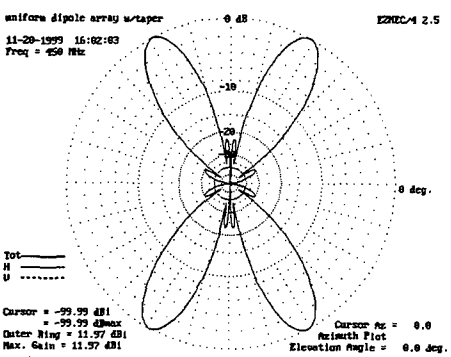


Figure 4: Beam pattern for 30° beam steer of the baseline dipole array. Note the presence of a large grating sidelobe.

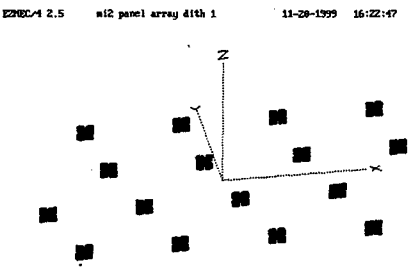


Figure 5: Array of MI2 dipoles with dithered positions in the *xz*-plane.

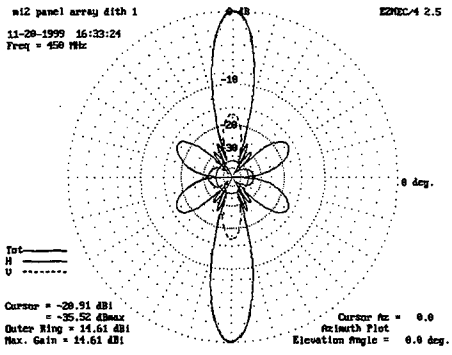


Figure 6: Beam pattern at zero beam steer for the dithered MI2 panel array.

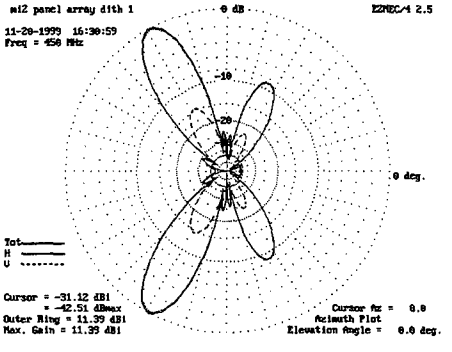


Figure 7: Beam pattern at 30° beam steer for the dithered MI2 panel array. Note that the amplitude of the grating sidelobe is significantly reduced.

The Radiation Characteristics of Recursively Generated Self-Scalable and Self-Similar Arrays

D. H. Werner and P. L. Werner
The Pennsylvania State University
Department of Electrical Engineering
University Park, PA 16802, USA

Abstract- There has been considerable recent interest in the radiation characteristics of self-scalable and self-similar planar arrays. For instance, array configurations based on Sierpinski carpets have been considered in [1,2]. The properties of self-scalable concentric circular Weierstrass arrays and self-similar concentric circular Cantor arrays have also been investigated in [3] and [4] respectively. In this paper we present an alternative design methodology for the mathematical construction of self-scalable and self-similar planar arrays. The technique is very general and consequently provides much more flexibility in the design of fractal and related arrays when compared to other approaches previously considered in the literature. This is primarily due to the fact that the generator in this case is based on a concentric circular ring array.

1. Introduction

A rich class of fractal and related arrays exist which can be formed recursively through the repetitive application of a generating array. A generating array is a small array at scale one ($P=1$) used to recursively construct larger arrays at higher scales (*i.e.*, $P>1$). In many cases the generating array has elements that are turned on and off in a certain pattern. A set formula for copying, scaling, and translating of the generating array is then followed in order to produce a family of higher order arrays. Hence, arrays which are created in this manner will be composed of a sequence of self-scalable or, in some cases, self-similar subarrays.

The array factor for such self-scalable or self-similar arrays may be expressed in the general form [1,2]

$$AF_P(\psi) = \prod_{p=1}^{P} GA(\delta^{p-1}\psi) \tag{1}$$

where $GA(\psi)$ represents the array factor associated with the generating array. The parameter δ is a scaling or expansion factor which governs how large the array grows with each recursive application of the generating array. We may regard (1) as representing a formal statement of the *pattern multiplication theorem* for self-scalable and self-similar (i.e., fractal) arrays.

2. The Concentric Circular Ring Array Generator

The generating array factor for the concentric circular ring array may be expressed in the form [5]

$$GA(\theta,\phi) = \sum_{m=1}^{M}\sum_{n=1}^{N_m} I_{mn} e^{j\psi_{mn}(\theta,\phi)} \tag{2}$$

where

$$\psi_{mn}(\theta,\phi) = kr_m \sin\theta\cos(\phi-\phi_{mn}) + \alpha_{mn} \tag{3}$$

$$k = 2\pi/\lambda \tag{4}$$

M = Total number of concentric rings (5)

N_m = Total number of elements on the mth ring (6)

r_m = Radius of the mth ring (7)

I_{mn} = Excitation current amplitude of the nth element on the mth ring (8)

α_{mn} = Excitation current phase of the nth element on the mth ring (9)

The array factor for a particular stage of growth P may be derived by substituting (2) directly into (1). The resulting expression for the array factor is then

$$AF_P(\theta,\phi) = \prod_{p=1}^{P}\left\{\sum_{m=1}^{M}\sum_{n=1}^{N_m} I_{mn} e^{j\delta^{p-1}\psi_{mn}(\theta,\phi)}\right\} \tag{10}$$

3. Examples

Several different examples of arrays that may be constructed via a concentric circular ring subarray generator will be presented and discussed in this section. The mathematical expressions that describe the radiation patterns of these arrays are all special cases of (10).

3.1 Planar Square Arrays

The radiation characteristics of Sierpinski carpet arrays have been considered in [1,2]. The generating subarray for a Sierpinski carpet may be represented by two concentric four-element circular arrays. Hence, the normalized Sierpinski carpet array factor may be expressed in the form

$$\hat{AF}_P(\theta,\phi) = \frac{1}{8^P}\prod_{p=1}^{P}\sum_{m=1}^{2}\sum_{n=1}^{4} e^{j3^{p-1}\psi_{mn}(\theta,\phi)} \tag{11}$$

where

$$\psi_{mn}(\theta,\phi) = \sqrt{m}\ \pi[\sin\theta\cos(\phi-\phi_{mn}) - \sin\theta_0\cos(\phi_0-\phi_{mn})] \tag{12}$$

$$\phi_{mn} = \left(\frac{mn-1}{m}\right)\frac{\pi}{2} \tag{13}$$

The geometry and the array factor for the first four stages (*i.e.*, P =1 - 4) of a Sierpinski carpet array are shown in Fig. 1.

3.2 Planar Triangular Arrays

The first category of triangular arrays that will be considered are those that can be constructed from the uniformly excited three-element circular subarray generator. This three-element circular array of radius $r = \lambda/(2\sqrt{3})$ can also be interpreted as an equilateral triangular array with half-wavelength spacing on a side (i.e., $d=\lambda/2$). The normalized array factor associated with this triangular generating subarray is

$$\hat{AF}_P(\theta,\phi) = \frac{1}{3^P}\prod_{p=1}^{P}\sum_{n=1}^{3} e^{j\delta^{p-1}\left[\frac{\pi}{\sqrt{3}}\sin\theta\cos(\phi-\phi_n)+\alpha_n\right]} \tag{14}$$

where

$$\phi_n = (n-1)\frac{2\pi}{3} \tag{15}$$

$$\alpha_n = -\frac{\pi}{\sqrt{3}}\sin\theta_0\cos(\phi_0-\phi_n) \tag{16}$$

If we choose $\delta = 2$, then (14) becomes

$$\hat{AF}_P(\theta,\phi) = \frac{1}{3^P}\prod_{p=1}^{P}\sum_{n=1}^{3} e^{j2^{p-1}\psi_n(\theta,\phi)} \tag{17}$$

where

$$\psi_n(\theta,\phi) = \frac{\pi}{\sqrt{3}}[\sin\theta\cos(\phi-\phi_n) - \sin\theta_0\cos(\phi_0-\phi_n)]$$

This represents the array factor for a triangular Sierpinski carpet array.

The second category of triangular arrays that will be explored are produced by a six-element generating subarray. This generating subarray consists of two three-element concentric circular arrays with radii $r_1 = \lambda/(2\sqrt{3})$ and $r_2 = \lambda/(\sqrt{3})$. If we treat the generating subarray as a pair of three-element concentric circular ring arrays, then it follows from (10) that the normalized array factor in this case may be expressed as

$$\hat{AF}_P(\theta,\phi) = \frac{1}{9^P}\prod_{p=1}^{P}\sum_{m=1}^{2}\sum_{n=1}^{3} I_{mn} e^{j\delta^{p-1}[kr_m\sin\theta\cos(\phi-\phi_{mn})+\alpha_{mn}]} \tag{18}$$

where

$$I_{mn} = (2/m) \tag{19}$$

$$kr_m = \frac{m\pi}{\sqrt{3}} \tag{20}$$

$$\phi_{mn} = (2n+m-3)\frac{\pi}{3} \tag{21}$$

$$\alpha_{mn} = -kr_m\sin\theta_0\cos(\phi_0-\phi_{mn}) \tag{22}$$

We will next consider a special case of (18), namely when $\delta = 2$. In this case (18) reduces to

$$\hat{AF}_P(\theta,\phi) = \frac{1}{9^P}\prod_{p=1}^{P}\sum_{m=1}^{2}\sum_{n=1}^{3} I_{mn} e^{j2^{p-1}\psi_{mn}(\theta,\phi)} \tag{23}$$

where

$$\psi_{mn}(\theta,\phi) = \frac{m\pi}{\sqrt{3}}[\sin\theta\cos(\phi-\phi_{mn}) - \sin\theta_0\cos(\phi_0-\phi_{mn})] \tag{24}$$

Fig.2 illustrates the geometry for the first three stages of this triangular array and the corresponding current distribution. This type of construction scheme can be exploited in order to realize low-sidelobe array designs. A sidelobe level of at least –20dB can be achieved by higher-order versions of these arrays.

3.3 Hexagonal Arrays

The standard hexagonal arrays are formed by placing elements in an equilateral triangular grid with spacings d (see for example Fig. 2.8 of [6]). The normalized form of the hexagonal array factor is given by [6]

$$\hat{AF}_P(\theta,\phi) = \frac{I_0 + \sum_{p=1}^{P}\sum_{m=1}^{p}\sum_{n=0}^{5} I_{pmn} e^{j[kr_{pm}\sin\theta\cos(\phi-\phi_{pmn})+\alpha_{pmn}]}}{I_0 + \sum_{p=1}^{P}\sum_{m=1}^{p}\sum_{n=0}^{5} I_{pmn}} \tag{25}$$

where

$$r_{pm} = d\sqrt{p^2 + (m-1)^2 - p(m-1)} \tag{26}$$

$$\phi_{pmn} = \cos^{-1}\left[\frac{r_{pm}^2 + d^2p^2 - d^2(m-1)^2}{2r_{pm}dp}\right] + \frac{n\pi}{3} \tag{27}$$

$$\alpha_{pmn} = -kr_{pm}\sin\theta_0\cos(\phi_0-\phi_{pmn}) \tag{28}$$

and P is the number of concentric hexagons in the array.

We now consider a uniformly excited six-element circular array of radius $r = \lambda/2$ as the generating subarray. Consequently, the normalized array factor associated with this generating subarray may be represented as:

$$\hat{AF}_P(\theta,\phi) = \frac{1}{6^P}\prod_{p=1}^{P}\sum_{n=1}^{6} e^{j\delta^{p-1}[\pi \sin\theta\cos(\phi-\phi_n)+\alpha_n]} \tag{29}$$

where

$$\phi_n = (n-1)\frac{\pi}{3} \tag{30}$$

$$\alpha_n = -\pi \sin\theta_0 \cos(\phi_0 - \phi_n) \tag{31}$$

Substituting the value of $\delta = 2$ into (29) yields an expression for the recursive hexagonal array factor given by

$$\hat{AF}_P(\theta,\phi) = \frac{1}{6^P}\prod_{p=1}^{P}\sum_{n=1}^{6} e^{j2^{p-1}\psi_n(\theta,\phi)} \tag{32}$$

where

$$\psi_n(\theta,\phi) = \pi[\sin\theta\cos(\phi-\phi_n) - \sin\theta_0\cos(\phi_0-\phi_n)] \tag{33}$$

Fig.3 shows the element locations and current distributions for the first four stages of this hexagonal array. One potential advantage of these arrays is that they are thinned and, therefore, may be realized with fewer elements. Another advantage of these arrays is that they possess low sidelobe levels, as indicated in Fig. 4. Finally, the compact product form given in (32) offers a significant advantage in terms of computational efficiency, especially for large arrays. For example, this property may be exploited to develop rapid beamforming algorithms.

When an element with two units of current is added to the center of the hexagonal generating subarray shown in Fig. 3, the array factor given in (29) must be modified in the following way:

$$\hat{AF}_P(\theta,\phi) = \frac{1}{8^P}\prod_{p=1}^{P}\left\{2+\sum_{n=1}^{6} e^{j\delta^{p-1}\psi_n(\theta,\phi)}\right\} \tag{34}$$

This allows a further reduction in sidelobe levels to be achieved and leads to a family of fully-populated hexagonal arrays.

References

[1] R. L. Haupt and D. H. Werner, "Fast Array Factor Calculations for Fractal Arrays," Proceedings of the *13th Annual Review of Progress in Applied Computational Electromagnetics (ACES)*, Vol.1, pp. 291-296, Naval Postgraduate School, Monterey, CA, March 1997.

[2] D. H. Werner and R. L. Haupt, "Fractal Constructions of Linear and Planar Arrays," Proceedings of the *IEEE Antennas and Propagation Society International Symposium*, Vol. 3, pp. 1968-1971, Montreal, Canada, July 1997.

[3] X. Liang, W. Zhensen and W. Wenbing, "Synthesis of Patterns From Concentric-Ring Arrays," *IEE Electronics Letters*, Vol. 32, No. 21, pp. 1940-1941, Oct. 1996.

[4] D. L. Jaggard and A. D. Jaggard, "Cantor Ring Arrays," Proceedings of the *IEEE Antennas and Propagation Society International Symposium*, Vol. 2, pp. 866-869, Atlanta, Georgia, June 1998.

[5] M. T. Ma, *Theory and Application of Antenna Arrays.* New York: Wiley, 1974.

[6] J. Litva and T. K. Y. Lo, *Digital Beamforming in Wireless Communications.* Boston, MA: Artech House, 1996.

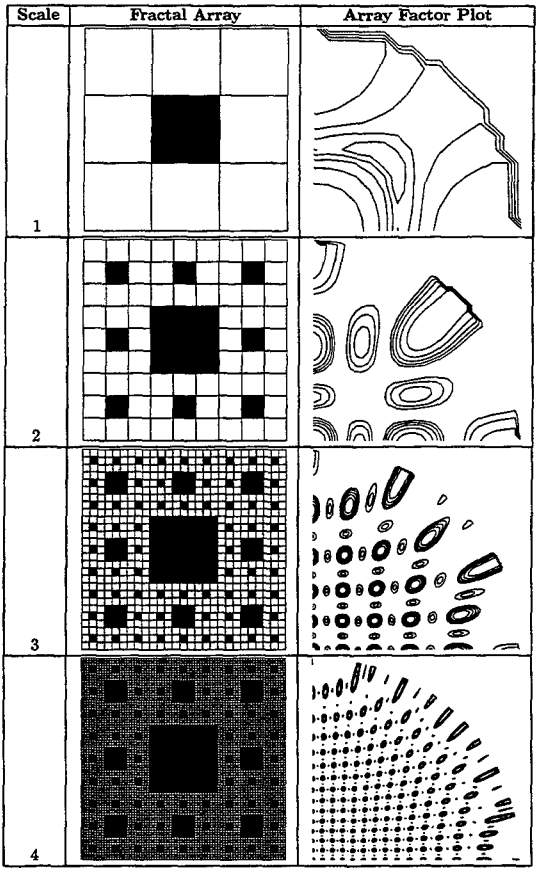


Fig.1. Scale 1 is the generator subarray. Column 2 is the geometrical configuration of the Sierpinski carpet array: white blocks represent elements that are turned on and black blocks represent elements that are turned off. Column 3 is the corresponding array factor where the angle phi is measured around the circumference of the plot and the angle theta is radially measured from the origin at the lower left.

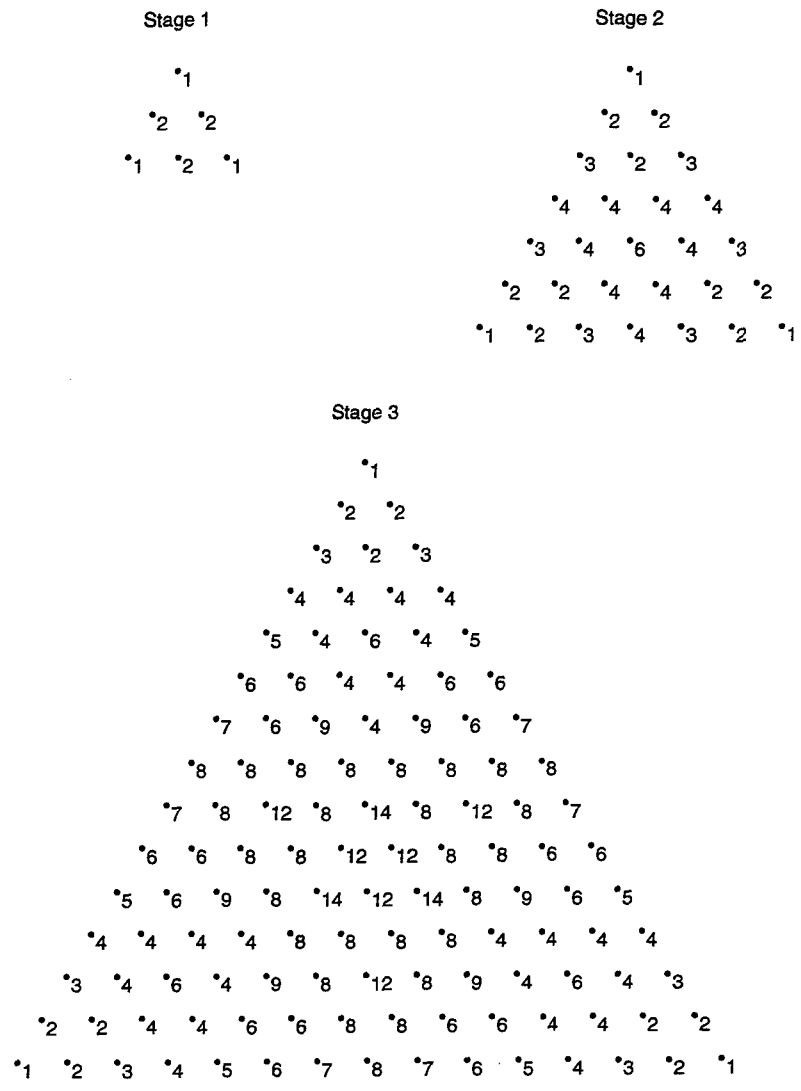


Fig.2. The geometry and current distribution for the first three triangular arrays.

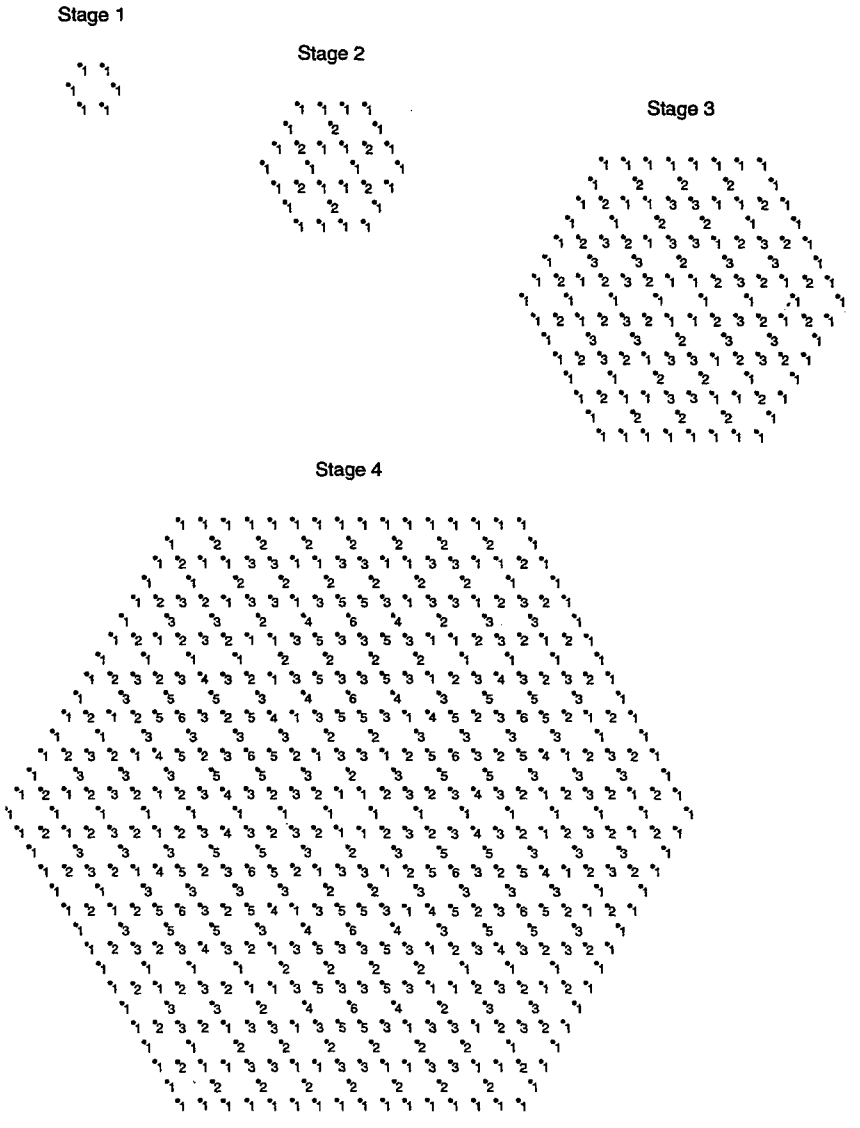


Fig.3. The element locations and associated current distributions for each of the four hexagonal arrays .

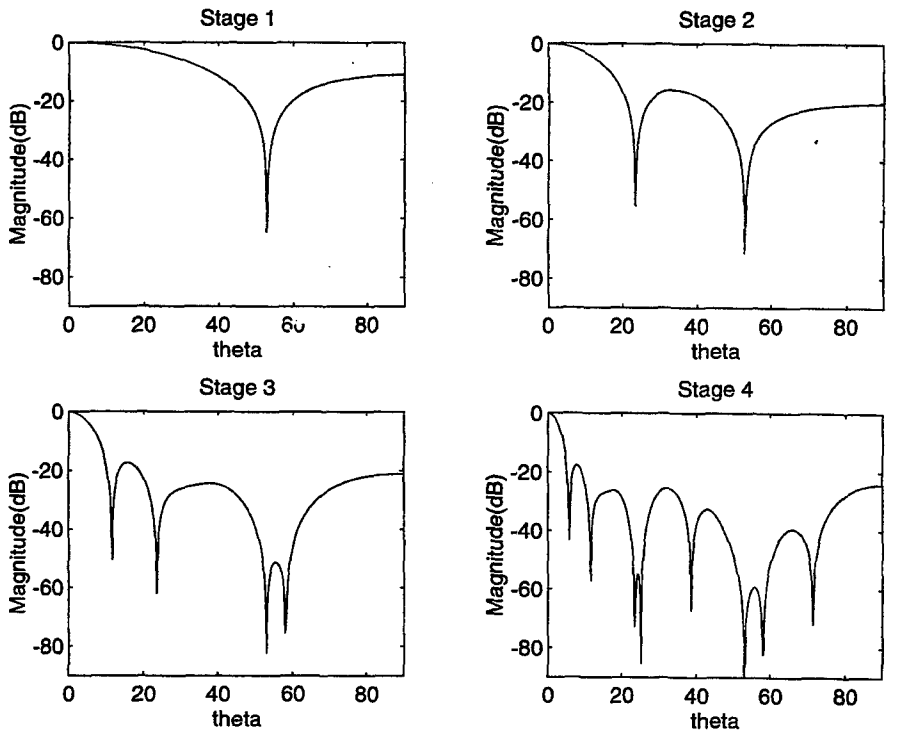


Fig.4. Plots of the far-field radiation patterns produced by the four hexagonal arrays shown in Fig.3.

SESSION 15

FAST AND EFFICIENT METHODS

Chairs: Weng C. Chew and Jiming Song

Three Dimensional Scattering Analysis in Stratified Medium using Fast Inhomogeneous Plane Wave Algorithm †

BIN HU AND WENG CHO CHEW

CENTER FOR COMPUTATIONAL ELECTROMAGNETICS
ELECTROMAGNETICS LABORATORY
DEPARTMENT OF ELECTRICAL AND COMPUTER ENGINEERING
UNIVERSITY OF ILLINOIS
URBANA, IL 61801

(Dedicated to the memory of James R. Wait for his expansive contributions to electromagnetics and his boundless energy)

1. Introduction

The scattering of electromagnetic waves in the presence of layered medium is a subject of great practical interests. Major applications include, but are not limited to, microstrip antenna and MIC. Among many techniques which have been proposed for this purpose, the Method of Moments (MOM) solution of the integral equation encountered in the layered medium studies, often named as full wave analysis method, has received considerable attention. However, two obstacles limit the analysis of practical problems.

First, for the layered medium problem, the spatial domain Green's function can be cast into a Sommerfeld-type integral (SI) from which no general analytic closed form is available. Numerical integration along the Sommerfeld Integration Path (SIP), though possible, converges too slowly to be practical. Second, the basic idea of MOM is to transform an integro-differential equation to a matrix equation, which is a dense one in the general case. Solving this matrix equation by using traditional scheme, such as Gaussian elimination, which requires $O(N^3)$ CPU time, or iterative solver with direct matrix vector multiplication, whose computational complexity scales as $O(N^2)$, quickly exhausts the currently available computing resources.

To address this problem, Fast Multipole Method (FMM) coupled with Discrete Complex Image Method (DCIM) has been proposed to solve stratified medium problems efficiently [1]. However, as we pointed out in [2], this approach is far from being optimal, partially because DCIM is basically an asymptotic method and not rigorous.

In this report, we propose a new approach, named Fast Inhomogeneous

†This work was supported by AFOSR under MURI Grant F49620-96-1-0025.

Plane Wave Algorithm (FIPWA). The major idea of this approach is to expand the Green's function encountered in layered medium study as the summation of the inhomogeneous plane wave, which is sampled along a carefully chosen Steepest Descent Path (SDP). By using the interpolation and extrapolation technique, the translation matrix is diagonalized. The advantages of this method, compared to the FMM/DCIM approach, include efficiency, accuracy, and versatility.

Throughout this paper, $e^{-i\omega t}$ time convention is assumed and suppressed.

2. Fast Inhomogeneous Plane Wave Algorithm in Layered Medium

2.1. Basic Formulation

By setting up the coordinate system as shown in Figure 1 and assuming that the scatterer is located entirely above the layered medium, the dyadic Green's function, which is expressed in the Sommerfeld-type integral, can be derived. For illustration purpose, the G_{xx} component is formulated as

$$G_{xx}(\mathbf{r}_j, \mathbf{r}_i) = \frac{i\mu}{8\pi} \int_{-\infty}^{\infty} dk_\rho \frac{k_\rho}{k_{1z}} H_0^{(1)}(k_\rho |\boldsymbol{\rho}_j - \boldsymbol{\rho}_i|) \left(e^{ik_{1z}|z_j - z_i|} + \tilde{R}^{TE}(k_\rho) e^{ik_{1z}(z_j - z_i + 2d)} \right) \tag{1}$$

where d is the distance from the source point, i.e., $\mathbf{r}_i$, to the interface of the layered medium and $\tilde{R}^{TE}(k_\rho)$ is the generalized reflection coefficient [3]. Separating Equation (1) into the direct and reflected field term, denoting $\mathbf{r}_{iI} = x_i\hat{x} + y_i\hat{y} + (z_i - 2d)\hat{z}$ as the mirror image point of the source point $\mathbf{r}_i$, and using $k_\rho = k\sin\theta$ and $k_{1z} = k\cos\theta$, we have

$$G_{xx}^d(\mathbf{r}_j, \mathbf{r}_i) = \frac{i\mu k}{8\pi} \int_\Gamma d\theta \sin\theta H_0^{(1)}(k\sin\theta |\boldsymbol{\rho}_j - \boldsymbol{\rho}_i|) e^{ik\cos\theta |z_j - z_i|} \tag{2}$$

$$G_{xx}^r(\mathbf{r}_j, \mathbf{r}_i) = \frac{i\mu k}{8\pi} \int_{\Gamma^I} d\theta \sin\theta \tilde{R}^{TE}(k\sin\theta) H_0^{(1)}(k\sin\theta |\boldsymbol{\rho}_j - \boldsymbol{\rho}_{iI}|) e^{ik\cos\theta (z_j - z_{iI})} \tag{3}$$

where Γ and Γ^I are the properly chosen paths on the complex θ plane. Application of FIPWA to the first term, which is the Green's function for free space, has been studied in [4]. Therefore, we will concentrate our discussion on the second term, which is used to account for the reflected wave contribution from the layered medium.

2.2. Steepest Descent Path

To determine the Steepest Descent Path for θ so that the integral converges quickly, we first use the asymptotic expansion of the Hankel function, i.e.,

$$H_0^{(1)}(k\rho\sin\theta) \sim \sqrt{\frac{2}{\pi k\rho\sin\theta}} e^{ik\rho\sin\theta - i\frac{\pi}{4}}. \tag{4}$$

Therefore, asymptotically, the integrand in Equation (3) takes the form $e^{ik\rho\sin\theta+ikz\cos\theta}$. The determination of the SDP for this kind of integrand has been extensively studied in the 2D FIPWA case [5]. In summary, to avoid the exponential large peaks, a modified SDP is defined and is shown in Figure 2. However, it is important to note the difference between this path with the one in the free space. After changing the integration path from the SIP to SDP, the possible pole and branch point contribution, as illustrated in Figure 2, cannot be neglected.

Therefore, denotes $f(\theta) = k\sin\theta\tilde{R}^{TE}(k\sin\theta)$, (θ_{q_1}, w_{q_1}) as the quadrature coefficients on the SDP path, θ_p as the contributing poles, and (θ_b, w_b) as the quadrature parameters on the branch cut, Equation (4) can be rewritten as

$$\begin{aligned}
G^r_{xx}(\mathbf{r}_j,\mathbf{r}_i) =& G^{rSDP}_{xx}(\mathbf{r}_j,\mathbf{r}_i) + G^{rP}_{xx}(\mathbf{r}_j,\mathbf{r}_i) + G^{rB}_{xx}(\mathbf{r}_j,\mathbf{r}_i) \\
=& \frac{i\mu}{8\pi}\sum_{q_1} w_{q_1} f(\theta_{q_1}) H_0^{(1)}(k\rho_{ji}\sin\theta_{q_1}) e^{ikz_{ji^I}\cos\theta_{q_1}} \\
&+ \frac{i\mu k}{8\pi}\sum_{p} \mathrm{Res}\{\theta_p\}\sin\theta_p H_0^{(1)}(k\rho_{ji}\sin\theta_p) e^{ikz_{ji^I}\cos\theta_p} \\
&+ \frac{i\mu}{8\pi}\sum_{b} w_b \left(f^+(\theta_b) - f^-(\theta_b)\right) H_0^{(1)}(k\rho_{ji}\sin\theta_b) e^{ikz_{ji^I}\cos\theta_b} \quad (5)
\end{aligned}$$

where $\mathrm{Res}\{\theta_p\}$ denotes the residue of $\tilde{R}^{TE}(k\sin\theta)$ at $\theta = \theta_p$ and $f^+(\theta)$ corresponds the upper Riemman sheet of k_{Nz} of the outmost layer. For layered medium backed with PEC ground plane, the contribution from the branch point disappears. as we have pointed out in [2]. G^{rSDP}_{xx}, G^{rP}_{xx}, and G^{rB}_{xx} represent the integral along SDP, the pole and branch point contribution, respectively. Up to this point, it is worth to point out that only $f(\theta)$ changes for different dyadic components.

2.3. Diagonalization

Before proceed to diagonalize the translation matrix, we group the source, i.e., $\mathbf{r}_{i^I}$, and observation point, i.e., $\mathbf{r}_j$, into groups, which are centered at $\mathbf{r}_{l'^I}$ and $\mathbf{r}_l$, as shown in Figure 1. Then, by applying the 2D Fast Multipole Method, the Hankel function in Equation (5) can be expressed as the summation of the two dimensional inhomogeneous plane waves. After that, G^{rSDP}_{xx} in Equation (5) can be expressed as

$$\begin{aligned}
& G^{rSDP}_{xx}(\mathbf{r}_j,\mathbf{r}_i) \\
=& \frac{i\mu}{8\pi}\sum_{q_1}\sum_{q_2} w_{q_1} w_{q_2} \beta_{jl}(\theta_{q_1},\phi_{q_2}) \cdot \beta_{l'^I i^I}(\theta_{q_1},\phi_{q_2}) \cdot \\
& f(\theta_{q_1}) T^{2DFMM}_{ll'^I}(k\sin\theta_{q_1},\phi_{q_2}) e^{ikz_{ll'^I}\cos\theta_{q_1}} \\
=& \sum_{q_1}\sum_{q_2} \beta_{jl}(\theta_{q_1},\phi_{q_2}) \cdot T_{ll'^I}(\theta_{q_1},\phi_{q_2}) \cdot \beta_{l'^I i^I}(\theta_{q_1},\phi_{q_2}) \quad (6)
\end{aligned}$$

where

$$T_{ll'l}(\theta_{q_1},\phi_{q_2}) = \frac{i\mu}{8\pi} w_{q_1} w_{q_2} f(\theta_{q_1}) T^{2DFMM}_{ll'l}(k\sin\theta_{q_1},\phi_{q_2}) e^{ikz_{ll'l}\cos\theta_{q_1}} \qquad (7)$$

In the above equations, $T^{2DFMM}_{ll'l}$ stands for the translation coefficients for 2DFMM and $\beta_{l'l_il}$ and β_{jl} represent the far field pattern function for the source and observation groups, respectively.

Denoting $I(\Omega_q,\Omega_s)$ as the interpolation and extrapolation kernel, where $\Omega_q = (\theta_{q_1},\phi_{q_2})$ is the quadrature samples in Equation (6) and Ω_s the samples on real θ and ϕ space, we have

$$\begin{aligned} G^{rSDP}_{xx}(\mathbf{r}_j,\mathbf{r}_i) &= \sum_q T_{ll'l}(\Omega_q) \sum_s I(\Omega_q,\Omega_s)\beta_{jl}(\Omega_s)\cdot\beta_{l'l_il}(\Omega_s) \\ &= \sum_s \beta_{jl}(\Omega_s)\cdot\tilde{T}_{ll'l}(\Omega_s)\cdot\beta_{l'l_il}(\Omega_s) \end{aligned} \qquad (8)$$

where

$$\tilde{T}_{ll'l}(\Omega_s) = \sum_q I(\Omega_q,\Omega_s) T_{ll'l}(\Omega_q) \qquad (9)$$

It is easy to see that Equation (8) yields a diagonal translator, $\tilde{T}_{ll'l}(\Omega_s)$. For the pole and branch point contribution, similar manipulation can be performed.

To this point, it is worth to note some merits of this approach in layered medium.

Observation 1. The information of the layered medium is embedded in the generalized reflection coefficient, i.e., $\tilde{R}^{TE}$ in Equation (1). Therefore, the algorithm developed above is independent of the structure of the layered medium, such as the number of layers, the thickness and the electromagnetic property of each layer.

Observation 2. It is not difficult to see that the contribution from the reflected wave can be accounted for by one term, which is equivalent to placing a source at the mirror image of the source point, although strictly speaking, no image source really exists. This property is desirable when analyzing non-planar structures, which currently is not feasible in FMM/DCIM approach, due to the non-linear relation between the source point and its complex image terms.

Observation 3. The computational complexity for including the reflected wave contribution is the same as that for free space, which is $O(N\log N)$ if multilevel scheme is used.

3. Numerical Results

For illustration purpose and without loss of the generality, we use a simple microstrip structure to validate our algorithm.

In Figure 3, the structure under study, which is a PEC sphere with radius $R = 0.5\lambda$ on top of a single layer medium backed with PEC ground, is shown.

The working frequency is chosen at $f = 0.15$ GHz. The permittivity of the substrate is $\varepsilon_r = 2.56$. The distance between the center of the sphere and the air-dielectric interface is 0.75λ.

Figure 4 and 5 plot the scattered field when the thickness of the substrate is chosen as $t = 0.25\lambda$ and the plane wave is incident from $(\theta^{inc}, \phi^{inc}) = (0^o, 0^o)$. The results are compared with those computed using the traditional CG solver with the matrix elements generated by direct Sommerfeld integration and direct matrix vector multiplication. The agreement is excellent. In Figure 6 and 7, we compare the current distribution on the sphere with or without the presence of the layered medium. The effect of the layered medium is obvious.

4. Conclusion

In this report, we propose the Fast Inhomogeneous Plane Wave Algorithm for the efficient analysis of stratified medium problems. Compared to the previously developed methods for this purpose, the new algorithm has several advantages, such as being simple, accurate, versatile for arbitrary scatterer shape and layered medium structure. Applying this approach to more general problems encountered in the layered medium, such as the electromagnetic scattering from the buried objects within lossy medium, is feasible in principle and is currently under investigation.

References

[1] Gurel, L., and M.I. Aksun, "Fast Multipole Method in Layered Medium: 2-D Electromagnetic Scattering Problems", *Proceedings of 1996 IEEE Antennas and Propagation Society International Symposium*, 1734-1737, 1996.

[2] Hu, B., and W.C. Chew, "Fast Inhomogeneous Plane Wave Algorithm for Electromagnetic Solutions in Layered Medium Structures - 2D Case", accepted by *Radio Science*.

[3] W.C. Chew, *Waves and Fields in Inhomogeneous Media*, Van Nostrand Reinhold, New York, 1990.

[4] Hu, B., W.C. Chew, and S. Velamparambil, "Fast Inhomogeneous Plane Wave Algorithm (FIPWA) for the Analysis of Electromagnetic Scattering", Tech. Rep., Center for Computational Electromagnetics, Dept. of Electrical and Computer Engineering, University of Illinois, Urbana, IL, 1999.

[5] Hu, B., W.C. Chew, E. Michielssen, and J.S. Zhao, "Fast Inhomogeneous Plane Wave Algorithm for the Fast Analysis of Two-Dimensional Scattering Problems", *Radio Science*, Vol. 34, No. 4, pp. 759-772, 1999.

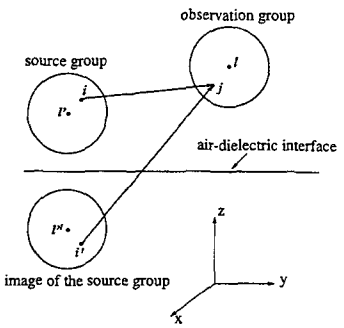


Figure 1. Structure under investigation.

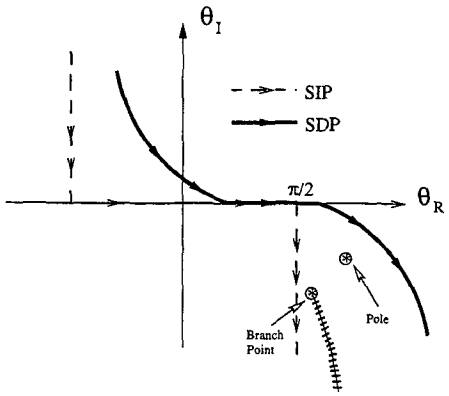


Figure 2. The steepest descent path.

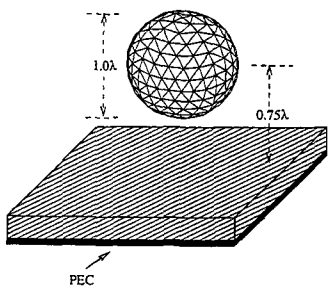


Figure 3. A sphere on top of one layer microstrip structure

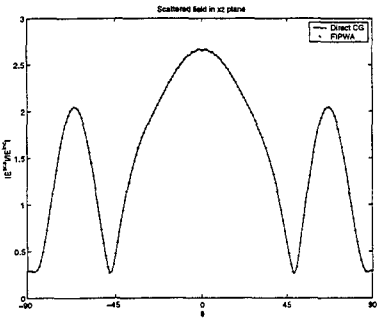


Figure 4. Scattered field in xz plane.

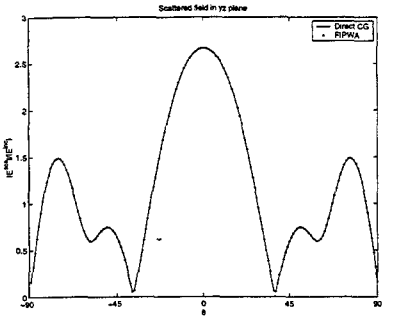


Figure 5. Scattered field in yz plane.

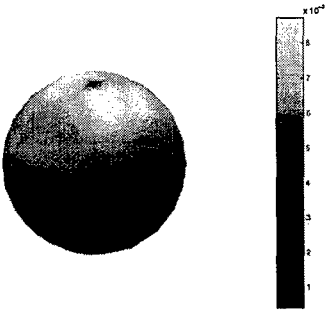


Figure 6. Current Distribution in Free Space

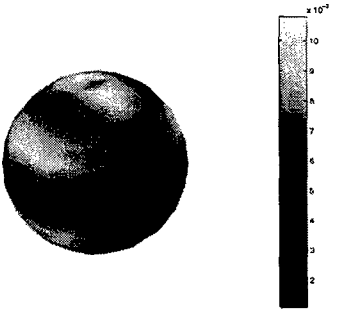


Figure 7. Current distribution with layered medium

Multilevel Fast Multipole Algorithm for Analysis of Large-Scale Microstrip Structures

Feng Ling, Jiming Song, and Jian-Ming Jin

Center for Computational Electromagnetics
Department of Electrical and Computer Engineering
University of Illinois at Urbana-Champaign
Urbana, Illinois 61801-2991

Abstract

An efficient algorithm combining multilevel fast multipole method and the discrete complex image method is presented for analyzing large-scale microstrip structures. The resulting algorithm has the memory requirement and the CPU time per iteration proportional to $O(N \log N)$, where N denotes the number of unknowns. Numerical results for microstrip antennas are presented to demonstrate the efficiency and accuracy of this method.

1 Introduction

The method of moments (MoM) has been widely used for the analysis of microstrip structures, such as microstrip antennas, microwave integrated circuits, and microstrip interconnects. To simulate large-scale complex microstrip structures, it is often necessary to employ a large number of unknowns. For the conventional MoM, the memory requirement is proportional to $O(N^2)$. The computing time can also become very excessive because direct matrix inversion solvers require $O(N^3)$ floating-point operations. When an iterative solver is employed for solving the MoM matrix equation, the operation count is $O(N^2)$ per iteration because of the need to evaluate the matrix-vector multiplication. This operation count is too high for an efficient simulation.

To make the iterative method more efficient, it is necessary to speed up the matrix-vector multiplication. There are several techniques developed for this purpose, including the adaptive integral method (AIM) [1], the fast multipole method (FMM) [2]–[4], and the singular value decomposition based algorithm [5]. Recently, effort has been made to extend these fast algorithms to microstrip problems. The AIM is successfully adapted in [6] with the aid of the discrete complex image method (DCIM) [7]. Extension of FMM is difficult because of its dependence on the Green's function. One approach is to combine FMM with DCIM [8]–[10]. In [8] and [9], which treat the static and 2-D problems, the equivalent problem is set up by adding N_c images at the corresponding complex coordinates, and therefore, represented by $N(N_c+1)$ basis functions. In the FMM implementation, the translation is different for different images. In [10], both the 2-D and 3-D FMMs are employed because the surface-wave poles are extracted in DCIM, which makes the implementation complicated. The multilevel algorithm is not implemented in those analyses. The other FMM approach is to express the Green's function in terms of a rapidly converging steepest descent integral and then to evaluate the Hankel function arising in the integrand by FMM [11]. This approach is good for thin-stratified media.

In this paper, the multilevel fast multipole algorithm (MLFMA) [2], [4] combined with DCIM is presented for efficient analysis of microstrip structures. Instead of being treated separately, the

image sources are grouped with the original source. By the use of the multilevel algorithm, the complexity is reduced to $O(N \log N)$. The algorithm requires little extra computation compared with that applied to free-space problems. Numerical results for microstrip antennas are presented to demonstrate the efficiency and accuracy of this method.

2 Formulations

Consider a general microstrip structure residing on an infinite substrate having relative permittivity ϵ_r and thickness h. The microstrips are in the x-y plane and excited by an applied field $\mathbf{E}^a$. The induced current on the microstrips can be found by solving the well-known mixed potential integral equation (MPIE) [12]. First, the microstrips are divided into triangular elements and then the current is expended using triangular rooftop basis functions. Applying Galerkin's method results in a matrix equation

$$\bar{\mathbf{Z}} \cdot \mathbf{I} = \mathbf{V} \tag{1}$$

in which the impedance matrix $\bar{\mathbf{Z}}$ has the elements given by

$$\begin{aligned} Z_{ij} = j\omega \int_{T_i} \int_{T_j} \Big[& \mathbf{f}_i(\mathbf{r}) \cdot \mathbf{f}_j(\mathbf{r}') G_a(\mathbf{r}, \mathbf{r}') \\ & - \frac{1}{\omega^2} \nabla \cdot \mathbf{f}_i(\mathbf{r}) \nabla' \cdot \mathbf{f}_j(\mathbf{r}') G_q(\mathbf{r}, \mathbf{r}') \Big] d\mathbf{r}' d\mathbf{r} \end{aligned} \tag{2}$$

where $\mathbf{f}_i$ and $\mathbf{f}_j$ represent the testing and basis function, respectively, T_i and T_j denote their supports, G_a is the xx-component of the Green's function for vector potential, and G_q is the Green's function for scalar potential. In general, both G_a and G_q can be expressed as an inverse Hankel transform of their spectral domain counterparts, which is commonly known as the Sommerfeld integral (SI). The analytical solution of the SI is generally not available, and the numerical integration is time consuming. This problem can be alleviated using DCIM [7], which yields closed-form expressions as

$$G(\mathbf{r}, \mathbf{r}') = \sum_{p=0}^{N_c} a_p \frac{e^{-jkr_p}}{4\pi r_p}, \quad r_p = |\mathbf{r} - (\mathbf{r}' + \hat{z} b_p)| \tag{3}$$

where a_p and b_p are the complex coefficients obtained from DCIM.

To use FMM, we first divide the entire structure into groups denoted by $G_m (m = 1, 2, \cdots, M)$. Letting $\mathbf{r}_i$ be the field point in group G_m centered at $\mathbf{r}_m$, and $\mathbf{r}_j$ be the source point in group $G_{m'}$ centered at $\mathbf{r}_{m'}$, we have

$$\begin{aligned} \mathbf{r}_{ij} &= \mathbf{r}_i - (\mathbf{r}_j + \hat{z} b_p) \\ &= (\mathbf{r}_i - \mathbf{r}_m) + (\mathbf{r}_m - \mathbf{r}_{m'}) + (\mathbf{r}_{m'} - \mathbf{r}_j) - \hat{z} b_p \\ &= \mathbf{r}_{im} + \mathbf{r}_{mm'} - \mathbf{r}_{jm'} - \hat{z} b_p. \end{aligned} \tag{4}$$

Employing the addition theorem and the elementary identity [3], we can rewrite the Green's function in (3) as

$$\begin{aligned} G(\mathbf{r}_i, \mathbf{r}_j) \approx \frac{k}{j16\pi^2} \oint \sum_{p=0}^{N_c} a_p e^{j\mathbf{k} \cdot \hat{z} b_p} \\ \times e^{-j\mathbf{k} \cdot (\mathbf{r}_{im} - \mathbf{r}_{jm'})} T(\hat{r}_{mm'} \cdot \hat{k}) d^2 \hat{k} \end{aligned} \tag{5}$$

where

$$T(\hat{r}_{mm'} \cdot \hat{k}) = \sum_{l=0}^{L} (-j)^l (2l+1) h_l^{(2)}(kr_{mm'}) P_l(\hat{r}_{mm'} \cdot \hat{k}). \tag{6}$$

Substituting (5) into (2), we obtain

$$Z_{ij} = \frac{\omega k}{16\pi^2} \Big[\oint S_a(\hat{k}) \mathbf{U}_{im}(\hat{k}) \cdot T(\hat{r}_{mm'}, \hat{k}) \mathbf{U}^*_{jm'}(\hat{k}) d^2\hat{k} - \frac{1}{\omega^2} \oint S_q(\hat{k}) V_{im}(\hat{k}) T(\hat{r}_{mm'}, \hat{k}) V^*_{jm'}(\hat{k}) \Big] d^2\hat{k} \tag{7}$$

where

$$\mathbf{U}_{im}(\hat{k}) = \int_{T_i} e^{-j\mathbf{k}\cdot\mathbf{r}_{im}} \mathbf{f}_i d\mathbf{r} \tag{8}$$

$$V_{im}(\hat{k}) = \int_{T_i} e^{-j\mathbf{k}\cdot\mathbf{r}_{im}} \nabla \cdot \mathbf{f}_i d\mathbf{r} \tag{9}$$

$$S(\hat{k}) = \sum_{p=0}^{N_c} a_p e^{j\mathbf{k}\cdot\hat{z}b_p}. \tag{10}$$

When an iterative method is used to solve (1), the matrix-vector multiplication can be performed in such a way that the contributions from nearby groups are calculated directly and the far interactions are calculated using (7).

The concept of FMM can be extended to multilevel using MLFMA [4]. To implement MLFMA, the entire solution region is first enclosed in a large box, which is divided into four smaller boxes. Each subbox is then recursively subdivided into smaller boxes until the edge length of the finest box is less than half a wavelength. For two elements in the same or nearby finest boxs, their interaction is calculated in a direct manner. However, when the two elements reside in different nonnearby boxes, their interaction is calculated by FMM, as described above. The level of boxes on which FMM is applied depends on the distance between the two elements.

3 Numerical Results

Before the proposed method is applied to realistic problems, the accuracy of this algorithm is examined. Consider a microstrip line on a substrate with relative permittivity $\epsilon_r = 2.17$ and thickness $h = 1.58$ mm. The frequency is 3.0 GHz. The line is 5 mm wide and 400 mm long. As shown in Fig. 1, the line is discretized into triangular elements with edge length 5 mm. Fig. 1 shows the values of matrix elements $Z_{1j}(j = 1, 2, \cdots, 80)$ obtained by using two different approaches. One approach is to use the original formulation (2). The other approach is to use MLFMA, where the group size d is $0.25\lambda_0$ with λ_0 being the wavelength in free space. Note that $Z_{1j}(j = 1, 2, \cdots, 14)$ is considered as the near interaction and is calculated directly, and $Z_{1j}(j = 15, 16, \cdots, 80)$ is considered as the far interaction and is calculated by MLFMA. As seen from Fig. 1, these two approaches agree well. In this calculation, the number of modes L is chosen to be $kd + 3\ln(\pi + kd)$.

Next, the complexity of this algorithm is evaluated. The CPU time per iteration and the memory requirement versus the number of unknowns are plotted in Fig. 2 for solving the problem of a rectangular microstrip patch antenna. It is seen that the CPU time per iteration is scaled as $O(N \log N)$ and the memory requirement is scaled as $O(N)$.

Now consider a corporate-fed microstrip antenna array, which involves 6569 facets and 8668 unknowns. At frequency $f = 9.42$ GHz, the current distribution and the radiation patterns in the

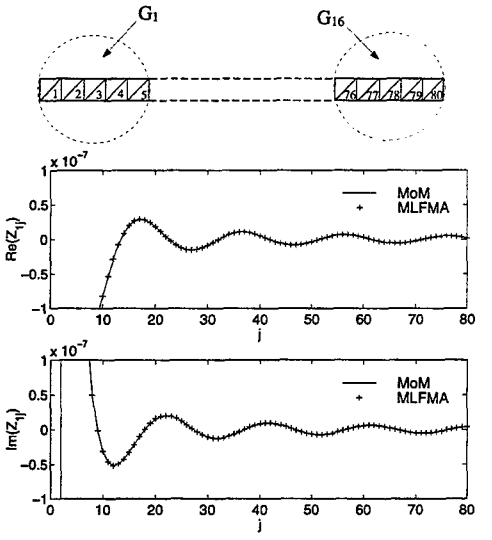


Figure 1: Matrix element $Z_{1j}(j = 1, 2, \cdots, 80)$ calculated by the conventional MoM and MLFMA.

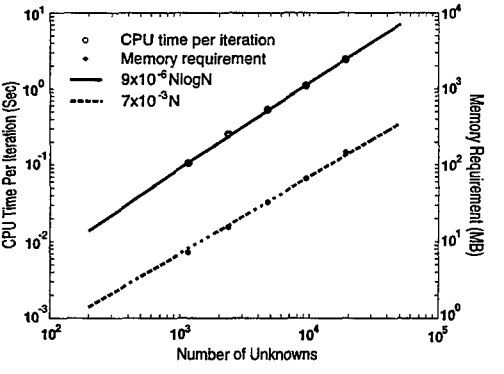


Figure 2: Complexity of MLFMA. The CPU time per iteration is close to $9 \times 10^{-6} N \log N$ and the memory requirement is close to $7 \times 10^{-3} N$.

two principal planes are given in Fig. 3, which shows excellent agreement between this method and the conventional MoM. For the conventional MoM, the memory requirement is over 600 MB and the CPU time per iteration is 15.8 seconds. However, it takes only 36.3 MB and 3.0 seconds for the 5-level MLFMA. The MLFMA also yields an over 70 percent reduction in the CPU time for the matrix fill comparing to the conventional MoM.

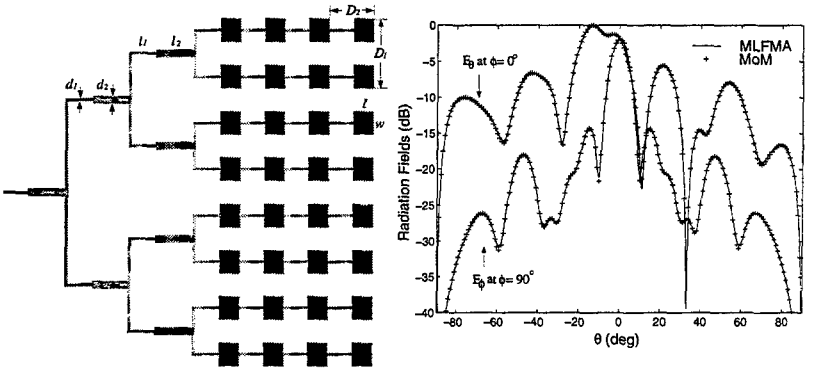


Figure 3: Current distribution and radiation patterns of the corporate-fed microstrip antenna array. $\epsilon_r = 2.2$, $h = 1.59$ mm, $l = 10.08$ mm, $w = 11.79$ mm, $d_1 = 1.3$ mm, $d_2 = 3.93$ mm, $l_1 = 12.32$ mm, $l_2 = 18.48$ mm, $D_1 = 23.58$ mm, $D_2 = 22.40$ mm. $f = 9.42$ GHz.

4 Conclusion

This paper presents a fast algorithm to deal with large-scale microstrip problems. The MLFMA originally developed for free-space problems is extended to microstrip problems with the aid of DCIM. The complexity of this algorithm is scaled as $O(N \log N)$. The efficiency and accuracy of this method is demonstrated by numerical results.

References

[1] E. Bleszynski, M. Bleszynski, and T. Jaroszewicz, "AIM: Adaptive integral method for solving large-scale electromagnetic scattering and radiation problems," *Radio Science*, vol. 31, pp. 1225-1251, Sept.-Oct. 1996.

[2] V. Rokhlin, "Rapid solution of integral equations of scattering in two dimensions," *J. Comput. Phys.*, vol. 86, pp. 414–439, Feb. 1990.

[3] R. Coifman, V. Rokhlin, and S. Wandzura, "The fast multipole method for the wave equation: A pedestrian prescription," *IEEE Antennas Propagat. Mag.*, vol. 35, pp. 7-12, June 1993.

[4] J. M. Song, C. C. Lu, and W. C. Chew, "Multilevel fast multipole algorithm for electromagnetic scattering by large complex objects," *IEEE Trans. Antennas Propagat.*, vol. 45, pp. 1488-1493, Oct. 1997.

[5] S. Kapur and D. E. Long, "IES^3: Efficient electrostatic and electromagnetic simulation," *IEEE Journal Computational Science and Engineering*, pp. 60-67, Oct.-Dec. 1998.

[6] F. Ling, C. F. Wang, and J. M. Jin, "An efficient algorithm for analyzing large-scale microstrip structures using adaptive integral method combined with discrete complex image method," *IEEE APS Int. Symp. Dig.*, vol. 3, pp. 1778-1781, 1998.

[7] Y. L. Chow, J. J. Yang, D. G. Fang, and G. E. Howard, "A closed-form spatial Green's function for the thick microstrip substrate," *IEEE Trans. Microwave Theory Tech.*, vol. 39, pp. 588-592, Mar. 1991.

[8] V. Jandhyala, E. Michielssen, and R. Mittra, "Multipole-accelerated capacitance computation for 3-D structures in a stratified dielectric medium using in a closed form Green's function," *Int. J. Microwave Millimeter-Wave Comput. Aided Engg.*, vol. 5, pp. 68-78, May 1995.

[9] L. Gurel and M. I. Aksun, "Electromagnetic scattering solution of conducting strips in layered media using the fast multipole method," *IEEE Microwave Guided Wave Lett.*, vol. 6, pp. 277-279, Aug. 1996.

[10] P. A. Macdonald and T. Itoh, "Fast simulation of microstrip structures using the fast multipole method," *Int. J. Numerical Modelling: Electronic Networks, Devices and Fields*, vol. 9, pp. 345-357, 1996.

[11] J. S. Zhao, W. C. Chew, C. C. Lu, E. Michielssen, and J. M. Song, "Thin-stratified medium fast-multipole algorithm for solving microstrip structures," *IEEE Trans. Microwave Theory Tech.*, vol. 46, pp. 395-403, Apr. 1998.

[12] J. R. Mosig, "Arbitrarily shaped microstrip structures and their analysis with a mixed potential integral eqtation," *IEEE Trans. Microwave Theory Tech.*, vol. 36, pp. 314–323, Feb. 1988.

A Novel Implementation of Multilevel Fast Multipole Algorithm for Higher-Order Galerkin's Method

K. C. Donepudi, J. M. Song, J. M. Jin, G. Kang, and W. C. Chew

Center for Computational Electromagnetics
Department of Electrical and Computer Engineering
University of Illinois, Urbana, IL 61801
donepudi@students.uiuc.edu

Abstract

A new approach is proposed to enhance the efficiency and reduce the memory requirements of the multilevel fast multipole algorithm (MLFMA) when applied to the higher-order Galerkin's method. This approach represents higher-order basis functions by a set of point sources such that a matrix-vector multiply is equivalent to calculating the fields at a number of points from given current sources at these points. The MLFMA is then applied to calculate the point-to-point interactions. This permits the use of more levels in MLFMA than applying MLFMA to basis-to-basis interactions directly and thus reduces the memory requirements significantly.

1 Introduction

The electromagnetic (EM) interactions with arbitrarily shaped objects can be characterized by seeking the solution of an integral equation whose unknown function is the induced current. In this process, the integral equation is first discretized into a matrix equation using the Galerkin-based method of moments (MoM) with subdomain basis functions such as roof-top functions for curvilinear quad patches and Rao-Wilton-Glisson (RWG) functions [1] for triangular patches. It is convenient to model objects with arbitrary shape using triangular patches and hence RWG functions are widely used for representing the unknown current distribution.

When iterative solvers are used to solve the MoM matrix equation, the calculations of matrix-vector multiplys can be accelerated using fast multipole method (FMM) or multilevel fast multipole algorithm (MLFMA) [2-4]. The FMM reduces the complexity of a matrix-vector multiply from $O(N^2)$ to $O(N^{1.5})$, where N is the number of unknowns. The MLFMA further reduces the complexity to $O(N\log N)$. The memory required by MLFMA is only $O(N\log N)$ and hence one can solve very large problems on existing computers. Integral-equation solvers that use RWG basis functions and employ the standard implementations of MLFMA such as FISC [5,6] and ScaleME [7-9] have been very successful in solving large-scale problems. However, these basis functions have a poor convergence and need a large number of unknowns for a desired accuracy. For example, a sampling rate of 10 unknowns per wavelength (about 200 unknowns per square wavelength for quad patches or 340 unknowns per square wavelength for triangular patches) typically results in an accuracy of 0.1dB in the radar cross section (RCS) calculation. The average edge size of the patches is about 0.1λ. As a result, it is very expensive to achieve a high accuracy by using RWG bases or any other low-order functions. Hence, it is imperative to use higher-order basis functions [10,11]

with vastly superior convergence properties to obtain accurate results using only a fraction of the unknowns required by low-order basis functions. It has been demonstrated [11] that using higher-order basis functions, the sampling rate for an accuracy of 0.1dB in RCS can be reduced to 40 $\sim$ 70 unknowns per square wavelength with an average edge length of $0.5 \sim 1\lambda$.

However, when MLFMA is used to accelerate the solution of the higher-order Galerkin-based MoM [12], its performance is limited for the reason explained below. In MLFMA, only the near interactions of the MoM matrix are computed explicitly whereas the far interactions are computed implicitly by using the multipole expansion of current distributions. In this procedure, the scatterer is first enclosed in a large cube, which is then divided into eight equally sized small cubes. Each of the small cubes is further divided into eight smaller cubes recursively until the smallest cube size is about several times bigger than the longest patch edge. Thus, the edge length limits the number of levels used in MLFMA.

In Galerkin-based MoM using RWG basis functions, since the edge length is about 0.1λ, the finest cube is about a quarter of a wavelength. However, because of the large patch size used with higher-order basis functions, the number of levels in MLFMA is at least one or two less than that for RWG basis functions. In MLFMA, the radiation pattern of each basis is calculated and stored. The number of samplings (K) in the radiation pattern is given by

$$K = 2L^2, \qquad L = kd + \alpha(kd)^{1/3}, \tag{1}$$

where k is the wavenumber, α depends on the accuracy, and d is the diameter of the group size, which is bigger than the cube as shown in Figure 1(a). Each higher-order basis needs much more samplings than the RWG basis. The average number of unknowns required is about 1.5 per patch for RWG basis, 5 and 10.5 for the first- and second-order basis functions, respectively. Thus, the number of unknowns in each group for higher-order basis functions is more than that for RWG basis. Therefore, more near interactions have to be calculated and stored for each higher-order basis. Consequently, MLFMA cannot work efficiently with higher-order Galerkin's method.

To overcome this problem, we propose to implement MLFMA based on point-to-point interactions, instead of the traditional basis-to-basis interactions. When we calculate the matrix elements for which the testing and source bases are not close to each other, we can apply Gaussian quadrature to evaluate the integrals. This process can be interpreted as replacing a continuous source distribution with discrete sources as shown in Figure 1(b). Thus, one matrix-vector multiply is similar to the calculation of the electromagnetic fields for a given distribution of N source bases and then testing them with these bases. In this implementation, we first find Q equivalent point sources from these N source bases, then calculate electromagnetic fields at these Q points, and finally test them with each testing basis. The value of Q depends on the number of patches and the quadrature rule used for each patch. The MLFMA is used to calculate electromagnetic fields at Q points generated by Q point sources. By doing so, the number of levels used is not limited by the size of basis functions, making MLFMA more efficiently. Furthermore, the near interaction part of the MoM matrix is redefined as the difference between the original matrix and the interactions calculated by MLFMA. Consequently, the memory requirement can be reduced as well. In the following section, this approach is first described in detail. Numerical results validating the point-based method are then presented, which are followed by the conclusion.

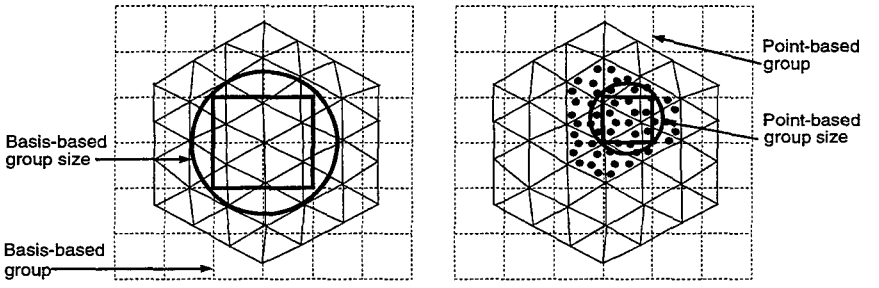


Figure 1: Applying MLFMA to (a) basis-based sources and (b) point-based sources.

2 Applying MLFMA to Point-Based Sources

By testing the electric field integral equation (EFIE) with the basis function $\boldsymbol{t}_j$, the matrix element Z_{ji} is written as

$$Z_{ji} = \int dS \boldsymbol{t}_j(\mathbf{r}) \cdot \int dS' \overline{\mathbf{G}}(\mathbf{r}, \mathbf{r}') \cdot \boldsymbol{t}_i(\mathbf{r}'), \tag{2}$$

where the dyadic Green's function is given by

$$\overline{\mathbf{G}}(\mathbf{r}, \mathbf{r}') = \frac{ik\eta}{4\pi} \left[\overline{\mathbf{I}} - \frac{\nabla\nabla'}{k^2} \right] \frac{e^{ik|\mathbf{r}-\mathbf{r}'|}}{|\mathbf{r}-\mathbf{r}'|}$$

and η denotes the impedance. When the testing basis ($\boldsymbol{t}_j$) is sufficiently far away from the source basis ($\boldsymbol{t}_i$), the integrals can be evaluated by using Gaussian quadrature to give

$$\begin{aligned} Z_{ji}^{\text{far}} &= \sum_{p=1}^{Q} W_{jp} \boldsymbol{t}_j(\mathbf{r}_p) \cdot \sum_{q=1}^{Q} \overline{\mathbf{G}}(\mathbf{r}_p, \mathbf{r}_q) \cdot W_{iq} \boldsymbol{t}_i(\mathbf{r}_q) \\ &= \sum_{p=1}^{Q} \boldsymbol{J}_j(\mathbf{r}_p) \cdot \sum_{q=1}^{Q} \overline{\mathbf{G}}(\mathbf{r}_p, \mathbf{r}_q) \cdot \boldsymbol{J}_i(\mathbf{r}_q), \end{aligned}$$

where Q is total number of quadrature points on all patches, W_{jp} is the quadrature weight at the pth point, which is non-zero only on the patch supporting the basis $\boldsymbol{t}_j$, and $\boldsymbol{J}_j(\mathbf{r}_p)$ is defined as $W_{jp}\boldsymbol{t}_j(\mathbf{r}_p)$. Correspondingly, the matrix-vector multiply for the far interactions is written as

$$\sum_{i=1}^{N} Z_{ji}^{\text{far}} x_i = \sum_{p=1}^{Q} \boldsymbol{J}_j(\mathbf{r}_p) \cdot \sum_{q=1}^{Q} \overline{\mathbf{G}}(\mathbf{r}_p, \mathbf{r}_q) \cdot \sum_{i=1}^{N} \boldsymbol{J}_i(\mathbf{r}_q) x_i, \tag{3}$$

where x_i is the coefficient of the ith basis function. By defining

$$\boldsymbol{E}_p = \sum_{q=1}^{Q} \overline{\mathbf{G}}(\mathbf{r}_p, \mathbf{r}_q) \cdot \boldsymbol{J}_q, \qquad \boldsymbol{J}_q = \sum_{i=1}^{N} \boldsymbol{J}_i(\mathbf{r}_q) x_i, \tag{4}$$

Equation (3) is simplified as

$$\sum_{i=1}^{N} Z_{ji}^{\text{far}} x_i = \sum_{p=1}^{Q} \boldsymbol{J}_j(\mathbf{r}_p) \cdot \boldsymbol{E}_p.$$

The above formulation means that for a given distribution of N source bases, calculate the electric fields and test them with these bases. The MLFMA can be used to calculate the fields generated by current sources very efficiently. Defining a variable I_{pq} such that

$$I_{pq} = \begin{cases} 1 & p\text{-}q \text{ interaction is calculated by MLFMA,} \\ 0 & \text{otherwise,} \end{cases}$$

the matrix-vector multiply calculated by MLFMA is modified as

$$\sum_{i=1}^{N} Z_{ji}^{\text{far}} x_i = \sum_{p=1}^{Q} \boldsymbol{J}_j(\mathbf{r}_p) \cdot \sum_{q=1}^{Q} I_{pq} \overline{\mathbf{G}}(\mathbf{r}_p, \mathbf{r}_q) \cdot \sum_{i=1}^{N} \boldsymbol{J}_i(\mathbf{r}_q) x_i. \tag{5}$$

Now, the near interaction part of the MoM matrix is redefined as the difference between the original matrix and the interactions calculated by MLFMA, so we have

$$Z_{ji}^{\text{near}} = Z_{ji} - Z_{ji}^{\text{far}}, \tag{6}$$

where

$$Z_{ji}^{\text{far}} = \sum_{p} \boldsymbol{J}_j(\mathbf{r}_p) \cdot \sum_{q} I_{pq} \overline{\mathbf{G}}(\mathbf{r}_p, \mathbf{r}_q) \cdot \boldsymbol{J}_i(\mathbf{r}_q).$$

Hence,

$$\begin{aligned} Z_{ji}^{\text{near}} &= Z_{ji} - Z_{ji}^{\text{far}} \\ &= \int dS \boldsymbol{t}_j(\mathbf{r}) \cdot \int dS' \overline{\mathbf{G}}(\mathbf{r}, \mathbf{r}') \boldsymbol{t}_i(\mathbf{r}') - \sum_{p} \boldsymbol{J}_j(\mathbf{r}_p) \cdot \sum_{q} I_{pq} \overline{\mathbf{G}}(\mathbf{r}_p, \mathbf{r}_q) \cdot \boldsymbol{J}_i(\mathbf{r}_q). \end{aligned}$$

If the testing basis $\boldsymbol{t}_j$ and the source basis $\boldsymbol{t}_i$ belong to the nearby groups but are not very close to each other, the same quadrature rule used for evaluating the far interactions is used to calculate the first term of the above equation. If all point-point interactions are calculated by MLFMA, Z_{ji}^{near} equals to zero. Therefore, Z^{near} is a sparse matrix and has less non-zero elements than the matrix for near interactions between bases.

Since the current vector in Equation (4) has two tangential components only, we write it in terms of two independent tangential vectors as

$$\boldsymbol{t}_i(\mathbf{r}_q) = \sum_{l'=1}^{2} \boldsymbol{\Lambda}_{l'}(\mathbf{r}_q) y_{il'}(\mathbf{r}_q). \tag{7}$$

Therefore, current $\boldsymbol{J}_q$ at the qth source point $\mathbf{r}_q$ is written as

$$\begin{aligned} \boldsymbol{J}_q &= \sum_{i=1}^{N} W_{iq} \boldsymbol{t}_i(\mathbf{r}_q) x_i = \sum_{i=1}^{N} W_{iq} \sum_{l'=1}^{2} \boldsymbol{\Lambda}_{l'}(\mathbf{r}_q) y_{il'}(\mathbf{r}_q) x_i \\ &= \sum_{l'=1}^{2} \boldsymbol{\Lambda}_{l'}(\mathbf{r}_q) Y_{l'}(\mathbf{r}_q), \end{aligned} \tag{8}$$

where

$$Y_{l'}(\mathbf{r}_q) = \sum_{i=1}^{N} W_{iq} y_{il'}(\mathbf{r}_q) x_i.$$

Substituting the above expression into Equation (3) yields

$$\sum_{i=1}^{N} Z_{ji}^{\text{far}} x_i = \sum_{p=1}^{Q} \sum_{l=1}^{2} W_{jp} y_{jl} \mathbf{\Lambda}_l(\mathbf{r}_p) \cdot \sum_{q=1}^{Q} \overline{\mathbf{G}}(\mathbf{r}_p, \mathbf{r}_q) \cdot \sum_{l'=1}^{2} \mathbf{\Lambda}_{l'}(\mathbf{r}_q) Y_{l'}(\mathbf{r}_q). \tag{9}$$

Applying the addition theorem to the dyadic Green's function [2-3] yields

$$\begin{aligned} \overline{\mathbf{G}}(\mathbf{r}_p, \mathbf{r}_q) &= \frac{ik\eta}{4\pi} \left[\overline{\mathbf{I}} - \frac{\nabla\nabla}{k^2} \right] \frac{e^{ik|\mathbf{r}_p - \mathbf{r}_q|}}{|\mathbf{r}_p - \mathbf{r}_q|} \\ &= \frac{ik\eta}{4\pi} \int d^2\hat{k} \left(\overline{\mathbf{I}} - \hat{k}\hat{k} \right) e^{-j\mathbf{k}\cdot(\mathbf{r}_{pm} - \mathbf{r}_{qm'})} \alpha(\mathbf{k}, \mathbf{r}_{mm'}), \end{aligned} \tag{10}$$

where

$$\begin{aligned} \alpha(\mathbf{k}, \mathbf{r}_{mm'}) &= \sum_{l=0}^{L} (-j)^l (2l+1) h_l^{(2)}(kr_{mm'}) P_l(\hat{r}_{mm'} \cdot \hat{k}), \\ \mathbf{r}_{pq} &= \mathbf{r}_p - \mathbf{r}_q = \mathbf{r}_p - \mathbf{r}_m + \mathbf{r}_m - \mathbf{r}_{m'} - \mathbf{r}_q = \mathbf{r}_{pm} + \mathbf{r}_{mm'} - \mathbf{r}_{qm'}, \end{aligned}$$

and $\mathbf{r}_m$ and $\mathbf{r}_{m'}$ are the group centers for the points p and q, respectively. Consequently, the far interactions of the matrix-vector multiply can be written as

$$\sum_{i=1}^{N} z_{ji}^{\text{far}} x_i = \sum_{l=1}^{2} U_{jl} \int d^2\hat{k} \mathbf{V}_{mlp}(\mathbf{k}) \sum \alpha_{mm'}(\mathbf{k}, \mathbf{r}_{mm'}) \sum_{q=1}^{Q} \sum_{l'=1}^{2} \mathbf{V}_{m'ql'}^{*}(\mathbf{k}) Y_{l'}(\mathbf{r}_q), \tag{11}$$

where $U_{jl} = W_{jp} y_{jl}$ and the radiation and receiving patterns are given by

$$\mathbf{V}_{mlp}(\mathbf{k}) = e^{i\mathbf{k}\cdot\mathbf{r}_{pm}} (\overline{\mathbf{I}} - \hat{k}\hat{k}) \cdot \mathbf{\Lambda}_l(\mathbf{r}_p). \tag{12}$$

Since the point sources do not have any spatial extent, we can refine the finest cube in MLFMA as small as a quarter of a wavelength. There are two advantages in applying MLFMA to point-to-point interactions. First of all, the group size is the same as the cube and there is no overlapping in sources as shown in Figure 1. Secondly, smaller group size means that much less samplings over the radiation patterns are needed. As a consequence, the memory requirements for the radiation pattern can be reduced. Further reductions can be obtained if the radiation patterns are calculated on the fly since no numerical integration is needed to calculate the radiation pattern.

3 Numerical Results

The inherent advantage in applying MLFMA to the point-based sources is shown by computing the RCS of a perfectly electric conducting (PEC) sphere with different diameters using

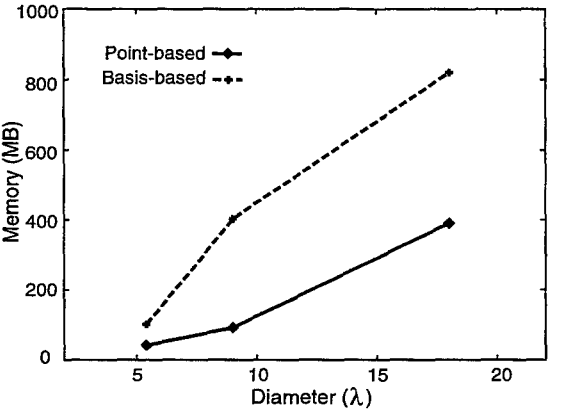


Figure 2: Memory requirements of MLFMA as applied to basis-based and point-based sources. A PEC sphere and the second-order basis functions are used.

the second-order basis functions [11] and then comparing the memory needed for applying MLFMA to basis-based sources as shown in Figure 2. The discretization is kept constant at 33 unknowns per square wavelength and the diameter of the sphere is increased from 5.4λ to 18λ. The corresponding bistatic RCS patterns are plotted in Figures 3 and 4. In Figure 3 the Mie series solution is compared with the basis-based approach and in Figure 4 the point-based and basis-based methods are compared. Compared with the Mie series solution, the RMS error is 0.138dB in the basis-based approach and 0.146dB in the point-based approach. The MLFMA kernel used for all examples in this paper is ScaleME [7-9].

4 Conclusion

A new approach is presented to make the higher-order Galerkin's method work more efficiently with the MLFMA. The far interactions in the matrix-vector multiply are calculated by applying MLFMA to the point interactions. This approach allows one to use two more levels in MLFMA than applying MLFMA to basis interactions directly, and hence reduces the memory requirements significantly. Further reductions can be obtained if the radiation patterns are calculated on the fly.

Acknowledgment: The authors would like to thank Dr. S. Velamparambil for the specialization of ScaleME and his personal communications.

References

[1] S.M. Rao, D.R. Wilton, and A.W. Glisson, "Electromagnetic scattering by surfaces of arbitrary shape," *IEEE Trans. Antennas Propagat.*, vol. 30, pp. 409-418, May 1982.

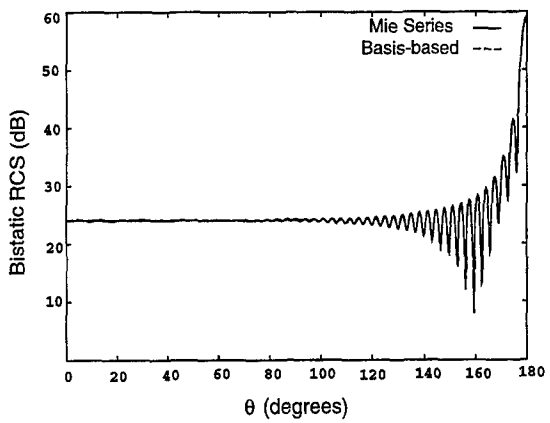


Figure 3: Bistatic RCS for a sphere of 18λ in diameter calculated by the Mie series and MLFMA applied to basis-based sources. The 4-level MLFMA and 820MB are used.

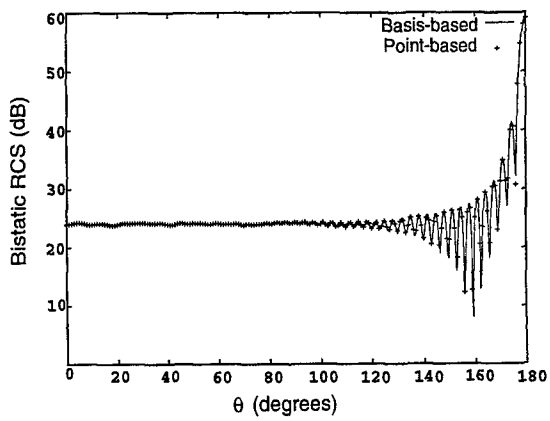


Figure 4: Bistatic RCS for a sphere of 18λ in diameter calculated by MLFMA as applied to basis-based and point-based sources, respectively. In the point-based approach, the 6-level MLFMA and 390MB are used.

[2] R. Coifman, V. Rokhlin and S. Wandzura, "The fast multipole method for the wave equation: A pedestrian prescription," *IEEE Antennas Propagat. Mag.*, vol. 35, no. 3, pp. 7-12, June 1993.

[3] J.M. Song and W.C. Chew, "Multilevel fast multipole algorithm for solving combined field integral equations of electromagnetic scattering," *Microwave Opt. Tech. Lett.*, vol. 10, no. 1, pp. 14-19, September 1995.

[4] J.M. Song, C.C. Lu, and W.C. Chew "MLFMA for electromagnetic scattering from large complex objects", *IEEE Trans. Antennas Propagat.*, vol. 45, PP. 1488-1493, October 1997.

[5] J.M. Song, C.C. Lu, W.C. Chew, and S.W. Lee, "Fast Illinois Solver Code (FISC)," *IEEE Antennas Propagat. Mag.*, vol. 40, no. 3, pp. 27-34, June 1998.

[6] J.M. Song and W.C. Chew, "The Fast Illinois Solver Code: requirements and scaling properties," *IEEE Computational Science and Engineering*, vol. 5, no. 3, pp. 19-23, July-Sept. 1998.

[7] S. Velamparambil, J.M. Song, and W.C. Chew, "A portable parallel multilevel fast multipole solver for scattering from perfectly conducting bodies," *IEEE APS Int. Symp. Dig.*, vol. 1, pp. 648-651, July 1999.

[8] S. Velamparambil and W.C. Chew, "ScaleME: Application interface. A programmer's guide and reference," Tech. Rep. CCEM-27-99, Univ. of Illinois, Oct. 8, 1999.

[9] S. Velamparambil, J.M. Song, and W.C. Chew, "ScaleME: A portable, distributed memory multilevel fast multipole kernel for electromagnetic and acoustic integral equation solvers," Tech. Rep. CCEM-23-99, Univ. of Illinois, Sept. 7, 1999.

[10] R.D. Graglia, D.R. Wilton, and A.F. Peterson, "Higher order interpolatory vector bases for computational electromagnetics," *IEEE Trans. Antennas Propagat.*, vol. 45, no. 3, pp. 329-342, March 1997.

[11] K. Donepudi, G. Kang, J.M. Song, J.M. Jin, and W.C. Chew, "Higher-order MoM implementation to solve integral equations," *IEEE APS Int. Symp. Dig.*, vol. 3, pp. 1716-1719, 1999.

[12] K. Donepudi, J.M. Jin, S. Velamparambil, J.M. Song, and W.C. Chew, "A higher-order parallelized multilevel fast multipole algorithm for 3d scattering," submitted to *IEEE Trans. Antennas Propagat.*, 1999.

Incomplete LU preconditioner for FMM implementation

Kubilay Sertel and John L. Volakis
Radiation Laboratory, EECS Department, University of Michigan
Ann Arbor, MI 48109-2122, USA
E-mail : {ksertel, volakis}@umich.edu

Abstract

Incomplete LU (ILU) preconditioner using the near-field matrix of the fast multipole method (FMM) is investigated to increase the efficiency of the iterative conjugate gradient squared (CGS) solver. Unlike the conventional LU, ILU requires no fill-ins hence no extra memory and CPU time in computing the LU decomposed preconditioner. It is shown that due to the nature of the near-field matrix, ILU preconditioning decreases the number of iterations dramatically.

Introduction

The FMM has been proposed and successfully applied to increase the efficiency of the method of moments (MoM) solution of large scale electromagnetic scattering and radiation problems [1, 2, 3, 4, 5, 6, 7, 8, 9, 10, 11]. The FMM is based on the iterative solution of the MoM matrix equation using an indirect fast computation of the matrix vector product. The convergence behavior is strongly dependent on the condition of the constructed matrix as well as the iterative solver being used. Various iterative solvers are available including the conjugate gradient (CG), biconjugate gradient (BiCG), conjugate gradient squared (CGS), quasi-minimal residual (QMR), and generalized minimal residual (GMRES). The convergence of all these iterative solvers is dictated by the matrix condition which typically deteriorates as the matrix size increases. Therefore, iterative solutions of such large, fully populated matrix systems inevitably requires some kind of preconditioning. Otherwise, propagation of numerical errors during the execution of the iterative solution may lead to convergence failure.

Various preconditioning techniques for improving the condition of the system can be found in [12]. Diagonal and block diagonal preconditioners for multilevel FMM implementations were reported in [6]. Here we present

an ILU preconditioner for MoM and FMM implementations. By its nature, the ILU preconditioner is constructed using the near-field FMM matrix and is shown to significantly reduce the number of iterations required for convergence.

Method of Moments and the Fast Multipole Method

The MoM formulation of electromagnetic scattering problems using 2^{nd} order curvilinear quadrilateral elements for surface modeling is given in [13]. The FMM implementation used herewith was built upon that in [13, 14].

Briefly, for the electric field integral equation (EFIE) the resulting linear system after Galerkin's testing is of the form

$$\sum_{n=1}^{N} Z_{mn} a_n = V_m, \qquad m = 1, 2, \ldots, N \tag{1}$$

where

$$Z_{mn} = \int_s ds \mathbf{f}_m(\mathbf{r}) \cdot \int_{s'} ds' \left[\mathbf{f}_n(\mathbf{r}') + \frac{1}{k^2} \nabla' \cdot \mathbf{f}_n(\mathbf{r}') \nabla \right] \frac{e^{ikR}}{R} \tag{2}$$

and

$$V_m = \frac{4\pi i}{k\eta} \int_s ds\, \mathbf{f}_m(\mathbf{r}) \cdot \mathbf{E}^i(\mathbf{r}). \tag{3}$$

Througout, an $e^{-i\omega t}$ time convention has been assumed and suppressed. Here, $\{a_n\}$ refers to the column containing the unknown coefficients of the surface current expansion

$$\mathbf{J}(\mathbf{r}) \approx \sum_{n=1}^{N} a_n \mathbf{j}_n(\mathbf{r}). \tag{4}$$

In the above expressions, $\mathbf{r}$ and $\mathbf{r}'$ denote the usual observation and source point locations, $\mathbf{E}^i(\mathbf{r})$ is the incident excitation plane wave at $\mathbf{r}$, $\hat{t}$ is the vector tangent to the surface at $\mathbf{r}$, $\eta = 120\pi$ denotes the free space impedance, and $k = 2\pi/\lambda$ is the free space wavenumber.

The key aspects of the FMM implementation are

- Iterative solution of the MoM system of equations $[Z]\{a\} = \{V\}$

- Fast evaluation of the matrix vector product $[Z]\{a\}$.

Fast evaluation of the matrix vector product (using $O(N^{1.5})$ or less resources, instead of $O(N^2)$) is attained by approximating the pertinent Green's function [1]. It can be shown [1] that the CPU time per iteration/matrix vector product for FMM is $O(N^{1.5})$ instead of $O(N^2)$.

The above CPU estimates are asymptotic in the sense that they represent values which are approached for very large N. The actual efficiency of the implementation depends on the choice of various parameters. These choices control the constant in front of the asymptotic behavior of the CPU requirements. However, choices of the FMM parameters for faster implementation inevitably lead to errors in the matrix vector product inducing erroneous minima for the iterative solver. This aspect may lead to unacceptable error since it may cause the solver to converge at one of these minima, especially when non-monotonic solvers (e.g. CG, BiCG, or CGS) are employed.

The specific integral equation formulation, be it the EFIE, MFIE, or CFIE, also affects the solution convergence.

Preconditioning Necessity

For large scale simulations possibly with geometrical surface details (e.g. antenna arrays on aircraft), the density of the surface mesh cannot be expected to be uniform. Nevertheless, a nonuniform mesh is well known to produce ill-conditioned MoM matrix equations. Also, different formulations of the same electromagnetic problem results in different system conditions, e.g. the CFIE formulation results in much better conditioned systems than the EFIE or MFIE. Also, as noted above, the FMM implementation introduces erroneous minima in the solution domain. Use of a preconditioner is therefore essential for robust implementations of iterative solvers.

Although the diagonal preconditioner is simple and leads to significant convergence improvements, it does so for diagonally dominant matrices. Block diagonal preconditioners are more robust but require renumbering of the grid or matrix rearranging so that the dominant matrix terms are clustered around the diagonal. This can easily be done for 2D problems, but is very difficult in 3D. Alternatively, when the FMM is used to speed up the iterative solution, we have the natural choice of using the near-field portion of the MoM matrix for preconditioning. These near-field elements

are the largest in magnitude and constitute the unapproximated portion of the system matrix.

To develop the preconditioner, the near-field matrix can be directly decomposed via LU. However, depending on the sparsity pattern of the near-field matrix, this LU process may require a significant amount of fill-ins. For large scale simulations, these fill-ins (hence the increase in memory usage) becomes a bottleneck in memory utilization. Alternatively, the fill-in requirement of direct LU can be resolved by using the ILU factorization. The ILU algorithm is the same as a direct LU algorithm except that it avoids fill-ins of elements in the decomposed LU matrices. This also results in less CPU utilization.

ILU Preconditioner for FMM

The algorithm for the ILU can be found in [12]. The pseudo code is repeated below for completeness:

```
for i = 2,...,n, do:
   for k = 1,...,i-1 and for (i,k) in NZ(Z) do:
      compute z_ik = z_ik / z_kk
      for j = k+1,...,n and for (i,j) in NZ(Z) do:
         compute z_ij = z_ij - z_ik z_kj
      end do
   end do
end do
```

Here `NZ(Z)` is the sparsity pattern of the near-field matrix `Z`, and the conventional LU decomposition algorithm is only applied to the non-zero entries of the matrix, hence the memory used is not affected and the sparsity pattern of the stored ILU matrix is the same as the original matrix which further saves memory in the sparse storage of the ILU matrix.

Performance of Preconditioned CGS Solver

To evaluate the performance of the ILU preconditioner, we considered a perfectly electrically conducting (PEC) ogive geometry (depicted in Fig. 1). For this study, the ILU preconditioner was implemented in the matrix systems

based on the EFIE, MFIE, and CFIE formulations. Again, the FMM near-field matrix is used as the preconditioner and the CGS iterative solver was used. The size of the matrix system was 480 and refers to a $10'' \times 2'' \times 2''$ ogive with its long axis coincident with the x-axis. All calculations were carried out at 5.91 GHz.

Fig. 2 shows the residual error as a function of iteration number for the EFIE matrix. It is seen that due to the irregular mesh around the sharp tips of the ogive, the CGS solver does not converge in less than 50 iterations without preconditioning. However, when the ILU preconditioner is used, convergence is dramatically improved, needing only and $N/50$ iterations to achieve an error of 10^{-5}.

Non-preconditioned and preconditioned solution data for the MFIE matrix are given in Fig. 3. Since the MFIE formulation produces better conditioned systems, the residual error behavior of the MFIE is better than that of the EFIE. Nevertheless, convergence without preconditioning is very slow. When the ILU preconditioner is included we reach convergence down to 10^{-5} in about $N/150$ iterations. Fig. 4 gives corresponding convergence curves for the CFIE matrix. Since the CFIE system is better conditioned, convergence is now achieved even without preconditioning. Use of ILU simply improves the convergence again from $N/25$ down to $N/150$ to reach an error of 10^{-5}.

Table 1 summarizes the performance of the ILU preconditioner for a larger problem. The scatterer in this simulation has sharp edges and tips as well as smooth sections. Also, the mesh is quite distorted and non-uniform around these edges. Nevertheless, the performance of the ILU preconditioner is quite impressive. Specifically, ILU improved the convergence of the CFIE ($\alpha = 0.5$) matrix down to $N/10,000$. leading to a solution time of only 5 minutes for a 53,000 unknown system on an 8-processor SGI Origin 2000.

Based on the above performance evaluations, we can conclude that the ILU preconditioner can be used to improve the performance of iterative solvers in FMM implementations without increasing memory utilization for the preconditioner matrix.

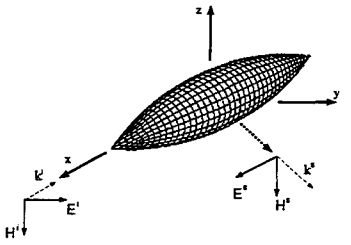


Figure 1: Ogive geometry and the simulation setup

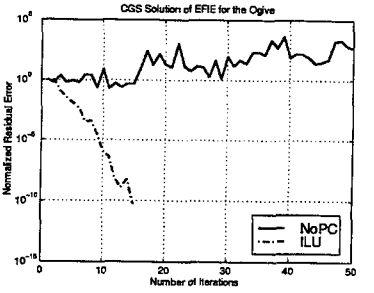


Figure 2: Performance of ILU in conjunction with EFIE formulation

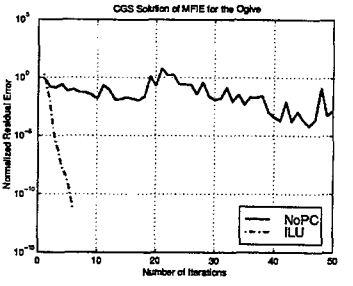


Figure 3: Performance of ILU in conjunction with MFIE formulation

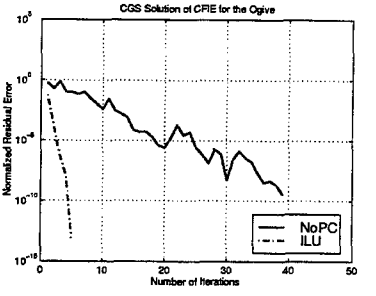


Figure 4: Performance of ILU in conjunction with CFIE($\alpha = 0.5$) formulation

Number of Unknowns	Matrix Fill Time(min) (8 proc.)	Precond. LU Time(min) (1 proc.)	Number of Iter.	Residual Error	Time per Solution(min) (8 proc.)
53000	77	81	5	0.001	5

Table 1: Performance of ILU for a large-scale complex target with sharp edges an tips on 8 processor SGI Origin 2000.

References

[1] Coifman, R., V. Rokhlin, and S. Wandzura, "The Fast Multipole Method for the Wave Equation: A Pedestrian Prescription," *IEEE Antennas and Propagat. Mag.*, vol. 35, pp. 7–12, Jun. 1993.

[2] Chew, W. C., J. Jin, C. Lu, E. Michielssen, and J. M. Song, "Fast Solution Methods in Electromagnetics," *IEEE Trans. Antennas Propagat.*, vol. AP-45, no. 3, pp. 533–543, Mar. 1997.

[3] Lu, N. and J.-M. Jin, "Application of the Fast Multipole Method to Finite–Element Boundary–Integral Solution of Scattering Problems," *IEEE Trans. Antennas Propagat.*, vol. AP-44, no. 6, pp. 781–786, 1996.

[4] Volakis, J. L., A. Chatterjee, and L. C. Kempel, *Finite Element Methods for Electromagnetics*, Piscataway, NJ:IEEE Press, 1998.

[5] Burkholder, R. J. and D. H. Kwon, "High frequency asymptotic acceleration of the fast multipole method," *Radio Sci.*, vol. 31, pp. 1199-1206, 1996.

[6] Song, J. M., C. C. Lu, and W. C. Chew, "Multilevel Fast Multipole Algorithm for Electromagnetic Scattering by Large Complex Objects," *IEEE Trans. Antennas Propagat.*, vol. AP-45, no. 10, pp. 1488–1493, 1997.

[7] Bindiganavale, S. S. and J. L. Volakis, "Comparison of Three FMM Techniques for Solving Hybrid FE/BI Systems," *IEEE Trans. Antennas Propagat.*, vol. AP-39, no. 4, pp. 47–59, Aug. 1997.

[8] R. L. Wagner and C. W. Chew, "A Ray-Propagation Fast Multipole Algorithm," *Microwave Opt. Tech. Lett.*, vol. 7, no. 7, pp. 435–438, Jul. 1994.

[9] Lu, N. and W. C. Chew, "Fast Far-Field Approximation for Calculating the RCS of Large Objects," *Microwave Opt. Tech. Lett.*, vol. 8, no. 5, pp. 238–241, 1995.

[10] Song, J. M. and W. C. Chew, "Multilevel Fast Multipole Algorithm for Solving Combined Field Integral Equations of Electromagnetic Scattering," *Microwave Opt. Tech. Lett.*, vol. 10, no. 1, pp. 14–19, Sep. 1995.

[11] Song, J. M. and W. C. Chew, "Fast Multipole Method Solution Using Parametric Geometry," *Microwave Opt. Tech. Lett.*, vol. 7, no. 16, pp. 760–765, Nov. 1994.

[12] Saad, Y., *Iterative Methods for Sparse Linear Systems*, Boston: PWS Pub. Co., 1996.

[13] G. E. Antilla and N. G. Alexopoulos, "Scattering from Complex 3D Geometries by a Curvilinear Hybrid Finite Element-Integral Equation Approach", *J. Opt. Soc. Am. A*, Vol. 11, No. 4, pp. 1445-1457, 1994

[14] Sertel, K. and J. L. Volakis, "The Effect of FMM Parameters on the Solution of PEC Scattering Problems," *IEEE Antennas Propagat. Symp.*, vol. 1, pp. 624–627, 1999.

A Fast, High-Order Scattering Code for Solving Practical RCS Problems

J. J. Ottusch, J. L. Visher, and S. M. Wandzura

HRL Laboratories, LLC
3011 Malibu Canyon Road
Malibu, CA 90265

Voice: (310) 317-5769 Fax: (310) 317-5958
e-mail: ottusch@hrl.com

Abstract

The FastScat(TM) scattering code has been adapted to solve RCS problems involving targets comprised of penetrable materials. Like its PEC-only predecessor, this code enjoys the simplicity and performance benefits provided by a high-order, point-based discretization and a scalable, parallel implementation of a multi-level, fast multipole method solver.

1 Introduction

The essential features of the general $3d$ scattering problem are contained in the more restricted problem of scattering from perfectly conducting (PEC) targets. Methods that are useful for solving this problem can often be profitably employed, with straightforward modification, to solve the general scattering problem.

These principles guided the initial development of FastScat, a frequency domain, boundary integral equation scattering code created over the past several years at HRL Laboratories. By restricting the target class to PECs, we could focus on developing and applying algorithmic advances to the practice of solving large scale RCS problems. The result was an improved tool for computational electromagnetics. The algorithmic advances incorporated into the PEC-only version of FastScat include a high-order, point-based (Nyström) discretization and an efficient, scalable parallel implementation of the multi-level FMM (fast multipole method). Previously-reported results[1] demonstrate that this code achieved its goal of greatly extending the range and improving the accuracy and efficiency of practical scattering calculations involving PECs.

Motivated by a desire to compute scattering from more realistic targets, we have recently rewritten our scattering code to be able to handle penetrable regions in addition to PECs. Although the transition to more general boundary conditions necessitated the addition of some new

data structures and involved some code restructuring, the numerical algorithms that form the basis of the PEC-only code carried through to the materials code with little or no modification. And they are similarly effective.

This paper is an overview of our method for computing scattering from targets comprised of homogeneous, isotropic regions (which includes dielectrics, PECs, impedance surfaces, and partially conducting surfaces). We describe the modifications that were needed to make the basic algorithms of the PEC-only code work with multiple regions and complex dielectric constants and present some preliminary results obtained with the materials code on simple targets. The presentation presupposes familiarity on the part of the reader with the multi-level FMM and high-order, point-based discretizations. Introductory presentations of these topics may be found in [2], [3], and [4]. Parallel implementation issues are discussed in [1].

2 Formulation

The two main differences between the penetrable material scattering problem and the PEC-only problem are: 1) the target may contain multiple volumes with different propagation constants and 2) at the interfaces between dielectric volumes it becomes necessary to compute magnetic currents[1] (corresponding to tangential electric fields) in addition to the usual electric currents (corresponding to tangential magnetic fields).

One can think of the composite scattering problem as that of several separate scattering problems, one for each penetrable volume, that are coupled by means of the boundary conditions on the fields at the interfaces between adjoining volumes. The equivalent sources $\mathbf{J}$ and $\mathbf{M}$ on (the inside of) the boundary S of a given volume V are related to the exciting fields $\mathbf{E}^i$ and $\mathbf{H}^i$ coming from the interior of V by

$$-\hat{\mathbf{n}} \times \mathbf{E}^i = \mu L\mathbf{J} + \left(K + \frac{1}{2}\right)\mathbf{M} \tag{1}$$

and

$$\hat{\mathbf{n}} \times \mathbf{H}^i = -\epsilon L\mathbf{M} + \left(K + \frac{1}{2}\right)\mathbf{J}, \tag{2}$$

where ϵ and μ are the dielectric constants of the volume, $\mathbf{J} \equiv \hat{\mathbf{n}} \times \mathbf{H}$, $\mathbf{M} \equiv -\hat{\mathbf{n}} \times \mathbf{E}$, $\hat{\mathbf{n}}$ is the unit normal pointing into the volume, L and K are integral operators given by

$$L \equiv \hat{\mathbf{n}} \times \int_S ds'\, i\omega \left(1 + \frac{1}{k^2}\nabla'\nabla'\right) G(\mathbf{x}, \mathbf{x}') \cdot \tag{3}$$

and

$$K \equiv \hat{\mathbf{n}} \times \int_S ds'\, \nabla' G(\mathbf{x}, \mathbf{x}') \times, \tag{4}$$

[1] Whereas the computed electric currents represent physical currents in the PEC case, both the magnetic and electric currents should be regarded merely as equivalent currents at certain interfaces, such as those between dielectrics.

and the kernel G is defined by

$$G(\mathbf{x},\mathbf{x}') \equiv \frac{e^{ikr}}{4\pi r}; \quad r = |\mathbf{x}-\mathbf{x}'|. \tag{5}$$

Note that the propagation wavenumber

$$k = \sqrt{\epsilon\mu}\omega \tag{6}$$

is specific to the dielectric properties inside the volume.

At an interface between two volumes, the relationship between $\mathbf{J}$ and $\mathbf{M}$ on either side of the interface is given by the boundary conditions. For example, at the interface between two dielectric volumes, the requirement that the tangential components of $\mathbf{E}$ and $\mathbf{H}$ be continuous across the boundary is equivalent to the statement that $\mathbf{J}$ and $\mathbf{M}$ must be opposites on the two sides. In this case, $\mathbf{J} = \mathbf{J}^+ = -\mathbf{J}^-$ and $\mathbf{M} = \mathbf{M}^+ = -\mathbf{M}^-$ can be determined by integral relations such as

$$-\hat{\mathbf{n}} \times \mathbf{E}^{i,\pm} = \pm(\mu L)^{\pm}\mathbf{J} + \left(\pm K^{\pm} + \frac{1}{2}\right)\mathbf{M} \tag{7}$$

and

$$\hat{\mathbf{n}} \times \mathbf{H}^{i,\pm} = \mp(\epsilon L)^{\pm}\mathbf{M} + \left(\pm K^{\pm} + \frac{1}{2}\right)\mathbf{J}, \tag{8}$$

where the $\pm$ superscript signifies the volume with which the source, field, or integral operator is associated (as written, the $+$ volume is the one into which a surface normal, uniquely defined on the boundary, points). There are different ways to combine these equations into a CFIE. We used the particular combination

$$-\hat{\mathbf{n}} \times \left(\mathbf{E}^{i,+} + \mathbf{E}^{i,-}\right) = \left((\mu L)^{+} - (\mu L)^{-}\right)\mathbf{J} + \left(K^{+} - K^{-} + 1\right)\mathbf{M} \tag{9}$$

$$\hat{\mathbf{n}} \times \left(\mathbf{H}^{i,+} + \mathbf{H}^{i,-}\right) = -\left((\epsilon L)^{+} - (\epsilon L)^{-}\right)\mathbf{M} + \left(K^{+} - K^{-} + 1\right)\mathbf{J} \tag{10}$$

which reduces to

$$-\hat{\mathbf{n}} \times \left(\mathbf{E}^{i,+} + \mathbf{E}^{i,-}\right) = \mathbf{M} \tag{11}$$

$$\hat{\mathbf{n}} \times \left(\mathbf{H}^{i,+} + \mathbf{H}^{i,-}\right) = \mathbf{J} \tag{12}$$

in the limit as the dielectric properties on the two sides become identical.

In some other cases, the $\mathbf{E}$ and $\mathbf{H}$ fields are discontinuous across the boundary (e.g. dielectric volumes separated by a partially conducting sheet), in which case the integral relations between $\mathbf{J}$ and $\mathbf{M}$ take a slightly different form. In all cases, however, one needs only to evaluate the L and K operators and the excitations (which may be zero) on one or both sides of the boundary to determine $\mathbf{J}$ and, if needed, $\mathbf{M}$.

3 Implementation

In the PEC-only code, two unknowns are associated with each discretization point on the surface. Each unknown corresponds to the amplitude of the electric current $\mathbf{J}$ in one of two independent surface tangent directions. The discretization points are distributed according to a high-order quadrature rule on a high-order representation of the physical scattering surface.

The method for numerically evaluating and applying the integral operators L and K is different depending on whether the operation connects field and source points that are nearby of far apart. Near interactions (including self interactions) are computed using locally-corrected quadrature rules. Local corrections restore high-order convergence to a quadrature rule in the presence of kernel singularities that would otherwise destroy the rule's high-order behavior. Since they are needed only for nearby interactions, the matrix of local corrections is sparse. It can be saved and reused.

Far interactions are computed by means of a multi-level FMM. The FMM makes use of the fact that relatively few multipoles are required to accurately compute interactions between well-separated collections of sources. By organizing sources into groups whose outgoing and incoming fields can be represented as sums of plane waves, one can significantly reduce the operation count needed to compute far interactions (e.g., with N interacting sources, the operation count is $\mathcal{O}\left(N^{3/2}\right)$ for a single-level FMM, as compared to $\mathcal{O}\left(N^2\right)$ for the direct interaction approach). Expanding the fields in terms of plane waves is key to making the FMM an efficient method; sparsity of the FMM decomposition depends on the fact that the operation of translating plane waves from a source group to a field group does not mix the terms associated with different propagation directions. The multi-level FMM obtains an additional speedup by organizing small groups (at the lowest level) into larger groups, these into still larger groups, and so on. The net result is that fewer plane wave translations are required and the overall operation count decreases (asymptotically) to $\mathcal{O}\left(N \log^2\left(N\right)\right)$. Storage requirements decrease similarly.

The transition from a PEC-only code to a materials code required:

- the addition of magnetic source unknowns at boundaries that can support non-vanishing tangential electric fields,
- computation of two sets of local corrections (one for each volume) at interfaces between penetrable volumes, and
- construction of separate FMM operators for each volume.

Contrary to what one might expect, it is not necessary to construct separate FMM operators for $\mathbf{E}$ and $\mathbf{H}$ fields. The reason is that, for each plane wave term in the expansion, one field is simply the a 90°-rotated version of the other.

Allowing for complex-valued dielectric constants, and therefore complex values for k, also had a negligible impact on the FMM. Its effect on the local corrections was not completely negligible, however, insofar as it necessitated that local corrections be computed not just for the real part of the kernel (which is singular) but also for its imaginary part (which is regular whenever k is real). The singularity in the imaginary part comes from the added factor of $\exp\left(-k_i r\right)$, which has a cusp at vanishing separation for non-zero values of the imaginary part of k.

4 Results

As in the PEC case, the canonical target for initial validation of a $3d$ scattering code is a sphere, because computed solutions can be compared against Mie series solutions. In the materials case, the sphere may consist of one or more dielectric shells. Figure 1 compares bistatic cross sections obtained from the Mie series against those computed by FastScat for a four-layer sphere consisting of a 1λ-radius IBC (impedance boundary condition) core surrounded by three 0.1λ-thick dielectric layers. Each dielectric layer has a partially-conductive coating. The (complex-valued) material parameters of the layers are given in Table 1.

The FastScat computation used a discretization produced by meshing each spherical boundary layer into 320 triangular spherical patches and placing a 15-point quadrature rule on each patch. The (admittedly over-refined) discretization that resulted had a total of 19200 sample points and 67200 unknowns. The RMS error of the computed solutions (as compared to the Mie series) are 0.001 dB ($\phi\phi$) and 0.005 dB ($\theta\theta$). The calculation made use of 3 FMM levels and a CFIE formulation.

The result of another calculation is displayed in Figure 2. In this case the target is a $6\lambda \times 3\lambda \times 1\lambda$ slab of uniform dielectric with index of refraction equal to 2. The graphic shows the intensity pattern of the equivalent electric current (i.e., surface magnetic field) for a vertically-polarized plane wave normally incident on the $3\lambda \times 1\lambda$ face. In this case, the surface was meshed into $1/4$-λ square patches and a 16-point quadrature rule (the product of two 4-point Gauss-Legendre product rules) was placed on each patch. The inside and outside FMM operators both had 5 levels.

The PEC-only version of FastScat can import high-order geometry descriptions produced by a CAD program. We regularly read in meshes generated by PATRAN, which can export a mesh composed of bicubic quadrilaterals. We are presently adapting this code to handle CAD descriptions of more general targets with material properties. When this task is complete, the new version of FastScat will be able to attack a large class of interesting problems involving realistic targets. We are also in the process of implementing a Nyström-discretized, high-order description of waveguide apertures and excitations [5].

5 Summary

The FastScat RCS code has been augmented to be able to handle targets comprised of homogeneous, isotropic penetrable materials in addition to PECs. The new code draws on the unique and powerful methods of its PEC-only predecessor, such as a high-order, point-based discretization and a scalable, parallel implementation of the multi-level fast multipole method. Enhancements to the code to allow for waveguide apertures and CAD-specified geometry descriptions are presently in development.

References

[1] J. J. Ottusch, M. A. Stalzer, J. L. Visher, and S. M. Wandzura, "Scalable electromagnetic scattering calculations for the SGI Origin 2000," in *Proceedings SC99*, (Portland, OR), IEEE,

Nov. 1999.

[2] R. Coifman, V. Rokhlin, and S. Wandzura, "The fast multipole method: A pedestrian prescription," *IEEE Antennas and Propagation Society Magazine*, vol. 35, pp. 7–12, June 1993.

[3] M. F. Gyure and M. A. Stalzer, "A prescription for the multilevel Helmholtz FMM," *IEEE Computational Science & Engineering*, vol. 5, pp. 39–47, July 1998.

[4] L. S. Canino, J. J. Ottusch, M. A. Stalzer, J. L. Visher, and S. M. Wandzura, "Numerical solution of the Helmholtz equation in $2d$ and $3d$ using a high-order Nyström discretization," *Journal of Computational Physics*, vol. 146, pp. 627–663, 1998.

[5] J. J. Ottusch, G. C. Valley, and S. Wandzura, "Integral equations and discretizations for waveguide apertures," *IEEE Transactions on Antennas and Propagation*, vol. 46, no. 11, pp. 1727–1738, 1998.

r(λ)	η	ϵ	μ	σ
1.0	0.1-0.2i			
1.1		1.6+0.3i	1.6-0.2i	0.3-0.2i
1.2		2.2+0.2i	2.6+1.2i	0.4-0.5i
1.3		1.6+0.7i	1.6+1.4i	1.4-0.5i

Table 1: Material parameters for 4-layer sphere. η (surface impedance); ϵ and μ (volume dielectric constants); σ (surface conductivity)

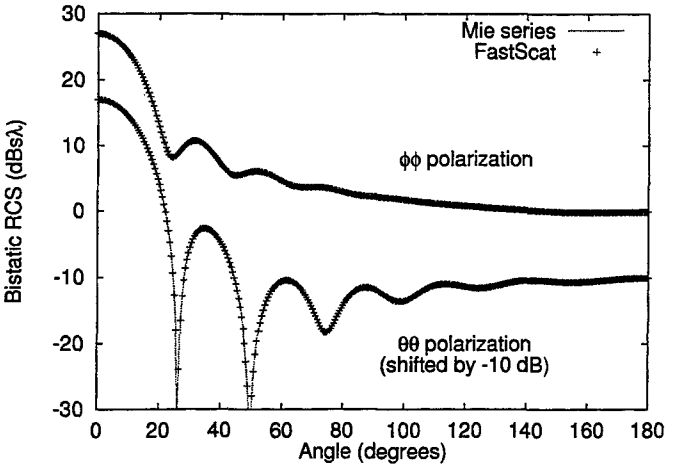


Figure 1: Comparison of Mie series and FastScat solutions for a 1λ-radius PEC sphere with three 0.1λ-thick dielectric coating layers.

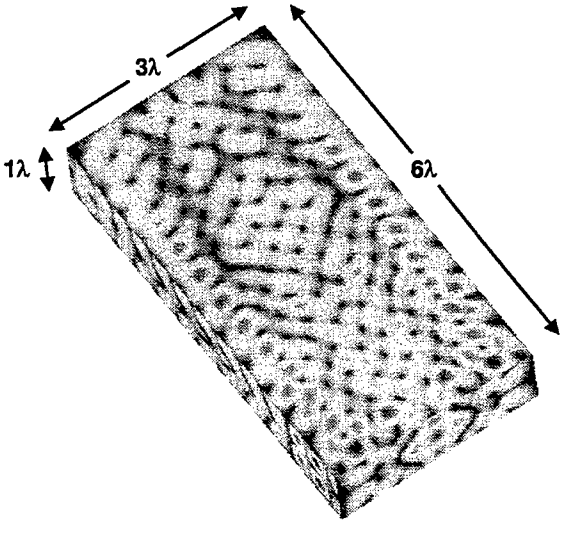


Figure 2: Intensity pattern of the equivalent electric current on a dielectric slab with $\epsilon = 4$, $\mu = 1$.

An Efficient Integral Equation Based Solution Method for Simulation of Electromagnetic Fields in Inhomogeneous Dielectric (Biological) Media

E. Bleszynski[1], M. Bleszynski[2], and T. Jaroszewicz[1]

[1] Monopole Research, Thousand Oaks, CA 91360

[2] EM Research, Thousand Oaks, CA 91360

Abstract

We describe a new approach for accurate and highly efficient numerical simulation of electromagnetic (EM) fields inside and in the vicinity of complex dielectric objects. Main elements of the approach are a novel coupled surface/volume integral-equation formulation and a modular solution technique consistent with the sparse block structure of the impedance matrix resulting from the proposed equations. The proposed approach utilizes also various impedance matrix compression techniques which are applied selectively for each block of the impedance matrix in a manner ensuring the optimal performance. The method is particularly well suited for simulation of EM field distribution in complex biological media.

1. Introduction

Numerical simulation of a broad spectrum of electromagnetic processes involving realistic dielectric objects encounters, generally, some or all of the following challenges: the geometries are several wavelength in size, they are highly inhomogeneous and rich in structural details of the order or orders of magnitude smaller than the wavelength.

For such class of problems, the integral equation based approaches (methods of moments (MoM)) are known to produce results of the highest degree of accuracy. The computer memory and computational time resources required by MoM have been recently significantly alleviated by the progress in the development of the impedance matrix compression techniques.

However, although a significant progress has been made in the application of compression techniques to electromagnetic processes involving simulation of perfectly conducting and resistive structures (which can be described in terms of surface integral equations), relatively much less attention has been given in the literature to the development and implementation of efficient integral equation techniques for electrically large and complex dielectric objects.

In this paper:

(1) *We describe a novel coupled surface/volume integral-equation formulation suitable for large dielectric geometries composed of coexisting homogeneous and inhomogeneous regions.* The pure

surface integral equations lead to block sparse structure of the impedance matrix however they are limited to fully describe models consisting only of piecewise homogeneous regions. The purely volumetric integral equations, although capable of capturing the inhomogeneities, lead to a dense impedance matrix. The formulation we propose is based on a representation of fields in terms of coupled surface currents and residual volumetric currents, and results in a block sparse impedance matrix.

(2) *We present an efficient solution strategy achieved through utilization of the sparse block structure of the resulting impedance matrix as well as the suitable impedance matrix compression techniques.* Our solution strategy was designed to be most efficient for geometries characterized by a clear hierarchy in the importance of individual components of the solution (i.e. of the induced current). One type of geometries which, in a natural way, display a hierarchy of the importance of individual components, are anatomical models. Here, because of the absorption in biological tissues, the magnitudes of fields and currents gradually decrease with the depth inside the body.

During the presentation we will show capabilities and efficiency of the proposed method for representative electrically large inhomogeneous dielectric objects.

2. Formulation

2.1. Coupled surface/volume integral equations

We first introduce and describe our coupled integral equation formulation on an example (Fig. 1a) of a single material region Ω_1, characterized by a position-dependent relative electric permittivity $\epsilon(\mathbf{r})$ and a magnetic permeability $\mu(\mathbf{r})$, surrounded by the free-space region Ω_0, with $\epsilon_0 = \mu_0 = 1$.

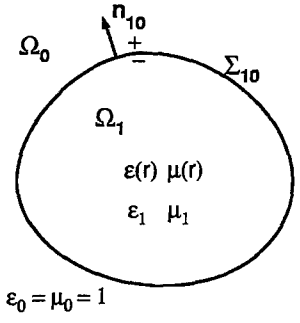


Fig. 1a: A single material region Ω_1 surrounded by the free-space region Ω_0.

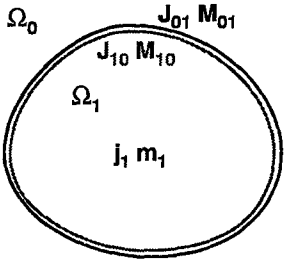


Fig. 1b: A representation of equivalent surface and volumetric currents in the problem of Fig. 1a.

We denote by ϵ_1 and μ_1 average values of the parameters $\epsilon(\mathbf{r})$ and $\mu(\mathbf{r})$ in Ω_1. In Fig. 1a, $\Sigma \equiv \Sigma_{10}$ denotes the interface between the regions, and $\mathbf{n} \equiv \mathbf{n}_{10}$ the unit normal vector oriented from Ω_0 to Ω_1. On the interface $\Sigma \equiv \Sigma_{10}$ there may be located a thin conducting sheet characterized by the (generally position-dependent) electric resistivity R, magnetic resistivity S, and a "cross-resistivity" W [1]. Such a sheet may be used to model a set of thin layers with various material properties.

We denote volumetric currents in region Ω_1 by $[\mathbf{j}_1 \quad \mathrm{i}\mathbf{m}_1]^{\mathrm{T}}$, and introduce two sets of equivalent surface currents on the interface Σ_{10}, $[\mathbf{J}_{01} \quad \mathrm{i}\mathbf{M}_{01}]^{\mathrm{T}}$ and $[\mathbf{J}_{10} \quad \mathrm{i}\mathbf{M}_{10}]^{\mathrm{T}}$, as shown in Fig. 1b. For convenience, we multiply here the magnetic fields and currents by the imaginary unit; this convention results in a manifestly symmetric complex impedance matrix.

The essence of our coupled integral equations is to represent the material parameters in dielectric regions as constant average values (for which the Green's function is known), and deviations, which will appear in the volumetric equations. We thus write, in region Ω_m, $\epsilon(\mathbf{r}) = \epsilon_m + (\epsilon(\mathbf{r}) - \epsilon_m)$ (and similarly for $\mu(\mathbf{r})$), and introduce matrix-valued Green's functions of the Maxwell's equations for *constant* parameters ϵ_m, μ_m,

$$G_m(\mathbf{r}) = \begin{bmatrix} \mathrm{i}k_0\mu_m\,(1+\frac{1}{k_m^2}\,\nabla\otimes\nabla)\,g_m(\mathbf{r}) & \mathrm{i}\,\nabla g_m(\mathbf{r})\times \\ \mathrm{i}\,\nabla g_m(\mathbf{r})\times & \mathrm{i}k_0\epsilon_m\,(1+\frac{1}{k_m^2}\,\nabla\otimes\nabla)\,g_m(\mathbf{r}) \end{bmatrix}. \tag{2.1}$$

Here $k_m = \sqrt{\epsilon_m\,\mu_m}\,k_0$ is the wave number in the homogeneous medium, and $g_m(\mathbf{r}) = \mathrm{e}^{\mathrm{i}k_m\,|\mathbf{r}|}\,/\,4\pi\,|\mathbf{r}|$ is the corresponding Green's function of the Helmholtz equation.

We represent fields in each region as due to the surface currents on the boundary of the region, and volumetric currents inside the region; both contributions involve the Green's function (2.1) (we use here the conventional integral representations [2, 3, 4]). By imposing the Maxwell equations on the fields, we obtain then a set of coupled equations for the surface and volumetric currents,

$$\begin{aligned} &\tfrac{1}{2}\,C_{10}\left\{(1+p)\begin{bmatrix}\mathbf{J}_{10}\\ \mathrm{i}\mathbf{M}_{10}\end{bmatrix}+(1-p)\begin{bmatrix}\mathbf{J}_{01}\\ \mathrm{i}\mathbf{M}_{01}\end{bmatrix}\right\}+G_1\begin{bmatrix}\mathbf{J}_{10}\\ \mathrm{i}\mathbf{M}_{10}\end{bmatrix}_{\Sigma_{10}} \\ &\qquad = -\tfrac{1}{4}\,T_{10}\,(1+p)\,G_1\begin{bmatrix}\mathbf{j}_1\\ \mathrm{i}\mathbf{m}_1\end{bmatrix}_{\Omega_1}-\tfrac{1}{2}\,G_1\begin{bmatrix}\mathbf{j}_1\\ \mathrm{i}\mathbf{m}_1\end{bmatrix}_{\Omega_1} \qquad \text{on } \Sigma_{10}, \end{aligned} \tag{2.2a}$$

$$\begin{aligned} &\tfrac{1}{2}\,C_{10}\left\{(1-p)\begin{bmatrix}\mathbf{J}_{10}\\ \mathrm{i}\mathbf{M}_{10}\end{bmatrix}+(1+p)\begin{bmatrix}\mathbf{J}_{01}\\ \mathrm{i}\mathbf{M}_{01}\end{bmatrix}\right\}+G_0\begin{bmatrix}\mathbf{J}_{01}\\ \mathrm{i}\mathbf{M}_{01}\end{bmatrix}_{\Sigma_{10}} \\ &\qquad = -\tfrac{1}{4}\,T_{10}\,(1-p)\,G_1\begin{bmatrix}\mathbf{j}_1\\ \mathrm{i}\mathbf{m}_1\end{bmatrix}_{\Omega_1}-\begin{bmatrix}\mathbf{E}^{\mathrm{in}}\\ \mathrm{i}\mathbf{H}^{\mathrm{in}}\end{bmatrix} \qquad \text{on } \Sigma_{10}, \end{aligned} \tag{2.2b}$$

and

$$\begin{bmatrix} [ik_0(\epsilon-\epsilon_1)]^{-1} & 0 \\ 0 & [ik_0(\mu-\mu_1)]^{-1} \end{bmatrix} \begin{bmatrix} \mathbf{j}_1 \\ \mathrm{i}\mathbf{m}_1 \end{bmatrix} + G_1 \begin{bmatrix} \mathbf{j}_1 \\ \mathrm{i}\mathbf{m}_1 \end{bmatrix}_{\Omega_1} = -G_1 \begin{bmatrix} \mathbf{J}_{10} \\ \mathrm{i}\mathbf{M}_{10} \end{bmatrix}_{\Sigma_{10}} \quad \text{in } \Omega_1. \quad (2.2c)$$

Here $\mathbf{E}^{\text{in}}$ and $\mathbf{H}^{\text{in}}$ are the external incident fields. The matrices $C_{10} \equiv C(\mathbf{n}_{10})$ and $T_{10} \equiv T(\mathbf{n}_{10})$ are defined as

$$C(\mathbf{n}) = \begin{bmatrix} -R & \mathrm{i}W\mathbf{n}\times \\ -\mathrm{i}W\mathbf{n}\times & -S \end{bmatrix}, \qquad T(\mathbf{n}) = 2\begin{bmatrix} W & -\mathrm{i}R\mathbf{n}\times \\ -\mathrm{i}S\mathbf{n}\times & -W \end{bmatrix}, \qquad (2.3)$$

and are, generally, position-dependent. The parameter $p = 1/4(RS+W^2)$ characterizes the degree of the electric penetrability of the sheet. In Eqs. (2.2) we use a compact operator notation, in which

$$G_0 \begin{bmatrix} \mathbf{J}_{01} \\ \mathrm{i}\mathbf{M}_{01} \end{bmatrix}_{\Sigma_{10}} (\mathbf{r}) = \int_{\Sigma_{10}} \mathrm{d}^2r'\, G_0(\mathbf{r}-\mathbf{r}') \begin{bmatrix} \mathbf{J}_{01}(\mathbf{r}') \\ \mathrm{i}\mathbf{M}_{01}(\mathbf{r}') \end{bmatrix}, \qquad (2.4)$$

$$G_1 \begin{bmatrix} \mathbf{j}_1 \\ \mathrm{i}\mathbf{m}_1 \end{bmatrix}_{\Omega_1} (\mathbf{r}) = \int_{\Omega_1} \mathrm{d}^3r'\, G_1(\mathbf{r}-\mathbf{r}') \begin{bmatrix} \mathbf{j}_1(\mathbf{r}') \\ \mathrm{i}\mathbf{m}_1(\mathbf{r}') \end{bmatrix}, \qquad (2.5)$$

etc.

We note that if the region Ω_1 is homogeneous, we have $\epsilon(\mathbf{r}) = \epsilon_1$ and $\mu(\mathbf{r}) = \mu_1$. In this case the volumetric currents, $\mathbf{j}_1$ and $\mathbf{m}_1$, must vanish, and Eqs. (2.2) reduce to purely surface equations.

The physical meaning of the coupled system of equations (2.2) is clear: Eqs. (2.2a) and (2.2b) have the form of the usual integral equations for equivalent surface currents, in which the sources on the right-hand-side include not only the incident wave, but also fields generated by the volumetric currents. We note that our integral equations differ substantially from the conventional volumetric integral formulation, which would have the form

$$\begin{bmatrix} [ik_0(\epsilon-1)]^{-1} & 0 \\ 0 & [ik_0(\mu-1)]^{-1} \end{bmatrix} \begin{bmatrix} \mathbf{j} \\ \mathrm{i}\mathbf{m} \end{bmatrix} + G_0 \begin{bmatrix} \mathbf{j} \\ \mathrm{i}\mathbf{m} \end{bmatrix}_{\Omega_1} = -\begin{bmatrix} \mathbf{E}^{\text{in}} \\ \mathrm{i}\mathbf{H}^{\text{in}} \end{bmatrix}. \qquad (2.6)$$

The essential differences are:

(1) The material-dependent term in Eq.(2.2c) involves only differences between the actual parameters $\epsilon(\mathbf{r})$ and $\mu(\mathbf{r})$ and their average values ϵ_1 and μ_1 in the medium, rather than the free-space values.

(2) The Green's function appearing in Eq.(2.2c) corresponds to a material with parameters ϵ_1 and μ_1 rather than to free-space, as in Eq.(2.6).

(3) While in Eq.(2.6) the right-hand side represents the incident free-space wave ($\mathbf{E}^{\text{in}}$, $\mathbf{H}^{\text{in}}$), in Eq.(2.2c) it is given by the field generated by the equivalent surface currents on the boundary of Ω_1.

We note that the currents $\mathbf{j}_1$ and $\mathbf{m}_1$ in Eqs. (2.2) are thus not the conventional volumetric currents $\mathbf{j}$ and $\mathbf{m}$ of Eq.(2.6), but rather "residual currents" due only to deviations of the material properties $\epsilon(\mathbf{r})$ and $\mu(\mathbf{r})$ from their average values ϵ_1 and μ_1.

2.2. Structure of integral equations and the impedance matrix for complex objects

Equations similar to (2.2) hold for objects with multiple regions and interfaces, such as the example of Fig. 2. Similarly to Fig. 1b, the interfaces between regions are represented as "doubled", so that each surface supports one pair of currents $(\mathbf{J}, \mathbf{M})$.

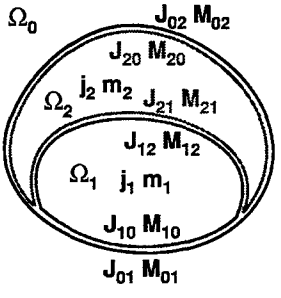


Fig. 2: A system of two material regions (Ω_1 and Ω_2) in free-space (Ω_0), with region boundaries supporting surface currents.

The most essential properties of these equations are as follows:

(1) *Surface currents on a boundary of a region couple only to:*
- *Surface currents on the same boundary.* Thus, in Fig. 2, currents $(\mathbf{J}_{10}, \mathbf{M}_{10})$ couple to $(\mathbf{J}_{12}, \mathbf{M}_{12})$ through the Green's function G_1 of region Ω_1.
- *Surface currents on the boundary of adjacent regions.* In this way, currents $(\mathbf{J}_{12}, \mathbf{M}_{12})$ couple to $(\mathbf{J}_{21}, \mathbf{M}_{21})$ through the material-dependent term C .
- *Volumetric currents in the considered region.* Thus, currents $(\mathbf{J}_{12}, \mathbf{M}_{12})$ couple to $(\mathbf{j}_1, \mathbf{m}_1)$ through G_1.

(2) *Volumetric currents in a region couple only to:*
- *Themselves,* with the material-dependent term in the volumetric equations (2.2c) and the region's Green's function. E.g., currents $(\mathbf{j}_1, \mathbf{m}_1)$ couple only to themselves, and no other *volumetric* currents.

- *Surface currents on the boundary of the region* with the Green's function of the region. Thus, $(\mathbf{j}_1, \mathbf{m}_1)$ couple to $(\mathbf{J}_{10}, \mathbf{M}_{10})$ and $(\mathbf{J}_{12}, \mathbf{M}_{12})$ with G_1.

(3) *Incident fields couple only to the surface currents on the interface with the free-space region.*

The most important of the above features is that the couplings between the currents are *local* – limited to the same region or adjacent regions.

After Galerkin discretization with locally-supported surface and volumetric basis functions by using conventional basis functions [5, 6] defined on triangles and tetrahedra, we obtain a matrix equation

$$Ax = b\,, \tag{2.7}$$

where x represents the unknown currents, b the incident fields, and A is the impedance matrix. Since, as we discussed above, there are only couplings of currents on adjacent interfaces and in adjacent regions, the matrix A is *block sparse*.

The block-sparse structure of the impedance matrix in our formulation contrasts with the purely volumetric formulation, which involves mutual couplings of *all* current elements in the entire object, and leads to a *dense* impedance matrix.

3. Solution Strategy

The structure and the block-sparseness of the impedance matrix following from the coupled surface/volume formulation presented above offers interesting possibilities of developing novel approaches to the impedance matrix compression and to iterative solution of the problem.

We describe here an iterative solution technique applicable, in particular, to geometries which exhibit a clear hierarchy in the importance of the individual components of the solution (i.e., of the induced currents). As an example of such geometries, one may consider anatomical models. There, due to the absorption in the tissues, the magnitude of the fields and currents gradually decreases with the depth inside the body. It is therefore natural to order the components of the objects, i.e., its volumetric regions and the interfaces between them, according to the magnitude of the currents they support.

Given the hierarchical ordering of the geometry components, and thus of the blocks of the current vector, a straightforward iterative solution method would be to: (i) solve for the currents on the first geometry component (in the absence of all the other components); (ii) use the currents on the first component as sources of the field incident on the second component, and solve for currents on the second component; etc. Then, if the desired accuracy has not been reached, repeat the entire process with the computed currents used as the starting point. The heuristic justification of the procedure is that, whereas the larger currents strongly affect the smaller currents (on the next component), the reverse influence is much weaker.

The solution procedure just described is precisely the classical block Gauss-Seidel method, in which the new approximation to the solution, x', is related to the previous approximation x by

$$x' = (I - L_A^{-1} A)\, x + L_A^{-1}\, b \equiv K\, x + N\, b\,, \tag{3.1}$$

where L_A is the lower-block-triangular part of A (*including* its diagonal blocks).

The iterative solution obtained from Eq.(3.1) is then the series

$$x = (I + K + K^2 + K^3 + \ldots)\, N\, b\,, \tag{3.2}$$

which may or may not converge, depending on whether or not the spectral radius of the matrix K is less than 1. This obvious deficiency of the block G-S method becomes clear when we realize that Eq.(3.2) is the Richardson-method solution of the *left-preconditioned* equation

$$L_A^{-1}\, A\, x = L_A^{-1}\, b\,, \tag{3.3}$$

with L_A^{-1} playing the role of the preconditioner matrix. The solution converges only when the matrix $L_A^{-1}\, A$ is sufficiently close to the identity matrix.

This deficiency can be, however, remedied, if we observe that it is associated only with the Richardson solution method, and not with the equation (3.3) itself. We can thus solve Eq.(3.3) by using any other iterative method whose convergence is guaranteed, such as the GMRES algorithm.

In practice, it is more convenient to use right-preconditioning. We thus solve the system of equations

$$A\, L_A^{-1}\, \widetilde{x} = b, \qquad x = L_A^{-1}\, \widetilde{x}\,, \tag{3.4}$$

where L_A^{-1} is the preconditioner matrix. We remark here that the preconditioner in Eq.(3.4) can be regarded as the inverse of the very simple approximation to the matrix A, $A \simeq L_A$ (which is a reasonable approximation under the assumption of the hierarchy of the solution components).

A possible alternative preconditioner, $U_A^{-1}\, D_A\, L_A^{-1}$ (where U_A and D_A are the block-upper-triangular part and the block-diagonal part of A), would result from the incomplete block LU decomposition of A, $A \simeq L_A\, D_A^{-1}\, U_A$.

For large problems it would become prohibitively expensive to compute the matrix L_A^{-1} explicitly. Thus, we developed the following scheme. We implement the preconditioner-vector multiplication, say $v = L_A^{-1}\, u$, by iteratively solving the system $L_A\, v = u$; this entails a sequential solution of a set of equations with diagonal blocks of A, and forward-substitution steps involving the off-diagonal blocks of A. The preconditioned iterative solution of the full system can be thus represented as

$$x = \left\{L_A\right\}_{\delta}^{-1} \left\{A \left\{L_A\right\}_{\delta}^{-1}\right\}_{\Delta}^{-1} b\,, \tag{3.5}$$

where $v = \left\{A\right\}_{\Delta}^{-1} u$ denotes an iterative solution of the equation $A\, v = u$, computed with the tolerance Δ, and similarly for $v = \left\{L_A\right\}_{\delta}^{-1} u$. Thus, δ and Δ in Eq.(3.5) are tolerances of the inner and outer iterations.

We note that since the computational cost of the block preconditioner-vector multiplication, $v = L_A^{-1} u$ associated with Eq. (3.5) is in general higher than the cost of the impedance matrix-vector multiplication $v = Au$, its use is advantageous if it leads to a significant reduction the number of outer iterations.

The application of our block preconditioner is even more advantageous in the out-of-core solution, in which individual blocks of the matrix A are stored on disk, and retrieved when needed. The gain results precisely from the fact that, for our block preconditioner, the cost of disk operations is approximately the same for the matrix-vector and preconditioner-vector multiplications, but the CPU time is higher for the latter. Therefore, the *relative* disk-operations overhead is lower for the preconditioned solution.

4. Numerical Examples

We have carried out extensive validation tests of the proposed method and were able to obtain highly accurate field distributions inside complex dielectric media modeled in terms of several hundred thousand of unknowns. For example, a field distribution within a complex anatomical model of 250,000 unknowns was obtained, with the residual tolerance of 0.01, in only 3 global (outer) iterations. Different impedance matrix compression techniques were used in for different regions, depending on their geometrical and electromagnetic characteristics. Compression methods were selected automatically by the code on the basis of the estimated matrix-fill and matrix-vector multiplication costs. Additional results of our analysis will be presented at the conference.

References

1. E. Bleszynski, M. Bleszynski, and T. Jaroszewicz, "Surface Integral Equations for Electromagnetic Scattering from Impenetrable and Penetrable Sheets", *IEEE Antennas and Propagation Magazine*, Vol. 35, pp. 14-25, 1993.
2. J.A. Stratton, *Electromagnetic Theory*, McGraw-Hill, New York, 1941.
3. A.J. Poggio and E.K. Miller, "Integral Equation Solution of 3-dimensional Scattering Problems", in *Computer Techniques for Electromagnetics*, R. Mittra (ed.), Pergamon Press, Oxford, New York, 1973, p. 218.
4. D. Colton and R. Kress, *Integral Equation Methods in Scattering Theory*, John Wiley & Sons, 1983.
5. S.M. Rao, D.R. Wilton, and A.W. Glisson, "Electromagnetic Scattering by Surfaces of Arbitrary Shape", *IEEE Trans. on Antennas and Propagation*, Vol. AP-30, pp. 409-418, 1982.
6. D.H. Schaubert, D.R. Wilton, and A.W. Glisson, "A Tetrahedral Modeling Method of Electromagnetic Scattering by Arbitrarily Shaped Inhomogeneous Dielectric Bodies", *IEEE Trans. on Antennas and Propagation*, Vol. AP-32, pp. 77-85, 1984.

Efficient Solution of Large-Scale Electromagnetic Eigenvalue Problems using the Implicitly Restarted Arnoldi Method

Daniel White and Joseph Koning
Lawrence Livermore National Laboratory
P.O. Box 808, Livermore, CA
dwhite@llnl.gov

1. Introduction

We are interested in determining the electromagnetic fields within closed perfectly conducting cavities that may contain dielectric or magnetic materials. The vector Helmholtz equation is the appropriate partial differential equation for this problem. It is well known that the electromagnetic fields in a cavity can be decomposed into distinct modes that oscillate in time at specific resonant frequencies. These modes are referred to as eigenmodes, and the frequencies of these modes are referred to as eigenfrequencies. Our present application is the analysis of linear accelerator components. These components may have a complex geometry; hence numerical methods are required to compute the eigenmodes and eigenfrequencies of these components.

The Implicitly Restarted Arnoldi Method (IRAM) is a robust and efficient method for the numerical solution of the generalized eigenproblem $\mathbf{A}x = \lambda \mathbf{B}x$, where $\mathbf{A}$ and $\mathbf{B}$ are sparse matrices, x is an eigenvector, and λ is an eigenvalue. The IRAM is an iterative method for computing extremal eigenvalues; it is an extension of the classic Lanczos method. The mathematical details of the IRAM are too sophisticated to describe here; instead we refer the reader to [1]. A FORTRAN subroutine library that implements various versions of the IRAM is freely available, both in a serial version named ARPACK and parallel version named PARPACK.

In this paper we discretize the vector Helmholtz equation using 1st order H(curl) conforming edge elements (also known as Nedelec elements). This discretization results in a generalized eigenvalue problem which can be solved using the IRAM. The question of so-called spurious modes is discussed, and it is shown that applying a spectral transformation completely eliminates these modes, without any need for an additional constraint equation. Typically we use the IRAM to compute a small set ($n < 30$) of eigenvalues and eigenmodes for a very large systems ($N > 100{,}000$).

2. Problem Formulation

We are interested in solving the vector Helmholtz equation in a 3-dimensional inhomogeneous volume Ω,

$$\nabla \times \mu^{-1} \nabla \times E - \omega^2 \varepsilon E = 0 \text{ in } \Omega, \tag{1}$$

with boundary condition $\hat{n} \times E = 0$ on $\partial\Omega$, where E is the electric field vector, μ and ε are the tensor permeability and permittivity, and ω is the radian frequency. Employing the Galerkin procedure using 1st order edge elements denoted by $_i$ results in the generalized eigenvalue problem

$$\mathbf{A}e = \omega^2 \mathbf{B}e \tag{2}$$

where e is the N-dimensional vector of degrees-of-freedom and the matrices **A** and **B** are given by

$$\mathbf{A}_{ij} = \int_{\Omega} \mu^{-1} \nabla \times W_i, \nabla \times W_j \,,\; \mathbf{B}_{ij} = \int_{\Omega} \varepsilon W_i, W_j \,. \tag{3}$$

The details of computing the matrices can be found in most finite element textbooks, for example [2][3]. Using terminology from continuum mechanics, the matrix **A** is referred to as the stiffness matrix and the matrix **B** is referred to as the mass matrix. When μ and ε are real, the matrices **A** and **B** are symmetric; the matrix **A** is semi-definite and the matrix **B** is positive-definite.

3. A Comment on Spurious Modes

Equation (1) admits to two types of solutions; irrotational field solutions and solenoidal field solutions. An irrotational field is the gradient of a scalar potential function

$$E_{ir} = -\nabla \phi. \tag{4}$$

Inserting (4) into (1) we see that $\omega = 0$ for irrotational fields. Conversely, by taking the divergence of (1) we see that if $\omega \neq 0$ then the field must be solenoidal,

$$\nabla \bullet \varepsilon E_s = 0. \tag{5}$$

Since the permittivity may not be continuous, equation (5) is best understood in the weak sense: we multiply (5) by a scalar potential ϕ that is zero on the boundary, and then integrate over the domain Ω and employ the divergence theorem to yield

$$\int_{\Omega} \varepsilon E_s \bullet \nabla \phi = 0. \tag{6}$$

Equation (6) states that a solenoidal solution of (1) is orthogonal to every irrotational solution. Solutions of (1) therefore can be decomposed into irrotational ($\omega = 0$) and solenoidal ($\omega \neq 0$) solutions, with every solenoidal solution being orthogonal to every irrotational solution. An important property of the vector finite element method is that the discrete Helmholtz equation (2) has the same decomposition of solutions as the original PDE. Let $L_h \subset H_1$ be the set of standard bi-linear nodal finite element basis functions, and let the discrete scalar potential be an element of L_h. It can be shown that the finite element spaces L_h and $_h$ are related by $\nabla L_h \in W_h$; therefore the gradient of every nodal basis function can be written as a linear combination of edge functions [4]. Because of this there exists exactly K discrete irrotational fields that are gradients of discrete scalar potentials, where K is the

number of internal nodes in the mesh. It can also be shown that these discrete irrotational fields form the null space of the stiffness matrix A; there are exactly K solutions of (2) with $\omega = 0$. These are the so-called spurious modes; they are static solutions of (2) with non-zero divergence. They are mathematically valid solutions of (2), but they are physically uninteresting. We are interested in the solenoidal solutions of (2). As in the continuous case, the discrete solenoidal solutions of (2) are orthogonal to the discrete irrotational solutions according to the inner product $u^T \mathbf{B} v$; this is a basic property of symmetric generalized eigenvalue problems.

4. Application of ARPACK for Electromagnetic Eigenvalue Problems

In this section we discuss the application of ARPACK, which is a specific implementation of the IRAM for computing the solenoidal eigenvectors and corresponding eigenvalues of (2). ARPACK provides several different subroutines depending upon whether the mass matrix **B** is the identity or not, whether the matrices **A** and **B** are symmetric or not, whether **A** and **B** are complex valued or not, etc. The mass matrix **B** would reduce to the identity matrix if Cartesian grid finite difference discretization of the vector Helmholtz equation was used. The matrices **A** and **B** would be complex valued and non-Hermitian if μ and ε were complex valued, representing lossy dielectric and magnetic materials. In our case **A** and **B** are real symmetric matrices.

The IRAM is an iterative method for computing a small set of extremal eigenvalues. In ARPACK the user can select to compute largest algebraic eigenvalues, smallest algebraic eigenvalues, largest absolute value eigenvalues, or smallest absolute value eigenvalues. ARPACK requires $N \bullet O(m) + O(m^2)$ storage where N is the dimension of the system and m the desired number of eigenvalues to compute. The basic user-specified parameters are:

a) N, the dimension of the system
b) m, the desired number of eigenvalues
c) WHICH, a character string denoting which eigenvalues to compute
d) *ncv*, the number of Lanczos basis vectors to use
e) *tol*, the numerical tolerance used to determine convergence
f) *maxit*, the maximum number of iterations

The number of Lanczos vectors must be at least $m+1$. The optimal choice of *ncv* with respect to m is problem dependent and experimentation is required. If the eigenvalues are well separated then $ncv \approx 2 \bullet m$ is acceptable, where well separated is defined as

$$|\lambda_i - \lambda_j| > C|\lambda_N - \lambda_1| \quad \text{for all } j \neq i \text{ with } C >> \varepsilon_M. \tag{7}$$

The numerical tolerance *tol* is used in the stopping criteria $|\lambda_c - \lambda_t| \leq tol \bullet |\lambda_t|$, where λ_c is the computed eigenvalue and λ_t is the exact eigenvalue closest to λ_c. It is tempting to make *tol* a very small number, however this increases the run time of the problem. If *tol* is too small convergence may not occur. It is important to remember that the eigenvalue problem (2) is itself an approximation to physical reality, so there is little point in computing the eigenvalues of (2) exactly.

The parameter *maxit* specifies the maximum number of iterations, or restarts, of the IRAM. The iteration process begins with an initial vector v_1, which is usually chosen at random. An Arnoldi factorization is computed, and the *ncv* eigenvalues of the $ncv \times ncv$ Arnoldi matrix are computed. This represents one iteration. The salient feature of the IRAM is the ability to automatically repeat this process with improved initial vectors v_i, where each new v_i is determined by application of a polynomial in **A** to the starting vector v_1. The repeated update of the starting vector through implicit restarting is designed to enhance the components of this vector in the direction of the desired eigenvalues and damp its components in the unwanted directions. The parameters *tol* and *maxit* are not independent; a large number of iterations may be required to converge with a small tolerance. Fortunately neither *tol* nor *maxit* affect the required amount of memory, these parameters only affect the run time of the calculation.

ARPACK does not require that users actually provide the matrices **A** and **B**; instead all that is required is the action of these matrices. Specifically, the user must provide $\mathbf{A}x \rightarrow w$, $\mathbf{B}x \rightarrow z$, and $\mathbf{B}^{-1}x \rightarrow y$. For small systems the mass matrix **B** can be factored, however since we are interested in large problems we employ iterative Krylov-type methods for computing $\mathbf{B}^{-1}x \rightarrow y$. If iterative methods are used for $\mathbf{B}^{-1}x \rightarrow y$ it is essential that the residual be significantly smaller than the requested eigenvalue tolerance *tol*.

We are interested in computing only a few of the solenoidal eigenvectors and corresponding eigenvalues of (2). Based on the discussion of spurious modes we know that the distribution of the eigenvalues is as shown in Figure 1.

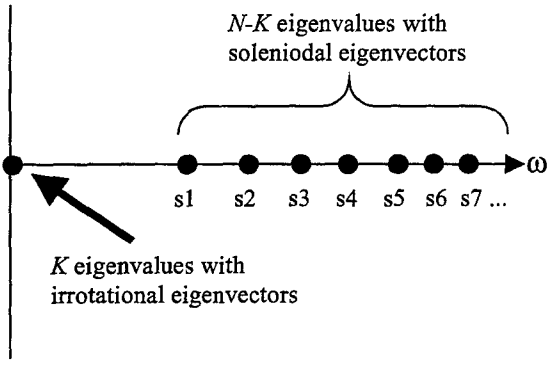


Figure 1: Eigenvalue distribution of $\mathbf{A}e = \omega^2\mathbf{B}e$

As illustrated in Figure 1, the solenoidal modes are not extremal and the IRAM cannot be directly applied to (2). Instead, a shift-and-invert spectral transformation is applied to enhance convergence to the desired part of the spectrum. If (x, λ) is an eigenpair of $(\mathbf{A}, \mathbf{B})$, and $\sigma \neq \lambda$, we form a new eigensystem

$$\mathbf{B}x = \gamma(\mathbf{A} - \sigma\mathbf{B})x$$
$$\text{with } \gamma = \frac{1}{\lambda - \sigma}. \tag{8}$$

We choose σ to be between 0 and *S1*, the smallest non-zero eigenvalue. The algebraically largest eiganvalues of the transformed system (8) correspond to the eigenvalues imediately to the right of σ in the original system (2). The zero-valued eigenvalues of the original problem are now the algebraically smallest eigenvalues of the transformed system. This is illustrated in Figure 2. The IRAM is applied to the transformed system computing the k algebraically largest eigenvalues and corresponding eigenvectors. The eigenvectors of (8) and (2) are identical. Once found, the eigenvalues of the original problem are computed via

$$\lambda_i = \sigma + \frac{1}{\gamma_i}. \tag{9}$$

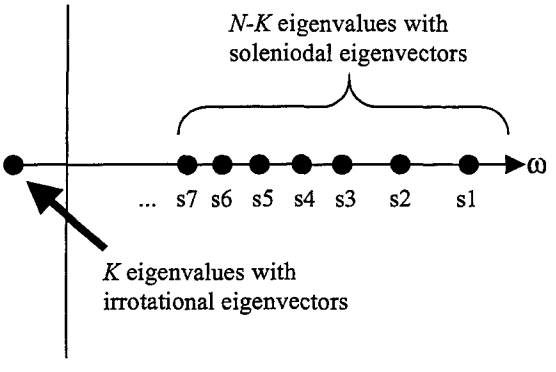


Figure 2: Spectrum of the transformed eigensystem

The shift-and-invert spectral transformation results in a new eigensystem where the desired eigenvalues are very well separated from the spurious eigenvalues. There is no need to add an additional constraint equation such as done in [5], nor is there any need to modify ARPACK. A disadvantage of this approach is that the user must have some knowledge of the problem to wisely choose σ. In addition, it is now necessary to provide the action of $(\mathbf{A} - \sigma\mathbf{B})^{-1}x \rightarrow y$. The matrix $\mathbf{A} - \sigma\mathbf{B}$ is indefinite and may be ill conditioned. However it is no more ill conditioned than the matrices that arise in standard frequency domain finite element electromagnetics where the frequency is a user-specified parameter and the right-hand side of (1) is non-zero.

5. Results

5.1 A Simple Sphere

The first problem is that of a simple homogeneous sphere. Although this seems trivial, it is in fact a difficult problem from a numerical point of view due to the numerous degenerate eigenvalues. The 20 smallest eigenvalues for a 36 cell per radius sphere are shown in Table 1, along with the exact solution. The sphere had a radius of 0.05855m and the speed of light is unity. The mesh had a total of 55296 hexahedral cells and the dimension of the eigensystem was $N = 162528$, the number of internal edges in the mesh. A sigma of $\sigma = 2000.0$ was used to perform the shift-and-invert spectral transformation.

Mode	Exact	Computed	Percent Error
TM11	2196.39	2200.44	0.184
TM11	2196.39	2200.44	0.184
TM11	2196.39	2200.44	0.184
TM21	4368.84	4382.21	0.306
TM21	4368.84	4382.21	0.306
TM21	4368.84	4384.45	0.357
TM21	4368.84	4384.45	0.357
TM21	4368.84	4384.45	0.357
TE11	5888.69	5911.07	0.380
TE11	5888.69	5911.07	0.380
TE11	5888.69	5911.07	0.380
TM31	7214.14	7248.11	0.470
TM31	7214.14	7248.21	0.470
TM31	7214.14	7248.21	0.470
TM31	7214.14	7248.21	0.470
TM31	7214.14	7252.40	0.530
TM31	7214.14	7252.40	0.530
TM31	7214.14	7252.40	0.530
TE21	9688.19	9731.82	0.450
TE21	9688.19	9731.82	0.450

Table 1: Exact vs computed eigenavlues (ω^2) for 36 cell per radius sphere

The data in Table 1 was computed using the following ARPACK input parameters:

a) $N = 162528$
b) $m = 20$
c) WHICH = largest algebraic eigenvalues
d) $ncv = 40$
e) tol = 1.0e-5
f) $maxit = 300$

Although *maxit* was set to 300, only six iterations were required for convergence of all 20 eigenvalues. The Jacobi-preconditioned conjugate residual method was used to evaluate $(\mathbf{A} - \sigma\mathbf{B})^{-1} x \rightarrow y$ with a residual tolerance of 1.0e-9. The total run time was 25 hours on a Compaq AlphaServer 8400 with a

theoretical peak performance of 880 Mflops. The run time was dominated by the cost of the conjugate residual method and not by ARPACK or by the calculation of the finite element mass and stiffness matrices.

5.2 A Linear Accelerator Induction Cell

The second problem is to compute the lowest eigenmodes of a linear accelerator induction cell. Of particular interest is the magnitude of the electric field in the accelerating gap, as this determines whether or not the particular mode will couple with the electron beam. A 33024 cell hexahedral mesh is used to model the induction cell. Part of the cell is vacuum, and another part consists of oil with a relative permittivity of $\varepsilon_r = 4.5$. The input parameters to ARPACK were the same as for the sphere problem above except that $N = 90237$ for this problem. Based on back-of-the-envelope estimations, a sigma of $\sigma = 0.001$ was chosen for the shift-and-invert spectral transformation. A total of 5 IRAM iterations were required for convergence of all 20 eigenmodes. The total run time was 15 hours on the same Compaq AlphaServer 8400. The computed eigenvalues are shown in Table 2, naturally for this problem there is no analytical solution for comparison. The column labeled ω^2 is the computed eigenvalues of (2) using unity speed of light, and the column labeled Mhz is the calibrated resonant frequencies of the induction cell.

Figure 3 shows the 1st, 5th, 13th, and 20th eigenmodes of the induction cell. The figures show electric field magnitude. Although it may be difficult to discern from the figures, the 1st and 20th modes have maximum field values in the accelerating gap and hence will couple strongly with the electron beam, whereas the 5th and 13th modes are examples of modes that will not couple strongly with the beam.

ω^2	Mhz
.00495	132.200
.01158	202.166
.01158	202.166
.01721	246.471
.02222	280.015
.02222	280.015
.02930	321.560
.02930	321.560
.03585	355.683
.03585	355.683
.05206	428.607
.05206	428.607
.05466	439.197
.05917	456.955
.05921	457.109
.05929	457.417
.05929	457.417
.07053	498.881
.07053	498.881
.08034	532.453

Table 2 : The 20 lowest eigenvalues and resonant frequencies for the induction cell

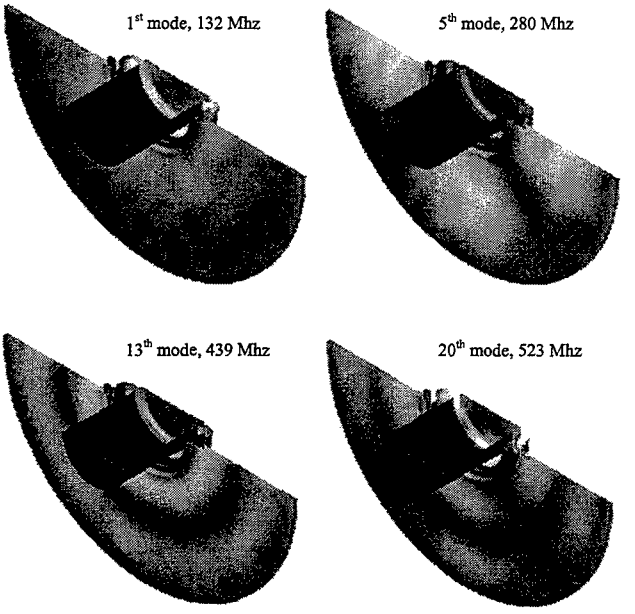


Figure 3: Selected eigenmodes for the linear accelerator induction cell. The geometry is clipped so that the internal structure of the modes can be seen.

6. References

[1] R. B. Lehoucq, D.C Sorensen, and C. Yang, ARPACK Users Guide: Solution of Large-Scale Eigenvalue Problems with Implicitly Restarted Arnoldi Methods, SIAM, 1998.

[2] J. L. Volakis, A. Chatterjee, L. C. Kempel, Finite Element Method for Electromagnetics: Antennas, Microwave Circuits, and Scattering Applications, IEEE Press, 1998.

[3] A. Bossavit, Computational Electromagentics: Variational Formulations, Complementarity, Edge Elements, Academic Press, 1998.

[4] J. C. Nedelec, "Mixed Finite Elements in R3", Numer. Math., vol. 35, pp. 315-341, 1980.

[5] S. G. Perepelitsa, R. Dyczij-Edinger, J. F. Lee, "Finite Element Analysis of Arbitrarily Shaped Cavity Resonators Using H1(curl) Elements," IEEE Trans. Mag., vol. 33, no. 2, pp. 1776-1779.

Fast Fourier Transform of Functions with Jump Discontinuities

Guo-Xin Fan and Qing Huo Liu
Department of Electrical and Computer Engineering
Duke University
Durham, NC 27708-0291

Abstract — A fast algorithm is presented for the evaluation of the Fourier transform of piecewise smooth functions with uniformly and non-uniformly sampled data by using a double interpolation procedure. The complexity of algorithm is $O(Np + N\log(N))$ where p is the interpolation order. Numerical experiments demonstrate the performance of the algorithm.

I. Introduction

The Fast Fourier Transform (FFT) algorithm, as one of most fundamental and powerful mathematical tools, has been widely used in computational science and engineering in general, and computational electromagnetics and signal and image processing in particular. As is well known, for a smooth periodic function, the FFT provides a high accuracy. However, if the function has singularities, such as jump discontinuities, the accuracy of the FFT results will be greatly reduced. It is easy to understand that this error is a result of the trapezoidal rule in the discretization of the Fourier transform integration. Sorets proposed a Fast Fourier Transform algorithm of piecewise constant functions via the Gaussian quadrature and Lagrange interpolation, together with an application of the standard FFT [1]. Beylkin also addresses the FFT of functions with similar singularities using piecewise polynomial splines [2].

In this paper, we develop an algorithm for piecewise smooth functions by using a double interpolation procedure. With the help of the double interpolation and Gaussian quadrature, the algorithm can be applied to both uniform and nonuniform sampled data. Hence, this algorithm can also perform nonuniform fast Fourier transform for unequally spaced data [2–6]. In the following sections, the formulation of algorithm is developed, followed by the implementation procedures and complexity analysis. Finally, we show the numerical results to demonstrate the performance of the algorithm.

This work was supported by the U.S. EPA through a PECASE grant CR-825-225-010, and by the NSF through a CAREER grant ECS-9702195.

II. Formulation

Consider the Fourier transform of a piecewise smooth function $f(x)$

$$\hat{f}(n) = \int_0^1 f(x) e^{-i2\pi nx}\, dx \qquad -N/2 < n \leq N/2 - 1 \tag{1}$$

where n is an integer. We divide the integration interval $[0, 1]$ into L subdivisions in which $f(x)$ is a smooth function. Step discontinuities are allowed at the boundaries of these subdivisions. In each subdivision, there are at most p uniformly or non-uniformly sampling points, where p is referred to as the order of interpolation as shown later. Then (1) can be written as

$$\hat{f}(n) = \sum_{l=1}^{L} \int_{x_{l-1}}^{x_l} f(x) e^{-i2\pi nx}\, dx \tag{2}$$

where $\{x_l\}(l = 1, \cdots, L)$ are the end points of the subdivisions. Using the change of variables

$$t = a^l + b^l x = \frac{x_l + x_{l-1}}{2} + \frac{x_l - x_{l-1}}{2}\, x \tag{3}$$

and the Gaussian Legendre quadrature

$$\int_{-1}^{1} f(t)\, dt \cong \sum_{k=1}^{q} f(t_k)\, \omega_k \tag{4}$$

where t_k and $\omega_k (k = 1, \cdots, q)$ are the Gaussian-Legendre nodes and weights, respectively, we obtain

$$\hat{f}(n) \cong \sum_{l=1}^{L} b^l \sum_{n=1}^{q} \omega_k\, f(t_k^l)\, e^{-i2\pi n t_k^l}. \tag{5}$$

In the above expression, the values of both function $f(x)$ and the exponential function at the nonuniform distributed points $\{t_k^l\}$ can be obtained via the Lagrange interpolation, i.e.

$$g(x) = \sum_{m=1}^{p} g(x_m)\, \delta_m(x) \tag{6}$$

where

$$\delta_m(x) = \prod_{\substack{n=1 \\ n \neq m}}^{p} \frac{x - x_n}{x_m - x_n}. \tag{7}$$

Here we perform this interpolation separately for $f(x)$ with order p_1 and $\exp(-i2\pi nx)$ with order p.

Note that we use this double interpolation scheme because these two functions to be interpolated have different properties. The former is a piecewise function, while the latter is a periodic analytic function but highly oscillating when n becomes large. Therefore we normally interpolate the two functions with different sets of sampling points and orders of interpolation. For the exponential function, we use a uniform grid in order to apply the uniform FFT for the discrete summation; and we always choose the interpolated points to locate at the center of the interpolation region to obtain the highest accuracy for a p-th order Lagrange interpolation. With this double interpolation, (6) becomes

$$\hat{f}(n) = \sum_{l=1}^{L} b^l \sum_{k=1}^{q} \omega_k^l \left(\sum_{m_1=1}^{p_1} f(t_{m_1}^l) \delta_{m_1}(t_k^l) \right) \left(\sum_{m=1}^{p} e^{-i2\pi n t_m^l} \delta_m(t_k^l) \right). \tag{8}$$

Transforming the local coordinate to global coordinate and changing the order of summation, we finally obtain

$$\hat{f}(n) = \sum_{m=1}^{\nu N} g_m \, e^{-i2\pi n x_m} \tag{9}$$

where

$$g_m = \sum_{l=1}^{L} b^l \sum_{k=1}^{q} \left(\sum_{m_1=1}^{p_1} f(t_{m_1}^l) \delta_{m_1}(t_k^l) \right) \omega_k^l \, \delta_m(t_k^l) \tag{10}$$

and ν is the oversampling factor. Since $\{x_m\}$ are now on a uniform grid in $[0, 1]$, (9) can be efficiently evaluated via a standard uniform FFT algorithm.

It is worth pointing out that the above double interpolation procedure has several advantages. First, the double interpolation can ensure the interpolation points for the exponential function to locate at the center of the interpolation region, leading to the highest accuracy for a given Lagrange interpolation order. In contrast, if a single interpolation were applied to the product of these two functions, the periodic property of the exponential function could not be used because of the piecewise property of the function to be transformed. Furthermore, the locations of the interpolated points would not be always located at the center of the interpolation region. The accuracy of the interpolation for the product, hence the accuracy of the FT, would be reduced, especially when n becomes large. Second, since the Lagrange interpolation allows the nonuniformly sampling, the above algorithm can be applied to both uniform and nonuniform sampled data with the same number of arithmetic operations. In contrast, a single interpolation allows only uniform sampled data in order to use uniform FFT to evaluate the summation. Third, the double interpolation allows a lower order interpolation, i.e., a lower sample density, for

the slowly varying function $f(x)$. Finally, the double interpolation allows other efficient algorithms, such as the fast multipole method (FMM) [7], to be incorporated readily into the interpolation procedure.

Implementation of the algorithm includes following steps:

1) Initialization of $\delta_{m_1}(t_k^l)$ and $\delta_m(t_k^l)$. This preprocessing is needed only once and has a complexity of $O(Np_1)$ and $O(Np^2)$ respectively, taking $q = p$;

2) Calculation of g_m in (10). The complexity is $O(Np)$;

3) Calculation of $\hat{f}(n)$ in (9) by a standard FFT. The complexity is $O(N\log(N))$.

The total complexity is $O(Np + N\log(N))$ for steps 3 and 4. The preprocessing step needs to be done only once.

III. Numerical Results

The algorithm described above has been implemented using Fortran and matlab programs. To illustrate the accuracy of the algorithm, we take two functions as examples. The functions to be transformed in example 1 and 2, as shown in Figs. 1 and 2, are respectively defined as

$$f_1(x) = \begin{cases} \dfrac{x - x_1}{x_2 - x_1} & x_1 \le x \le x_2 \\ 0 & \text{elsewhere} \end{cases} \tag{11}$$

and

$$f_2(x) = \begin{cases} \alpha + \sin(2\pi\beta x) & x_1 \le x \le x_2 \\ 0 & \text{elsewhere} \end{cases} \tag{12}$$

In the calculations, we take $\nu = 4$, $p = 32$, and $p_1 = 2$ (Fig. 1) or $p_1 = 16$ (Fig. 2). Both uniformly and nonuniformly sampled data are used in each example. The nonuniformly spaced points are randomly distributed. We compare the numerical results with the analytical solutions. The error is defined as

$$E_\infty = \max_{-N/2 \le n \le N/2-1} |\hat{f}(n) - \hat{f}_a(n)| \tag{13}$$

where $\hat{f}_a(n)$ is the analytical solution. The difference between the results for the uniformly and nonuniformly sampled data is negligible. Table 1–3 show the accuracy and computer time of the algorithms. The CPU times is obtained on a SUN Ultra 1 workstation. For comparison, we also give the results of a direct application of FFT for a uniform grid with size N.

Finally, similar to a standard 2-D FFT algorithm, we calculate an example of 2-D FFT by the row-column deposition along with the above 1-D FFT algorithm. The function to be transformed in example 3 is

$$f(x,y) = f_1(x)\, f_2(y) \tag{14}$$

where f_1 and f_2 are defined in (12) and (13). In this example, the precalculations in both x- and y-direction 1-D FFTs are needed only once. Table 4 compares the accuracy of our algorithm with those obtained by a standard 2-D FFT.

In all examples, we note that with a comparable CPU time (excluding preprocessing which is needed only once), our algorithm is 10 order of magnitude more accurate than the standard FFT for double precision computations.

IV. Conclusion

In conclusion, we presented a fast algorithm for the evaluation of Fourier transform of piecewise smooth functions. By using a double interpolation procedure, the algorithm can be applied to both uniform and nonuniform sampled data. The complexity of algorithm is $O(Np + N\log(N))$ plus $O(Np^2)$ for precalculation. The numerical experiments show the accuracy and efficiency of the algorithm. This algorithm is useful for signal processing and for simulations.

References

[1] E. Sorets, "Fast Fourier transforms of piecewise constant function," *J. Computational Physics*, vol. 116, pp. 369–379, 1995.

[2] G. Beylkin, "On the fast Fourier transforms of functions with singularities," *Appl. Comput. Harmon. Anal.*, vol. 2, pp. 363–381, 1995.

[3] A. Dutt and V. Rokhlin, " Fast Fourier transforms for nonequispaced data," *SIAM J. Sci. Comput.*, vol. 14, pp. 1368–1393, 1993.

[4] A. Dutt and V. Rokhlin, " Fast Fourier transforms for nonequispaced data, II" *Appl. Comput. Harmon. Anal.*, vol. 2, pp. 85–100, 1995.

[5] Q. H. Liu, and N. Nguyen, "An accurate algorithm for nonuniform fast Fourier transforms (NUFFT)," *IEEE Microwave Guided Wave Lett.*, vol. 8, no. 1, pp. 18–20, 1998.

[6] N. Nguyen, and Q. H. Liu, "The regular Fourier matrices and nonuniform fast Fourier transforms," *SIAM J. Sci. Compt.*, vol. 21, no. 1, pp. 283–293, 1999.

[7] A. Dutt, M. Gu and V. Rokhlin, "Fast algorithms for polynomial interpolation, integration, and differentiation," *SIAM J. Numer. Anal.*, vol. 33, pp. 1689–1711, 1996.

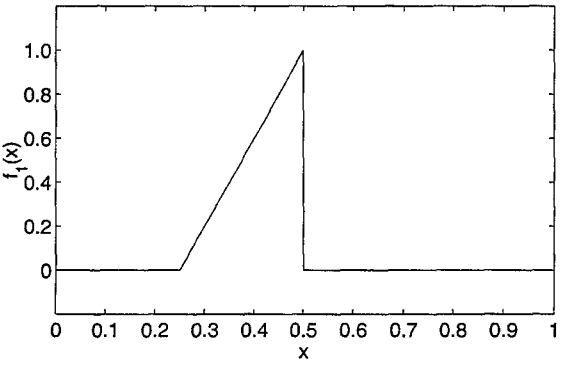


Figure 1. A triangle function for $0.25 \leq x \leq 0.5$.

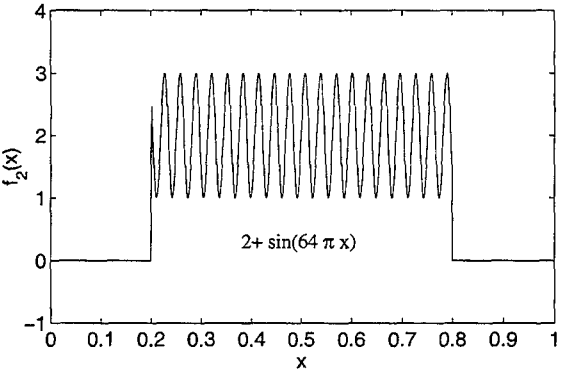


Figure 2. A sinusoidal function for $0.2 \leq x \leq 0.8$.

Table 1. Errors and run times for example 1 (double precision)

N	Errors (E_∞)		Timings (sec)			
	This paper	Direct	Init.	Eval.	FFT	Direct
64	1.130e-13	9.683e-03	0.198	0.006	0.008	0.002
128	1.120e-13	4.824e-03	0.346	0.012	0.017	0.004
256	1.130e-13	2.408e-03	0.768	0.024	0.037	0.008
512	1.120e-13	1.203e-03	1.535	0.049	0.081	0.017

Table 2. Errors and run times for example 1 (single precision)

N	Errors (E_∞)		Timings (sec)			
	This paper	Direct	Init.	Eval.	FFT	Direct
64	1.856e-07	9.683e-03	0.027	0.002	0.008	0.002
128	6.038e-07	4.824e-03	0.053	0.004	0.016	0.004
256	6.747e-07	2.408e-03	0.104	0.007	0.036	0.008
512	7.058e-07	1.203e-03	0.206	0.013	0.078	0.016

Table 3. Errors and run times for example 2 (double precision)

N	Errors (E_∞)		Timings (sec)			
	This paper	Direct	Init.	Eval.	FFT	Direct
512	1.471e-11	5.820e-02	0.591	0.020	0.081	0.017
1024	1.080e-12	2.920e-02	1.164	0.037	0.176	0.036

Table 4. Errors for the 2-D problem in example 3 (double precision)

N × M	Errors (E_∞)	
	This paper	Direct
128 × 512	2.916e-12	1.697e-03
256 × 1024	2.700e-13	8.511e-04

Applications of Nonuniform Fast Transform Algorithms in Numerical Solutions of Integral Equations

Q. H. Liu, X. M. Xu, and Z. Q. Zhang
Department of Electrical and Computer Engineering
Duke University
Durham, NC 27708
Email: Qing.Liu@duke.edu

Abstract

We review our recent efforts to apply the nonuniform fast Fourier transform (NUFFT) and fast Hankel transform (NUFHT) algorithms to numerical solutions of electromagnetic integral equations in frequency domains. The NUFFT is a fast algorithm to perform the discrete Fourier transform of data sampled nonuniformly with $O(N \log_2 N)$ arithmetic operations. Using the NUFFT scheme, we develop the nonuniform fast Hankel transform (NUFHT) algorithm. These NUFFT and NUFHT algorithms are then combined with the conjugate-gradient method to solve integral equations in Cartesian and cylindrical coordinates.

I. Introduction

In this work, we review our recent efforts to develop numerical solutions of Maxwell's equations using the nonuniform fast Fourier transform (NUFFT) and nonuniform fast Hankel transform algorithms.

The conventional method for solving integral equations in electromagnetics is the method of moment (MOM) [1]. Although effective for small-scale problems, this method requires $O(N^3)$ arithmetic operations, where N is the number of unknowns, because of the need to invert a dense matrix. It is therefore impractical to use the MOM for large-scale problems.

To reduce the computational complexity of integral equation methods, the conjugate-gradient fast Fourier transform (CG-FFT) method has been proposed which combines the iterative CG procedure with the FFT algorithm (see [2, 3] and the references therein). It results in a scheme with $O(KN \log_2 N)$ arithmetic operations, where K is the required number of CG iterations. Furthermore, there is no need to store the MOM matrix since the matrix-vector multiply is carried out implicitly in the convolution calculation using FFT. The memory requirement is only $O(N)$, much smaller than $O(N^2)$ required by the MOM. For cylindrical coordinates, a similar method, called the CG-FFHT (conjugate-gradient fast Fourier Hankel transform) method [4, 5], has been proposed.

However, because of the limitations of the available fast transform algorithms, these methods require the grid points to distribute uniformly in certain scales. Specifically, because of the FFT algorithm, the CG-FFT method require a uniform distribution of the grid points; The CG-FFHT method requires the grid points to distribute logarithmically uniform in the radial direction because of a coordinate transformation involving an exponential function in the FHT algorithm. This poses an undesirable limitation to the accuracy and flexibility of the spectral domain methods. For example, for problems with both electrically large and small regions, it is more efficient to sample nonuniformly so that a higher resolution is achieved in the electrically small region. This is not possible unless fast Fourier and Hankel transforms can be achieved for nonuniformly sampled data.

Recently, the nonuniform fast Fourier transform algorithm have attracted considerable attention because of its importance in many applications [6–10]. With the NUFFT and the related nonuniform fast Hankel transform (NUFHT) algorithms [11], this work aims to remove this important limitation of a uniform grid in the spectral domain methods for integral equations.

II. Formulation

The objective of this section is to develop the formulation for spectral domain methods using the nonuniform fast transform algorithms. The NUFFT algorithm provides a fundamental tool to nonuniform fast Hankel transform algorithm. These algorithms are then incorporated in the CG-FFT and CG-FFHT methods for integral equations.

A. The NUFFT and NUFHT Algorithms

NUFFT Algorithms. We first define a nonuniform discrete Fourier transform (NUDFT-1, denoted by $\mathcal{F}_1$) of $\{\alpha_k\}$

$$f_j \equiv \{\mathcal{F}_1[\alpha]\}_j = \sum_{k=-N/2}^{N/2-1} \alpha_k e^{it_k \cdot \omega_j}, \quad j = -N/2, \cdots, N/2-1 \tag{1}$$

where the frequency samples $\{\omega_j = 2\pi j/N\}$ are uniform, but the time samples $\{t_k\} \in [-N/2, N/2]$ are nonuniform. A related nonuniform discrete Fourier transform (NUDFT-2, denoted by $\mathcal{F}_2$) of $\{\beta_k\}$ is defined as

$$g_j \equiv \{\mathcal{F}_2[\beta]\}_j = \sum_{k=-N/2}^{N/2-1} \beta_k e^{ik\omega_j}, \quad j = -N/2, \cdots, N/2-1 \tag{2}$$

where the frequency samples $\{\omega_j\} \in [-\pi, \pi]$ are nonuniform but the time samples $\{t_k = k\}$ are uniform. The input data $\{\alpha_k\}$ and $\{\beta_k\}$ are the data at time sample points $\{t_k\}$. Note that the regular FFT algorithms do not apply to these DFT's. A direct summation of (1) and (2) requires $O(N^2)$ operations.

In [6–10] fast algorithms with $O(N \log_2 N)$ arithmetic operations have been developed for these DFT's. In particular, in [8, 10] we use a least-squares method to interpolate an exponential function at a set of nonuniform points with another set of oversampled $(q+1)$ uniform points. Using this method, for example, (1) is rewritten as

$$f_j s_j = \sum_{k=-N/2}^{N/2-1} \alpha_k \sum_{\ell=-q/2}^{q/2} x_\ell(t_k) e^{i2\pi j([mt_k]+\ell)/mN}, \quad j = -N/2, \cdots, N/2-1 \tag{3}$$

where $s_j = \cos(j\pi/mN)$ is called the accuracy factor, m is the oversampling rate (usually equal to 2), $[mt_k]$ denotes the nearest integer of mt_k, and $x_\ell(t_k)$ are the interpolation coefficients. Using the least-squares method we find that the interpolation coefficients array of length $(q+1)$ can be written as $x(t_k) = F^{-1}a(t_k)$, where array a and matrix F are in closed forms. More importantly, $F = F(m, N, q)$ is independent of t_k, a remarkable property that gives an efficient interpolation since F of dimension $(q+1) \times (q+1)$ and its inverse only need to be calculated once, rather than N times. Once the interpolation coefficients are known, the DFT of the interpolated data on the uniform points can be performed efficiently by the regular FFT algorithm.

The inverse DFT's, i.e. to find $\{\alpha_k\}$ and $\{\beta_k\}$ from $\{f_j\}$ and $\{g_j\}$ respectively, cost $O(N^3)$ operations if the direct matrix inversion is performed. Instead, noting that the product of the matrix $[A_{jk}] = [\exp(it_k\omega_j)]$ in (1) and its complex-conjugated transpose produces a Toeplitz matrix, we use a CG-FFT method for the inversion which costs only $O(KN \log_2 N)$ operations [6, 9]. We refer to these inverse algorithms as NUIFFT-1 and NUIFFT-2, and denote them as $\mathcal{F}_1^{-1}$ and $\mathcal{F}_2^{-1}$ respectively. In this work, we employ the fast algorithms in [8–10] for these DFT's which are optimal with the least-squares errors. They use the regular Fourier matrices for the interpolation of nonuniform data.

NUFHT Algorithm. The Hankel transform of a function $f(\rho)$ is defined as

$$\tilde{f}(k_\rho) = \int_0^\infty f(\rho) J_n(k_\rho \rho) \rho d\rho \tag{4}$$

where J_n is the Bessel function of order n. Making the change of variables $\rho = \tilde{\rho} e^{ax}$ and $k_\rho = \tilde{k} e^{-ax}$, we can write (4) as a convolution. Using the convolution theorem, we then obtain the Fourier transform of $\tilde{k} \exp(-ax) \tilde{f}(\tilde{k} e^{-ax})$ as

$$H(\omega) = H_n(\omega) F(\omega) \tag{5}$$

where $F(\omega)$ is the Fourier transform of $\tilde{\rho} e^{ax} f(\tilde{\rho} e^{ax})$, and $H_n(\omega)$ is a closed-form Fourier transform of function $a\check{k}\tilde{\rho} \exp(ax) J_n[\check{k}\tilde{\rho} \exp(ax)]$. In the discrete form, if $\{x_m\}$ $(m = -N/2, \cdots, N/2-1)$ are nonuniform, we can find $F(\omega_j)$, thus $H(\omega_j)$, at some uniform $\{\omega_j\}$ using the NUFFT-1 algorithm. Finally, from the definition of the NUDFT-1, the nonuniform Hankel transform is obtained as

$$\tilde{f}(k_{\rho j}) \equiv \{\mathcal{H}_n[f(\rho_k)]\}_j = \frac{e^{ax_j}}{\Delta x_j \tilde{k}} \left\{\mathcal{F}_1^{-1}[H(\omega_k)]\right\}_j, j = -N/2, \cdots, N/2-1 \tag{6}$$

Alternatively, equation (6) can be replaced by an NUFFT-2 algorithm (see the following discussions on convolution for more details). The inverse Hankel transform can be obtained in the same way since its definition is identical to (4). The number of arithmetic operations is $O(N \log_2 N)$ [11].

B. Convolution on a Nonuniform Grid

We now discuss the fast convolution on a nonuniform grid. To approximate this continuous operation, we assume that the input functions are band-limited and the truncation error is negligible.

We consider the convolution of two functions $g(x)$ and $f(x)$ with the desired results at a set of N nonuniform points $\{x_k\} \in [x_{\min} = -N/2, x_{\max} = N/2]$:

$$h(x_k) = \{g(x) \otimes f(x)\}(x_k) \tag{7}$$

where $f(x)$ is assumed zero outside $[x_{\min}, x_{\max}]$, while $g(x)$ is the convolution kernel and may have an infinite support. In order to use the convolution theorem, we pad $\{f(x_k)\}$ with $N/2$ zeros on both ends; The kernel function $g(x)$ is calculated with $2N$ points, possibly all nonzero. With a slight abuse of notations, we denote these two finite arrays of length $2N$ by f and g, respectively.

Now, using the convolution theorem, the NUDFT's of h, g and f are related by

$$H(\omega_j) = G(\omega_j) F(\omega_j) = \sum_{k=-N}^{N-1} \Delta x_k h(x_k) e^{ix_k \omega_j}, \quad j = -N, \cdots, N-1 \tag{8}$$

where $x_k \in [-N, N]$, $\omega_j = (j + 1/2)\pi/N$, and G and F are the NUDFT's of $\{g(x_k)\Delta x_k\}$ and $\{f(x_k)\Delta x_k\}$, respectively, with a length of $2N$. Note G and F are defined in the same way as the right-hand side of (8). Therefore, the convolution result is approximated by

$$h(x_k) \approx \left\{ \frac{e^{-ix_k \pi/2N}}{\Delta x_k} \cdot \mathcal{F}_1^{-1}[H] \right\}_k, \quad k = -N/2, \cdots, N/2-1 \tag{9}$$

where $\mathcal{F}_1^{-1}[H]$ stands for the NUIFFT-1 with a length of $2N$.

Alternatively, the convolution can also be calculated by using the NUFFT-2 algorithm instead of the NUIFFT-1 algorithm. Note that the continuous inverse Fourier transform is

$$h(x) = \frac{1}{2\pi} \int_{-\infty}^{\infty} H(\omega) e^{-i\omega x} d\omega. \tag{10}$$

Approximating this integral by the trapezoidal rule, we have

$$h(x_k) \approx \frac{e^{-ix_k\pi/2N}}{2N} \left\{ (\mathcal{F}_2[H^*])^* \right\}_k, \quad k = -N/2, \cdots, N/2-1 \tag{11}$$

where $\mathcal{F}_2$ stands for the NUFFT-2 of length $2N$, and the asterisk denotes the complex conjugation.

Thus, we have developed an efficient method to compute the convolution on a nonuniform grid with $O(N \log_2 N)$ arithmetic operations. Note that in the above formulation, for convenience we have assigned x to a special range. In practice, x can take any range which can be easily transformed to the above range with a linear coordinate transformation.

B. The CG-NUFFT Method

We now combine the CG method and the NUFFT algorithm to solve integral equations in electromagnetic wave scattering problems. For simplicity, consider a 2-D TM_z plane wave incident on an isotropic, inhomogeneous cylinder $S(x, y)$ with electric permittivity $\epsilon(x, y)$, electric conductivity $\sigma(x, y)$, and magnetic permeability $\mu = \mu_0$. From Maxwell's equations we can derive the integral equation for the electric field

$$E_z(x, y) + \omega^2 \mu_0 \int_S [\tilde{\epsilon}(x', y') - \tilde{\epsilon}_b] g(x - x', y - y') E_z(x', y') dx' dy' = E_z^{\text{inc}} \tag{12}$$

where $\tilde{\epsilon} = \epsilon + i\sigma/\omega$ and $\tilde{\epsilon}_b = \epsilon_b + i\sigma_b/\omega$ are the complex permittivity of the cylinder and background medium, respectively, E_z^{inc} is the incident field in the background medium, and S is the support of the scatterer. Note that the integral in (12) is convolutional. Hence, by using the convolution theorem we arrive at an operator equation

$$\mathcal{L} E_z(x, y) = E_z^{\text{inc}}(x, y) \tag{13}$$

where

$$\mathcal{L}[\,\cdot\,] = [\,\cdot\,] + \mathcal{F}^{-1}\{\mathcal{F}[\omega^2 \mu_0 (\tilde{\epsilon} - \tilde{\epsilon}_b)(\,\cdot\,)] \cdot \mathcal{F}[g(x, y)]\} \tag{14}$$

Here, $\mathcal{F}$ and $\mathcal{F}^{-1}$ stand for forward and inverse Fourier transforms in two dimensions.

Similar to the CG-FFT method (see [2, 3] and references therein), the CG-NUFFT method solves equation (13) iteratively using the conjugate-gradient method. Within each CG iteration, the forward and inverse NUDFT's are obtained efficiently by the NUFFT algorithms with $O(N \log_2 N)$ arithmetic operations. Therefore the CG-NUFFT retains the computational efficiency of the CG-FFT method, but gives the important flexibility of nonuniform sampling.

C. The CG-NUFFHT Method

Similarly we can formulate the integral equation in cylindrical coordinates for axisymmetric problems. For a circular loop antenna located at (ρ_0, z_0) in an axisymmetric medium with permittivity $\epsilon(\rho, z)$, permeability $\mu = \mu_0$, and conductivity $\sigma(\rho, z)$, the integral equation can be derived as

$$E_\phi(\rho, z) = E_\phi^{\text{inc}} + \int_{-\infty}^{\infty} dz' \int_0^{\infty} d\rho' g(\rho, \rho', z - z') \Delta k^2(\rho', z') E_\phi(\rho', z') \tag{15}$$

where $\Delta k^2 = \omega^2\mu_0(\tilde{\epsilon} - \tilde{\epsilon}_b)$ is the contrast function, and g is the Green's function for the axisymmetric problem in cylindrical coordinates. Using the convolution theorem in z and Hankel transform in ρ, this integral equation can be written in an operator form [4, 5]

$$\mathcal{L}[E_\phi(\rho, z)] = E_\phi^{\text{inc}}(\rho, z) \tag{16}$$

where

$$\mathcal{L}[\cdot] = [\cdot] - \mathcal{F}^{-1}\mathcal{H}_1^{-1}\left\{\frac{1}{(k_\rho^2 + k_z^2 - k_b^2)} \cdot \mathcal{F}\mathcal{H}_1[(k^2 - k_b^2)\,(\cdot)]\right\} \tag{17}$$

and $\mathcal{H}_1$ denotes the Hankel transform of order 1 in ρ direction, while $\mathcal{F}$ stands for the Fourier transform in z direction. These transforms are obtained by the NUFHT algorithm and NUFFT algorithms, respectively. Then the operator equation (16) can be solved by the CG method. In each iteration of the CG method, NUFHT and NUFFT algorithms perform the operation in (17) with $O(N \log_2 N)$ arithmetic operations.

III. Numerical Results

We now present some numerical results for the above methods. Figure 1 shows the convolution of a function $f(x) = \cos(x)\exp[-36(x-2.5)^2/L^2]$ with another function $g(x) = \exp(-|x-2.5|)$ on the nonuniform grid within $L = 11.4$, $-3.2 \le x \le 8.2$. The function is sampled by $N = 64$ nonuniform points with the cell size Δx shown in Figure 1(a). The ratio between maximum and minimum Δx is $\Delta x_{\max}/\Delta x_{\min} = 40.7$.

We have applied the CG-NUFFT method to solve 2-D scattering problems. A square cylinder ($\epsilon_r = 2.56$) in Figure 2(a) is coated with a very thin layer of dielectric ($\epsilon_r = 4$). With a plane TM_z wave incident from the left, the induced electric current density calculated by the CG-NUFFT method is compared with the MOM results in Figures 2(b) and 2(c), respectively across the center lines in x and y directions. The radar scattering width is shown in Figure 2(d). For this problem, the number of unknowns is $N_x \times N_y = 48 \times 48$ for both methods. The nonuniform grid is set up such that there are two grid points inside the thin coating, and larger cell size is used outside the coating. The CG-NUFFT method requires much smaller computer memory than the MOM.

Finally we show an application of the CG-NUFFHT method for electromagnetic induction well logging. The axisymmetric, inhomogeneous medium is shown in Figure 3(a), where an induction tool consisting of two coaxial coil antennas, one as transmitter and the other as receiver, moves along the borehole axis. Because of the presence of the thin bed and the slightly different invasion radii in the two thick beds, a nonuniform grid is necessary both in z and ρ directions. Figure 3(b) shows the CG-NUFFHT results compared with the numerical mode-matching [12] results. If a uniform grid with the same cell size as in the thick beds is used, the CG-FFHT result will miss the thin bed, as clearly shown in the figure.

Conclusions

With the recent progress in the development of nonuniform fast Fourier transform and Hankel transform algorithms, it is now possible to use a nonuniform grid in an iterative solution of integral equations in electromagnetics. Here we have reviewed the applications of these nonuniform fast transform algorithms in the CG-NUFFT and CG-NUFFHT for two-dimensional integral equations in Cartesian and cylindrical coordinates. Compared to the conventional methods with a uniform grid, these spectral domain methods provide the important flexibility in modeling media with both electrically large and electrically small regions. Furthermore, we believe that the nonuniform grid can handle Gibbs phenomenon much better than a uniform grid. Much further investigation is needed in this regard to remove or reduce the Gibbs phenomenon associated with spectral domain methods.

Acknowledgment

This work was supported by Environmental Protection Agency through a PECASE grant CR-825-225-010, and by the National Science Foundation through a CAREER grant ECS-9702195.

References

[1] R. F. Harrington, *Field Computation by Moment Method*, New York: Macmillan, 1968.

[2] T. K. Sarkar, *Application of Conjugate Gradient Method to Electromagnetics and Signal Analysis*, PIER 5, Progress in Electromagnetics Research, New York: Elsevier, 1991.

[3] M. F. Catedra, R. P. Torres, J. Basterrechea, and E. Gago, *The CG-FFT Method: Application of Signal Processing Techniques to Electromagnetics*, Boston: Artech House, 1995.

[4] Q. H. Liu, and W. C. Chew, "A CG-FFHT method for the scattering solution of axisymmetric inhomogeneous media," *Microwave Opt. Tech. Lett.*, vol. 6, pp. 101–104, 1993.

[5] Q. H. Liu, and W. C. Chew, "Applications of the conjugate gradient fast Fourier Hankel transfer method with an improved fast Hankel transform," *Radio Sci.*, vol. 29, pp. 1009–1022, 1994.

[6] A. Dutt and V. Rokhlin, "Fast Fourier transforms for nonequispaced data," *SIAM J. Sci. Comput.*, vol. 14, No. 6, pp 1368-1393, November 1993.

[7] G. Beylkin, "On the fast Fourier transform of functions with singularities," *Appl. Computat. Harmonic Anal.*," vol. 2, pp. 363–382, 1995.

[8] Q. H. Liu, and N. Nguyen, "An accurate algorithm for nonuniform fast Fourier transforms," *IEEE Microwave Guided Wave Lett.*, vol. 8, no. 1, pp. 18–20, 1998.

[9] Q.H. Liu and X.Y. Tang, "Iterative algorithm for nonuniform inverse fast Fourier transform (NU-IFFT)," *Electronics Letters*, vol. 34, No. 20, pp. 1913–1914, 1998.

[10] N. Nguyen, and Q. H. Liu, "The regular Fourier matrices and nonuniform fast Fourier transforms," *SIAM J. Sci. Compt.*, vol. 21, no. 1, pp. 283–293, 1999.

[11] Q. H. Liu, and Z. Q. Zhang, "A nonuniform fast Hankel transform (NUFHT) algorithm," *Applied Optics*, scheduled for vol. 38, no. 32, 1999.

[12] W. C. Chew, Z. Nie, Q. H. Liu, and B. Anderson, "An efficient solution of electrical well logging tools in a complex environment," *IEEE Trans. Geosci. Remote Sensing*, vol. GE-29, pp. 308–313, 1991.

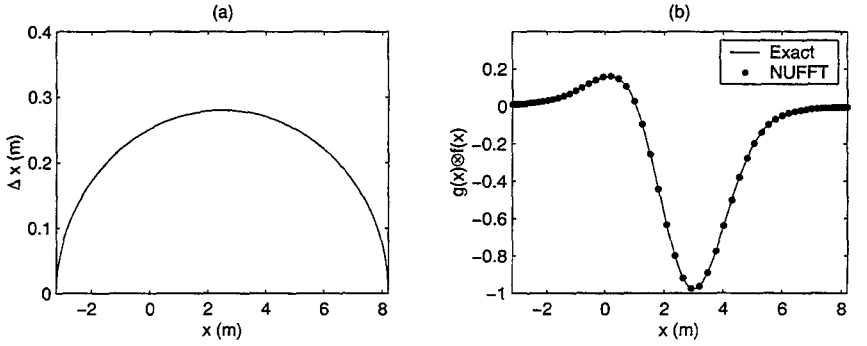


Figure 1. The convolution of function $f(x)\cos(x)\exp[-36(x-2.5)^2/L^2]$ and $g(x) = \exp(-|x-2.5|)$ at a nonuniform grid through the NUFFT algorithm. (a) Cell size Δx as a function of the position. (b) The convolution on the nonuniform grid.

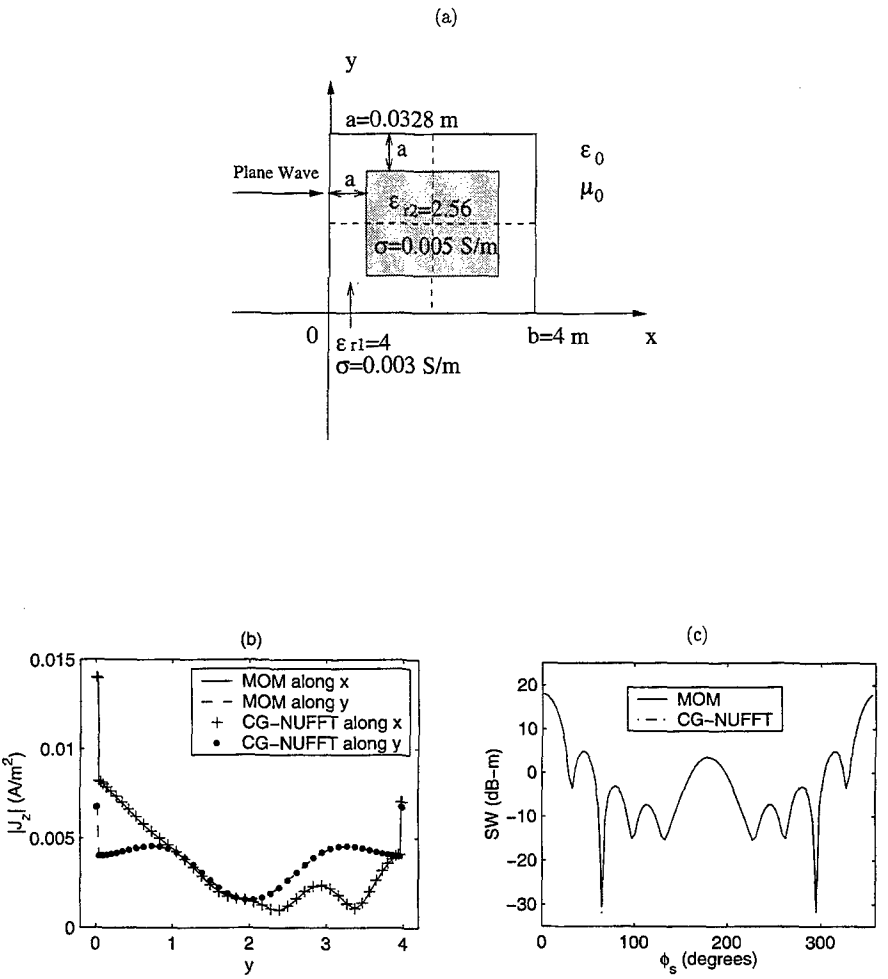


Figure 2. The scattering of a square cylinder coated with a thin dielectric layer. (a) Geometry. (b) The induced electric current density along the center lines in x and y directions compared with the MOM results. (c) The radar scattering width from the CG-NUFFT and the MOM.

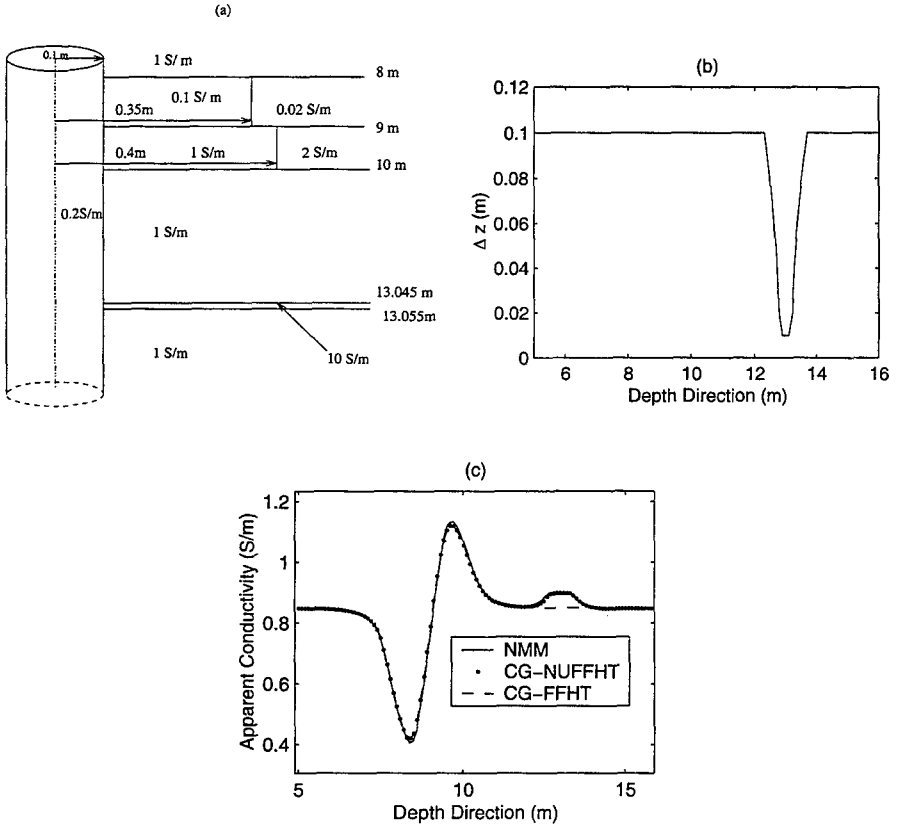


Figure 3. Induction measurement in an axisymmetric medium with a thin bed. (a) Geometry. (b) Cell size Δz in the vertical direction. (c) Comparison of apparent conductivity calculated by CG-NUFFHT, CG-FFHT, and NMM methods.

SESSION 16

APPLICATIONS OF THE FDTD TECHNIQUE

Chairs: Atef Elsherbeni and Wenhua Yu

A Non-Dissipative Staggered Fourth-Order Accurate Explicit Finite Difference Scheme for the Time-Domain Maxwell's Equations.

A. Yefet and P. G. Petropoulos
New Jersey Institute of Technology
University Heights, Newark, NJ 07105.
yefet@m.njit.edu, peterp@m.njit.edu

Abstract

We consider a divergence-free non-dissipative fourth-order explicit staggered finite difference scheme for the hyperbolic Maxwell's equations. Special one-sided difference operators are derived in order to implement the scheme near metal boundaries and dielectric interfaces. Numerical results show the scheme is long-time stable, and is fourth-order convergent over complex domains that include dielectric interfaces and perfectly conducting surfaces. We also examine the scheme's behavior near metal surfaces that are not alligned with the grid axes, and compare its accuracy to that obtained by the Yee scheme.

1 Maxwell Equations

We consider the two dimensional case with $J = 0$. The only sources for the problem are incident waves. These waves will be scattered after they encounter an obstacle. Furthermore, in free space ϵ and μ are constants. The extension of the method to three space dimensions, sources and variable coefficients is straightforward. Maxwell's equations now decouples into two independent sets of equations. We shall consider the TM system. Let $\tau = ct = t/\sqrt{\mu\epsilon}$ and $Z = \sqrt{\frac{\mu}{\epsilon}}$, where ϵ and μ are the permittivity and permeability coefficients, in free space, respectively and c is the speed of light. The TM wave equations then become:

$$\frac{\partial E_z}{\partial \tau} = Z(\frac{\partial H_y}{\partial x} - \frac{\partial H_x}{\partial y})$$

$$\begin{aligned} \frac{\partial H_x}{\partial \tau} &= -\frac{1}{Z}\frac{\partial E_z}{\partial y} \\ \frac{\partial H_y}{\partial \tau} &= \frac{1}{Z}\frac{\partial E_z}{\partial x} \end{aligned} \tag{1}$$

2 Finite Differences Scheme

We approximate the spatial derivatives to fourth order, using the following explicit method for $\frac{\partial U}{\partial y}$:
explicit(2,4):

$$\left.\frac{\partial U}{\partial y}\right|_{i,j+1/2} = \frac{1}{24\Delta y}\left(U_{i,j-1} - 27U_{i,j} + 27U_{i,j+1} - U_{i,j+2}\right) \tag{2}$$

We shall refer to 2 as the explicit(2,4) scheme. At the first and last points we use a fourth order and fifth order accurate one sided approximation to the derivative. We note that this is used only in order to globally approximate the derivative. No physical boundary conditions are included at this stage. The approximations are as follows:

$$\begin{aligned} \left.\frac{\partial U}{\partial y}\right|_{i,1/2} &= \frac{1}{24\Delta y}\left(-22U_{i,0} + 17U_{i,1} + 9U_{i,2} - 5U_{i,3} + U_{i,4}\right) \\ \left.\frac{\partial U}{\partial y}\right|_{i,1} &= \frac{1}{24\Delta y}\left(-23U_{i,1/2} + 21U_{i,3/2} + 3U_{i,5/2} - U_{i,7/2}\right) \\ \left.\frac{\partial U}{\partial y}\right|_{i,N-1} &= \frac{1}{24\Delta y}\left(23U_{i,N-1/2} - 21U_{i,N-3/2} - 3U_{i,N-5/2} + U_{i,N-7/2}\right) \\ \left.\frac{\partial U}{\partial y}\right|_{i,N-1/2} &= \frac{1}{24\Delta y}\left(22U_{i,N} - 17U_{i,N-1} - 9U_{i,N-2} + 5U_{i,N-3} - U_{i,N-4}\right) \end{aligned}$$

Define

$$\mathbf{A_H} = \frac{\mathbf{1}}{\mathbf{24}}\begin{bmatrix} -23 & 21 & 3 & -1 & . & . & 0 \\ 1 & -27 & 27 & -1 & . & . & 0 \\ 0 & 1 & -27 & 27 & -1 & . & 0 \\ . & . & . & . & . & . & \\ 0 & . & . & 1 & -27 & 27 & -1 \\ 0 & . & . & 1 & -3 & -21 & 23 \end{bmatrix}. \tag{3}$$

$$\mathbf{A_E} = \frac{\mathbf{1}}{\mathbf{24}} \begin{bmatrix} -22 & 17 & 9 & -5 & 1 & . & 0 \\ 1 & -27 & 27 & -1 & . & . & 0 \\ 0 & 1 & -27 & 27 & -1 & . & 0 \\ . & . & . & . & . & . & \\ 0 & . & . & 1 & -27 & 27 & -1 \\ 0 & . & -1 & 5 & -9 & -17 & 22 \end{bmatrix}. \tag{4}$$

The matrix form of The TM equations is:

$$[EZ_{i,j}]^{n+1} = [EZ_{i,j}]^n + \frac{\Delta t}{\Delta x}\mathbf{A_H}[\mathbf{HY_{i+1/2,j}}]^{\mathbf{n+1/2}} - \frac{\mathbf{\Delta t}}{\mathbf{\Delta y}}[\mathbf{HX_{i,j+1/2}}]^{\mathbf{n+1/2}}\mathbf{A_H^t}$$

$$[HX_{i,j+1/2}]^{n+1/2} = [HX_{i,j+1/2}]^{n-1/2} - \frac{\Delta t}{\Delta y}[EZ_{i,j}]^n\mathbf{A_E^t}$$

$$[HY_{i+1/2,j}]^{n+1/2} = [HY_{i+1/2,j}]^{n-1/2} - \frac{\Delta t}{\Delta x}\mathbf{A_E}[\mathbf{EZ_{i,j}}]^{\mathbf{n}}$$

3 Time Step

For each numerical method one must choose a time step for the numerical integration. This time step is based on two considerations: stability and accuracy. Since all the schemes have stability limits this places an upper bound on the usable time step.

Since we wish higher order accuracy it is also necessary to limit the time by accuracy requirements. We do not want the accuracy of the scheme to be determined by the time integration. Hence, the temporal error should be equal to or less than the spatial error. For the explicit(2,4) scheme the time step chosen depends on the accuracy desired. As the mesh is refined the spatial error decreases as a fourth order scheme and so decreases faster than the temporal error. Thus, the time step should depend on $(\Delta x)^2$. If the error requirements are too severe then this is inefficient and the leapfrog in time should be replaced by a fourth order Runge-Kutta method. However, for the experiments in this paper we shall use the same leapfrog method for this scheme.

4 Computational Results

We wish to compare the efficiency of three different schemes: the standard Yee scheme ([1]), the explicit(2,4) scheme and the Ty(2,4) ([2]) scheme advanced in time by a leapfrog method. For conciseness of notation we shall refer to these schemes as Yee, and explicit(2,4) and the Ty(2,4) respectively. For all computations we choose $Z = 1$ unless it's stated otherwise. In some of the cases we used the Berenger PML layer in the far field or Gedney's PML method, where it was needed. In all cases the error is measured between the exact E_z and the numerical E_z in L_2 norm.

We first consider the simplest mode of propagation in a rectangular cross section wave guide. We take the walls to be perfect conductors. For simplicity, we assume that the permeability is everywhere 1. We take the followin boundary and initial conditions:

$$\begin{aligned}
E_z(x,y,0) &= \sin(3\pi x)\sin(4\pi y) \\
H_y(x,y,\frac{\Delta t}{2}) &= -\frac{3}{5}\sin(3\pi x - \frac{5\pi\Delta t}{2})\sin(4\pi y) \\
H_x(x,y,\frac{\Delta t}{2}) &= -\frac{4}{5}\cos(3\pi x - \frac{5\pi\Delta t}{2})\sin(4\pi y) \\
E_z(0,y,t) &= -\sin(5\pi t)\sin(4\pi y) \\
E_z(1,y,t) &= \sin(3\pi - 5\pi t)\sin(4\pi y) \\
E_z(x,0,t) &= 0 \\
E_z(x,1,t) &= 0
\end{aligned}$$

The solution is then:

$$E_z(x,y,t) = \sin(3\pi x - 5\pi t)\sin(4\pi y).$$

For the three schemes we choose uniform gridspacing. For the Yee, the explicit(2,4) and the Ty(2,4) schemes we take: $h = \Delta x = \Delta y = 1/20, 1/40, 1/80$. For the Yee scheme we take $\Delta t = 2h/3$ and for the explicit(2,4) scheme we take $\Delta t = h^2$.

In table 1 we present the errors in L_2 norm for the Yee and the explicit(2,4) scheme. In both cases the errors are almost linear in time. However as the mesh is refined the Yee scheme yields second order accuracy while the explicit(2,4) yields between fourth and fifth order accuracy.

scheme	h	Δt	$Max(\|\|error\|\|_{L_2})$ $0 \leq t \leq 10$	*rate*
$explicit(2,4)$	$\frac{1}{20}$	$\frac{1}{400}$	0.014	
$explicit(2,4)$	$\frac{1}{40}$	$\frac{1}{1600}$	1.9316×10^{-4}	6.2
$explicit(2,4)$	$\frac{1}{80}$	$\frac{1}{3200}$	6.48×10^{-6}	4.896
$Ty(2,4)$	$\frac{1}{20}$	$\frac{1}{400}$	0.0242	
$Ty(2,4)$	$\frac{1}{40}$	$\frac{1}{1440}$	7.9304×10^{-5}	8.15
$Ty(2,4)$	$\frac{1}{80}$	$\frac{1}{3440}$	2.329×10^{-6}	5.089
Yee	$\frac{1}{20}$	$\frac{1}{30}$	0.1889	
Yee	$\frac{1}{40}$	$\frac{1}{60}$	0.0476	1.9885
Yee	$\frac{1}{80}$	$\frac{1}{120}$	0.0119	2.0032

Table 1: The maximal errors in L_2 norm.

We next consider the treatment of a domain which contains air and a lossless dielectric with a relative permittivity of ϵ_2 as shown in Fig(1).

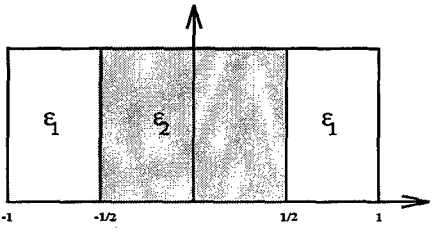


Figure 1: The computational domain

E_z is continuous but its second derivatives are discontinuous. To overcome this problem we use an innovative approach, which is presented in [6] and [7]. This approach helps to preserve the fourth order accurcy of the explicit scheme. In this approach we divide the computational domain into three subdomains. Two contain air and the third one contains the lossless dielectric. On the interfaces the treatment differs. On the interfaces both the electric and magnetic fields are approximated. Suppose the interfaces are located at $i = I_1$ and $i = I_2$ and $\epsilon = \epsilon_2$ for $I_1 < i < I_2$ and $\epsilon = \epsilon_1$ at $i > I_2$ and $i < I_1$. We approximate H_y at $i = I_1$ and $i = I_2$ by using the following fifth order extrapolation:

$$H^{n+1/2}_{y_{I_1,j}} = \frac{315}{128}H^{n+1/2}_{y_{I_1-1/2,j}} - \frac{105}{32}H^{n+1/2}_{y_{I_1-3/2,j}} + \frac{189}{64}H^{n+1/2}_{y_{I_1-5/2,j}} - \frac{45}{32}H^{n+1/2}_{y_{I_1-7/2,j}} + \frac{35}{128}H^{n+1/2}_{y_{I_1-9/2,j}}$$

$$H^{n+1/2}_{y_{I_2,j}} = \frac{315}{128}H^{n+1/2}_{y_{I_2+1/2,j}} - \frac{105}{32}H^{n+1/2}_{y_{I_2+3/2,j}} + \frac{189}{64}H^{n+1/2}_{y_{I_2+5/2,j}} - \frac{45}{32}H^{n+1/2}_{y_{I_2+7/2,j}} + \frac{35}{128}H^{n+1/2}_{y_{I_2+9/2,j}}$$

$H^{n+1/2}_{y_{I_1},j}$ can be extarpolated by using the points to the left of I_1 or to the right of I_1. This is true because H_y is a continuous function. Once H_y is approximated on the interface we approximte the x derivative of H_y using $H_{y_{I_1},j}$ and $H_{y_{I_2},j}$ This is done in order to approx imate the time derivative of E_z. This is done the following way:

$$\frac{\partial}{\partial x}H^{n+1/2}_{y_{I_1},j} \sim \tfrac{352}{105}H_{y_{I_1},j} - \tfrac{35}{8}H_{y_{I_1+1/2}} + \tfrac{35}{24}H_{y_{I_1+3/2},j} - \tfrac{21}{40}H_{y_{I_1+5/2},j} + \tfrac{5}{46}H_{y_{I_1+7/2},j}$$
$$\frac{\partial}{\partial x}H^{n+1/2}_{y_{I_2},j} \sim -\tfrac{352}{105}H_{y_{I_2},j} + \tfrac{35}{8}H_{y_{I_2-1/2}} - \tfrac{35}{24}H_{y_{I_2-3/2},j} + \tfrac{21}{40}H_{y_{I_2-5/2},j} - \tfrac{5}{46}H_{y_{I_2-7/2},j}$$

Once $\frac{\partial}{\partial x}H^{n+1/2}_{y_{I_1},j}$ and $\frac{\partial}{\partial x}H^{n+1/2}_{y_{I_2},j}$ are calculated we can evaluate $EZ^{n+1}_{I_1,j}$ and $EZ^{n+1}_{I_2,j}$ the following way:

$$\begin{aligned} EZ^{n+1}_{I_1,j} &= EZ^{n}_{I_1,j} - \tfrac{dt}{24\Delta y}\left(H_{x_{I_1,j-3/2}} - 27H_{x_{I_1,j-1/2}} + 27H_{x_{I_1,j+1/2}} - H_{x_{I_1,j+3/2}}\right) \\ &+ \tfrac{dt}{\Delta x}\left(\tfrac{352}{105}H^{n+1/2}_{y_{I_1},j} - \tfrac{35}{8}H^{n+1/2}_{y_{I_1+1/2},j} + \tfrac{35}{24}H^{n+1/2}_{y_{I_1+3/2},j} - \tfrac{21}{40}H^{n+1/2}_{y_{I_1+5/2},j} + \tfrac{5}{46}H^{n+1/2}_{y_{I_1+7/2},j}\right) \end{aligned}$$

$$\begin{aligned} EZ^{n+1}_{I_2,j} &= EZ^{n}_{I_1,j} - \tfrac{dt}{24\Delta y}\left(H_{x_{I_2,j-3/2}} - 27H_{x_{I_2,j-1/2}} + 27H_{x_{I_2,j+1/2}} - H_{x_{I_2,j+3/2}}\right) \\ &+ \tfrac{dt}{\Delta x}\left(-\tfrac{352}{105}H^{n+1/2}_{y_{I_2},j} + \tfrac{35}{8}H^{n+1/2}_{y_{I_2+1/2},j} - \tfrac{35}{24}H^{n+1/2}_{y_{I_2+3/2},j} + \tfrac{21}{40}H^{n+1/2}_{y_{I_2+5/2},j} - \tfrac{5}{46}H^{n+1/2}_{y_{I_2+7/2},j}\right) \end{aligned}$$

Since $\frac{\partial}{\partial x}H^{n+1/2}_{y_{I_1},j}$ and $\frac{\partial}{\partial x}H^{n+1/2}_{y_{I_1},j}$ are approximated where $\epsilon = \epsilon_2$ we set $\epsilon = \epsilon_2$ at $i = I_1$ and $i = I_2$. The extension of this innovation to two and three dimensions can be found in [6].

The slope of the Yee scheme is 2 and the slope of the Ty(2,4) scheme and the explicit(2,4) converges to 4 as can be seen in table 2

scheme	h	Δt	$Max(\|\|error\|\|_{L_2})$ $0 \le t \le 10$	*rate*
explicit(2,4)	$\frac{1}{20}$	$\frac{1}{400}$	6.9239×10^{-5}	
explicit(2,4)	$\frac{1}{40}$	$\frac{1}{1600}$	3.5486×10^{-6}	4.286
explicit(2,4)	$\frac{1}{80}$	$\frac{1}{3200}$	2.0112×10^{-7}	4.141
$Ty(2,4)$	$\frac{1}{20}$	$\frac{1}{400}$	2.7043×10^{-5}	
$Ty(2,4)$	$\frac{1}{40}$	$\frac{1}{1600}$	1.4233×10^{-6}	4.249
$Ty(2,4)$	$\frac{1}{80}$	$\frac{1}{6400}$	1.1040×10^{-7}	3.688
Yee	$\frac{1}{20}$	$\frac{1}{30}$	0.0095	
Yee	$\frac{1}{40}$	$\frac{1}{60}$	0.00237	2.003
Yee	$\frac{1}{80}$	$\frac{1}{120}$	5.9442×10^{-4}	1.9953

Table 2: The maximal errors in L_2 norm with $\epsilon_2 = 4$.

Next we consider a monochromatic isotropic point source of wavelength 0.25, that is switched on at $t = 0$ in the presence of an infinit perfect conductor (fig(2)).

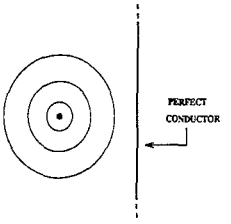


Figure 2: The computational domain.

The domain is $-\infty \leq x, y \leq \frac{1}{2}$, $-\infty \leq y \leq \infty$. For Yee's scheme we choose $h = \frac{1}{40}$, $\Delta t = \frac{2h}{3}$, for the explicit(2,4) and theTy(2,4) schemes $h = \frac{1}{40}$, $\Delta t = h^2$. The point source is modeled by adding a term representing a current $I_z(t) = 0.01 \sin(8\pi t)\epsilon(t)$ at $(x, y) = (\frac{1}{4}, \frac{1}{4})$ where $\epsilon(t)$ denotes the Heaviside unit-step function. The equations in this case are:

$$\begin{aligned}
\frac{\partial E_z}{\partial t} &= Z(\frac{\partial H_y}{\partial x} - \frac{\partial H_x}{\partial y}) - Z I_z(t)\delta(r - r_s) \\
\frac{\partial H_x}{\partial t} &= -\frac{1}{Z}\frac{\partial E_z}{\partial y} \\
\frac{\partial H_y}{\partial t} &= \frac{1}{Z}\frac{\partial E_z}{\partial x} \quad .
\end{aligned}$$

With the boundary conditions:

$$E_z(1/2, y, t) = 0 \tag{5}$$

In figures 3 we draw the errors in L_2 norm.

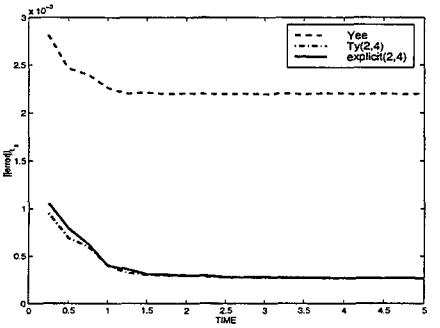


Figure 3: The errors in L_2 norm between the numerical solutions and the exact solution of 5.

Next we test these three schemes in $[0, 1/2] \times [0, 1/4] \times [01/2]$ domain. An exact solution in this case can be [8]:

$$\begin{aligned}
H_x &= \sin(\omega t)\sin(Ax + By + Cz) \\
H_y &= \sin(\omega t)\sin(Ax + By + Cz) \\
H_z &= \sin(\omega t)\sin(Ax + By + Cz) \\
E_x &= \frac{C - B}{\omega}\cos(\omega t)\cos(Ax + By + Cz) \\
E_y &= \frac{A - C}{\omega}\cos(\omega t)\cos(Ax + By + Cz) \\
E_z &= \frac{B - A}{\omega}\cos(\omega t)\cos(Ax + By + Cz)
\end{aligned}$$

Where

$$\begin{aligned}
\omega^2 &= A^2 + B^2 + C^2 \\
0 &= A + B + C
\end{aligned}$$

We choose:

$$A = \pi, \quad B = -2\pi, \quad C = \pi, \quad \omega = \sqrt{6}\pi.$$

In table 3, we can see that for the explicit(2,4) and the Ty (2,4) schemes we have used $\Delta t = h^2$ and for the Yee scheme we have used $\Delta t = \frac{4h}{7}$. The explicit(2,4) as well as the Ty(2,4) schemes behave better than expected and gives almost fifth order of accuracy.

scheme	h	Δt	$Max(\|\|error\|\|_{L_2})$ $0 \leq t \leq 10$	rate
$explicit(2,4)$	$\frac{1}{20}$	$\frac{1}{400}$	5.375×10^{-4}	
$explicit(2,4)$	$\frac{1}{40}$	$\frac{1}{1600}$	2.184×10^{-5}	4.621
$explicit(2,4)$	$\frac{1}{80}$	$\frac{1}{3200}$	9.071×10^{-7}	4.590
$Ty(2,4)$	$\frac{1}{20}$	$\frac{1}{400}$	3.621×10^{-4}	
$Ty(2,4)$	$\frac{1}{40}$	$\frac{1}{1600}$	1.144×10^{-5}	4.983
$Ty(2,4)$	$\frac{1}{80}$	$\frac{1}{6400}$	3.5621×10^{-7}	5.005
Yee	$\frac{1}{20}$	$\frac{1}{35}$	0.0027	
Yee	$\frac{1}{40}$	$\frac{1}{70}$	7.3×10^{-4}	1.9028
Yee	$\frac{1}{80}$	$\frac{1}{140}$	1.8252×10^{-4}	2.0015

Table 3: Comparison of the errors in L_2 norm

5 Computational Cost Comparisons

In order to compare the efficiency of the explicit(2,4), the Ty(2,4) and Yee scheme we take the following boundary conditions:

$$\begin{aligned} E_z &= \sin(3\pi x)\sin(4\pi y) \\ H_y &= (3/5)\cos(3\pi x)\sin(4\pi y)\sin(\frac{5\pi\Delta t}{2}) \\ H_x &= -(4/5)\sin(3\pi x)\cos(4\pi y)\sin(\frac{5\pi\Delta t}{2}) \end{aligned}$$

The exact solution in this case is:

$$E_z = \sin(3\pi x)\sin(4\pi y)cos(5\pi t)$$

For the Ty(2,4) scheme and the explicit(2,4) scheme we use a uniform gridspacing with $\Delta x = \Delta y = \frac{1}{30}$. For the Yee scheme we also use uniform gridspacing with $\Delta x = \Delta y = \frac{1}{260}$. We chose these mesh sizes in order to get the same error between the exact E_z and the approximated E_z in L_2 norm. The comparison is shown in table 4. The programs were written in fortran and run on a Digital Alpha workstation.

scheme	h	Δt	$Max(\|\|error\|\|_{L_2})$ $0 \leq t \leq 10$	$CPU - time$
$explicit(2,4)$	$\frac{1}{30}$	$\frac{1}{900}$	1.99×10^{-3}	0.9 sec
$Ty(2,4)$	$\frac{1}{30}$	$\frac{1}{900}$	1.25×10^{-3}	5.7 sec
Yee	$\frac{1}{240}$	$\frac{1}{360}$	1.31×10^{-3}	91 sec

Table 4: CPU-time using various difference schemes.

The CPU time needed to achieve the same accuracy in Yee's case is more than 15 times larger than required for the Ty(2,4) scheme and 91 times larger than required for the explicit(2,4) scheme.

6 Discussion and Conclusion

The results demonstrate that we can use a coarser mesh with the fourth order scheme and still get the same accuracy as with the Yee scheme. This is true even in the presence of a dielectric media.

Although this scheme is not as good as the Ty(2,4) scheme[2], it is still easier to modify an existing code based on the Yee scheme and make it fourth order accurate, by using the explicit(2,4) scheme. This is true because in the Ty(2,4) scheme one has to inverse a matrix by using a LU decomposition.

References

[1] K.S. Yee, *Numerical Solution of Initial Boundary Value Problems Involving Maxwell's Equation in Isotropic Media, IEEE Transactions on Antennas and Propagation*, Vol.AP-14, pp. 302-307, May 1966.

[2] E. Turkel and A. Yefet, *Fourth Order Accurate Compact Impl icit Method for the Maxwell Equations,* submitted to IEEE Transactions on Antennas and Propagation.

[3] H.O. Kreiss and J. Oliger, "Comparison of Accurate Methods for the Integration of Hyperbolic Equations," *Tellus* Vol. 24, pp. 199-215, 1972.

[4] A. Taflove, *Computational Electrodynamics The Finite-Difference Time-Domain Method,*

[5] D. Gottlieb and B. Yang, "Comparisons of Staggered and Non-Staggered Schemes for Maxwell's Equations," *12th Annual Review of Progress in Applied Computational Electromagnetics*, 1996.

[6] K. H. Dridi, J. S. Hesthaven and Adi Ditkowski,*Staircase Free Finite-Difference Time-Domain Formulation for Arbitrary Material Distributions in General Geometries,* submitted to IEEE Transactions on Antennas and Propagation.

[7] A. Ditkowski and J. S. Hesthaven. Private communications

[8] A. Yefet and E. Turkel,*Construction of Three Dimensional Solutions for the Maxwell Equations, NASA/CR-1998-208954 ICASE Interim Report No. 34*

[9] S. Abarbanel, Adi ditkowski and A. Yefet,*Bounded Error Schemes for the Wave Equation on Complex Domains, NASA/CR-1998-208740 ICASE Report No. 98-50*

[10] P. Petropoulo ,*Phase Error Control for FD-TD Methods of Second and Fourth Order Accuracy , IEEE Transaction on Antennas and Propagation* , Vol42, no. 6, pp 859-862, 1994.

[11] C.W. Manry, S.L. Broschat and J.B. Scneider *Higher-Order F DTD Methods for Large Problems, J. Applied Computational Electromagnetics Society* , Vol 10, no. 2, pp 17-29, 1995.

[12] J. Fang ,*Time Domain Finite Difference Computation for Maxwell's Equation , PhD. Dissertation, University of California at Berkeley*, 1989.

FDTD Method for Maxwells Equations in Complex Geometries

A. Ditkowski[†1], K. Dridi[‡], and J.S. Hesthaven[†]

[†]*Division of Applied Mathematics, Brown University, Box F, Providence, RI 02912, USA;* [‡]*Research Center COM, Technical University of Denmark, DK-2800 Lyngby, Denmark*

E-mail: adit@cfm.brown.edu; kd@com.dtu.dk; Jan_Hesthaven@brown.edu

A stable second order Cartesian grid finite difference scheme for the solution of Maxwells equations is presented. The scheme employs a staggered grid in space and represents the physical location of the material and metallic boundaries correctly, hence eliminating problems caused by staircasing, and, contrary to the popular Yee scheme, enforces the correct jump-conditions on the field components across material interfaces.

To validate the analysis several test cases are presented, showing an improvement of typically 1-2 orders of accuracy at little or none additional computational cost over the Yee scheme, which in most cases exhibits first order accuracy.

Key Words: Finite difference schemes, Maxwells equations, Complex geometries, Embedded interfaces, Stability, Staircasing

1. INTRODUCTION

The development of efficient, yet simple, computational methods for the accurate time-domain solution of Maxwells equations remains a very significant challenge. In recent years attempts were made to apply high-order finite difference scheme, and multi-domain spectral methods to solve the problem. These methods, however, share the disadvantage that they either are restricted to simple geometries or that a multi-domain framework must be introduced to facilitate the correct treatment of general metallic boundaries and material interfaces.

The very popular Yee scheme, introduced in [3] uses 2nd order finite-difference scheme on a staggered grid. This straightforward approach remains the by far most popular time-domain computational techniques for the modeling and design of problems in computational electromagnetics. An updated review on this method can be found in [1, 2].

The implementation of the Yee scheme in complex geometries presents the difficulties of approximation the boundary and the boundary-conditions. The straightforward using of a staircased curve affects the overall accuracy and essentially reduces the scheme to first order. In the case of metallic boundaries this problem has received considerable interest in the past, see e.g. [5] and references therein. Most proposed methods, however, sacrifice the simplicity of the original Yee scheme to achieve the improved accuracy.

[1]Corresponding Author

A more subtle problem that has received significantly less attention is the effect of using staircasing around a non-metallic embedded interface, i.e., a transparent interface. While the conditions connecting the field components on both sides of such media are well known, no effort is made in the Yee scheme to enforce these conditions. To overcome the problems associated with such an approach the standard technique is to extend the size of the interface by introducing a transition zone in which averaged material properties are employed. While such techniques appears to improve the overall accuracy, it has nevertheless been shown that the global accuracy of the scheme is reduced to first order [4]. This is a one-dimensional result and, as we shall show here, the situation is much worse for problems beyond one dimension.

To specifically address the problems associated with embedded metallic and general material interfaces when solving Maxwells equations, we present in this work a novel finite-difference scheme that maintains global second convergence in the presence of arbitrary interfaces, curved as well as straight. It is worth noting that staircasing problems at metallic boundaries are resolved at no additional computational cost and internal material interfaces are treated in an equally efficient way. Indeed, the main additional computational cost of this new scheme lies in a preprocessing stage and adds only little to the cost of solving the time-dependent problem.

2. THE ONE-DIMENSIONAL SCHEME

To illustrate the central elements of the proposed scheme, let us consider the solution of the one-dimensional Maxwell equation

$$\begin{aligned} \varepsilon \frac{\partial E}{\partial t} &= \frac{\partial H}{\partial z} \ , \\ \mu \frac{\partial H}{\partial t} &= \frac{\partial E}{\partial z} \ , \end{aligned} \tag{1}$$

where $E(z,t)$ and $H(z,t)$ signifies the normalized, mutually perpendicular tangential electric and magnetic field components, while ε and μ refers to the relative permitivity and permeability, respectively, of the materials.

In case of a perfectly conducting wall (PEC) the boundary conditions becomes

$$E(z_{\text{pec}},t) = 0 \quad \text{or} \quad \left.\frac{\partial H}{\partial z}\right|_{z_{\text{pec}}} = 0 \ , \tag{2}$$

where z_{pec} signifies the position of the wall. In case the interface has finite conductivity the field components, termed $(E^{(1)}, H^{(1)})$ and $(E^{(2)}, H^{(2)})$ are continuous across the material interface, situated at z_{mat}, as

$$E^{(1)}(z_{\text{mat}},t) = E^{(2)}(z_{\text{mat}},t) \ , \quad H^{(1)}(z_{\text{mat}},t) = H^{(2)}(z_{\text{mat}},t) \ . \tag{3}$$

To numerically solve Eq.(1), we introduce a spatially staggered grid with grid size h as

$$z_j = hj \ , \quad z_{j+\frac{1}{2}} = h\left(j+\tfrac{1}{2}\right) \ , \tag{4}$$

and embed the full problem into this simple Cartesian grid. To account for the possibility of the physical problem not being aligned with the grid, we introduce $\gamma \in [0, \frac{1}{2}]$ which measures the relative distance between the physical boundary and the first grid point, see Fig. 1.

The two field components, E and H, are collocated as

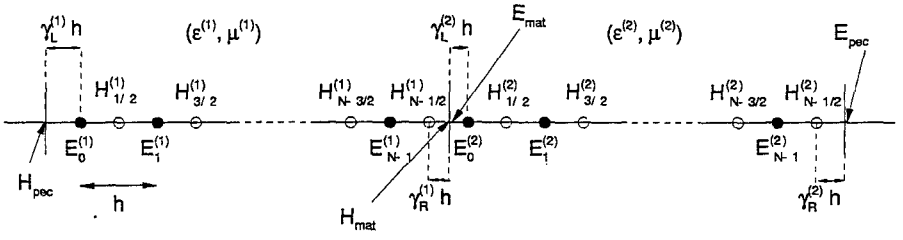


FIG. 1. Definition of grid, numbering and various parameters for solving the one-dimensional Maxwells equations in a PEC cavity filled with two materials.

$$E(z_j, t) = E_j \ , \ H(z_{j+\frac{1}{2}}, t) = H_{j+\frac{1}{2}} \ ,$$

as illustrated in Fig. 1. The actual limits on j depends on the individual computational problem and it should be clear that the first and last grid points in the computational domain can be an E- as well as an H-nodes. We recall that ϵ as well as μ may depend on z, possibly in a discontinuous manner, and that the location of such material interfaces as well as the enclosing walls need not be aligned with the grid.

Let us consider the situation of a perfectly conducting cavity, enclosed by two PEC walls situated at $z_{\rm pec}^{(1)}$ and $z_{\rm pec}^{(2)}$. The cavity is assumed to be filled with two regions of different materials, having properties $(\varepsilon^{(1)}, \mu^{(1)})$ and $(\varepsilon^{(2)}, \mu^{(2)})$, and with the interface situated at $z_{\rm mat}$ as illustrated in Fig. 1. We introduce the two sets of fields, $(E^{(k)}, H^{(k)})$ with $k = 1, 2$, representing the solution in the two regions of different materials and it assume that the two solutions are given on two separate grids and connected only through the conditions across the material interface, Eq.(3), much like in a multi-domain solution technique. For simplicity we assume here that N, being the number of grid points in each domain, is the same in both regions. This, however, is done purely to simplify the notation and the generalization for the general case is straightforward.

To account for the situation where the interfaces, be they material interfaces or PEC walls, do not coincide with a grid point we associate with each region two parameters, $\gamma_L^{(k)}$ and $\gamma_R^{(k)}$, which measure the distance from the first/last grid-point to the physical position of the wall or interface relative to the grid size h. Clearly, $\gamma^{(k)} \in [0, \frac{1}{2}]$ and, due to the global equidistant grid, $\gamma_R^{(k)} + \gamma_L^{(k+1)} = \frac{1}{2}$, across a material interface. Since these parameters are only geometry dependent, they can be computed and stored in a preprocessing stage once the grid has been defined.

In the interior of each of the two regions with constant material parameters, we shall use the standard staggered scheme as

$$j \in [1, N-1] \ : \ \varepsilon^{(k)} \frac{\partial E_j^{(k)}}{\partial t} = \frac{H_{j+\frac{1}{2}}^{(k)} - H_{j-\frac{1}{2}}^{(k)}}{h} \ , \tag{5}$$

and

$$j \in [0, N-2] \ : \ \mu^{(k)} \frac{\partial H_{j+\frac{1}{2}}^{(k)}}{\partial t} = \frac{E_{j+1}^{(k)} - E_j^{(k)}}{h} \ , \tag{6}$$

where $k = 1, 2$ and the numbering follows that in Fig. 1. Without loss of generality we assume that the material properties are constant within each region of the cavity. This, however, extends trivially to include problems where the materials vary smoothly within each domain.

To complete the scheme we shall introduce special schemes for updating $E_0^{(k)}$ and $H_{N-\frac{1}{2}}^{(k)}$ in such a way that the boundary conditions at the PEC walls, the material interface and the physical position of these relative to the grid is accounted for correctly.

For $E_0^{(1)}$ we use the following second order approximation

$$\varepsilon^{(1)}\frac{\partial E_0^{(1)}}{\partial t} = \frac{\gamma_L^{(1)}}{1+\gamma_L^{(1)}}\frac{H_{\frac{3}{2}}^{(1)} - H_{\frac{1}{2}}^{(1)}}{h} \quad . \tag{7}$$

The scheme for updating $H_{N-\frac{1}{2}}^{(2)}$ is simpler as we can explicitly exploit that $E^{(2)}(z_{\text{pec}}) = E_{\text{pec}} = 0$ to obtain

$$\mu^{(2)}\frac{\partial H_{N-\frac{1}{2}}^{(2)}}{\partial t} = \frac{2}{2\gamma_R^{(2)}+1}\frac{E_{\text{pec}} - E_{N-1}^{(2)}}{h} = \frac{2}{2\gamma_R^{(2)}+1}\frac{-E_{N-1}^{(2)}}{h} \quad . \tag{8}$$

Let us now consider the treatment of the material interfaces across which we know that the individual field components must remain continuous. However, one should not, as is implicitly done in the traditional Yee scheme, assume that the fields are smooth across the boundary and simply use $E_{N-1}^{(1)}$ and $E_0^{(2)}$ to update $H_{N-1/2}^{(1)}$.

To solve this problem, we introduce the extrapolated value

$$E_{\text{mat}} = (1+\gamma_L^{(2)})E_0^{(2)} - \gamma_L^{(2)}E_1^{(2)} \quad , \tag{9}$$

and complete the scheme for updating $H_{N-1/2}^{(1)}$ as

$$\mu^{(1)}\frac{\partial H_{N-1/2}^{(1)}}{\partial t} = \frac{2}{2\gamma_R^{(1)}+1}\frac{E_{\text{mat}} - E_{N-1}^{(1)}}{h} \quad . \tag{10}$$

Likewise we compute the flux of $E_0^{(2)}$ by using the extrapolated magnetic field

$$H_{\text{mat}} = (1+\gamma_R^{(1)})H_{N-1/2}^{(1)} - \gamma_R^{(1)}H_{N-3/2}^{(1)} \quad , \tag{11}$$

to obtain

$$\varepsilon^{(2)}\frac{\partial E_0^{(2)}}{\partial t} = \frac{2}{2\gamma_L^{(2)}+1}\frac{H_{1/2}^{(2)} - H_{\text{mat}}}{h} \quad . \tag{12}$$

The rigorous proof of stability and accuracy of this scheme is given in [5]. It should be noted that $\gamma^{(k)}$ always appear as $c\gamma^{(k)}+1$ ($c=1$ at metals, otherwise $c=2$) when ever being in the denominator. As a consequence the scheme can be expected to be well behaved for all values of γ_R and γ_L.

The application of the scheme in multi dimension domain is more complex due to the boundary conditions, which involve a combination of all the components of the vector-fields $\mathbf{E}$ and $\mathbf{H}$. In order to deal with this

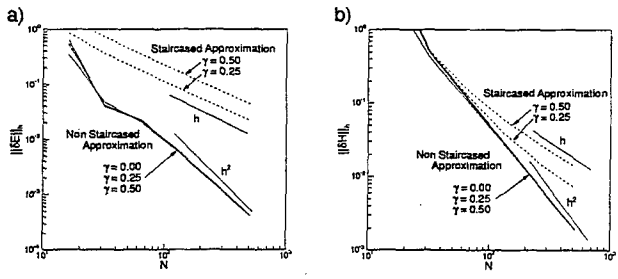


FIG. 2. The discrete L^2-error at $t = 2\pi$ for the electric (a) and the magnetic (b) field components in an air-filled metallic cavity as a function of the resolution $h = 2/N$. The dashed curves are obtained without properly accounting for the correct position of the metallic walls while the full curves are obtained with the new scheme.

problem extrapolation of the fields should be made to and along the boundaries. A comprehensive discussion on the boundary condition representation in two and three dimensions is given in [5].

3. A FEW NUMERICAL TESTS

Let us consider a simple test case consisting of a one-dimensional electromagnetic resonator with perfectly conducting walls located at $z_{\text{pec}}^{(1)} = -1$ and $z_{\text{pec}}^{(2)} = 1$. The interior of the resonator can be either air-filled or filled with two di-electric media with the material interface at $z_{\text{mat}} = 0$ and $\mu^{(1)} = \mu^{(2)} = 1.0$.

For $n^{(1)} = n^{(2)}$ the solution to Eq.(1) is a standing sinusoidal waves. In the case $n^{(1)} \neq n^{(2)}$ the solution is sinusoidal in each of the domains and is continuous but non smooth at the material interface.

We shall seek the numerical solution to the cavity problem on the staggered grid, Eq.(4). Note that for $\gamma = 0$ the grid coincides with the boundaries as well as the material interface at $z_{\text{mat}} = 0$ while for $\gamma > 0$, the whole grid is simply shifted towards the right, creating a situation exactly as sketched in Fig. 1 with $\gamma_L^{(k)} = \gamma$ and $\gamma_R^{(k)} = \frac{1}{2} - \gamma$.

Let us begin by considering just the vacuum filled cavity, i.e., $n^{(1)} = n^{(2)} = 1.0$. In Fig. 2 we plot the global error at $t = 2\pi$ as a function of $N = 2/h$ for various values of γ. As discussed in [5, Sec 2.2], the classic staggered scheme and the new scheme are equivalent for the perfectly conducting homogeneous cavity with $\gamma = 0$ and we observe, as expected, a global $\mathcal{O}(h^2)$ convergence in Fig. 2 for both the E and the H component. However, for $\gamma > 0$ the schemes yield very different results with the classic scheme being reduced to $\mathcal{O}(h)$ convergence as a direct result of the geometry of the actual problem being approximated to first order only. The new scheme, however, maintains second order global convergence for both field components, yielding a dramatic improvement in accuracy at no additional computational cost, compared to the classical scheme.

The situation for a metallic cavity filled with two different materials, having $n^{(1)} = 1.0$ and $n^{(2)} = 1.5$, is even more alarming when one considers the performance of the classic Yee scheme. In Fig. 3 we show the decay of the global error with increasing resolution when using the staircased approximation as well as the new scheme where no staircasing is introduced. We note in particular that even when the grid is aligned with the geometry is the staircased approximation reduced to a first order scheme at best.

For the new scheme the global second order convergence is recovered for all values of γ, confirming the analysis of [5, Sec 2.2].

To illustrate the particular importance of correctly imposing the jump-conditions when solving multidimensional problems, we consider the TE problem in a square cavity filled with two di-electric materials. The boundary between those materials is a straight line tilted with respect to the z-axis by an angle θ.

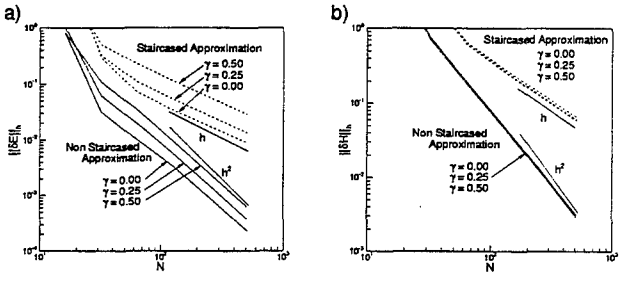


FIG. 3. The discrete L^2-error at $t = 2\pi$ for the electric (a) and the magnetic (b) field components in a metallic cavity as a function of the resolution $h = 2/N$. The cavity is filled with two materials with the interface being positioned at $z = 0$. The dashed curves are obtained without properly accounting for the position of the interfaces and the correct jump conditions while the full curves is obtained using the new scheme.

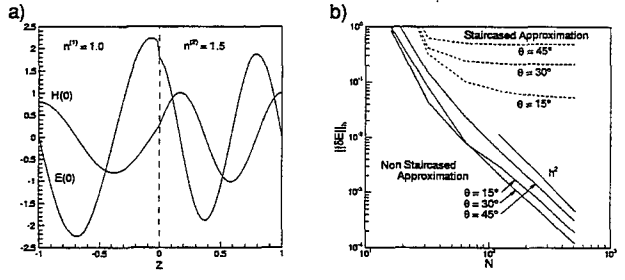


FIG. 4. In a) we illustrate the initial conditions for the modified one-dimensional cavity problem in the case where the material interface is assumed tilted at $\theta = 30°$. In b) we show the global L^2-error of E for different angles, i.e., the degree of discontinuity of E at the interface, as computed using the staggered Yee scheme and the new non-staggered approximation.

We consider a situation in which a plane wave impinges on the interface from the left propagating along the z-axis.

$$E^{x,(1)} = \frac{\varepsilon^{(2)}}{\varepsilon^{(2)}\hat{n}_z^2 + \hat{n}_x^2} E^{x,(2)} = \frac{\varepsilon^{(2)}}{1 + (\varepsilon^{(2)} - 1)\cos^2\theta} E^{x,(2)} \quad , \tag{13}$$

We observe that for $\theta = 0$, E^x is continuous as expected while for $\theta = \pi/2$ it experiences a maximum jump as it becomes a purely normal component. The degree of discontinuity of E^x across the interface in controlled solely by ε and θ.

We shall now attempt to model this problem using the Yee scheme and the newly developed scheme. To make things even simpler we shall assume that $\gamma = 0$, i.e., the material interface is located at a grid point although the interface generally is tilted at some angle.

Due to the nature of the Yee scheme, it is naturally unable to correctly model the discontinuous field component. As we see in Fig. 4, a consequence of this is that the Yee scheme is globally non-convergent for a problem with a discontinuous solution. One should recall that while one observes global non-convergent behavior, the solution is locally divergent.

Using the new method, however, the correct solution is recovered to global 2nd order accuracy. That is orders of magnitude better than obtained with the Yee scheme at the same work.

The relevance of this study is two-fold. On one hand it demonstrates the ability of the new scheme to accurately and efficiently model problems with discontinuous solutions. Secondly, and perhaps most importantly, it illustrates the inability of the Yee scheme to handle such problems. For more examples an a detailed analysis see [5, Sec 2.2].

4. FINAL REMARKS

The purpose of this paper has been twofold. On one hand, we wanted to show that the need in the Yee scheme to introduce a staircased approximation of curved metallic boundaries dramatically reduces the overall accuracy of the scheme which at best is first order. However, the situation at transparent interfaces is much more troubling. As the Yee scheme is applied everywhere in the computational domain no effort is made to impose the proper jump conditions on the electric and magnetic fields. Since these are continuous at best, this clearly introduces another source of significant error which has received limited attention in the literature. Indeed, as we have argued and confirmed through a very simple computational example, this may result in a non-convergent approximation. No averaging of material properties or a variety of other simple techniques can restore this property.

It has been the purpose of the second topic of this paper to present a novel second order scheme, building on the superior behavior of the Yee scheme in homogeneous regions and utilizing the same spatially staggered grid, yet modified in such a way that the need for staircasing is eliminated and physical jump-conditions are imposed to the order of the scheme. The new scheme is globally second order accurate for arbitrarily embedded interfaces. Moreover, there is no extra running-time computational cost with respect to the Yee scheme.

The aim of the current research is to extend the ideas introduced in this paper to high order schemes. The first steps in a development of suitable fourth order schemes have been taken in [6] where a fourth order scheme has been studied computationally, yielding very promising results. Encouraged by these results as well as our own initial studies, we hope to be able to present a stable fourth order Cartesian grid method for Maxwells equations in the near future.

ACKNOWLEDGMENT

This work was partially supported by AFOSR grant F49620-96-1-0426.

REFERENCES

1. A. Taflove (Ed.), *Advances in Computational Electrodynamics: The Finite-Difference Time-Domain Method*, Aztech House, Boston, 1998.

2. A. Taflove, *Computational Electrodynamics - The Finite-Difference Time-Domain Method*, Aztech House, Boston, 1995.

3. K. S. Yee, *Numerical Solution of Initial Boundary Value Problems involving Maxwells Equations in Isotropic Media*, IEEE Trans. Antennas Propaga. 14(1966), pp. 302-307.

4. E. Luo and H.O. Kreiss, *Pseudospectral vs. Finite Difference Methods for Initial Value Problems with Discontinuous Coefficients*, SIAM J. Sci. Comput. 20(1999), pp. 148-163.

5. A. Ditkowski, K. H. Dridi, and J. S. Hesthaven, and A. *Stable Cartesian Grid Methods for Maxwells Equations in Complex Geometries*, J. Comput. Phys. 1999 – submitted.

6. A. Yefet and P. G. Petropoulos, *A Non-Dissipative Staggered Fourth-Order Accurate Explicit Finite Difference Scheme for the Time-Domain Maxwells Equations*. ICASE Report 99-30, NASA Langley Research Center, VA. 1999.

FDTD ANALYSIS OF TAPERED MEANDER LINE ANTENNAS FOR RF AND WIRELESS COMMUNICATIONS

Chun-Wen Paul Huang, Atef Z. Elsherbeni, and Charles E. Smith
Electrical Engineering Department, The University of Mississippi
University, MS 38677

Abstract

Small printed antennas are becoming one of the most popular designs in personal wireless communication systems. Recently, a new type of printed meander line antenna was introduced. In this paper, the characteristics of a novel tapered meander line antenna are presented and analyzed using the finite difference time domain technique. Experimental verification is applied to ensure the effectiveness of the numerical model, and very good agreement is found between numerical analysis and measurements. A new design of this antenna features an operation frequency of 2.55 GHz with a 230 MHz bandwidth, which supports future generations of mobile communication systems.

Introduction

With the advancements of modern integrated circuit technologies, personal communication systems (PCS) features light weight, small size, high frequency operation, and high transmission efficiency. Mobile antenna design is one of the major tasks in PCS designs, which requires easy integration with the interior circuitry. One of the most widely used wireless communications systems is the global system for mobile (GSM) communications, which operates at 890-915 MHz for uplink and 935-960 MHz for downlink. The new generation of personal communication systems, such as digital communication systems (DCS) 1800, operates at 1.710-1.785 GHz for uplink and 1.805-1.880 GHz for downlink. Another widely adopted telecommunication system for PCS is the code division multiple access (CDMA) system, which operates at 1.8 to 2.0 GHz. In addition, recently, indoor cordless phones and modems for wireless local area networks (WLAN) operating at 2.4 GHz are also available in the market. Therefore, antennas for current and future generation of personal communication systems are designed to operate at the frequency range from 0.9 GHz to 2.5 GHz. If the future use of higher frequency PCS and the possibility of applying PCS for military purposes are considered, then antenna designs for wireless personal communication systems should be expanded in scope to cover the frequency range from the current 0.9-2.5 GHz to 0.9-3.0 GHz range. New types of printed meander line antennas have been recently investigated by several authors [1-6].

In this paper, studies for the characteristics of a novel tapered meander line antenna, using the finite difference time domain (FDTD) [6] techniques with Berenger's perfectly matched layers (PML) [7] absorbing boundaries are presented. The presented designs of the antenna shown in Fig 1, feature small dimensions (32 x 21 x 3.17 mm^3), and approximately 50 Ω input impedance with a dual printed sleeve tuner, and it operates within the 0.9-3.0 GHz range on a comparably small ground plane (60 x 27 mm^2). The validation of the numerical analysis used in this investigation is made by computing the return loss of the tapered antenna and comparing it with

measurements. Very good agreement is found using the developed FDTD code. Analysis and design based on this numerical model are thus performed. A wideband design is achieved by using a dual sleeve tuner [2, 6], whose operating bandwidth is centered at 2.5 GHz and with 230 MHz of band-width. This optimal design can be used for future generation of wireless phone or current other wireless applications operating around this frequency.

Analysis

The antenna considered in this investigation, as shown in Figure 1, is a tapered meander line trace printed on a 21-mm dielectric slab sitting on a 60 x 27 mm^2 perfectly conducting ground plane. The parameters e1 and e2 represent the lengths of the vertical and horizontal printed traces, respectively. The vertical segment length e1 = 2 mm, and the horizontal segment length e2 starting from 4 mm ending at 17 mm with a 1 mm increment for each horizontal segment, which results in the vertical length of the antenna L_{ax} = 29 mm. The distance between the edge of the dielectric slab and the edge of the ending segment of the meander line is set equal to e1. The reason for modeling the meander line antenna on a small ground plane (60 x 27 mm^2) is to simulate its performance when this antenna is placed on top of a PCS handset or a small effective ground plane of wireless appliances. The main objective of this research is to design a meander line antenna with 50 Ω input impedance at the operating frequencies within 0.9 to 3.0 GHz. The frequency range under study is extended from 0.9-3.0 GHz to 0.001-10.0 GHz for clearer observations of the resonance behavior of the antenna.

The finite difference time domain (FDTD) technique is applied to model the antenna inside a 3-dimensional air chamber terminated with the artificial boundaries of Berenger's perfectly matched layers (PML) [7]. The PML is adopted to reduce the numerical reflection from the truncated boundaries of the finite problem space, which resembles the anechoic chamber for antenna measurements. An array of voltage sources with a Gaussian waveform is placed between the ground plane and the edge of the first vertical segment of the trace line for excitations. After the characteristics of the tapered meander monopole are analyzed, dual printed sleeves are employed in the design to enlarge the bandwidth and tune the input impedance toward 50 Ω. Another tuning method using dual floating printed sleeves is studied, which can be used to model the behavior of the dual sleeves that are not well grounded.

Results

In order to verify the numerical analysis, a tapered meander line antenna is built and measured. To prevent bending of the dielectric substrate, the width is increased 2 mm more on each side than the width specified in the previous section. The thickness of the PCB is one half of that is used in the simulations. The performance of this antenna is measured on a 1.5 x 2-m^2 large ground plane to avoid the influence from surrounding objects. This ground plane is effective to simulate a semi-infinite ground plane for GHz application. The test is done using HP 8510C network analyzer, by measuring the return loss sweeping frequency up to 10 GHz. As shown in Figure 1b, there is a 43-mm coaxial cable connected to the fixture of the antenna that serves as an antenna feed. This coaxial cable is excluded in measurement results by applying port

extension to the electrical length of the cable, for establishing a reference plane at the antenna feed, as determined by the time domain reflectometry (TDR).

After calibration, the analyzer is switched to time domain mode, and the antenna characterizations are measured in the time domain. To locate the starting plane of the antenna trace, the antenna is shorted to the ground at the feed point, which results in total reflection with 180 degrees out of phase. Therefore, by locating the reflection with magnitude of 1 and by measuring of the time difference between this reflection spike and analyzer's reference plane, the information to translate the network analyzer reference to the apparent antenna reference plane is obtained. Therefore, the actual electrical delay can be determined by using one half of the time difference between the analyzer reference plane and the total reflection spike, which is 212.5 picosecond for this antenna model. The one half factor is required because the analyzer presents the time domain reflectometry (TDR) data for twice the traveling time between source and load to detect this total reflection. The computed impedance for the taper meander line antenna placed on a semi-infinite ground plane can be obtained by computing half of the meander line dipole configuration impedance, which is analyzed using a cell size of 0.5 mm with 2 cells used for modeling the source. Very good agreement is observed up to 10 GHz between the numerical and experimental results. The slight frequency shift in magnitude and phase differences at higher frequency range are mainly accounted by the different feeds used in the numerical and experimental methods and the conductor and dielectric losses at higher frequencies which are not considered in the FDTD simulation. From comparisons of results in Figure 2, the effectiveness of the numerical model and methodology are reassured.

The return loss of the tapered meander line antenna on a comparably small ground plane is shown in Figure 3. From Figure 3, the first and the third resonance of this taper line is at 1.2 GHz and 2.7 GHz, respectively, which may be tuned as a 50-Ω input impedance for current wireless application. Instead of using a 0.5-mm cell size, the computed return loss for the small ground plane case uses 1-mm cell size, which is small enough for effective simulation. To simplify the tuning design, the dual-sleeve method [2, 6] is adopted to improve the input impedance. Because the taper line is not a uniform segment ratio trace, the optimal sleeve length l is not necessarily ½ of L_{ax}, as suggested in [2]. Choosing a spacing of 1mm away from the longest horizontal segment, the effects of different sleeve length is observed in Figure 3(a). From Figure 3(a), the optimal sleeve length for lower frequency end is found when sleeve is 24 mm, 83 % of L_{ax}.

Since the optimal sleeve length is determined for the current antenna configuration, the following analysis is made to determine the best location for dual-sleeves. From Figure 3(b), the optimal return loss is found when the spacing between the longest segment and a sleeve is at the edge of the substrate, 3-mm. The case is operates at 2.55 GHz with 230 MHz bandwidth, which is effective for future wideband mobile phones and current wireless applications in the vicinity of this frequency.

To analyze the case with the sleeve tuners are not connected to the ground; another study is conducted for dual floating printed lines. The lines are simulated by printed traces at the center of the tapered meander line trace. From Figure 4, the effects of floating traces are found to be trivial at frequencies below 5 GHz, but detectable above 5 GHz. From this study, the results indicate that the tuning effectiveness is greatly reduced when the dual sleeves are not well

grounded.

Conclusions

The reliability of the numerical model in this study is demonstrated by comparing FDTD simulations with prototype test results. A detailed investigation for optimizing the operating frequncy and input impedance of a taper meander monopole for wireless communication has been presented. The presented tapered meander line monopoles can be tuned for a broad bandwidth of 230 MHz, operation at 2.55 GHz, and for a 50 Ω input impedance using printed tuning sleeves, which is appropriate for support of current and future generations of wideband wireless communication systems. Optimal results for lower frequency applications, between 1 and 2 GHz, may be achieved by increasing the meander line trace segments or by employing other tuning methods. Future studies will be focused on finding simple tuning methods to tune the lower frequncy modes and the optimization of the radiation pattern parameters of the current design.

REFERENCES

[1] K. Noguchi, M. Mizusawa, T. Yamaguchi, and Y. Okumura, "Numerical analysis of the radiation characteristics of the meander line antennas consisting of two strips," *IEEE AP-S Digest,* pp. 1598-1601, 1996.

[2] M. Ali, S. S. Stuchly, and K. Caputa, "A wide-band dual meander-sleeve antenna," *Journal of Electromagnetic Waves and Applications,* vol. 10, no. 9, pp. 1223-1236, 1996.

[3] A. Z. Elsherbeni, J. Chen, and C. E. Smith, and Y. Rahmatt-Sami, "FDTD analysis of meander line antennas for personal communication applications," Progress in Electromagnetics Research Symposium (*PIERS*), Cambridge, MA, 1997.

[4] M. Ali, S. S. Stuchly, and M. Okoniewski, "Characterization of planar printed meander line antennas using the finite difference time domain technique," *IEEE AP-S Dig.,* pp. 1546-1549, 1997.

[5] H. Y. Wang and M. J. Lancaster, "Aperture-coupled thin-film superconducting meander line antennas," *IEEE Trans. Antennas Propagat.,* vol. 47, no.5, pp. 829-836, May 1999.

[6] C. P. Huang, A. Z. Elsherbeni, J. J. Chen, and C. E. Smith, "FDTD characterization of meander line antennas for RF and wireless communications," Progress in Electromagnetics Research Symposium (*PIERS*), vol. 24, pp. 185-200, 1999.

[7] J. P. Berenger, "A perfectly matched layer for the absorption of electromagnetic waves," *J. Computat. Phys.,* Oct. 1994.

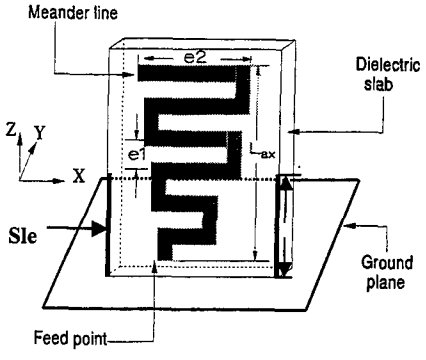


Figure 1(a) Tapered meander monopole with dual sleeves on a small ground plane

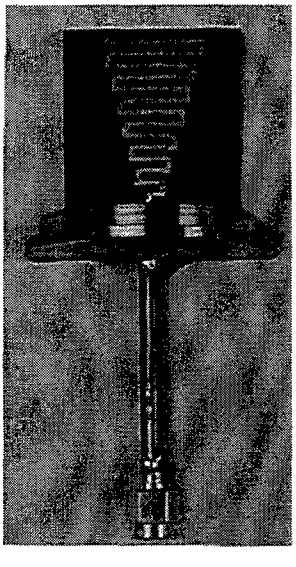


Figure 1(b) The prototype of a tapered meander line monop

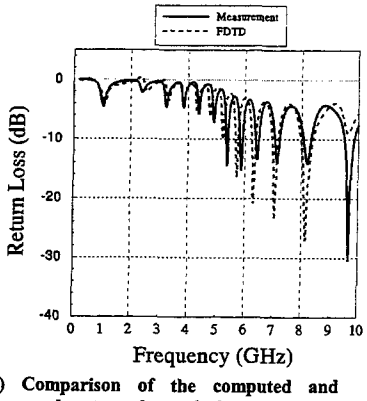


Figure 2(a) Comparison of the computed and measured return loss of the prototyped tapered meander line monopole.

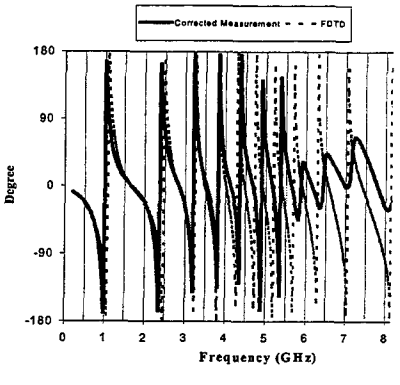


Figure 2(b) Comparison of the computed and measured phase of the reflection coefficient of the prototyped tapered meander line monopole.

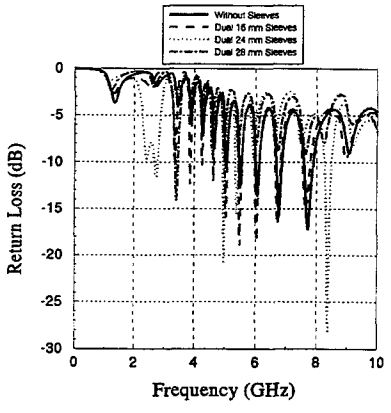


Figure 3(a) Return loss of the tapered meander monopole versus sleeve length.

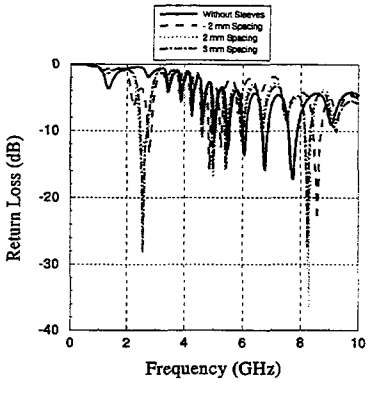


Figure 3(b) Return loss of the tapered meander monopole versus sleeve spacing.

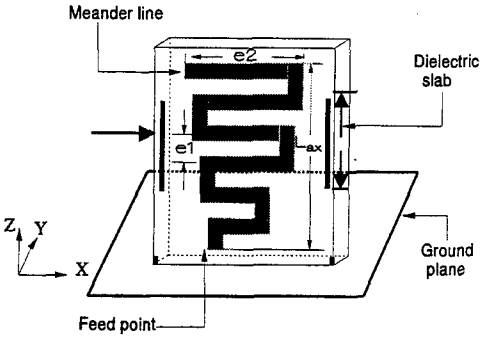


Figure 4(a) Tapered meander monopole with dual floating lines.

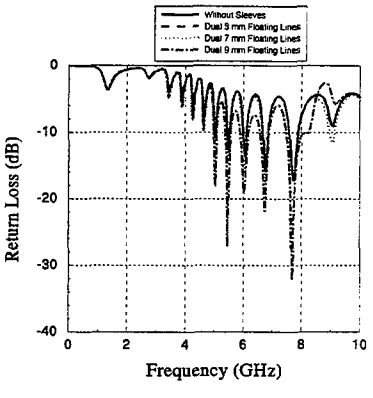


Figure 4(b) Return loss of the tapered meander monopole versus floating line length.

FDTD Modeling of an Electron Cyclotron Resonance Reactor Driven by a Lisitano Coil

Gaetano Marrocco[(1)] Fernando Bardati[(1)] Francesco De Marco[(2)]

[(1)] DISP, University of Rome Tor Vergata, Via di Tor Vergata 110, 00133 Roma (Italy)
[(2)] ENEA, Divisione Fusione, Frascati, Roma (Italy)

Abstract - **Theoretical models of modern plasma tools for surface processing need accurate electromagnetic computation for field prediction. A numerical code based on the FDTD method for electromagnetic field computation at microwave frequencies inside a region non-uniformly filled by a magnetized collisional plasma has been validated by computation of the resonant frequencies for a circular cylindrical uniformly-filled cavity. A realistic model of an ECR camera, sourced by a Lisitano coil antenna, has been proposed.**

I. INTRODUCTION

Surface processing by plasma is an established technical and industrial procedure since long time. The most common method is to excite the plasma with a 13.56 MHz radiofrequency source. In the last years a plasma reactor based on microwave absorption at the electron cyclotron resonance was developed. In this Electron Cyclotron Resonance (ECR) reactor, plasma is formed inside a magnetic field generated by a solenoid. The advantage of the ECR reactor is that the formation zone of the plasma can be away from the target where the surface to process is placed. Plasma streams down from the formation zone along the field lines to surface. This should allow better control of the process and of the geometry. Several versions of the ECR reactors are now on the market. The microwave frequency is generally 2.45 GHz, consequently the magnetic field intensity is about 875 Gauss and is slowly variable in space in order to control the absorption zone [1,2].

One of the research goals in the field of ECR is to improve the method in order to be able to process wafers having larger and/or non planar surfaces. Possible theoretical models are based on the analysis of electromagnetic wave propagation in a collisional plasma confined by a magnetic field in a rectangular or cylindrical cavity. The magnetic field is spatially varying so that the wave propagates along the field lines in regions where the wave frequency is slightly below the cyclotron frequency (whistler wave). In the process of propagation the wave approaches the resonance zone and it is absorbed.

Cold plasma can be generated inside the cavity (Fig.1) by a Lisitano slotted coil antenna [3], which excites an electric field pattern similar to that of the TE_{011} mode in a cylindrical cavity. As additional advantage, the coil diameter can be determined independently of the microwave frequency. The plasma is excited within the coil not only near the slots but also in the central area. To obtain a uniform field inside the coil, the radius r_L compared with wavelength should be such that: $\lambda/60 < r_L < 3\lambda$. Moreover the Lisitano coil also works as a plasma ejector.

The plasma dielectric tensor is a function of space and frequency as well as of plasma parameters and further computational complexity is originated for a realistic model by boundary conditions on non-simple surfaces. Therefore the electromagnetic wave propagation problem can only be solved by numerical tools. We use an extension of the FDTD method to the analysis of

gyrotropic media [4].

In this paper the results of a numerical simulation for an ECR camera with a realistic model for the launcher are reported. Previously, the algorithm has been validated for a cylindrical cavity which was homogeneously filled by a collisional axially-magnetized plasma. For this structure resonant frequencies can be obtained in closed form, therefore a comparison with FDTD computed data can be easily performed.

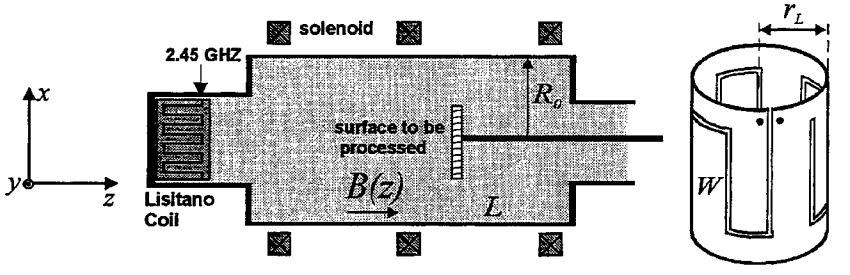


Fig.1: ECR camera typical set-up with axial symmetry along z (left). A simplified scheme of a Lisitano coil antenna (right) showing the slot line

II. METHOD

The relationship between electric flux and electric field for a magnetized cold plasma is

$$\underline{D}(\omega)/\epsilon_0 = \epsilon_{xx}(\omega)\underline{E}(\omega) + \hat{z}[\epsilon_{zz}(\omega) - \epsilon_{xx}(\omega)]\hat{z}\cdot\underline{E}(\omega) + j\epsilon_{xy}(\omega)\hat{z}\times\underline{E}(\omega) \qquad (1)$$

where it has been assumed that the biasing field is parallel to the z-axis; $\underline{B}_0 = \hat{z}B_0$, ω is the angular frequency and $\underline{\underline{\epsilon}}$ is the dielectric tensor. The plasma angular frequency, ω_{kp} and the cyclotron angular frequency, ω_{kc} are respectively defined for the k – particle of a general cold plasma as

$$\omega_{kp}^2 = \frac{Z_k^2 e^2 n_k}{m_k \epsilon_0} \quad , \quad \omega_{kc} = \frac{Z_k e B_0}{m_k} \qquad (2)$$

where $Z_k e$, m_k and n_k denote the particle charge, mass and density, respectively. Hereafter we shall consider a two-particle plasma (ion and electron) for which the tensor components are reported in [5]. The products in (1) correspond to convolutions in time. Hunsberger et al. [4] extended the standard FDTD algorithm to include the discrete convolution of the electric field with a time-domain susceptibility tensor $\underline{\underline{\chi}} = \underline{\underline{\epsilon}} - \underline{\underline{I}}$, ($\underline{\underline{I}}$ the identity matrix), for the case of pure electron modes in a cold plasma. In such a case the magnetic field is updated as in the standard FDTD scheme, while the electric field components are updated according to the following equations:

$$
\begin{aligned}
E_x^{n+1} &= \frac{1}{1+\chi_{xx}^0}\cdot\left[E_x^n + \chi_{xy}^0 E_y^{n+1} + \sum_{m=0}^{n-1} E_x^{n-m}\Delta\chi_{xx}^m - \sum_{m=0}^{n-1} E_y^{n-m}\Delta\chi_{xy}^m + \frac{\Delta t}{\varepsilon_0}(\nabla\times\mathbf{H})_x^{n+0.5}\right] \\
E_y^{n+1} &= \frac{1}{1+\chi_{yy}^0}\cdot\left[E_y^n - \chi_{yx}^0 E_x^{n+1} + \sum_{m=0}^{n-1} E_y^{n-m}\Delta\chi_{yy}^m + \sum_{m=0}^{n-1} E_x^{n-m}\Delta\chi_{yx}^m + \frac{\Delta t}{\varepsilon_0}(\nabla\times\mathbf{H})_y^{n+0.5}\right] \\
E_z^{n+1} &= \frac{1}{1+\chi_{zz}^0}\cdot\left[E_z^n + \sum_{m=0}^{n-1} E_z^{n-m}\Delta\chi_{zz}^m + \frac{\Delta t}{\varepsilon_0}(\nabla\times\mathbf{H})_z^{n+0.5}\right]
\end{aligned}
\tag{3}
$$

where the components of $\underline{\underline{\chi}}$ take into account the recursive convolution. As further generalization we considered a z-variable biasing field $B_0(z)$ and a non-uniform plasma with density variation on transversal cross-sections. This generalization requires plasma parameters to be averaged over each cell.

According to previous investigations [6], a slotted-type Lisitano coil with N longitudinal slots can be regarded approximately as an array of N thin z-oriented slot antennas, of length W, uniformly distributed over the surface of a cylinder (Fig.2). A simple model to account for slot radiation was therefore an annular array of sinusoidal magnetic line currents radiating in front of short-circuited slots.

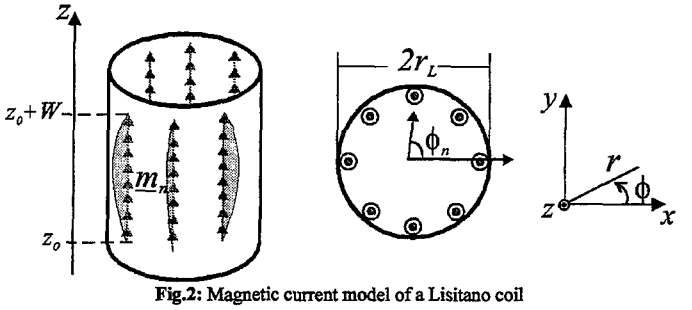


Fig.2: Magnetic current model of a Lisitano coil

This model can be easily implemented in an FDTD computer code. To this purpose, the azimuthal electric field in the slot placed at $\phi = \phi_n$ is:

$$
e_{\phi_n}(r_L,\phi_n,z,t) = i(t)\sin\left(\frac{z-z_0}{W}\pi\right)\delta(r-r_L)\delta(\phi-\phi_n)\frac{1}{r}; \qquad z_0 \le z \le z_0+W \tag{4}
$$

where z_0 is the coordinate of the slot down-end in the FDTD grid and $i(t)$ accounts for the time-domain dependence (a sinusoid or a gaussian pulse). The equivalent magnetic line current will be therefore:

$$
\underline{m}_n(r_L,\phi_\ell,z,t) = -\hat{\underline{r}}\times(e_{\phi_n}\hat{\underline{\phi}}) \tag{5}
$$

Furthermore, $r_L\Delta\phi \ll \lambda$, where $\Delta\phi$ is the angular distance between consecutive axial slots. Therefore , when the reverse direction of the current in two adjacent slots is considered, we conclude that the currents $\underline{m}_n$ radiate in phase for any n. The expression in (5) can be directly inserted in the H_z update equation at points of the slots:

$$H_z^{(n_t+0.5)}(i_0,j_0,k)=H_{z,FDTD}^{(n_t+0.5)}(i_0,j_0,k)+m_n(R_0,\phi_n,k\Delta z,(n_t+0.5)\Delta t) \qquad (6)$$
$$i_0\Delta x=r_L\cos(\phi_n),\qquad j_0\Delta y=r_L\sin(\phi_n)$$

where the subscript "*FDTD*" is for the corresponding FDTD equation in homogeneous media.

III. VALIDATION

The accuracy of the modified FDTD algorithm in modeling cylindrical cavities filled by cold plasma can be discussed by means of a test case involving the computation of resonant frequencies according to the procedure described in [7] for magnetized ferrites. The reference data can be obtained by means of a closed form procedure. Starting from the Maxwell's equations for gyrotropic media, it can be demonstrated [5] that the characteristic equation for the resonant modes of a cylindrical cavity of length L and radius R_0 is:

$$kk_0\in_b\frac{\chi}{b}[qJ_m(pR_0)J'(qR_0)-pJ_m(qR_0)J'(pR_0)]=-j\omega\mu_0\{\in_a[q\frac{\chi^2}{bd}J_m(pR_0)J'(qR_0)+pJ_m(qR_0)\cdot J'(pR_0)]+\frac{m}{R_0}\in_b(\frac{\chi^2}{bd}+1)J_m(pR_0)J(qR_0)\} \qquad (7)$$

where $\in_a=\in_{xx}-k^2,\in_b=-\in_{xy},\in_c=\in_{xx}^2-\in_{xy}^2-\in_{xx}k^2,p^2=a+\chi;\ q^2=c-\chi;$

$\chi=\sqrt{bd+(\frac{a-c}{2})^2}-\frac{a-c}{2};\ a=-k_0^2\in_{zz}\in_a\eta;\ b=-j\omega\mu_0kk_0\in_b\eta;\ c=-k_0^2\in_c\eta;$

$d=j\omega\in_0kk_0\in_b\in_{zz}\eta;\ \eta=(\in_a^2-\in_b^2)/(k^2\in_b^2-\in_a\in_c);\ k_0=\omega/c_0,\ kk_0=h\pi/L_0$

h is an integer and (7) is solved for k_0. If n denotes the n-th zero of (7) for given h and m, then $\omega_{hmn}=c_0k_0$ is the corresponding angular resonant frequency. The limit $\in_b\to 0$ corresponds to zeroing off-axis tensor components. It is easy to show that (7) reduces to

$$J'_m(R_0\sqrt{a})J_m(R_0\sqrt{c})=0 \qquad (8)$$

The roots of (8) correspond to *TE* and *TM* resonant modes, respectively, and can be found in closed form. In this work, therefore, the modes are first computed in the above limit, then they are tracked on the complex plane [8] when the value of the off-axis components is restored.

Numerical resonant frequency are computed by FDTD [9] in combination with another technique which, starting from the time response, will provide the resonant frequencies of the structure. The cavity is excited by an electric z-directed current element located on z-axis [10]. Therefore only rotationally symmetric modes will be excited. Gaussian time-dependence for wide-band analysis is adopted. Since resonant frequencies for plasma cavities can be very densely distributed in bands close to the plasma characteristic frequencies, the standard procedure, involving the Fourier transform of field time-response and peak detection, may result inaccurate. We applied an algorithm for parametric spectral estimation in time domain. In fact the FDTD late-time response (after the excitation has died down) of an eigenvalue problem can be expressed as a superposition of resonant modes

$$E_\ell^{(n)}=\sum_{i=1}^{M}R_ie^{(\alpha_i+j\omega_i)n\Delta t} \qquad (9)$$

where R_i is complex modal amplitude, α_i is damping factor and ω_i is resonant angular frequency of the i-th resonant mode and M is twice the number of resonant modes. Resonance parameters can be computed via a pole-residue extraction procedure such as the Matrix Pencil algorithm [11] which does not require a Fourier transform. The procedure can be repeated for different electromagnetic field components and at different observation points. Finally, resonant frequencies can be obtained by averaging these data.

The results of Tab.I have been obtained by the FDTD and Matrix Pencil method for a cavity with L=7.3cm, R_0=5cm, filled with a plasma having electron density n_0=5 $10^{16}m^{-3}$, B_0=1200 G, ν_c=0.3GHz. For comparison, the corresponding resonant frequencies which are obtained by the closed-form method, are also reported, showing a good agreement between the outcomes of the two procedures.

TABLE I
CAVITY RESONANT FREQUENCIES

mode	f [GHz] (analytical)	f [GHz] (FDTD)	Error (%)
quasi TE_{200}	2.759	2.782	0.85
quasi TE_{400}	3.150	3.120	0.95
quasi TM_{410}	3.560	3.550	0.28
quasi TM_{220}	3.681	3.656	0.67
quasi TM_{120}	3.847	3.877	0.78
quasi TE_{210}	5.872	5.894	0.37

IV. NUMERICAL EXAMPLE

As a realistic example, a camera with L=0.6m, Ro=0.1m was considered. The Lisitano coil parameters were: N=8, r_L=14cm, W=6.1cm. The frequency was 2450 MHz. Plasma parameters were $n_0 = 2.5\,10^{17}\,m^{-3}$, $\nu_c = 24.5\,MHz$. The biasing magnetic induction was zero within the coil and decrease linearly from 950 Gauss to 750 Gauss outside the coil. The camera and the coil were meshed on a $(5mm \times 5mm \times 2mm)$-cell grid resulting in 530.000 voxels. Fig.3 shows the computed electric field on a vertical cross-section of the camera. An important local maximum appears along the camera axis at about 10cm from the Lisitano coil termination. This peak is due to the plasma resonance and, as expected, the field is strongly dumped hereafter. The object to be processed could be placed in the hot-spot area where the field is almost uniform around the axis (Fig.4a). Finally, the electric field within the coil is shown in (Fig.4b). It can be observed that the field exhibits small variation on the cross-section (approximately 5dB). Moreover the picture is not exactly symmetrical for the coil staircasing in FDTD modeling.

V. CONCLUSIONS

The FDTD method has been used for electromagnetic field computations at microwave frequencies inside a cylindrical camera inhomogeneously filled by a magnetized collisional plasma and excited by a slotted circular array.

To validate the numerical method, computations were performed on a simple structure, i.e., a cylindrical cavity filled by a uniform axially-magnetized plasma. Comparisons among resonant frequencies obtained in closed form and by means of FDTD and Matrix Pencil method show a good agreement and a relative difference less than 1%. A realistic simulation of an ECR camera with an FDTD model of the Lisitano coil launcher has been successfully performed, showing the electric field hot-spot which can be associated to plasma resonance.

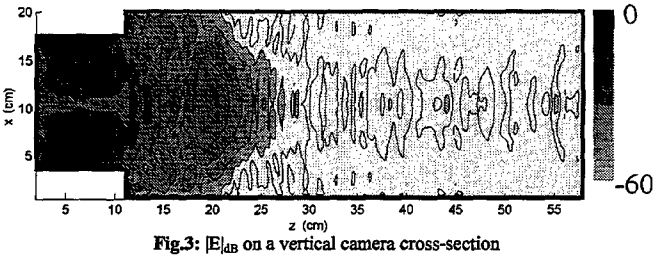
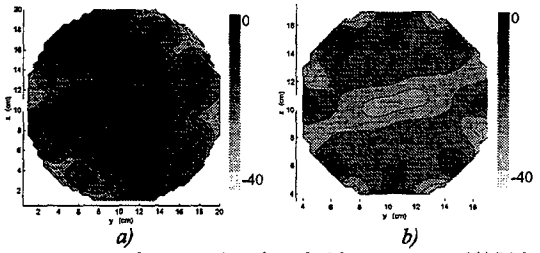


Fig.3: $|E|_{dB}$ on a vertical camera cross-section



a) *b)*

Fig.4: $|E|_{dB}$ on two transversal cross-sections through a) hot spot area and b) Lisitano coil

REFERENCES

[1] M. Tanaka, M. Tamaoki, S. Higashi, M. Matsuoka, A. Komori, and Y. Kawai, "Production of plasma with large area for plasma application," *Jpn. J. Appl. Phys.* Vol. 32, pp. 5028, 1994.

[2] J. E. Stevens, "RF Physics Issues for electron cyclotron resonance plasma etch tool operation," *ISPP-13 Piero Caldirola , Industrial Applications of Plasma Physics*, G. Bonizzoni, W. Hooke and E. Sindoni (Eds.) , Bologna: SIF 1993.

[3] G. Lisitano, "Microwave plasma generation with slotted-line radiator structures", *ISPP-13 Piero Caldirola , Industrial Applications of Plasma Physics*, G. Bonizzoni, W. Hooke and E. Sindoni (Eds.) , Bologna: SIF 1993.

[4] F. Hunsberger, R. Lubbers, and K. Kunz, " Finite difference time-domain analysis of gyrotropic media - I: Magnetized plasma," *IEEE Trans. Antennas Propagat.*, Vol. 40, pp. 1489-1495, December 1992.

[5] T. H. Stix, *The Theory of Plasma Waves*, New York: McGraw-Hill, 1962.

[6] Y. Suetsugu, Y. Kaway, "RF Field distribution in a slotted-type Lisitano Coil", Japanese J. Applied Physics, Vol.23, pp.1101-1106, 1984

[7] G. C. Chinn, L. W. Epp, and G. M. Wilkins, "Determination of the eigenfrequencies of a ferrite-filled cylindrical cavity resonator using the finite element method," *IEEE Trans. Microwave Theory Tech.*, Vol. 43, pp. 1207-1209, May 1995.

[8] L. M. Delves, and J. N. Lyness, "A numerical method for locating the zeros of an analytic function," *Math. Comp.*, Vol. 21, pp. 543-560, 1967.

[9] J. D. Wills, "Spectral estimation for TE transmission line matrix method", *IEEE Trans. Microwave Theory Thech.* Vol. 38, pp.447-451, April 1990.

[10] G. Marrocco, L. Tirone, F. Bardati, "FDTD Computation of Resonant Frequencies for Cavity Filled with a Collisional Magnetized Plasma", proceedings of *IEEE-URSI-98 International Symposium*, p.69, Atlanta 1998

[11] Y. Hua, T. K. Sarkar, "Matrix Pencil method for estimating parameters of exponentially damped/undamped sinusoids in noise", *IEEE Trans. Acoust. Speech, Signal Processing*, vol. 38, pp.814-824, May 1990

Modelling Microwave and Hybrid Heating using FDTD

J. Haala, W. Wiesbeck
Institut für Höchstfrequenztechnik und Elektronik, Universität Karlsruhe, Germany
Kaiserstr. 12, D-76128 Karlsruhe
Tel: +49 721 608-2522
Fax: +49 721 691865
E-Mail: Jens.Haala@etec.uni-karlsruhe.de

Abstract

This paper presents an efficient simulation tool for microwave and hybrid heating. Computational results illustrate the usefulness for such a tool. A new thermal modeling technique for the simulation of conductive and radiant heat transfer is presented. The conductive heat transfer is modeled by a finite difference algorithm. A finite difference scheme is not applicable for the radiant heat transfer, as radiation from a material surface is not bounded to the immediate vicinity as is the conductive transfer. Therefore ray optical methods are used. Rays connecting mutually visible surfaces are obtained by a new fast method. The algorithms are combined with an electromagnetic FDTD program to simulate the electromagnetic fields within ovens. Simulations are presented for an oven heated by microwaves, or by a combination with a conventional heating.

Introduction

Thermal modeling is mandatory for the optimization of heating processes in ovens. Especially in combination with microwaves, the heating process has to be carefully designed to achieve a fast and uniform heating. Nowadays, most thermal models for ovens include only heat conduction or simplified models for heat radiation. This simplification neglects the transportation of heat radiation from one object to another and only the emission of heat from a surface. This becomes questionable at higher temperatures. In fact, with increasing temperature radiant heat exchange becomes more and more important, since the energy emitted from a material surface increases proportional to the fourth power of temperature. In contrast energy transported by heat conduction is only proportional to the temperature. Radiant heat transfer eventually prevails conductive heat transfer. If ovens are designed for higher temperatures radiant heat transfer is not neglectable and an accurate model has to be used for simulation.

For the optimization of microwave ovens one needs to determine the dynamic heat process. Hence, a combination of thermal and electromagnetic simulation must be used. Both radiation and the influence of varying material parameters due to increasing temperature must be considered.

The Finite Difference Time Domain (FDTD) method has been found to be an excellent algorithm for the calculation of electromagnetic fields, especially in closed structures like ovens. Narrowband and broadband calculations are easily performed. The FDTD method applied to the heat conduction equation is similar to the electromagnetic FDTD. A combination with an electromagnetic FDTD leads to a very efficient and powerful simulation tool. Self-consistent modeling is possible as well as analyzing dynamic heating processes.

Both, the conductive thermal and the electromagnetic algorithm are of local character as the temperature and the fields in one discretisation cell is only related to its neighboring cells. When considering radiant heat transfer, energy may be transported through the whole computational space. Mutually visible surfaces, view factors and material parameters have to be determined and used for the calculation. This usually means high computational effort. A very fast algorithm has been developed that is optimized for calculation of radiant heat transfer.

The mechanism and the modeling of the conductive and radiant heat transfer is shown and combined with an electromagnetic FDTD algorithm. The resulting code is applied to a single mode oven where a polyvinyl chloride (PVC) sample is heated. As this material is likely to produce hot spots in an electromagnetic field the microwave heating is combined with conventionally heated walls. The heat distribution within the sample for the different heat sources is shown.

Heat Conduction

The finite difference scheme [1] is applied for the conductive heat transfer to a rectangular non-uniform grid with cells indexed by *(i, j, k)*. Inside a cell the temperature is assumed to be homogeneous. Heat flux density vectors describing the heat exchange with the neighboring cells are defined in the middle of the six cell surfaces as shown in Fig. 1 for the discretisation cell *(i,j,k)*

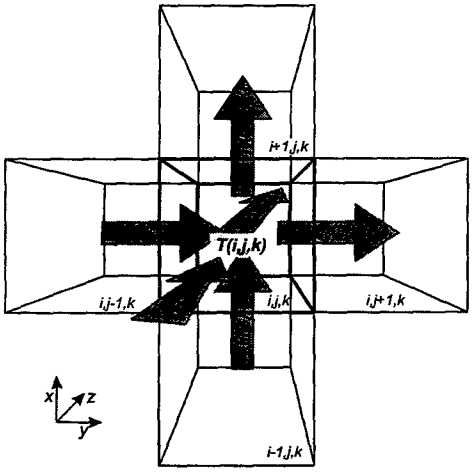


Fig. 1: Discretisation cell (i,j,k) and the position of the scalar field components T and the vectors j

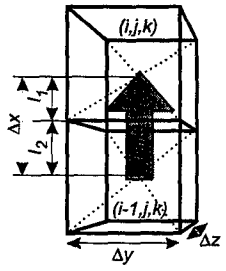


Fig. 2: Geometrical properties for the calculation of the discretised field component j_x

The calculation of the temperature distribution is divided into two steps. The conductive heat flux densities are caused by the temperature gradients between neighboring cells and given by

$$\vec{j}(\vec{x},t) = -\sigma(\vec{x},t)\,\mathrm{grad}\big(T(\vec{x},t)\big) \tag{1}$$

with $\vec{j}$ the heat flux density, and σ the thermal conductivity. Considering only the x component of $\vec{j}$ in Fig. 1 as shown in Fig. 2 the gradient in equation (1) is expressed using the finite difference expression

$$\mathrm{grad}\big(T(\vec{x},t)\big) = \frac{T(i,j,k) - T(i-1,j,k)}{\Delta x} \tag{2}$$

The thermal conductivity at $\vec{x}$ is the average of two neighboring cells. With

$$\sigma(\vec{x},t) = \Delta x \frac{\sigma(i,j,k)\sigma(i-1,j,k)}{\sigma(i,j,k)l_2 + \sigma(i-1,j,k)l_1} \tag{3}$$

one obtains

$$j_x(i,j,k) = \frac{\sigma(i,j,k)\sigma(i-1,j,k)}{\sigma(i,j,k)l_2 + \sigma(i-1,j,k)l_1}\left(T(i-1,j,k) - T(i,j,k)\right) \quad . \tag{4}$$

The thermal conductivity is assumed to be constant over the volume of one discretisation cell. As the heat flux density is supposed to be constant over the surface, the power P_x flowing through the interface between the cells *(i,j,k)* and *(i-1,j,k)* is determined by

$$P_x(i,j,k) = \iint_A j_x \, dA = j_x(i,j,k)\Delta y \Delta z \quad . \tag{5}$$

All other components of $\vec{j}$ and P are obtained accordingly.

The next step is the application of the conservation of energy. The change of temperature within a discretisation cell is derived from the change of energy. When the conservation of energy

$$\operatorname{div} \vec{j}(\vec{x},T) + c_s(\vec{x},T)\rho(\vec{x},T)\frac{\Delta T(\vec{x})}{\Delta t} = 0 \tag{6}$$

is applied to one cell *(i,j,k)* the divergence of $\vec{j}$ equals the power that flows through the surfaces of the cell. c_s and ρ are the specific heat capacity and the density, respectively. The divergence of $\vec{j}$ is expressed by the discretised surface integral in equation (5). This leads to

$$\operatorname{div} j(\vec{x}) \Rightarrow \oiint_A j(\vec{x})\, dA = P_x(i,j,k) - P_x(i+1,j,k) + P_y(i,j,k) - P_y(i,j+1,k) + P_z(i,j,k) - P_z(i,j,k+1) \tag{7}$$

in the finite difference scheme.

The right hand side term in equation (6) applied to the cell volume leads to

$$c_s(\vec{x},T)\rho(\vec{x},T)\frac{\Delta T(\vec{x},t)}{\Delta t} \Rightarrow \iiint_V c_s(\vec{x},T)\rho(\vec{x},T)\frac{\Delta T(\vec{x},t)}{\Delta t}\, dV = \Delta x \Delta y \Delta z\, c_s(i,j,k)\rho(i,j,k)\frac{\Delta T(i,j,k)}{\Delta t} \tag{8}$$

and finally the time derivative is also expressed by a finite difference

$$\frac{\partial T(\vec{x})}{\partial t} = \frac{T^{n+1}(i,j,k) - T^n(i,j,k)}{\Delta t} \tag{9}$$

where T^n denotes the temperature at timestep n. Using equations (7), (8) and (9) one obtains

$$T^{n+1}(i,j,k) = T^n(i,j,k) + \frac{\Delta t}{\Delta x \Delta y \Delta z\, c_s(i,j,k)\rho(i,j,k)} \cdot \left[P_x(i,j,k) - P_x(i+1,j,k) + P_y(i,j,k) - P_y(i,j+1,k) + P_z(i,j,k) - P_z(i,j,k+1)\right] \tag{10}$$

With equations (10) and (5) the temperature is updated at each time step.

Radiant Heat Transfer

Radiant heat transfer applies only to surfaces. Additionally, radiant heat transfer is not bounded to the immediate vicinity, as energy may be transported through gases without any interaction. The main tasks of the simulation is to determine mutually visible surfaces and geometric parameters. The algorithm is therefore quite different to the algorithm for the heat conduction above.

With increasing time in the simulation the increase of temperature may cause a variation of the electric and thermal properties, but the geometry remains constant. Therefore geometry checks are performed only once before calculation starts.

The checks include the determination of radiant surfaces, testing for visibility and the calculation of view factors.

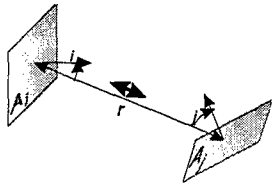


Fig. 3: Radiation between two rectangular planes.

The radiant heat transfer only applies to interfaces between solid and gaseous materials. Therefore the first step is to determine those surfaces within the finite difference grid. The surfaces of the solids are assumed to be rough. The Stefan-Boltzmann and Lambert equations determine for this case the specific heat radiation. In closed environments like ovens, all the radiated energy is absorbed by other surfaces. For the calculation of the radiant heat all energy exchanges between surfaces have to be calculated. As shown in Fig. 3 the radiation of surface A_i is partially absorbed by surface A_j. The absorbing surface A_j, however, also emits thermal radiation. A part of this radiation is in turn absorbed by A_i. The power exchanged between the two surfaces i and j is

$$P_{\text{rad}} = \Phi_i - \Phi_j \tag{12}$$

where

$$\begin{aligned} \Phi_{ij} &= \varepsilon_i \alpha_j F_{ij} \sigma_i T_i^4 \\ \Phi_{ji} &= \varepsilon_j \alpha_i F_{ji} \sigma_j T_j^4 \end{aligned} \tag{13}$$

where α_i and ε_i are the absorption and emission coefficient of surface A_i, respectively. Kirchhoff's law states that α_i equals ε_i. The view factors F_{ij} and F_{ji} are coefficients determined by the geometry only. They express the part of energy that is transmitted by surface A_i and actually received by surface A_j, divided by the total energy emitted by surface A_i. The view factors F_{ij} are given by

$$F_{ij} = \frac{1}{\pi A_i} \iint_{A_i A_j} \frac{\cos(\theta_i)\cos(\theta_j)}{r^2} dA_j \, dA_i \tag{14}$$

and are determined by geometrical properties as shown in Fig. 3. The factors have values between 0 for infinitesimally small surfaces infinitely separated and 1 for two parallel, infinitely extended planes. The F_{ij} are constant with respect to temperature.

The final temperature distribution is determined by the energy exchange between all surfaces. The radiant power flowing through the surfaces of cell *(i,j,k)* is now used to calculate the variation of the temperature. When applying the conservation of energy, equation (6), to the radiant heat transfer one finally obtains

$$T^{n+1}(i,j,k) = T^n(i,j,k) + \frac{\Delta t}{\Delta x \Delta y \Delta z \, c_s(i,j,k) \rho(i,j,k)} \sum_{\text{Surface}} P_{\text{rad}} \tag{15}$$

Implementation

For maximum versatility, the simulations are based on a cartesian, but non-uniform grid. This allows an enormous simplification for the determination of view factors. An efficient calculation is obtained if the geometrical properties are checked and the view factors are calculated and stored only once before the calculation starts. During the calculation the

stored values are simply processed in a look-up table.

The preprocessing is divided into two steps. First the relevant cells are determined. Only cells representing solid materials bordered by a gas or vacuum are relevant as only those cells radiate or absorb energy.

The next step is to determine surface pairs. Two surfaces are called a surface pair when they exchange energy. Energy exchanges only apply to surfaces that are mutually visible. Every possible combination of surfaces has to be checked whether they are linked by a line of sight. Depending on the size and properties of the oven and the discretisation millions of possible surface pairs exist. Hence, the visibility check has to be very efficient.

Here a modified Bresenham algorithm is used which combines versatility and efficiency. This algorithm determines very fast the pixels that are penetrated by a line [2,3]. However, this algorithm has been developed for two dimensional uniform grids. Here the algorithm is extended to three dimensional non-uniform grids.

For each surface pair the view factors F_{ij} are calculated. Using the reciprocity

$$A_i F_{ij} = A_j F_{ji} \tag{16}$$

the view factors are calculated only once for each surface pair. As the surfaces are either parallel or perpendicular oriented in the rectangular grid, the integrals in equation (13) can be simplified. Hsu [4] showed a method for evaluating the view factor without integration making the calculation much faster.

Microwave Heating

The heating of materials by microwaves is determined directly using

$$P_{\text{elec}} - \iiint_V c_s(\vec{x},T)\,\rho(\vec{x},T)\frac{\partial T(\vec{x},t)}{\partial t} = 0 \tag{17}$$

where P_{elec} is the microwave power dissipated. As shown in Fig. 4 there are twelve electric field components dissipating power within one cell. The electromagnetic power

$$P_{\text{elec}} = \frac{\Delta x\,\Delta y\,\Delta z}{4}\sum_{n=1}^{12}\kappa|E_n|^2 \tag{18}$$

is determined by the conductivity κ of the material . Combining (17) and (18) and setting up the finite difference scheme one obtains

$$T^{n+1}(i,j,k) = T^n(i,j,k) + \frac{\Delta t}{4\,c_s(i,j,k)\,\rho(i,j,k)}\sum_{n=1}^{12}\kappa|E_n|^2 \tag{19}$$

The computation of the electric energy dissipated in one cell is done by a standard FDTD scheme, and includes linear and frequency-dependent materials.

Additionally, equations (10), (15) and (19) are combined to update the temperature in only one computational step. The radiant, conductive and electric power is summed up leading to

$$T^{n+1}(i,j,k) = T^n(i,j,k) + \frac{\Delta t}{\Delta x\,\Delta y\,\Delta z\,c_s(i,j,k)\,\rho(i,j,k)}\left[\sum_{\text{Surface}}P_{\text{rad}} + \sum_{\text{Surface}}P_{\text{cond}} + \sum_{\text{Volume}}P_{\text{elec}}\right] \tag{20}$$

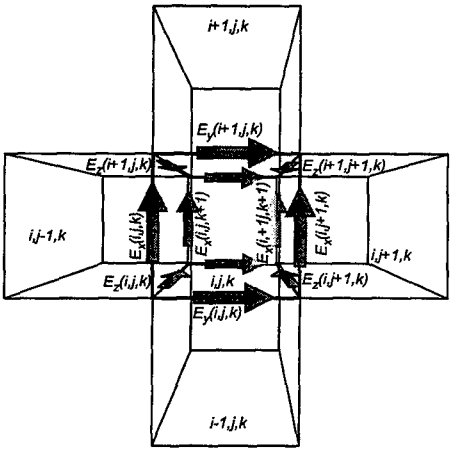


Fig. 4: Placement of the electric field components within the discretisation cell (i,j,k).

Selfconsistent Simulation

In the previous sections all material parameters are assumed to be constant over temperature. However, for most materials this assumption is not valid. The variation of material parameters like electric or heat conductivity is very important for the heat process. To obtain a realistic simulation of a heat process the variation has to be included.

The variation of material parameters is slow in comparison to the variation of the electromagnetic field. In most cases it is not necessary to adapt the material parameters after every calculation step. A good way to include variant parameters and restrict computational effort is to adapt parameters only if temperature has changed significantly.

The combination of electromagnetic and thermal simulation can be done in two different ways:

- *Direct Coupling of the two methods:* Thermal variations are much slower than electromagnetic ones. Therefore a direct coupling would lead to enormous computational effort, as calculations would have to proceed very long to get temperature variations. This can be avoided if the simulations use different time steps. For the electromagnetic simulations a rather small time step is needed to fulfill the stability criterion for this algorithm. The timestep for the thermal FDTD code may be much greater. For e.g. simulations at 2.45 GHz the timestep for the electromagnetic code is approximately 10 ps. For thermal simulations the timestep is in the region between milliseconds and seconds. Using different timesteps causes an unphysical acceleration of the thermal processes and may lead to inaccurate results. Therefore this technique has to be handled with care.
- *Separation of the two methods:* This means electromagnetic and thermal calculations are done separately. First the electromagnetic field is calculated and assumed to be constant for the thermal simulation started afterwards. When temperature and therefore parameters change significantly, the thermal simulation is interrupted and the electromagnetic field is determined again with the adapted parameters.

Both of these methods involve advantages and disadvantages and for a given problem only one method may be applicable.

Investigation of Heating Processes

To show the applicability of this method a small single mode oven is used. In this oven a polyvinyl chloride (PVC) sample is heated. Fig. 5 shows the oven and the placement of the sample. PVC has a very low thermal and electric conductivity. Additionally, the electric conductivity is temperature dependent and increases with temperature. In microwave ovens thermal hot spots arise in such materials. Areas within those materials with higher electromagnetic fieldstrength become warmer and losses increase. This causes a higher energy absorption in those areas and the temperature increases faster. The thermal conductivity is too low to compensate this effect.

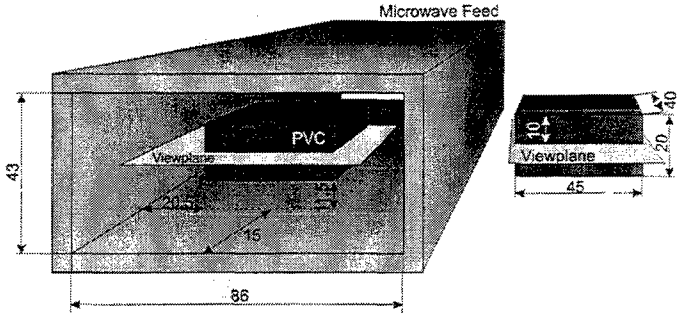


Fig. 5: Single Mode Applicator for heating PVC samples with removed front wall.

Fig. 6 shows the calculated electric field distribution in a horizontal viewplane in the middle of the sample. One can see that a standing wave arises causing a strong maximum in the middle of the sample. In the calculated temperature distribution within the sample one can see the resulting hot spot (Fig. 7).

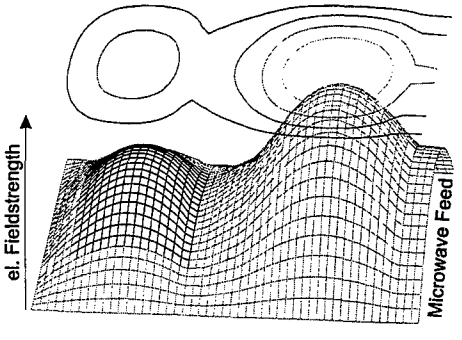


Fig. 6: Electric field within the oven. The area with darkened lines represents the field within the sample.

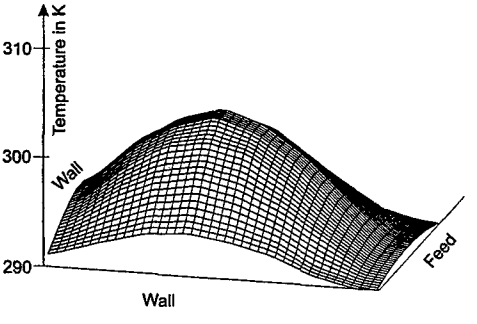


Fig. 7: Temperature distribution within the oven after 60 s.

To avoid the hot spot a conventional heating is added. The walls of the applicator are heated in addition to the microwaves with a constant heating rate of 0.83 K/s. In Fig. 8 the results for the combination of both heatings is shown. It is clear that the surfaces of the sample pointing to a hot wall are heated up. The surface pointing to the microwave feed is not heated and a temperature gradient arises. To avoid this the sample is placed 5 mm nearer to the front wall. The hot spot is moved

to the cooler surface and compensates the missing absorption of radiated heat by that wall. The results are shown in Fig. 9.

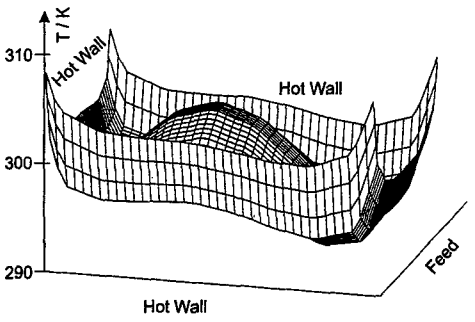


Fig. 8: Temperature Distribution within the sample if the walls are heated conventionally (t=60 s).

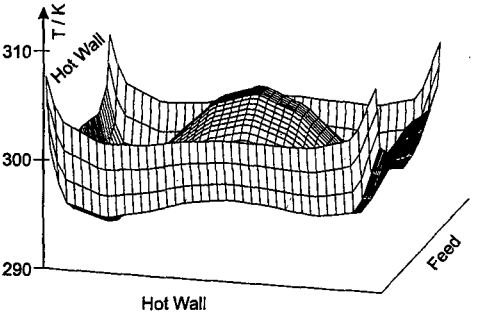


Fig. 9: Temperature Distribution within the sample. The sample is placed 10 mm away from the front wal (t=60 s)l.

Conclusion

A new method was presented to simulate heating processes including conduction and radiation. The algorithms are implemented in an electromagnetic FDTD-code, allowing the calculation of microwave and conventionally heated ovens. For the conductive heat transfer a finite difference scheme is shown. Ray optical methods are introduced to check visibility of surfaces and consequently the possibility of radiant heat exchange. The resulting simulation tool is very powerful and helpful to design ovens. As shown in an example microwave ovens cause hot spots in materials with low thermal conductivity and electric losses that increase with temperature. In hybrid ovens microwave and conventional heat sources can be adjusted and hot spots can be minimized. Temperature distributions can be determined inside a material to optimise the heating pattern. As a determination by measurements needs much more effort and is difficult to realise, the program is an excellent tool to perform heating adjustments and offers an excellent opportunity to simulate heating processes.

References

[1] M. Shashkow, Conservative Finite-Difference Methods on General Grids, CRC Press, 1996.

[2] B. Zalik, G. Clapworthy and C. Pblonsek, "An efficient codebased voxel-traversing Algorithm", Computer Graphics Forum, vol. 16, no. 2, pp. 119-147, june 1997.

[3] C. Yuesheng and C. Zhenchu, "The Bresenham's line algorithm line algorithm in multi-dimension", Proceedings of the 4th Int. Conf. on Computer-Aided Drafting, Design and Manufacturing Technology, Bejing, China, pp. 133-139, aug 1994.

[4] C. J. Hsu, "Shape Factor Equations for Radiant Heat Transfer between Two Arbitrary Sizes of Rectangular Planes", Canadian Journal Chem. Eng., vol. 45, 1967.

A Conformal Finite Difference Time Domain (CFDTD) Algorithm For Modeling Perfectly Conducting Objects

Wenhua Yu, Raj Mittra, Dean Arakaki, and Douglas H. Werner

Department of Electrical Engineering
The Pennsylvania State University
University Park, PA 16802
Email: wxy6@psu.edu

Abstract: In this paper, the authors present a new and robust conformal Finite Difference Time Domain (FDTD) algorithm for the accurate modeling of perfectly conducting objects with curved surfaces and edges. We illustrate the application of this approach by analyzing a number of representative antenna and cavity problems. These include a quarter wave monopole mounted on a perfectly conducting elliptic disk, a circular patch antenna, and a cylindrical cavity. We validate the method by comparing the results for the pattern, impedance and resonant frequency, etc., with those derived by using other techniques.

I. INTRODUCTION

The finite difference time domain method (FDTD), though it has been widely used to model various electromagnetic phenomena [1,2,3,4], continues to present a challenge when used to analyze structures with curved surfaces and edges. Although, in the past, there have been many attempts to address this problem via the use of conformal FDTD methods [2-19], the problems of mesh generation and instabilities have continued to plague most of these approaches. In this paper we present a generalization of the conformal FDTD method, which substantially preserves the conventional FDTD update algorithm as introduced by Yee [1]. We show, through several examples, that the present CFDTD approach is accurate, numerically efficient, and stable.

We begin by providing a brief review of the various techniques that have been employed for analyzing objects with curved surfaces. These include:

(i) *Methods based on a globally-distorted and body-fitted grid model*

These methods use non-Cartesian grids that conform to smoothly-shaped structures [6,7], and are limited in their application to special classes of geometries.

(ii) *Hybrid methods*

These approaches combine the FDTD method with other numerical methods, such as the Finite Element Method (FEM) [8,9] and the Method of Moments (MoM) [10]. In these approaches, the problem of interfacing the FDTD regions with the MoM or FEM domains in a manner such that spurious reflections are minimized and the solution is stable, is a challenging one and must be addressed to obtain satisfactory results.

(iii) *Locally distorted grid models*

These methods have the advantage of preserving the basic Cartesian nature of the grid in the entire computational domain [11-17]. However, they frequently suffer from the problems of late time instability and difficulties with mesh generation.

II. THE CONFORMAL FDTD APPROACH

Let us now describe briefly the conformal FDTD technique presented in this paper. It begins by dividing the cells, that are partially-filled with metallic conductors (assumed to be PECs), into two parts, *viz.*, the inside and outside subregions (see Fig. 1). The E-fields on the edges of the inside subregions are set to zero, whereas they are updated by using a modified algorithm in the outside subregions.

The magnetic fields inside the partially-filled cells are updated by using a slightly modified form of the conventional FDTD algorithm which accounts for the deformation of the cell. Unlike past approaches, however, we no longer employ the deformed cell area for updating the H-field--but use the entire cell area instead (see Fig. 2)--and this serves to eliminate the instability problems experienced in the past. The magnetic field component H_y is written as

$$H_y^{n+1/2}(i,j,k) = H_y^{n-1/2}(i,j,k) + \frac{\Delta t}{\mu_y(i,j,k)} \times \left[\begin{array}{l} \dfrac{\Delta z(i,j,k)E_z^n(i,j,k) - \Delta z(i-1,j,k)E_z^n(i-1,j,k)}{dx(i) \times dz(k)} \\ + \dfrac{\Delta x(i,j,k-1)E_x^n(i,j,k-1) - \Delta x(i,j,k)E_x^n(i,j,k)}{dx(i) \times dz(k)} \end{array} \right] \quad (1)$$

In the next section we present the numerical results for a number of representative problems to illustrate the application of the method just described above.

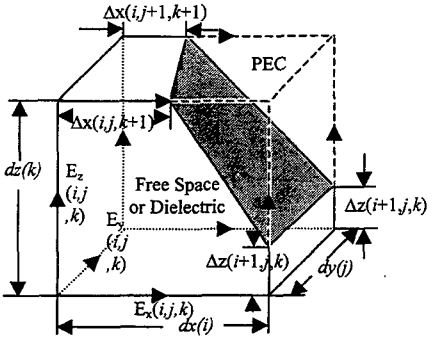


Fig. 1 FDTD cell partially filled with PEC

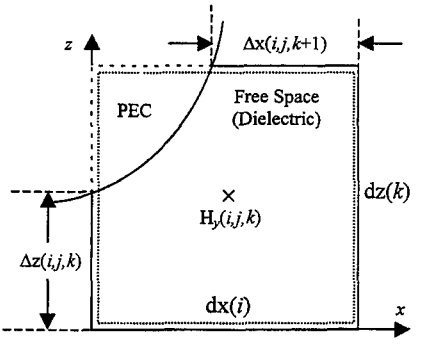


Fig.2 Intersection between the FDTD mesh and a PEC in the *x*-*z* plane

III. NUMERICAL RESULTS

To illustrate the versatility of the modified Finite Difference Time Domain program described above, referred to herein as the CFDTD code, we now present the numerical results for three different problems. They include: (i) the computation of the far-zone pattern for a quarter-wave monopole mounted on a perfectly conducting elliptic disk; (ii) evaluation of the impedance of a circular patch antenna; and, (iii) computation of resonant frequencies for a cylindrical cavity. In all of these cases, a 10-layer unsplit PML is used to truncate the FDTD domain, and the time step is chosen to be

$$\Delta t = \frac{0.995}{c\sqrt{\left(\frac{1}{dx}\right)^2 + \left(\frac{1}{dy}\right)^2 + \left(\frac{1}{dz}\right)^2}} \tag{2}$$

3.1. *Monopole on elliptic and circular ground planes*

First, we consider a quarter-wave monopole, mounted on a perfectly conducting elliptic disk, as shown in Fig. 3. The accuracy of the fields in the shadow region of the monopole depends on our ability to model the ground plane accurately.

The major and minor axes of the elliptic disk (b and a) are assumed to be 1.7 and 1.5 meters, respectively. The excitation source is a Gaussian pulse with a 3 dB cutoff frequency of 300 MHz, modulated by a sine function. The antenna is excited at the gap between the monopole and the ground plane. The FDTD domain is discretized into 79 × 87 × 30 cells, with a uniform mesh, whose dimensions are: $dx(i) = 0.05\ m$, $dy(j) = 0.05\ m$ and $dz(k) = 0.05\ m$. The normalized far zone field patterns for $\phi = 0^0$ and $\phi = 90^0$ at a frequency of 300 MHz are shown in Fig. 4 and Fig. 5, respectively. We observe that the CFDTD results are in good agreement with those obtained by using the MoM technique for both cuts.

Next we change the disk shape to be a circular one with a radius of 0.62 m, and use a non-uniform version of the CFDTD to calculate the far zone field pattern of the same monopole antenna at 1 GHz (see Fig. 6). We observe, once again, that the conformal FDTD results are in good agreement with those reported elsewhere in [21,22].

3.2 *Circular patch antenna*

Next, we compute the impedance of a microstrip patch antenna, circular in shape, as shown in Fig. 7. The computational domain for this problem is subdivided into 55 × 44 × 10 cells. The cell dimensions are chosen to be 0.002 m, 0.002 m and 0.000795 m, in the x, y and z directions, respectively. The simulation is run for 25,000 time steps (though 15,000 were found to be adequate), with a time step of $\Delta t = 2.29847\ ps$, and the solution is found to be entirely stable. The impedance of the circular patch antenna versus frequency is shown in Fig. 8. The results reported in [2,18,19] via the application of the symmetric and asymmetric PGY approaches, and those obtained by using the MoM [22], are also plotted in the same figure for the sake of comparison. The CFDTD results are seen to compare quite favorably with that obtained via the MoM; however, both the PGY (symmetric) and PGY (non-symmetric) methods exhibit a slight downward shift in the resonant frequency. We also

point out that in the PGY simulations a time step of $\Delta t = 0.725\ ps$ [2] was used, which is one-third of that needed in the CFDTD simulations.

3.3 *Cylindrical cavities*

As a final example, we turn to the problem of computing the resonant frequencies of the dominant TE and TM modes of a circularly-cylindrical cavity. The dimensions of the cylindrical cavities and results are presented in Table 1, along with the dimensions of the cavity, with R and H denoting the radius and height, respectively. The spatial discretization for this problem was chosen to be 0.005 *m*, and 5000 time steps were used to derive the results. Once again, we observe very good agreement between the new CFDTD results and the analytical solutions. In addition, no instabilities were observed, for this closed region problem, even though the program was tested up to 40,000 time steps.

TABLE 1. Resonant Frequencies of Cylindrical Cavities

	Methods	Geometry I R×H= (0.1m×0.1m)	Geometry II R×H= (0.1m×0.08m)	Geometry III R×H= (0.1m×0.06m)	Geometry IV R×H= (0.06m×0.06m)
TE_{111}	CFDTD	1.734	2.062	2.639	3.133
	Analytic	1.738	2.071	2.650	3.148
	Error	0.23%	0.43%	0.42%	0.48%
TM_{011}	CFDTD	1.88	2.194	2.742	2.872
	Analytic	1.889	2.199	2.751	2.897
	Error	0.48%	0.23%	0.33%	0.86%

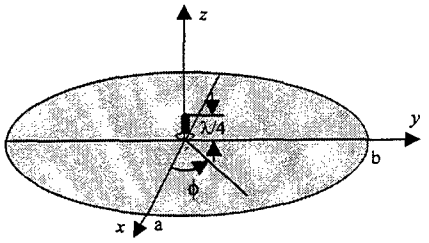


Fig. 3 Geometry for the radiation from a λ/4 monopole on an elliptic disk

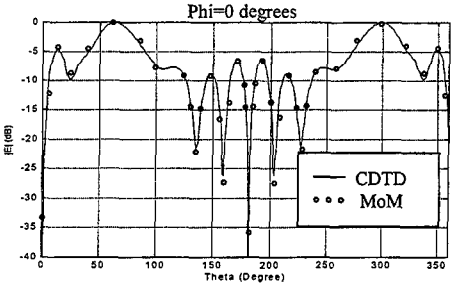


Fig.4 Normalized total electric field pattern for a λ/4 monopole on an elliptic disk with a=1.5 m and b=1.7 m at a frequency of 300 MHz.

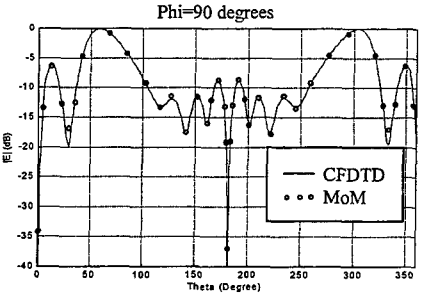


Fig.5 Normalized total electric field pattern for a λ/4 monopole on an elliptic disk with a=1.5 m and b=1.7 m at a frequency of 300 MHz.

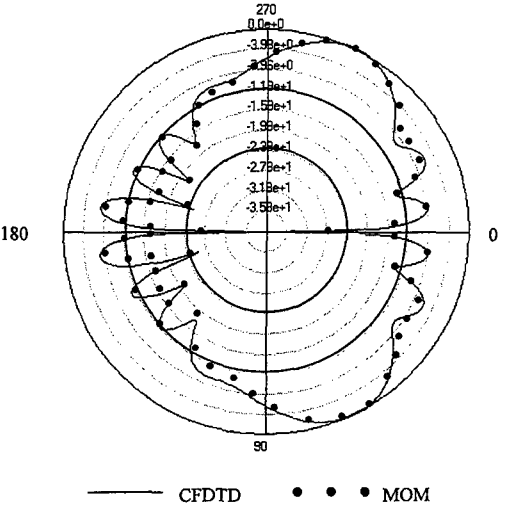


Fig. 6 Normalized total electric field pattern for a λ/4 monopole on a circular disk with a=b= 0.61 m at a frequency of 1 GHz.

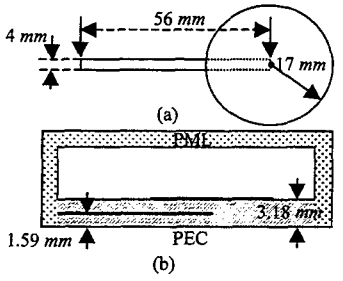


Fig. 7 Microwave coupled circular patch antenna. The microstrip is printed on a 1.59 *mm* substrate of $\varepsilon_r = 2.62$ over a ground plane, and the patch antenna is printed above a 1.59 *mm* superstrate of $\varepsilon_r = 2.62$. (a) top view; (b) side view.

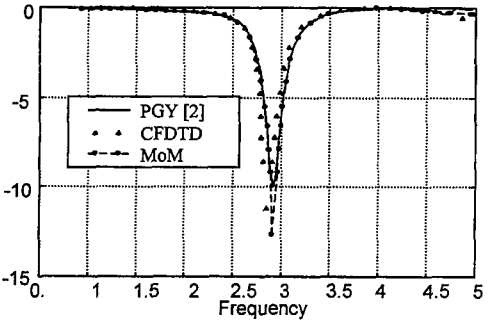


Fig. 8 Comparison of the reflection loss for a microstrip coupled circular patch antenna computed using CFDTD, MoM, and PGY.

REFERENCES:

[1] K. S. Yee, "Numerical Solution of Initial Boundary Value Problems Involving Maxwell's Equations in Isotropic Media," *IEEE Trans. Antennas and Propagat.*, vol. AP-14, pp. 302-307, May 1966.

[2] A. Taflove (editor), *Advances in Computational Electromagnetics: The Finite-Difference Time-Domain Method*, Boston, MA: Artech House, 1998.

[3] T. Itoh (Editor), *Time-Domain Methods for Microwave Structures*, IEEE Press, 1998.

[4] A. Taflove, *Computational Electromagnetics: The Finite-Difference Time-Domain Method*, Boston, MA: Artech House, 1995.

[5] J. P. Berenger, "A Perfectly Matched Layer for the Absorption of Electromagnetic Waves," *J. Comput. Phys.*, vol.114, pp.185-200, 1994.

[6] M. Fusco, "FDTD Algorithm in Curvilinear Coordinates," *IEEE Trans. Antennas and Propagat.*, vol. AP-38, no.1, pp. 76-89, January 1990.

[7] J-F. Lee, R. Palandech, and R. Mittra, "Modeling Three-Dimensional Discontinuities in Waveguides Using a Nonorthogonal FDTD Algorithm," *IEEE Trans. Antennas and Propagat.*, vol. AP-40, no.2, pp. 346-352, February 1992.

[8] K. S. Yee and J. S. Chen, "The Finite-Difference Time-Domain (FDTD) and the Finite-Volume Time-Domain (FVTD) Methods in Solving Maxwell's Equations," " *IEEE Trans. Antennas and Propagat.*, vol. AP-45, no.3, pp. 355-363, March 1997.

[9] Monorchio, A., and R. Mittra, "Time-Domain (FE/FDTD) Technique for Solving Complex Electromagnetic Problems," *IEEE Microwave and Guided Wave Letters*, vol. 8, no.2, pp. 93-95, February 1998.

[10] A. R. Bretones, R. Mittra, and R. G. Martin, "A Hybrid Technique Combining the Method of Moments in the Time Domain and FDTD," *IEEE Microwave and Guided Wave Letters*, vol. 8, no.8, pp. 281-283, August 1998.

[11] T. G. Jurgens, A. Taflove, K. Umashankar, and T. G. Moore, "Finite-Difference Time-Domain Modeling of Curved Surfaces," *IEEE Trans. Antennas and Propagat.*, vol. AP-40, no. 4, pp. 357-366, April 1992.

[12] T. G. Jurgens, and A. Taflove, "Three-Dimensional Contour FDTD Modeling of Scattering from Single and Multiple Objects," *IEEE Trans. Antennas and Propagat.*, vol. AP-41, no.12, pp. 1703-1708, December 1993.

[13] J. B. Schneider, and K. L. Shlager, "FDTD Simulations of TEM Horns and the Implications for Staircased Representations," *IEEE Trans. Antennas and Propagat.*, vol. AP-45, no.12, pp. 1830-1838, December 1997.

[14] Y. Nishioka, O. Maeshima, T. Uno, and S. Adachi, "FDTD Analysis of Resistive-Loaded Bow-Tie Antennas Covered with Ferrite-Coated Conducting Cavity for Subsurface Radar," *IEEE Trans. Antennas and Propagat.*, vol. AP-45, no. 12, pp. 970-977, December 1997.

[15] C. J. Railton, and J. B. Schneider, "An Analytic and Numerical Analysis of Several Locally Conformal FDTD Schemes," *IEEE Trans. Microwave Theory Tech.*, vol. 47, no.1, pp. 56-66, Jan. 1999.

[16] S. Dey and R. Mittra, "A Locally Conformal Finite Difference Time Domain (FDTD) Algorithm for Modeling 3-D Objects with Curved Surfaces," *IEEE AP-S International Symposium*, Montreal, Canada, 1997.

[17] S. Dey and R. Mittra, "A Locally Conformal Finite Difference Time Domain (FDTD) Algorithm for Modeling Three-Dimensional Perfectly Conducting Objects," *IEEE Microwave and Guided Wave Letters*, vol.7, no.9, pp. 273-275, September 1997.

[18] S. Gedney, F. Lansing, "A parallel Plane Generalized Yee Algorithm for the Analysis of Microwave Circuit Devices," J. Numerical Modeling, (Electric Networks and Fields), vol. 8, 1995, pp. 265-276.

[19] S. Gedney, F. Lansing, and D. Rescoe, "A Full Wave Analysis of Passive Monolithic Integrated Circuit Devices Using a Generalized Yee Algorithm," *IEEE Trans. Microwave Theory Tech.*, vol. 44, 1996, pp. 1393-1400.

[20] Wenhua Yu, and R. Mittra, "A Technique for Improving the Accuracy of the Non-uniform Finite Difference Time Domain (FDTD) Algorithm," *IEEE Trans. Microwave Theory Tech.*, vol. 47, no. 3, pp. 353-356, March 1999.

[21] P. A. Tirkas and C. A. Balanis, "Finite-Difference Time-Domain Method for Antenna Radiation," *IEEE Trans. Antennas and Propagat.*, vol. AP-40, no.3, pp. 334-340, March 1992.

[22] C. A. Balanis, *Advanced Engineering Electromagnetics,* John Wiley & Sons, New York, 1989, chapters 13 and 14.

[23] Zeland Software, 39120 Argonaut Way, Suite 499, Freemont, CA 94538.

A finite-difference algorithm for modeling of conductive wedges in 2D

Piotr Przybyszewski*

Abstract

This paper presents a fast finite-difference approach to the analysis of 2D structures containing conductive wedges. Such wedges may lead to singularity of some of the field components causing the local truncation error of the standard finite-difference methods to be unbounded and leading to high inaccuracy of the global results. The new method is expressed in the form of modification of two simple basic matrices. Such an approach gives a common method for discretization of various electromagnetic problems, since the basic operators allow one to represent Maxwell's equations. The new algorithm for modeling of conductive wedges supports inhomogeneous domains and unlike other algorithms found in the literature, makes no assumption about positioning of the edge with respect to Yee's cell. The numerical tests performed to validate the new approach give very good results in all range of parameters.

1 Introduction

Finite difference techniques using Yee's mesh are widely used for solving electromagnetic problems. However, one of the assumptions of these methods is that the variation of field within Yee's cell is not significantly different from linear. This condition is not satisfied in the vicinity of conductive wedges, where some of the field components may become singular [1]. This causes the local truncation error to be unbounded and leads to high inaccuracy of the global results. Various solutions of this problem were published in the literature. However, all of them have limitations. They assume the central location of the edge within Yee's cell [2][3] and/or support only wedges placed in the homogeneous domain [4]. In this paper, we present a new technique which does not have these limitations. The new approach gives significant reduction of error associated with the singularity for an arbitrary location of the wedge within the cell. Moreover, the domain in the vicinity of the wedge may be inhomogeneous. The new methods are implemented in the form of modification of basic matrices. All these matrices arise from discretization of basic operators, such as transverse gradient $\nabla_t(.)$, transverse divergence $\nabla_t \cdot (.)$ or operator $\vec{i}_z \times (.)$. Such an approach gives a common method for discretization of every differential problem in 2D electromagnetics, since the basic operators are directly related to Maxwell's equations. This method of discretization is similar to the one proposed in [5] but uses different basic operators.

2 Formulation of 2D electromagnetic problems

In this paper, we assume that the analyzed structure is lossless, isotropic and uniform in direction z. We decompose the fields into transverse (indiced with t) and longitudinal (indiced with z) components. Maxwell's equations may be written as follows.

$$\begin{bmatrix} -j\beta_z \mathbf{Z_m} & -\mathbf{Z_m G_{tm}} \\ -\mathbf{D_{te} Z_m} & 0 \end{bmatrix} \begin{bmatrix} h_t \\ h_z \end{bmatrix} = j\omega \begin{bmatrix} \mathbf{E_{tt}} & 0 \\ 0 & \mathbf{E_{zz}} \end{bmatrix} \begin{bmatrix} e_t \\ e_z \end{bmatrix} \tag{1}$$

$$\begin{bmatrix} -j\beta_z \mathbf{Z_e} & -\mathbf{Z_e G_{te}} \\ -\mathbf{D_{tm} Z_e} & 0 \end{bmatrix} \begin{bmatrix} e_t \\ e_z \end{bmatrix} = -j\omega \begin{bmatrix} \mathbf{M_{tt}} & 0 \\ 0 & \mathbf{M_{zz}} \end{bmatrix} \begin{bmatrix} h_t \\ h_z \end{bmatrix} \tag{2}$$

β_z is the propagation constant, ω is the angular frequency, e and h denote, respectively, electric and magnetic intensity fields. All the basic operators are written in a symbolic form. They have dual forms depending on

*Technical University of Gdańsk, Department of Electronics, Telecommunications and Informatics,
ul. Narutowicza 11/12, 80-952, Gdańsk, tel. (+ 48 58) 347 23 24, fax. (+ 48 58) 347 12 28, e-mail: pip@pg.gda.pl

the fields they are acting on. This allow one to introduce the boundary conditions to the operators and treat the boundary value problem in a uniform way. This gives us a common approach for the operator equations in continuous space and matrix equations in discrete space. The following table presents relations between the symbols, continuous operators and matrices:

Continuous space	$\nabla_t \cdot (.)$		$\nabla_t(.)$		$\vec{i}_z \times (.)$		$\bar{\bar{\epsilon}}_{tt}$	ϵ_{zz}	$\bar{\bar{\mu}}_{tt}$	μ_{zz}
Symbol	$\mathbf{D_{te}}$	$\mathbf{D_{tm}}$	$\mathbf{G_{te}}$	$\mathbf{G_{tm}}$	$\mathbf{Z_e}$	$\mathbf{Z_m}$	$\mathbf{E_{tt}}$	$\mathbf{E_{zz}}$	$\mathbf{M_{tt}}$	$\mathbf{M_{zz}}$
Discrete space	$\underline{D}_{te}$	$\underline{D}_{tm}$	$\underline{G}_{te}$	$\underline{G}_{tm}$	$\underline{Z}_e$	$\underline{Z}_m$	$\underline{E}_{tt}$	$\underline{E}_{zz}$	$\underline{M}_{tt}$	$\underline{M}_{zz}$

2.1 Properties of basic operators

Analysis of basic operators in continuous space in eqs. (1) and (2) leads, for lossless structures and nonradiative modes, to the following properties:

$$\mathbf{D_{te}} = -\mathbf{G_{te}^T} \tag{3}$$
$$\mathbf{D_{tm}} = -\mathbf{G_{tm}^T} \tag{4}$$
$$\mathbf{Z_e} = -\mathbf{Z_m^{-1}} = -\mathbf{Z_m^T} \tag{5}$$

In the lossless domain, the operators associated with material tensors should be hermitian symmetric:

$$\mathbf{E_{tt}} = \mathbf{E_{tt}^H} \qquad \mathbf{E_{zz}} = \mathbf{E_{zz}^H} \qquad \mathbf{M_{tt}} = \mathbf{M_{tt}^H} \qquad \mathbf{M_{zz}} = \mathbf{M_{zz}^H} \tag{6}$$

Furthermore, from the property $\nabla \cdot \nabla \times (.) = 0$, we get:

$$\mathbf{D_{tm}Z_eG_{te}} = 0 \tag{7}$$
$$\mathbf{D_{te}Z_mG_{tm}} = 0 \tag{8}$$

If the domain is isotropic and homogeneous, we have $v^2 = (\epsilon\mu)^{-1}$, where v is the wave speed. This implies:

$$\mathbf{E_{tt}^{-1}Z_mM_{tt}^{-1}Z_e} = v^2\mathbf{I_{tt}} \tag{9}$$

where $\mathbf{I_{tt}}$ is the identity operator defined on the transverse fields. This condition guarantees that the propagation constant and the frequency are related to each other by the following equation:

$$\omega^2 - \omega_0^2 = v^2\beta_z^2 \tag{10}$$

where ω_0 is the cutoff angular frequency of the corresponding mode.

All the properties presented above may be seen as constraints which have to be fulfilled by the discrete operators. However, most of them will be satisfied in a natural way, as a consequence of the field behavior and properties of Maxwell's equations and Yee's grid.

2.2 Electromagnetic eigenproblems

Various eigenproblems may be formulated based on eqs. (1), (2). Here, we point out only a few examples. β_z^2 formulation for the transverse electric intensity field components may be written as follows:

$$\begin{aligned}\beta_z^2 e_t &= -\omega^2\mathbf{Z_mM_{tt}Z_eE_{tt}}e_t - \mathbf{Z_mM_{tt}G_{tm}M_{zz}^{-1}D_{tm}Z_e}e_t \\ &+ \mathbf{G_{te}E_{zz}^{-1}D_{te}E_{tt}}e_t\end{aligned} \tag{11}$$

At cutoff, we get two scalar eigenproblems dealing with, respectively, modes E and H:

$$\mathbf{E_{zz}^{-1}D_{te}Z_mM_{tt}^{-1}Z_eG_{te}}e_z = \omega^2 e_z \tag{12}$$
$$\mathbf{M_{zz}^{-1}D_{tm}Z_eE_{tt}^{-1}Z_mG_{tm}}h_z = \omega^2 h_z \tag{13}$$

Analogously, we may write two scalar eigenproblems for the static case. By discretizing separately the basic operators rather than full equations, we get a common approach to the discretization of eigenproblems including the ones presented above.

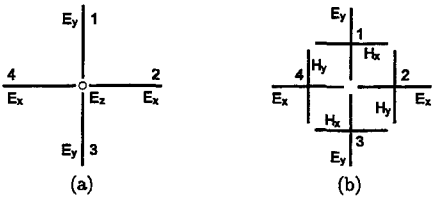


Figure 1: *Fragments of 2D Yee's grid corresponding to the domains and contradomains of matrices* $\underline{\underline{D}}_{te}$ *(a) and* $\underline{\underline{Z}}_e$ *(b).*

3 Discretization of basic operators

Fragment of matrix $\underline{\underline{D}}_{te}$ corresponding to nodes in fig. 1(a) may be written as follows:

$$\underline{\underline{D}}_{te} = \begin{bmatrix} \frac{1}{\Delta y} & \frac{1}{\Delta x} & -\frac{1}{\Delta y} & -\frac{1}{\Delta x} \end{bmatrix} \tag{14}$$

In a similar manner, we may define matrix $\underline{\underline{D}}_{tm}$. Matrices corresponding to transverse gradient, have the form $\underline{\underline{G}}_{te} = -\underline{\underline{D}}_{te}^T$ and $\underline{\underline{G}}_{tm} = -\underline{\underline{D}}_{tm}^T$, satisfying conditions (3) and (4). Fragments of matrices $\underline{\underline{Z}}_e$, $\underline{\underline{Z}}_m$ corresponding to the nodes in fig. 1(b) have the following form:

$$\underline{\underline{Z}}_e = \begin{bmatrix} 1 & 0 & 0 & 0 \\ 0 & -1 & 0 & 0 \\ 0 & 0 & 1 & 0 \\ 0 & 0 & 0 & -1 \end{bmatrix} \qquad \underline{\underline{Z}}_m = \begin{bmatrix} -1 & 0 & 0 & 0 \\ 0 & 1 & 0 & 0 \\ 0 & 0 & -1 & 0 \\ 0 & 0 & 0 & 1 \end{bmatrix} \tag{15}$$

Material matrices corresponding to the material tensors are in the homogeneous parts of the domain simply the values of the appropriate material constant at the corresponding point.

Further on, we define local algorithms for modeling of conductive wedges, arbitrarily located electric walls and boundaries between dielectrics. All these algorithms are written in the form of modification of material matrices. Such an approach guarantees the right interpretation of the fields.

3.1 Conductive wedges

Conductive wedges may lead to singularity of some of the field components in the vicinity of the edge. This cause the local truncation error to be unbounded and leads to high inaccuracy of the global results. Here, we present the new algorithm for modeling of such structures reducing this kind of errors. A general idea is to modify matrices $\underline{\underline{E}}_{tt}$, $\underline{\underline{M}}_{tt}$ so that the field behavior is correctly represented by the standard grid equations.

General algorithm based on cutoff solutions We expand the longitudinal field components in the region of singularity into a series of functions:

$$e_z = \sum_i c_{ei} e_{zci} \qquad h_z = \sum_i c_{hi} h_{zci} \tag{16}$$

where c_{ei}, c_{hi} are unknown coefficients. Functions e_{zci}, h_{zci} are the solutions of cutoff scalar equations, respectively (12) and (13), for $\omega = 0$ in the vicinity of the singularity. Let us concentrate on field e_z. Limiting the sum in (16) to the first few terms and writing it for a few grid points e_z we may present it in the following matrix form:

$$\underline{e}_z = \underline{\underline{B}}_{ec} \underline{c}_e \tag{17}$$

Further on, we assume, that the number of elements in the sum is equal to the number of grid points, and hence $\underline{\underline{B}}_{ec}$ is a square matrix. We also assume, that the location of these points does not lead to singularity of the matrix.

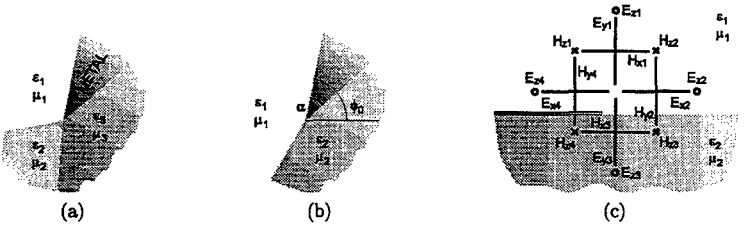


Figure 2: *Conductive wedge in an inhomogeneous domain: general case (a), wedge symmetrically placed between two dielectrics (b), nodes used in the correction algorithm for the wedge of angle $\alpha = 0$ at $\phi_0 = 180°$ (c).*

Element ij of matrix $\underline{\underline{B}}_{ec}$ is equal to the value of function e_{zci} of series (16) at grid point e_{zj}:

$$B_{ecij} = e_{zci}|_{e_{zj}} \tag{18}$$

Let us now write Maxwell's cutoff equation for field $\underline{b}_t$ in terms of field $\underline{e}_z$:

$$-j\omega \underline{b}_t = -\underline{\underline{Z}}_e \underline{\underline{G}}_{te} \underline{e}_z \tag{19}$$

Inserting eq. (17) into (19) and inverting the operator in order to express vector $\underline{c}_e$ in terms of vector $\underline{b}_t$, we get:

$$\underline{c}_e = -j\omega \underline{\underline{B}}_{ec}^{-1} \underline{\underline{G}}_{te}^{I} \underline{\underline{Z}}_m \underline{b}_t \tag{20}$$

Operation $(.)^I$ is a quasi-inversion and will be discussed in one of the next paragraphs. At this stage of discussion, we may assume that it is equivalent to inversion. Vector $\underline{h}_t$ may be expressed in terms of $\underline{c}_e$ as follows:

$$-j\omega \underline{h}_t = \underline{\underline{G}}_{tm} \underline{\underline{A}}_{ec} \underline{c}_e \tag{21}$$

Matrix $\underline{\underline{A}}_{ec}$ in this equation converts coefficients c_{ei} into indefinite integrals. Further on, matrix $\underline{\underline{G}}_{tm}$ converts them to the definite integrals. Element ij of matrix $\underline{\underline{A}}_{ec}$ is the value of appropriate indefinite integral of function e_{zci} at grid point h_{zj}:

$$A_{ecij} = \int \frac{1}{\mu_{xx}} \frac{\partial}{\partial x} e_{zci} dy \Big|_{h_{zj}} = -\int \frac{1}{\mu_{yy}} \frac{\partial}{\partial y} e_{zci} dx \Big|_{h_{zj}} \tag{22}$$

Putting eq. (20) into (21), we get:

$$\underline{h}_t = \underline{\underline{G}}_{tm} \underline{\underline{A}}_{ec} \underline{\underline{B}}_{ec}^{-1} \underline{\underline{G}}_{te}^{I} \underline{\underline{Z}}_m \underline{b}_t \tag{23}$$

The above equation shows relation between fields $\underline{h}_t$ and $\underline{b}_t$. This defines operator $\underline{\underline{M}}_{tt}^{-1}$:

$$\underline{\underline{M}}_{tt}^{-1} = \underline{\underline{G}}_{tm} \underline{\underline{A}}_{ec} \underline{\underline{B}}_{ec}^{-1} \underline{\underline{G}}_{te}^{I} \underline{\underline{Z}}_m \tag{24}$$

In the same manner, we construct matrix $\underline{\underline{E}}_{tt}^{-1}$:

$$\underline{\underline{E}}_{tt}^{-1} = -\underline{\underline{G}}_{te} \underline{\underline{A}}_{hc} \underline{\underline{B}}_{hc}^{-1} \underline{\underline{G}}_{tm}^{I} \underline{\underline{Z}}_e \tag{25}$$

Analogous procedure may be performed when constructing the basis from static equations for $\beta_z = 0$. This leads to definitions of matrices $\underline{\underline{E}}_{tt}$ and $\underline{\underline{M}}_{tt}$, which are equivalent to the equations given above.

Symmetrization of matrices $\underline{\underline{E}}_{tt}$ and $\underline{\underline{M}}_{tt}$ We should note, that operators $\underline{\underline{M}}_{tt}^{-1}$, $\underline{\underline{E}}_{tt}^{-1}$ (or $\underline{\underline{E}}_{tt}$, $\underline{\underline{M}}_{tt}$) defined this way are not symmetric, and hence do not satisfy condition (6). Fortunately, the algorithm is not sensitive to small deformations of Yee's cells in the vicinity of the wedge. Therefore, we may choose the locations of the appropriate nodes in the way leading to symmetric operators. This may be also achieved in a simpler way, where we symmetrize nonsymmetric matrices as follows:

$$\underline{\underline{C}} \leftarrow 0.5(\underline{\underline{C}} + \underline{\underline{C}}^T) \tag{26}$$

where $\underline{\underline{C}}$ denotes the operator to be symmetrized. In order to not disturb condition (9) for homogeneous domains, we should symmetrize only one of the pairs $\underline{\underline{E}}_{tt}$, $\underline{\underline{M}}_{tt}^{-1}$ or $\underline{\underline{M}}_{tt}$, $\underline{\underline{E}}_{tt}^{-1}$.

Quasi-inversion of matrices $\underline{\underline{G}}_{te}, \underline{\underline{G}}_{tm}$ Expressions describing matrices $\underline{\underline{E}}_{tt}, \underline{\underline{M}}_{tt}$ include inversions of matrices $\underline{\underline{G}}_{te}$ and $\underline{\underline{G}}_{tm}$. Unfortunately, in many cases, these matrices cannot be inverted, because they are singular. Let us note, however, that zero eigenvalue of these operators corresponds to one of the static modes $e_{zi} = \text{const}$ or $h_{zi} = \text{const}$. These modes do not have the transverse field components, and hence have no influence on matrices $\underline{\underline{E}}_{tt}$ and $\underline{\underline{M}}_{tt}$. Therefore, we may assume that these modes do not exist in the global field. In this case we may remove zero eigenvalue as follows:

$$\underline{\underline{G}}'_{tm} = \underline{\underline{G}}_{tm} + \underline{h}_{t0}\underline{h}^T_{z0} \tag{27}$$

where $\underline{h}_{z0}$ is nonzero eigenvector corresponding to zero eigenvalue, and $\underline{h}_{t0}$ is an arbitrary nonzero vector in space $\{\underline{h}_t\}$. Operator $\underline{\underline{G}}'_{tm}$ is not singular and may be inverted. We call operator $\underline{\underline{G}}'^{-1}_{tm}$ the quasi-inversion of $\underline{\underline{G}}_{tm}$ ($\underline{\underline{G}}^I_{tm} = \underline{\underline{G}}'^{-1}_{tm}$).

Conductive wedge When a conductive wedge is the source of singularity (fig. 2(a)), series (16) takes up the form [1]:

$$e_z = \sum_{i=1}^{\infty} \alpha_{ej} c_{ei} r^{\nu_i} sin(\nu_i \phi) \qquad h_z = \sum_{i=0}^{\infty} \alpha_{hj} c_{hi} r^{\nu_i} cos(\nu_i \phi) \tag{28}$$

where α_{ej}, α_{hj}, ν_i have to be chosen in a way satisfying all boundary conditions. The following table presents definition of basic operators for the conductive wedge placed symmetrically between two dielectrics (figs. 2(b,c)). One may note, that this includes a very common case of a thin metal strip placed on a dielectric boundary, which may be seen as a conductive wedge of angle $\alpha = 0$.

$$\underline{\underline{B}}_{ec} = \begin{bmatrix} 0 & s_{11} & s_{12} & s_{13} \\ 0 & s_{21} & (\mu/\mu_1)s_{22} & s_{23} \\ 0 & s_{31} & (\mu_2/\mu_1)s_{22} & s_{33} \\ 1 & 0 & 0 & 0 \end{bmatrix} \qquad \underline{\underline{A}}_{ec} = \frac{1}{\mu_1} \begin{bmatrix} 1 & c_{11} & c_{12} & c_{13} \\ 1 & c_{21} & c_{22} & c_{23} \\ 1 & (\mu_1/\mu_2)c_{31} & c_{32} & (\mu_1/\mu_2)c_{33} \\ 1 & (\mu_1/\mu_2)c_{41} & c_{42} & (\mu_1/\mu_2)c_{43} \end{bmatrix}$$

$$\underline{\underline{B}}_{hc} = \begin{bmatrix} 1 & c_{11} & c_{12} & c_{13} \\ 1 & c_{21} & c_{22} & c_{23} \\ 1 & (\epsilon_2/\epsilon_1)c_{31} & c_{32} & (\epsilon_2/\epsilon_1)c_{33} \\ 1 & (\epsilon_2/\epsilon_1)c_{41} & c_{42} & (\epsilon_2/\epsilon_1)c_{43} \end{bmatrix} \qquad \underline{\underline{A}}_{hc} = \frac{1}{\epsilon_1} \begin{bmatrix} 0 & s_{11} & s_{12} & s_{13} \\ 0 & s_{21} & (\epsilon_1/\epsilon)s_{22} & s_{23} \\ 0 & s_{31} & (\epsilon_1/\epsilon_2)s_{32} & s_{33} \\ 1 & 0 & 0 & 0 \end{bmatrix}$$

$$\underline{\underline{G}}_{tm} = \underline{\underline{H}}^{-1} \begin{bmatrix} -1 & 1 & 0 & 0 \\ 0 & 1 & -1 & 0 \\ 0 & 0 & 1 & -1 \\ 0 & 0 & 0 & 0 \end{bmatrix} \qquad \underline{\underline{G}}^I_{tm} = \begin{bmatrix} -0.75 & 0.5 & 0.25 & 0 \\ 0.25 & 0.5 & 0.25 & 0 \\ 0.25 & -0.5 & 0.25 & 0 \\ 0.25 & -0.5 & -0.75 & 0 \end{bmatrix} \underline{\underline{H}}$$

$$\underline{\underline{G}}_{te} = \underline{\underline{H}}^{-1} \begin{bmatrix} 1 & 0 & 0 & 0 \\ 0 & 1 & 0 & 0 \\ 0 & 0 & -1 & 0 \\ 0 & 0 & 0 & 0 \end{bmatrix} \qquad \underline{\underline{G}}^I_{te} = \begin{bmatrix} 1 & 0 & 0 & 0 \\ 0 & 1 & 0 & 0 \\ 0 & 0 & -1 & 0 \\ 0 & 0 & 0 & 0 \end{bmatrix} \underline{\underline{H}}$$

$$\underline{\underline{H}} = \text{diag}(\Delta x, \Delta y, \Delta x, \Delta y)$$

$$s_{ij} = r_i^{\nu_j} \sin \nu_j \phi_i \qquad c_{ij} = r_i^{\nu_j} \cos \nu_j \phi_i \qquad \nu_i = \frac{i\pi}{2\pi - \alpha}$$

3.2 Modeling of boundaries

Boundaries between dielectrics or magnetics and electric and magnetic walls may be modeled by setting appropriate effective permittivities and/or permeabilities on the diagonal elements of material arrays corresponding to nodes close to the boundary. The equations for the effective material constants are based on the integral interpretation of the finite difference methods and are given below without derivation. These equations are needed to perform the tests presented in sec. 4. Since, in this paper, we want to concentrate on modeling of conductive wedges, the reader may skip the rest of this section.

Boundary between dielectrics Fig. 3(a-c) presents three cases of location of dielectric boundary with respect to the electric field within Yee's cell. When the electric field is parallel to the boundary (fig. 3(a)), the effective

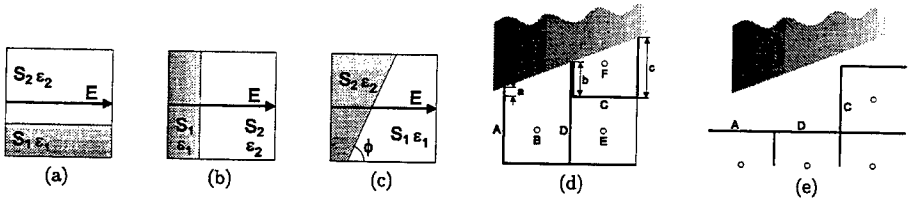


Figure 3: *Modeling of boundaries. Electric field parallel (a), normal (b) and at an arbitrary angle with respect to the dielectric boundary (c). Electric wall crossing 2D Yee's grid. Nodes H_z, E_x, E_y (d) and E_z, H_x, H_y (e).*

permittivity may be calculated from the following equation:

$$\epsilon_{||} = \frac{\epsilon_1 S_1 + \epsilon_2 S_2}{S} \tag{29}$$

In the case of the field normal to the boundary (fig. 3(b)), we get the following formula:

$$\epsilon_{\perp} = \frac{S}{\frac{S_1}{\epsilon_1} + \frac{S_2}{\epsilon_2}} \tag{30}$$

In a more general case, when electric vector is placed at an arbitrary angle with respect to the boundary (fig. 3(c)), the effective permittivity may be expressed by $\epsilon_{||}$ and $\epsilon_{\perp}$:

$$\epsilon_{eff} = \epsilon_{\perp} \sin^2 \phi + \epsilon_{||} \cos^2 \phi \tag{31}$$

where ϕ is the angle between the boundary and x field component.

In a similar manner, we may express the effective permeability μ_{eff} at the boundary between two magnetics.

Electric walls Looking at Yee's cells crossed by an electric wall in fig. 3(d,e), we may note, that they are deformated with respect to the standard cells. This means, that there appear different integration paths and surfaces than in the standard case in the integral interpretation of the finite difference methods. This difference may be carried out by introducing appropriate effective permittivities and permeabilities at the cells close to the boundary. We may note, that there are three types of cells crossed by electric plane, namely A, B and C in fig. 3(d,e). Node D is of the same type as node A, node E is a standard Yee's cell which requires no modification, and cell F corresponds to cell B. The effective material constants for all three types of cells are presented in the following table:

Node	Nodes H_z, E_x, E_y	Nodes E_z, H_x, H_y
A	$\epsilon_{eff} = \epsilon \frac{\Delta y}{\Delta y + a}$	$\mu_{eff} = \mu \frac{\Delta y + a}{\Delta y}$
B	$\mu_{eff} = \mu \frac{\Delta y + 0.5(a+b)}{\Delta y}$	
C	$\epsilon_{eff} = \epsilon \frac{\Delta x}{\Delta x + b}$	$\mu_{eff} = \mu \frac{\Delta x + b}{\Delta x}$

4 Numerical results

In order to present the abilities of the approach presented in the previous sections, the new algorithms were implemented in the form of a computer code and used for computing of the cutoff frequencies of an inhomogeneous line with a single conductive wedge shown in fig. 4. The following table compares the results for E_1 and H_1 modes for the algorithm without and with correction for the conductive wedge presented in sec. 3.1, for the case $\alpha = 0$, $\phi_0 = 0$ and the edge corner located in the center of Yee's cell.

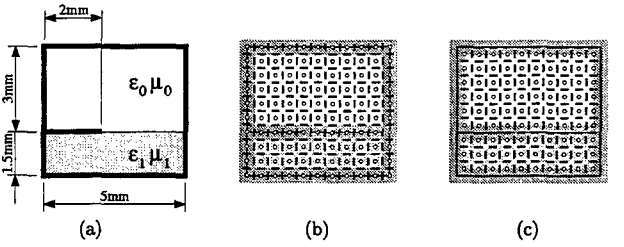


Figure 4: *Tested structure (a) and the same structure placed in Yee's grid: nodes E_z, H_x, H_y (b) H_z, E_x, E_y (c).* $\epsilon_1 = 4\epsilon_0$. $\mu_1 = \mu_0$.

	Standard					New
	20×18	40×36	80×72	160×144	Ext.	20×18
E_1	**38.04**	37.85	37.75	37.70	**37.64**	**37.58**
	1.06%	0.57%	0.30%	0.15%		**-0.17%**
H_1	**14.01**	14.22	14.32	14.37	**14.42**	**14.39**
	-2.80%	-1.39%	-0.69%	-0.35%		**-0.16**

In the standard algorithm the error for the coarsest grid 20×18 is -2.80% for the H_1. When the new algorithm is applied, the coarsest grid leads to an error of -0.16%,

To show the behavior of the algorithm when the edge corner is not located in the center of the cell, a series of simulations was carried out for the same structure but the 20×18 grid translated in the x, y space by the normalized distance $-0.5 \leq x_t/\Delta x \leq 0.5$, $-0.5 \leq y_t/\Delta y \leq 0.5$. The contour plots showing the relative error for the algorithm with and without correction are shown in figs. 5, 6. For the standard method the largest error is at the level of 2.5% (E_1 mode) or 8% (H_1) while the modified algorithm reduces this error to 0.4% and 0.6% in the worst case.

Acknowledgments

Computations reported in this paper were performed using the facilities in at the Academic Computer Center in Gdańsk (CI TASK). The research was supported by the Polish State Committee for Scientific Research under contract 8 T11D 030 15.

References

[1] J. Meixner, "The Behavior of Electromagnetic Fields at Edges", *IEEE Trans. Antennas Propagat.*, vol. AP-20, pp. 442–446, Jul. 1972.

[2] G. Mur, "The Modelling of Singularities in the Finite-Difference Approximation of the Time-Domain Electromagnetic-Field Equations", *IEEE Trans. Microwave Theory Tech.*, vol. MTT-29, pp. 1073–1077, Oct. 1981.

[3] Ngoc-Hoa Huynh, W. Heinrich, "Efficient Finite-Difference Description of 3D Edge Singularities for Coplanar MMICs Including Metalization Thickness", proc. 29th European Microwave Conference, Munich, 1999.

[4] P. Przybyszewski, M. Mrozowski. "A conductive wedge in Yee's mesh". *IEEE Microwave and Guided Wave Letters*, pp. 66-68, Feb. 1998.

[5] T. Weilandt, "Eine Mathode zur Loesung derMaxwellschen Gleichungen fuer sechskomponentinge Felder auf diskreter Basis", *Arch. Elek. Übertragung.*, vol. 31, pp. 116–120, 1977.

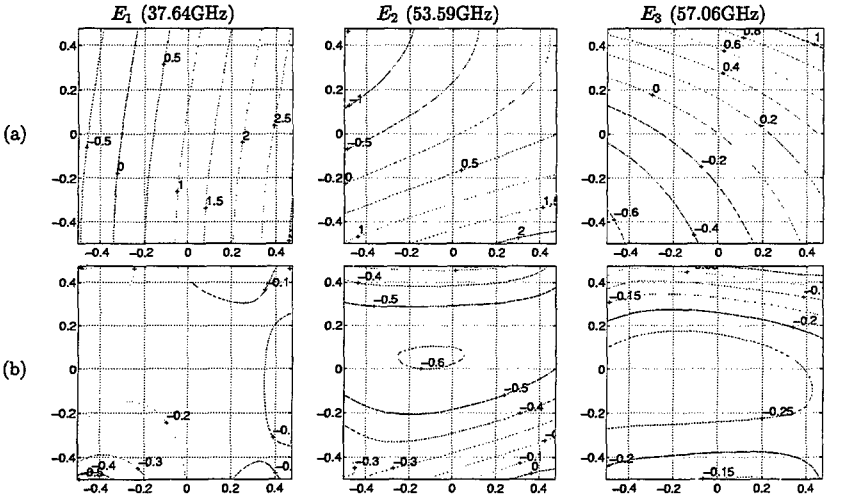


Figure 5: *Contours of relative error [%] of the cutoff frequancies of E modes versus normalized wedge location within Yee's cell for the finite difference algorithm without (a) and with (b) correction.*

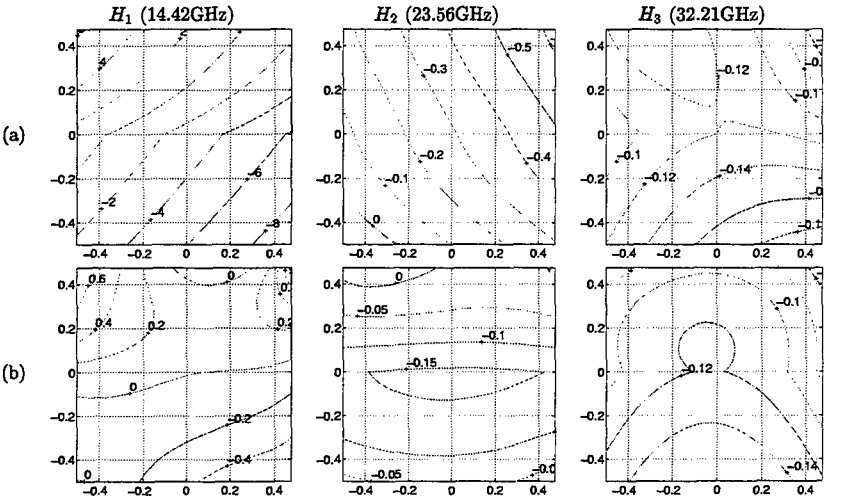


Figure 6: *Contours of relative error [%] of the cutoff frequencies of H modes versus normalized wedge location within Yee's cell for the finite difference algorithm without (a) and with (b) correction.*

ADVANCED TECHNIQUES OF GEOMETRICAL MODELLING AND CFDTD

F. Rivas*, J.P. Roa*, M.F. Cátedra**

* Departamento de Electrónica, EUP de Linares, Universidad de Jaen.
**Escuela Politécnica, Universidad de Alcalá
28806 Alcalá de Henares, (Madrid), SPAIN
Fax +34 91 885.6699
e-mail: felipe.catedra@alcala.es

Abstract

An FDTD-based code for treating 3D arbitrary conducting and material bodies is presented. The geometry is modeled using NURBS surfaces, one of the most powerful and flexible tools for the geometrical representation of objets. On the other hand, the use of the CFDTD technique avoids the use of a staircase to shape the body, what improves the solution. The CFDTD method has been slightly modified when it is applied to material bodies by considering the discontinuity of electric and magnetic fields crossing the medium-air interface. The method has been applied to obtain RCS values of both conducting and dielectric bodies modeled by NURBS surfaces. Good agreement with results from other methods is observed.

Introduction

The FDTD method has been successfully applied to a wide variety of electromagnetic problems. Originally, its main limitation was its application to Cartesian orthogonal grids that involves the use of a staircase model to represent the body. It is known that this kind of representation introduces spurious responses and therefore degrades the solution. There are several ways of avoiding the use of the staircase model. In this communication the solution presented in [1] has been chosen. In [1] the orthogonal grid is preserved in almost the whole computational domain except in a few cells, those intersecting the geometry. In such cells, the contours in which Ampere's and Faraday's laws are applied in order to update E and H are adjusted to the shape of the conducting body. This method is known as CFDTD (Conformal Finite Difference Time Domain). As is presented in reference [1], this method is limited to perfect electrical conductor (PEC) bodies. Next, in [2], the same authors extended the method to deal with dielectric media, obtaining the portion of the contour inside the dielectric body and defining an effective dielectric constant.

The contribution of this communication is double. In one hand, the formulation developed in [1] is applied to the study of perfectly conducting bodies modeled by NURBS surfaces, and in the other hand an alternative approach to the method of [2] is provided in order to deal with material bodies.

NURBS (Non Uniform Rational B-Splines) [3] surfaces are curved surfaces of an arbitrary degree. Because of their arbitrary degree, they shape complex bodies accurately with limited (few) information. NURBS are becoming one of the most universal tools for the geometrical representation of objects. The application of NURBS and other geometrical tools to solve electromagnetic problems has provided excellent results in many cases. In [4-6] several codes to analyze the RCS from complex targets using high and low frequency techniques are presented.

An FDTD-based program that analyzed arbitrary geometry modeled by NURBS surfaces has been developed. The scatter is embedded inside a regular computational space (orthogonal grid) which is only deformed for the field components located next to the geometry to accommodate the curvature of the surface. The computational space is ended with UPML [7] absorbing boundary conditions and the far-field computations are performed using NF-FF (Near Field -Far Field Formulation) as it is done in [8]

Theory

As stated before, conducting (PEC) and material bodies are considered. Depending on the nature of the body the equations which update the $\vec{E}$ *and* $\vec{H}$ components will be whether those of [1] for PEC case or an improved version of [2] for material bodies.

For the sake of completeness, the updated equations for the PEC case are presented, in particular, for a $\vec{H}$ field component close to the geometry. Thus, $H_z|_{i,j,k}$ is updated from the following equation -for more details see reference [1].

$$H_z^{n+\frac{1}{2}}(i,j,k) = H_z^{n-\frac{1}{2}}(i,j,k) + \frac{\Delta t}{\mu * Area(i,j,k)} * E_x^{\,n}(i,j+1,k) * l3 - E_x^{\,n}(i,j,k) * l1 + E_y^{\,n}(i,j,k) * l2 \quad (1)$$

Where Area (i,j,k) is the area enclosed by the contour C_A

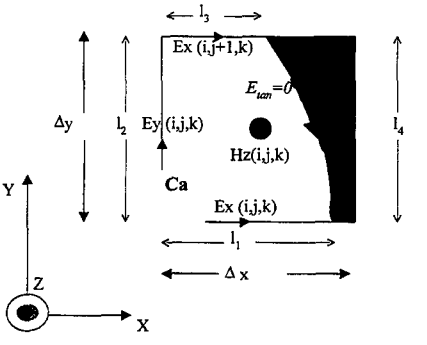


Figure 1.- CFDTD on perfecly conducting bodies

Because the geometry is defined by NURBS surfaces, geometrical rendering algorithms have been developed in order to obtain the intersecting points of the contour with the geometry.

For the treatment of dielectric media, the approximation presented in [2] is improved when the discontinuity of electrical and magnetic fields crossing the medium-air interface is considered (assuming the scatterer surrounded by air). The process to update a particular component of magnetic field H ($H_z|_{i,j,k}$) following Faraday's law is developed below.

Expressing Maxwell's laws in integral form, fields $\vec{E}$ *and* $\vec{B}$ are related following Faraday's law:

$$\frac{-\partial \int_S \vec{B}\vec{ds}}{\partial t} = \oint_{C1} \vec{E}\vec{dl} \qquad (2)$$

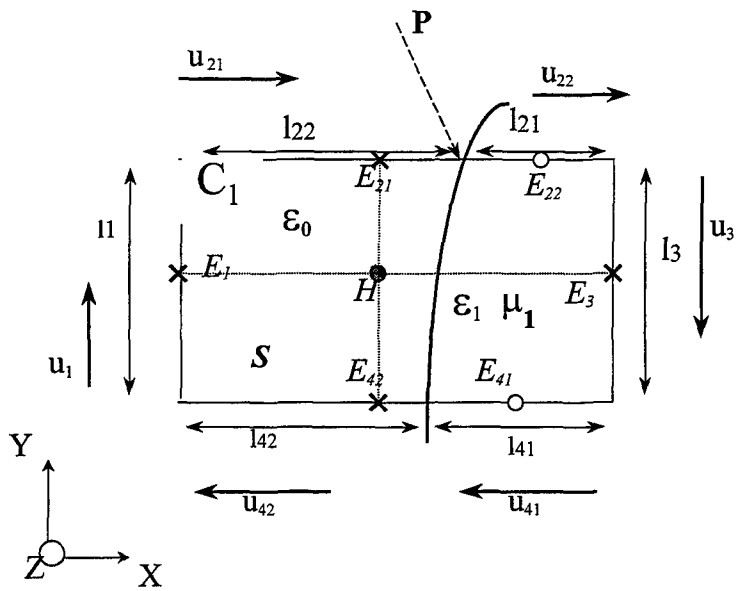


Figure 2.- Parameters to consider when $H_{Z|i,j,k}$ *is updated (material media)*

Let us suppose that $H_z|_{i,j,k}$ is close to the geometry (that is to say, the contour C1 that surrounds it, intersects the geometry). In that case, a new formulation has been developed to update that component in time. Otherwise, Yee's formulation [9] is used.

In figure 2 are μ_1 and ε_1 are the permeability and dielectric constant of the material medium and S is the area bounded by contour C1. Applying Ampere's law to the perpendicular contour C1, the variation of the flux of $\vec{B}_z$ is related to the values of $\vec{E}_x$ and $\vec{E}_y$ in C_1. Otherwise, the contour C_1 is defined by segments $C_1 = \{L_1, L_{21}, L_{22}, L_3, L_{41}, L_{42}\}$ as is shown in figure2.

Applying Faraday's law and assuming that $\vec{E}$ is constant in the segments which conform C_1, the right term in (2) is developed as follows:

$$\frac{-\partial \int_S \vec{B}\vec{ds}}{\partial t} = L_1 \vec{E}_1 \vec{u}_1 + L_{21} \vec{E}_{21} \vec{u}_{21} + L_{22} \vec{E}_{22} \vec{u}_{22} + L_3 \vec{E}_3 \vec{u}_3 + L_{41} \vec{E}_{41} \vec{u}_{41} + L_{42} \vec{E}_{42} \vec{u}_{42} \quad (3)$$

where $\vec{u}_j, \vec{E}_j$ y $\vec{L}_j$ are respectively the unitary vector, the electrical field and the length of segment j -see figure 2-

Notice that the fields $\vec{E}_1, \vec{E}_{21}, \vec{E}_3$ y $\vec{E}_{42}$ are defined on the middle points of the segments that define the contour surrounding the surface S (points represented with crosses in figure 2). These fields are updated at every time step using CFDTD equations and they are always known. In equation (3) $\vec{E}_{22}$ y $\vec{E}_{41}$ are still left to define (points represented by circles in the figure).

In the segment l_{22}, $\vec{E}_{22}$ is determined from $\vec{E}$ in l21, enforcing continuity if the tangential electric field across the material boundary.

Using as a reference figure 3, the point P represents the point where segment l_{21} intersects the geometry. Using geometric algorithms, it is possible to obtain in P the unitary tangential and normal vector (called $\vec{n}$ y $\vec{t}$) and decompose $\vec{E}_{21}$ is terms of those vectors:

$$\vec{E}_{21} = (\vec{E}_{21}\vec{t})\,\vec{t} + (\vec{E}_{21}\vec{n})\,\vec{n} \quad (4)$$

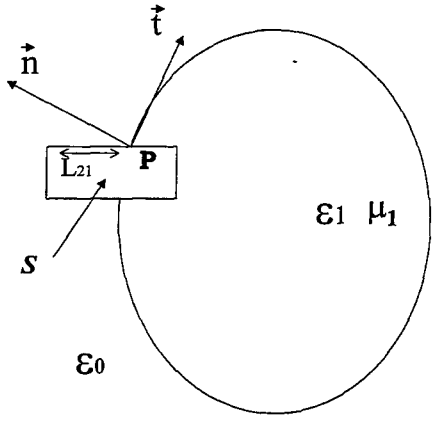


Figure 3.- Characterization of a trimmed contour

From (4), $\vec{E}_{21}$ is splitting into its normal and its tangential components with respect to point P. Enforcing the boundary conditions (continuity of tangential components and discontinuity of normal components) $\vec{E}_{22}$ is expressed as:

$$\vec{E}_{22}=\left(\vec{E}_{21}\,\vec{t}\right)\vec{t}+\left(\left(\frac{\varepsilon_1}{\varepsilon_0}\right)\vec{E}_{21}\,\vec{n}\right)\vec{n} \tag{5}$$

where ε_0 is the permittivity of free space (because it is assumed the body surrounded by air).

Similarly, $\vec{E}_{41}$ is obtained from $\vec{E}_{42}$.

$$\vec{E}_{41}=\left(\vec{E}_{42}\,\vec{t}\right)\vec{t}+\left[\left(\frac{\varepsilon_1}{\varepsilon_0}\right)\vec{E}_{42}\,\vec{n}\right]\vec{n} \tag{6}$$

The above formulation has to do with the development of the right term in (2) – that is to say, the circulation of $\vec{E}$ along contour C_1-. Next, the left term will be considered – variation of flux of vector $\vec{B}$ through surface S (see figure 1) that we rewrite in order to clarity:

$$\frac{-\partial \int_S \vec{B}\vec{ds}}{\partial t} \tag{7}$$

Considering that B=μH, assuming that $\vec{H}$ is constant in S and averaging the value of μ in S; the value of $\vec{H}_z$ component, is updated as follows

$$H_z^{n+\frac{1}{2}} = H_z^{n-\frac{1}{2}} - \frac{\Delta t}{\overline{\mu}} \oint_{C1} \vec{E}\,\vec{dl} \tag{8}$$

where $\overline{\mu}$ is defined as:

$$\overline{\mu} = \int_S \mu\, ds \tag{9}$$

and Δt is the time step.

In a similar way, we can derive finite-difference expressions for the $\vec{H}y$ and $\vec{H}_X$ field components and the 3 components of E.

RESULTS

Bistatic RCS values of a perfectly conducting sphere of radio 0.03819 with ka=2.3 is shown in figure 4. The result is compared with the MM formulation of [6]. Each quadrant of hemisphere is modeled using only one NURBS surface; therefore eight NURBS surfaces are needed to conform the geometry. The sphere is illuminated by a theta-polarized plane wave that is incident in the way indicated in the sketch of figure 4.

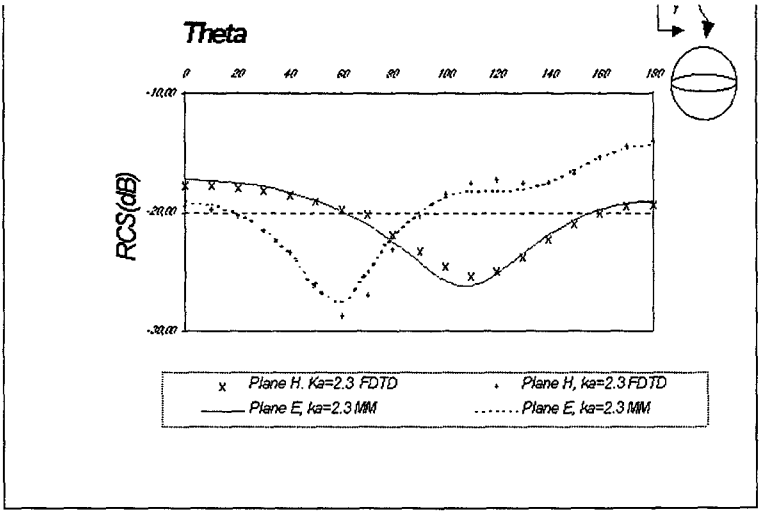


Figure 4.- RCS of a conducting sphere with ka=2.3

The behavior of arbitrary media is tested with a dielectric sphere with ε_r=5. The incidence is the same that of the previous case. Bistatic RCS for E and H planes is presented. Once again, there is very good agreement between the present formulation and those of those of [8]

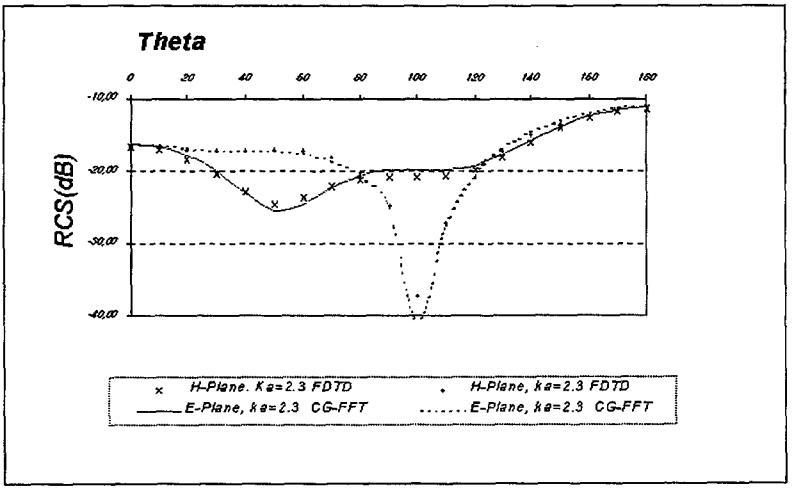


Figure 5.- Bistatic RCS of a dielectric sphere with ε_r=5

Conclusions

A FDTD approach to the analysis of complex tree-dimensional arbitrary conducting and material bodies has been presented. The geometry of the body is modeled by NURBS surfaces, which is and advanced geometrical tool. For material bodies, the CFDTD formulation is

improved by considering the discontinuity of field components crossing the medium-air interface.

References.

[1] Dey bistatic bistatic S. , Mittra R. "A Locally Conformal Finite Difference Time Domain (FDTD) Algorithm for modelling Three-Dimensional Perfectly Conducting Objects. *IEEE Microwave and Guided Letters*, Vol 7 n° 9 pp 273-275

[2] Dey S. , Mittra R. "A locally conformal Finite Difference Time Domain Technique for modelling arbitrary shaped bodies". *IEEE AP-S International Symposium*, 1998 pp 584-589.

[3] G. Farin. "Curves and Surfaces for Computer Aided Geometric Design: A practical Guide". *Academic Press*, 1988.

[4] J. Pérez,, M.F. Cátedra, "Application of Phisical Optics to the RCS Computation of Bodies Modeled with NURBS surfaces". *IEEE Trans. Antennas and Propagat*, vol. AP-42, no. 10, pp. 1401-1411.

[5] M. Domingo, F. Rivas, J. Pérez, R.P. Torres, M.F. Cátedra. "Computation of the RCS of Complex Bodies Modeled using NURBS surfaces". *IEEE Magazine, Antennas Propagat.* Vol. 37, no. 6, pp-36-47, Dec. 1995.

[6] L. Valle, F. Rivas, M.F. Cátedra. "Combining the Moment Method with Geometrical Modelling by NURBS surfaces and Bezier Patches". *IEEE Trans. Antennas and Propagation.* Vol 42, no3, pp 373-381, Mar. 1994.

[7] Gednet, S.D. "An anisotropic perfectly matched layer absorbing media for the truncation of FDTD lattices", *IEEE Trans. Antennas and Propagation*, Vol 44, 1996 pp.1630-1639.

[8] Luebbers, R.J.,K. S. Kunz,, m. Schneider, F.Hunsberger "A finite-difference time-domain near zone to far zone transformation", *IEEE Trans. Antennas and Propagation*, Vol 39, 1991 pp. 429- 433.

[9] Yee, K. S. "Numerical solution of initial boundary value problems involving Maxwell's equations in sotropic media". *IEEE Trans. Antennas and Propagation*, Vol 14, 1966 pp. 302-307.

[10] M. F. Cátedra, E. Gago, L, Nuño. " A numerical Scheme to obtain the RCS of Three-dimensional bodies of resonant size using the conjugate gradient method and the fast Fourier transform". *IEEE Trans. Antennas and Propagation,* May 1989, pp. 528-537.

SESSION 17

HYBRID TECHNIQUES

Chairs: Agostino Monorchio and P.H. Pathak

A Three-Dimensional Hybrid Technique for Combining the Finite Element and Finite Difference Methods in Time Domain

Agostino Monorchio[1] and Raj Mittra[2]

[1] Department of Information Engineering, University of Pisa, Pisa, Italy
via Diotisalvi 2, I-56126 Pisa, Italy.
E-mail: mono@iet.unipi.it

[2] Electromagnetic Communication Laboratory, Pennsylvania State University,
319 Electrical Engineering East, University Park, PA 16802.
E-mail: rxm53@psu.edu

Abstract- A hybrid, three-dimensional Finite Element/Finite Difference Time Domain (FE/FDTD) technique for solving complex electromagnetic problems is presented in this paper. The method combines the computational simplicity of the structured FDTD scheme with the versatility as well as flexibility of the Finite Element method, and enables us to accurately model curved geometries without resorting to staircasing. In the scheme presented herein, the interfacing between the FE and FDTD algorithm is accomplished without the use of any overlapping in the transition region between the corresponding meshes. Preliminary numerical results that illustrate the accuracy of the method are included in the paper.

I. INTRODUCTION

It is well known that the staircasing approach employed in the conventional Finite Difference Time Domain (FDTD) method can introduce significant errors in the field solution when modeling curved geometries. In contrast, the Finite Element method (FEM) method is well suited for handling complex geometries as it employs an unstructured mesh that conforms to these geometries. Moreover, the weak form based on the Faedo-Galerkin formulation provides a very natural way for handling the field and flux continuity conditions at the material interfaces, and yields accurate results that can be further improved by using higher-order interpolating functions [1]. However unlike the FDTD, the the FEM requires the solution of a matrix equation with a number of unknowns that can be fairly large, especially when the tetrahedral elements are used. Even when a skyline band or a non-zero value storage is employed in conjunction with a sparse matrix solver, the solution of the system matrix can become an excessive burden on the CPU time. This attribute of FEM is especially inconvenient in its

time domain application, where a matrix solution is needed at each iteration step [2-3] in time. In contrast, the FDTD requires no matrix inversion and, hence, is numerically efficient.

In this paper, we present a hybrid numerical techniques that combines the above two methods in a manner that retains the advantages of both. In particular, the FE is used only in regions with curved surfaces and high degree of inhomogeneities; thus its computational burden is kept low. The balance of the computational domain is analyzed via the FDTD, fully exploiting its numerical efficiency. A similar technique has already been presented in recent literature for the 2-D case in [4], and extended to the 3-D case in [5]. However, the hybridization of the FDTD and FEM schemes in [4] and [5] requires the knowledge of the electric fields at two different locations in the overlapping region, where the two boundaries (exterior and secondary) are defined. Experience shows that the use of such an overlapping region can introduce some difficulties in the mesh generation procedure. A different approach has been followed in [6] that circumvents this problem, where the interlacing between the FDTD and FEM is realized by using an interpolation scheme in the interface region. However, the two regions still partially overlap in this case, even though they do not need to be interlaced as in [4] and [5]. Additionally, the analysis presented in [6] is restricted to the use of prism elements in the FEM procedure. In contrast to the above-mentioned works, the method presented herein, which is based upon the technique presented earlier in [7] and [8] for two-dimensional problems, does not employ an overlapping region, and enables one to fully exploit the capabilities of modern mesh generators utilizing general elements. Indeed, the hybridization of the FDTD and FEM schemes is realized by using the electric field only at a single location on the interface, thus circumventing the need for an overlapping region between the FDTD and FEM domains. The main contribution of this paper is to present the three-dimensional extension of the technique described in [7], and to illustrate its application via some numerical examples.

II. FORMULATION

We begin by dividing D, the computational domain, into two sub-domains D_{FD} and D_{FE}, corresponding to the FDTD and FE regions, respectively, such that $D = D_{FD} \cup D_{FE}$. Next, we mesh these two regions by using structured and tetrahedral meshes, respectively, with common nodes shared at the interface but with no overlapping ($D_{FD} \cap D_{FE} = \varnothing$). The unstructured grid is confined to the vicinity of the irregular region of the domain, and this allows us to limit the number of unknowns in the FE region to a moderate size.

The FDTD solution in D_{FD} is conventional in nature and, hence, requires no further discussion. In D_{FE}, an FE formulation with curl-conforming vector edge basis functions is employed in the time domain to discretize the second-order vector wave equation.

The specific FE-TD formulation adopted herein relies on the discretization of the second-order vector wave equation with appropriate boundary conditions. The solution for the electric field is considered in a volume Ω [3]:

$$\nabla\times\frac{1}{\mu}\nabla\times\vec{E}+\sigma\frac{\partial\vec{E}}{\partial t}+\varepsilon\frac{\partial^2\vec{E}}{\partial t^2}=-\frac{\partial\vec{J}}{\partial t}, \tag{1}$$

where μ, ε and σ are the permeability, permittivity and conductivity of the medium, respectively. Next, the fields are expanded by using the edge elements and a Galerkin testing procedure is employed. This enables us to numerically express the above equation as:

$$\varepsilon\,\underline{\underline{A}}\frac{\partial^2\underline{e}}{\partial t^2}+\sigma\,\underline{\underline{A}}\frac{\partial\underline{e}}{\partial t}+\frac{1}{\mu}\underline{\underline{B}}\,\underline{e}=-\underline{\underline{A}}\frac{\partial\underline{j}}{\partial t} \tag{2}$$

where $A_{ij}=\int_{\Omega}\vec{W}_i\cdot\vec{W}_j\,d\Omega$ and $B_{ij}=\int_{\Omega}\nabla\times\vec{W}_i\cdot\nabla\times\vec{W}_j\,d\Omega$, and $\vec{W}_i$ are the edge vector basis functions used for expanding the field, though it is possible to employ other basis functions as well. Specifically, curl-conforming vector edge basis functions [2] have been utilized in the present work. Their expression in simplex coordinates reads: $\vec{W}_i=\left(\xi_j\nabla\xi_k-\xi_k\nabla\xi_j\right)$, $i=1,2,3,4$, where $\vec{W}_i$ is the basis function pertaining to the i-th edge delimited by nodes j and k. Assuming $j<k$, the above functions constitute six vector basis functions that have zero divergence and constant curl.

By resorting to a mixed central and backward difference scheme for the derivatives with respect to time, (2) can be transformed into a *marching-on-in-time* algorithm as follows:

$$\underline{e}^{n+1}=\underline{\underline{M}}^{-1}\left(\underline{\underline{N}}\,\underline{e}^{n}+\underline{\underline{P}}\,\underline{e}^{n-1}+\underline{f}^{n}\right), \tag{3}$$

where

$$\underline{\underline{M}}=\left[\frac{\varepsilon}{\Delta T^2}+\frac{(\Theta_1+1/2)\sigma}{\Delta T}\right]\underline{\underline{A}}+(\Theta_1+2\Theta_2)\frac{1}{\mu}\underline{\underline{B}}, \tag{4a}$$

$$\underline{\underline{N}}=\left[\frac{2\varepsilon}{\Delta T^2}+\frac{4\Theta_1\sigma}{\Delta T}\right]\underline{\underline{A}}+\frac{4\Theta_2-1}{\mu}\underline{\underline{B}}, \tag{4b}$$

$$\underline{\underline{P}}=\left[-\frac{\varepsilon}{\Delta T^2}-\frac{(\Theta_1-1/2)\sigma}{\Delta T}\right]\underline{\underline{A}}-\frac{(2\Theta_2-\Theta_1)}{\mu}\underline{\underline{B}}, \tag{4c}$$

$\underline{e}^{n}$ denotes the unknowns vector at time step n, and $\underline{f}^{n}$ is the vector expansion coefficients for the current density $\underline{j}$. With a proper choice of the two stability parameters Θ_1 and Θ_2, this scheme is unconditionally stable; in particular, for $\Theta_1\geq 0$ and $\Theta_2\geq 1/8$ the results are stable [3] regardless of the choice of the time step. It is especially crucial to employ an unconditionally-stable time domain formulation for the FEM algorithm in problems with very small features that lead to large variations in the element size across the problem domain. This enables us to employ a time step which is identical to that dictated by the Courant condition in the FDTD domain, and which is typically much larger than the corresponding one in the FE domain. An added advantage of this hybrid method is that, unlike the classical subgridding techniques in FDTD, the present approach requires no interpolation in the time domain.

III. TIME-MARCHING SCHEME

Next, we turn to the time marching scheme that has been implemented in our algorithm. Let $H_{BD}^{n-1/2}$ be a generic component of the magnetic field close to the interface between the FDTD and FE regions in D_{FD}, at a generic time step t^n, while $H_{BE}^{n-1/2}$ is the adjacent magnetic field located in the D_{FE} domain (see Fig. 1a). The electric field component E_B^n can be evaluated in accordance with the FDTD algorithm, provided that the location of $H_{BE}^{n-1/2}$ coincides with that of the magnetic field in a fully-structured grid. We address this problem by first identifying the tetrahedral element in the FE region which contains the point location of the desired $H_{BE}^{n-1/2}$, and then evaluating it exactly from the knowledge of the electric fields in the element. It is important to point out that, in the most general case, the tetrahedral element is different for each component due to the staggered location of the magnetic field components. Indeed, this is crucial for the implementing the hybrid procedure in a correct manner.

In the following, we illustrate the computation of the magnetic field from the knowledge of the corresponding electric field values at the edges. In particular, if we expand the electric field over the 4 edges of a tetrahedral element in the FEM domain, we can write

$$\vec{E}(\vec{r}_k,t)=\sum_{j=1}^{4} e_j(t)\vec{W}_j(\vec{r}_k); \tag{5}$$

where $\vec{r}_k$ is a generic position located within the element k; the corresponding magnetic field is obtained by discretizing the relationship:

$$\vec{H}(\vec{r},t)=-\frac{1}{\mu}\int_t \nabla\times\vec{E}(\vec{r},t)dt, \tag{6}$$

which leads to the recursive formula:

$$\vec{H}_k^{n+1/2}=-\frac{1}{\mu}\sum_{n=1}^{N_t}\sum_{j=1}^{4} e_j^n\,\nabla\times\vec{W}_j\Delta T=\left(-\frac{1}{\mu}\sum_{j=1}^{4} e_j^n\,\nabla\times\vec{W}_j\Delta T\right)+\vec{H}_k^{n-1/2}. \tag{7}$$

In (7), the index n refers to the temporal discretization. We note that the edge elements have the property that $\nabla\times\vec{W}_j$ is constant, implying that the magnetic field is constant within a generic tetrahedron.

Let us now go on to describe the time-marching scheme. We begin by updating all of the electric fields $\vec{E}_{FD}^n$ in the region D_{FD} in accordance with the FDTD algorithm, using the values of the magnetic fields $\vec{H}_{FD}^{n-1/2}$ in the region D_{FD} together with the magnetic fields $\vec{H}_{BE}^{n-1/2}$ at the interface. All of the magnetic fields $\vec{H}_{FD}^{n+1/2}$ in the region D_{FD} can next be evaluated from $\vec{E}_{FD}^n$. The electric field $\vec{E}_B^n$ along the interface between D_{FD} and D_{FE} is used as a boundary condition (initial value in time, boundary value in space) for the FE procedure. We note that, at this stage, we also need the electric field at the edge not coincident with the FDTD grid (see Fig. 1b); this can be

computed by using a simple linear interpolation between the values at the sides. Once these boundary conditions are fully specified, the electric field $\vec{E}_{FE}^{n}$ at the time step t^n can be evaluated throughout the region D_{FE}. The procedure can now be repeated to continue the time iteration.

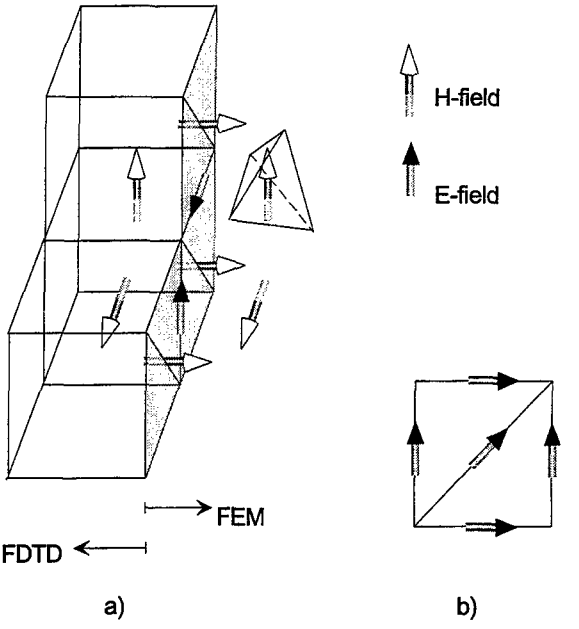


Fig. 1 – Interfacing the FEM and the FDTD regions.

IV. NUMERICAL RESULTS

We will now present some numerical results to validate the hybrid technique. Specifically, we examine the problem of scattering from a PEC cube 60 *cm* on a side, illuminated by a dipole source located at a distance of 80 *cm* from one of its faces and oriented along the *z*-direction of a cartesian coordinate system (Fig.2a). The results obtained from an "FDTD-only" scheme are compared with those derived for the same problem by employing an FEM region within the computational domain. The FDTD computational domain comprises 50×50×50 cubic cells, 10 *cm* on a side, and uses second order Absorbing Boundary Conditions (ABC). For testing the hybrid technique, an FEM region $1m \times 1m \times 1m$ containing the PEC cube has been embedded in the FDTD computational domain. The region between the cube and the FDTD domain has been meshed by using 3141 tetrahedral elements

with 5829 edges, which include1800 boundary edges and 600 PEC edges. In both of these cases, the time step was $\Delta T = 1.8 \cdot 10^{-10}$ *sec*, and the FE stability parameters were chosen to be $\Theta_1 = 0.2$ and $\Theta_2 = 0.3$. The dipole source radiates a gaussian pulse with a –3dB frequency equal to 150 MHz. In Fig. 2b, we plot the *y*-component of the electric field observed at a distance of 80 *cm* below the cube, computed with the two methods alluded to above. Excellent agreement between the two results serves to adequately validate the accuracy of the hybrid scheme presented in this paper. Before closing we mention that satisfactory results also have been obtained for different observation points and for all of the components of the electric and magnetic fields. Additional tests performed on problems with different geometrical and electrical parameters have further confirmed the accuracy of the procedure.

V. CONCLUSIONS

A three-dimensional hybrid technique for combining the Finite Element and Finite Difference methods in time domain has been presented. The hybridization between the two algorithms has been achieved without the use of any overlapping or transition region. This not only enables us to take full advantage of modern mesh generators, but also renders the technique flexible as well as accurate for solving complex electromagnetic problems.

REFERENCES

[1] P. P. Silvester and R. L. Ferrari, *Finite Elements for electrical engineers*, Cambridge University Press, 1983.

[2] K. Mahadevan and R. Mittra, "Use of Whitney's edge and face elements for efficient finite element time domain solution of Maxwell's equations", *J. of Electromag. Waves and Applicat.*, Vol. 8, No. 9/10, pp. 1173-1191, 1994.

[3] J.-F. Lee, R. Lee and A. Cangellaris, "Time-Domain Finite-Element Methods", *IEEE Trans. on Antennas and Propagat.*, vol. 45, no. 3, pp. 430-441, March 1997.

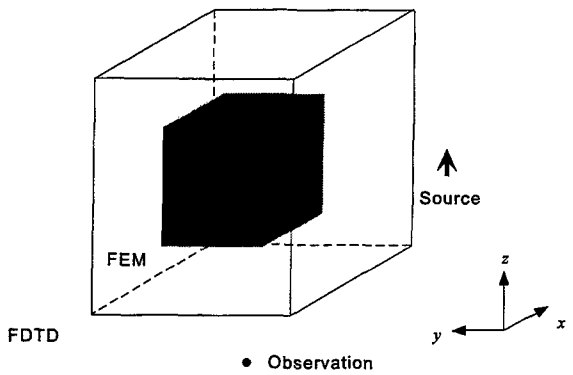
[4] R-B. Wu and T. Itoh, "Hybridizing FD-TD analysis with unconditionally stable FEM for objects of curved boundary," *IEEE MTT-Symposium Digest*, pp. 833-836, May 1995.

[5] R-B. Wu and T. Itoh, "Hybrid finite-difference time-domain modeling of curved surfaces using tetrahedral edge elements" *IEEE Trans. on Antennas and Propagat.*, vol. 45, n.8, pp. 1302-1309, Aug. 1997.

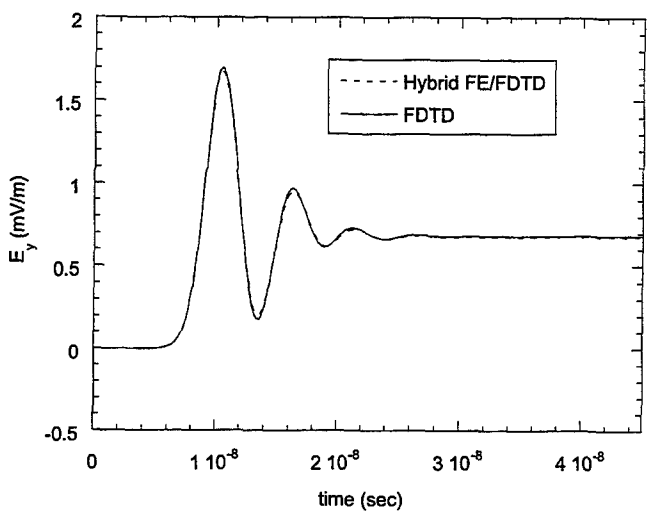
[6] D: Koh, H.-b. Lee and T. Itoh, "A Hybrid Full-Wave Analysis of Via-Hole Grounds Using Finite-Difference and Finite-Element Time-Domain Methods," *IEEE Trans. on Microwave Theory and Techniques*, vol. 45, no. 12, Dec. 1997.

[7] A. Monorchio and R. Mittra, "A Hybrid Finite-Element/Finite-Difference Time-Domain (FE/FDTD) Technique for Solving Complex Electromagnetic Problems," *IEEE Microwave and Guided Waves Letters,* vol. 8, no. 2, pp. 93-95, Feb. 1998.

[8] A. Monorchio and R. Mittra, "A Novel Subgridding Scheme Based on a Combination of the Finite Element and Finite Difference Time Domain Methods," *IEEE Trans. on Antennas and Propagation,* vol. AP-46, no. 9, pp. 1391-1392, Sept. 1998.



a)



b)

Fig. 2 – a) Geometry of the problem; b) E_y component at the observation point computed by using a fully FDTD scheme (continuous line) and the present hybrid technique (dashed line).

Vertical Antenna Near-Field Computation in Complex Environments by a Hybrid Method

F. Bardati[(1)], E. Di Giampaolo[(2)], A. Durantini [(1)], G. Marrocco[(1)],

(1) DISP, University of Rome Tor Vergata, Via di Tor Vergata 110, 00133 Roma (Italy)
(2) DIE, University of L'Aquila, Monteluco, 67100 L'Aquila (Italy)

Abstract – **Evaluation of the electromagnetic field radiated by base station antennas in complex surroundings requires the development of hybrid methods joining local and asymptotic techniques. In the proposed method, geometrical optics rays are traced from a suitably defined quasi-constant-phase surface located in the near field region of a vertical antenna where the usual far-field approximation fails. Such a near-field wave front is determined by processing near field data, which are obtained by a conventional analysis of the field radiated by a stand-alone antenna. Results of a preliminary application of the method to a planar array of elementary dipoles are reported showing the practicability of the method.**

I. INTRODUCTION

Base station antennas for mobile communications are normally installed in complex environments including walls, buildings, pylons and humans. Environmental effects on electromagnetic propagation must be taken into account to comply with coverage requirements and exposition restrictions of people and things. To this purpose an accurate and efficient numerical prediction of electromagnetic near field is desirable. Ordinary local algorithms, based on Method of Moments, Finite-Difference Time-Domain or Finite Elements, although very accurate in the detailed modelling of stand-alone antennas, fail in modelling electrically large environments. On the contrary, high frequency methods, based on ray tracing including edge diffraction, are fast and robust in modelling electromagnetic propagation and interactions with scatterers, but they are accurate only if the scatterer is large in terms of wavelength and does not exhibit small features. Recently hybrid procedures were presented which employ local methods for the antenna and asymptotic methods for the environment. In [1] the FDTD method was applied to model a bounded region including dielectric bodies while the field interaction in the external region with large conducting bodies was modelled by a generalised ray expansion. The interface between the ray region and the FDTD region was defined by means of equivalent surface sources. In [2] a moving frame procedure was proposed, where an asymptotic technique was used for wave packet propagation while interactions of each wave packet with environmental scatterers were FDTD modelled. In [3] a hybrid procedure takes advantage from ray tracing to build a modified Green function accounting for the antenna complex environment. The antenna radiation pattern is then obtained solving a Boundary Element or Finite Element problem. In the last method, changing the antenna position with respect to the environment requires a complete new simulation to be restarted.

In this paper we present a preliminary investigation on a hybrid procedure for direct

application of ray tracing methods to the antenna near field. The method works as follows. First a "near field wave front" is obtained close to the antenna by retrieving a quasi-constant-phase (QCP) surface. Then the wave front is partitioned according to a polyhedral mesh and astigmatic ray beams are launched and traced in the environment [4]. The retrieval of a QCP surface for the antenna near field is a non-linear problem, which can be computationally expensive for real antennas. Therefore the antenna stand-alone near-field, that is obtained once and for all by means of a numerical simulation with a local method (or even by measurements), is sampled and efficiently interpolated on a surface enclosing the antenna. Since the antennas of radio-base stations have generally vertical structure, a vertical circular cylinder is adopted as the enclosing surface, from which the field is propagated as a superposition of cylindrical waves for the computation of QCP surfaces. (Fig.1). Under the hypothesis that the antenna field is not modified by the environment, which is acceptable for the computation of exposition volumes, ray-tracing only has to be repeated for any antenna location with respect to the environment. The procedure to obtain the near-field wave front will be presented in the next sections, while the integration with an efficient ray-tracer will be the subject of future work.

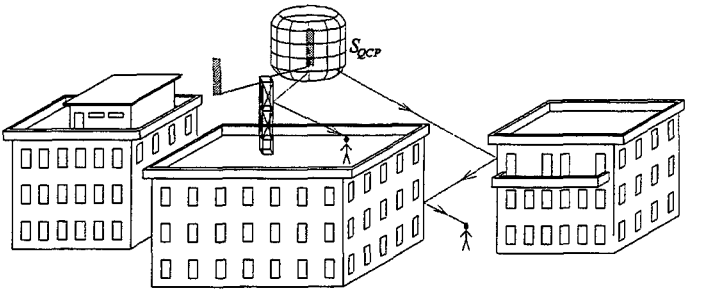


Fig. 1: Schematic view of the hybrid procedure: A wave front S_{QCP} is retrieved from near field data close to the antenna. Ray tracing is performed outside S_{QCP}.

II. METHOD

A vertical antenna, with the main size in the z-direction, is placed at the origin of a cylindrical co-ordinate system (ρ,ϕ,z). Consider the electromagnetic field radiated by the stand-alone antenna and an unbounded cylinder S_0 having radius R_0, axis z and enclosing the antenna. The field can be obtained at a discrete set of points $\{P_i\}_{i=1}^{N}$ belonging to S_0 by means of a numerical procedure (or by measurements).

The field outside S_0, can be expressed as superposition of elementary inhomogeneous cylindrical waves [5]:

$$\psi_m = e^{-jm\phi} H_m^{(2)}(\kappa\rho) e^{-jz\beta} \tag{1}$$

with $H_m^{(2)}$ the Hankel function of second kind and order m, $\kappa = \sqrt{k_0^2 - \beta^2}$, $\mathrm{Im}[\kappa] < 0$, $k_0 = 2\pi/\lambda$ (λ is wavelength), β is longitudinal wave number. The resulting representation splits into TM and TE waves. TM equations are:

$$E_\rho = -j\beta \sum_{m=-\infty}^{\infty} a_m^{TM} \frac{d\psi_m}{d\rho}$$
$$E_\phi = -\frac{\beta}{\rho} \sum_{m=-\infty}^{\infty} a_m^{TM} m\psi_m \qquad H = Y_0 \hat{z} \times \underline{E} \qquad (2)$$
$$E_z = (k_0^2 - \beta^2) \sum_{m=-\infty}^{\infty} a_m^{TM} m\psi_m$$

where $Y_0 = \omega\varepsilon/\beta$. Dual equations can be derived for TE waves with $\underline{E} = Z_0 \underline{H} \times \hat{z}$, $Z_0 = \omega\mu/\beta$. For a given radiation field, the coefficients a_m^{TM} and a_m^{TE} are functions of β. Coefficients a_m^{TM} and a_m^{TE} can be retrieved from the field evaluations at $\{P_i \equiv (R_0, \phi_i, z_i)\}_{i=1}^N$. In fact we have for $E_{z,i} = E_z(R_0, \phi_i, z_i)$:

$$E_{z,i} = \sum_m m e^{-jm\phi_i} \left(\frac{1}{2\pi} \int_{-\infty}^{+\infty} a_m^{TM} (k_0^2 - \beta^2) H_m^{(2)} (R_0 \sqrt{k_0^2 - \beta^2}) e^{-jz_i\beta} d\beta\right) \qquad (3)$$

while a similar equation holds for $H_{z,i} = H_z(R_0, \phi_i, z_i)$ from which coefficients a_m^{TE} are determined.

A wave front is normally defined as a constant-phase surface in the antenna far field, where all the field components have the same phase function, moreover $\underline{E}$, $\underline{H}$ and the normal, $\hat{n}$, to the wave front are mutually orthogonal. Nevertheless it is possible to define a quasi-constant-phase surface in the antenna near field if the above conditions are not strictly enforced. This surface can be computed according to the following iterative procedure:

1) Starting from a radial distance $R_1 \geq R_0$, a constant-phase surface S_{QCP} for the dominant field component (H_ϕ for vertical, z-directed antennas) is carried out via a search procedure on z-slices. H_ϕ is computed by equations (2). S_{QCP} is obtained as stacked constant-phase lines.
2) The Poynting vector $\underline{S}_R + j\underline{S}_I$ is computed at points of S_{QCP}. Then two tests are performed: (i) $|\underline{S}_I|/|\underline{S}_R| < \varepsilon_1$; (ii) $\cos^{-1}(\hat{n} \cdot \underline{S}_R/|\underline{S}_R|) < \varepsilon_2$, where ε_1 and ε_2 are positive small numbers. These tests are repeated for a sufficiently dense grid of points on S_{QCP}.
3) If the tests are passed then S_{QCP} is considered as a quasi wave front surface. Otherwise, the initial distance is increased: $R_1 \to R_1 + \Delta\rho$ and the procedure restarts.

A particular field interpolation on the cylinder S_0 proved to be useful to solve for a_m^{TM} by equation (3). Though the electromagnetic field exists all over S_0, nevertheless it is expected to be substantially localised within a cylindrical waist of S_0 centred on $z=0$. Therefore each electromagnetic-field component, e.g. E_z, is expanded on a Hermite polynomial basis [6,7,8] accounting for z- dependence as follows:

$$E_z(R_0,\phi,z)=\sum_{m=-\infty}^{\infty}\sum_{n=0}^{\infty}A_{mn}h_n(z)e^{-jm\phi} \tag{4}$$

with:

$$h_n(z)=e^{-\frac{c^2z^2}{2}}\frac{H_n(cz)}{(\sqrt{\pi}2^n n!)^{1/2}} \tag{5}$$

$H_n(cz)$ is the scaled Hermite polynomial of order n, and c is a scaling factor. The set $\{h_n\}$ constitutes a complete orthonormal basis, defined on the whole real axis z, which provides a compact support, around $z=0$, controlled by the scaling factor. A further property of functions h_n (also called associate Hermite functions) is used for solving equation (3), i.e., the Fourier transform of h_n also is an associate Hermite function. The set $\{A_{mn}\}$ constitutes the spectrum of H_ϕ with respect to the chosen basis. The summations in equation (4) are truncated to M and N, respectively, for numerical computation.

III. NUMERICAL EXAMPLE

To test the method we considered a curtain array of 8×2 elements, with $\lambda/4$ horizontal spacing and $\lambda/2$ vertical spacing. Infinitesimal electrical dipoles of unitary moment $I\ell$ oriented along the z-axis (Fig. 2a) were used.

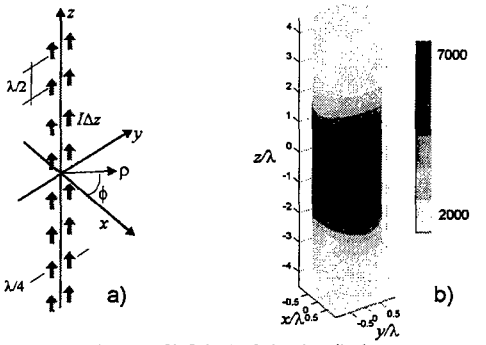


Fig.2: a) curtain array of infinitesimal electrical dipoles;
b) $|E_z|$ on cylinder $\rho = R_0 = \lambda$, for $I\ell = 1$.

This geometry is quite similar to that of standard antennas for mobile-communication base-stations, with the electrical dipoles replaced by half-wavelength wire radiators. Since the overall length of the reference antenna is $D=3.5\lambda$, the conventional far-field transition distance from the antenna is $2D^2/\lambda = 24.5\lambda$. This antenna radiates a TM field since H_z is zero everywhere. The

spectrum A_{mn} was obtained from closed-form computations of E_z at points of a cylinder S_0 with radius $R_0 = \lambda$ (Fig. 2b). Only a few spectral terms were necessary to obtain an accurate field representation for $\rho \geq R_0$. As an example, the reconstruction of H_ϕ by M=6 and N=9 terms is shown in Fig. 3 for comparison with the exact results.

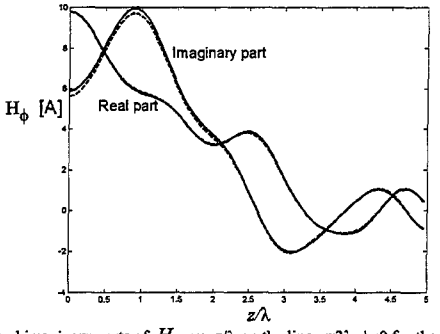


Fig. 3: Real and imaginary parts of H_ϕ vs. z/λ on the line ρ=3λ, ϕ=0 for the array in Fig. 2: Exact solution (dashed line) and numerical solution (continuos line).

An example of QCP surface, computed by the iterative procedure with initial distance $R_1 = 3\lambda$, is shown in Fig. 4a. This surface exhibits a nearly cylindrical cross-section in the central region, where the Poynting vector takes larger values. Surface normal and Poynting vector real-part direction are superimposed at points of the QCP surface in Fig. 4b. A substantial parallelism can be appreciated from the diagram, except for larger values of *z*, which, however, provide less contribution to the overall radiation.

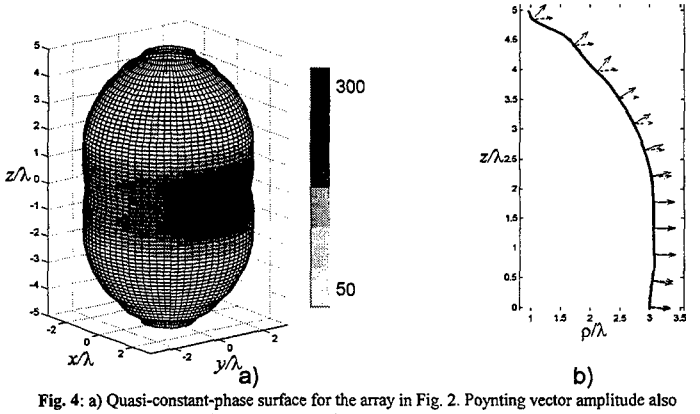


Fig. 4: a) Quasi-constant-phase surface for the array in Fig. 2. Poynting vector amplitude also shown. b) Cut ϕ=0 showing surface normal (continuous line) and Poynting vector real part direction (dashed)

IV. CONCLUSION

The radiation-field computation problem for a vertical antenna in the presence of scatterers in the antenna near field has been considered. The results of a preliminary investigation on a hybrid procedure have been presented, that is based on a ray-tracing interface with field data for stand-alone antennas. Ray tracing is started from a near-field wave front close to the antenna. Therefore the problem addressed by this paper was that of finding a quasi-constant-phase surface in a region close to the antenna, where the usual conditions for the validity of ray optics are only partially met. Initially the field is computed on a vertical cylinder enclosing the antenna by a suitable method (e.g., method-of-moments) to account for antenna geometrical and physical characteristics. The propagation outside the cylinder is modelled as the sum of cylindrical waves, whose coefficients are retrieved by enforcing the continuity to the stand-alone antenna field at a set of points of the cylinder. The formulation takes advantage from field data interpolation on a basis of Hermite polynomials. A preliminary application to a simple curtain array has shown that ray tracing can be applied from a 3λ distance onwards.

REFERENCES

[1] R.Lee, "Analysis of electromagnetic scattering from a cavity with a complex Termination by means of a Hybrid Ray-FDTD Method", IEEE *Trans. Antennas Propagat.* Vol. 41, pp. 1560- 1569, 1993

[2] B. Fidel, E. Heyman, R. Kastner, "Hybrid Ray-FDTD moving frame approach to pulse propagation", *IEEE Antennas Propagat. Symposium*, Vol.3, pp.1414-1417, Seattle 1994

[3] M. Alaydrus, V. Hansen, "A hybrid method combining FE/BEM with the UTD for calculating the effects of real surroundings on antenna characteristics", proceedings of *European Wireless* pp.465-470, Munchen 1999

[4] E. Di Giampaolo, M. Sabbadini, F. Bardati, "An astigmatic beam model to be used in beam tracing", submitted to ACES 2000

[5] J.A.Stratton, "Teoria dell'elettromagnetismo", pp. 499-500, Einaudi 1952

[6] L.R. Lo Conte, R. Merletti, G.V. Sandri, "Hermite expansions of compact support waveforms: applications to myoelectric signals", *IEEE Trans. Biomed. Eng.*, Vol.41, pp.1147-1159, 1994

[7] E. Di Giampaolo, F. Bardati, "Near-field microwave radiometry by non-contacting antennas", *Atti della Fondazione G. Ronchi*, Anno LIV, N. 3-4, pp. 561-566, 1999.

[8] M.M. Rao, T.K. Sarkar, T. Anjali, R.S. Adve, "Simultaneous extrapolation in time and frequency domains using Hermite expansions", IEEE *Trans Antennas Propagat.* Vol. 47, pp.1108-1115, 1999

3-D EM Problem Modelling by Geometry Decomposition and Combination of the FE, FDTD and BIE Techniques

Hendrik Rogier* (IWT), Daniël De Zutter and Frank Olyslager (FWO-V).
Department of Information Technology (INTEC), University of Gent
St.-Pietersnieuwstraat 41, B-9000 Gent, Belgium
Tel: 32-9-264.3316 Fax: 32-9-3-264.3593
E-mail: hendrik.rogier@intec.rug.ac.be

Abstract— A hybrid approach that relies on the decomposition of the simulation geometry into a number of uniformly meshed subregions is proposed to model complex three-dimensional structures. The 3-D boundary integral technique is used for homogeneous bounded and unbounded regions. Each inhomogeneous subregion is either described at one frequency by a finite eliment method combined with a frontal elemination algorithm, or an interaction matrix is calculated at multiple frequencies using FDTD. The interaction matrices and the excitation vectors resulting from the three different techniques are assembled into one global matrix equation by expressing continuity of the tangential fields at all the interfaces between the subregions.

I. Introduction

With the drastic increase of the computer power, conventional numerical techniques such as the finite element (FE) method, the finite-difference time-domain technique (FDTD) and the boundary integral equation (BIE) approach have proven their use in versatile modeling of 3-D EM configurations. However, the applicability of the FE and FDTD method mostly lies in describing problems with an inhomogenous and bounded character, whereas the BIE technique is very efficient in handling unbounded structures composed of a limited number of homogeneous subdomains. This clearly suggests that new, more powerful formalisms can be found by decomposing the simulation geometry into different subregions and by describing each of them with the most efficient numerical approach for that domain. Up to now, the most popular of these hybrid methods has been the combination of finite elements with a boundary integral equation in the frequency domain.

Quite recently, we have developed a new formalism in which both the FE method and FDTD algorithm are combined with a BIE approach [1, 2]. The FE method or the FDTD technique then takes into account the inhomogeneous parts of the configuration whereas the BIE approach is used to rigorously model the open character of the structure and the interactions between the different subregions. In previous publications, much attention was devoted to the coupling of the FDTD formalism with a BIE formulation in the frequency-domain [3–5]. The technique allows to obtain a system matrix for a given inhomogeneous subregion within a certain frequency band, by performing a number of FDTD simulations. In this contribution, it will be shown how the FE formulation can also be efficiently incorporated into the hybrid formalism, by means of a frontal elimination technique. In [1, 2], this technique was applied to study the radiation of lossless structures. In this paper, lossy configurations and plane wave incidence are also considered.

II. Geometry decomposition

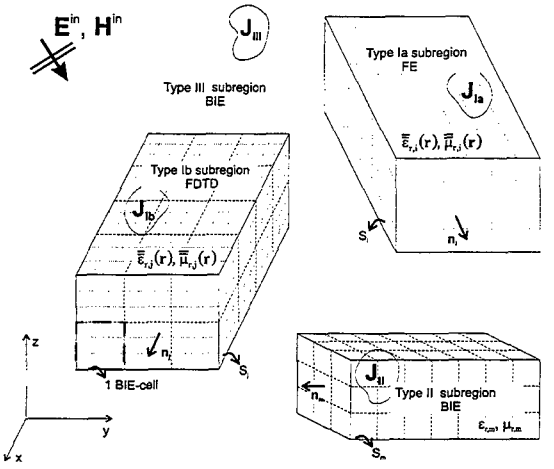


Fig. 1. Sample 3-D geometry with partitioning into subregions.

Consider a 3-D configuration consisting of scatterers and sources, schematically represented in Figure 1. Let us now assume that the simulation geometry can be decomposed into a number of subregions. The field equivalence theorem then allows a separate description of each subregion by introducing additional virtual sources $\mathbf{J}_{virt} = \hat{\mathbf{n}} \times \mathbf{H}$ and $\mathbf{M}_{virt} = \mathbf{E} \times \hat{\mathbf{n}}$ on the interfaces between the different subregions. These latter sources act as the problem's unknowns.

Such a partitioning scheme can considerably enhance the efficiency of the EM problem description. First of all, each subregion can be described with a different modelling strategy, specifically adapted to the particular EM features of that subdomain in the following way. For inhomogeneous and bounded subregions, one can chose between two numerical techniques: either one uses the FE method for the type Ia subregions or the FDTD algorithm for the type Ib subregions. For homogeneous bounded type II and unbounded type III subregions, a BIE formulation is applied. Current sources (schematically represented by the source regions $\mathbf{J}_I$, $\mathbf{J}_{II}$ and $\mathbf{J}_{III}$ in Figure 1) can be present in all the bounded subregions, and a plane wave can be incident from within the type III subregion. Second, the description of a particular subregion can be reused in the presence of several identical subregions within the configuration. This is typically the case when modelling frequency selective surfaces [3].

III. Hybrid FE-FDTD-BIE formulation

A. BIE formulation

Homogeneous bounded or unbounded regions are described by means of a BIE technique. Consider a type II subregion V_m, with virtual interface S_m between this subregion and the rest of the simulation geometry. We use the 3-D Poggio and Miller [6] integral expressions to find the electric and magnetic fields at the interface S_m due to the virtual sources on S_m:

$$\mathbf{E} = -j\mu_r \iiint_{V_m} G\mathbf{J}\, dV - \iint_{S_m} [\nabla G \times (\mathbf{E} \times \hat{\mathbf{n}}) + \nabla \cdot (\mathbf{H} \times \hat{\mathbf{n}}) \frac{\nabla G}{j\epsilon_r} + j\mu_r G(\mathbf{H} \times \hat{\mathbf{n}})]\, dS \quad (1)$$

$$\mathbf{H} = -\iiint_{V_m} \nabla G \times \mathbf{J}\, dV - \iint_{S_m} [\nabla G \times (\mathbf{H} \times \hat{\mathbf{n}}) - \nabla \cdot (\mathbf{E} \times \hat{\mathbf{n}}) \frac{\nabla G}{j\mu_r} - j\epsilon_r G(\mathbf{E} \times \hat{\mathbf{n}})]\, dS \quad (2)$$

with $G(\mathbf{r} \mid \mathbf{r}') = \frac{e^{-j\omega\sqrt{\mu\epsilon}|\mathbf{r}-\mathbf{r}'|}}{4\pi|\mathbf{r}-\mathbf{r}'|}$. Similar expressions hold for the type III subregion in Figure 1, involving virtual sources on interfaces S_i, S_j and S_m and with addition of an incident plane wave source contribution $\mathbf{E}^{\text{in}}$ and $\mathbf{H}^{\text{in}}$. Note that by using both tangential electric and magnetic field components in the formulation, the problem of interior resonances is avoided.

Since we will solve the global problem using a method of moments technique, it will be necessary to discretize the virtual boundaries S_i, S_j and S_m into a uniform mesh of rectangular cells and to represent the unknown virtual sources by rooftop basis functions $\mathbf{w}_r$:

$$\mathbf{E}(\mathbf{r}) = \sum_{r=1}^{N} E_r \mathbf{w}_r(\mathbf{r}), \quad \mathbf{H}(\mathbf{r}) = \sum_{r=1}^{N} H_r \mathbf{w}_r(\mathbf{r}), \quad \mathbf{r} \in S_i \cup S_j \cup S_m \tag{3}$$

To determine the set of unknown expansion coefficients (E_r, H_r), these same rooftop functions will be used to apply Galerkin weighting to the boundary integral expressions. For each type II and III subregion, the discretization process results in a matrix expression of the following form:

$$\begin{pmatrix} E_r \\ H_r \end{pmatrix} = \begin{pmatrix} E_r^{\text{in}} \\ H_r^{\text{in}} \end{pmatrix} + \overline{\overline{Z}}_{\text{BIE}} \cdot \begin{pmatrix} E_r \\ H_r \end{pmatrix} \tag{4}$$

It will now be shown how similar matrix expressions can be found for the inhomogenous subregions, either with an FE method or an FDTD formalism.

B. FE technique

Let us now focus on the inhomogeneous Type Ia subregion V_i with boundary S_i. The following Galerkin FE formulation is used to describe subregion V_i:

$$\begin{aligned} &\iiint_{V_i} (\nabla \times \mathbf{w}_r) \cdot \overline{\overline{\mu}}_r^{-1} \cdot (\nabla \times \mathbf{E})\, dV - k_0^2 \iiint_{V_i} \mathbf{w}_r \cdot \overline{\overline{\epsilon}}_r \cdot \mathbf{E}\, dV + j\omega\mu_0 \iiint_{V_i} \mathbf{w}_r \cdot \mathbf{J}\, dV \\ &= +j\omega\mu_0 \iint_{S_i} \mathbf{w}_r \cdot (\hat{\mathbf{n}} \times \mathbf{H})\, dS \end{aligned} \tag{5}$$

$$\begin{aligned} &\iiint_{V_i} (\nabla \times \mathbf{w}_r) \cdot \overline{\overline{\epsilon}}_r^{-1} \cdot (\nabla \times \mathbf{H})\, dV - k_0^2 \iiint_{V_i} \mathbf{w}_r \cdot \overline{\overline{\mu}}_r \cdot \mathbf{H}\, dV - \iiint_{V_i} (\nabla \times \mathbf{w}_r) \cdot \overline{\overline{\epsilon}}_r^{-1} \cdot \mathbf{J}\, dV \\ &= -j\omega\epsilon_0 \iint_{S_i} \mathbf{w}_H \cdot (\hat{\mathbf{n}} \times \mathbf{E})\, dS \end{aligned} \tag{6}$$

The formulation is discretized by covering the volume of a type Ia subregion with a uniform mesh of bricks and chosing expansion and weighting functions $\mathbf{w}_r$ to be the 3-D versions of the rooftop basis functions applied in (3). Discretisations of the FE subregion and the adjacent BIE subregions are chosen conform, meaning that the boundary discretisation and the field expansion for the BIE formulation is found as the restriction of the FE mesh to the boundary of the subregion.

During the construction of the FE system matrix, a frontal technique is used to condense the sparse matrix to a dense matrix containing only the coefficients within the expansions (3) of the fields on the boundary S_i of the Type Ia subregion as unknowns. By chosing the grids uniform and conform to each other, the frontal elimination can be done in a very efficient and robust way. For each type Ia subregion, the process leads to following matrix expression, similar to (4):

$$\begin{pmatrix} E_r \\ H_r \end{pmatrix} = \begin{pmatrix} J_r^E \\ J_r^H \end{pmatrix} + \overline{\overline{Z}}_{\text{FE}}^{\text{cond}} \cdot \begin{pmatrix} E_r \\ H_r \end{pmatrix} \tag{7}$$

C. Constructing a subregion's interaction matrix using FDTD

In [4], it is shown how a matrix expression, similar to (4) and (7), can be constructed for each type Ib inhomogeneous subregion V_i with FDTD.

$$\begin{pmatrix} E_r \\ H_r \end{pmatrix} = \begin{pmatrix} J_r^E \\ J_r^H \end{pmatrix} + \overline{\overline{Z}}_{\text{FDTD}} \cdot \begin{pmatrix} E_r \\ H_r \end{pmatrix} \tag{8}$$

To find an EM description of a type I subregion V_i, the interaction matrix $\overline{\overline{Z}}_{\text{FDTD}}$ must be constructed , which relates the electric and magnetic fields on the boundary S_i to the virtual

currents $\mathbf{J}_{virt}$ and $\mathbf{M}_{virt}$ on S_i. We therefore define a mesh of rectangular BIE cells on its boundary S_i and expand the unknown fields on S_i into rooftop basis functions following (3). Since the subregion is described by performing FDTD simulations, its volume V_i must also be subdivided into a mesh of Yee cells. We choose the FDTD and BIE discretizations in such a way that one BIE cell comprises an integer number of Yee cell facets, as shown in Fig. 1.

The subregion V_i is then excited by each basis function, implemented as an electric or magnetic current source within a separate FDTD simulation. The resulting electric and magnetic fields on S_i yield one column of the FDTD interaction matrix. By performing a number of FDTD simulations equal to the number of basis functions, the complete interaction matrix is formed. To take into account the excitations $\mathbf{J}_I$ within a type Ia domain, an additional FDTD simulation is required [5]. The geometry of V_i remains the same as for constructing $\overline{\overline{Z}}_{\text{FDTD}}$, but now $\mathbf{J}_I$ acts as source and no virtual currents are present.

Because of the large number of simulations to obtain a system matrix, special measures are taken to perform fast FDTD calculations by reducing transients within the FDTD simulation domain. This is done by invoking field equivalence, since fields are zero outside the FDTD subdomain, because of the presence of the virtual currents $\mathbf{J}_{virt}$ and $\mathbf{M}_{virt}$ on S_i. To avoid inefficient FDTD simulations due to long lasting transients, the FDTD grid is terminated in the region outside V_i by an absorbing boundary condition or by absorbing Berenger material. Obviously, the introduction of absorption does not affect the accuracy of the final results, because fields are zero outside V_i.

As demonstrated in [4], the fields at the boundary due to the excitation of one basis function can be derived at multiple frequencies in one FDTD run, by chosing a suitable time dependence for the current sources (e.g. sum of sines or Gaussian pulse). After exciting all the rooftop basis functions, an FDTD interaction matrix is stored on disk for the different frequencies under consideration. Since geometrically identical subregions have identical interaction matrices, such a matrix can be reused each time a subregion with that specific geometry occurs.

D. Assembling the global geometry's interaction matrix

A global description of the geometry is found by imposing the continuity of the tangential fields at $S_{i/j}$ in a weak sense through Galerkin weighting:

$$\lim_{\mathbf{r}\to S_{i/j}} \iint_{S_{i/j}} \mathbf{w}_r \cdot (\hat{\mathbf{n}} \times \mathbf{E}^{\text{BIE}}(\mathbf{r}))\, dS = \lim_{\mathbf{r}\to S_{i/j}} \iint_{S_{i/j}} \mathbf{w}_r \cdot (\hat{\mathbf{n}} \times \mathbf{E}^{\text{FE/FDTD}}(\mathbf{r}))\, dS \qquad (9)$$

$$\lim_{\mathbf{r}\to S_{i/j}} \iint_{S_{i/j}} \mathbf{w}_r \cdot (\hat{\mathbf{n}} \times \mathbf{H}^{\text{BIE}}(\mathbf{r}))\, dS = \lim_{\mathbf{r}\to S_{i/j}} \iint_{S_{i/j}} \mathbf{w}_r \cdot (\hat{\mathbf{n}} \times \mathbf{H}^{\text{FE/FDTD}}(\mathbf{r}))\, dS \qquad (10)$$

for all basis functions $\mathbf{w}_r$ and at each boundary $S_{i/j}$.

This yields a matrix equation of the form $(\overline{\overline{Z}}_{\text{FDTD}} + \overline{\overline{Z}}_{\text{FE}} - \overline{\overline{Z}}_{\text{BIE}}) \cdot \mathbf{X} = \mathbf{B}$ with $\mathbf{X}$ containing the unknowns E_r and H_r and $\mathbf{B}$ a source vector due to the current sources and/or incident fields. In Fig. 2, a schematic overview is presented that summarizes the proposed hybrid scheme.

IV. Numerical example

Let us consider the configuration drawn in Fig. 3. The structure consists of a microstrip substrate, consisting of a dielectric with $\epsilon_r = 12$ and dimensions 9mm × 9mm × 550μm, and a cupper ground plane with $\sigma = 5.8\ 10^7$ and thickness 50μm. A y-oriented Hertzian dipole, radiating at 10GHz, is placed at the air-substrate interface, in the middel of the substrate. Above this configuration, a frequency selective surface (FSS) is defined, consisting of a 4 by 4 array of dielectric patches with permittivity $\epsilon_r = 12$. Each of the patches is tilted over 45°.

For modelling purposes, following decomposition of the configuration is proposed: The substrate together with the dipole are placed within a FE subregion (resolution $11 \times 11 \times 13$ and cell dimensions 1mm × 1mm × 50μm), whereas each plate of the FSS is embedded

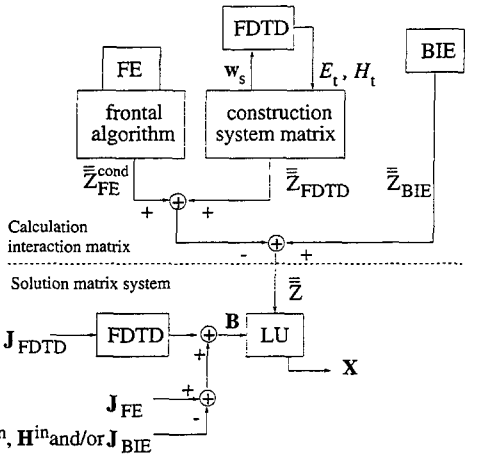


Fig. 2. Overview of the FE-FDTD-BIE Technique.

within a separate FDTD subregion. For one such region an FDTD mesh is defined with cell dimensions 0.5mm × 0.5mm × 0.5mm together with a surface mesh on the virtual boundary (resolution 6 × 6 × 2 and cell dimensions 2.5mm × 2.5mm).

Using the technique described in section III-C, an FDTD interaction matrix is generated within a frequency range from 6 GHz to 15 GHz. The resulting interaction matrix can be reused for all cells of the FSS. The interaction matrix is then retrieved from disk for $f = 8$ GHz and $f = 10$ GHz and coupled with the FE and BIE descriptions. In Fig. 4 and Fig. 5, the radiation patterns in the xz- and yz-plane are shown at resp. 8 GHz and 10 GHz, and in Fig. 6 and Fig. 7, the bistatic RCS is presented for a incident plane wave $\mathbf{E}^{in} = e^{+jkz}\mathbf{u}_y$ at resp. 8 GHz and 10GHz. A good agreement is seen between the hybrid FE-FDTD-BIE technique and FE-BIE approach, with the patches placed in FE subregions.

References

[1] H. Rogier, D. De Zutter, and F. Olyslager, "Modelling complex structures by combining the FE, FDTD and BIE techniques", *IEEE AP-S Int. Symp.*, vol. 2, pp. 1062–1065, Jul. 1999.

[2] H. Rogier, D. De Zutter, and F. Olyslager, "An overview of hybrid techniques to model three-dimensional EM problems", *URSI General Assembly*, p. 697, Invited Paper, Aug 1999.

[3] H. Rogier, D. De Zutter, and F. Olyslager, "Rigorous analysis of frequency selective surfaces of finite extent using a hybrid finite difference time domain-boundary integral equation technique", *1998 URSI Electromangetic Theory Symposium*, vol. 1, pp. 366-368, May 1998.

[4] H. Rogier, F. Olyslager, and D. De Zutter, "A new hybrid FDTD-BIE approach to model electromagnetic scattering problems", *IEEE Microwave and Guided Wave Lett.*, vol. 8, no. 3, pp. 138–140, Mar 1998.

[5] H. Rogier, D. De Zutter, and F. Olyslager, "Modelling radiation from complex structures using a hybrid FDTD-BIE technique", *IEEE AP-S Int. Symp.*, pp. 1808–1811, June 1998.

[6] A. J. Poggio, E. K. Miller, and R. Mittra, *Computer Techniques for Electromagnetics and Antennas*, vol. 2, Danish Association of Professional Engineers, Copenhagen, 1971.

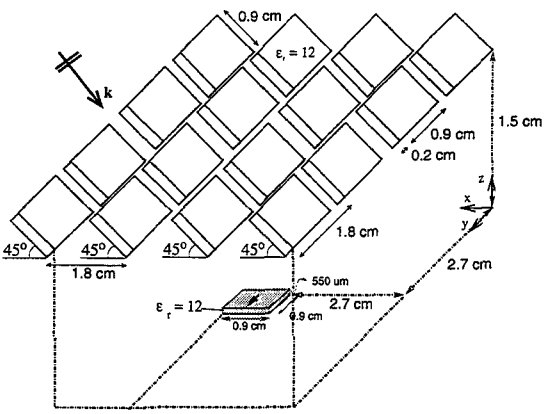


Fig. 3. Problem geometry: FSS above a substrate with radiating dipole.

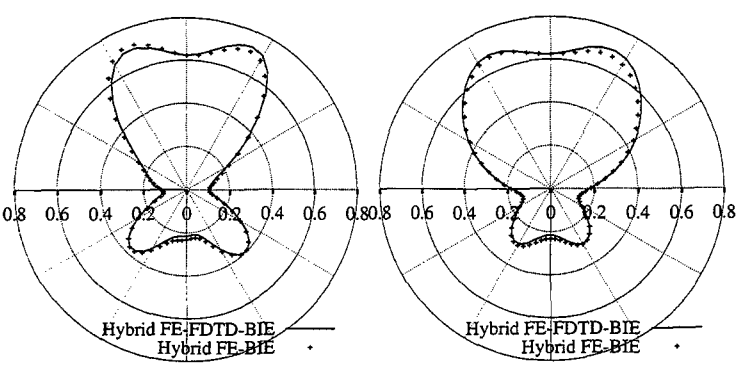


Fig. 4. Radiation patterns in the xz-plane and yz-plane at 8 GHz, for the geometry of Figure 3

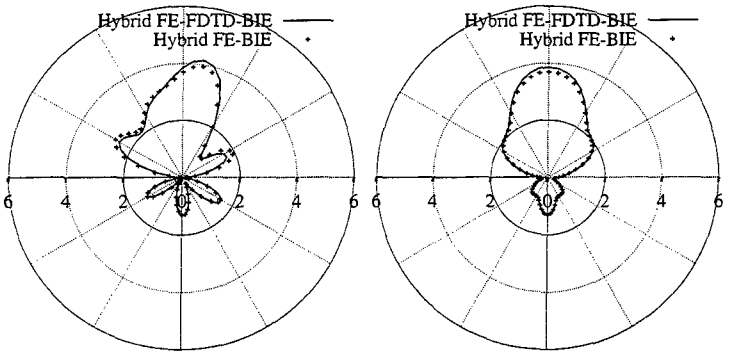


Fig. 5. Radiation patterns in the xz-plane and yz-plane at 10 GHz, for the geometry of Figure 3

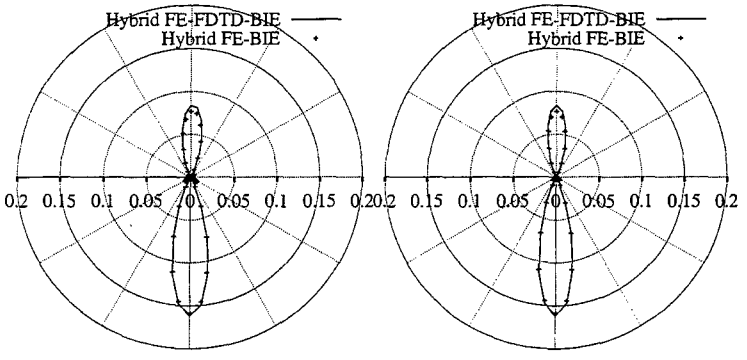


Fig. 6. Bistatic RCS in the xz-plane and yz-plane for normal plane wave incidence at 8 GHz

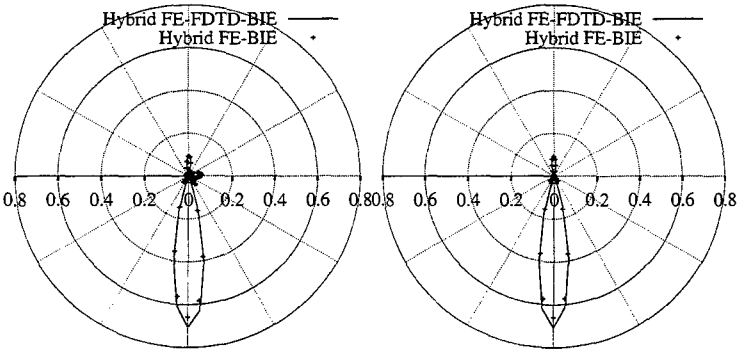


Fig. 7. Bistatic RCS in the xz-plane and yz-plane for normal plane wave incidence at 10 GHz

Hybrid FDTD-Frequency Dependent Network Simulations using Digital Filtering Techniques

Ian Rumsey
Melinda Piket-May
University of Colorado at Boulder
Dept. of Electrical and Computer Engineering
Campus Box 425
Boulder, CO 80309-0425
rumsey@colorado.edu mjp@colorado.edu

Abstract

Microwave and high-speed circuits are reaching ever-increasing speeds and physical complexity. As a result the need for accurate simulation of both lumped circuit elements and complex geometries has also increased. The finite-difference time-domain (FDTD) method is capable of modeling arbitrary materials and physical geometries, but the implementation of frequency-dependent lumped circuit loads is not trivial. This paper presents a new method for representing multiport devices with arbitrary frequency responses in FDTD simulations using approximate recursive digital filters.

Introduction

The FDTD method has been used in the past to model lumped circuit elements using the extended FDTD method [1]. This method utilizes an additional lumped circuit current density in Ampere's Law to include the device behavior into the FDTD update equations. This method has recently been extended [2] to model arbitrary two-port linear networks by applying digital filtering techniques to this lumped circuit current density. This paper presents an approach based on the equivalent source method [3] for including lumped devices which can model networks with an arbitrary number of ports [4]. The equivalent source method relies on derived voltages and currents in the FDTD grid rather than directly modifying the Yee update equations. Through the use of approximate digital filters, the convolution usually required to include dispersive materials and devices in FDTD is implemented in a straight-forward manner.

The equivalent source method allows for transmission line voltages and currents to be calculated at all device ports at every time step. Manipulation of these total voltages and currents provides the incident voltage wave at each port, and a recursive digital filter is used to calculate reflection and transmission from each port to all other ports.

The time-stepping scheme used in the FDTD method is by nature a discrete-time system, so the techniques used in digital signal processing can be applied directly without modification. The sampling rate in FDTD is much higher than that used in normal DSP applications due to numerical stability constraints. At the highest resolved FDTD frequency such that the grid spacing Δx is equal to $\lambda/20$, the FDTD sampling rate is at least 20 samples per cycle, well above the Nyquist limit of 2 samples per cycle. This leads to a very low ratio of the digital filter pole and zero frequencies to the sampling frequency, which can lead to inaccuracy and instability in digital filters [5].

Potential applications of this method include system-level electromagnetic simulations of large systems with many subsystems. These subsystems could be simulated individually, and then combined to determine overall performance, particularly in systems with transmission line interconnects between lumped circuit devices.

Formulation

The total voltage and current on a transmission line is given by the combination of forward (towards a port) and reverse (away from a port) travelling waves. The convention for defining these total

parameters is that the forward (V_a) and reverse (V_b) voltages add, and reverse current (I_b) subtracts from the forward current (I_a). The forward and reverse voltages are related to the forward and reverse currents by the characteristic impedance of the line, Z_o.

$$V = V_a + V_b \qquad I = I_a - I_b$$

$$V_a = Z_o I_a \tag{1}$$

Combining the total voltage and current with knowledge of the line impedance, the forward travelling voltage can be extracted from the total instantaneous voltage.

$$V_a = \frac{V + Z_o I}{2} \tag{2}$$

Using the reflection and transmission coefficients at a port, the reverse voltage that would be observed due to the attached load can be calculated using the extracted forward voltage. The total voltage at any port is thus given by the superposition of the forward voltage at that port and the reverse voltages due to all other ports. Using the notation of S-parameters, which are generalized reflection transmission coefficients, the reverse voltage V_{bj} at the jth port due to the forward voltage V_{ai} at port i is given by:

$$S_{ij} = \left.\frac{V_{bj}}{V_{ai}}\right|_{V_{ak \neq i} = 0} \tag{3}$$

where S_{ij} is the reflection/transmission coefficient relating V_{ai} to V_{bj}. These reflection and transmission coefficients have been used in the FDTD algorithm [6] to implement multiport devices with constant coefficients. Examples of such devices are idealized gain stages and isolators. FDTD implementation in this work uses a microstrip line of known impedance with a gap where the device is located. Total voltage and current at the open microstrip ends are calculated from the magnetic and electric fields in the FDTD grid. Equation (2) is applied to get the incident voltage at each port, and then equation (3) is used to derive the reverse travelling voltages. The new total voltage (V_a+V_b) is then enforced in the FDTD grid using equivalent voltage sources at the microstrip ends, and then the simulation is advanced one more time step before repeating the process.

This method can be extended to frequency-dependent loads by considering discrete convolution at each port. In this case the discretized reverse voltage $V_b[k]$ at a port is given by the convolution of $V_a[k]$ with the reflection impulse response h[k] at the port.

$$V_b[k] = \sum_{n=0}^{k} V_a[n] h[k-n] \tag{4}$$

where k and n are indices into the discrete variables V_b, V_a, and h. While this is an adequate method for calculating the reverse voltage, a recursive formulation is desirable. Fortunately, a recursive form of the discrete convolution is readily available in the form of and infinite impulse response (IIR), or recursive digital filter. This type of filter is described in the Z-domain by equation (5).

$$V_b(z) = \frac{A(z)}{B(z)} V_a(z) \tag{5}$$

where

$$A(z) = \sum_{k=0}^{L} a_k z^{-k} \qquad B(z) = 1 - \sum_{k=1}^{M} b_k z^{-k} \tag{6}$$

L is the number of filter poles, and M is the number of filter zeroes. The operator z^{-1} is a delay of one sample in the time domain, so converting equation (5) to the discrete time domain and cross-multiplying yields:

$$V_b[k] - b_1 V_b[k-1] - \cdots - b_M V_b[k-M] = \quad a_0 V_a[k] + a_1 V_a[k-1] + \cdots + a_L V_a[k-M] \tag{7}$$

which can be rearranged to solve for $V_b[k]$ by moving all other terms to the right side of equation (7). This produces a formulation for the most current value of V_b in terms of the previous values of V_b as well as the current and previous values of V_a.

$$V_b[k] = \sum_{m=1}^{M} b_m V_b[k-m] + \sum_{l=0}^{L} a_l V_a[k-l] \tag{8}$$

The generalized reflection and transmission coefficients in equation (3) can be put in the form of equation (4) to provide recursive discrete convolution at all ports. This involves approximating the Z-domain response at each of the ports as the ratio of two polynomials, known as the Padé approximation [7]. This approximation is accomplished using the discrete impulse response *h[k]* at each port, and transforming it into the Z-domain. The port discrete impulse response can be thought of as a summation of time-shifted impulse functions, so the Z-transform can be found by inspection.

$$h[k] = \sum_{k=0}^{\infty} c_k \delta(t - kT) \qquad H(z) = \sum_{k=0}^{\infty} c_k z^{-k} \tag{9}$$

H(z) is the Z-transform of *h[k]*, *T* is the time between samples, and c_k is the amplitude of the *k*th sample. Using the Padé approximation, H(z) can be written as [7,8]:

$$\sum_{k=0}^{\infty} c_k z^{-k} = \frac{\sum_{i=0}^{L} a_i z^{-i}}{1 + \sum_{i=1}^{M} b_i z^{-i}} + O(z^{-(L+M+1)}) \tag{10}$$

where $O(z^{-(L+M+1)})$ is an error term in the $L+M+1$ sample due to the approximation. The filter coefficients a_i and b_i can be found by multiplying out the denominator in equation (10) and matching coefficients of like powers of z^{-1} [7]. If the negative of the b_i coefficients in equation (10) are used, this form is identical to that in equation (5) and thus an approximate digital filter for the port impulse response has been found. Equation (7) can be implemented using the a_i and b_i coefficients found from the Padé approximation, provided that the port impulse response is sampled at the same rate as the FDTD time step.

Multiplying the denominator of equation (10) over to the left side of the equation and equating coefficients of equal powers of z^{-1} yields a system of equations which can be stated as a matrix equation [7]:

$$\begin{bmatrix} c_{L-M+1} & c_{L-M+2} & \cdots & c_L \\ c_{L-M+2} & c_{L-M+3} & \cdots & c_{L+1} \\ \vdots & \vdots & & \vdots \\ c_L & c_{L+1} & \cdots & c_{L+M-1} \end{bmatrix} \begin{bmatrix} b_M \\ b_{M-1} \\ \vdots \\ b_1 \end{bmatrix} = - \begin{bmatrix} c_{L+1} \\ c_{L+2} \\ \vdots \\ c_{L+M} \end{bmatrix} \tag{11}$$

where the c_k's are coefficients of the system impulse response, and the b_i's are the coefficients of the polynomial in the denominator of equation (10). This can be solved by a number of matrix solution methods. The numerator coefficients, a_i in equation (10), can then be found by:

$$a_0 = c_0 \qquad a_1 = c_1 + b_1 c_0 \qquad \cdots \qquad a_L = c_L + \sum_{i=1}^{\min(L,M)} b_i c_{L-i} \tag{12}$$

where L is the order of the numerator polynomial in equation (10), and M is the order of the denominator polynomial. As can be seen from these equations, only the first (L+M) terms of the discrete impulse response *c[k]* are used, which can lead to very large numbers of poles and zeros in the approximate filter for long impulse responses.

An alternative method for determining the approximate filter coefficients is a least-squares fit using the time-domain input *u[k]* and output *y[k]* of the system [9]. The input-output relationship is fit to a recursive model in the form of equation (8).

$$y[k] = b_1 y[k-1] + \cdots + b_M y[k-M] + a_0 u[k] + \cdots + a_L u[k-L] \tag{13}$$

A vector θ of filter coefficients and another ϕ of input and output signal parameters can be defined:

$$\theta = [b_1 \cdots b_M \quad a_0 \cdots a_L]^T \qquad \phi = [y[k-1] \cdots y[k-M] \quad u[k] \cdots u[k-L]]^T \tag{14}$$

where the approximate reconstructed output signal $\hat{y}[k|\theta]=\phi^T\theta$. Taking the sum-squared error of (y[k]-$\hat{y}$[k|θ]) for a sequence of length N and then differentiating with respect to θ to find a minimum of the error yields a matrix formulation to solve for θ.

$$\begin{bmatrix} \sum_{k=1}^{N} y[k-1]^2 & \sum_{k=1}^{N} y[k-1]y[k-2] & \cdots & \sum_{k=1}^{N} y[k-1]u[k-L] \\ \sum_{k=1}^{N} y[k-2]y[k-1] & \sum_{k=1}^{N} y[k-2]^2 & \cdots & \sum_{k=1}^{N} y[k-2]u[k-L] \\ \vdots & \vdots & & \vdots \\ \sum_{k=1}^{N} u[k-L]y[k-1] & \sum_{k=1}^{N} y[k-1]^2 & \cdots & \sum_{k=1}^{N} u[k-L]^2 \end{bmatrix} \begin{bmatrix} b_1 \\ \vdots \\ b_M \\ a_0 \\ \vdots \\ a_L \end{bmatrix} = \begin{bmatrix} \sum_{k=1}^{N} y[k-1]y[k] \\ \sum_{k=1}^{N} y[k-2]y[k] \\ \vdots \\ \sum_{k=1}^{N} u[k-L]y[k] \end{bmatrix} \quad (15)$$

This method has the feature of using all the time samples of u[k] and y[k], and 'degrades gracefully' when a suboptimal number of poles and zeros are used in the approximate filter. Both of these features are advantageous over the Padé approach presented in equations (10-11). Figure 1 illustrates the effect of using the Padé approximation and a least-squares solution when attempting to reproduce the pulse response of a simple IIR filter, for which there is an exact solution in the form of equation (8). The filter being approximated has:

$$a_{exact} = [0.5 \quad 0.1 \quad 0.1] \qquad b_{exact} = [0.1 \quad 0.1 \quad 0.1 \quad 0.1] \quad (16)$$

for the filter coefficients. When the number of poles (M) and zeros (L) used in the Padé and least-squares solutions are equal to the number of poles and zeros in the original IIR filter, both techniques arrive at the exact solution, shown in figure 1a. When the solution space for these two methods is restricted to include only three poles, the exact filter response lies outside the solution space. The Padé approximation shows marked degradation in performance, while the least-squares solution still closely follows the original pulse response, shown in figure 1b. For the restricted solution space the two methods yield:

$$\begin{aligned} a_{LSQ} &= [0.5007 \quad 0.0996 \quad -0.1172] & a_{Pade} &= [0.5 \quad 0.0783 \quad -0.3174] \\ b_{LSQ} &= [0.1009 \quad 0.5364 \quad 0.0188] & b_{Pade} &= [0.1435 \quad 0.9217 \quad -0.1609] \end{aligned} \quad (17)$$

The results presented in this paper use the Padé approximation to arrive at the filter recursion coefficients. Future work will utilize least-squares approximations.

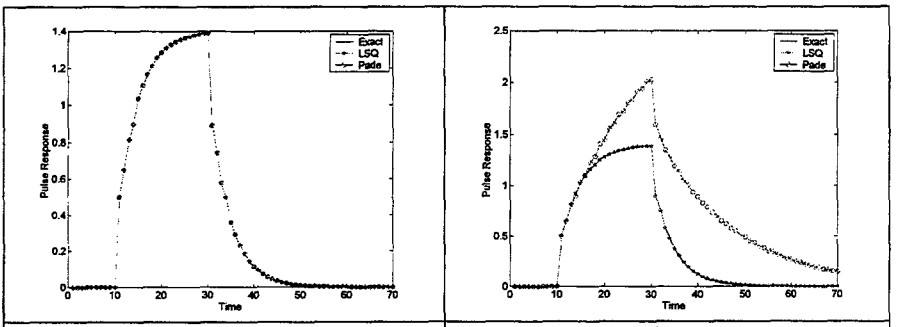


Figure 1— Padé (circles) and Least-Squares (stars) approximations to an IIR filter pulse response when (a) the exact solution is included in the solution space and (b) when the solution space is restricted to not include the exact filter response

Simple Digital Filters

In order to validate this technique, several canonical digital filters were implemented in FDTD. The a and b coefficients for these filters can be found from analytic expressions, which eliminated the Padé approximation as a source of error. Section IV presents a digital filter approximation for a three section quarter-wave impedance matching circuit, which does utilize the Padé approximation to find the filter coefficients.

The FDTD model used to validate these digital filters was a 1mm wide microstrip transmission line on a 0.25mm thick air substrate with a 10mm gap. The model boundaries were terminated with a PML absorbing boundary condition. The microstrip line was excited by a Gaussian pulse modulated at 20GHz with a bandwidth of 40GHz. The filter output voltage was measured on the other side of the gap from the source, and then normalized by the spectrum of the exciting function to find the filter response. The phase is corrected for the time delay between the source and the gap, and between the gap and the measurement location. The time step used for this model yields a sampling frequency f_s=2.3983THz.

The first recursive filter validated was the cascade connection of four single-pole lowpass filters with the same cutoff frequency. The coefficients for this filter can be found by multiplying four single-pole lowpass transfer functions together, which produces the following expressions for the aggregate filter coefficients:

$$a_0 = (1-x)^4 \qquad b_1 = 4x$$
$$b_2 = -6x^2 \qquad b_3 = 4x^3 \qquad b_4 = -x^4 \tag{18}$$
$$x = e^{-14.445\frac{f_c}{f_s}}$$

the cutoff frequency f_c for this filter is 8GHz. The ideal IIR filter response and the FDTD implementation are shown together in figure 1a, with good agreement. This principle of combining filter transfer functions can be applied to any cascade or parallel combination of IIR filters.

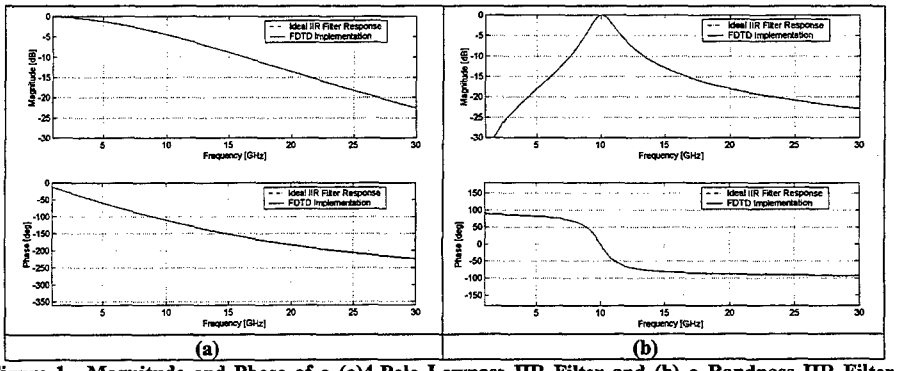


Figure 1—Magnitude and Phase of a (a)4-Pole Lowpass IIR Filter and (b) a Bandpass IIR Filter shown with the FDTD Implementation

The second simple filter used in this validation was a bandpass filter. This type of filter is defined by the center frequency f_c and bandwidth f_{BW} of the passband. The recursion coefficients for this filter are given by [5]:

$$a_0 = 1-K \quad a_1 = 2(K-R)\cos\left(2\pi f_c/f_s\right)$$
$$a_2 = R^2 - K \quad b_1 = 2R\cos\left(2\pi f_c/f_s\right) \quad b_2 = -R^2 \tag{19}$$

where R and K are defined in equation (20).

$$R = 1 - 3\frac{f_{BW}}{f_s} \qquad K = \frac{1 - 2R\cos\left(2\pi f_c / f_s\right) + R^2}{2 - 2\cos\left(2\pi f_c / f_s\right)} \tag{20}$$

f_c was chosen to be 10GHz, and the 3dB bandwidth f_{BW} to be 2GHz. Figure 2b shows the ideal IIR filter response with the FDTD implementation, with good agreement.

Other filters used to validate this method include single-pole low pass, single-zero high pass, Chebychev, and notch filters. All of these filter types showed good agreement between the ideal IIR filter response and the FDTD implementation.

Impedance Matching Network

As an application of this method to practical microwave circuit design, the frequency response of a microstrip three-section quarter-wave impedance transformer was included in FDTD as a recursive digital filter.

S_{11} and S_{21} for a maximally flat three-section transformer [10] between 50Ω and 77Ω at 10GHz were found using Hewlett-Packard's Microwave Design System (MDS) software package. Using the calculated frequency-domain S_{11} and transmission S_{21} characteristics, the reflection and transmission impulse responses were found by inverse Fast Fourier Transform (FFT) [11], and fit to the FDTD time step. The Padé approximation in equation (10) was applied to these discrete impulse responses to produce approximate recursive digital filters that could be implemented in FDTD using equation (8).

The FDTD implementation depends only on the value of the reflection and transmission coefficients and not on the actual impedance of the connecting lines, so the same FDTD model as in section III was used for simplicity. The modulated Gaussian pulse used in the validation studies was excited at port 1, and the time-domain reflection and transmission were measured. These signals were transformed to the frequency domain and normalized by the spectrum of the source waveform. The magnitude and phase of the desired response, the IIR filter found by Padé approximation, and the FDTD implementation are shown together in figure 3a for S_{11} and figure 3b for S_{21}.

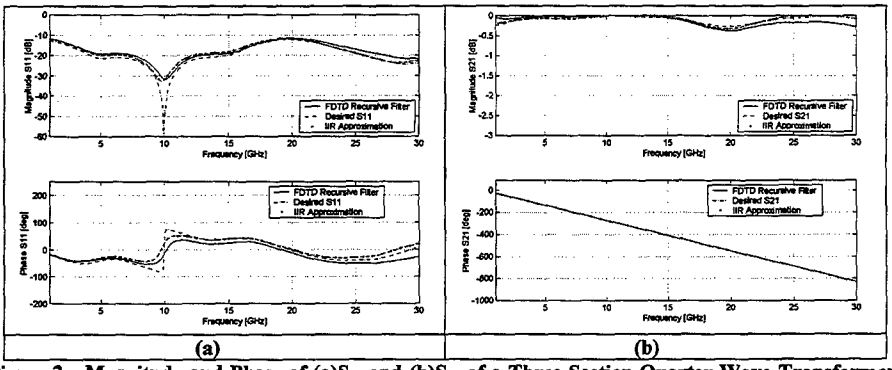


Figure 2—Magnitude and Phase of (a)S_{11} and (b)S_{21} of a Three-Section Quarter Wave Transformer found using MDS (dashed), Padé Approximation of the MDS results (dotted), and FDTD implementation (solid)

Figures 3a and 3b show that while the Padé approximation does not reproduce the full depth of the S_{11} null at 10GHz, the overall response shape for magnitude and phase is acceptably reproduced for both S_{11} and S_{21}. The Padé approximation introduces some error because the method for finding a_i and b_i utilizes

only the first $L+M$ samples of the impulse response, losing information at the end of the impulse response. The multiple reflections taking place within the three-section transformer yield a very long impulse response, and even a large number of poles and zeros ($L+M$=1000) does not capture enough information to reproduce the full depth of the 10GHz null. Continuing work is focusing on methods, such as least-squares approximation and frequency domain techniques, for finding an optimum set of poles and zeros using all the information available in the impulse response. Another source of error, exhibited by the IIR filter and FDTD responses deviating at high frequencies is due to parasitic reactance at the microstrip open-end in the FDTD model. Future models will include a method for calibrating out the minor effect of these parasitics.

Conclusions

A new method for including arbitrary frequency-dependent linear networks with an arbitrary number of ports in FDTD using digital filtering techniques has been introduced. This technique relies on the equivalent source method for describing lumped circuit elements to implement the interface between the field interactions in FDTD and the voltage and currents used to describe the port characteristics of a device. A number of simple digital filters were implemented in FDTD to validate the use of IIR filters, and an example involving a three-section quarter-wave impedance transformer was shown.

Sources of error in this method include the direct application of the Padé approximation, which does not use all available information in the impulse response, and parasitics in the microstrip gap used in the FDTD model. Future work will calibrate out these parasitics, and will use a more sophisticated method for identifying the approximate IIR filter poles and zeros.

Acknowledgements

This work was supported in part by National Science Foundation CAREER Award #ECS-9703467.

References

[1] M. Piket-May, et.al., "FD-TD Modeling of Digital Signal Propagation in 3-D Circuits with Active and Passive Loads", *IEEE Trans. Microwave Theory & Tech*, **vol 42, no. 8,** Aug. 1994, pp.1514-1523

[2] J.A. Pereda, et.al., "A New Algorithm for the Incorporation of Arbitrary Linear Lumped Networks into FDTD Simulators", *IEEE Trans. Microwave Theory & Tech*, **vol. 47, no. 6,** June 1999, pp. 943-949

[3] J.Mix, et al, "Modeling Nonlinear Devices in FD-TD: The Equivalnet Source Method", USNC/URSI National Radio Science Meeting, 1998 Digest, Atlanta, GA, pp.75

[4] I.Rumsey, et al, "Digital Filtering Embedded in a Finite-Difference Time-Domain (FDTD) code" Proceedings of the International Conference on Electromagnetics in Advanced Applications (ICEAA99) Torino, Italy, Sept. 1999, pp. 669-672.

[5] S. Smith, The Scientist and Engineer's Guide the Digital Signal Processing, California Technical Publishing, San Diego, CA 1998

[6] I. Rumsey, et al, "Methods for Including Lumped Elements in FDTD Simulations", Proceedings of the 15th Annual Review of Progress in Applied Computational Electromagnetics (ACES), Monterey, CA, 1999, pp. 12-15

[7] G.A. Baker and P. Graves-Morris, Padé Approximants, Encyclopedia of Mathematics and its Applications, **vol. 13,** Addison-Wesley Publishing Company, Inc., 1981

[8] M. AbuShaaban, et al, "Recursive Causal Convolution", Proceedings of the IEEE International Microwave Symposium, MTT-S, Denver, CO, June 1997, pp. 631-634

[9] L. Ljung, System Identification: Theory for the User, 2nd Edition, Prentice Hall Inc., Upper Saddle River, NJ, 1999

[10] D.H. Schrader, Microstrip Circuit Analysis, Prentice Hall Inc., Upper Saddle River, NJ, 1995

[11] T.J. Brazil, "Causal-Convolution—A New Method for the Transient Analysis for Linear Systems at Microwave Frequencies" *IEEE Trans. on Microwave Theory & Tech.*, **vol. 43, no. 2,** Feb. 1995, pp. 315-323

Study of Electrically-Short Thin-wire Antennas Located in the Proximity of Inhomogeneous Scatterers Using a Hybrid NEC/FDTD Approach.

A. Rubio Bretones[1], R. Mittra[2] and R. Gómez Martín[1]

(1)Departamento de Electromagnetismo
Facultad de Ciencias, Univ. Granada
10871 Granada, SPAIN
Email: arubio@goliat.ugr.es, rgomez@goliat.ugr.es

(2)Electromagnetic Communication Laboratory
Department of Electrical Engineering
The Pennsylvania State University
University Park, PA 16802
Email: rxm53@psu.edu

Abstract: *The paper presents a hybrid technique, which combines the Method of Moments (MoM) with the Finite Difference Time Domain (FDTD) method to analyze electrically-short, thin-wire antennas located in the vicinity of inhomogeneous dielectric bodies. The antennas are dealt with in the frequency domain using the NEC code, while the FDTD is used to analyze the inhomogeneous part of the problem. The two sub-problems are linked together and hybridized by invoking the equivalence theorem.*

I. INTRODUCTION

The analysis of thin-wire antennas located in the vicinity of inhomogeneous dielectric scatterers is important in numerous electromagnetic applications, *e.g.*, wireless communication, electromagnetic compatibility and ground radar. A hybrid method that combines two numerical techniques, viz., the Method of Moments in the time domain (MoMTD) and the Finite Difference Time Domain (FDTD) scheme, was recently introduced in [1] to investigate this type of problem. The above approach takes advantage of the versatility of the FDTD for handling complex structures with arbitrary material properties, and the ability of the MoM to deal with thin wires; and yet, it overcomes some of the drawbacks [2] of using the FDTD alone to handle the same problem. The above time-domain hybrid method is quite general in its application, and is useful for studying the problems of transient excitation of an arbitrary thin-wire configuration in the presence of inhomogeneous objects that may also be arbitrary. However, it is not as numerically efficient as one might desire, at least for the case of harmonic excitation of wire antennas located in the vicinity of an inhomogeneous medium [3,4], and the method proposed in this paper has been designed to provide improved performance for such problems. The proposed scheme is a new hybrid method that combines the well-known NEC code [5] for frequency domain analysis with the FDTD technique. For the specific case of harmonically-excited short antennas, the new scheme uses fewer computational resources than the time-domain hybrid

method [1], and yet yields excellent results. The present method [6] is formulated in a self-consistent way, which does not require the use of iterative procedures to model the coupling between the different sub-regions.

II. DESCRIPTION OF THE METHOD

In this section we describe the proposed hybrid approach for combining the FDTD technique and the NEC code by considering the problem of a thin wire located in the vicinity of a dielectric body (see Fig. 1). The two numerical schemes are used to analyze specific parts of the problem for which they are best suited individually, *viz.*, the integral-equation technique for the wire and the FDTD for the dielectric body. The first step is to divide the original problem into the following two sub-problems: (a) thin wire antenna located in an unbounded free space; and, (b) the inhomogeneous object inside surface S', with the thin-wire antenna removed. The solutions of the two sub-problems are interconnected through the surface equivalence theorem (Huygen's principle). The process for linking the frequency domain variables used in NEC, to the time domain ones needed in the FDTD, is described below.

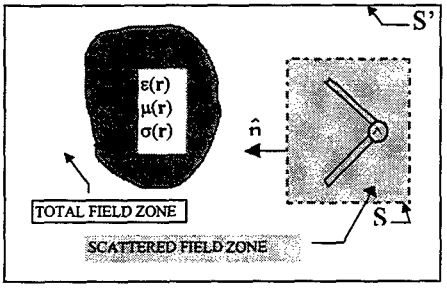


Fig. 1: Thin wire antenna in the vicinity of a dielectric scatterer and the FDTD computational domain

First, the Electric Field Integral equation (EFIE) for the current $I(s)$, induced on the surface of the thin-wire antenna by an incident field $\vec{E}^i$, is formulated by enforcing the boundary condition on the tangential electric field along the wire axis. Including the contribution of the field scattered by the inhomogeneous body, $\vec{E}^B$, within the total electric field at position s on the wire, the EFIE can be written as

$$\hat{s} \cdot [\vec{E}^i(s) + \vec{E}^S(s) + \vec{E}^B(s)] = 0 \qquad (1)$$

where s is the distance along the wire axis, $\hat{s}$ is the unit vector tangential to the wire axis at position s, and $\vec{E}^S$ is the electric field that would be scattered at the same position if it were in free space. The field $\vec{E}^B$ in (1) is an unknown, with a linear dependence on $I(s)$, for which we do not have a closed-form expression in general; however, it can be computed numerically.

The point matching form of the method of moments is applied to (1) by dividing the wire into N_S straight segments and expanding the unknown function $I(s)$ into the sum of the N_S basis functions, $f_j(s)$, (j=1,...,N_S) used in NEC [5]. For the antenna case, this transforms (1) into the matrix equation:

$$\sum_{j=1}^{Ns}[Z_{i,j} + Z^{B}_{i,j}]\cdot\alpha_j = \frac{V(s_i)}{\Delta s_i};\quad i = 1,..., N_S \qquad (2)$$

where α_j are the coefficients of the current expansion; $V(s_i)$ is the applied voltage at position s_i on the wire; Δ_i is the length of segment i; $Z_{i,j}$ are the elements of the NEC-impedance matrix $[Z]$ when the wire is located in free space; and, $Z^{B}_{i,j}$ are the contributions arising in the presence of the dielectric body. They represent the tangential electric fields at positions s_i on the wire, scattered by the inhomogeneous region by the jth basis function $f_j(s)$, and are computed numerically.

To obtain the row j of the matrix $[Z^B]$, we assume that the current is given by $f_j(s)$, and then compute the tangential electric field on the sampled points along the wire. To this end, we begin by introducing a Huygens' surface, S, around the thin-wire antenna (see Fig. 1), where the time-domain values of the equivalent sources are deduced from the magnitude and phase of field radiated by the antenna in free space, that were computed previously by using NEC. Next, the FDTD algorithm is applied, in the presence of these equivalent sources [7] but in the absence of the antenna, to the entire computational domain consisting of the total field (outside S) and the scattered field (inside S) zones. The tangential electric fields are calculated at the specific locations s_i (i=1,...N_S) on the antenna after the steady state condition has been reached inside S, and interpolation is used if the points are not coincident with the FDTD grid points. Finally, we obtain the elements $Z^{B}_{i,j}$ (i=1,...N_S) we were seeking, after transforming the time domain data into the frequency domain. The procedure is repeated for j=1,...,N_S, until all the rows of the matrix $[Z^B]$ have been filled.

Subsequently, a modified version of NEC is run to solve (2) and to obtain the current $I(s)$ induced on the antenna, from which all of the fields in the FDTD computational domain can be derived. We can obtain these fields either by repeating the procedure described in the above paragraph for the actual current $I(s)$, or by applying linearity if the observation variables have been kept in memory when solving for each of the $f_j(s)$'s.

The entire procedure entails a running of the FDTD code N_S times and, hence, the method is only useful for antennas that can be modeled accurately by using a small number of basis functions. It should be pointed out, however, that the computational burden in running the program N_S times is still smaller than that in the FDTD scheme employing a very small cell size, which may be required to accurately model the thin wire antenna.

III. NUMERICAL RESULTS

To validate the technique described in the last section, the hybrid method has been employed to solve several simple problems for which independent solutions can be obtained with NEC alone is possible. We now present the results obtained for a V antenna and a circular loop operating in a two-media environment.

3.1 V antenna

We have investigated a V-antenna located in the proximity of an interface between free space, and either a homogeneous half space with a relative dielectric permittivity $\varepsilon_r=4$, or a perfectly conducting (PEC) plane. The inner angle of the antenna is $\alpha=120^o$, and the length of each of its arms is *6.6 cm*, its radius is *0.8 mm*, and the distance to the interface between the two media is *0.3 m*. The antenna was excited by applying a *900 MHz* voltage source, of strength 0.5 *V*, at each of the two central segments. It was modeled with $N_S=6$ segments, after determining that the results for free space simulations did not vary significantly when N_S was increased beyond 6. The FDTD solution space contained 80x80x80 cells, and a size of 1.5 *cm*. Figure 2 shows the magnitude and phase of the x-component of the electric field sampled at a set of observation points plotted with a dashed line in Fig.2b. The points are located at a distance of 7.5 *cm* away from the interface, with the first one at $D=0.3$ *m* from the antenna. The solid lines plot the NEC results and the (■) symbol lines designate the ones obtained by applying the hybrid method proposed herein. It is evident that the results obtained with the hybrid scheme are in very good agreement with those derived via the MoM approach.

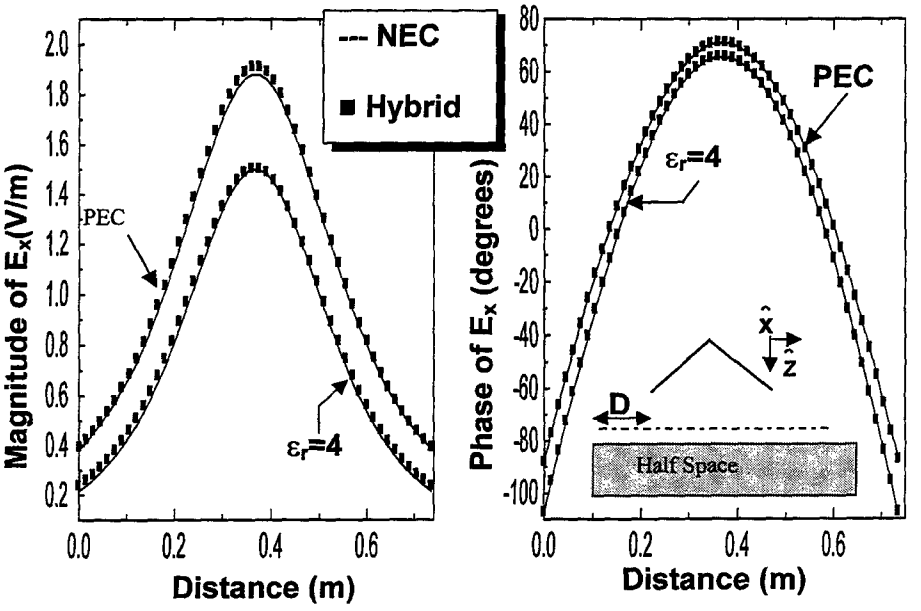
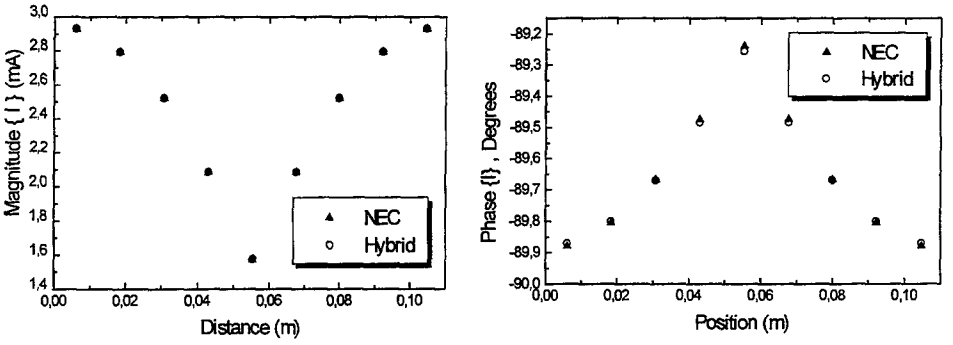


Fig. 2: V antenna: Magnitude and phase of E_x sampled at a set of observation points

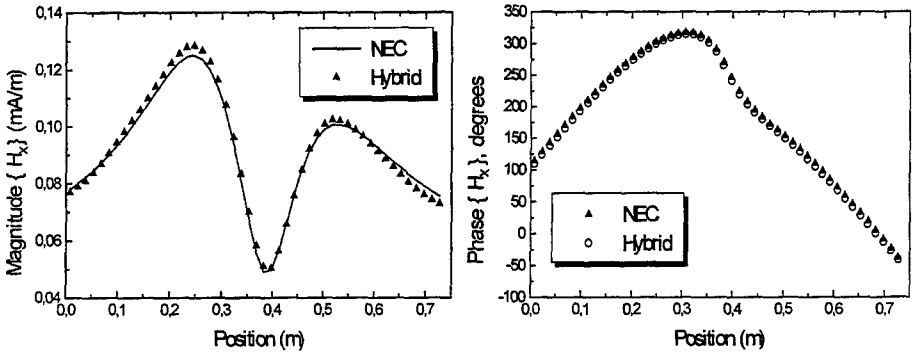
3.2 Circular loop antenna

For the second example, we analyze the problem of a circular loop antenna located parallel to the same interface, between free space and a homogeneous half space with $\varepsilon_r=4$, as was the case in the previous example. The distance from the loop to the interface is *0.3 m*, the radius of the loop is *1.8 cm* and the radius of the wire is *0.8 mm*. The antenna was divided into 9 segments, and one of these was excited with a 900 *MHz* voltage source. Figure 3 shows the current at the feed point obtained by using NEC alone, as well as with the hybrid method described here. Figures 4 and 5 show the z-component of the electric field and the x-component of the magnetic field at the same set of observation points as used for the plots in Fig. 2b. Specifically, they are located parallel to the interface and at a distance of *7.5 cm* from it. Again the agreement between the two methods is seen to be excellent.



(a) (b)

Fig. 3: Circular loop antenna: Current at the feed point. a) Magnitude. b) Phase



(a) (b)

Fig. 4. Circular loop antenna: E_z at a set of points. (a) Magnitude. (b) Phase.

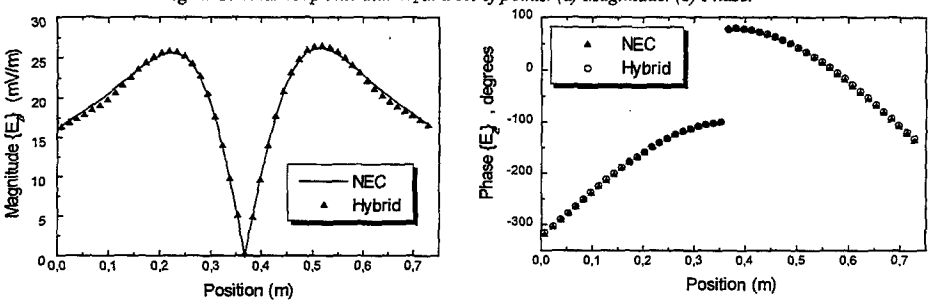


Fig. 5: *Circular loop antenna: H_z at a set of points. (a) Magnitude. (b) Phase.*

Acknowledgements: This work was supported in part by the Spanish CICYT Project TIC98-1037-C03-01 and by the U.S.- Spain Science & Technology Program 1999.

REFERENCES:

[1] RUBIO BRETONES, A., MITTRA, R. and GÓMEZ MARTÍN., R., "A new Hybrid Method Combinig the Method of Moments in the Time Domain and FDTD", *IEEE Microwave and Guided Wave Letters*; vol.8, pp. 281-283, 1998

[2] MONTOYA, T.P. and SMITH, G.S., "Modeling staircase wires using FDTD method", *IEEE Antennas and Propagation International Symposium*, Orlando, USA, pp. 180-183, July 1999

[3] CHEN, W. and CHUANG, H., "Numerical Computation of Human Interaction with Arbitrarily Oriented Superquadratic Loop Antennas in Personal Communications, *IEEE Trans. Antennas and Propagat*, vol.46, n. 6, pp. 821-828, 1998.

[4] LEPELAARS, E., "Transient electromagnetic excitation of biological media by circular loop antennas", Ph D. Dissertation (Eindhoven University of Technology, The Netherlands), ISBN: 90-386-0320-7, 1997.

[5] BURKE, G.J. and POGGIO, A.J.: Numerical Electromagnetic Code (NEC) – Method of Moments, Lawrence Livermore Laboratory, *Technical Document NOSC TD 116*, 1981

[6] RUBIO BRETONES, A., MITTRA, R. and GÓMEZ MARTÍN., R., "Hybrid NEC/FDTD approach for analyzing electrically short thin-wire antennas located in proximity of inhomogeneous sactterers", *Electronics Letters*; vol. 35, n. 19, pp. 1594-1596, 1999

[7] MEREWETHER D. E., FISHER R., SMITH F. W., "On Implementing a Numerical Huygen's Source Scheme in a Finite Difference Program to Illuminate Scattering Bodies", *IEEE Trans. on Nuclear Sciences*, vol. 27, n. 6, pp. 1829-1833, 1980.

A REVIEW OF SOME HYBRID HIGH FREQUENCY AND NUMERICAL SOLUTIONS FOR RADIATION/SCATTERING PROBLEMS

P.H. Pathak and R.J. Burkholder
The Ohio State University ElectroScience Laboratory, Dept. of Electrical Engineering,
1320 Kinnear Road, Columbus, Ohio 43212, U.S.A.
(pathak.2@osu.edu; burkholder.1@osu.edu)

Abstract— A review of some hybrid combination of asymptotic high frequency and numerical methods is presented for solving a variety of electromagnetic (EM) radiation/scattering configurations which cannot otherwise be analyzed in a tractable fashion by either of the methods when they are used alone. The numerical (or low frequency) methods are best suited to deal with electrically small portions of the radiation/scattering object because they generally become highly inefficient and even intractable for treating electrically large portions, whereas the high frequency methods are ideally suited for dealing with the electrically large portions but cannot deal with electrically small parts. Specifically, examples of hybrid solutions will be described for analyzing the coupling of edge and surface diffraction effects on a large, smooth convex boundary containing edges when illuminated by a distant wave, the scattering from a large inlet cavity containing a complex interior termination, the radiation from a cavity backed slot antenna on a large aircraft, and the radiation/scattering from a large planar phased array containing small antenna elements, respectively.

I. INTRODUCTION

This paper presents a review of some hybrid asymptotic high frequency and numerical methods for analyzing a variety of electrically large EM radiation/scattering problems. Such hybrid methods become necessary when the radiating/scattering objects become electrically large, and also when they contain some electrically small portions as well. It is noted that the use of purely numerical methods is primarily restricted to low frequency regimes (or electrically small problems), because the number of unknowns to be solved increases dramatically with frequency. In contrast, asymptotic high frequency methods are best suited for analyzing electrically large problems. However, most large practical structures contain both, electrically large as well as small parts, in general. Clearly, therefore, no single technique, i.e. either low or high frequency technique, can be used to adequately analyze electrically large configurations containing electrically small features if the latter are significant contributors to the overall radiation/scattering effects.

Some of the earliest works in the development of hybrid combinations of high frequency and numerical methods are found in [1,2], where a combination of ray methods and moment method solutions of governing integral equations are described. Subsequently, several other authors have introduced different hybrid combinations of high and low frequency techniques, as for example in [3] which combines physical optics and moment method solution of governing integral equations and also

introduces iterative techniques within the hybrid framework to further improve the accuracy. The present work reviews hybrid solutions that demonstrate their ability to solve relatively complex and fairly realistic radiation/scattering configurations. In particular, four different radiating/scattering configurations are selected and their hybrid solutions are briefly described in the following section.

II. BRIEF DESCRIPTION OF SOME HYBRID SOLUTIONS

In this section, the hybrid solutions to the following four radiating/scattering configurations are briefly reviewed in items (A) through (D).

(A) Scattering by a Half-Moon Configuration

Consider a perfectly-conducting cylindrical scatterer with a semi-circular or half-moon cross-sectional shape, which is excited by an EM plane wave. This two-dimensional (2-D) problem is assumed to have an electrically large half-moon cross-section. Such a canonical geometry is selected to study the coupling between the edge and surface diffraction effects; it is actually ideally suited for analysis via the high frequency, ray-based uniform geometrical theory of diffraction (UTD) [4]. However, the UTD requires a knowledge of the relevant edge diffraction coefficients that also simultaneously provide expressions for the launching of surface rays on the curved portion of the cylinder. These UTD coefficients can generally be found from the analytical solutions to appropriate canonical problems [4]. While the UTD coefficients for the diffraction by an edge have been known for the geometry in question for rays diffracted directly into external space by an arbitrary curved wedge [4], the edge excited surface ray launching coefficients have been found analytically only recently for describing the coupling of edge and smooth convex surface diffraction effects. Clearly, if UTD expressions are not currently available to describe some diffraction phenomena, then the method of analysis similar to that used for the half-moon geometry can be employed to efficiently obtain such UTD diffraction or launching coefficients, etc., in a numerical fashion via the hybrid approach described here. Such numerical UTD coefficients can be obtained if the functional forms of the fields are known analytically away from the diffraction/launching point; the unknown initial amplitude of the diffracted/launched field which constitutes the relevant UTD diffraction/launching coefficient for a discontinuity is then obtained numerically via the hybrid scheme. The solution discussed here for the scattering by a half-moon essentially provides numerical values for the UTD launching coefficients of the edge excited surface rays on the convex portion of the half-cylinder. Since the analytical UTD solutions for this case have only been found recently, its accuracy can be checked by comparison with the numerical hybrid solution being discussed here. The hybrid solution to the half-moon (semi-circular cylinder) begins by formulating an integral equation for the unknown currents induced on this configuration by an externally incident plane wave. This unknown current is expanded into a set of mixed basis functions; a very small subsectional basis set is utilized only at and very near the two edges of this half-moon, whereas a very small entire domain set is used elsewhere on the flat and curved portions. The entire domain basis functions contain the well known UTD Fock-type functions on the curved side and the ordinarily and slope-type UTD edge transition functions on the flat side, respectively, corresponding to two oppositely-travelling ray paths on this geometry, as described by the present authors in [5]. The subsectional basis set can be pulse (or other suitable) functions. The unknown amplitudes of these handful of total basis sets can then be found numerically, via the moment method (MoM) solution which utilizes UTD functional forms for representing the unknown

current away from the discontinuities, thereby drastically reducing the number of unknown which needs to be solved via the MoM. The conventional MoM solution would require dramatically more unknowns since it does not utilize *a priori* knowledge of the current behavior away from the edges. Thus, the present hybrid approach utilizes the physics of the problem to achieve not only efficiency but insights into the scattering mechanisms. Numerical results for this case show that the edge excited surface ray phenomena is significant for certain aspects of incidence and scattering even for a very large half-moon as shown by the present authors in [5].

(B) Radiation/Scattering by a Planar Finite Array Configuration

Consider a planar, electrically large rectangular array of short, thin dipole antennas in air. Such a configuration is selected for simplicity in illustrating the hybrid analysis of large finite arrays. The theory of periodic structures cannot be applied directly to solve a finite periodically-spaced phased array. Also, conventional numerical solutions based on element by element field superposition become highly inefficient and even intractable for large arrays. Following the ideas discussed in problem (A) above, one can again formulate an integral equation for the array element currents due to an external plane wave illumination (for the scattering problem) or due to a known voltage excitation at the feed location of each dipole element of the array (for the antenna problem). The unknown current shape on each dipole element is represented by a set of standard basis functions for thin wire dipoles, and requires only a pair of piecewise sinusoidal basis set for a dipole whose length is less than or equal to half a wavelength. The unknown amplitudes of these dipole currents defined at the feed points must then be solved via the MoM procedure. The number of unknowns is generally greater than or equal to the number of antenna elements of the array in the conventional approach; thus, the number of unknowns can become exorbitantly high for large arrays. On the other hand, if one can incorporate the recently-developed high frequency UTD ray-based functional forms for describing the behavior of the unknowns for elements which are not at or extremely close to the edge (boundary) of the array, based on the work in [6,7], then one can achieve a drastic reduction of the unknowns as demonstrated by the present authors in [7,8]. The unknowns at and near the edge can also be related along the edges via the impressed phase variation which in known [7,8] leading to a further reduction in unknowns. The only unknowns which remain are then primarily concentrated in very small regions near the array corners. Such a hybrid UTD-numerical procedure is found to be very efficient, and it also lends physical insight because of the UTD functional forms utilized in this approach. Numerical results based on this hybrid approach for arrays are shown to be quite accurate when compared to results obtained via the conventional or direct numerical schemes.

(C) Scattering by Inlet Cavities

It is not an easy task to determine the scattering from electrically large inlet cavities, especially when their interior termination is complex, as might be the case when modeling the scattering by a jet inlet cavity. However, it is seen here that a hybrid approach for predicting the scattering from inlet cavities provides a useful tool that leads to a relatively tractable solution. This problem is important because inlet scattering can contribute significantly to the overall RCS of modern jet aircraft. The hybrid approach described here is based on breaking the problem up into its component parts, then treating each part separately in an efficient way, and finally combining the different solutions appropriately. Here, the finite difference time domain (FDTD) method is used to determine the reflection matrix associated with the termination in terms of the circular waveguide modes since the jet inlet region near

the engine termination is generally circular. The FDTD method is employed since it is more efficient than the frequency domain methods in obtaining a broadband frequency information. On the other hand, the long front portion of the relatively arbitrarily shaped inlet is analyzed via high frequency iterative physical optics (IPO), or the generalized ray expansion (GRE) and its modifications to include elliptic ray tube basis functions. The fields within the inlet are excited by an externally incident plane wave, and the fields are tracked from the open front end to the circular cross-section termination region via IPO, or via GRE. The IPO or GRE-based fields are then expanded into a circular waveguide modal sum; these are then coupled to the termination region FDTD solution which is converted to the frequency domain and also expanded in a set of circular waveguide modes. The coupling is carried out via mode matching. This hybrid procedure has been developed by the present authors in [9]. Numerical results based on this hybrid IPO/GRE-FDTD analysis are shown to give very reasonable accuracy when compared to reference solutions for simple circular inlet shapes. The RCS of relatively complex inlet shapes have also been obtained.

(D) Radiation from a Cavity Backed Slot Antenna on Aircraft

In this problem, a cavity backed slot antenna with a probe feed inside the cavity is flush mounted on the fuselage of a relatively realistic aircraft model. The cavity backed antenna is first placed on an infinite planar perfectly conducting surface, and the fields in the slot are obtained by solving an integral equation for the equivalent magnetic currents corresponding to the slot fields. Since the cavity is rectangular in shape, the interior Green's function is expanded into a set of interior rectangular cavity modes, whereas, the external fields are obtained via the free space Green's function in the integral equation formulation. The integral equation is solved via MoM. Once the equivalent sources are found via the conventional MoM, they are then assumed to be unchanged to a first order of approximation when placed on an electrically large smooth aircraft fuselage. These sources are then allowed to radiate in the presence of the aircraft, and the radiated fields are found using the high frequency UTD method via the NEWAIR code developed at The Ohio State University ElectroScience Laboratory. This hybrid procedure which has been developed by the present authors [10] is different form the previous ones discussed above, but at the same time is in some manner distantly related to that described in problem (C) above. Numerical results based on this hybrid approach have been obtained for sufficiently realistic aircraft models such as for the F-16 fighter configuration.

III. CONCLUSION

It is shown that the hybrid approaches which systematically combine asymptotic high frequency and numerical methods can be employed successfully to solve a variety of electrically large EM radiation and scattering problems which cannot otherwise be solved in an efficient or even tractable manner by any one method alone.

REFERENCES

[1] W.D. Burnside, C.L. Yu and R.J. Marhefka, "A technique to combine the geometrical theory of diffraction and the moment method," *IEEE Trans. Antennas Propagat.*, *23*, 551-558, July 1975.

[2] G.A. Thiele, "Overview of selected hybrid methods in radiating system analysis," *Proc. IEEE*, *80*(1), 66-78, Jan. 1992.

[3] R.E. Hodges and Y. Rahmat-Samii, "An iterative current-based method for complex structures," *IEEE Trans. Antennas Propagat.*, *45*(2), 265-276, Feb. 1997.

[4] R.G. Kouyoumjian and P.H. Pathak, "A uniform geometrical theory of diffraction for an edge in a perfectly conducting surface," *Proc. IEEE*, *62*, 1448-1461, Nov. 1974.

[5] S. Srikanth, P.H. Pathak and C.W. Chuang, "Hybrid UTD-MM analysis of the scattering by a perfectly-conducting semi-circular cylinder," *IEEE Trans. Antennas Propagat.*, *34*(10), 1250-1257, Oct. 1986.

[6] F. Capolino, M. Albani, S. Maci and L.B. Felsen, "Floquet wave diffraction theory for truncated dipole arrays: Propagating and evanescent spectra," paper presented at URSI EMT symposium in Thessaloniki, Greece, May 1998.

[7] O.A. Civi, P.H. Pathak and H.-T. Chou, "A hybrid UTD MoM for efficient analysis of EM radiation/scattering from large finite planar arrays," paper presented at URSI EMT symposium in Thessaloniki, Greece, May 1998.

[8] O.A. Civi, P.H. Pathak, H.-T. Chou and P. Nepa, "A hybrid UTD-MoM for efficient analysis of EM radiation/scattering from large finite planar arrays," paper to appear in a special issue of *Radio Science* devoted to the 1998 URSI EMT symposium in Thessaloniki, Greece.

[9] T.-T. Chia, R.J. Burkholder and R. Lee, "The application of FDTD in hybrid methods for cavity scattering analysis," *IEEE Trans. Antennas Propagat.*, *43*(10), 1082-1090, Oct. 1995.

[10] H.-W. Tseng and P.H. Pathak, "Hybrid UTD-MM analysis of the radiation from a composite slot-blade cavity backed antenna on realistic aircraft configurations," *Radio Science*, pp. 587-598, May-June 1999.

An Hybrid method combining Integral Equations and Modal expansion applied to the RCS modulation of Antennas and Rotating Fans

André Barka* (barka@onera.fr) Paul Soudais (soudais@onera.fr)

ONERA BP 72 92322 Châtillon Cedex, France

1 Introduction

The electromagnetic scattering from the interior of a complex jet engine inlet contributes significantly to the overall radar cross section (RCS) of a modern jet aircraft. The scattering mechanisms in jet or missile inlets are complicated and difficult to simulate accurately. The geometry is both complicated (engine face, structural obstacles, materials) and electrically large. Several authors have developped hybrid numerical methods in the frequency domain to solve this problem ([2, 3]).

Recently, an hybid method combining Integral Equations, Partial Differential Equations and Modal expansion has been developped at ONERA ([1]). In this paper we present several results obtained with this method called FACTOPO applied to the RCS modulation of Antennas and Rotating Fans.

The global target Ω is split into N_V subdomains $(V_i)_{i=1,N_V}$ separated by N_I fictitious surfaces $(\Gamma_j)_{j=1,N_I}$ (Figure 1). For each subdomain (even the exterior three-dimensional volume), the generalized Scattering matrix S_i is computed with different methods such as the three-dimensional finite-element method (FEM) or the electric field integral equation (EFIE) combined with a generalized waveguide modal representation of the fields on the fictitious surfaces ([4]). We use waveguide modes as expansion functions on the fictitious surfaces to model the coupling of sub-domains.Then, the different objects are connected by cascading the different S matrices. In a context of parametric investigations, the scattering matrices of the modified domains have to be re-evaluated, the other ones are simply re-used in the connection step. This strategy reduces significantly the computation time compared to traditional hybrid methods for which a geometric or electromagnetic modification requires a new computation of the complete target.

We will emphasize the strong reduction in computational ressources obtained with this coupling scheme and especially the waveguide modal expansion. The advantages of this formulation for parametric studies will be illustrated by two cases: computing the RCS of an air-intake terminated by a flat PEC or a rotating fan, and of an antenna structure coupled to an electronic feed with a varying parameter.

2 Formulation

The target Ω is split into N_V subdomains $(V_i)_{i=1,N_V}$ by N_I fictitious surfaces $(\Gamma_j)_{j=1,N_I}$ (Figure 1). Note that V_0 is an unbounded volume, and the volumes $\{V_1, .., V_{N_V}\}$ are bounded. In each bounded or unbounded volume V_i of the decompozition, the boundary ∂V_i is made of n_i fictitious surfaces Γ_j and a part of Γ_0. The surrounding medium has permittivity ε_0 and permeability μ_0. The scatterer is illuminated by an incident wave $\{E_{source}, H_{source}\}$ with wavenumber $k = \omega/c$.

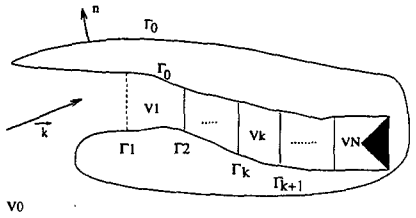


Figure 1: Target decompozition.

2.1 Modal functions on the fictitious surfaces

On each fictitious surface Γ_j of V_i, the tangential fields $(n \times E,\ n \times H)$ are expanded in a set of waveguide mode functions $(n \times E_p^j,\ n \times H_p^j)$. These modes are computed on planar surfaces of any shape with a finite element method ([4]). If p_j denotes the number of modes on Γ_j, the total tangential fields are written as:

$$\begin{cases} (n \times E)_{\Gamma_j} = \sum_{p=1,p_j} (a_{i,p}^j + b_{i,p}^j)(n \times E_p^j) \\ (n \times H)_{\Gamma_j} = \sum_{p=1,p_j} (a_{i,p}^j - b_{i,p}^j)(n \times H_p^j) \end{cases} \tag{1}$$

We shall now introduce these field decompozitions in the EFIE formulations. By linearity of the Maxwell equations, the tangent magnetic field on each of the n_i fictitious surfaces Γ_j of the volume V_i is a linear combination of the following fields:

$$(n \times H)_{\partial V_i} = \sum_{j=1,n_i} \sum_{p=1,p_j} (a_{i,p}^j + b_{i,p}^j)(n \times H_{excitation}^{j,p})_{\partial V_i} + (n \times H_{source})_{\partial V_i} \tag{2}$$

EFIE operators P,Q,B,S ([1]) can be used in this formulation to compute the $H_{excitation}^{j,p}$ fields for both bounded and unbounded volumes:

$$(B - S)(J_p^j) = (P + Q)(K_p^j) \tag{3}$$

with $J_p^j = n \times H_{excitation}^{j,p}$, $K_p^j = E_p^j \times n$.

The scatterer is illuminated by an incident wave $\{E_{source}, H_{source}\}$ located in the exterior unbounded domain V_0. The $J_{source} = n \times H_{source}$ field is computed with the integral equation ([1]):

$$(B - S)(J_{source}) = 2P(E_{sources} \times n) \tag{4}$$

2.2 Scattering matrices

We shall now characterize the volume V_i by its scattering matrix S_i. On all of the n_i fictitious surfaces Γ_j, the tangential components of the total magnetic fields are written:

$$\sum_{p=1,p_j} (a^j_{i,p} - b^j_{i,p}).(n \times H^j_p) = (n \times H_{source,\partial V})_{/\Gamma_j} + (\sum_{j=1,n_i} \sum_{p=1,p_j} (a^j_{i,p} + b^j_{i,p}).(n \times H^{j,p}_{excitation}))_{/\Gamma_j} \tag{5}$$

We define the hermitian scalar product of the vectors u, v : $\langle u, v \rangle_{\Gamma_j} = \int_{\Gamma_j} u.v^* ds$. By expressing the b^j_i coefficients associated with the outgoing waves in terms of the a^j_i coefficients associated with the incoming waves on the n_i fictitious surfaces, we obtain the following system:

$$\begin{pmatrix} b^1_i \\ . \\ . \\ b^{n_i}_i \end{pmatrix} = \begin{bmatrix} U^{11}_i & . & . & U^{1n_i}_i \\ . & . & . & . \\ . & . & . & . \\ U^{n_i1}_i & . & . & U^{n_in_i}_i \end{bmatrix}^{-1} . \left\{ \begin{bmatrix} V^{11}_i & . & . & V^{1n_i}_i \\ . & . & . & . \\ . & . & . & . \\ V^{n_i1}_i & . & . & V^{n_in_i}_i \end{bmatrix} . \begin{pmatrix} a^1_i \\ . \\ . \\ a^{n_i}_i \end{pmatrix} + \begin{pmatrix} I^1_i \\ . \\ . \\ I^{n_i}_i \end{pmatrix} \right\} \tag{6}$$

The scattering matrix of V_i is defined by the S_i=$U_i^{-1}.V_i$ matrix of the right hand side of equation (6). The vector b_{source}=$U_0^{-1}.I_0$ corresponds to the outgoing waves generated by the H_{source} fields in V_0 .

After the scattering matrices S_1,..,S_{N_V} of the cavity domains have been computed, the interior domain is assembled with a standard connection scheme ([5]) yielding the scattering matrix S_{Int}. Finally, the exterior domain V_0 and the interior V_{Int} are assembled by identification of the outgoing waves on the fictitious surface Γ_1. We get the following linear system:

$$[I_d - S_0 S_{Int}] \left\{ b^1_0 \right\} = \{ b_{source} \} \tag{7}$$

Then, once the vector $\{b^1_0\}$ has been determined, the total electromagnetic field is recombined on ∂V_0 for all the incident waves.

3 Modelization of the fan rotations

The blade rotations in the engine subdomain is a particular case of parametric investigations. The challenge is obtain the RCS for all the angular positions of the engine from the computation of a reference position. In a general manner, a scattering matrix is associated to a linear application $\mathcal{S}$ and a base (f_p) and express the outgoing waves in function of the incomming waves on each interface of the subdomain. The algorithm consists in writting the scattering matrix S in a new base (g_p). If P is the matrix transforming base (f_p) in base (g_p), the associated matrix $\tilde{S}$ in the (g_p) base is derived by : $\tilde{S}$= $P^{-1}.S.P$. The modelization of the engine rotation is then

realized with a simple rotation of the basis functions (f_p). In this particular case, the fields are expanded on modal circular functions and the matrix $P(\varphi)$ for a rotation angle φ is analytical as well as its inverse $P^{-1}(\varphi)$. In addition $P(\varphi)$ and $P^{-1}(\varphi)$ have no more than two non zero coefficients on each row. The engine scattering matrix $\tilde{S}(\varphi)$ for a blade position making an angle φ with a reference position φ=0 is then obtained with only two matrix products $\tilde{S}(\varphi)$= $P^{-1}(\varphi).S(0).P(\varphi)$. If N is the total number of edges unknowns of the engine subdomain, NB the number of modal functions on the interface, then we need $16.K.NB^3$ operations to compute the scattering matrices associated with K different positions of the engines blades. The same investigation with a full analysis for the K blades positions will required $K*(\frac{4}{3}N^3+8.N^2.NB)$ operations.

4 Test-cases

4.1 Air intake geometry : "CHANNEL"

The geometry of this case is an evolutive channel enclosed in a circular cylinder. The entry of the channel has an elliptic cross-section, the end of the channel has a circular cross-section. The object is perfectly conducting. The geometry is presented in figure 2.
The wave vector of the incident wave for ϕ=0 is directed along -X, and the electric field is parallel to Y ($\phi\phi$ polarization) or to Z ($\theta\theta$ polarization).

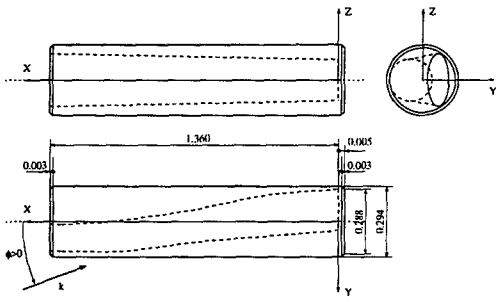


Figure 2: Geometry of the problem (all dimensions are in meters).

The location of (y_s, z_s) the center of the waveguide cross-section is a function of x:

$$y_s = -0.04878 + 0.116\sin^2(\frac{\pi}{2}\frac{x}{1.360}) \quad ; \quad z_s = 0$$

The elliptic cross-section is also a function of x:

For $0 \leq x \leq 1.300$

$$(\frac{z-z_s}{0.11803+0.02568\frac{x-1.300}{1.300}})^2 + (\frac{y-y_s}{0.05877-0.03358\frac{x-1.300}{1.300}})^2 = 1$$

For $1.300 \leq x \leq 1.360$

$$(\frac{z-z_s}{0.11803})^2 + (\frac{y-y_s}{0.05877})^2 = 1$$

The far field RCS is computed at 3 GHz for the two polarizations $\phi\phi$ and $\theta\theta$. We have introduced a spherical incident wave emitted at 8.73 m from the point (0.592,0,0) so as to reproduce the measurement conditions . The target is split in two volumes V_0 (39,627 unknowns) and V_{Int} (33,316 unknowns) each one computed with the EFIE. The tangent fields on Γ_1 are expanded with 13 propagating modes. The figure 3 show the RCS versus the angle of incidence in the $\phi\phi$ and $\theta\theta$ polarizations. The results are in agreement with the measurements.

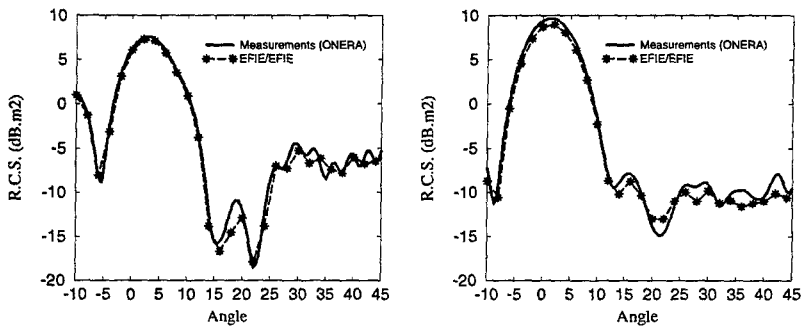


Figure 3: Comparison of measured and computed near field RCS for the air intake, $\phi\phi$ and $\theta\theta$ polarization , F=3 Ghz.

4.2 Antenna geometry: "DENEB"

The geometry of this case is a rectangular horn enclosed in a circular cylinder. The horn is fed by an electronic network. The object is perfectly conducting. The geometry is defined by figure 4 .

The wave vector of the incident wave is directed along -Z, and the electric field is parallel to X ($\phi\phi$ polarization) or to Y ($\theta\theta$ polarization). The target is split into three volumes : V_0 the exterior domain, V_1 the rectangular horn and V_2 the rectangular waveguide fed by the electronic network.

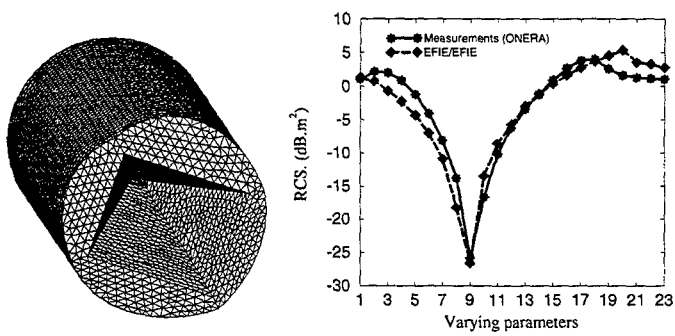


Figure 4: Comparison of measured and computed Modulated RCS for DENEB, Incidence zero degree, $\theta\theta$ polarization , F=4.5 Ghz.

The frequency of interest is 4.5 Ghz. The spherical incident wave is generated at 8.71 m from the point (0,0,0.251). The mesh of V_0 leads to 32,904 surface unknowns and the scattering matrix S_0 is computed with the EFIE formulation. The interior horn domain V_1 has also been computed with the EFIE solver (7,161 surface unknowns). The fictitious surface Γ_1 between V_0 and V_1 is located at 0.03333 m from the aperture. The tangent fields on Γ_1 are expanded with 30 propagating modes. The vertical fundamental mode (electric field parallel to Y) is used on the second fictitious surface Γ_2 localized in the rectangular waveguide V_2 at 0.03333 meter from the junction with the rectangular horn. The scattering matrix S_2 of V_2 is measured for 23 states of the electronic network. These parameters are defined on the reference plane localized at the junction between the horn and the rectangular waveguide i.e at 0.0763 m from the termination of the cavity.

Figure 4 shows the comparison between the computed and measured RCS versus the varying parameters of the electronic alimentation for an incidence angle of zero degree in the $\theta\theta$ polarization. The results are in agreement with the measurements.

4.3 Engine modulation

The following test (Figure 5) is the evolutive inlet CHANNEL (interior domain V_{Int} is the connection of the inlet subdomain V_1 and the engine subdomain V_2) inserted in a cylinder (exterior domain V_0). The frequency of interest is 3 Ghz and the RCS are computed in the two polarizations from -10 to 45 degree. The fields are expanded on 17 propagating modes on the engine interface. The V_2 subdomain is a single rotating blade as described on Figure 5. The 3 GHz monostatic RCS for two different blades position φ are computed by cascading the S_1 and $\tilde{S}_2(\varphi)$ matrices and solving the linear system (7). One complete period of the RCS modulation pattern has been computed in a post-processing phase with the above algorithm for an azimuth angle of 30 degree using the reference scattering matrix (φ=0) caracterizing the V2 subdomain (Figures 6). The agreement with a full analyzis using the EFIE solver is very good.

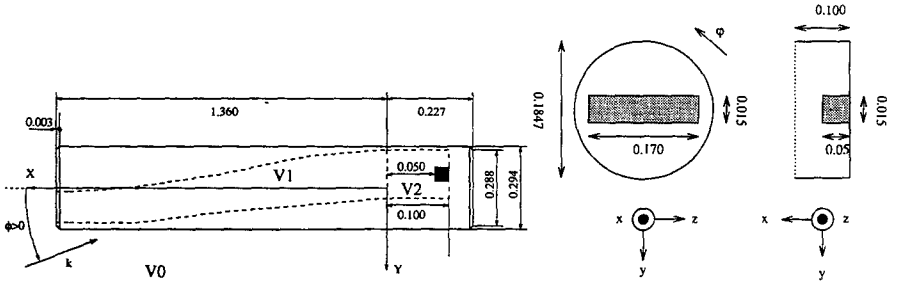


Figure 5: Air-Intake terminated by a simple rotating structure

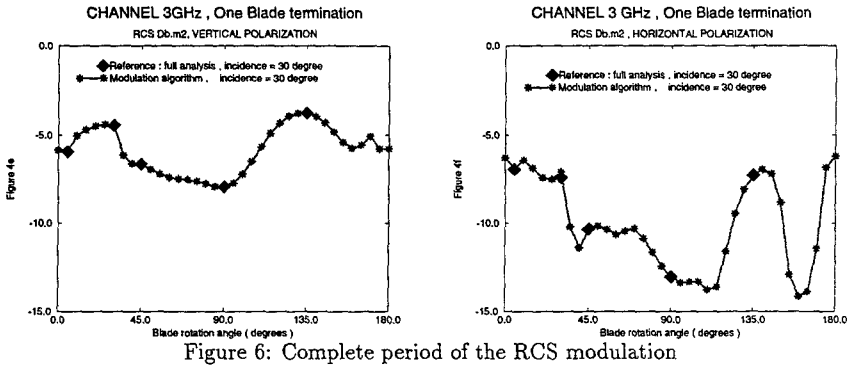


Figure 6: Complete period of the RCS modulation

5 Conclusion

In this paper, we have introduced a multi-domain and multi-method technique for analyzing the EM scattering from 3-D cavities. The Electric Field Integral Equation is used to compute the generalized Scattering matrices of the subdomains. We have used waveguide modes for modeling the field propagation from the cavity opening down to the obstacles or the engine face. RCS patterns of various complex cavities including modulation were presented and compared to measurements to show the accuracy of this method, the reduction in computation time and the advantage of this method for parametric studies.

References

[1] A. Barka, P. Soudais, D. Volpert, *Scattering from 3-D Cavities with a Plug and Play Numerical Scheme Combining IE, PDE and Modal Techniques*, Submitted at IEEE Trans. on Antennas and Propagation.

[2] D.C Ross,J.L Volakis, H.Hannastassiu , *Hybrid Finite Element-Modal Analysis of Jet Engine Inlet Scattering*, IEEE Trans. on Antennas and Propagation, Vol 43 , $n°3$, March 1995.

[3] J.M Jin, J.L Volakis, *"A finite element-boundary integral formulation for scattering by three-dimensional cavity-backed apertures"*, IEEE Trans. on Antennas and Propagation, VOL. 39(1), pp. 97-104 , Jan. 1991.

[4] A.Barka, A.Cosnuau, F.X Roux. *Parallel organization of air intake electromagnetic mode computation on a distributed memory machine.* La Recherche Aérospatiale, 1995, $n°$ 6.

[5] Graeme L. James, *"Analysis and Design of TE_{11} to HE_{11} corrugated cylindrical waveguide mode convectors"*. IEEE Transactions on Microwave Theory and Techniques, Vol MTT-29, $n°10$, October 1981.

A 2D TLM and Haar MRTD Real-Time Hybrid Connection Technique

Masafumi Fujii, Poman P.M So, Enqiu Hu, Wei Liu and Wolfgang J.R. Hoefer

Computational Electromagnetics Laboratory
Department of Electrical and Computer Engineering
University of Victoria
PO BOX 3055, Victoria, B.C. CANADA V8W 3P6
E-mail: fujii@ece.uvic.ca

Abstract

A real-time interface between Transmission Line Matrix (TLM) and Haar-Wavelet based Multi-Resolution Time Domain (MRTD) algorithms is presented and described. Like other hybrid combinations of different methods, the present scheme may offer improvements in computational efficiency and permits embedding of special features and boundaries into MRTD. Since the Haar MRTD scheme is operated at a time step twice that of the TLM scheme for equal spatial sampling density, the connection algorithm does not require any interpolation or extrapolation either in time or in space. The proposed algorithm exhibits smooth field distribution without spurious distortions even around discontinuities or obstacles, which could not be achieved with conventional MRTD schemes.

I. Introduction

Application of wavelets in the time-domain numerical modeling of electromagnetic fields has been extensively studied [1], [2], [3] for the purpose of reducing computational expenditure of the analysis methods. The advantage of those wavelet based techniques resides in their highly linear numerical dispersion property and the possibility of using much coarser discretization compared to the conventional space discrete methods, thus leading to significant reduction of the number of unknowns in the analysis region. Even the simple Haar wavelets can improve the computational efficiency of the numerical analysis through the coupling of scaling and wavelet basis functions at excitation and boundary conditions [4], [5], [6], [7].

However, when the analysis region contains complicated boundary conditions or small structure features, the discretization is restricted by the smallest feature of the geometry. Therefore, embedding boundary conditions of small structures curtail the advantage of the wavelet based techniques, and hence it is one of the critical issues to be addressed.

One possible way to overcome this difficulty is to combine with other methods. Hybrid connection schemes between the TLM and Finite-Difference Time-domain (FDTD) methods were proposed for both the two-dimensional (2D) [8] and the three-dimensional (3D) [9] cases. Since Haar MRTD algorithms lead to update schemes that are similar to those of FDTD, the hybrid connection with TLM has certain similarities with the TLM-FDTD connection algorithm. However there are a number of differences due to the different size of the MRTD and TLM cells, and due to the difference in time step.

In this paper, the details of the algorithm will be presented and the results of numerical validation will be reported.

II. Connection algorithm

An algorithm for connecting 2D Haar MRTD for the TE polarization and the 2D TLM shunt network will be described. As shown in Fig.1, one MRTD Yee cell and two TLM cells are over-

lapped at the interface such that the sampling points of the Haar MRTD cell and the centers of the TLM cells are collocated. This alignment allows us to avoid both spatial interpolation and extrapolation at the interface.

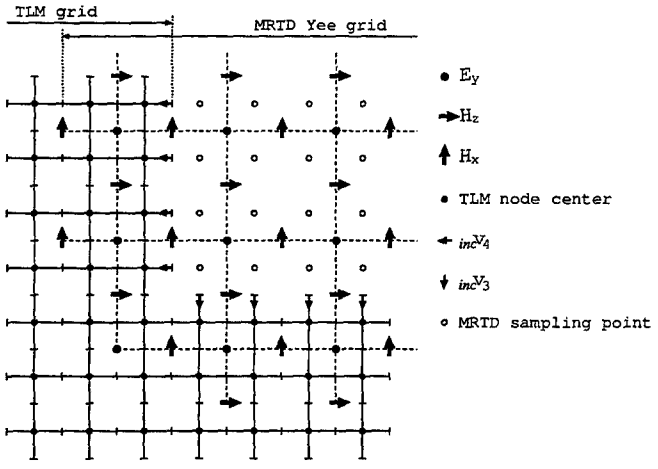


Fig. 1. Connection between the 2D Haar MRTD with the TE polarization and the 2D TLM shunt network.

The connection algorithm consists of four steps; A-1) at the end of the MRTD region, transfer data from TLM node voltages to MRTD E-fields, A-2) at the end of the TLM region, transfer data from MRTD E-fields to TLM incident pulses, B) update MRTD H-fields, and perform TLM scattering and connection, C-1) at the end of the MRTD region, transfer data from TLM node currents to MRTD H-fields, C-2) at the end of the TLM region, transfer data from MRTD H-fields to TLM incident pulses, and D) update and excite MRTD E-fields, and perform TLM scattering, connection and excitation, then go back to A-1,2) to repeat the cycle.

The time synchronization of the connection algorithm is depicted in Fig.2. Since the time step of Haar MRTD is twice that of TLM, the TLM scattering and connection processes are performed twice while MRTD E- and H-fields are updated once. The advantage of combining MRTD with TLM is that, in the TLM scheme, both voltages and currents are defined at the same location and at the same time. Therefore, field data can be transfered either from TLM to the MRTD E-field or from TLM to the MRTD H-field, and vice versa. Because of this advantage, no interpolation or extrapolation neither in time nor in space is required.

III. Formulation

The formalism will now be described for each step of the connection algorithm. Let us consider the interface shown in Fig.3.

A. At Time Step "n"

The connection is first made between TLM node voltages and Haar MRTD E-fields. For data transfer from TLM to the MRTD E-field, we first sample TLM node voltages at four TLM nodes

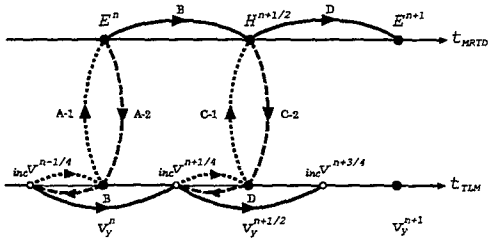


Fig. 2. Time synchronization between the Haar MRTD and the TLM methods. —— : update TLM and MRTD, – – – : transfer from MRTD to TLM, ····· : transfer from TLM to MRTD.

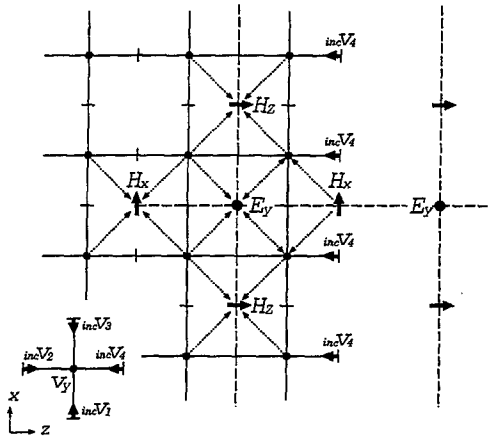


Fig. 3. Data transfer between the 2D Haar MRTD and the 2D TLM shunt nodes at the interface. Arrows with dotted lines represent the transfer of field data between the two methods. The definition of the incident pulses at the TLM branches are shown in the lower left corner.

that surround the MRTD E_y node as

$$v_y^n = \frac{1}{2}[{}_{inc}v_1^{n-1/4} + {}_{inc}v_2^{n-1/4} + {}_{inc}v_3^{n-1/4} + {}_{inc}v_4^{n-1/4}]. \tag{1}$$

The relation between the TLM node voltage and the Haar MRTD E-field is defined by

$$E_y^n \equiv v_y^n. \tag{2}$$

Then those four voltages are decomposed into the Haar wavelet basis by

$$\begin{bmatrix} \phi\phi E_y^n \\ \phi\psi E_y^n \\ \psi\phi E_y^n \\ \psi\psi E_y^n \end{bmatrix} = \frac{1}{4}\begin{bmatrix} 1 & 1 & 1 & 1 \\ 1 & -1 & 1 & -1 \\ 1 & 1 & -1 & -1 \\ 1 & -1 & -1 & 1 \end{bmatrix}\begin{bmatrix} {}^{ll}E_y^n \\ {}^{lu}E_y^n \\ {}^{ul}E_y^n \\ {}^{uu}E_y^n \end{bmatrix} \tag{3}$$

where ll, lu, ul and uu denote the corresponding Haar MRTD sampling points, for example, lu denotes the sampling point at the lower side in the x-direction and the upper side in the z-direction.

For data transfer from the MRTD E-field to TLM, the MRTD E-field at the TLM node centers on the last column of the TLM nodes are reconstructed by

$$\begin{bmatrix} {}^{ll}E_y^n \\ {}^{lu}E_y^n \\ {}^{ul}E_y^n \\ {}^{uu}E_y^n \end{bmatrix} = \begin{bmatrix} 1 & 1 & 1 & 1 \\ 1 & -1 & 1 & -1 \\ 1 & 1 & -1 & -1 \\ 1 & -1 & -1 & 1 \end{bmatrix} \begin{bmatrix} {}^{\phi\phi}E_y^n \\ {}^{\phi\psi}E_y^n \\ {}^{\psi\phi}E_y^n \\ {}^{\psi\psi}E_y^n \end{bmatrix}. \tag{4}$$

Since these E-field values are equivalent to TLM node voltages as in (2), the incident pulses at the end of the TLM region can be estimated by

$$\begin{aligned} {}_{inc}v_4^{n-1/4} &= 2v_y^n - ({}_{inc}v_1^{n-1/4} + {}_{inc}v_2^{n-1/4} + {}_{inc}v_3^{n-1/4}) \\ &= 2E_y^n - ({}_{inc}v_1^{n-1/4} + {}_{inc}v_2^{n-1/4} + {}_{inc}v_3^{n-1/4}). \end{aligned} \tag{5}$$

Thus we have all the TLM incident pulses required for the following TLM scattering process.

B. Transition from "n" to "$n+1/2$"

The fields are now to be updated both in the TLM and Haar MRTD regions individually. For H-field update through Haar MRTD,

$${}_z^{\xi\eta}H_{i+1/2,k}^{n+1/4} = {}_z^{\xi\eta}H_{i+1/2,k}^{n-1/4} - \frac{\Delta t_M}{\mu \Delta l_M}\left({}_y^{\xi\eta}E_{i+1,k}^n - {}_y^{\xi\eta}E_{i,k}^n\right) \tag{6}$$

$${}_x^{\xi\eta}H_{i,k+1/2}^{n+1/4} = {}_x^{\xi\eta}H_{i,k+1/2}^{n-1/4} - \frac{\Delta t_M}{\mu \Delta l_M}\left({}_y^{\xi\eta}E_{i,k+1}^n - {}_y^{\xi\eta}E_{i,k}^n\right) \tag{7}$$

for $\xi, \eta = \phi, \psi$, where Δt_M and Δl_M denote the Haar MRTD time and space increments, i, k and n denote the index in the x-, z-directions and time, respectively.

For TLM, the standard 2D shunt node algorithm is performed, which consists of scattering and connection procedures

$${}_{ref}[V]^{n+1/4} = [S]\ {}_{inc}[V]^{n-1/4} \tag{8}$$

$${}_{inc}[V]^{n+1/4} = [C]\ {}_{ref}[V]^{n+1/4} \tag{9}$$

where $[S]$ is the scattering matrix and $[C]$ is the connection matrix. Note that for consistent excitation of TLM and MRTD regions, excitation is not occurred at this moment but occurred only at the following update step described later.

C. At Time Step "$n+1/2$"

After updating H-fields in MRTD, field data are transfered between TLM node currents and Haar MRTD H-fields. For data transfer from the TLM node currents to the Haar MRTD H-fields, TLM node currents i_x are sampled at four TLM nodes that surround the MRTD H_z node as

$$i_x^{n+1/2} = \frac{1}{Z_l}[{}_{inc}v_1^{n+1/4} - {}_{inc}v_3^{n+1/4}] \tag{10}$$

where Z_l is the TLM link-line impedance. Similarly, i_z are sampled at four TLM nodes that surround the MRTD H_x node as

$$i_z^{n+1/2} = \frac{1}{Z_l}[{}_{inc}v_2^{n+1/4} - {}_{inc}v_4^{n+1/4}]. \tag{11}$$

Then these currents are converted to the MRTD H-field by

$$H_x^{n+1/2} \equiv -i_z^{n+1/2} \tag{12}$$

$$H_z^{n+1/2} \equiv i_x^{n+1/2}. \tag{13}$$

Then the H-fields are decomposed into the Haar basis by

$$\begin{bmatrix} {}^{\phi\phi}H_w^{n+1/2} \\ {}^{\phi\psi}H_w^{n+1/2} \\ {}^{\psi\phi}H_w^{n+1/2} \\ {}^{\psi\psi}H_w^{n+1/2} \end{bmatrix} = \frac{1}{4}\begin{bmatrix} 1 & 1 & 1 & 1 \\ 1 & -1 & 1 & -1 \\ 1 & 1 & -1 & -1 \\ 1 & -1 & -1 & 1 \end{bmatrix}\begin{bmatrix} {}^{ll}H_w^{n+1/2} \\ {}^{lu}H_w^{n+1/2} \\ {}^{ul}H_w^{n+1/2} \\ {}^{uu}H_w^{n+1/2} \end{bmatrix} \tag{14}$$

for $w = x$ and y.

Inversely, data transfer from Haar MRTD H-fields to TLM node currents is achieved first by reconstructing H_x-fields

$$\begin{bmatrix} {}^{ll}H_x^{n+1/2} \\ {}^{lu}H_x^{n+1/2} \\ {}^{ul}H_x^{n+1/2} \\ {}^{uu}H_x^{n+1/2} \end{bmatrix} = \begin{bmatrix} 1 & 1 & 1 & 1 \\ 1 & -1 & 1 & -1 \\ 1 & 1 & -1 & -1 \\ 1 & -1 & -1 & 1 \end{bmatrix}\begin{bmatrix} {}^{\phi\phi}H_x^{n+1/2} \\ {}^{\phi\psi}H_x^{n+1/2} \\ {}^{\psi\phi}H_x^{n+1/2} \\ {}^{\psi\psi}H_x^{n+1/2} \end{bmatrix} \tag{15}$$

and then, with the relation (10),(11),(12) and (13), the incident pulses at the end of the TLM region can be estimated by

$$\begin{aligned} {}_{inc}v_4^{n+1/4} &= -Z_l i_z^{n+1/2} + {}_{inc}v_2^{n+1/4} \\ &= Z_l H_x^{n+1/2} + {}_{inc}v_2^{n+1/4}. \end{aligned} \tag{16}$$

It is then possible to perform the next TLM scattering process.

D. Transition from "$n+1/2$" to "$n+1$"

The field values are now updated again with TLM and a Haar MRTD E-update equation. The Haar MRTD E-update equation is given by

$$\begin{aligned} {}^{\xi\eta}_{y}E_{i,k}^{n+1} &= {}^{\xi\eta}_{y}E_{i,k}^{n} \\ &\quad + \frac{\Delta t_M}{\epsilon \Delta l_M}[{}^{\xi\eta}_{x}H_{i,k+1/2}^{n+1/2} - {}^{\xi\eta}_{x}H_{i,k-1/2}^{n+1/2} - ({}^{\xi\eta}_{z}H_{i+1/2,k}^{n+1/2} - {}^{\xi\eta}_{z}H_{i-1/2,k}^{n+1/2})] + {}^{\xi\eta}_{y}e_{i,k}^{n} \end{aligned} \tag{17}$$

for $\xi, \eta = \phi, \psi$, where ${}^{\xi\eta}_{y}e_{i,k}^{n}$ is the amplitude of an E-field excitation.

The same TLM algorithm as described above, together with an excitation process at this time, is executed as follows:

$${}_{ref}[V]^{n+1/4} = [S]\ {}_{inc}[V]^{n-1/4} + \frac{1}{2}e[I] \tag{18}$$

where [I] is the identity matrix. This excitation procedure gives smooth excitation distribution over the TLM and the Haar MRTD regions. This concludes the connection algorithm, and the cycle is repeated.

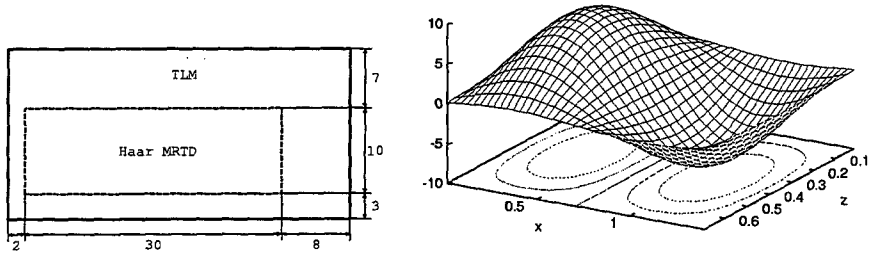
IV. Numerical Validation

Two cases, a simple rectangular resonator and a square resonator loaded with a perfect conductor fin, were analyzed with the present method.

A. Simple Rectangular Resonator

An air filled simple rectangular resonator was first analyzed. Preliminary experiments showed that the connection algorithm was stable when the propagation of wave fronts was at 45 degrees with respect to the main axes. In order to separate effects due to the symmetry of boundaries and effects due to symmetries of the interface topology while maintaining 45 degree oblique propagation, the width and the length of the resonator were taken to be $\sqrt{2}$ and $\sqrt{2}/2$ as shown in Fig.4 (a). The interface region was placed asymmetrically and the TE_{12} mode was excited such that the field is a superposition of plane waves propagating at 45 degrees with respect to the main axes. All the numbers are normalized such that the speed of light is unity.

In this analysis, the algorithm was stable at time step 10^5 and no instability was observed. The E-field distribution at that time step is shown in Fig.4 (b) and exhibits no spurious distortion. The Fourier transform of the time signal indicated that the resonant frequency was exactly 1.0 with an error less than 1.0×10^{-5}. This is reasonable because the 2D TLM and Haar MRTD methods have no numerical dispersion for the 45 degree diagonal propagation; TLM gives accurate results for the 45 degree propagation regardless of the discretization level, and so does the Haar MRTD when the stability factor is the maximum allowable value, i.e. $s = c\Delta t_M/\Delta l_M = 1/\sqrt{2}$.



(a) (b)

Fig. 4. (a) Configuration of the simple resonator. The size of the resonator is $\sqrt{2} \times \sqrt{2}/2$. The dotted lines show the connection interfaces. The numbers beside the arrows indicate the number of equivalent TLM cells. (b) The E-field distribution in the simple resonator.

B. A Metal Fin Loaded Square Resonator

The connection algorithm was applied to the analysis of a square resonator loaded with a perfect conductor fin (Fig.5).

In this case the algorithm was stable for 800 time steps, and an abrupt amplification of the field values, so-called late-time instability, was observed. The time signal is shown in Fig.6 (a). The resonant frequency was 1.09445. However, until the onset of the instability, the field distribution

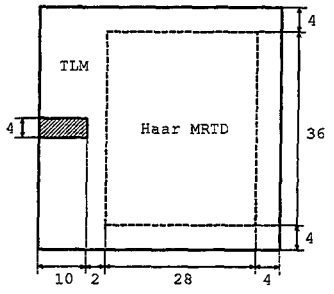
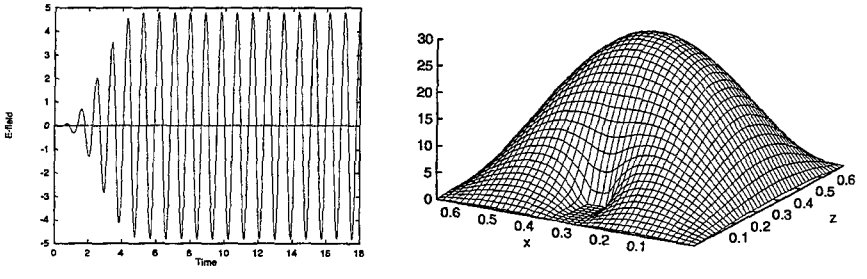


Fig. 5. Configuration of a square resonator and waveguide loaded with a perfect conductor fin. The size of the structure is $\sqrt{2}/2 \times \sqrt{2}/2$. The numbers beside the arrows indicate the number of equivalent TLM cells.

remained smooth without spurious distortions even around the edge of the fin (Fig.6 (b)), which was difficult to achieve with the conventional boundary implementation in the MRTD method.



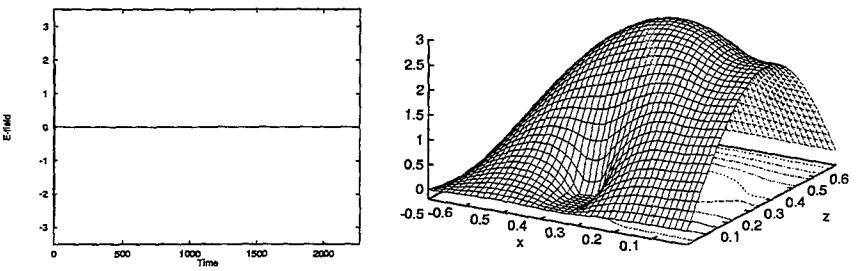
(a) (b)

Fig. 6. (a) The time signal of the square resonator loaded with a perfect conductor fin. (b) The E-field distribution in the square resonator loaded with a perfect conductor fin.

C. A Metal Fin Loaded Waveguide

The same structure as the previously analyzed fin-loaded square resonator (Fig. 5) was then analyzed as a waveguide. The top and the bottom walls were replaced with narrow-band absorbing walls; the reflection coefficient for the TLM link lines at those boundaries were set to be -0.1715 to realize approximate zero-reflection walls. Due to these narrow-band absorbing walls, the excitation signal was also band-limited with the normalized center frequency 1.0.

Interestingly, as shown in Fig. 7 (a), the algorithm is stable at time step 10^5 and no late-time instability is observed. In the analysis of open structures using absorbing walls, numerical errors associated with the interface do not accumulate in the analysis region, and the late-time instability disappears or delays far behind. The field distribution is also smooth even in the vicinity of the metal corners as shown in Fig. 7 (b).



(a) (b)

Fig. 7. (a) The time signal of the waveguide loaded with a perfect conductor fin for 10^5 time steps. (b) The E-field distribution in the waveguide loaded with a perfect conductor fin. The wave travels from right to left.

V. Conclusions

A real-time connection algorithm between the TLM and the Haar MRTD methods has been presented. The algorithm is stable for the case where a wave propagates at 45 degrees with respect to the main axes and is practically stable for open structures such as waveguides loaded with metal fins. It is stressed that the algorithm provides smooth field distribution without spurious distortions even in the vicinity of metal corners. Since the implementation of boundary conditions in the MRTD method is one of the most critical problems, the present combination technique is a first step towards overcoming this difficulty.

References

[1] M.Krumpholz and L.P.B.Katehi, "MRTD: New time-domain schemes based on multiresolution analysis", *IEEE Trans. Microwave Theory Tech.*, vol. 44, no. 4, pp. 555–571, Apr. 1996.

[2] M.Werthen and I.Wolff, "A novel wavelet based time domain simulation approach", *IEEE Microwave Guided Wave Lett.*, vol. 6, no. 12, pp. 438–440, Dec. 1996.

[3] Y.W.Cheong, Y.M.Lee, K.H.Ra, J.G.Kang, and C.C.Shin, "Wavelet-Galerkin scheme of time-dependent inhomogeneous electromagnetic problems", *IEEE Microwave Guided Wave Lett.*, vol. 9, no. 8, pp. 297–299, Aug. 1999.

[4] K.Goverdhanam, E.Tentzeris, M.Krumpholz, and L.P.B.Katehi, "An FDTD multigrid based on multiresolution analysis", *Proc. IEEE Antennas and Propagation Society Int. Symposium 1996*, pp. 352–355.

[5] M.Fujii and W.J.R.Hoefer, "Formulation of a Haar-wavelet-based multi-resolution analysis similar to the 3-D FDTD method", *1998 IEEE MTT-S Int. Microwave Symposium Digest*, pp. 1393–1396, 1998.

[6] M.Fujii and W.J.R.Hoefer, "A three-dimensional Haar-wavelet-based multiresolution analysis similar to the FDTD method — derivation and application", *IEEE Trans. Microwave Theory Tech.*, vol. 46, no. 12, pp. 2463–2475, Dec. 1998.

[7] M.Fujii and W.J.R.Hoefer, "Numerical dispersion in haar-wavelet based mrtd scheme – comparison between analytical and numerical results", *Proc. 15th Annual Review of Progress in Applied Computational Electromagnetics*, pp. 602–607, Mar. 1999.

[8] C.Eswarappa and W.J.R.Hoefer, "Bridging the gap between TLM and FDTD", *IEEE Microwave Guided Wave Lett.*, vol. 6, no. 1, pp. 4–6, Jan. 1996.

[9] C.Eswarappa and W.J.R.Hoefer, "A hybrid 3D TLM-FDTD model of microwave fields", *1996 IEEE MTT-S Int. Microwave Symposium Digest*, pp. 1063–1066.

AUTHORS INDEX

Abbott, T. I-221
Akyurtlu, A. I-181
Allard, J. 1-73
Amrhein, J. I-28
Andersen, L.S. II-734
Antonini, G. II-654
Arakaki . D. II-742, 944
Archambeault, B. I-423, 431, 436
Aydin, K. I-181
Balanis, C.A. I-387
Barba, I. II 534, 635
Bardati , F. II 930, 975
Barka, A. II-1006
Batchelor, J.C. II-562
Bevensee, R.M. I-214
Beyer, A. I-255
Bleszynski, E. II-874
Bleszynsk, M. II-874
Bluck, M.J. 4, II-662
Borkes, J. I-255
Boyer, D. I-515
Breakall, J.K. II-814
Brench, C.E. I-410
Burkholder, R.J. II-1001
Burke, G.J. I-452
Cabrera, F.J. II-699
Canales, R.R. I-189
Cangellaris, A.C. I-108
Catedra, M.F. II-959
Chamberlin, K. I-501
Chew, W.C. II-668, 691, 838, 851
Christopoulos, C. II-587
Chtchekatourov, V. II-580
Coccetti , F. II-580
Cohen, N. II-822
Cravens, L.A. II-677
Cuevas del Rio, J.G. II-699
Cui , W. I-436
Cwik, T. I-308
Cybert, K.J. I-395, II-806
Davis, D. I-493
Dawson, T.W. I-333
DeCarlo, D. I-365
De Marco, F. II-930
De Zutter , D. II-981
Demkowicz, L. I-11,19
Di Giampaolo, E. II-975
Ditkowski, A. II-917
Doncov, N.S. I-233
Donepudi, K. II-691, 716, 851
Drewniak, J.L. I-130, 431, 436
Dridi, K. II-917
Durantini, A. II-975
DuRieu, D. I-341
Ellingson, D. I-S6
Elsherbeni, A.Z. I-294, II-924
Erdemli, J.E. II-734
Ergin, A.A. II-647
Fan, G-X II-890
Fan,K. I-130
Fear, E.C. I-310
Fonseca, L.F. I-189
Franceschetti, G. I-485
Fujii, M. II-526, 534, 1013
Gaudine, D. I-356
Georgakopoulos, S.V. I-387
Gjonaj, E. I-241
Glisson, A.W. II-683
Goldberg, D.E. I-78
Goldsmith, K. I-341, II-750
Gomez Martin, R. II-627, 995
Gres, N.T. II-647
Grotjohn, T. I-28
Guidry, R.D. II-765
Guy, A.W. I-317
Haala, J. II-936
Hagen, J.V. II-670, 758
Hagness, S.C. I-310
Hammes, P. I-247
Han, D-H. I-387
Hesthaven, J.S. II-917
Hill, K.C. II-677
Hoefer, W.J.R. II-526, 534, 635, 1013
Hohlfeld, R.G. II-822
Holtby, L. II-780
Holzheimer, T.R. I-198, II-726, 798
Hoorfar, A. I-63
Horvatic, P. I-501
Hu, B. II-838
Hu, E. II-526, 838, 1013
Huang, C-W.P. II-924
Hubing, T.H. I-444
Huttunen, T. I-49
Jacobs, M.W. II-814
Jaroszewicz, T. II-874
Ji, Y. I-444
Jiang, B.N. II-604
Jiao, D. 166, II-611
Jimenez, E. II-699
Jin, J-M. I-166, II-611, 691, 716, 845, 851
Johnson, P. II-750
Kang, G. II-691, 851
Katehi, L.P.B. II-540
Kawakami, H. I-206
Kayano, T. I-349
Kempel, L. I-28, II-765, 772
Kent, W.J. II-677
Kishk, A.A. II-683
Knighten, J.L. I-130
Kogiso, S. I-206
Koning, J. II-882
Kubina, S.J. I-356
Lammers, T. I-160
Langley, R.J. II-562
Layden, R.G. II-677
Lee, Y.H. I-70
Liao, N. II-604
Li, X. I-310
Lindenmeier, S. II-587
Ling, F. II-716, 845
Liu, Q.H. II -890, 897
Liu, W. II-526, 1013
Liu, Y. I-63
Iizuka, Y. I-206
Long, B.R. I-86
Loeffler, D. II-758
Luebbers, R.J. I-462, 470, 477
Lysiak, K. II-790
Macon, C. II-772
Magnusson, R. I-198
Manara, G. I-56
Manara, G. II-640
Mangold, T. II-570
Marano, S. I-485
Marrocco, G. II-930, 975
Martin, R.A. I-286
Marvin, A.C. I-70
Michielssen, E. I-78, II-647
Miller, E.K. I-99
Milovanovic, B.D. I-233
Mittra, R. I-2, 56, II-742, 944, 968, 995
Miyata, K. I-349
Monk, P. I-49
Monorchio, A. I-56, II-640, 968
Mueller, G. I-123
Munn, D.R. I-373, 381
Myers, C.D. I-365
Ng, M.W.R. II-562
Nott, A. I-325
Ohashi, K. I-349
Ojiro, Y. I-206
Ordovas, R. I-4,
Orlandi, A. II-654
Ottusch, J.J. II-867
Olyslager, F. II-981
Ouyang, C.C. II-604
Paknys, R. I-493
Pantoja, M.F. II-627
Pasquino, N. I-485
Pathak, P.H.II-1001
Paul, J. II-556
Perez, R. I-416
Pertz, O. I-255
Peterson, A.F. I-43
Petropoulos, P.G. II-906
Pham, H. I-515
Pickelsimer, J. I-477
Piket-May, M. I-160, II-988
Pinto, I.M. I-485
Polycarpou, A.C. I-35, 387
Porter, S.J. I-70
Priest, T. I-341, II-750
Przybyszewski, P. II-951
Railton, C.J. I-115
Ramahi, O.M. I-146, 152
Rebel, J. II-570
Reiss, K. I-123
Remis, R.F. I-93
Represa, J. II-534, 635
Reuster, D.D. I-395, II-806
Rivas, F. II-959
Roa, J.P. II-959
Rodriguez-Pereyra, V. I-294
Rogier, H. II-981
Rubio Bretones, A. II-627, 995
Rummel, P. I-28
Rumsey, I. II-988
Russer, P. I-401, II-570, 580, 587, 594
Ryan, F.J. I-507
Sarris, C.D. II-540
Sato, G. I-206
Schuhmann, R. I-247
Schneider, S. II-772
Schunn, F. II-619
Schuster, J.W. I-462, 470
Segal, B. I-493
Seledtsov, M. I-501
Sertel, K. II-859
Setzer, S. I-247
Shang, J.S. II-611
Shanker, B. II-647
Shi, H. I-130
Shin, J. II-683
Shlepnev, Y.O.I-138
Singer, H. II-619
Slater, M. I-281
Smith, C.E. I-294, II-924

So, P.P.M.S. II-526, 594, 1013
Sobhy, M.I. II-562
Song, J. II-691, 845, 851
Soudais, P. II-1006
Speciale, R.A. I-263
Staker, S.W. I-160
Stamm, J.M., II-814
Steich, D.J. I-452
Stuchly, M.A. I-310, 333
Sunderland, K.V. I-226
Sabet, S.N. I-365
Sakahashi, N. I-349
Sentzeris, M.M. II-548
Thomas, C. II-662
Thomas, D.W.P. II-556
Trapp, B. I-247
Trenkic, V.M. I-233
Trott, K.D. II-765, 772
Trueman, C.W. I-281, 356, 373, 381, 493
Tuerk, U. I-401
van den Berg, P.M. I-93
Vardapetyan, L. I-11
Vietzorreck, L. II-580
Visher, J.L. II-867
Volakis, J.L. II-734, 859
Walker, S.P. I-4, II-662
Wandzura, S.M. II-867
Wang, H. I-444
Wasi, S. I-43
Weiland, T. I-247
Weile, D.S. I-78
Wiesbeck, W. II-670, 936
Werner, D.H. I-86, 173, 181, 286, II-742,
Werner, D.H. II-829, 944
Werner, P.L. I-86, II-829
White, Daniel II-882
White, Doug I-436
Wiesbeck, W. II-758
Wood, Jr., W.D. II-677
Xu, X.M. II-897
Ye, X. I-436
Yefet, A. II-906
Young, P.P. I-198
Yu, W. II-944
Zhang, Z.Q. II-897
Zhao, J. I-493
Zmyslo, J.S. I-173
Zubaidah, S. I-349
Zypman, F.R. I-189